Yucca Mountain Seismic Source Characterization Workshop #2

October 16-18, 1996

John Stamatakos

Center for Nuclear Waste Regulatory Analyses (CNWRA)
San Antonio, Texas

Geological and Geophysical Studies of Crater Flat and Bare Mountain

9611260175 -Part 2

Data

- Apatite and Zircon Fission Track
- Paleomagnetic (Bare Mountain and Regional)
- Geothermometry (Calcite Twin Deformation)
- Tectonic Sedimentation (Alluvial Fans)
- Ground Magnetic Surveys
- GPS Surveys (with Cal. Tech)
- Structural data (Cross-sections, bedding dips, faults, folds, intersections, kinematics)

Additional Resources

- 3DSTRESS
- Analog Modeling
- Numerical Modeling
- SEISM

Publications

Slip-tendency analysis and Fault reactivation, **Geology** (24), p. 275-278, 1996

Quaternary slip history of the Bare Mountain fault (Nevada) from the morphology and distribution of alluvial fans deposits, **Geology** (24), p. 559-562, 1996

Quaternary basin evolution and basaltic volcanism of Crater Flat, Nevada, from detailed ground magnetic surveys of the Little Cones, **Journal of Geology**, in press

Geometric, thermal, and temporal constraints on the development of extensional faults at Bare Mountain, Nevada and implications for Neotectonics of the Yucca Mountain region, in review at **Geological Society of America Bulletin**

Physical Analog Modeling of pull-apart basin evolution, in review **Tectonophysics**

Unleashing the Potential of ground magnetic surveys with improved instrumentation: Examples from the Yucca Mountain area, Nevada, in review **EOS**

Mechanical analyses of listric normal faulting with emphasis on seismicity assessment, in review **Tectonophysics**

Late Paleozoic to Tertiary Tectonic evolution of Bare Mountain, Nevada, from zircon, fission track thermochronology and paleomagnetism, in prep for **Geological Society of America**

Exhumation of Bare Mountain from Apatite fission-track thermochronometry, in prep **Geology**

CNWRA Reports

Finite Element Modeling of Listric Normal faulting

Faulting in the Yucca Mountain region (NUREG)

Semi-Annual reports (1994, 1995)

Ground Magnetic Surveys of the Little Cones, Crater Flat, Nevada

SEISM1.1

Outline

1. Sources of uncertainties in paleoseismic trenching studies.

2. Fault length-displacement scaling relationships
   - Bare Mountain fault appears anomalous (southern tip ?)
   - Windy Wash and Ghost Dance

3. Bare Mountain-Crater Flat-Yucca Mountain balanced cross-sections
   - curved or listric geometry

4. Bare Mountain alluvial fans
   - increased slip on Bare Mountain Fault from north to south

5. Ground Magnetic Surveys
   - Buried Little Cones flows
   - Accumulation rate of 0.03 mm/yr. (1 Ma) ~10 Ma rate from VH2
   - Change in dip of the Bare Mountain Fault
   - Faults at Northern Cone
   - Alignment of buried centers in Amargosa desert

6. Apatite fission track - exhumation from track length data
   - mean uplift rate of 0.19 mm/yr.

7. Slip and dilation tendency analysis
   - additional criteria for Type I faults

8. Geodetic surveys (GPS, level-line surveys)
   - Rapid uplift of Bare Mountain (?) (5.0 +/- 3.5mm/yr.)
   - Hunter Mountain fault locked (?)
   - Total strain rate across eastern Cal-western Nev of ~12 mm/yr.

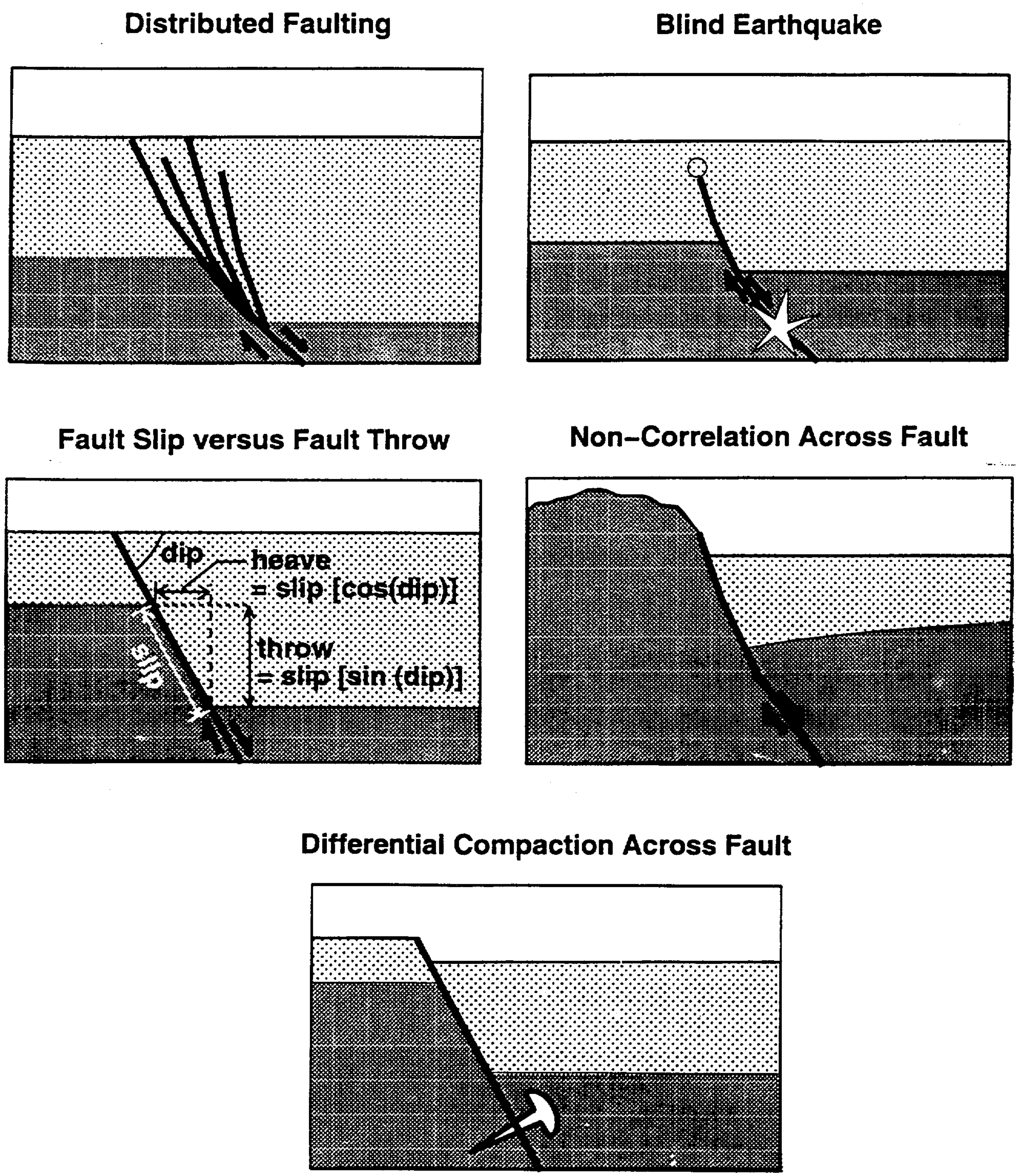

Figure 2-1. Potential sources of uncertainty in fault-trenching analyses of paleoseismicity. Relationships between heave, throw, and slip are illustrated for a dip-slip fault.

ALTERNATIVE MODELS FOR YUCCA MOUNTAIN FAULTS

For balance of sections

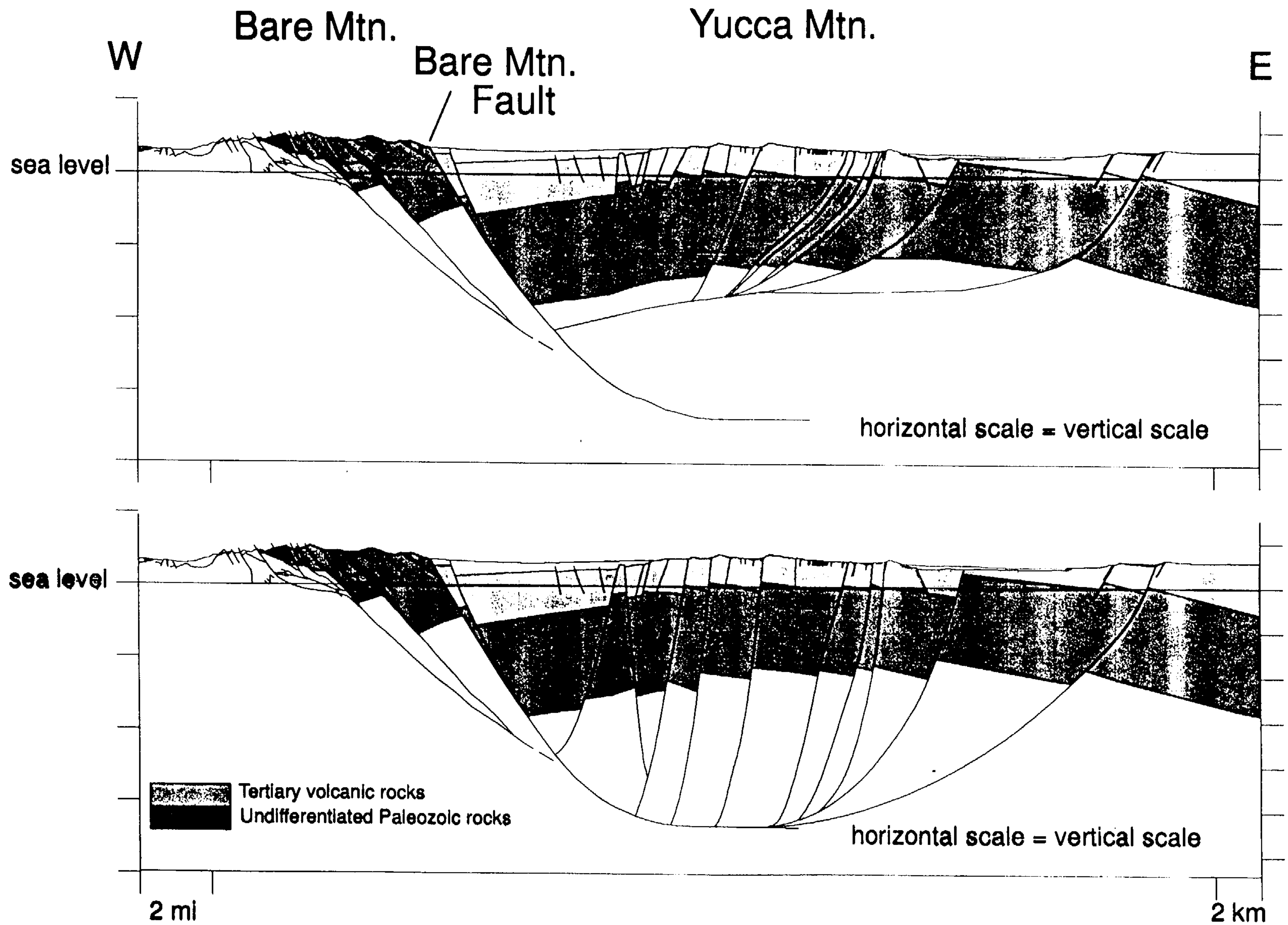

Fits the surface data better

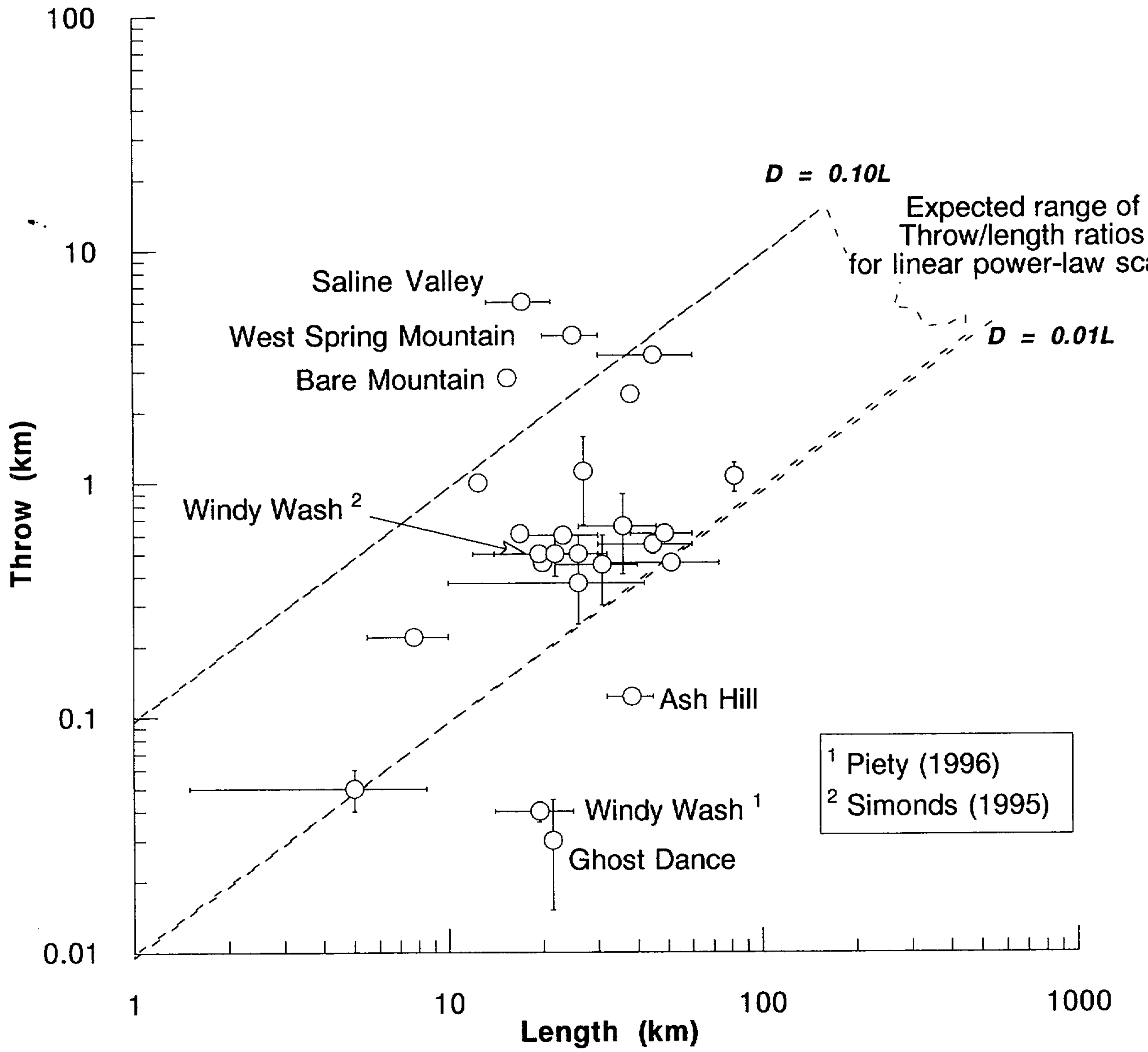

100
10
1
0.1
0.01
Throw (km)
1
10
100
1000
Length (km)
D = 0.10L
D = 0.01L
Expected range of
Throw/length ratios
for linear power-law sca
Saline Valley
West Spring Mountain
Bare Mountain
Windy Wash 2
Ash Hill
Windy Wash 1
Ghost Dance
1 Piety (1996)
2 Simonds (1995)

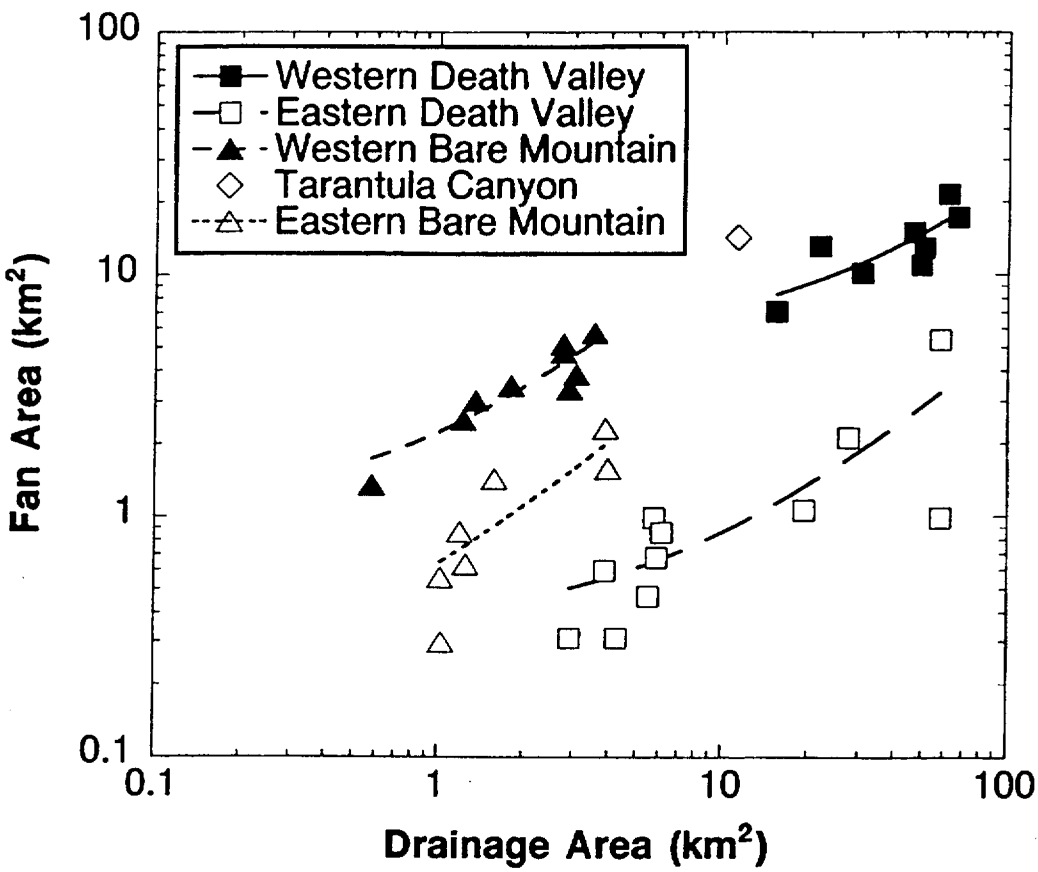

Western Death Valley
Eastern Death Valley
Western Bare Mountain
Tarantula Canyon
Eastern Bare Mountain
Fan Area (km^2)
Drainage Area (km^2)
100
10
1
0.1
0.1
1
10
100

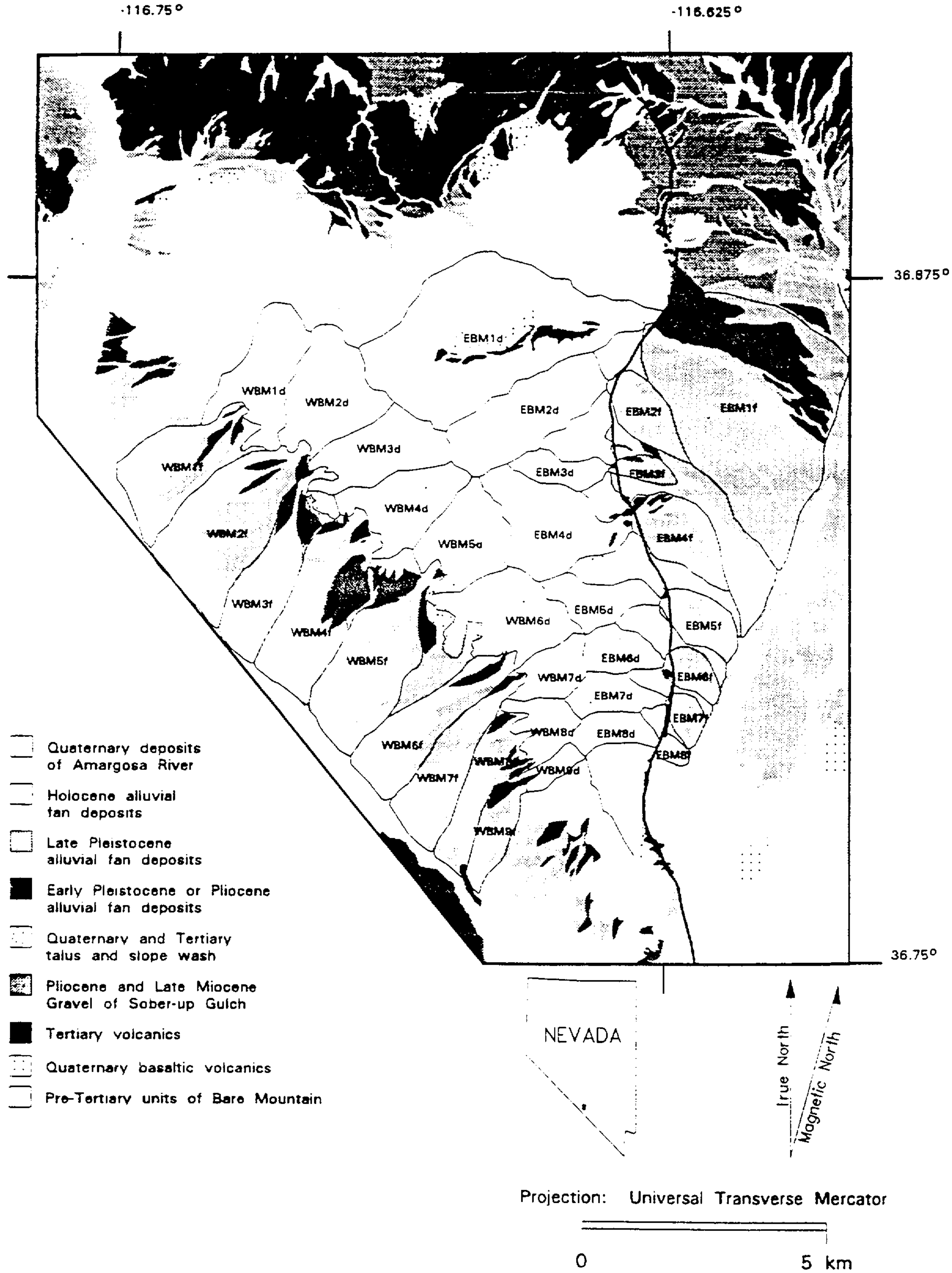
-116.75°
-116.625°
36.875°
36.75°
EBM1d
WBM1d
WBM2d
EBM2d
EBM2f
EBM1f
WBM1f
WBM3d
EBM3d
EBM3f
WBM4d
EBM4d
EBM4f
WBM2f
WBM5d
WBM3f
WBM6d
EBM5d
EBM5f
WBM4f
WBM5f
EBM6d
WBM7d
EBM6f
EBM7d
EBM7f
WBM8d
EBM8d
WBM6f
EBM8f
WBM7f
WBM9d
WBM9f
Quaternary deposits of Amargosa River
Holocene alluvial fan deposits
Late Pleistocene alluvial fan deposits
Early Pleistocene or Pliocene alluvial fan deposits
Quaternary and Tertiary talus and slope wash
Pliocene and Late Miocene Gravel of Sober-up Gulch
Tertiary volcanics
Quaternary basaltic volcanics
Pre-Tertiary units of Bare Mountain
NEVADA
True North
Magnetic North
Projection: Universal Transverse Mercator
0
5 km

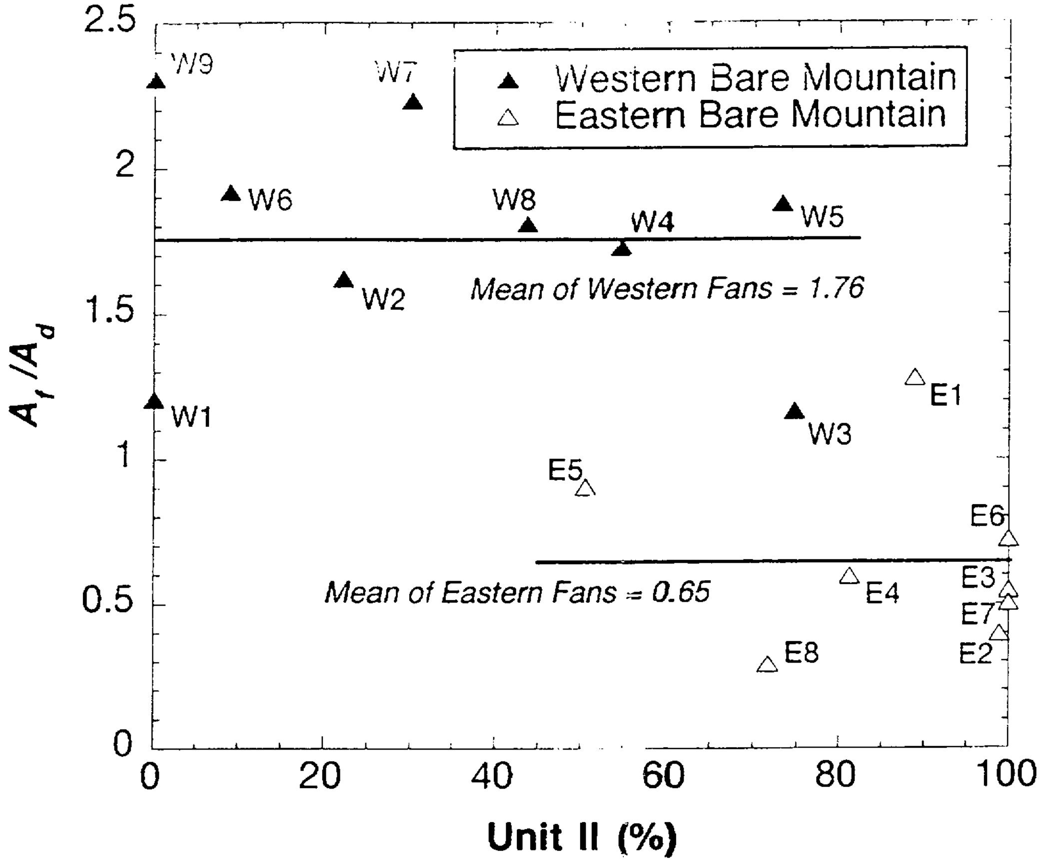

Western Bare Mountain
Eastern Bare Mountain
W9
W7
W6
W8
W4
W5
W2
W1
W3
E1
E5
E6
E3
E7
E2
E4
E8
Mean of Western Fans = 1.76
Mean of Eastern Fans = 0.65
A_f / A_d
Unit II (%)
2.5
2
1.5
1
0.5
0
0
20
40
60
80
100

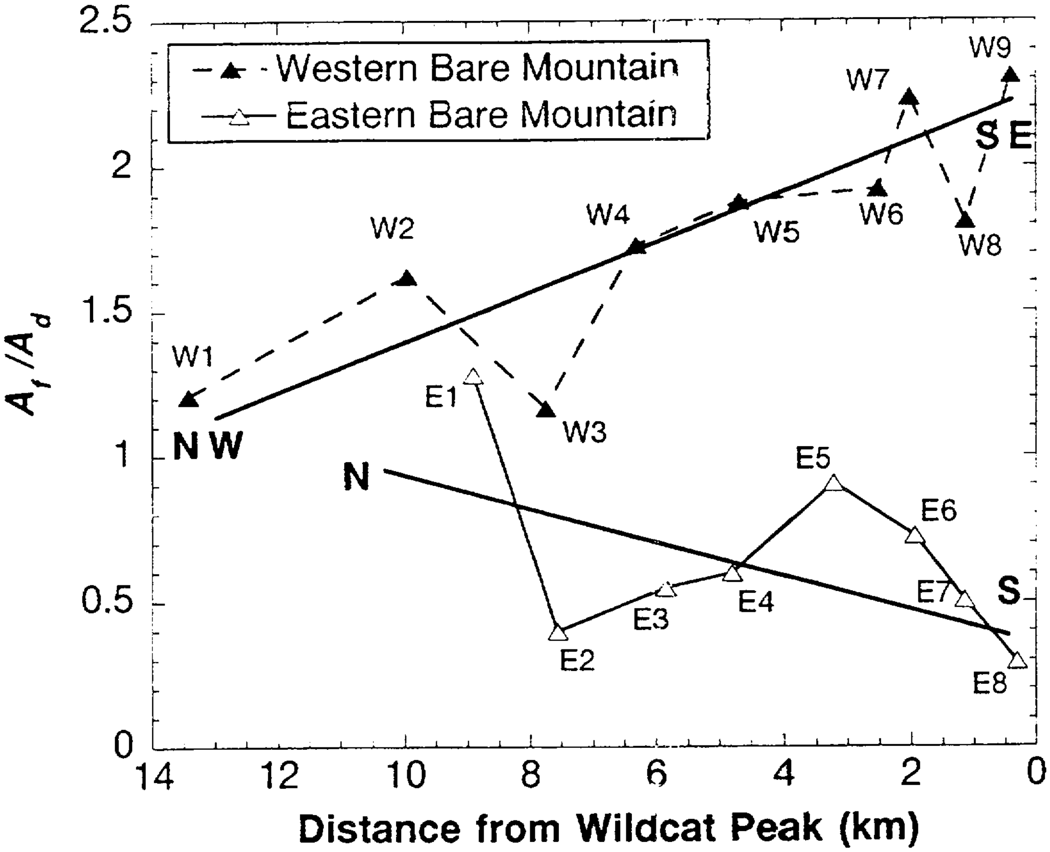

Western Bare Mountain
Eastern Bare Mountain
W1
W2
W3
W4
W5
W6
W7
W8
W9
E1
E2
E3
E4
E5
E6
E7
E8
N W
S E
N
S
2.5
2
1.5
1
0.5
0
14
12
10
8
6
4
2
0
A_f / A_d
Distance from Wildcat Peak (km)

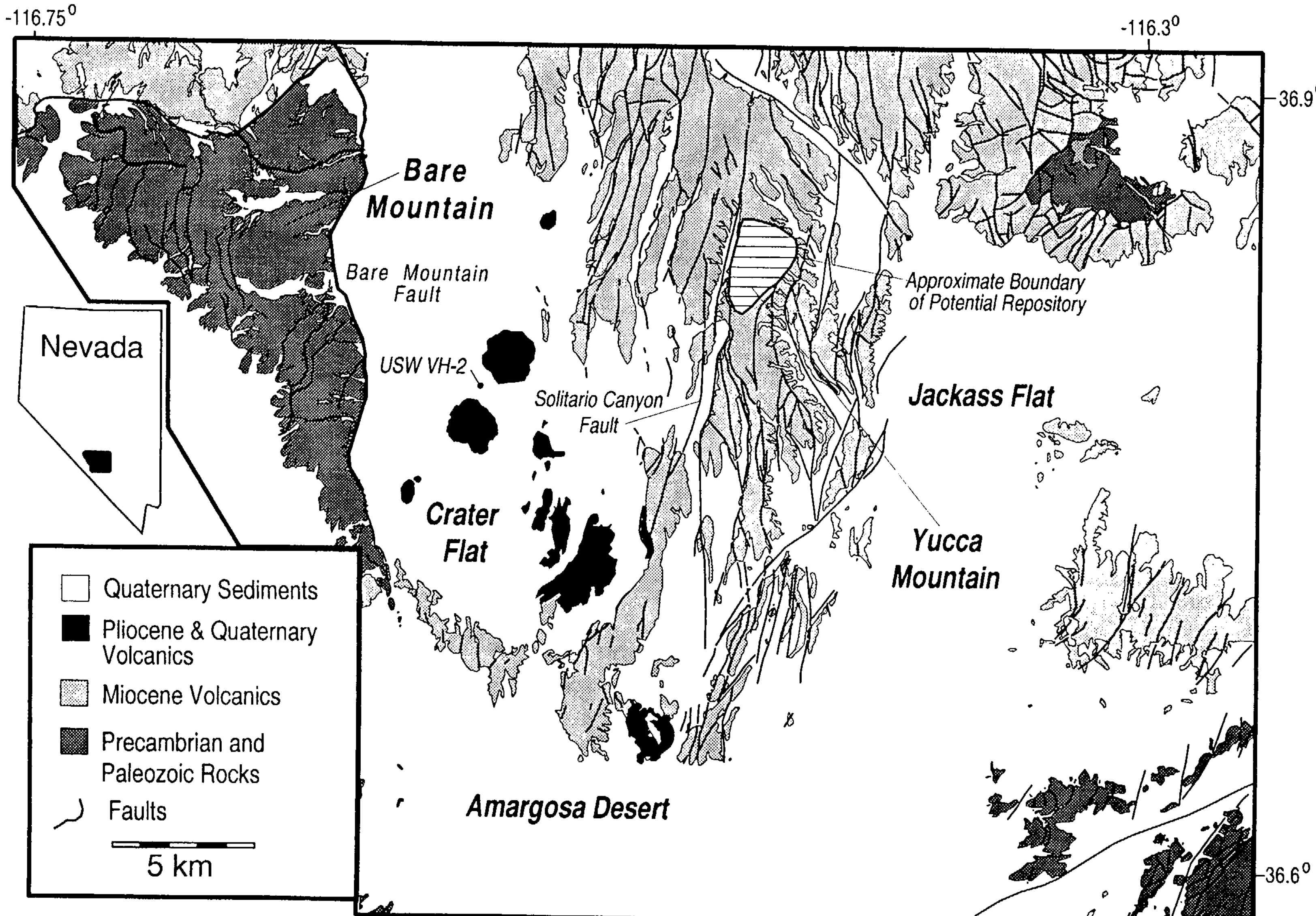

Stamatakos, Connor, and Martin - figure 1

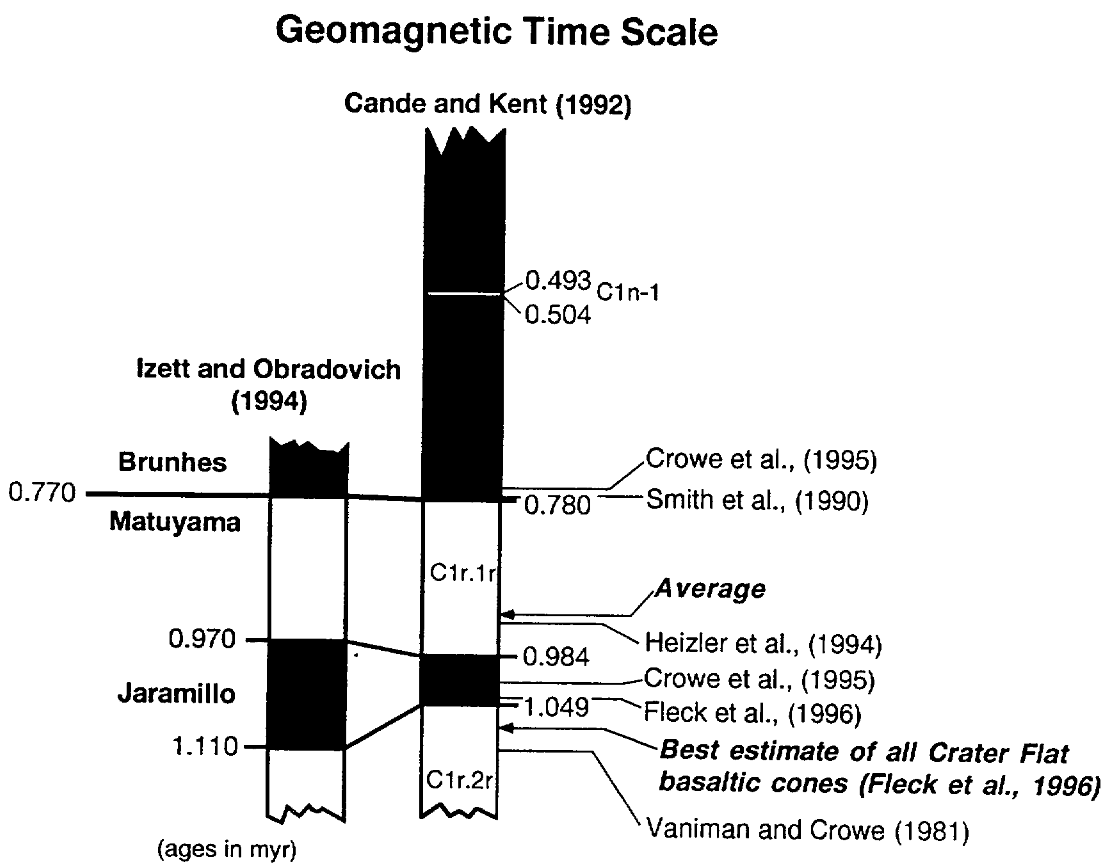

Stamatakos, Connor, and Martin - Figure 3

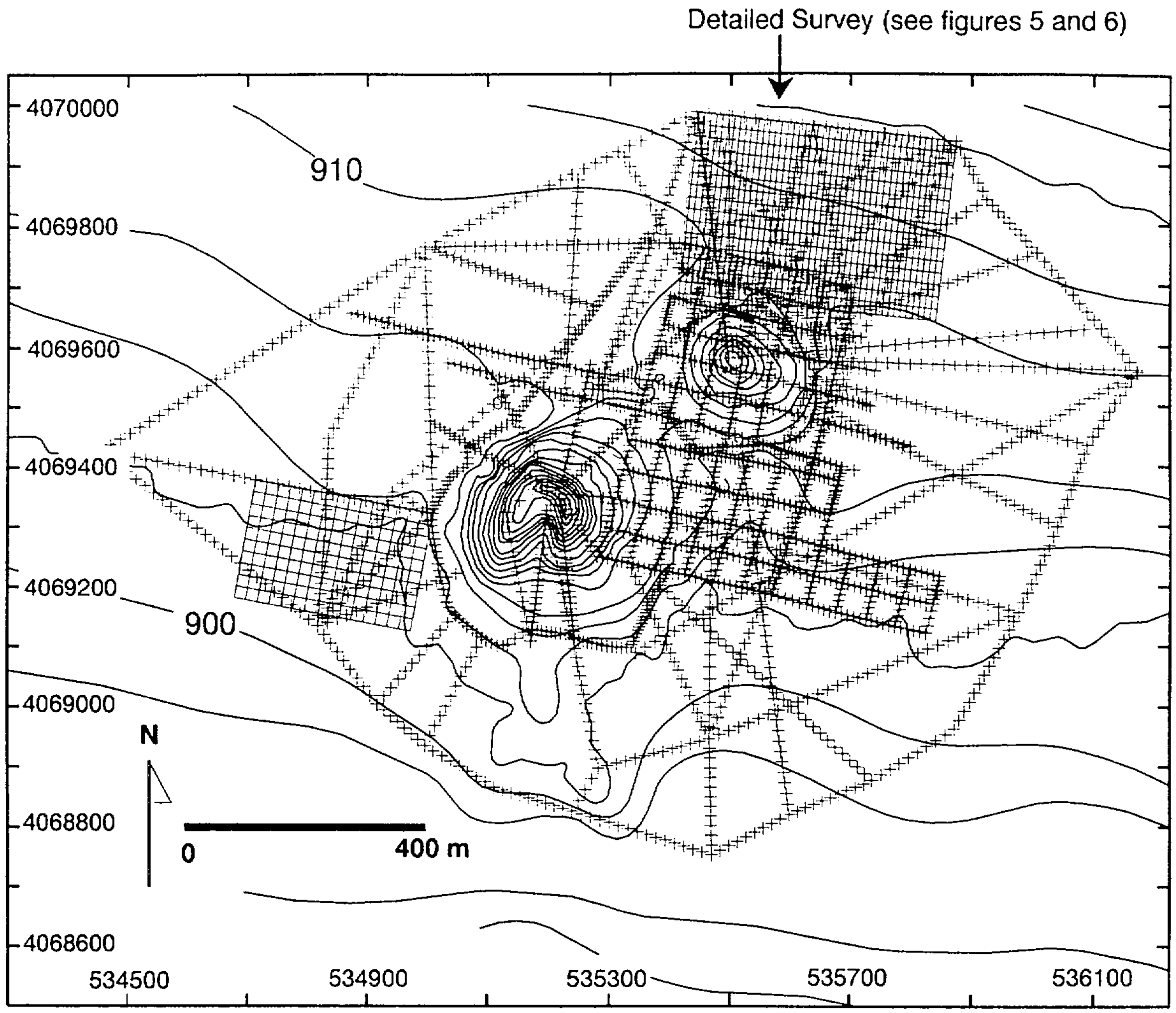

Stamatakos, Connor, and Martin - Figure 4

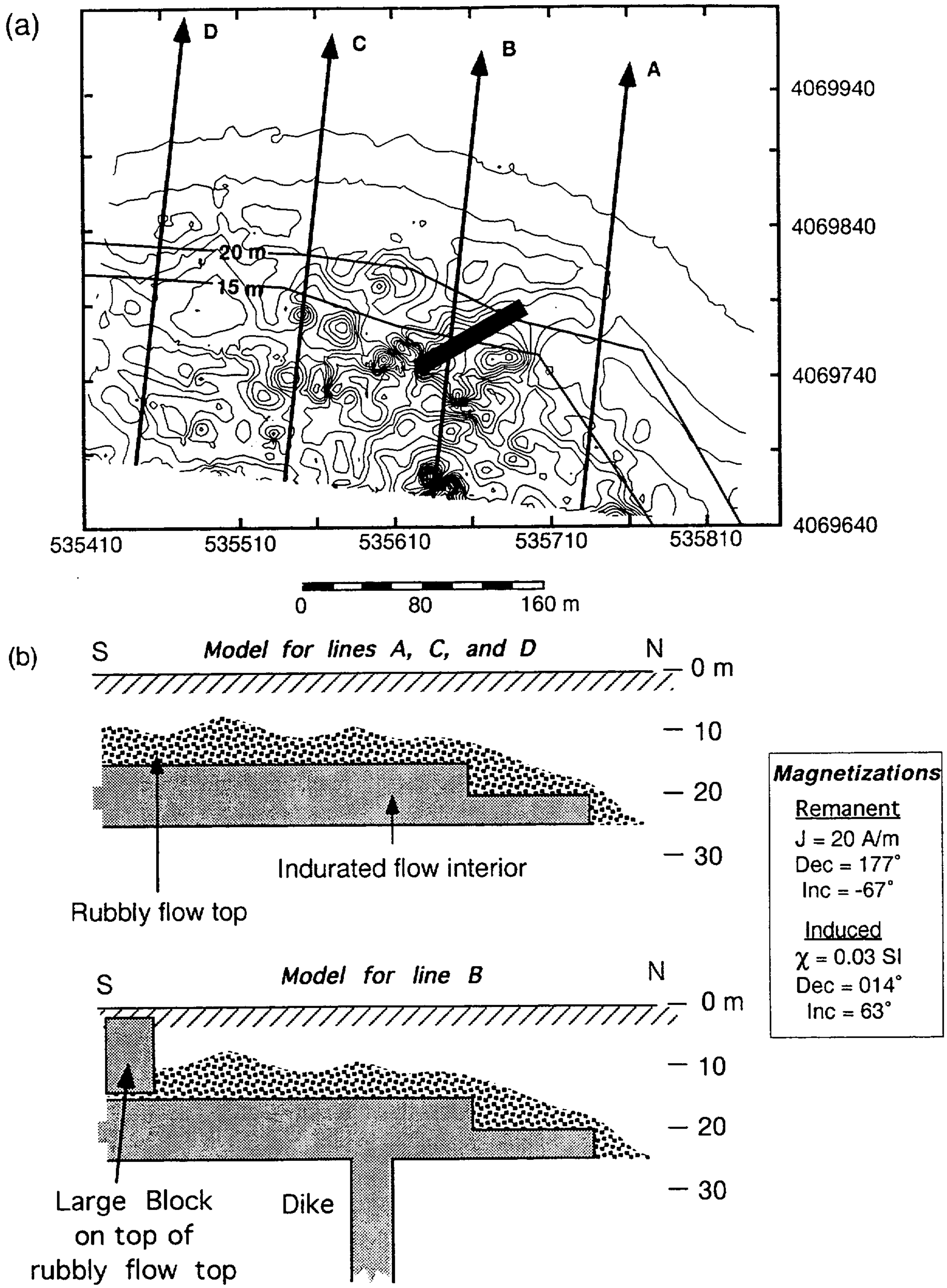

Stamatakos, Connor, and Martin - Figure 7

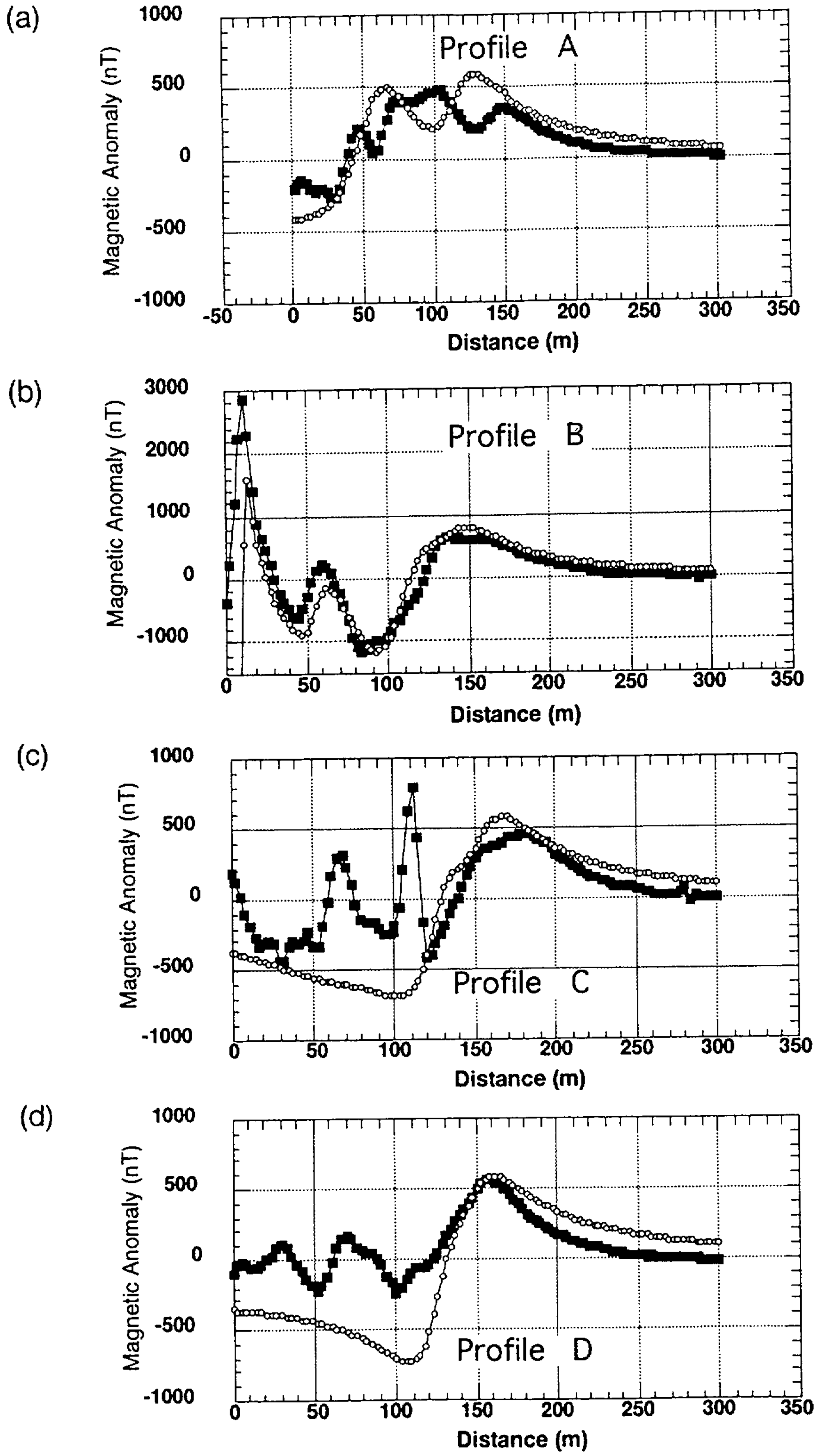

Stamatakos, Connor, and Martin - Figure 8

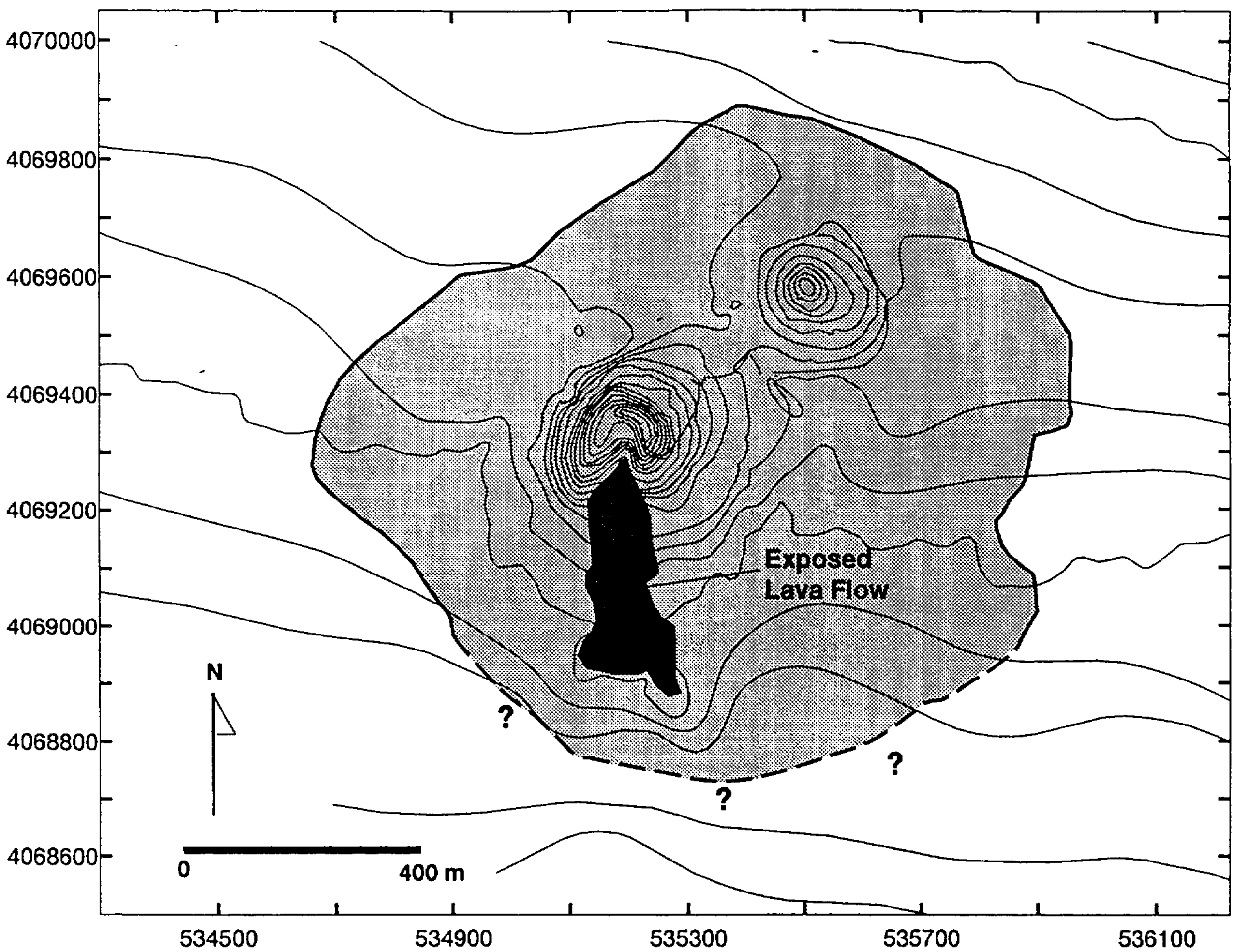

Stamatakos, Connor, and Martin - Figure 9

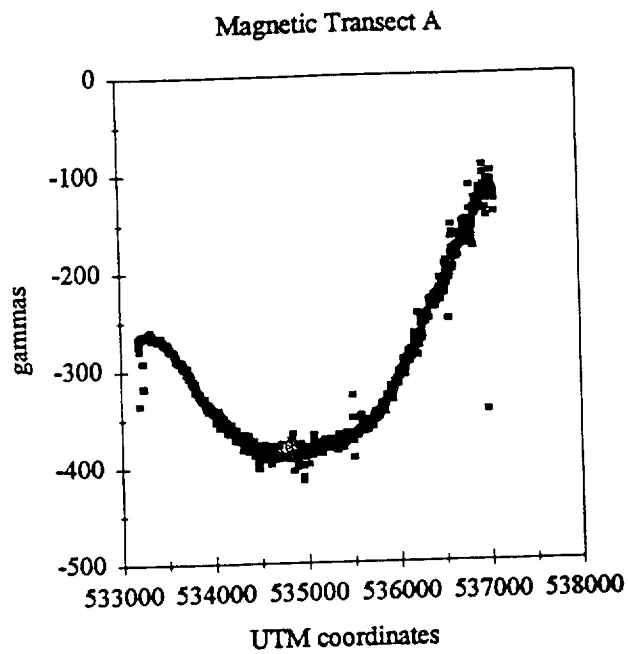
Magnetic Transect A
0
-100
-200
-300
-400
-500
gammas
533000 534000 535000 536000 537000 538000
UTM coordinates

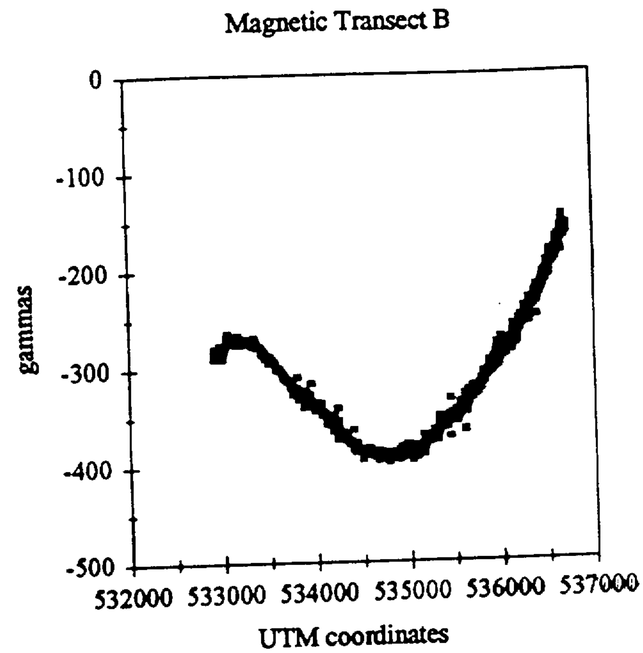
Magnetic Transect B
0
-100
-200
-300
-400
-500
gammas
532000 533000 534000 535000 536000 537000
UTM coordinates

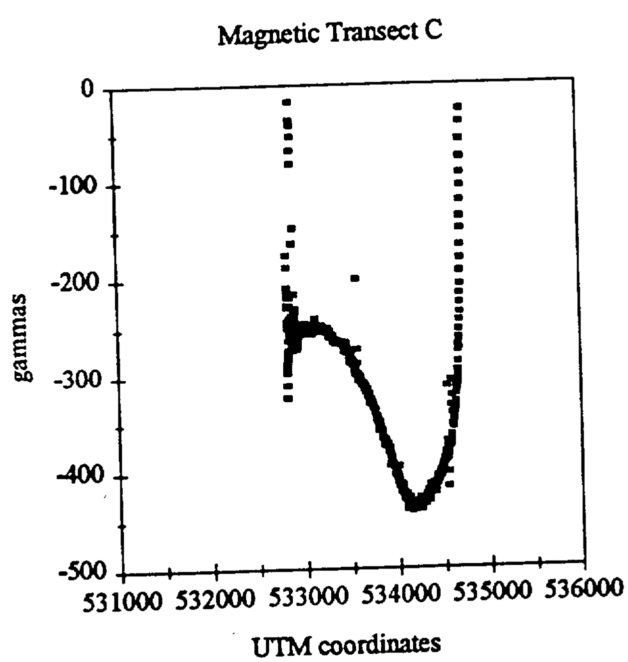
Magnetic Transect C
0
-100
-200
-300
-400
-500
gammas
531000 532000 533000 534000 535000 536000
UTM coordinates

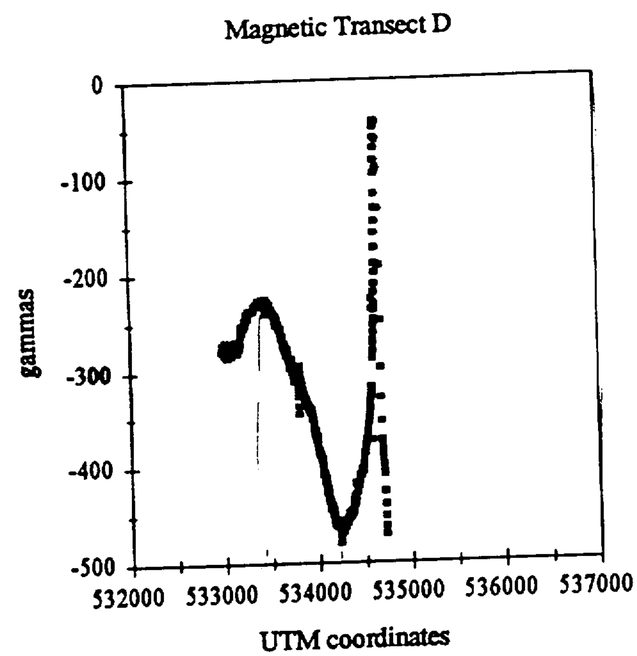
Magnetic Transect D
0
-100
-200
-300
-400
-500
gammas
532000 533000 534000 535000 536000 537000
UTM coordinates

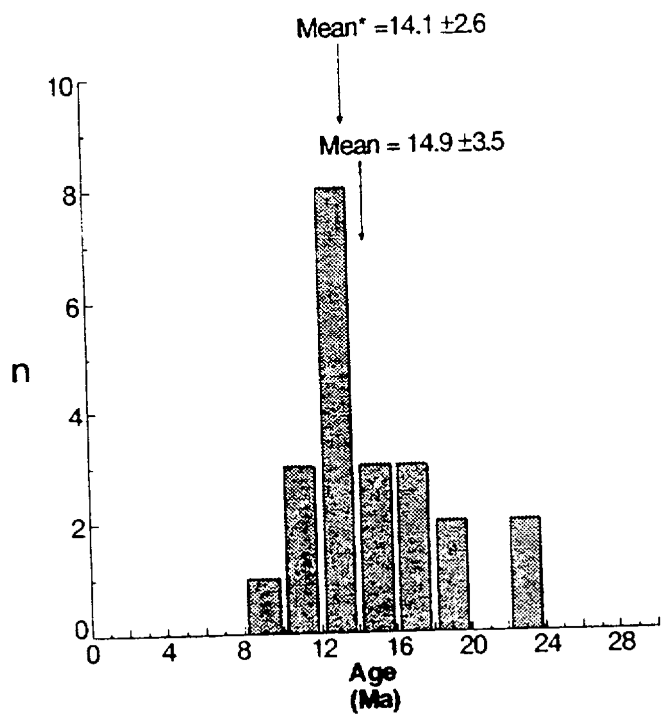

Stamatakos et al., Figure 4.

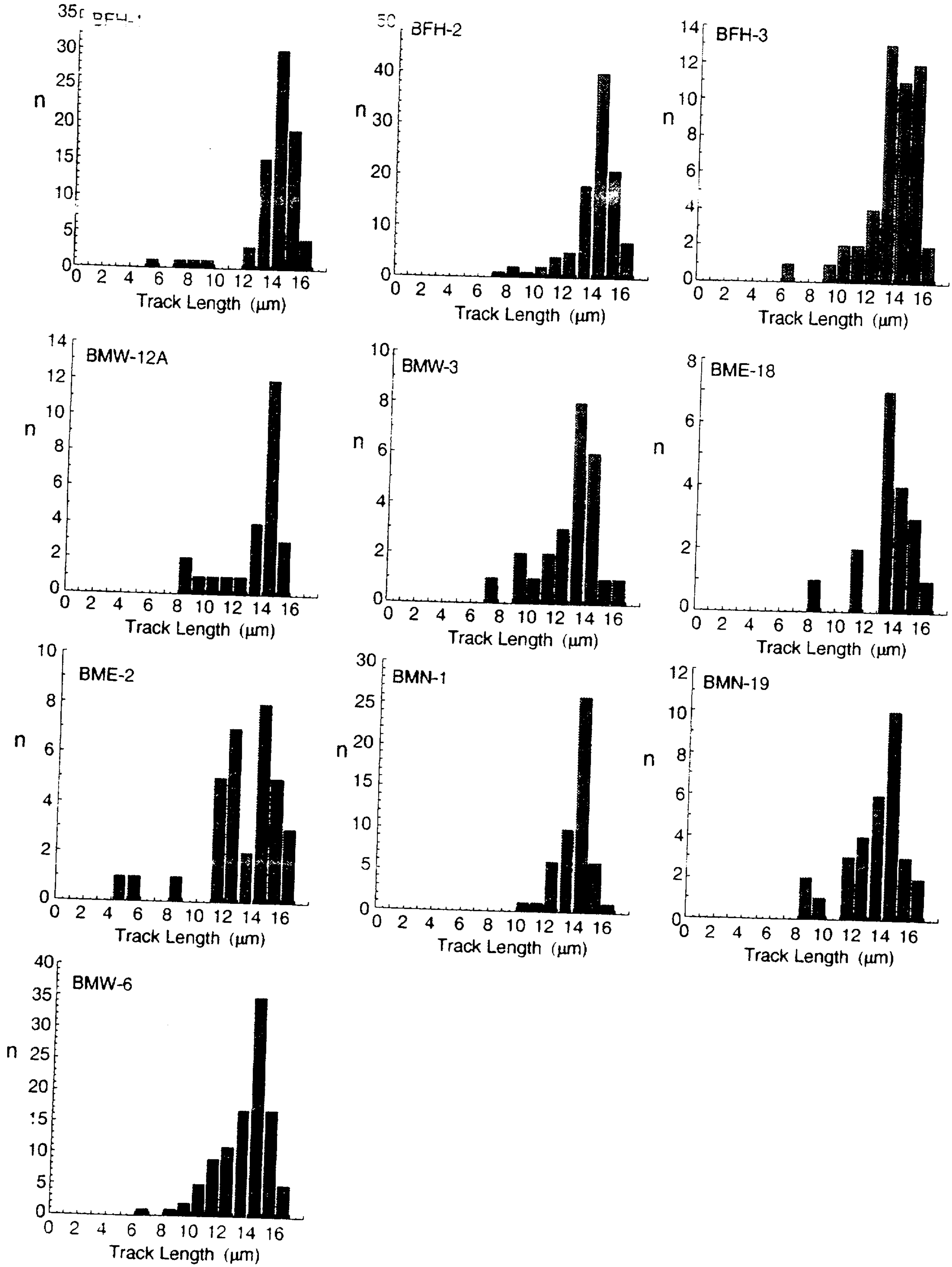

Stamatakos et al., Figure 7.

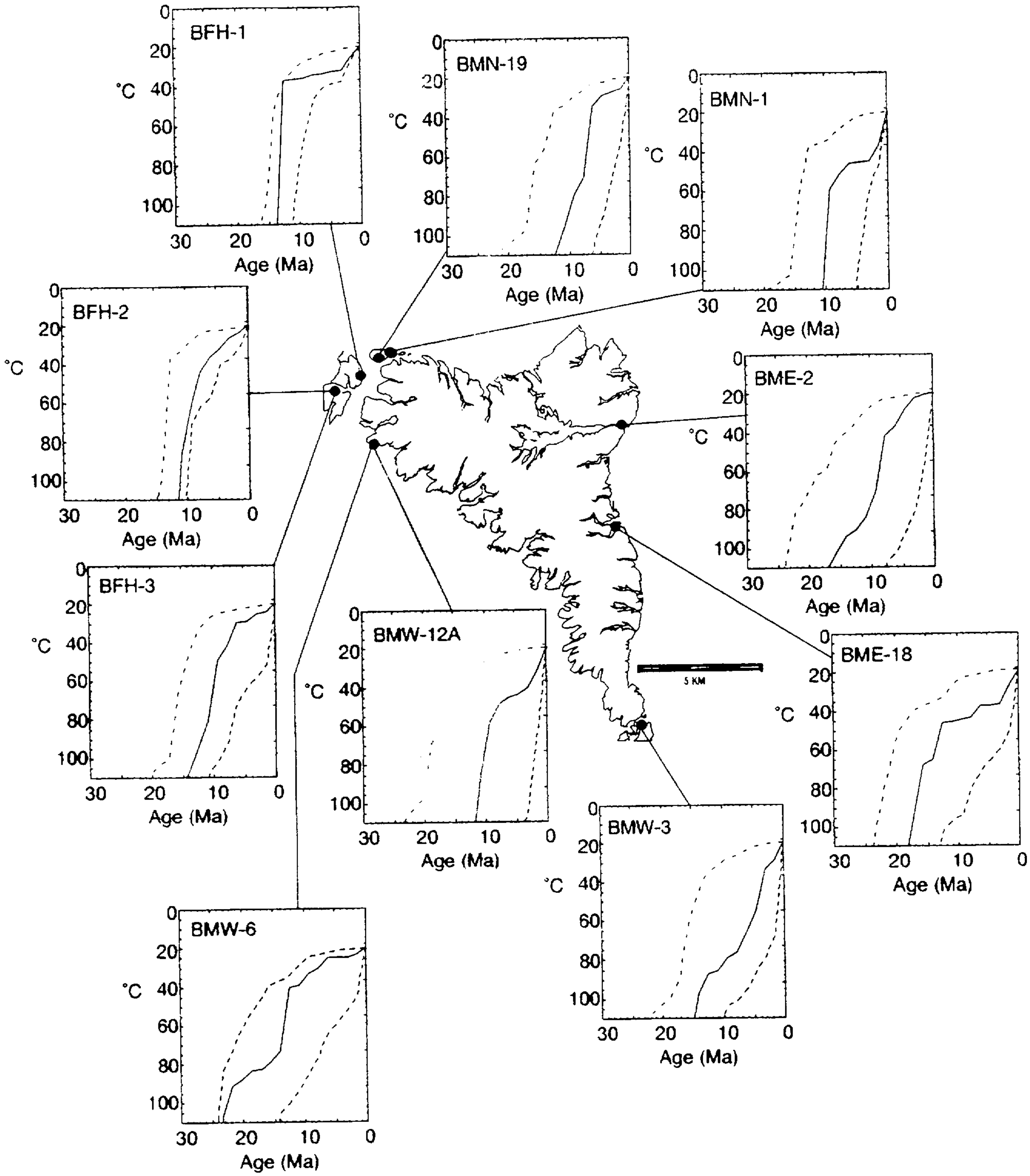

Stamatakos et al., Figure 8.

DEFINITION OF SLIP AND DILATION TENDENCY

Slip Tendency = $T_s = \tau/\sigma_n$

and

Dilation Tendency = $T_d = (\sigma_1 - \sigma_n)/(\sigma_1 - \sigma_3)$

where,

τ = resolved shear stress
σ_n = resolved normal stress
σ_1 = maximum principal compressive stress
σ_3 = minimum principal compressive stress

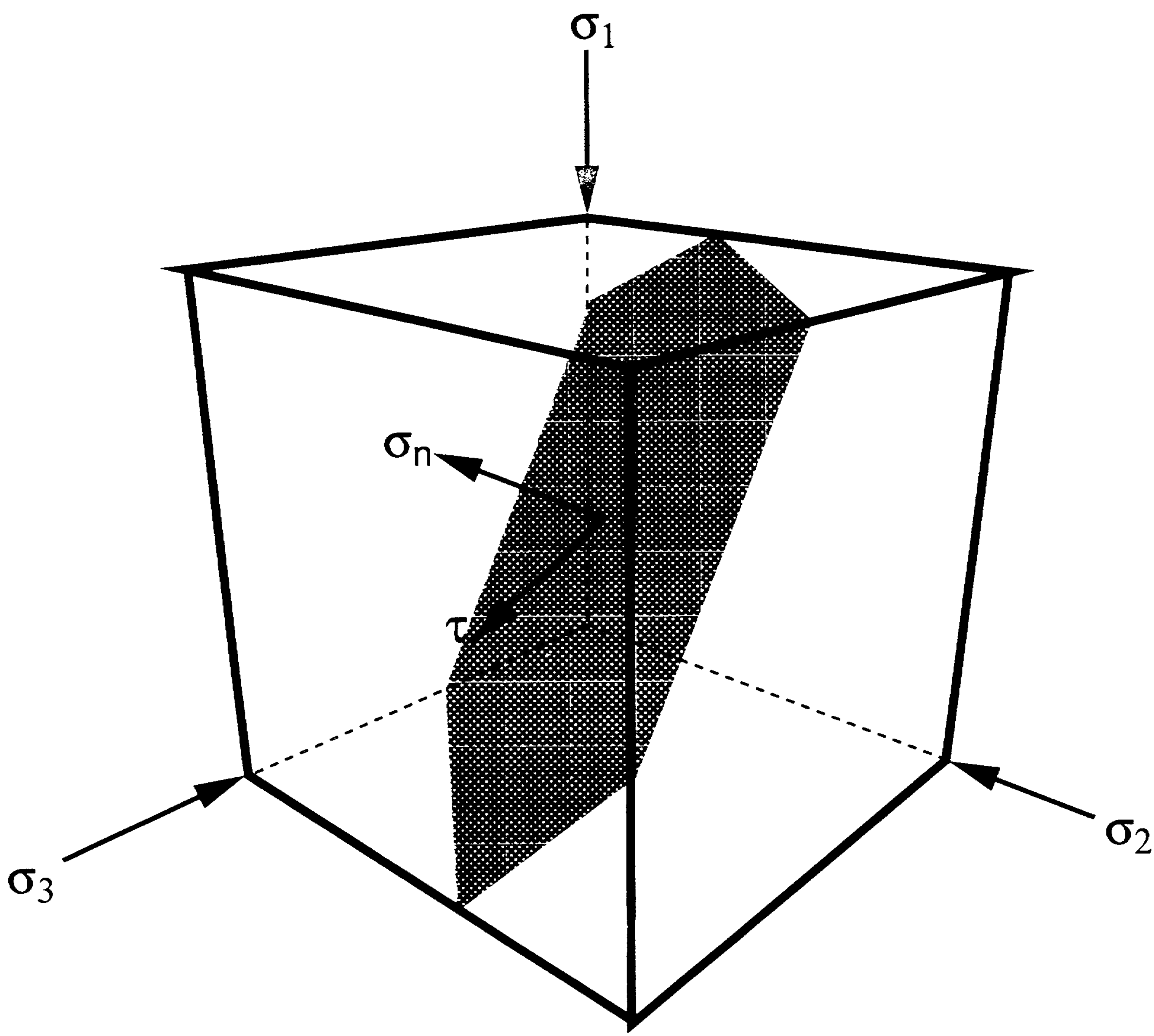

σ_1, σ_2, σ_3 = maximum, intermediate, and minimum principal stresses

σ_n = resolved normal stress

τ = resolved shear stress

YUCCA MOUNTAIN STRESS STATE

Normal Faulting Regime

$$R = (\sigma_1 - \sigma_2) / (\sigma_1 - \sigma_3)$$

$$K = (\sigma_1 / \sigma_2) / (\sigma_2 / \sigma_3)$$

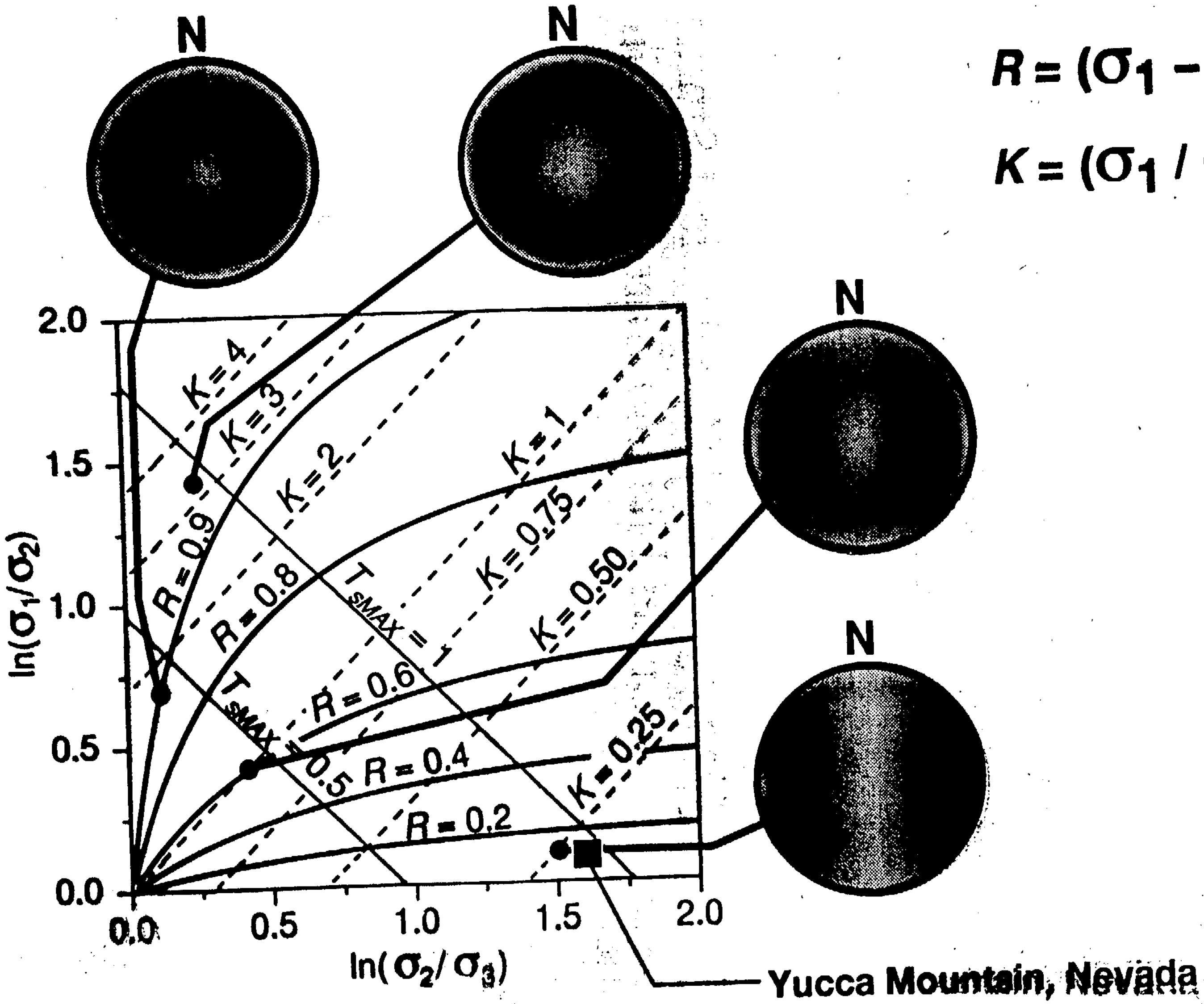

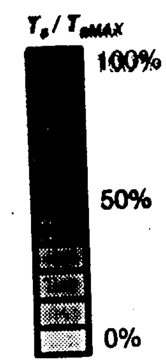

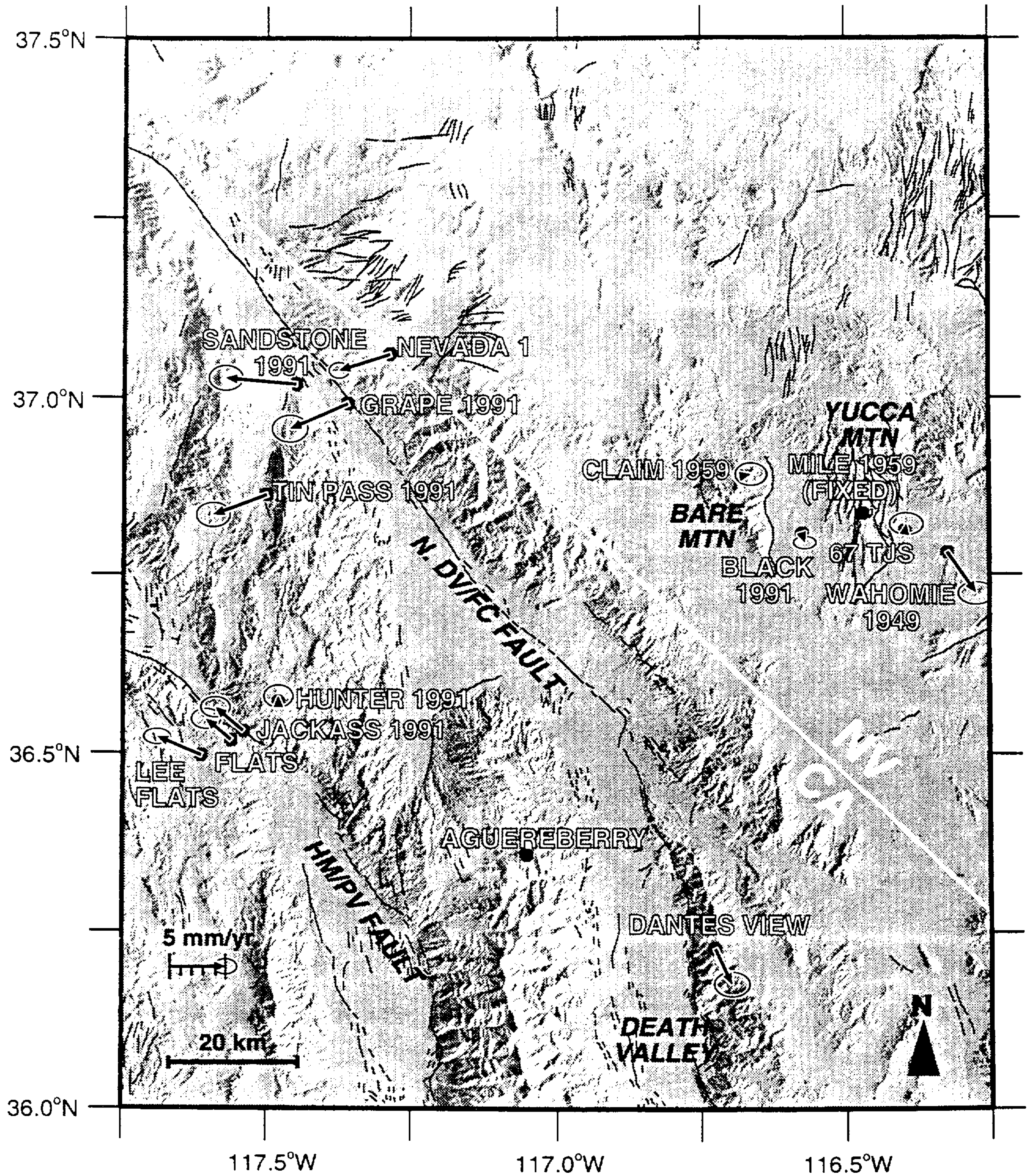

Figure 4-1. Map showing location of network sites and relative motions based on 1991, 1993, and 1994 Global Positioning System surveys, relative to site Mile. Ellipses show estimated 1σ errors.

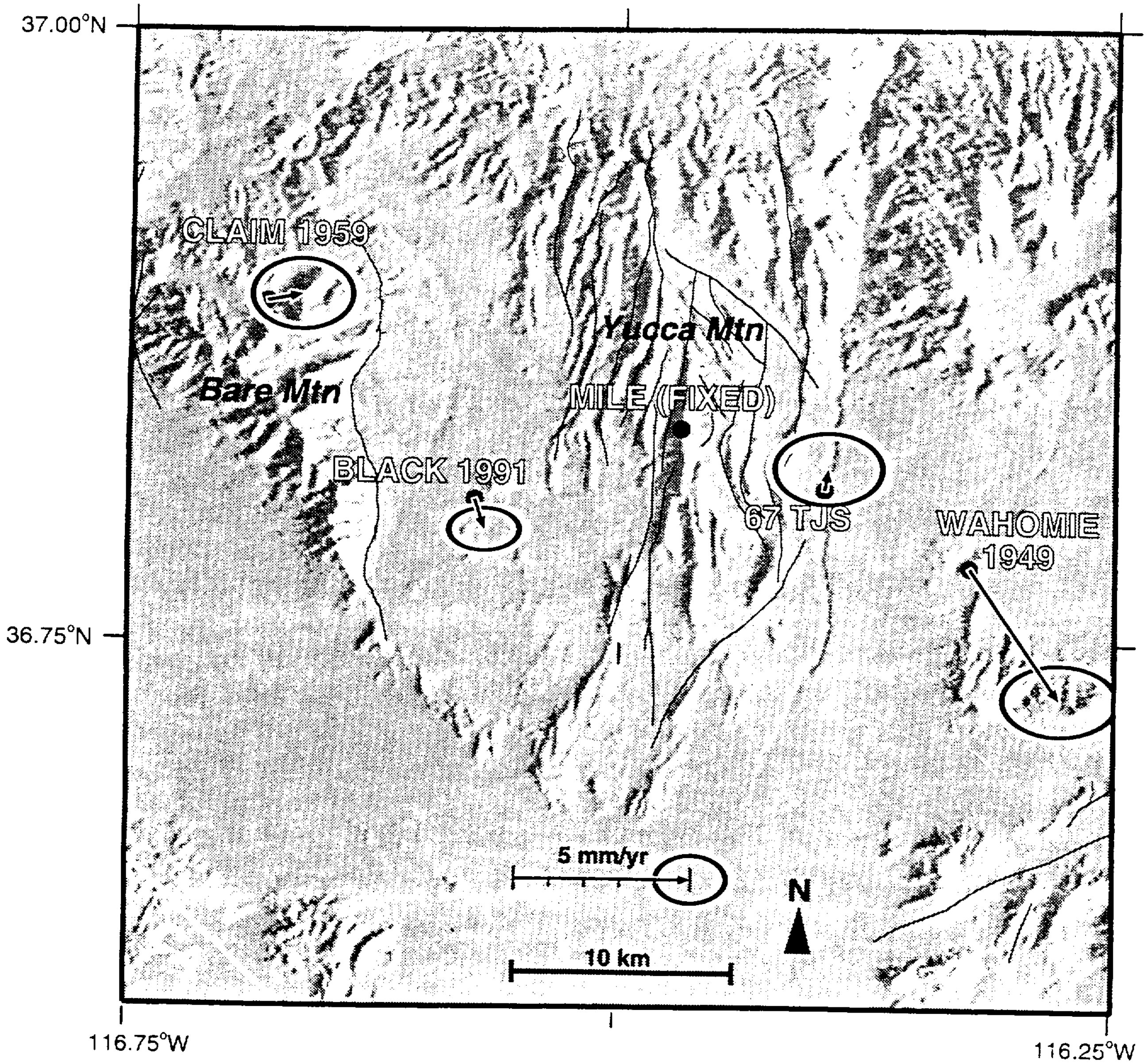

Figure 4-2. Map showing relative motions based on the 1991, 1993, and 1994 Global Positioning System surveys within the Yucca Mountain subnet. Ellipses show estimated 1σ errors.

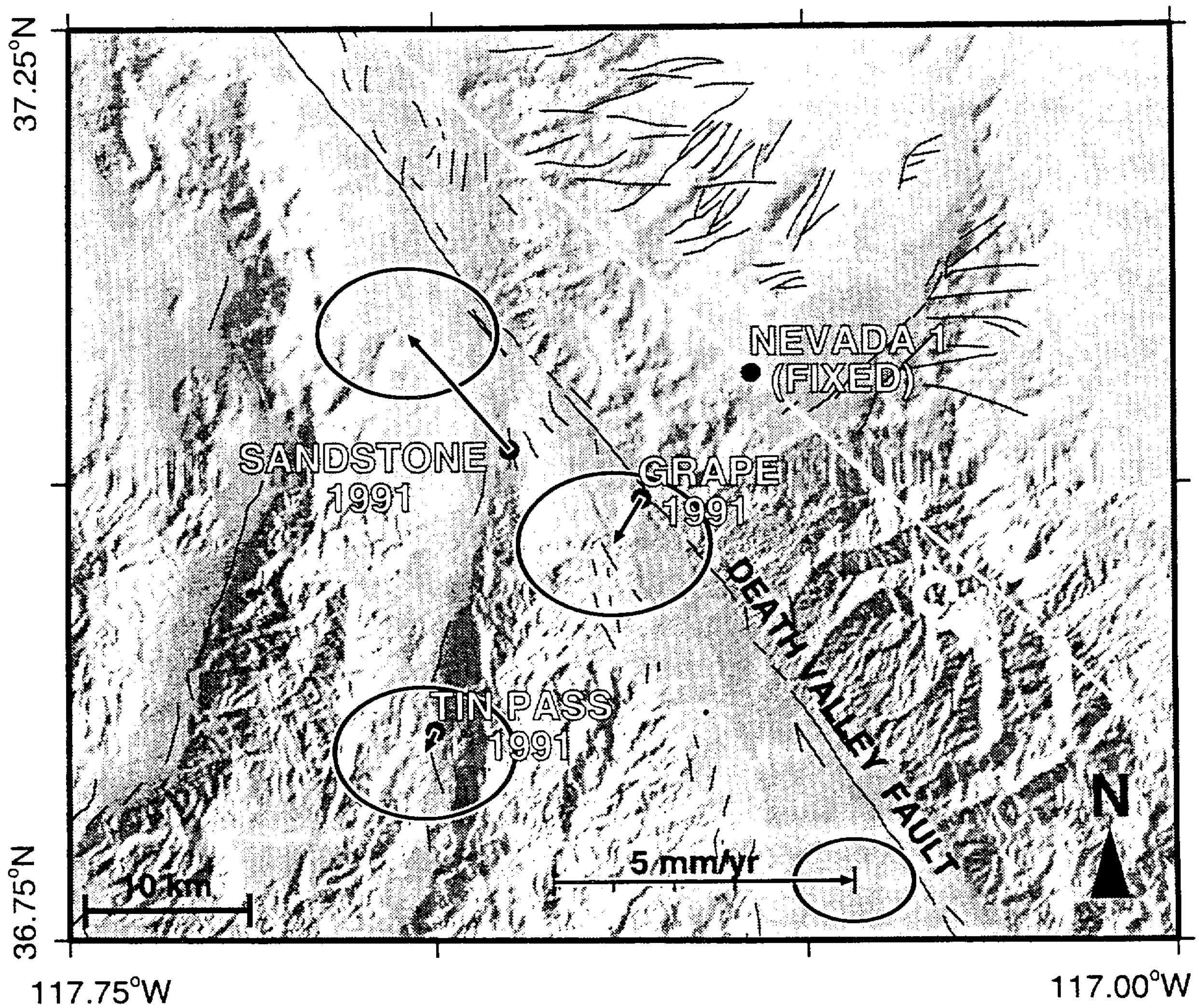

Figure 4-3. Maps showing relative motions based on the 1991, 1993, and 1994 Global Positioning System surveys within the Death Valley subnet. Ellipses show estimated 1σ errors.

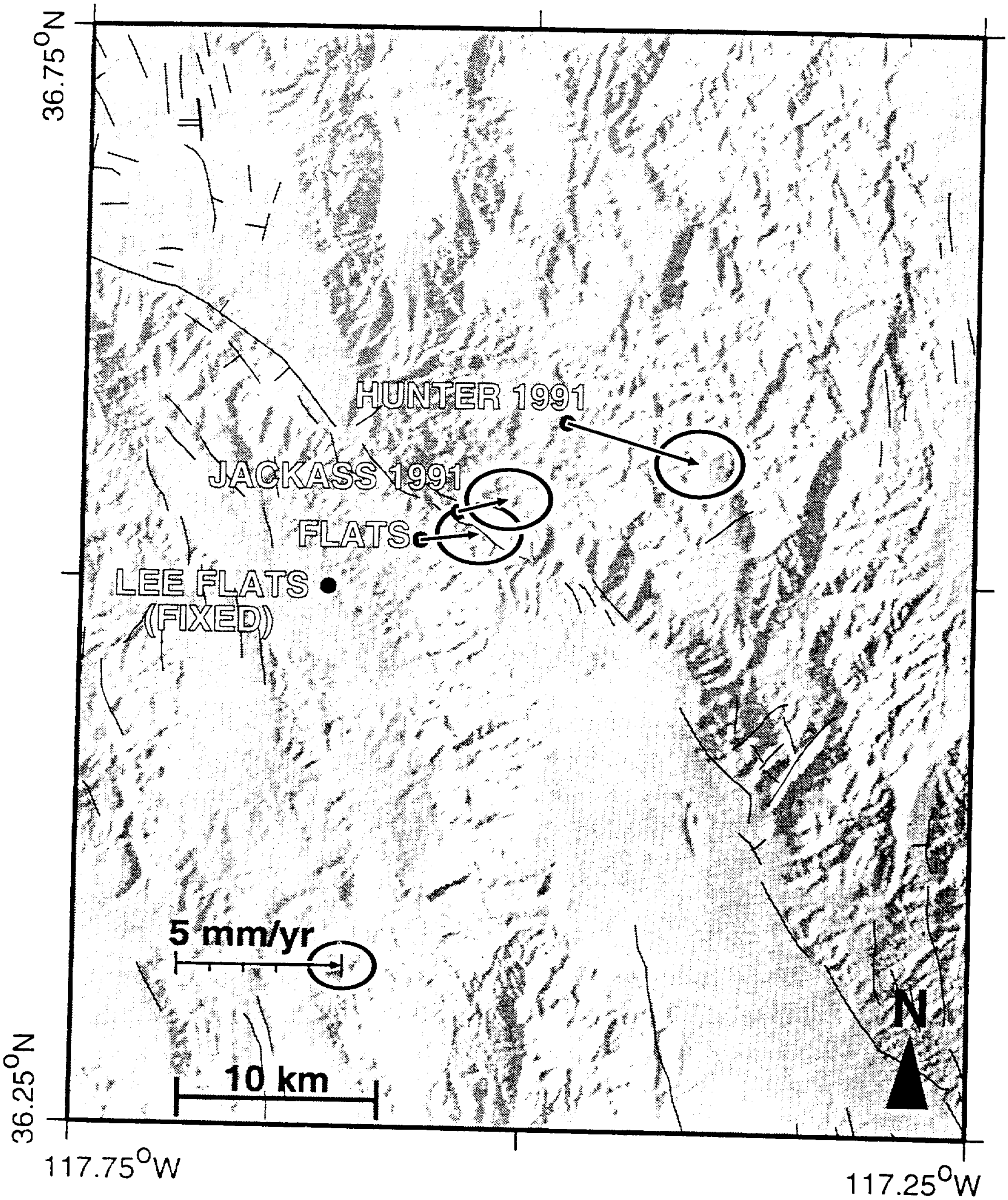

Figure 4-4. Map showing relative motions based on the 1991, 1993, and 1994 Global Positioning System surveys within the Hunter Mountain subnet. Ellipses show estimated 1σ errors.

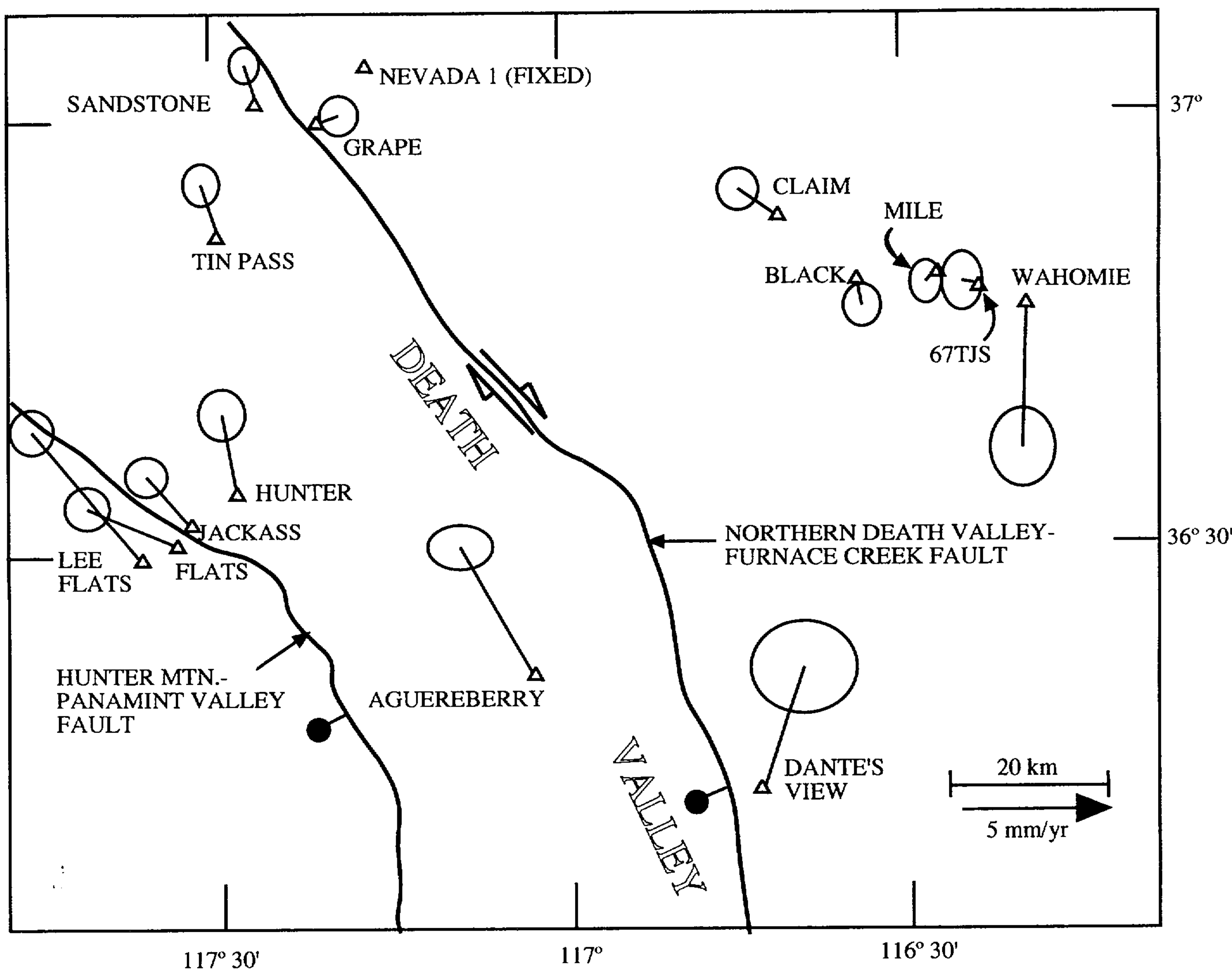
NEVADA 1 (FIXED)
SANDSTONE
GRAPE
TIN PASS
CLAIM
MILE
BLACK
WAHOMIE
67TJS
DEATH
HUNTER
JACKASS
LEE FLATS
FLATS
NORTHERN DEATH VALLEY-FURNACE CREEK FAULT
HUNTER MTN.-PANAMINT VALLEY FAULT
AGUEREBERRY
VALLEY
DANTE'S VIEW
20 km
5 mm/yr
37°
36° 30'
117° 30'
117°
116° 30'

1995 SURVEY

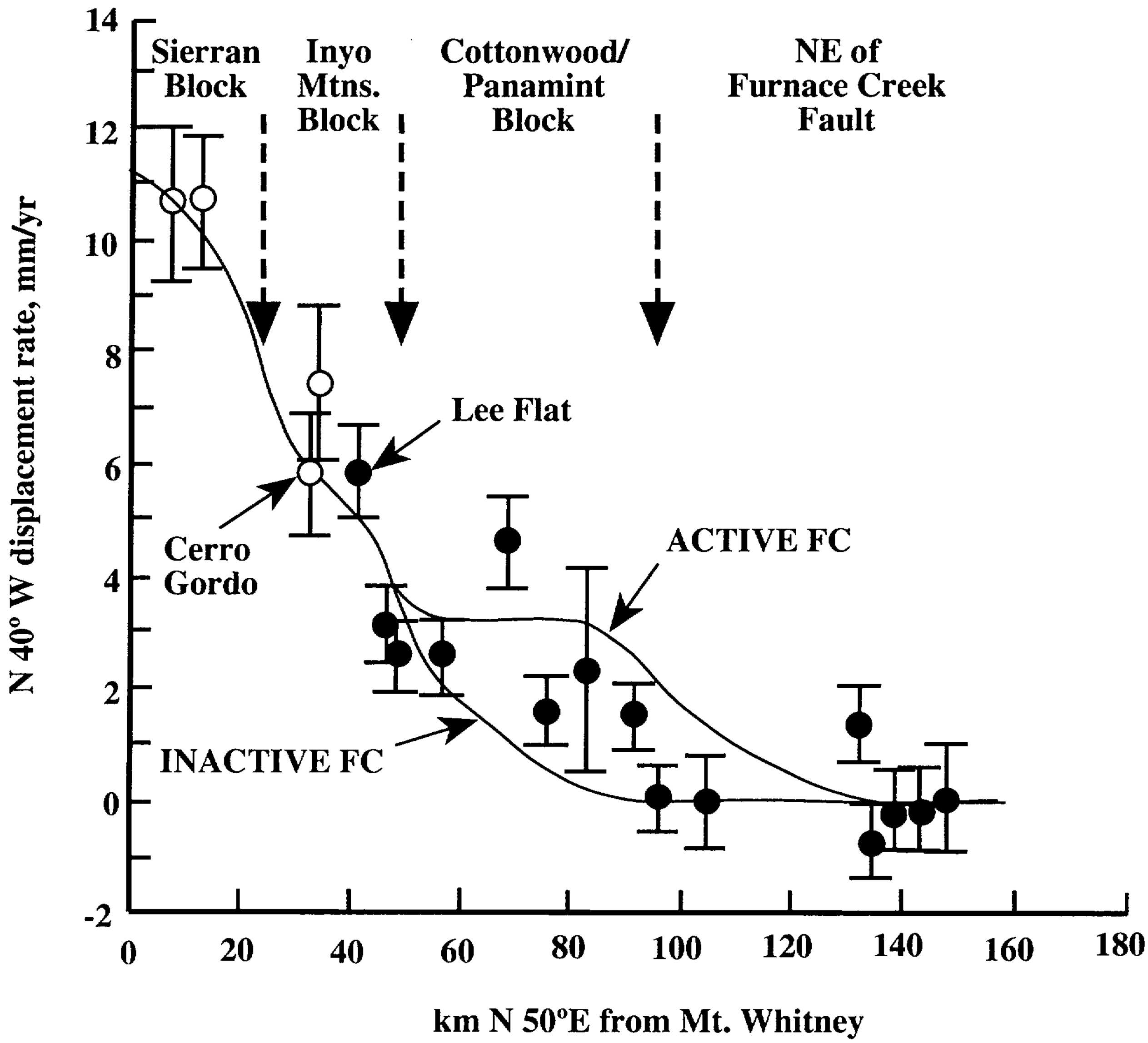

Sierran Block
Inyo Mtns. Block
Cottonwood/ Panamint Block
NE of Furnace Creek Fault
Lee Flat
Cerro Gordo
ACTIVE FC
INACTIVE FC
N 40° W displacement rate, mm/yr
14
12
10
8
6
4
2
0
-2
0
20
40
60
80
100
120
140
160
180
km N 50°E from Mt. Whitney

Geodetic Leveling Data Used to Define Historical Height Changes Between Beatty and Mercury, Nevada

Source: Gilmore, 1992

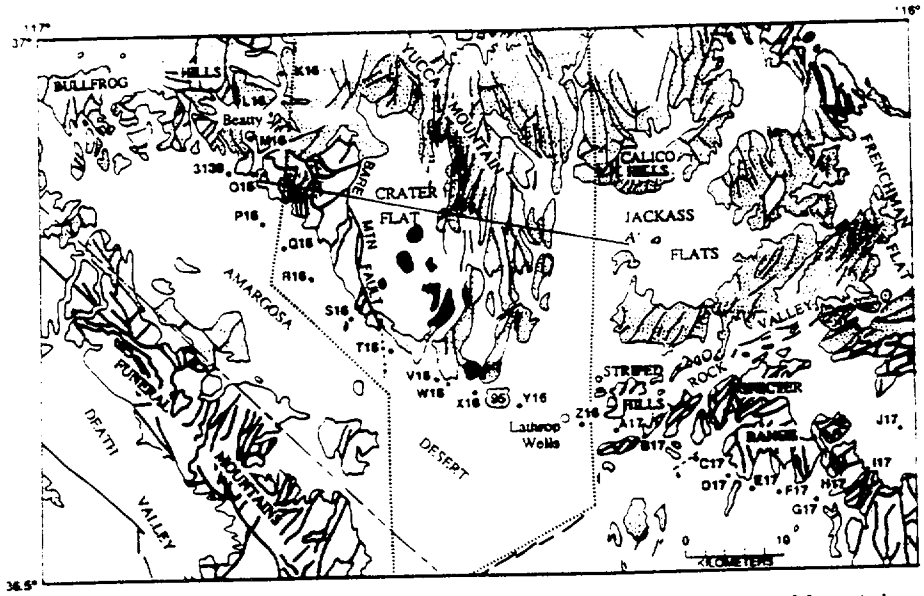

Routes of repeated geodetic levelings in the vicinity of Yucca Mountain

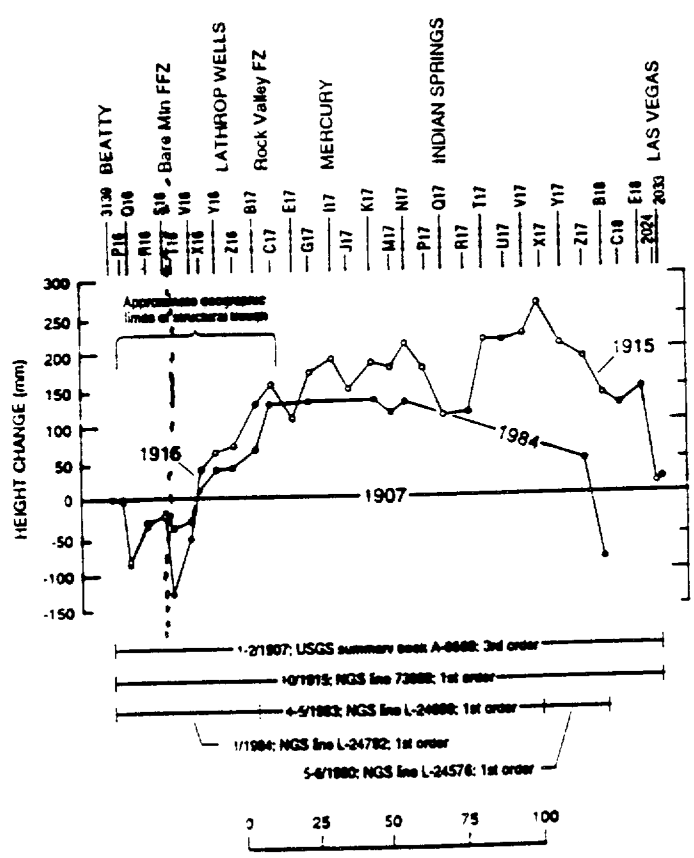

Profile showing height changes with respect to 1907 baseline between Beatty and Las Vegas, Nevada

US Geological Survey Geodetic Data at Yucca Mountain

Leveling, Trilateration, and Global Positioning System Data

presented by

Silvio Pezzopane

U.S. Geological Survey

Yucca Mountain Project

GEODETIC LEVELING DATA USED TO DEFINE HISTORICAL HEIGHT CHANGES BETWEEN TONOPAH JUNCTION AND LAS VEGAS, NEVADA

GILMORE (1992)

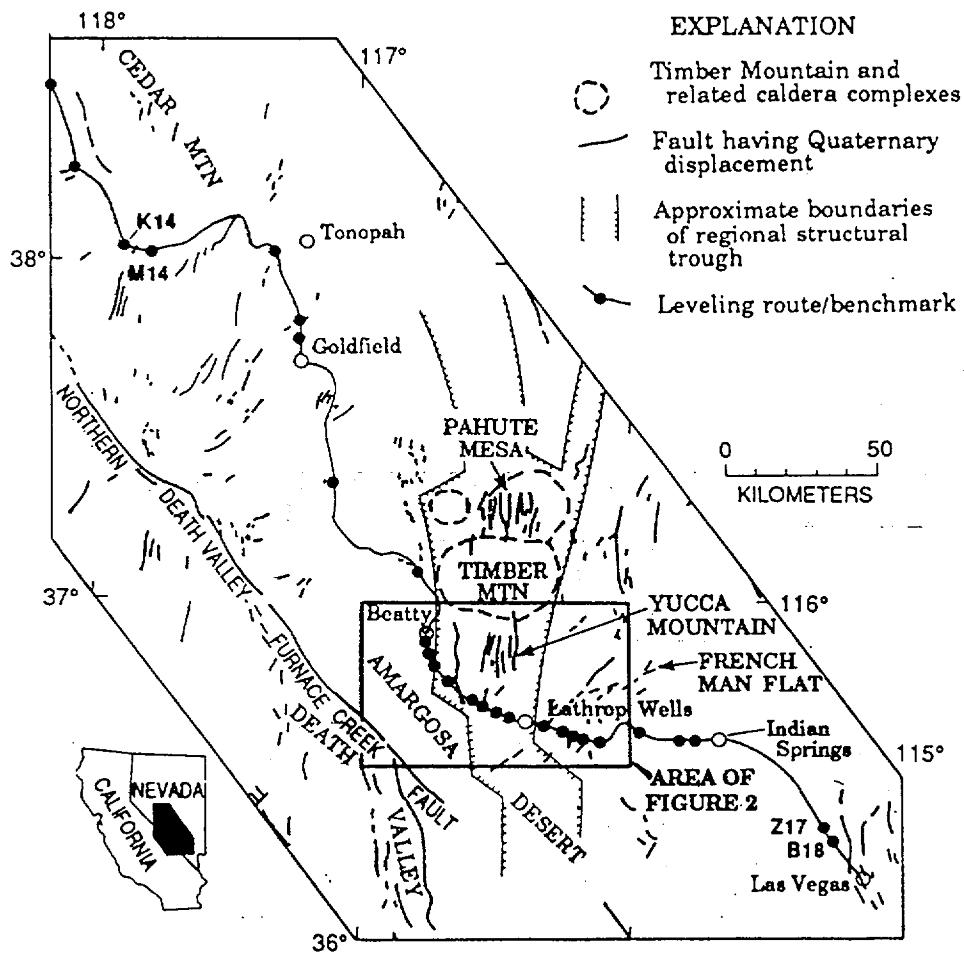

Figure 1. Generalized map showing faults with Quaternary rupture in southwestern Nevada and route of repeated geodetic levelings between Tonopah and Las Vegas. Bench marks used in 1915 to 1984 comparison (fig. 3) represented by dots along leveling route. Leveling route follows highway U.S. 95, shown as solid line connecting bench marks. Upland areas underlain by bedrock are shaded; Quaternary surficial deposits are unpatterned. Faults modified after Nakata and others (1982) and Reheis and Noller (1989).

ALSO USGS SEISMOTECTONIC REPT – CHAPTER 6

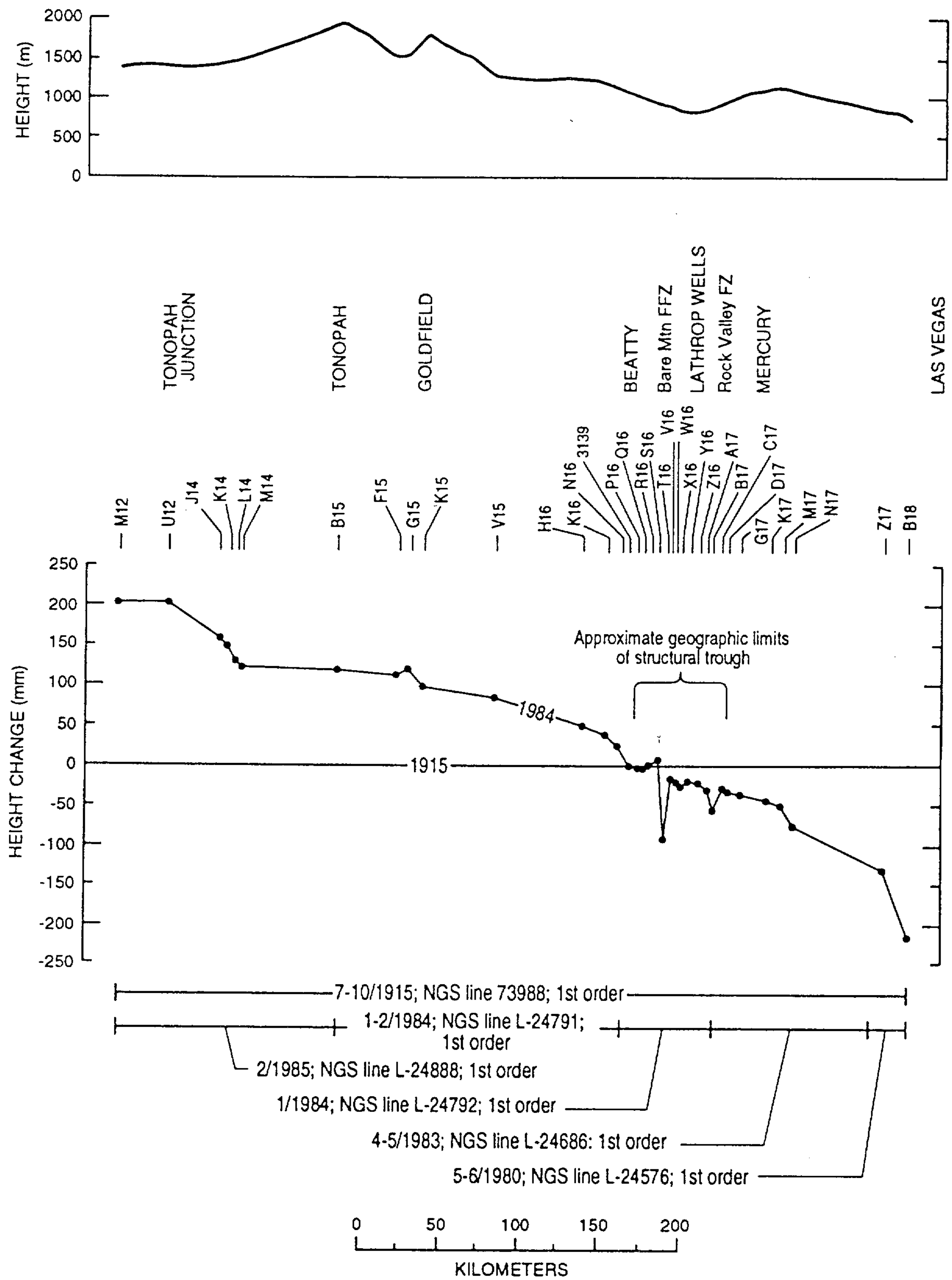

Figure 3. Profiles showing terrain and height changes with respect to 1915 baseline between Tonopah Junction and Las Vegas.

FROM GILMORE 1992 - OFR 92-450

ALSO USGS SEISMOTECTONIC REPT - CHAPT 6

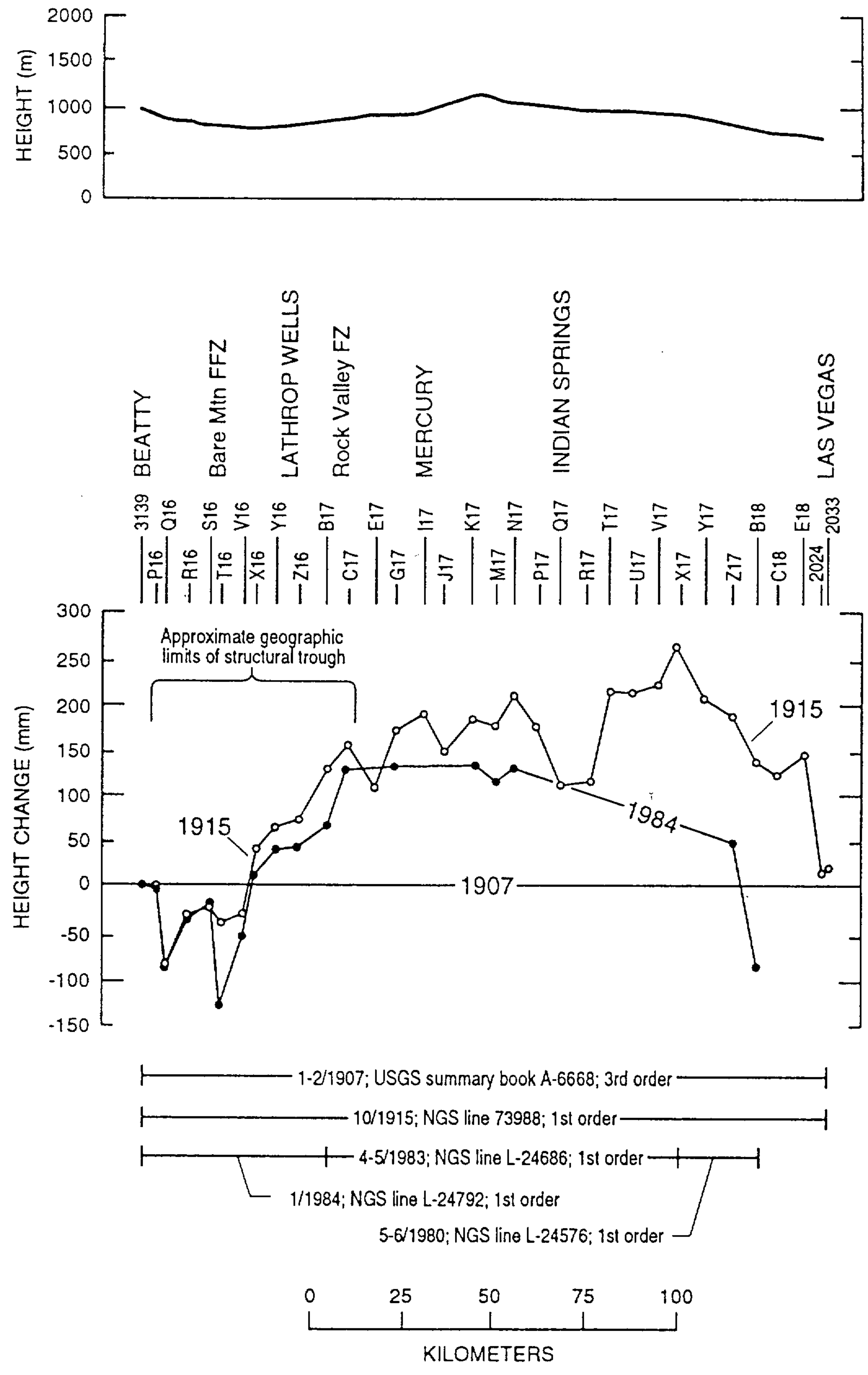

Figure 4. Profiles showing terrain and height changes with respect to 1907 baseline between Beatty and Las Vegas. Note that the horizontal scale of this figure is one half that of figure 3.

FROM GILMORE 1992 - OFR 92-450
USGS SEISMOTECTONIC RPT. CHAPT 6

First-Order Level Lines Across Yucca Mountain

- 92-km-long line
- 133 bench marks every kilometer
- across YM, every 1/2 kilometer
- first surveyed during the period 1956-1959
- surveyed every 1 or 2 yrs since 1983
- difference recent survey elevations from 1985-1986 survey elevations
- Little Skull Mountain earthquake caused negative elevation change over a 17-km-wide zone with a maximum of 22 mm
- maximum downdrop is 2 km northwest of Little Skull Mountain
- zone lies between Mine Mountain and Rock Valley faults
- typical signal for an event of this size (~ M6)

Map of Leveling Lines, Benchmark Locations, and Reference Marks

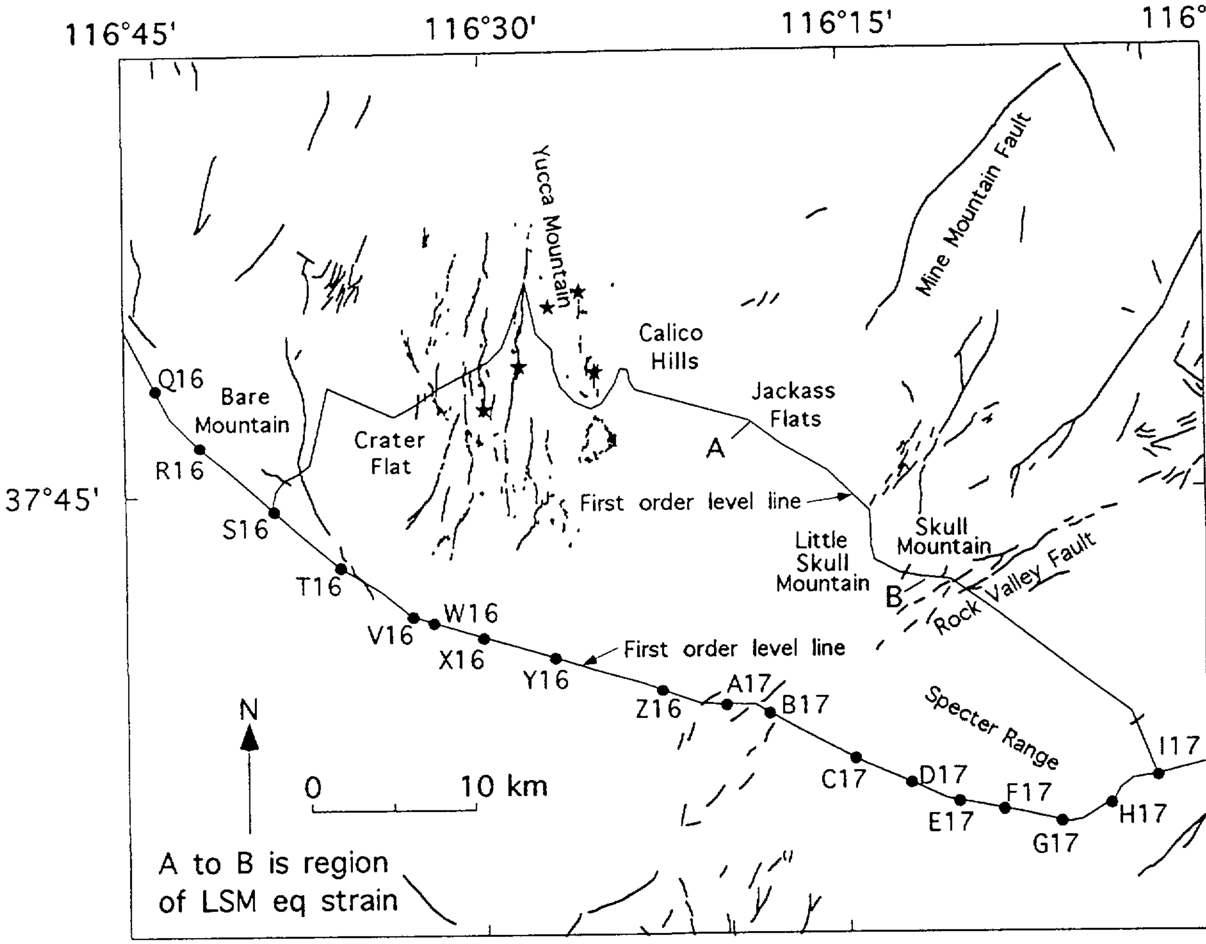

- the region between marks A and B downdropped during the Little Skull Mountain Earthquake

in USGS Seismotectonic Report— Chapter 6

Profile plots showing data from surveys of level line across Yucca Mountain during the period 1983 - 1993

from K.S. Koepsell, National Geodetic Survey, written commun., 1996
also see USGS Seismotectonic Report— Chapter 6

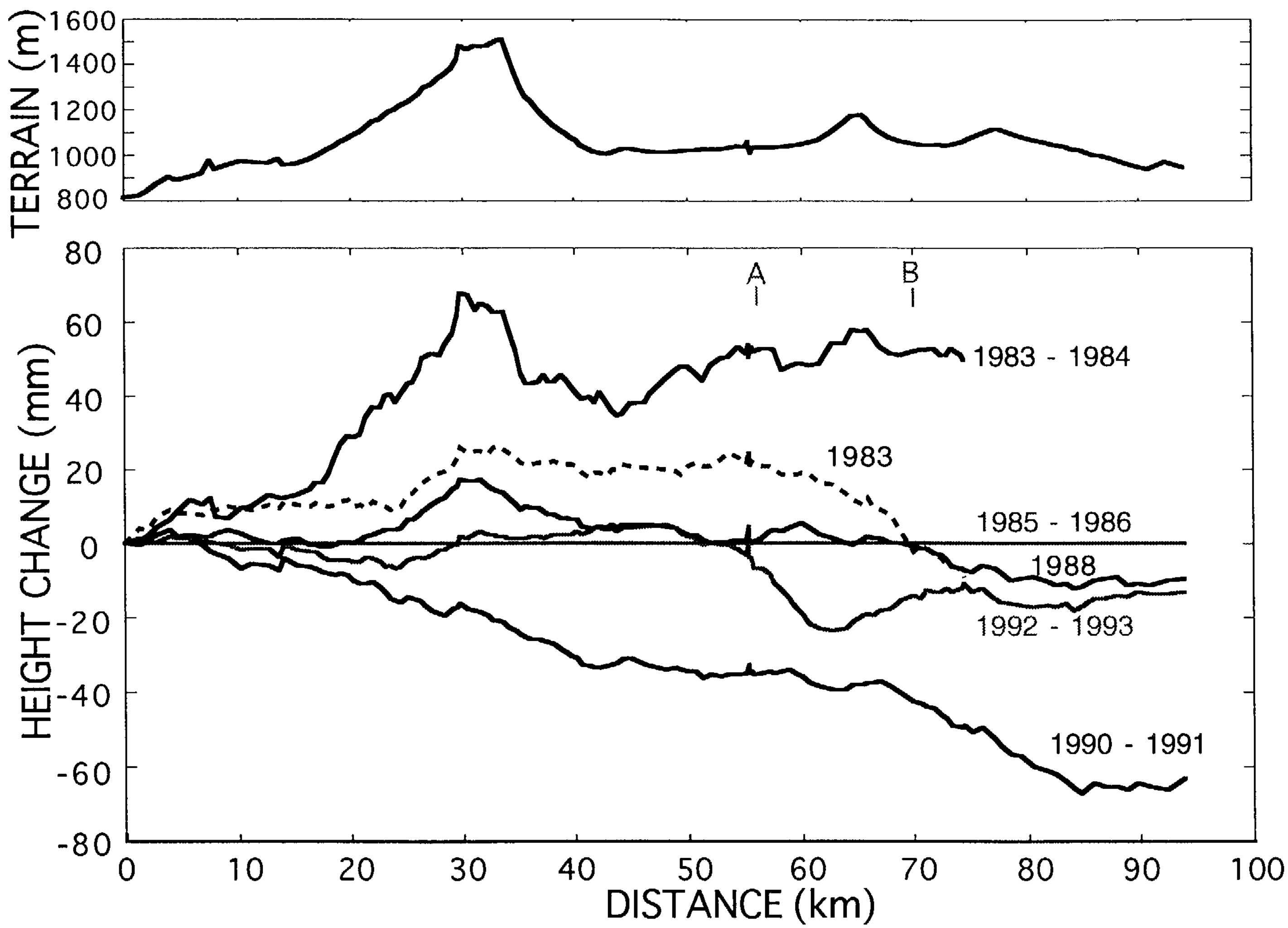

Map of Trilateration Network at Yucca Mountain

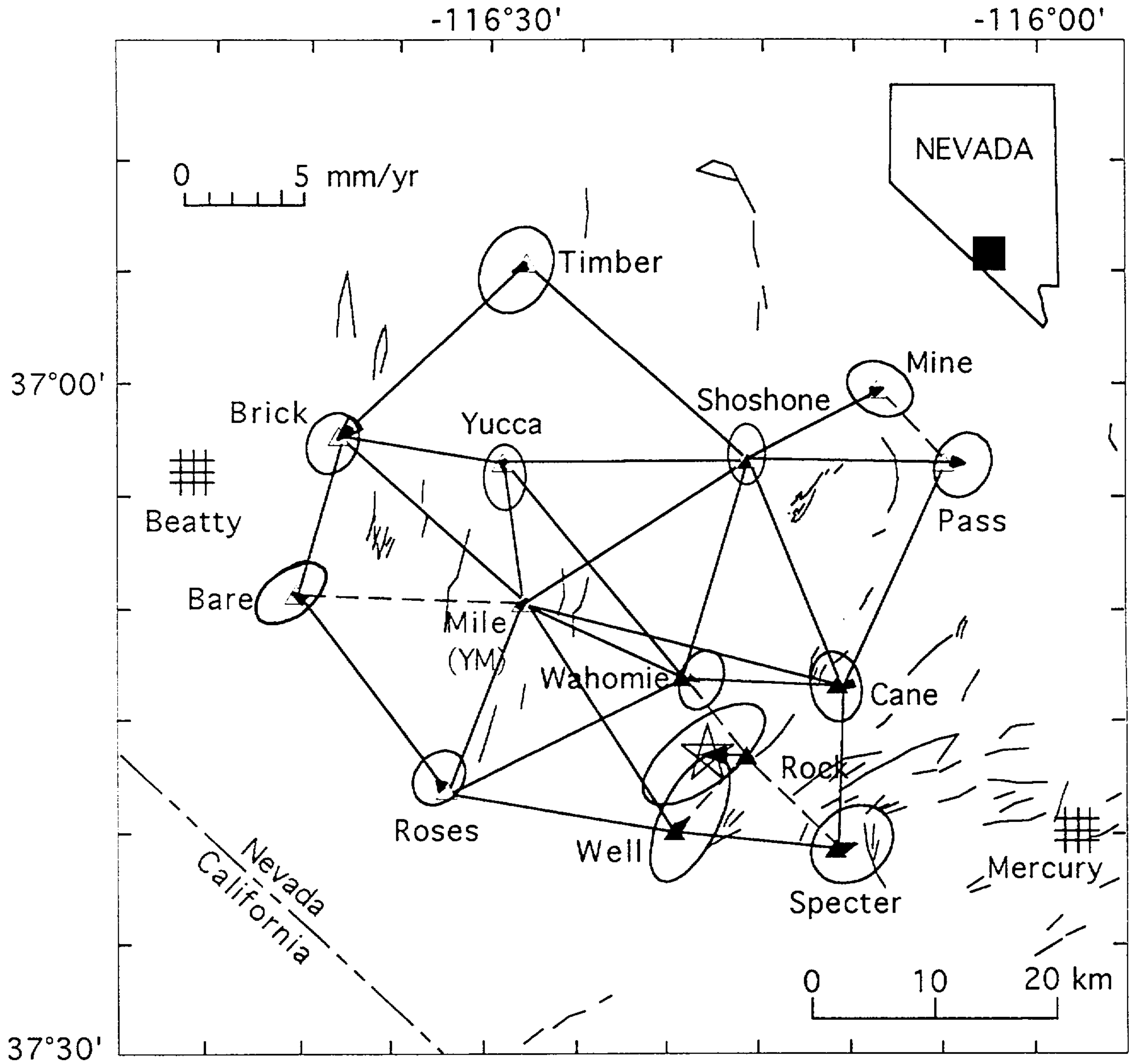

- from Savage and others (1994) JGR
- no detectable deformation across network except LSM Eq
- star marks Little Skull Mtn Earthquake
- ellipses show 95% confidence intervals on motions

USGS-YMP Pezzopane Oct 96

—Summary—
Geodetic Data at Yucca Mountain

- Early Leveling Lines along Highway U.S. 95—Topopah to Las Vegas—may Reveal Elevation Changes in Vicinity of Yucca Mountain—Rock Valley
  - » 1907 Baseline is Questionable
- First-Order Leveling across Yucca Mountain and Rock Valley reveal Little Skull Mountain Earthquake produced a negative elevation change of as much as 22 mm over a 17-km-wide zone
  - » Typical of M ~ 6 Strain Pattern
- Trilateration and GPS surveys (1983-1993) reveal no Detectable Deformation except for Little Skull Mountain Eq. strain
  - » Modeled as a 5-km-square rupture surface at a depth of ~ 8 km with ~ 0.58±0.075 m of slip
- USGS Seismotectonic Report—Chapt 6

HISTORICAL EARTHQUAKE CATALOGUE FOR YUCCA MOUNTAIN

Ivan Wong, Jacqueline Bott, and Doug Wright
Woodward-Clyde Federal Services
Oakland, CA

Yucca Mountain Seismic Source Characterization Workshop
Salt Lake City, Utah
17 October 1996

OBJECTIVES

To allow experts to:

(1) characterize the regional seismicity around the site;

(2) evaluate the seismicity for any possible associations with geologic structures particularly late-Quaternary faults; and

(3) compute earthquake recurrence parameters for the various seismotectonic provinces which make up the Yucca Mountain region.

CATALOGUE VITAL STATISTICS

TIME PERIOD	**1868 to 31 January 1994 (being updated through 1995)**
AREA OF COVERAGE	**300 km radius around Yucca Mountain**
NUMBER OF EVENTS	**247,717 (NTS explosions, cavity collapses and quarry blasts removed)**
MAGNITUDE RANGE	**M< 1.0 - 7.8**

DATA SOURCES

- **Southern Great Basin earthquakes, 1868 to 1978 (Meremonte and Rogers, 1987)**
- **Southern Great Basin network, 1978 to 1991 (Rogers *et al.*, 1987)**
- **California, 1868 to 1932, California Division of Mines and Geology**
- **Southern California, 1932 to 1994, California Institute of Technology/USGS**
- **Northern California, 1910 to 1972, University of California at Berkeley**
- **Northern and Central California, 1969 to 1995, USGS**

DATA SOURCES (CONT.)

- Nevada, 1874 to 1994 including the SGB for 1992 to 1994, University of Nevada, Reno
- Decade of North American Geology, 1868 to 1985 (Engdahl and Rinehart, 1988)
- Arizona, 1891 to 1992, Northern Arizona University
- State catalogues for Utah and Arizona, 1881 to 1985, Stover, Reagor and Algermissen (NEIS)
- Utah, 1881 to 1994, University of Utah
- PDEs for Utah and Arizona, 1938 to 1991, NEIS

CATALOGUE ISSUES

Goal: Cataloging Truly independent EQ events

- Magnitude errors
- Common M_w scale
- Maximum intensity-magnitude conversion
- Removal of nuclear explosions, collapses, and quarry blasts
- Removal of nuclear explosion-induced aftershocks
- Removal of Lake Mead RIS?
- Completeness
- Declustering
- Definition of seismotectonic provinces

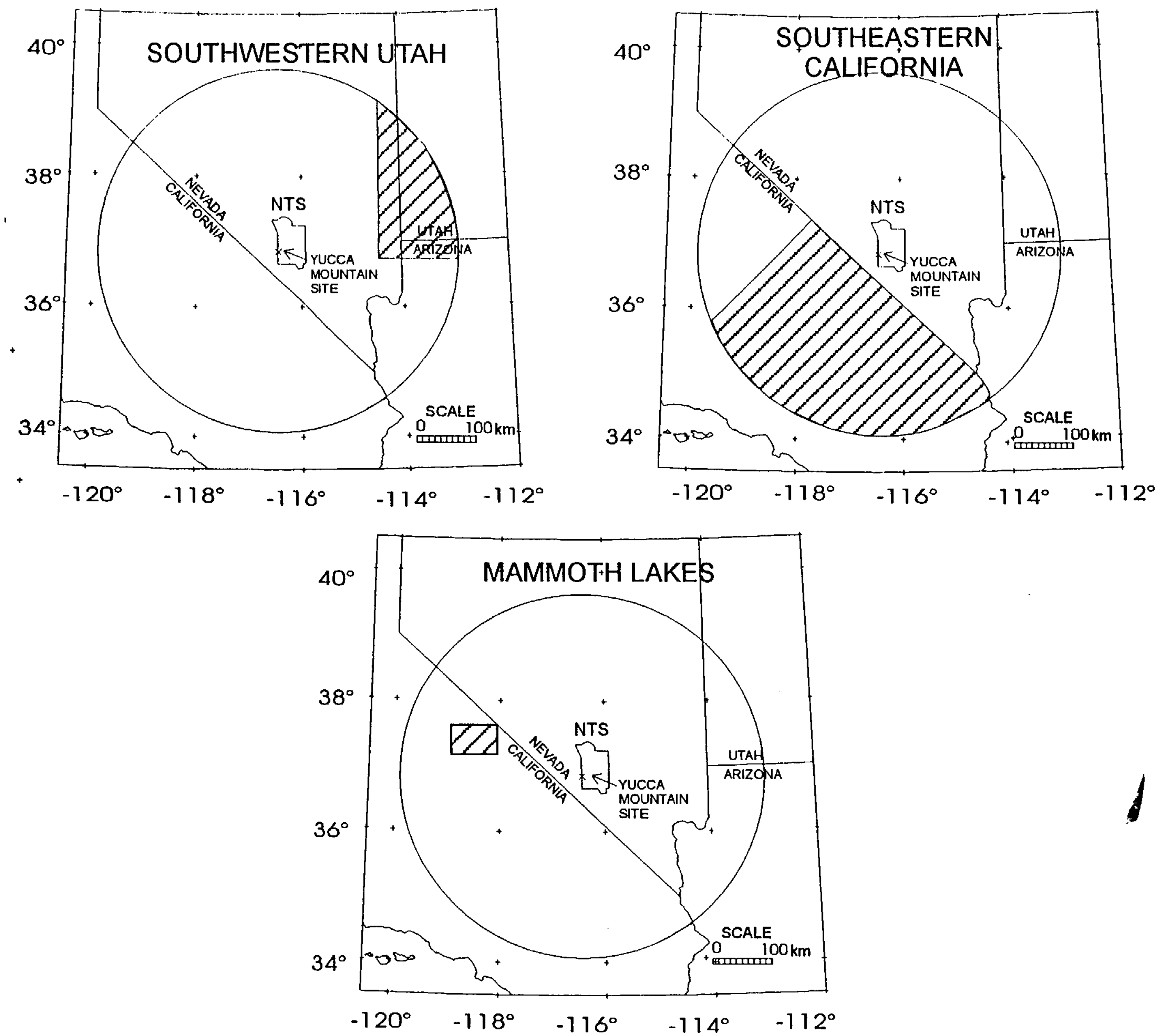

Project 5001A	Yucca Mountain Project	SUBREGIONS THAT COMPRISE THE 300-KM RADIUS YUCCA MOUNTAIN CATALOGUE (CONTD)	Figure 1
Woodward-Clyde Federal Services			

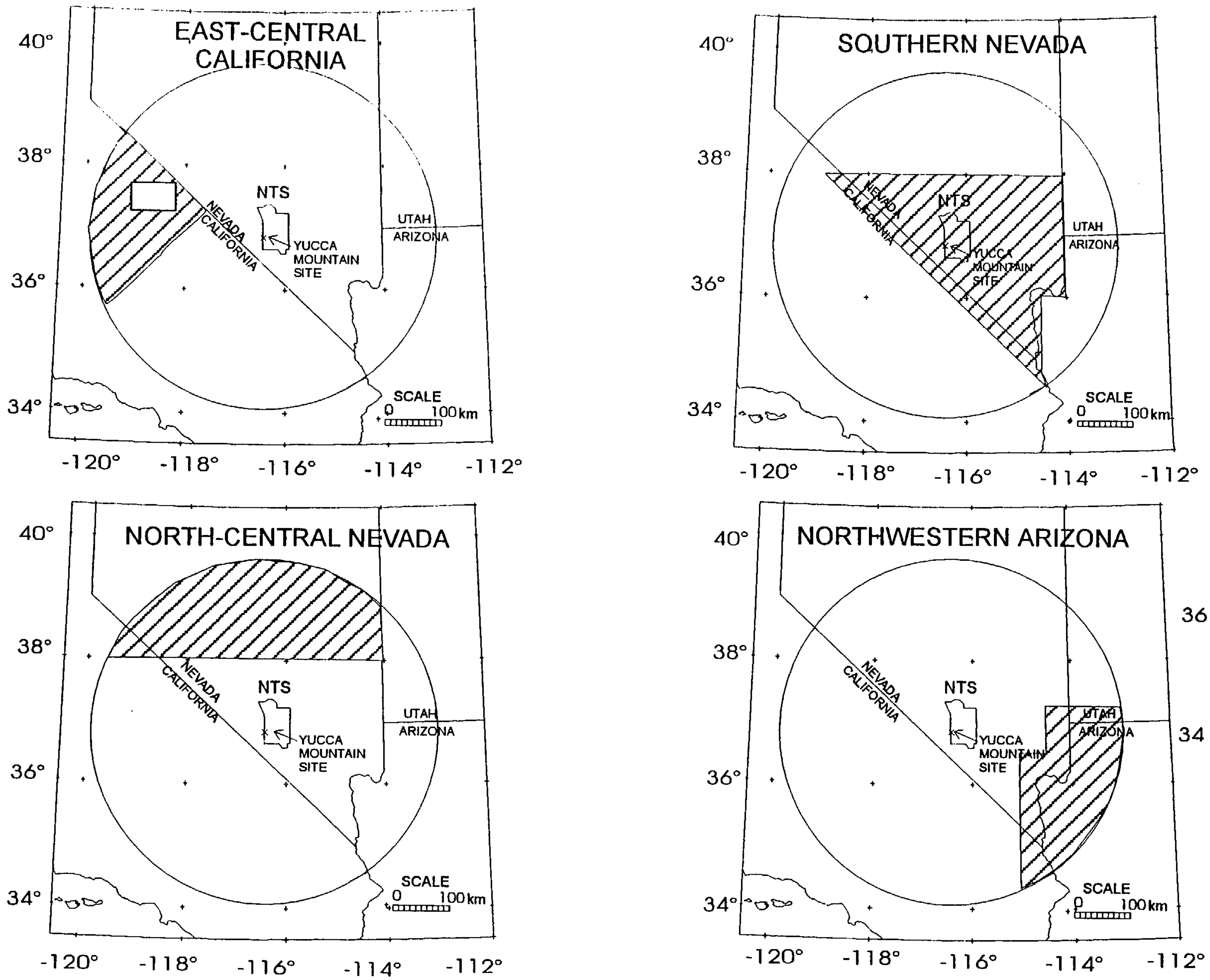

Project 5001A	Yucca Mountain Project	SUBREGIONS THAT COMPRISE THE 300-KM RADIUS YUCCA MOUNTAIN CATALOGUE	Figure 1 (continued)
Woodward-Clyde Federal Services			

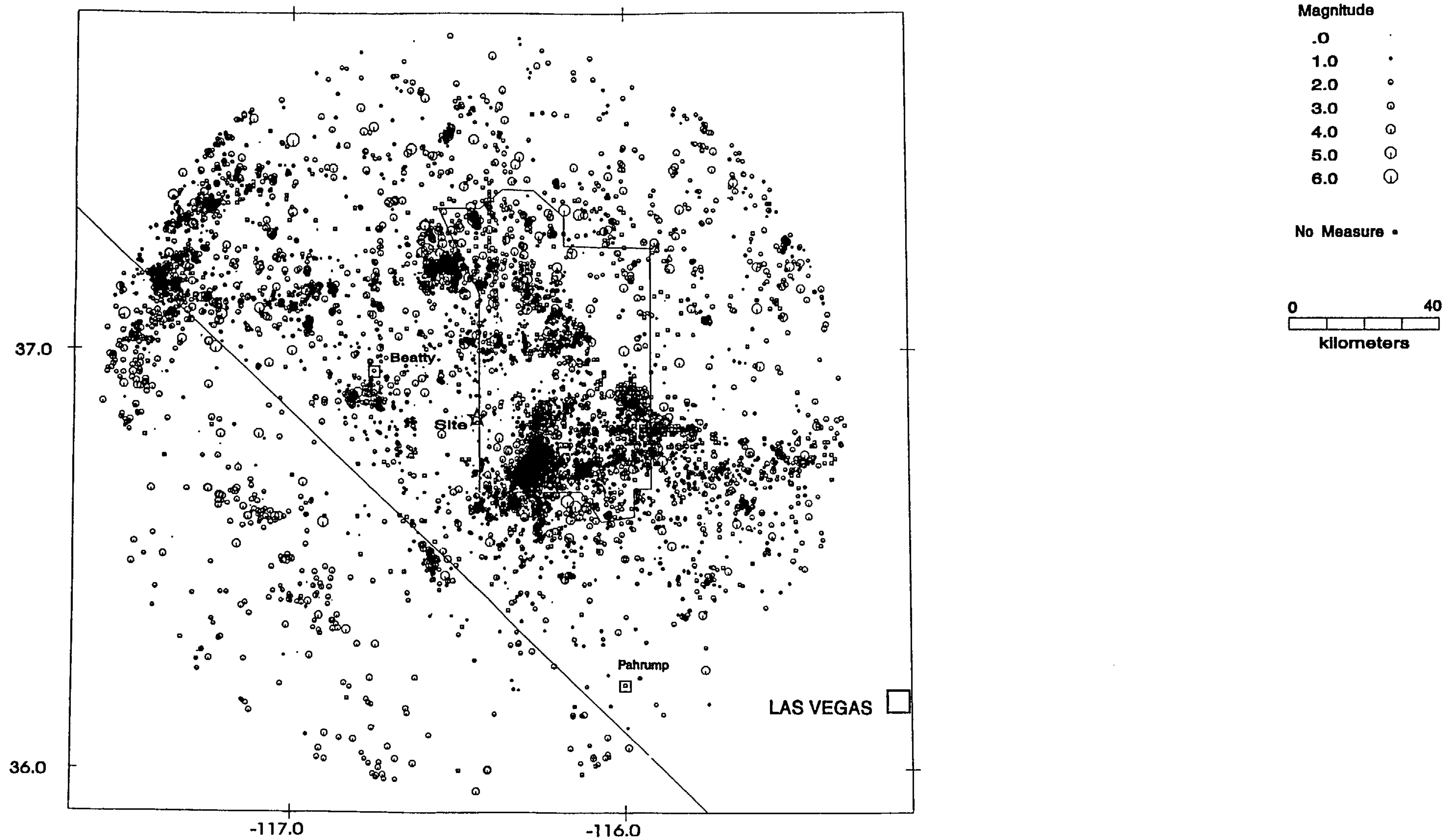

Project No. 5001A	YUCCA MOUNTAIN WHB	HISTORICAL SEISMICITY (1904 - 1994) WITHIN 100 KM OF THE YUCCA MOUNTAIN SITE	Figure
Woodward-Clyde Federal Services			

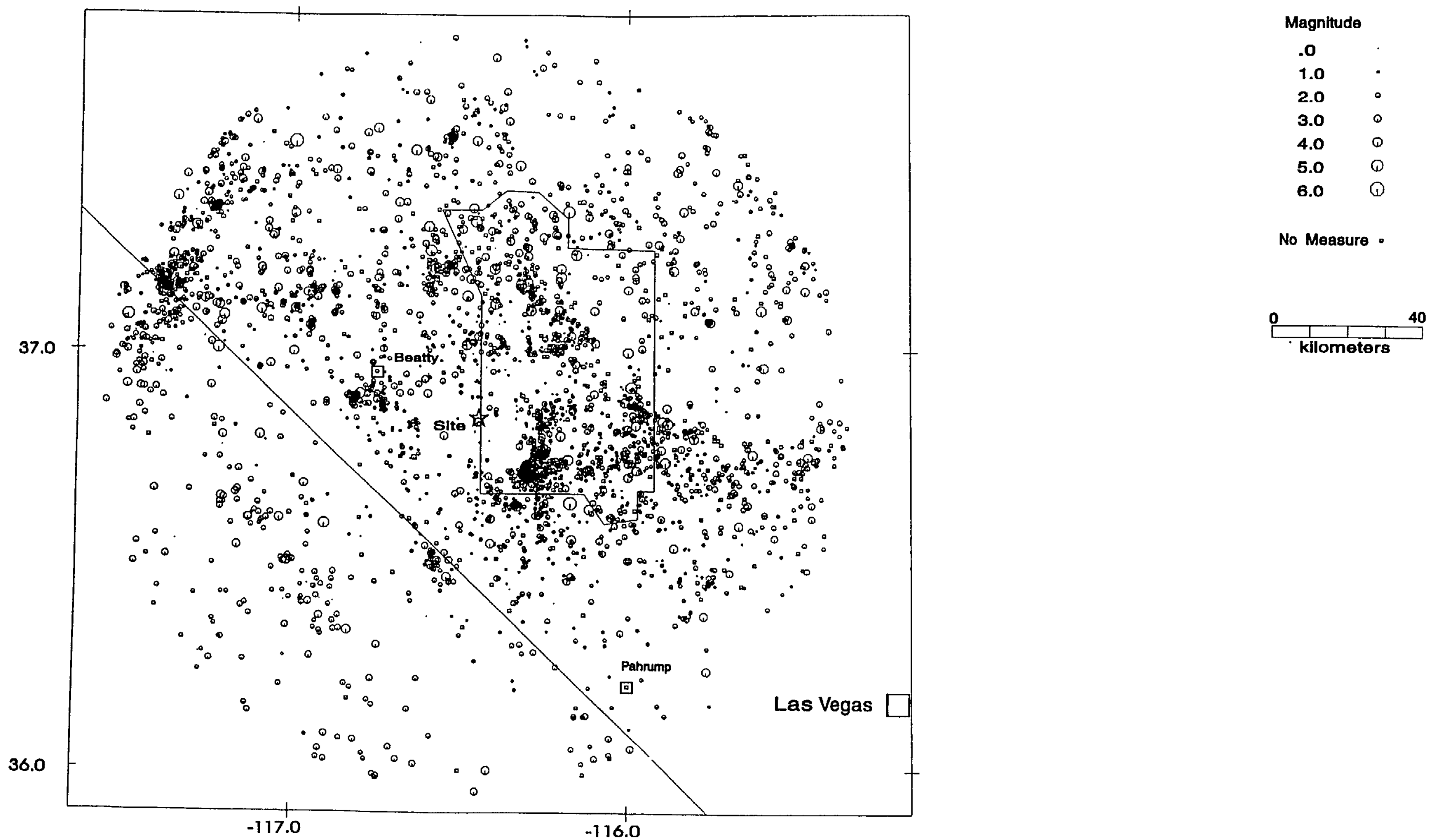

Project No. 5001A	YUCCA MOUNTAIN WHB	HISTORICAL SEISMICITY (1904-1994) WITHIN 100 KM OF THE YUCCA MOUNTAIN SITE USED IN RECURRENCE	Figure
Woodward-Clyde Federal Services			

CATALOGUE ISSUES

- Magnitude errors
- Common M_W scale
- Maximum intensity-magnitude conversion
- Removal of nuclear explosions, collapses, and quarry blasts
- Removal of nuclear explosion-induced aftershocks
- Removal of Lake Mead RIS?
- Completeness
- Declustering
- Definition of seismotectonic provinces

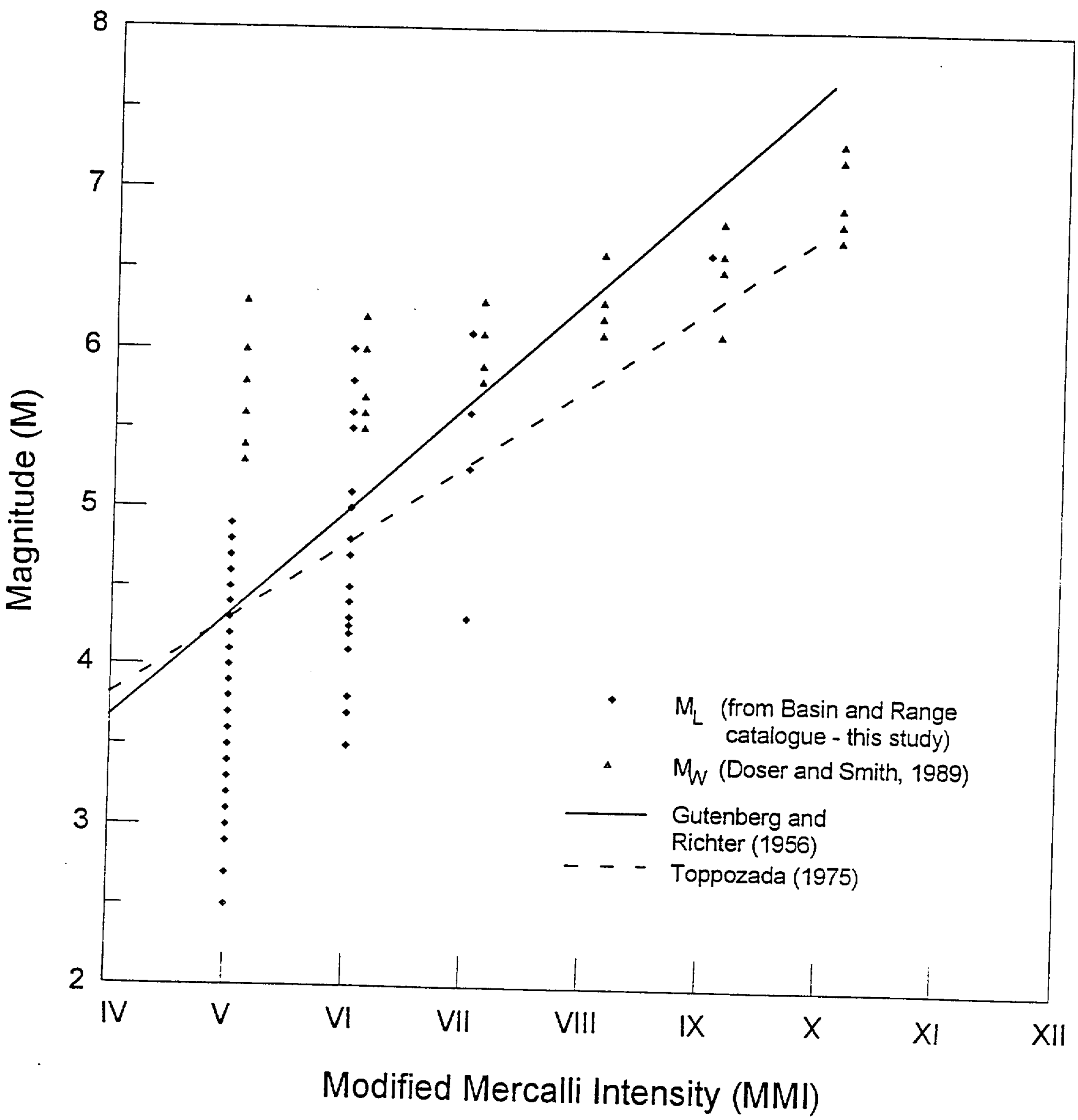

Project No.	Yucca Mountain Project	MAGNITUDE VS. INTENSITY FOR BASIN & RANGE EARTHQUAKES COMPARED TO TWO COMMONLY USED RELATIONSHIPS	Figure
Woodward-Clyde Federal Services			

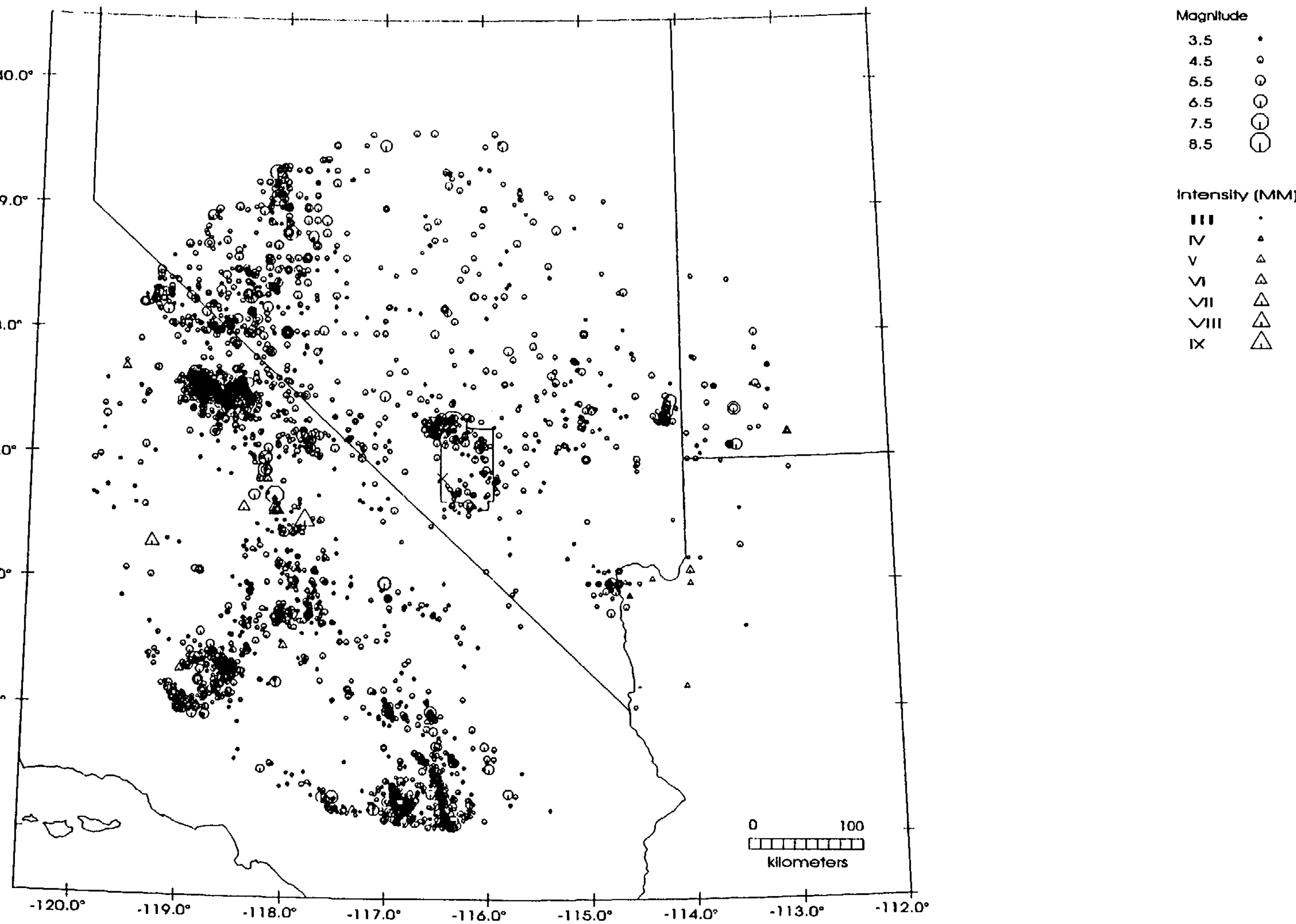

Project 5001A	Yucca Mountain Project	HISTORICAL SEISMICITY GREATER THAN M 3.5 OR MM III WITHIN THE 300-KM RADIUS YUCCA MOUNTAIN CATALOGUE (1868-1994)	Figure 2
Woodward-Clyde Federal Services			

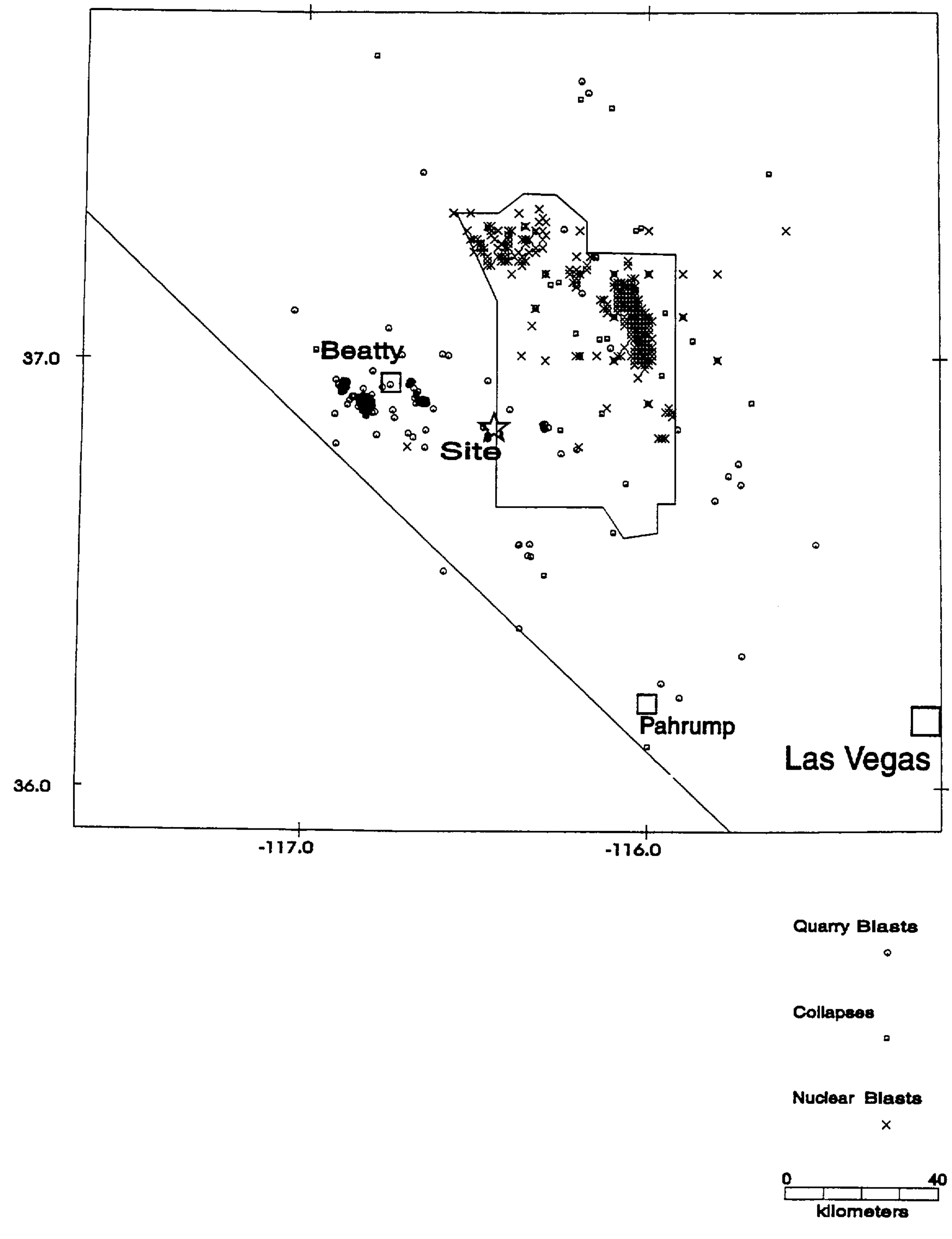

Project No. 5001A	YUCCA MOUNTAIN WHB	NUCLEAR BLASTS, CAVITY COLLAPSES AND QUARRY BLASTS	Figure
Woodward-Clyde Federal Services			

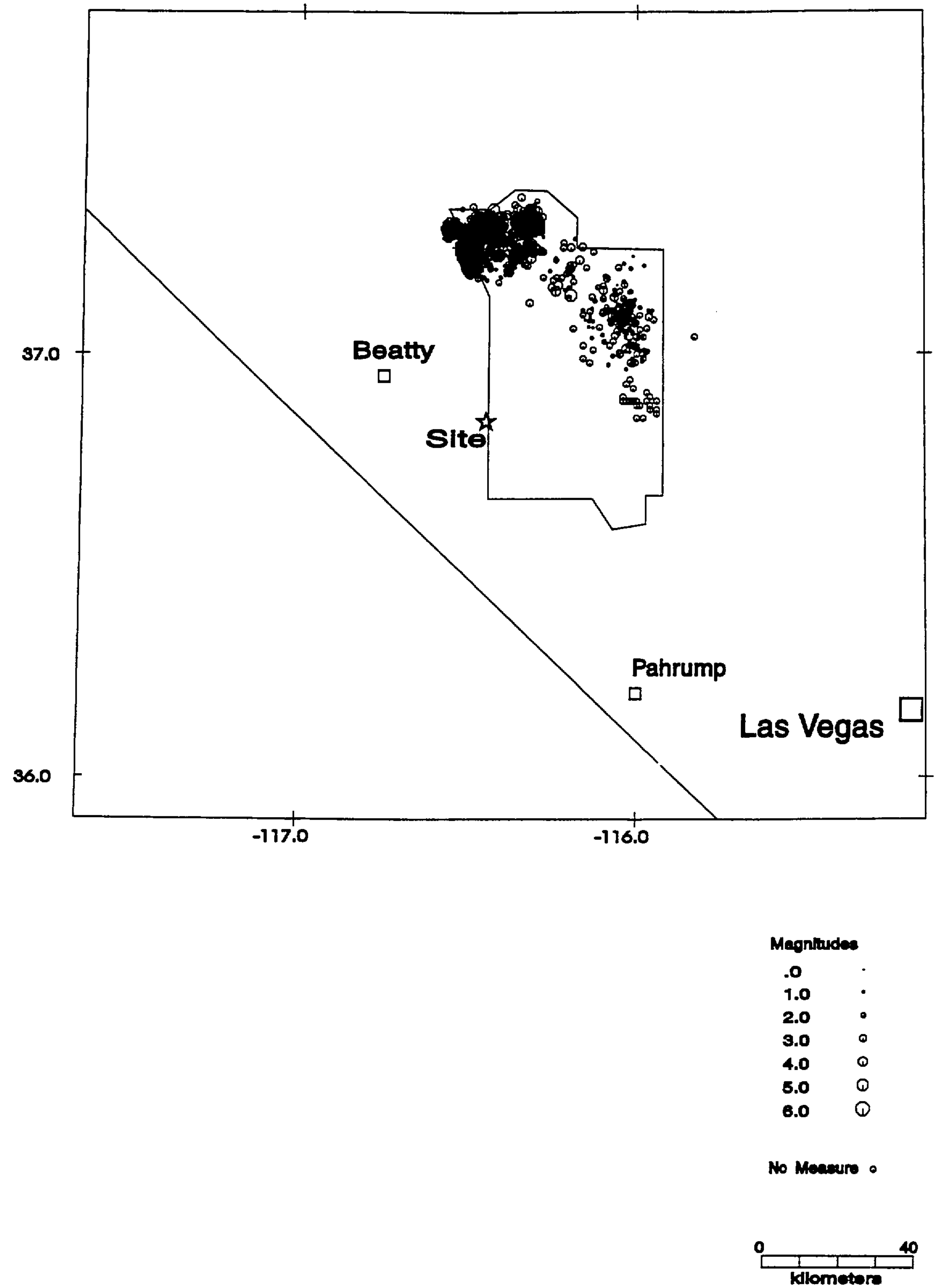

Project No. 5001A	YUCCA MOUNTAIN WHB	EARTHQUAKES DEPENDENT ON NUCLEAR BLASTS	Figure
Woodward-Clyde Federal Services			

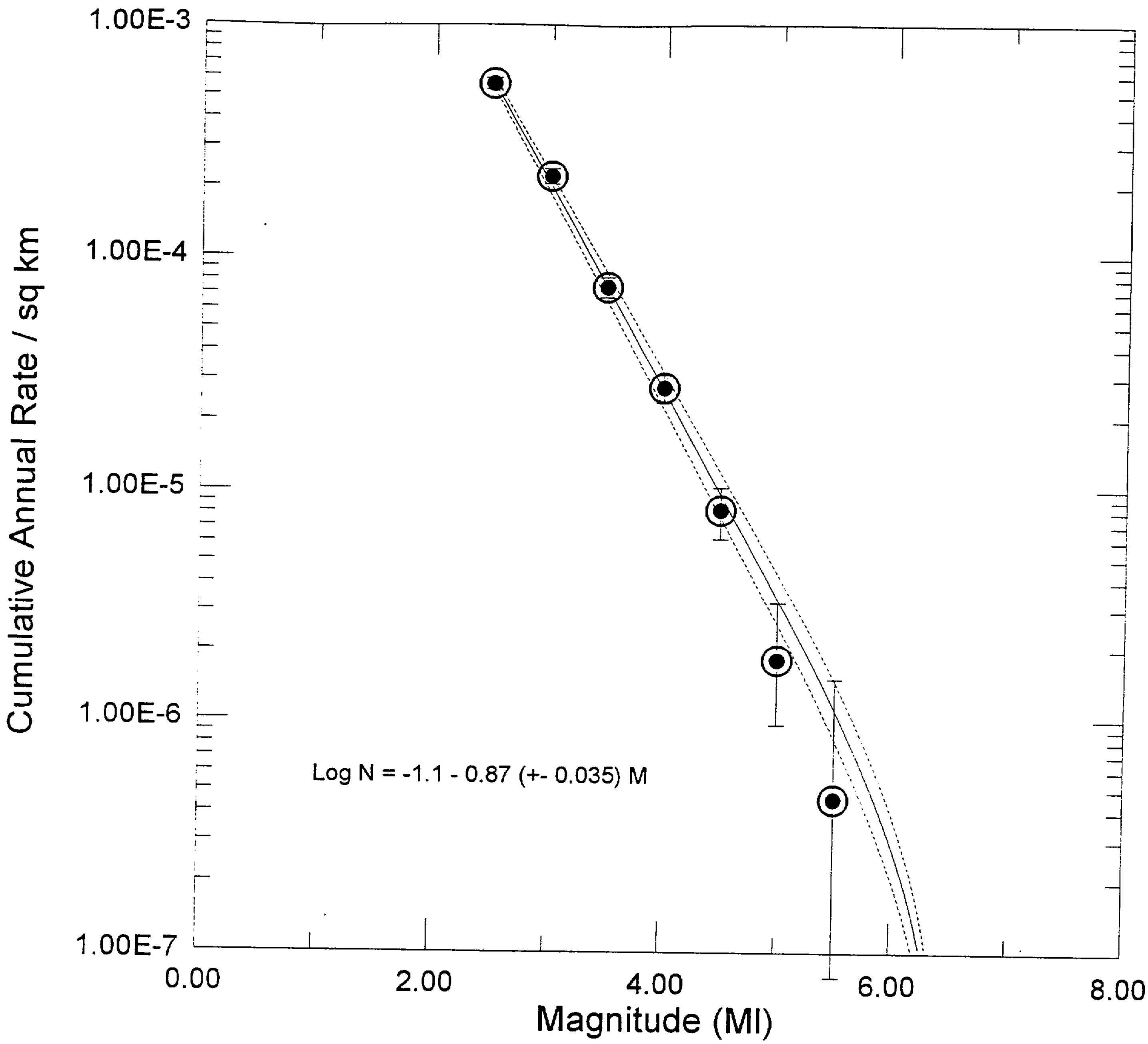

Recurrence curve for Yucca Mtn.
Using 1996 Yucca Mtn. Catalogue

YM-SSC Workshop #2

October 16-18, 1996

Methods for Assessing Fault Displacement Hazard

Robert Youngs
Geomatrix Consultants

Expression of Fault Rupture Hazard

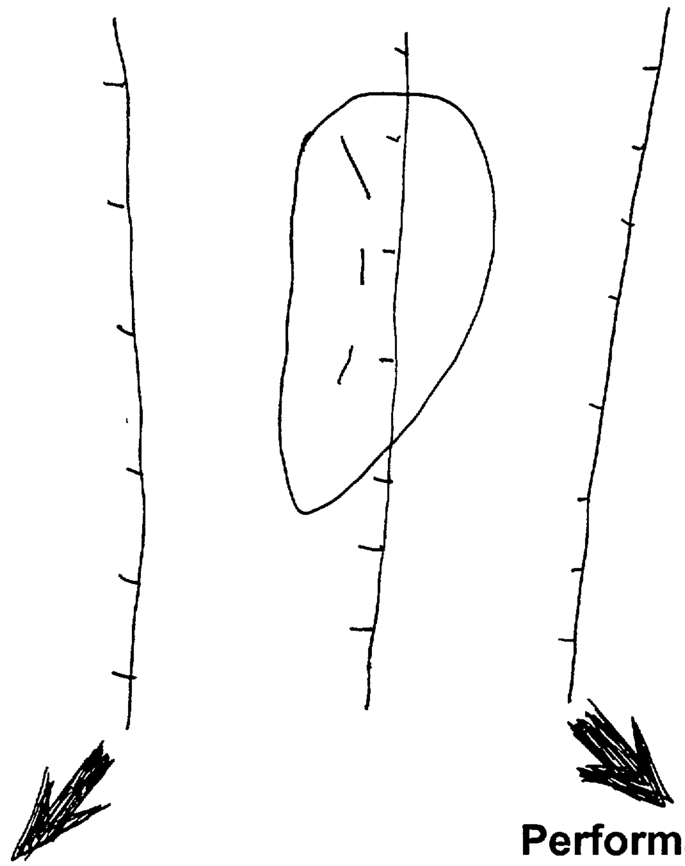

Design

Performance Assessment

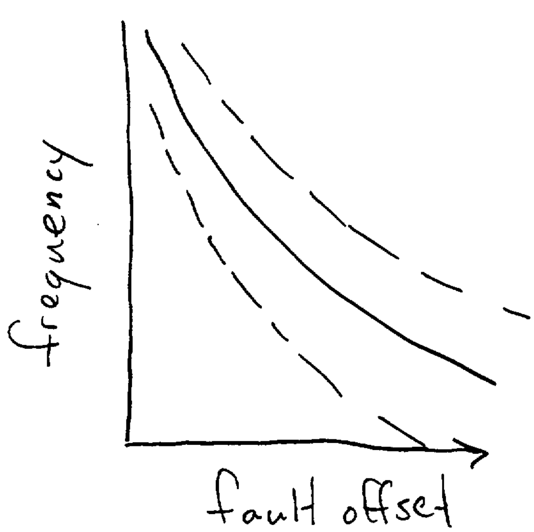

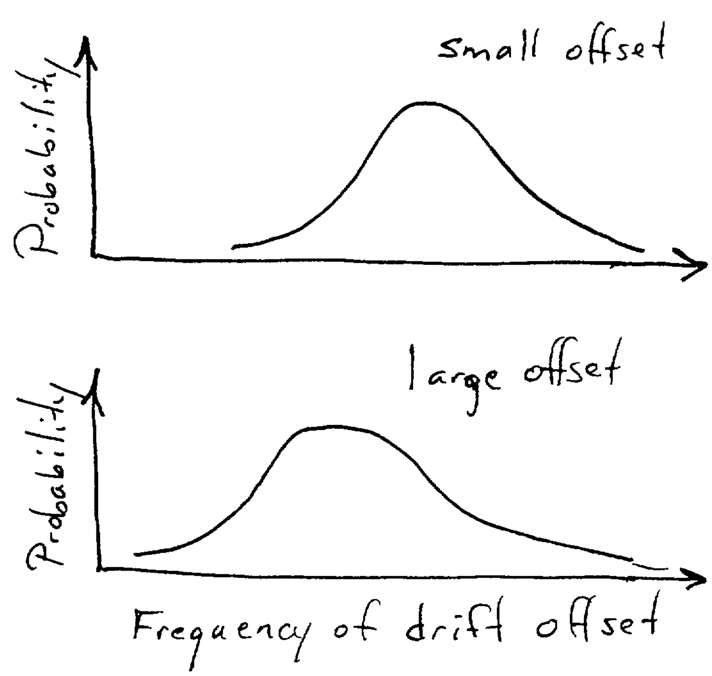

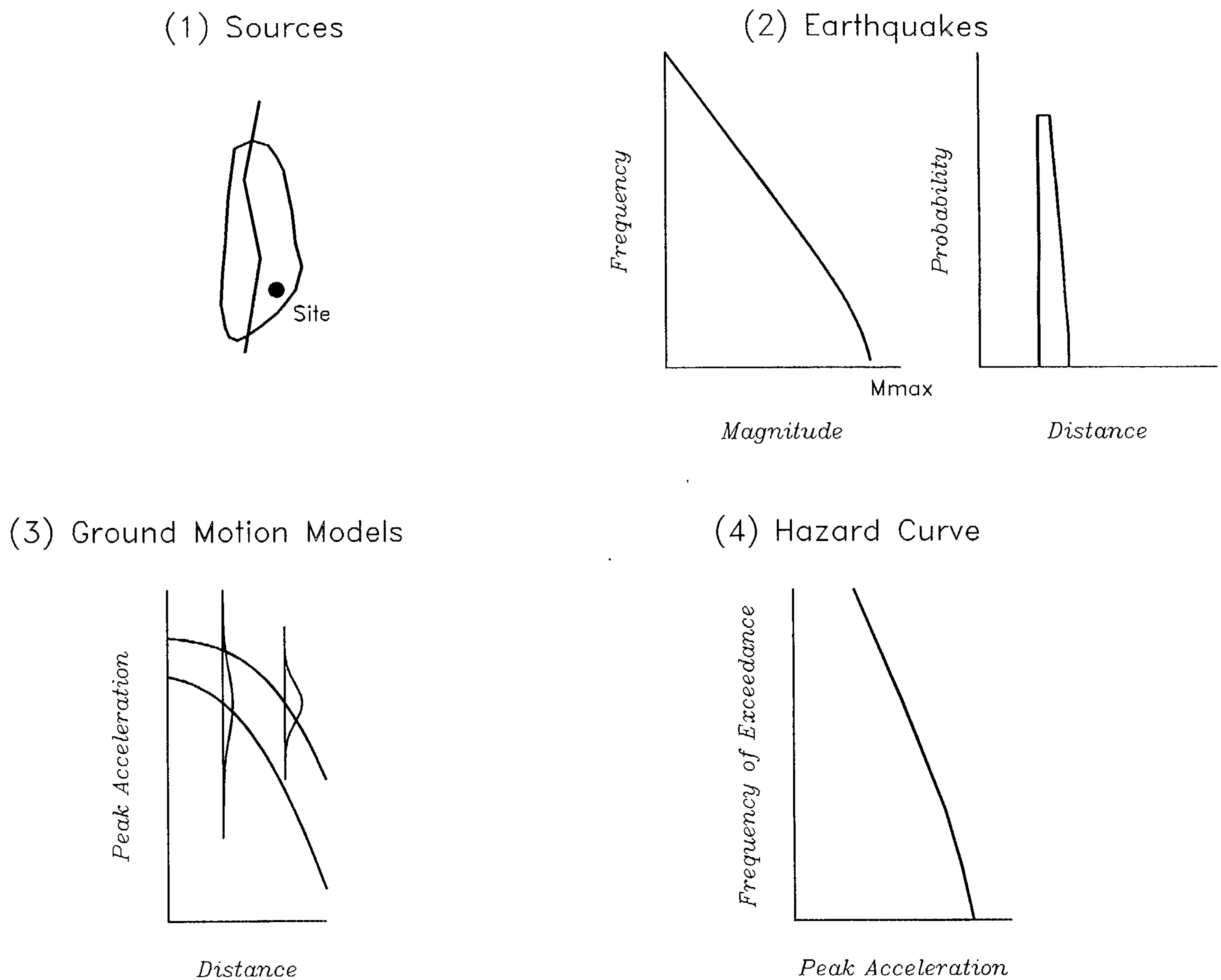

Schematic diagram of the components of PSHA for Ground Motion

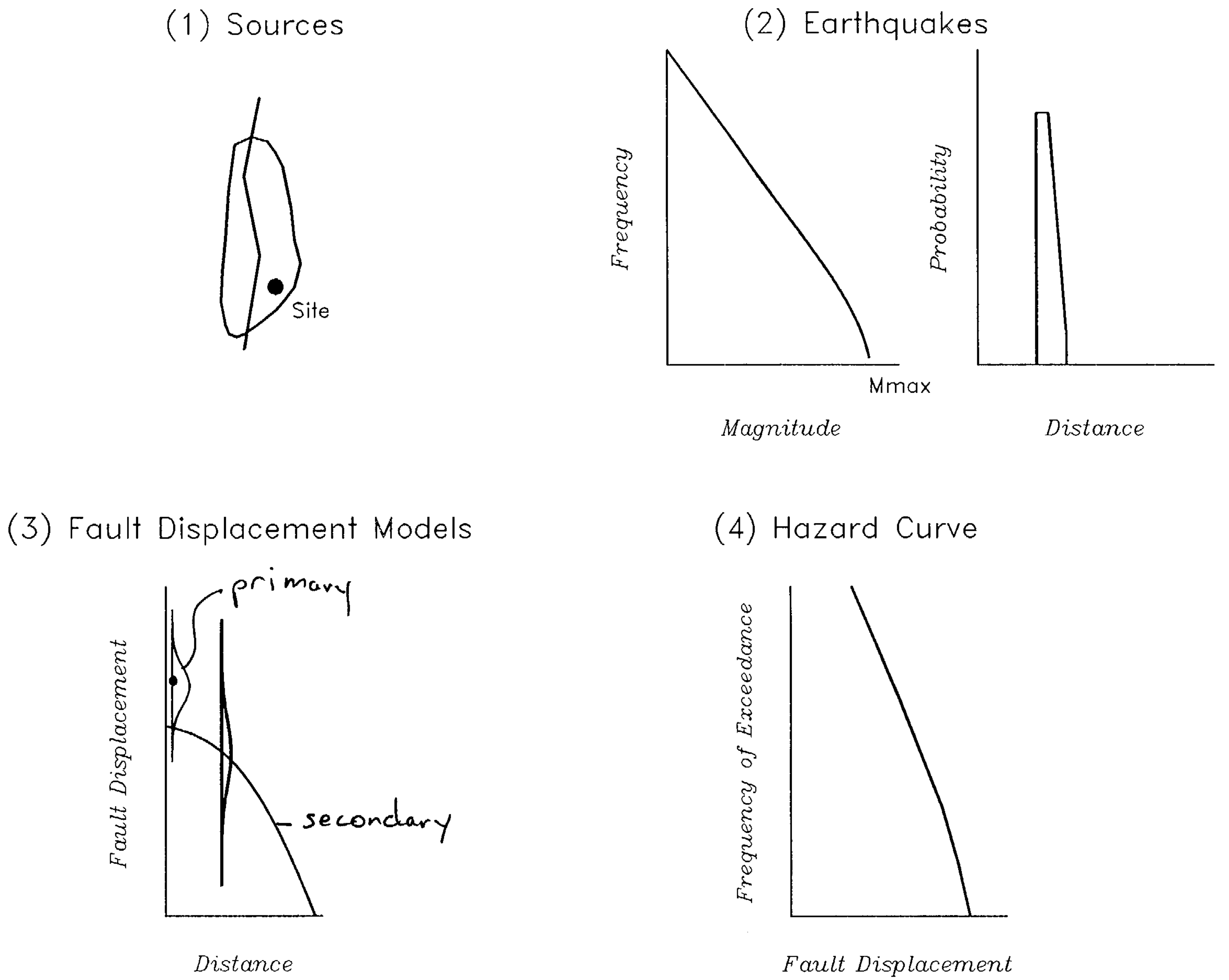

Schematic diagram of the components of PSHA for Fault Rupture

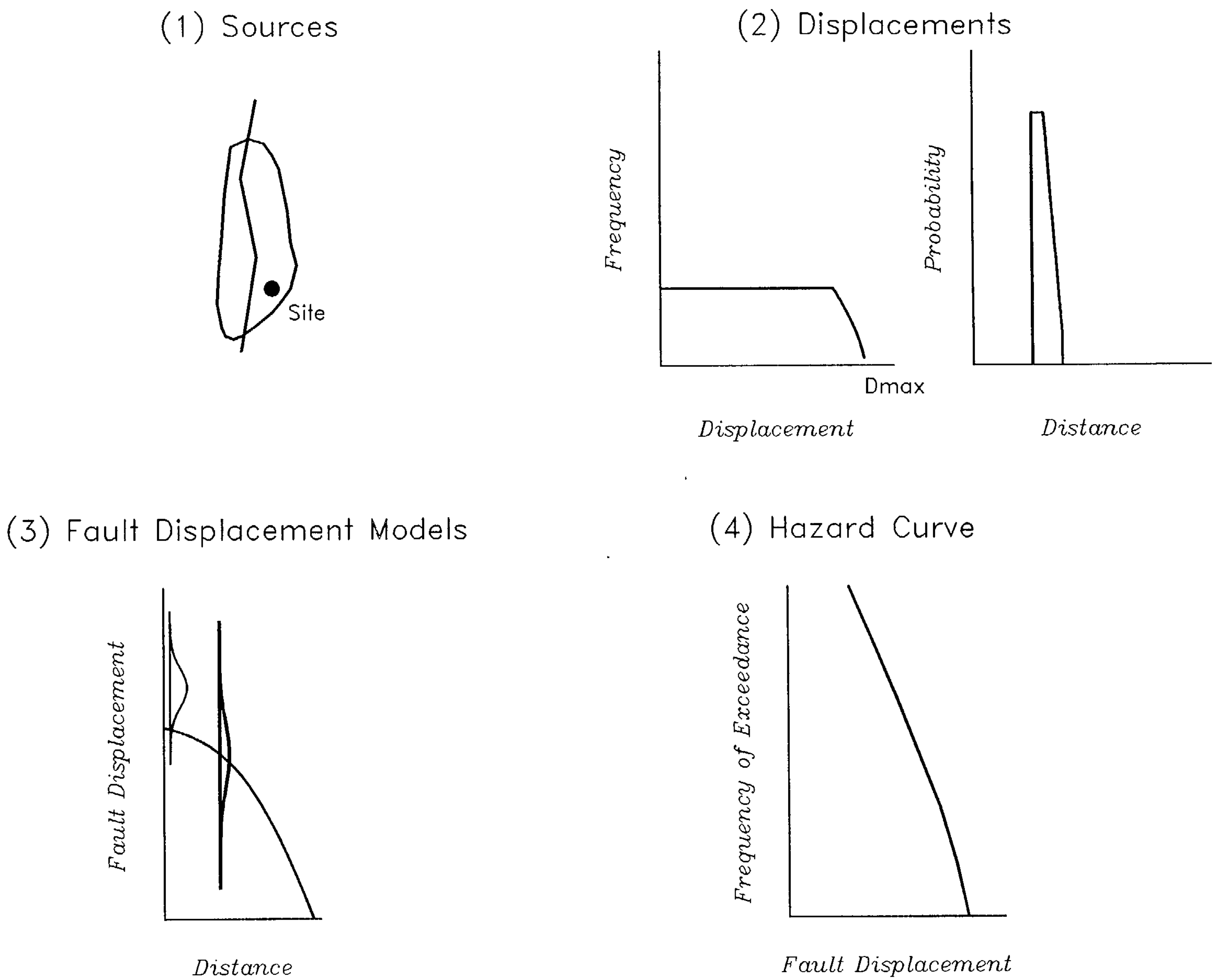

Schematic diagram of the components of PSHA for Fault Rupture

Approaches for characterizing displacement events

- Earthquake source model from ground motion hazard
- Direct modelling of observed displacements

Approaches for estimating freqency of events

- Geodetic Geologic fault slip rate
- Paleoseismic recurrence intervals
- strain rate

Approaches for estimating effects in repository

- Mapped faults and fractures only
- Mapped faults with random secondary rupture in a zone
- Random rupture in a zone

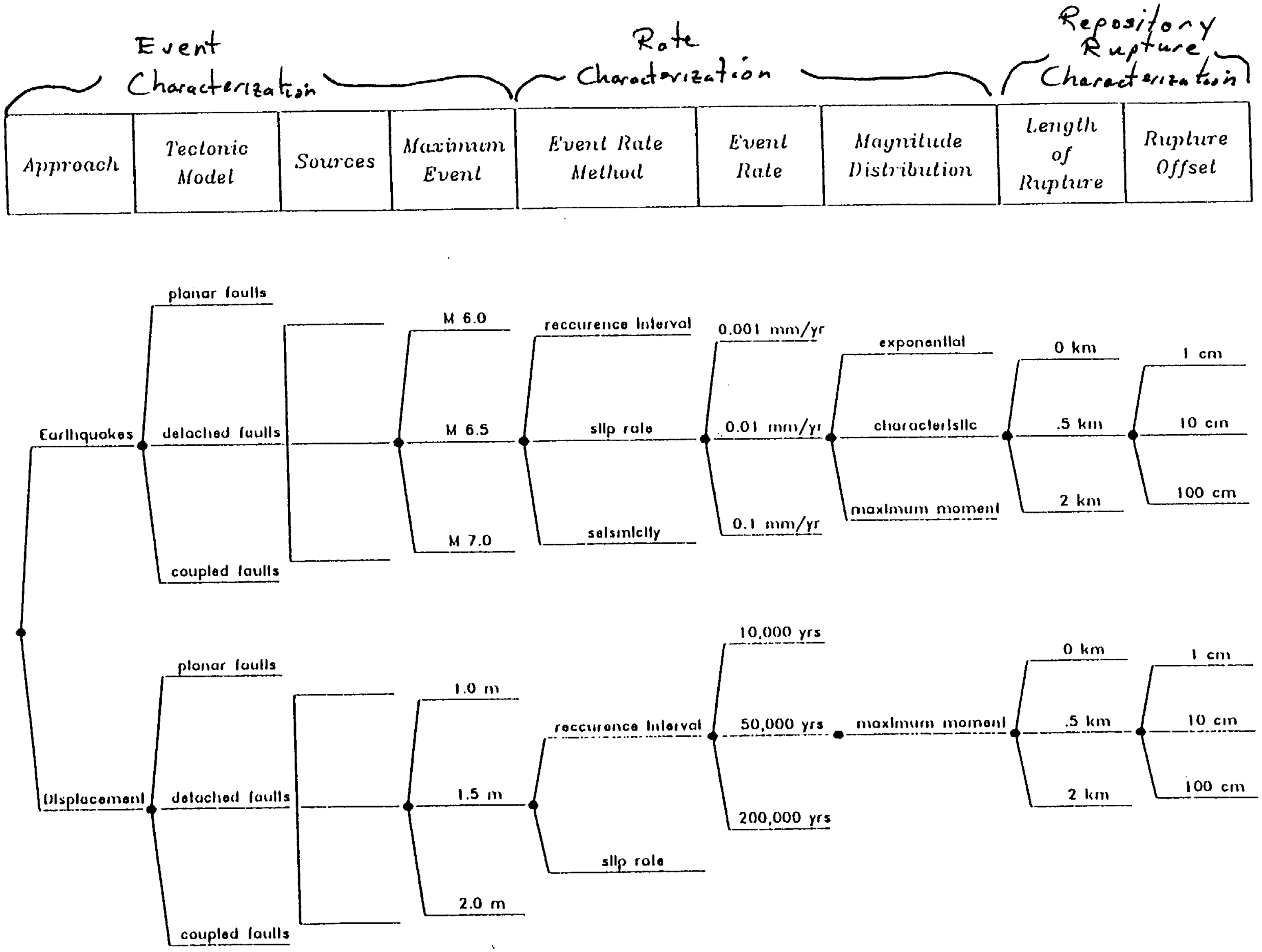

Figure 1 Schematic logic tree for expert elicitations and aggregated fault rupture hazard model. Each node of the logic tree represents a component of the model. Each branch of the logic tree represents an alternative parameter of each component of the model. (Parameter values shown are for illustration purposes only). Each branch is assigned a relative weight that specifies the relative likelihood that each parameter value is the correct value.

"Information" on Rupture Distribution

- Mapped larger faults that may be "seismogenic"
- Mapped minor faults
- Fault density
- Analogs
- Generalization of analogs into empirical models

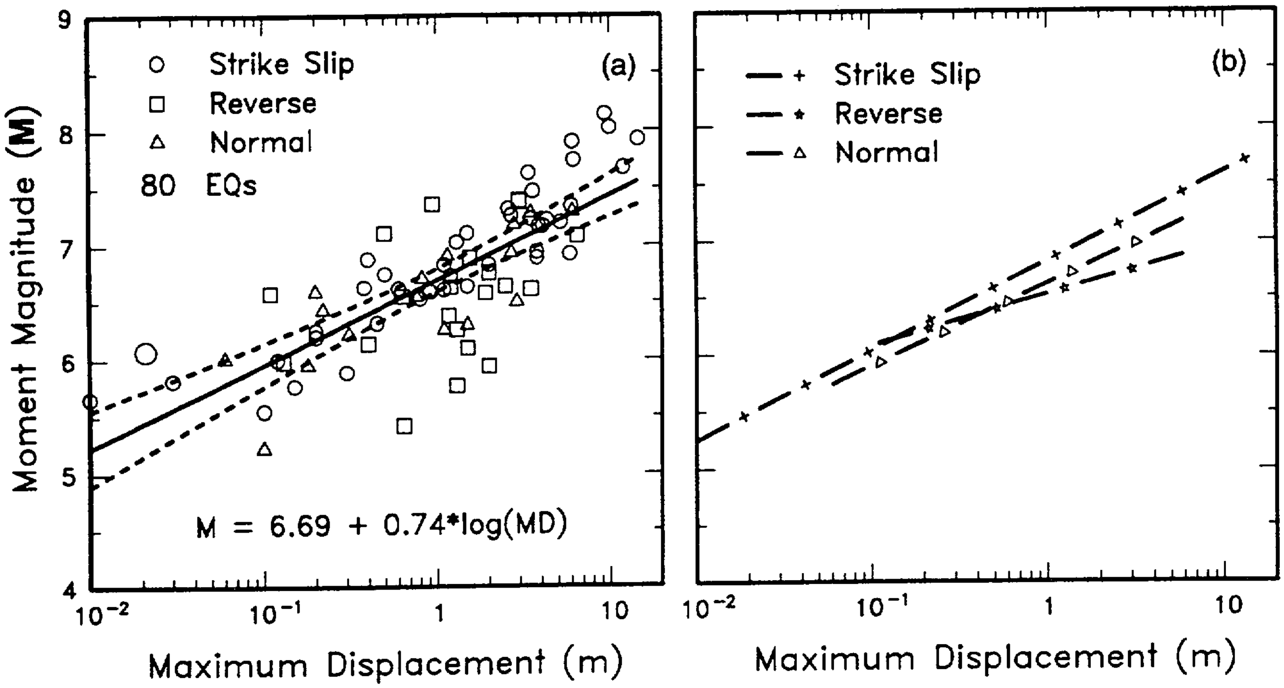

Figure 10. (a) Regression of maximum surface displacement on magnitude (M). Regression line shown for all-slip-type relationship. Short dashed line indicates 95% confidence interval. (b) Regression lines for strike-slip, reverse, and normal-slip relationships. See Table 2 for regression coefficients. Length of regression lines shows the range of data for each relationship.

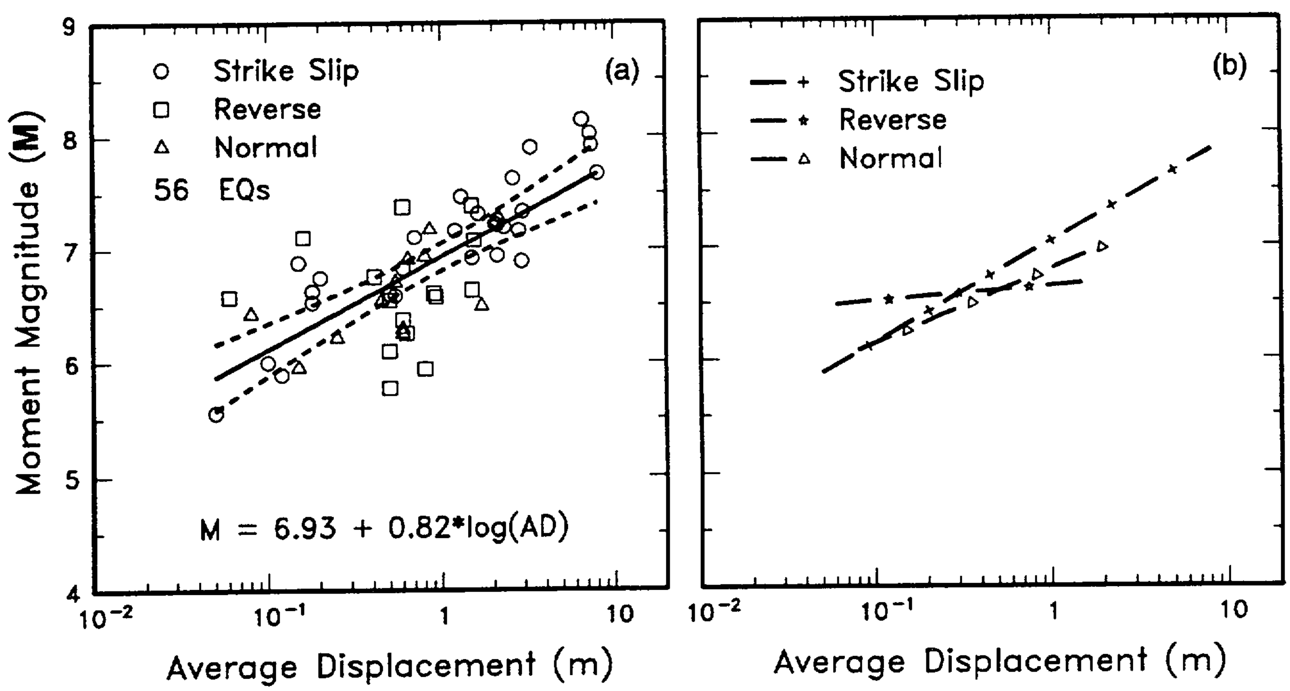

Figure 11. (a) Regression of average surface displacement on magnitude (M). Regression line shown for all-slip-type relationship. Short dashed line indicates 95% confidence interval. (b) Regression lines for strike-slip, reverse, and normal-slip relationships. See Table 2 for regression coefficients. Length of regression lines shows the range of data for each relationship.

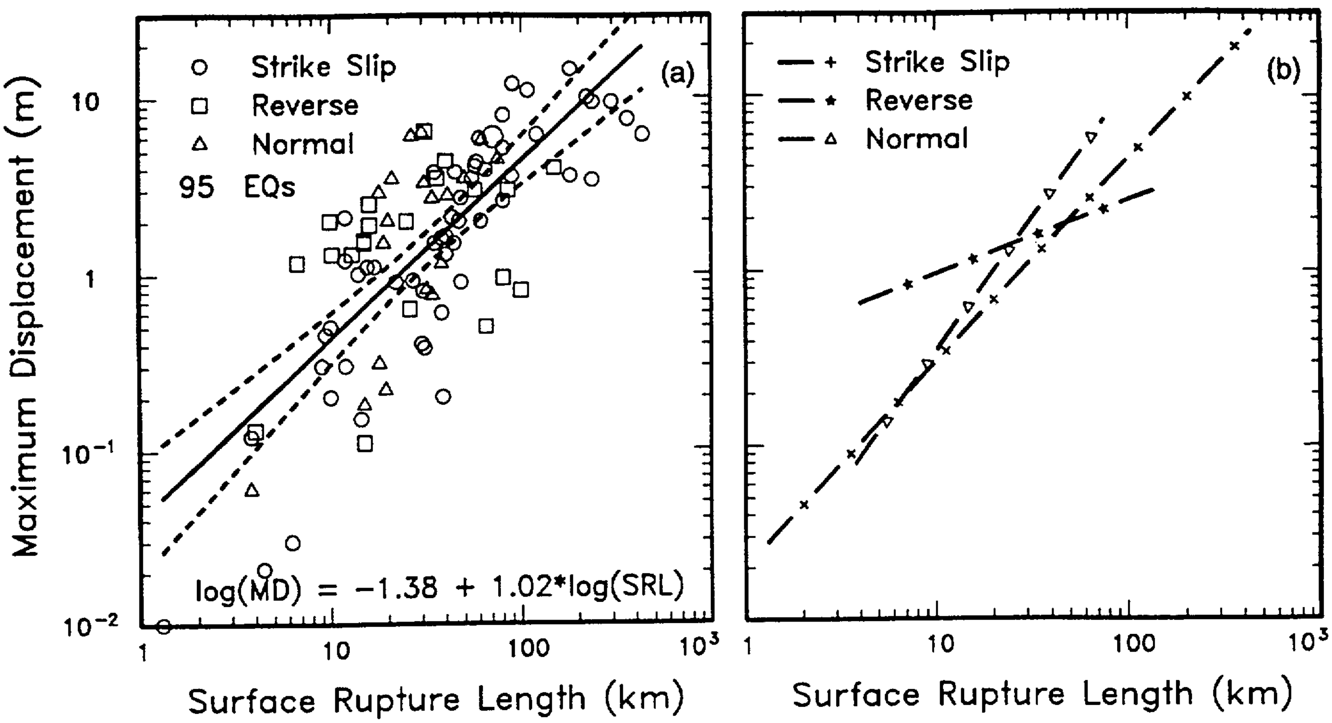

Figure 12. (a) Regression of surface rupture length on maximum displacement. Regression line shown for all-slip-type relationship. Short dashed line indicates 95% confidence interval. (b) Regression lines for strike-slip, reverse, and normal-slip relationships. See Table 2 for regression coefficients. Length of regression lines shows the range of data for each relationship.

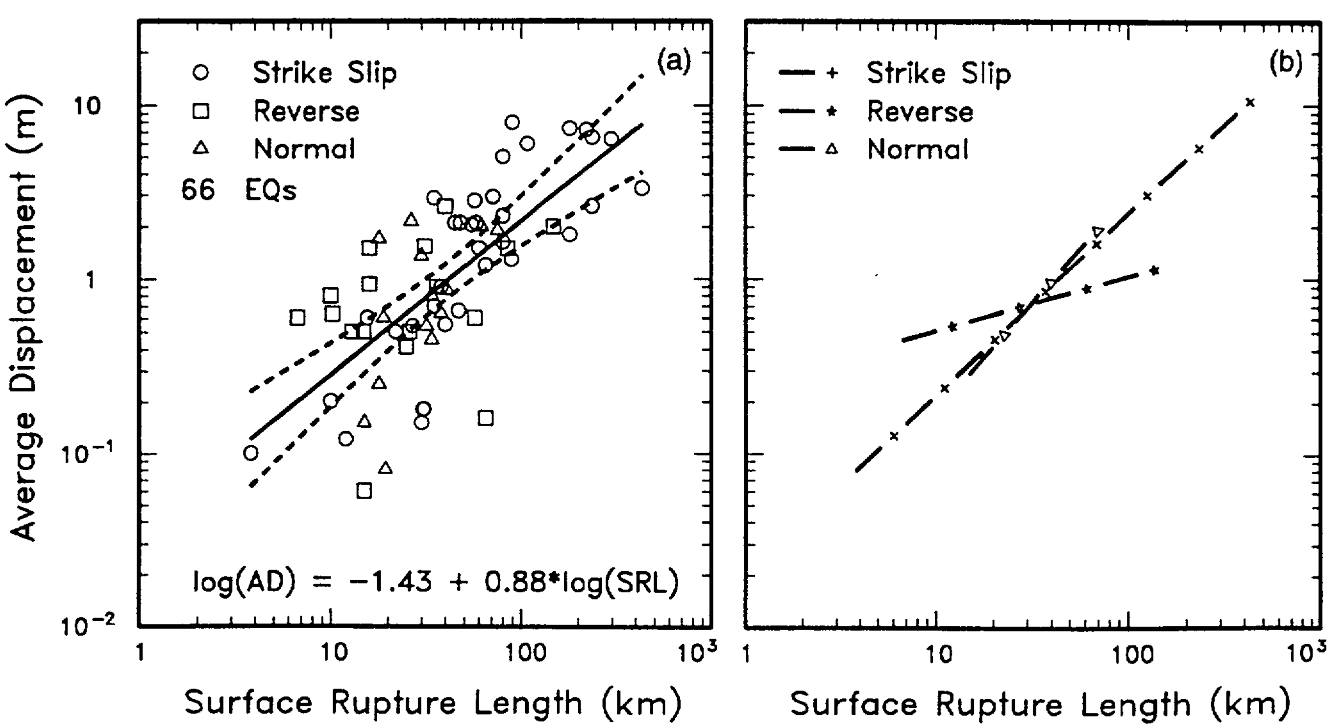

Figure 13. (a) Regression of surface rupture length on average displacement. Regression line shown for all-slip-type relationship. Short dashed line indicates 95% confidence interval. (b) Regression lines for strike-slip, reverse, and normal-slip relationships. See Table 2 for regression coefficients. Length of regression lines shows the range of data for each relationship.

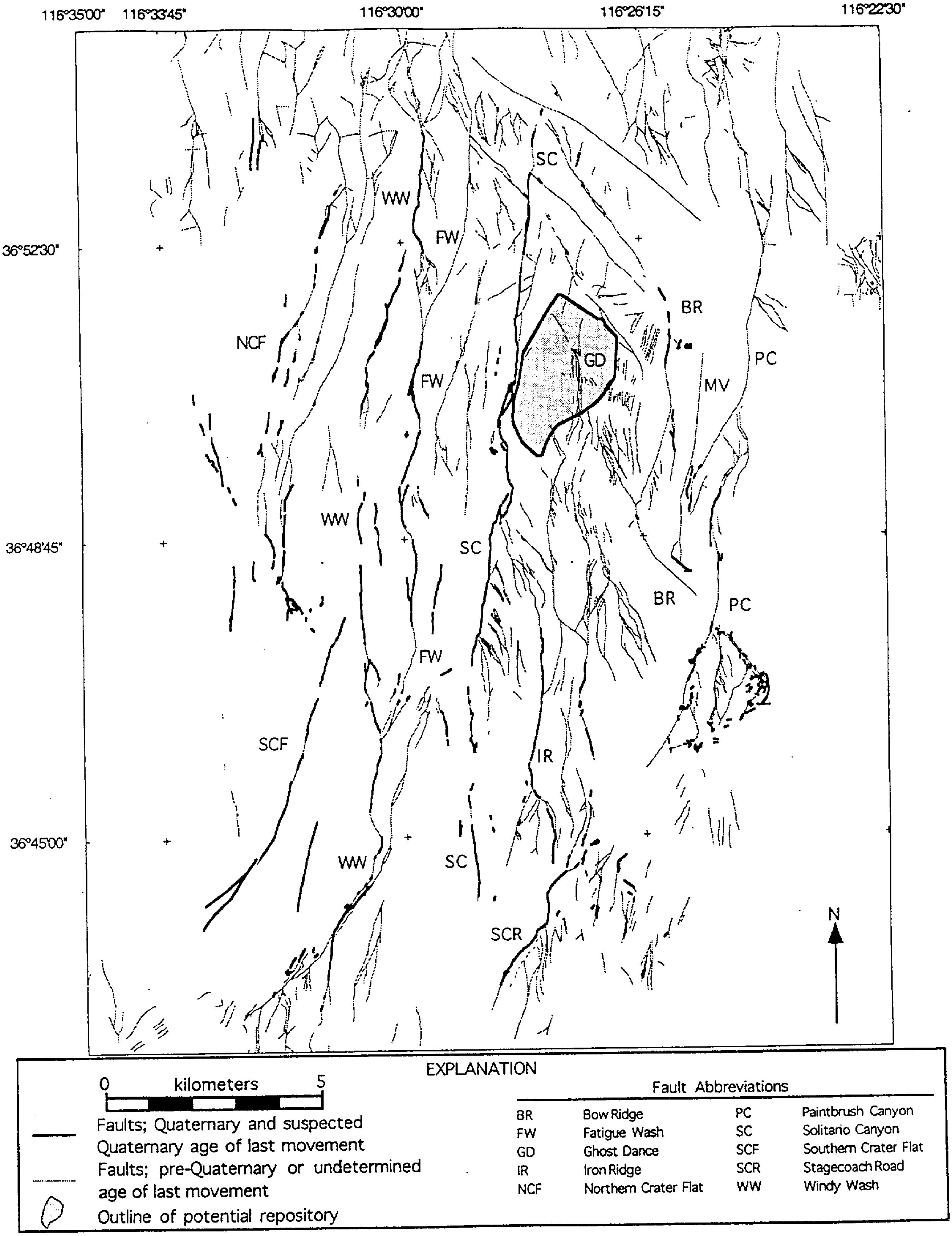

Figure 9-17. Map of faults at Yucca Mountain and proposed sites of potential repository and surface facilities. Simplified from Simonds and others (1995).

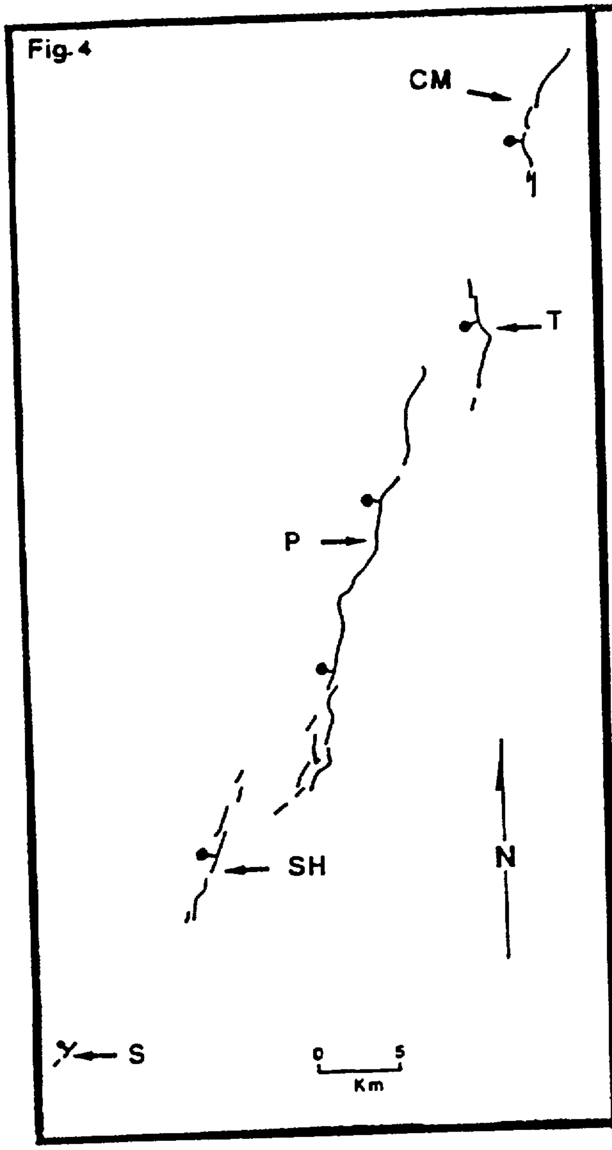

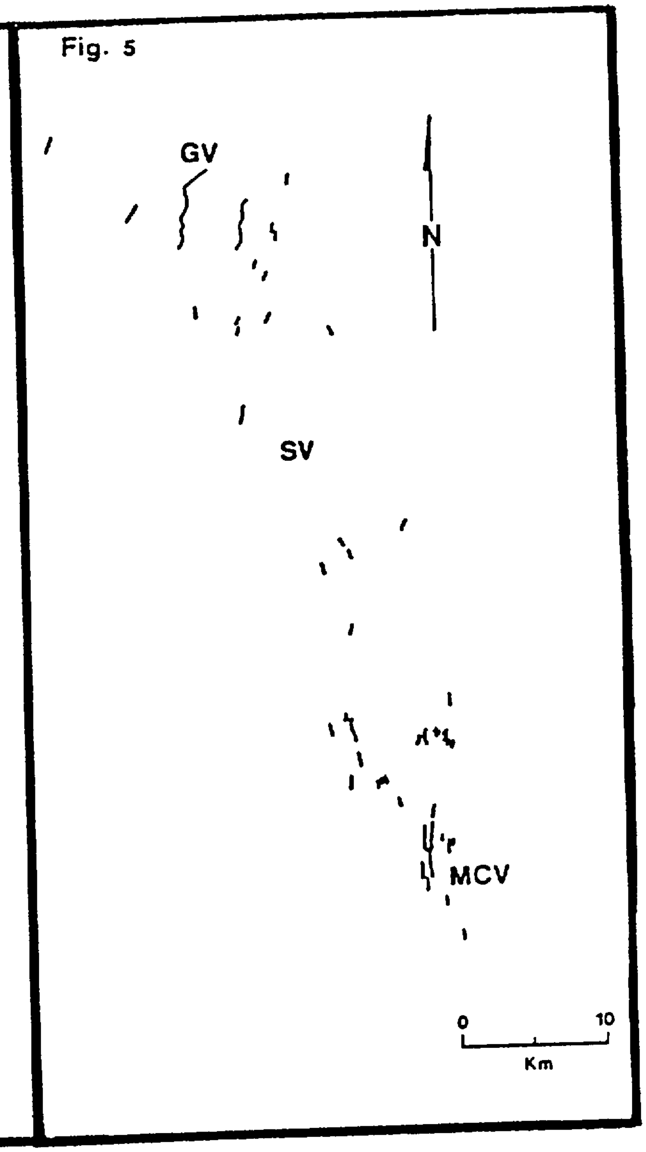

De Polo et al., 1990

Figure 4. 1915 Pleasant Valley (from Wallace, 1984), CM=China Mountain scarp, P=Pearce scarp, S=Stillwater scarp, SH=Sou Hills scarp, T=Tobin scarp.

Figure 5. 1932 Cedar Mountain (from Gianella and Calleghan, 1934), GV=Gabbs Valley, MCV=Monte Cristo Valley, SV=Stewart Valley.

Example Application

- Identify sources of "primary" rupture

- Estimate length and amount of offset for primary rupture

- Estimate extent and amount of "secondary" rupture
  - size of zone of faulting
  - length of secondary faulting
  - amount of secondary offset

8

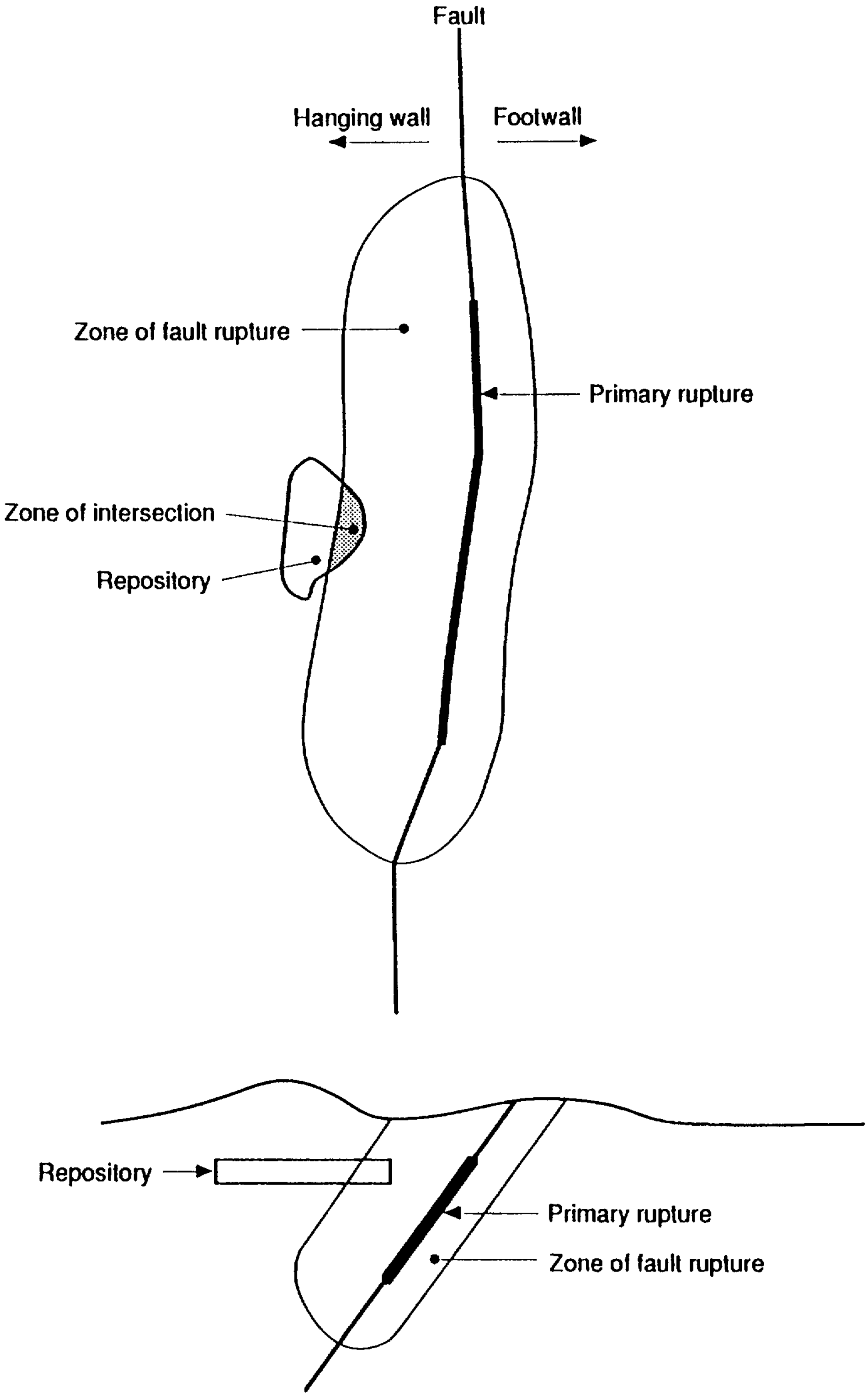

1504/zonefaultrupture

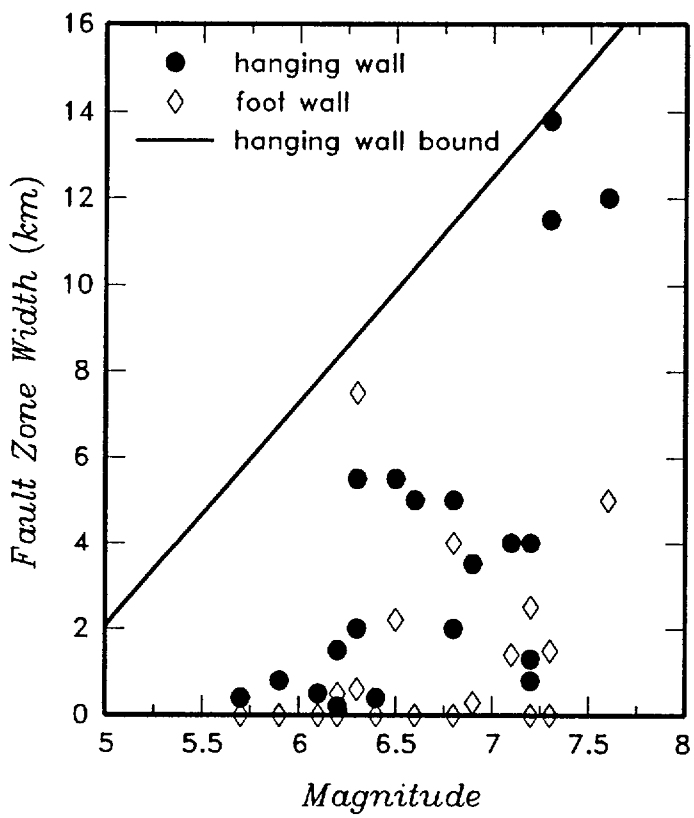
hanging wall
foot wall
hanging wall bound
Fault Zone Width (km)
Magnitude
0
2
4
6
8
10
12
14
16
5
5.5
6
6.5
7
7.5
8

f5

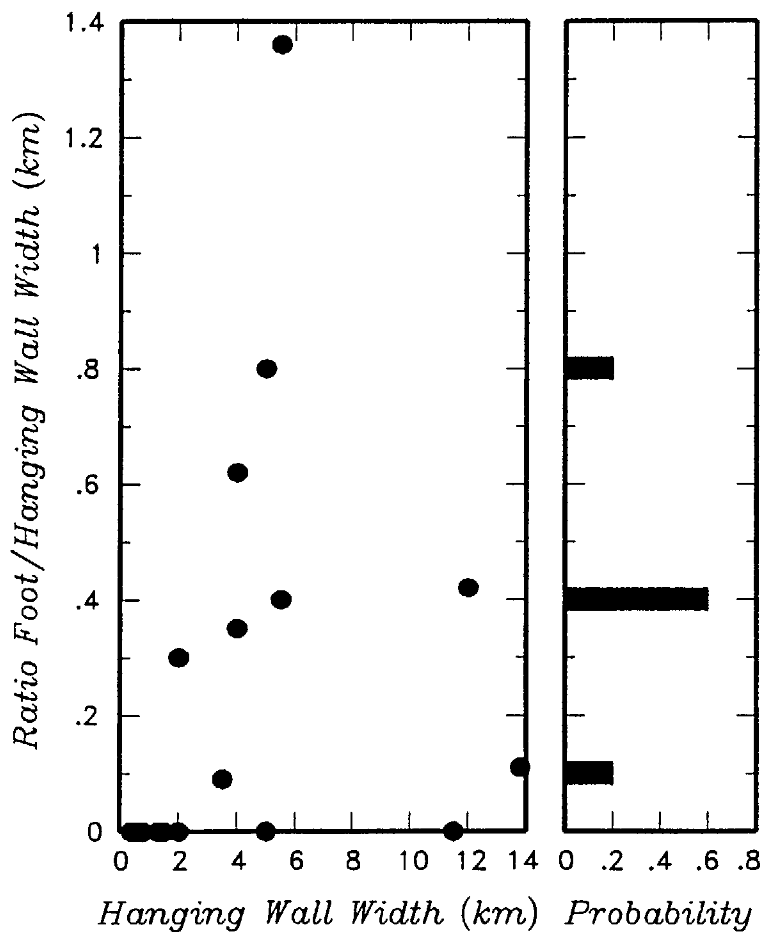

Ratio Foot/Hanging Wall Width (km)
1.4
1.2
1
.8
.6
.4
.2
0
0 2 4 6 8 10 12 14
Hanging Wall Width (km)
0 .2 .4 .6 .8
Probability

f 6

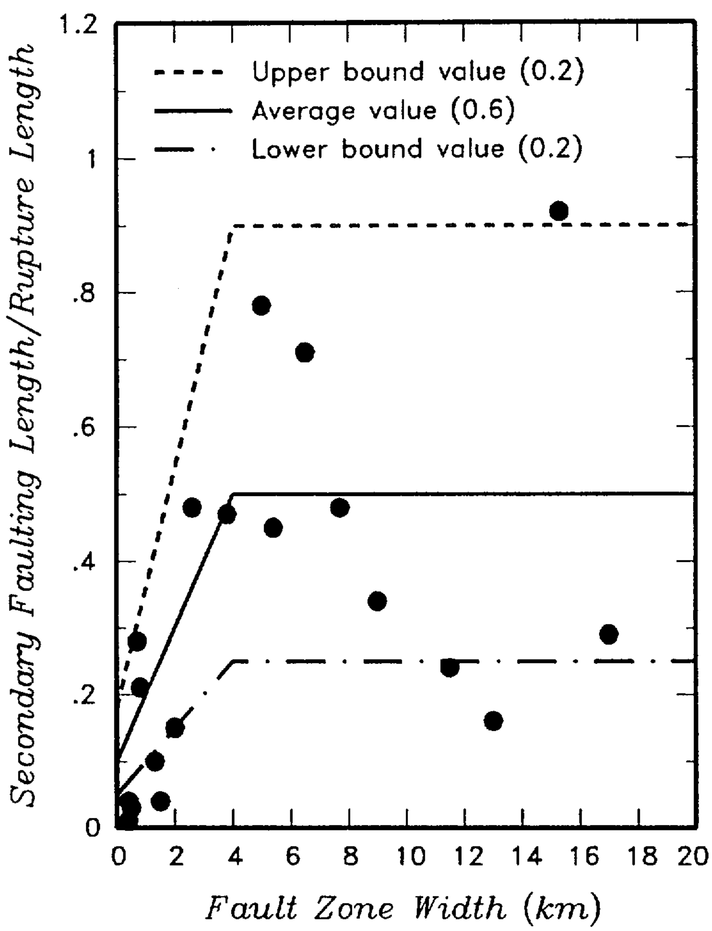
Upper bound value (0.2)
Average value (0.6)
Lower bound value (0.2)
Secondary Faulting Length/Rupture Length
Fault Zone Width (km)
1.2
1
.8
.6
.4
.2
0
0 2 4 6 8 10 12 14 16 18 20

f 7

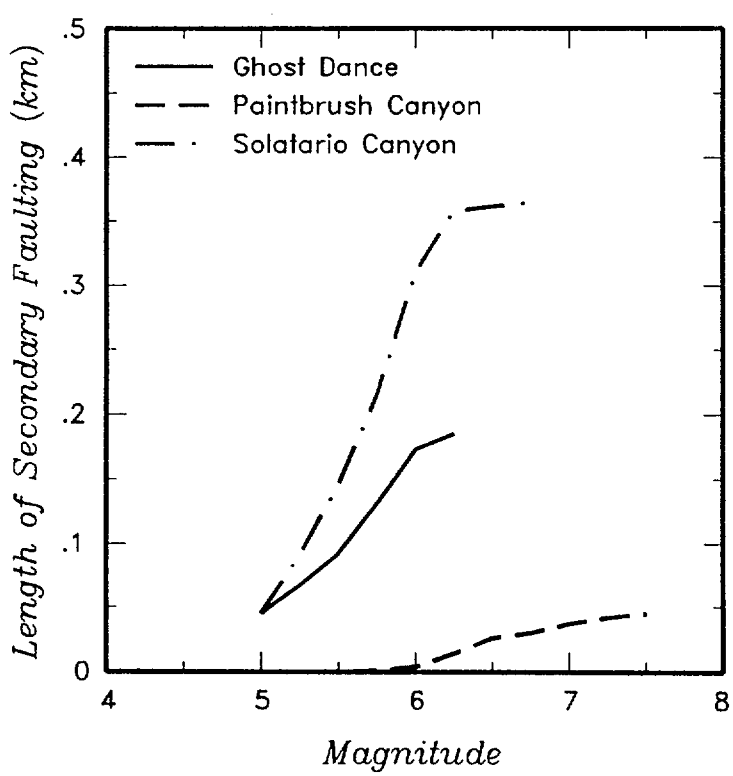

Ghost Dance
Paintbrush Canyon
Solatario Canyon
Length of Secondary Faulting (km)
Magnitude
0
.1
.2
.3
.4
.5
4
5
6
7
8

f 9

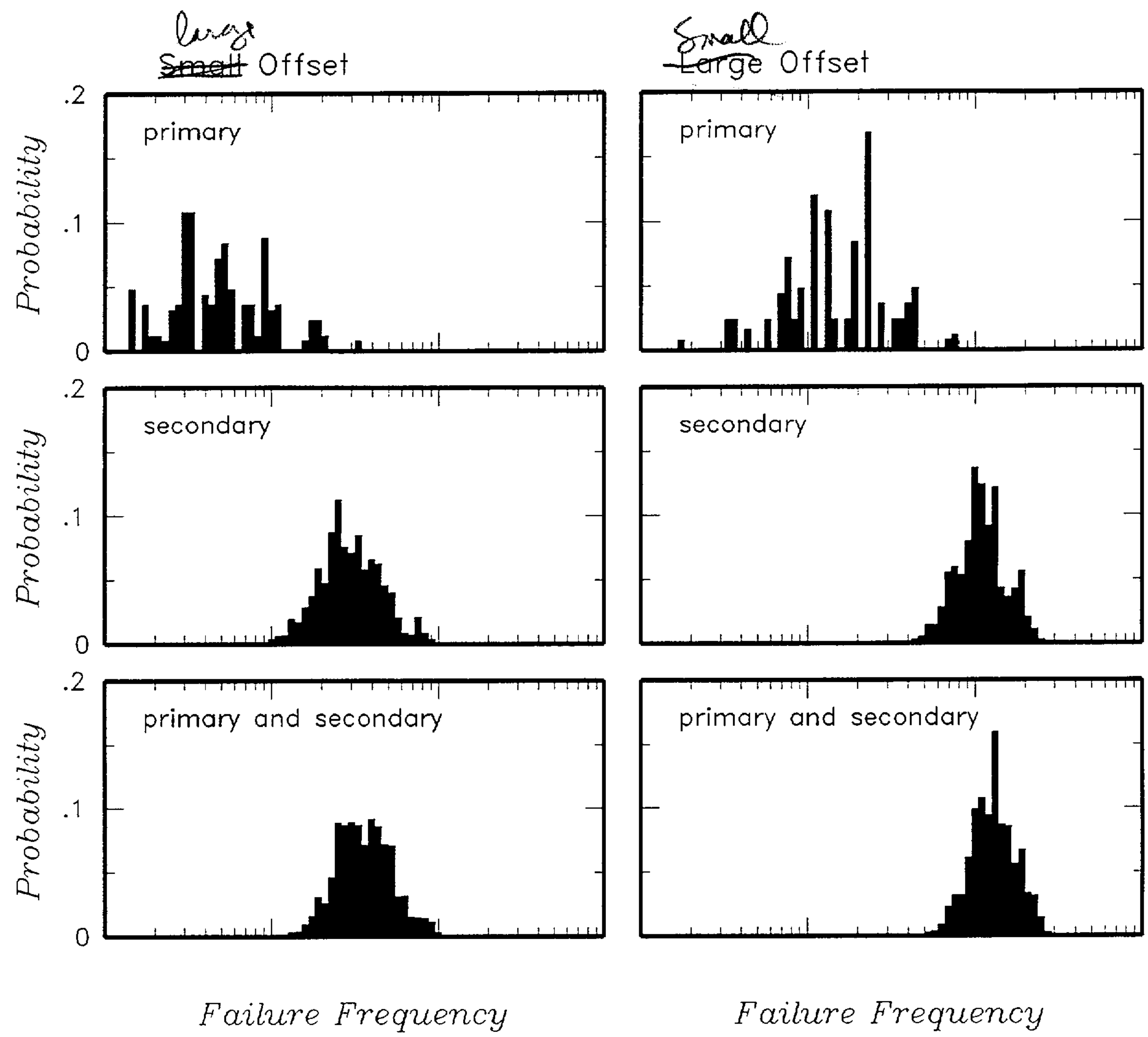
Large ~~Small~~ Offset
Small ~~Large~~ Offset
primary
secondary
primary and secondary
Probability
.2
.1
0
Failure Frequency

Yucca Mountain Seismic Source Characterization Workshop #2:

Hazard Methodologies
October 16-18, 1996

Bedrock Geologic Mapping at Yucca Mountain

—Review who we are and where we were, where we are, and where we're going

Presenter: Warren C. Day, USGS Structural Studies Project

OBJECTIVES OF TODAY'S TALK

- **COMPARE NEW RESULTS WITH EARLIER MAPPING**
- **PRESENT SOME HIGHLIGHTS OF NEW MAPPING**
- **REVIEW FAULT TYPES AND CHARACTERISTICS**

FUNCTION AS A RESOURCE FOR TECTONIC MODELS IN FURTHER DISCUSSIONS

Handout Materials:

- **Notes From This Talk**
- **Bedrock Geologic Map of the Central Block Area and Text**
- **Photocopies of Abstracts for Reference**

USGS YMP Structural Studies Project

—Who We Are

Chris J. Potter, *PhD (Mapping, PISA report)*

Don Sweetkind, *PhD (Fracture Studies)*

Robert Dickerson, *MSc (Mapping)*

Carma San Juan, *MSc (GIS)*

Dana Polacsek *(MSc Thesis: Fracturing and Fault Mechanics-Hydrologic Implications)*

Warren C. Day, *PhD (Mapping, Project Lead, etc.)*

USGS YMP Structural Studies Project

Applicable FY96 Products

- ***Bedrock Geologic Map of the Central Block Area, Yucca Mountain, Nye County, Nevada (Day and others)***
  - Geologic map of central block area (1:6,000-scale)
  - Cross Sections near North and South Ghost Dance Alcove and South Ramp areas
  - Accompanying Text:
    - Structural setting
    - Geometry, Interconnectivity, and Kinematics of Dominant Faults
      - Classification: Block-Bounding, Northwest-Striking, Intrablock Faults
    - Synopsis of the Structural Development
    - Rock Unit Descriptions

USGS YMP Structural Studies Project

FY96 Products (continued)

- *Preliminary Geologic Map of the Yucca Mountain Area, Nye County, Nevada (Day and others)*
  - Digital compilation of all available relevant geologic maps for the Framework 3-d Model area
- *Fracture Synthesis Report (Sweetkind and Williams-Stroud)*
  - Compilation and distillation of all surface-based fracture studies
  - Digital database of all data available as of 3/96 from surface, some drill hole, and ESF (through 30+00m)

Relative Accuracy of Geologic Maps

- *Geologic Map of the Central Block (1:6,000-scale)*
  - Each contact was walked and/or visually inspected
  - Fault offsets could be confidently established at 1/2 the
  - contour interval (≥5 feet)
  - High quality orthophoto maps superimposed with
  - 10' topographic contours
  - Projection of the surface-based mapping to the ESF
  - has been extremely successful

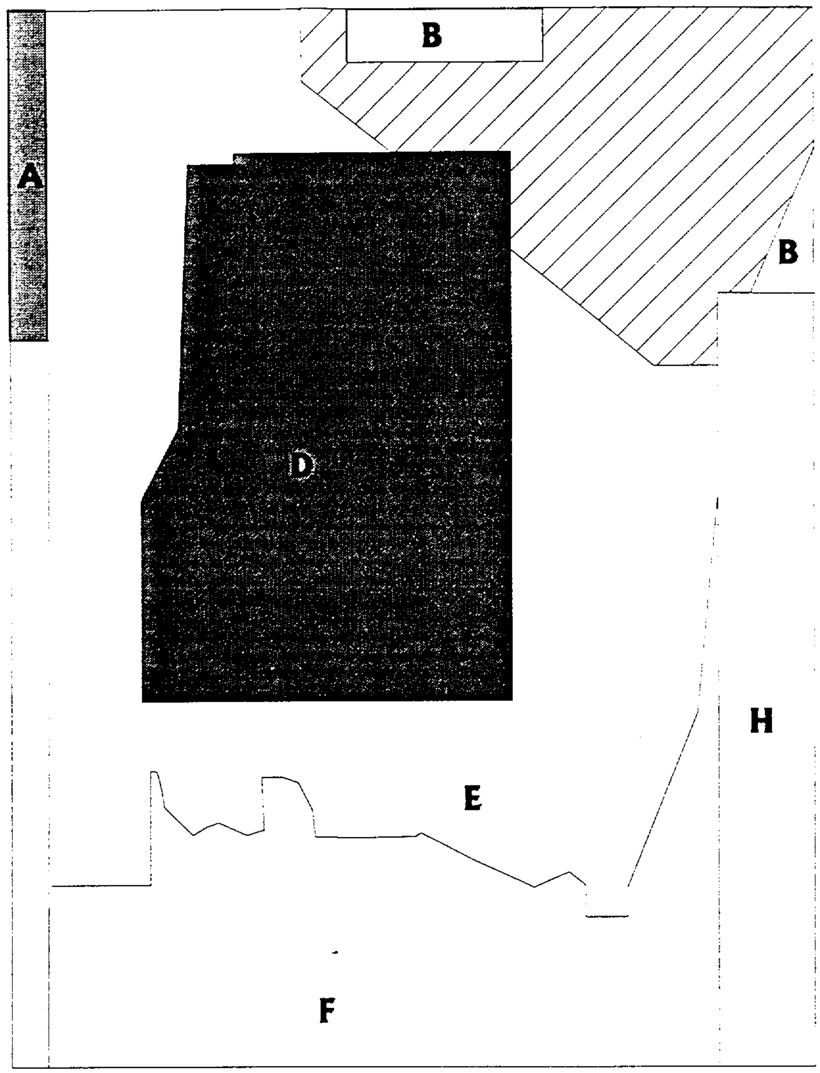

Index to Supporting Geologic Map Data

A. Fridrich, C. (unpublished; 1:12k)
B. Christian and Lipman, 1965 (1:24k)
C. Dickerson and Drake (in TDB, 1:6k)
D. Day and others (Central Block Map; 1:6k)
E. This study; Scott and Bonk (1983; 1:12k)
F. This study; Scott (1992; 1:12k)
G. Faulds and others (1994; 1:24k)
H. Lipman and McKay (1965; 1:24k)

Relative Accuracy of Maps (continued)

- *Preliminary Geologic Map of Yucca Mountain (1:24,000)*
  - Map presented today is a compilation (1:6k-1:24k)
  - Final Product (8/97):
    - Areas which have not been mapped by our team will be examined and remapped as needed
    - Mapping done under standard methods for scale
    - Numerous map edge busts are obvious
    - Problems internal to the supporting maps identified
    - Cartographic reality is that the map units must be at least about 30-40 feet thick
      - Map will include Formations, Members, and a few zones (where appropriate)
    - The new 1:24k map will have a lower degree of resolution compared to 1:6k Central Block Map, which is typical of map scale constraints

PREVIOUS MAPPING
—Where We Were

- Lipman and McKay (1965), Christian and Lipman (1965)
  - Basic 1:24,000-scale GQ mapping of the entire area
    - Provided Geologic Framework for Yucca Mountain as was Critical in Selecting Yucca Mountain for Further Investigation
- Scott and Bonk (1984)
  - Detailed 1:12,000-scale Reconnaissance of Yucca Mountain
    - Critical Input into Initial Repository Design, Hydrologic Investigations, Process Models, etc..
- Braun and others (OFR 96-109, in press)
  - Detailed Mapping Focused on the Ghost Dance Fault in the Repository Area
    - Delineated complexities along part of Ghost Dance Fault

RESULTS OF SCOTT AND BONK (1984)

- **Established location of major and minor faults**
- **Proposed Listric Model for Geometry of Block-Bounding faults**
  - **Out of vogue now**
- **"Imbricate Fault" Zone**
  - **Bad name**
- **Did NOT Recognize Members (crystal-rich/-poor) of Tiva and Topopah**
  - **VERY POWERFUL TOOL FOR DELINEATING FAULTS**
- **Naturally, there is some breakdown due to differences in scale**

COMPARISON WITH PREVIOUS STUDIES

Examples of Intrablock Faults

- **Ghost Dance Fault (splays, width, and displacement variations)**
- **Sundance Fault (not delineated by Scott and Bonk, 1984)**
- **Orientation of minor faults (Scott and Bonk had unrealistically uniform NW-strikes)**
- **Numerous minor faults incorrectly mapped**

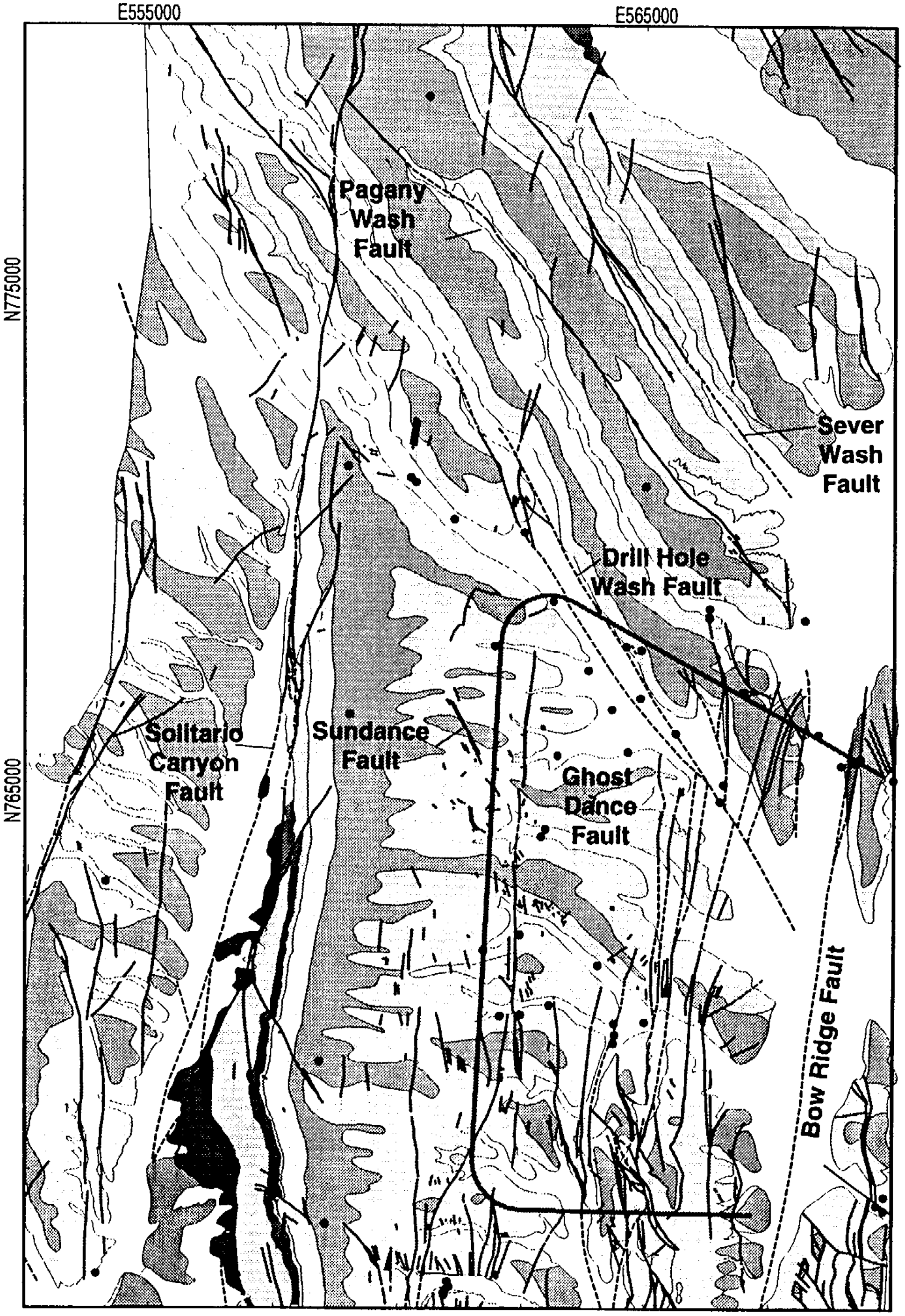

Bedrock Geologic Map of the Central Block Area, Yucca Mountain, Nevada

by
W.C. Day, C.J. Potter, D.S. Sweetkind, and R.P. Dickerson

Explanation

Quaternary
- Alluvium & Colluvium

Tertiary
- Rainier Mesa Tuff
- Comb Peak Rhyolite
- Tiva Canyon & Topopah Spring Tuff

Tiva Canyon Tuff
- Crystal - rich member
- Crystal - poor member

Pah Canyon, Yucca Mountain Tuffs - undivided

Topopah Spring Tuff
- Crystal - rich member
- Crystal - poor member

0 2,500 Feet

Preliminary Data for Information Only
USGS
July, 1996

Day 8A

SOME HIGHLIGHTS OF THE NEW MAP —Where We Are

- Defined branching of faults (vertical & horizontal)
  - Ghost Dance Fault
  - Abandoned Wash (on cross section)
- Connectivity of Faults
  - Projection of faults in hanging wall of Bow Ridge Fault ("imbricate fault" zone) into the Bow Ridge Fault
  - Dune Wash and "imbricate fault" zone
  - Northward continuation of the Abandoned Wash Fault into the Ghost Dance Fault

SOME HIGHLIGHTS (continued)

- *Solitario Canyon growth fault splays*
  - Offsetting of Topopah>PTn>Tiva
  - Apparent thickness increase of the PTn
  - Implication: evidence for post-Topopah Spring pre-Tiva deformation, extent of which is obscured b overlying blanket of Tiva Canyon Tuff

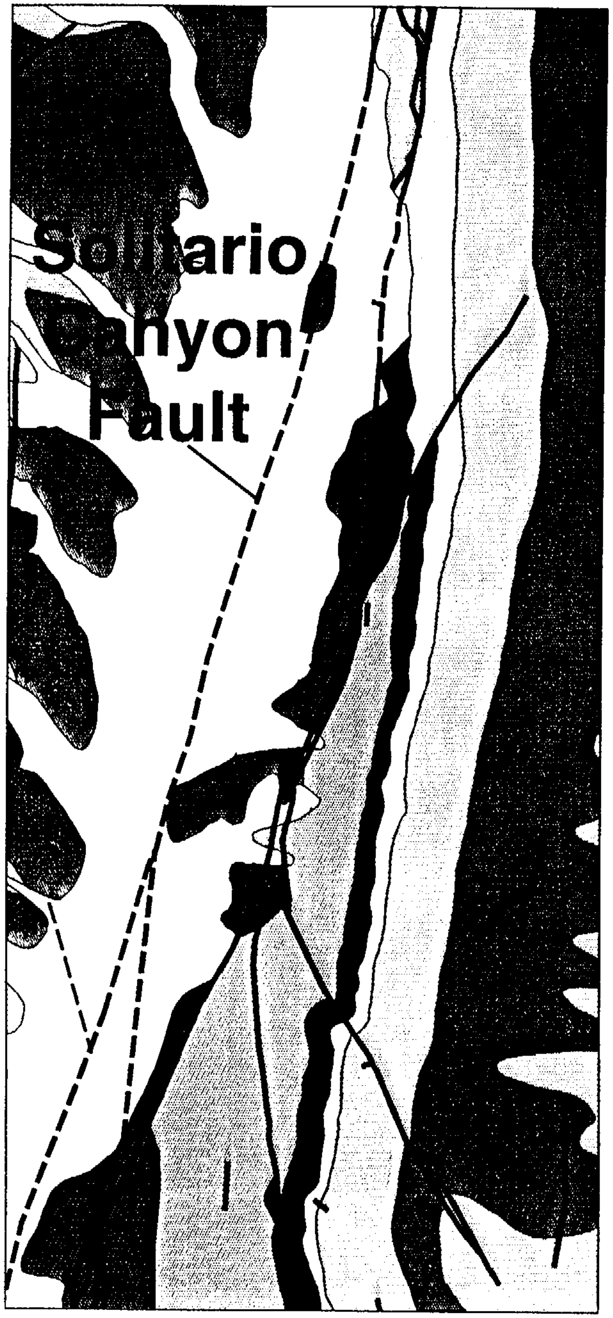

Explanation

Quaternary

- Alluvium & Colluvium

Tertiary

- Rainier Mesa Tuff
- Comb Peak Rhyolite
- Tiva Canyon & Topopah Spring Tuff

Tiva Canyon Tuff

- Crystal - rich member
- Crystal - poor member

- **Pah Canyon, Yucca Mountain Tuffs - undivided**

Topopah Spring Tuff

- Crystal - rich member
- Crystal - poor member

0 2,500 Feet

Types and Characteristics of Faults at Yucca Mountain

- **Block-Bounding Faults**
  - (Solitario Canyon, Bow Ridge, Paintbrush Canyon, etc.)
- **Intrablock Faults**
  - (Ghost Dance, Sundance, etc.)
- **Northwest-Striking Faults**
  - Intrablock Faults (Drill Hole, Pagany Wash, Sever Wash faults, and numerous minor faults)
  - Bridging Faults: Northwest-striking faults that connect (and bleed displacement from) Block-Bounding Faults

Characteristics of Block-Bounding Faults
(Solitario Canyon, Bow Ridge, Paintbrush Canyon, etc..)

In the Central Block Area, they are:

- Generally continuous, 10's of km in length
- North-striking faults with discontinuous splays
- Dip at surface 55-75^0 to the West (shallower than intrablock faults)
  - *Fault planes are inferred to curve at depth to produce roll-over in dips of units exposed at surface*
- Can have mineral lineations on fault scarps
- Offset was left-lateral oblique coupled with normal dip-slip motion

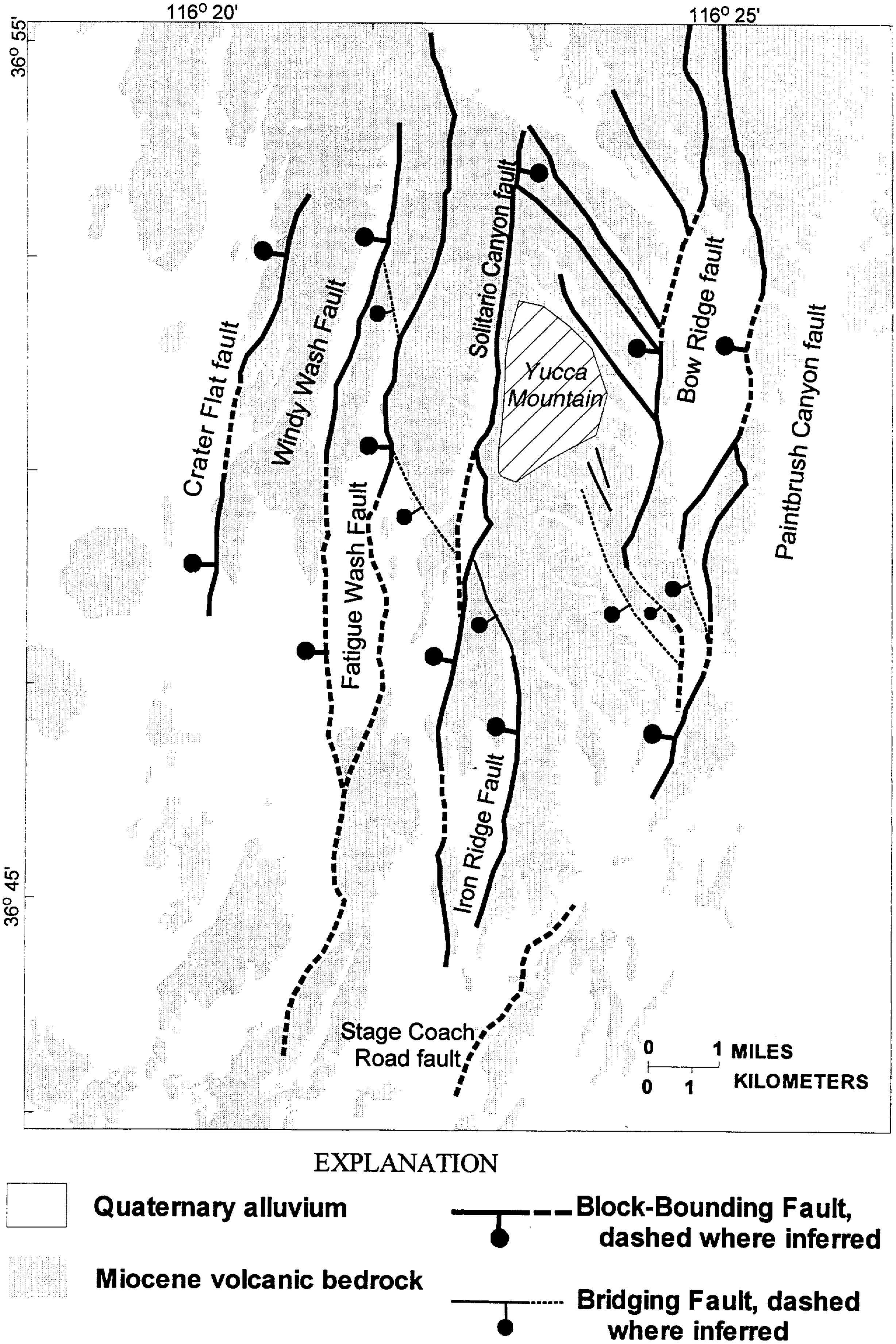
116° 20'
116° 25'
36° 55'
36° 45'
Crater Flat fault
Windy Wash Fault
Fatigue Wash Fault
Solitario Canyon fault
Yucca Mountain
Bow Ridge fault
Paintbrush Canyon fault
Iron Ridge Fault
Stage Coach Road fault
0 1 MILES
0 1 KILOMETERS
EXPLANATION
Quaternary alluvium
Miocene volcanic bedrock
Block-Bounding Fault, dashed where inferred
Bridging Fault, dashed where inferred

Characteristics of Block-Bounding Faults (*continued*)

- Commonly have parallel graben structures (east-side-down faults) in hanging wall
  - Important Example: "*Imbricate Fault Zone*" in the proposed repository area
- Splays of Solitario Canyon fault (Solitario Canyon) and faults related to Paintbrush Canyon fault (Fran Ridge) active prior to eruption of 12.7 m.y. Tiva Canyon Tuff (syn-PTn time)
- Most of the motion pre-dated deposition of the 11.6 m.y. Rainer Mesa Tuff

Characteristics of Intrablock Faults

- Generally discontinuous, meters to few kms in length
  - Longest in Central Block: Ghost Dance/Abandoned Wash (about 9 km long)
- Both north- and northwest-striking, with fewer northeast-striking faults
- Dips are steep (80°-90°)
- No tectonic mineral lineations found at surface
- Lateral component hard to determine: dominantly dip-slip
- Formed as local accommodation zones, which can interconnect with block-bounding faults
- In the upper block of the proposed repository area, few connect with block-bounding faults
- Interpreted to be result of local adjustments to deformation along block-bounding faults, most of which was >11.6 m.y.

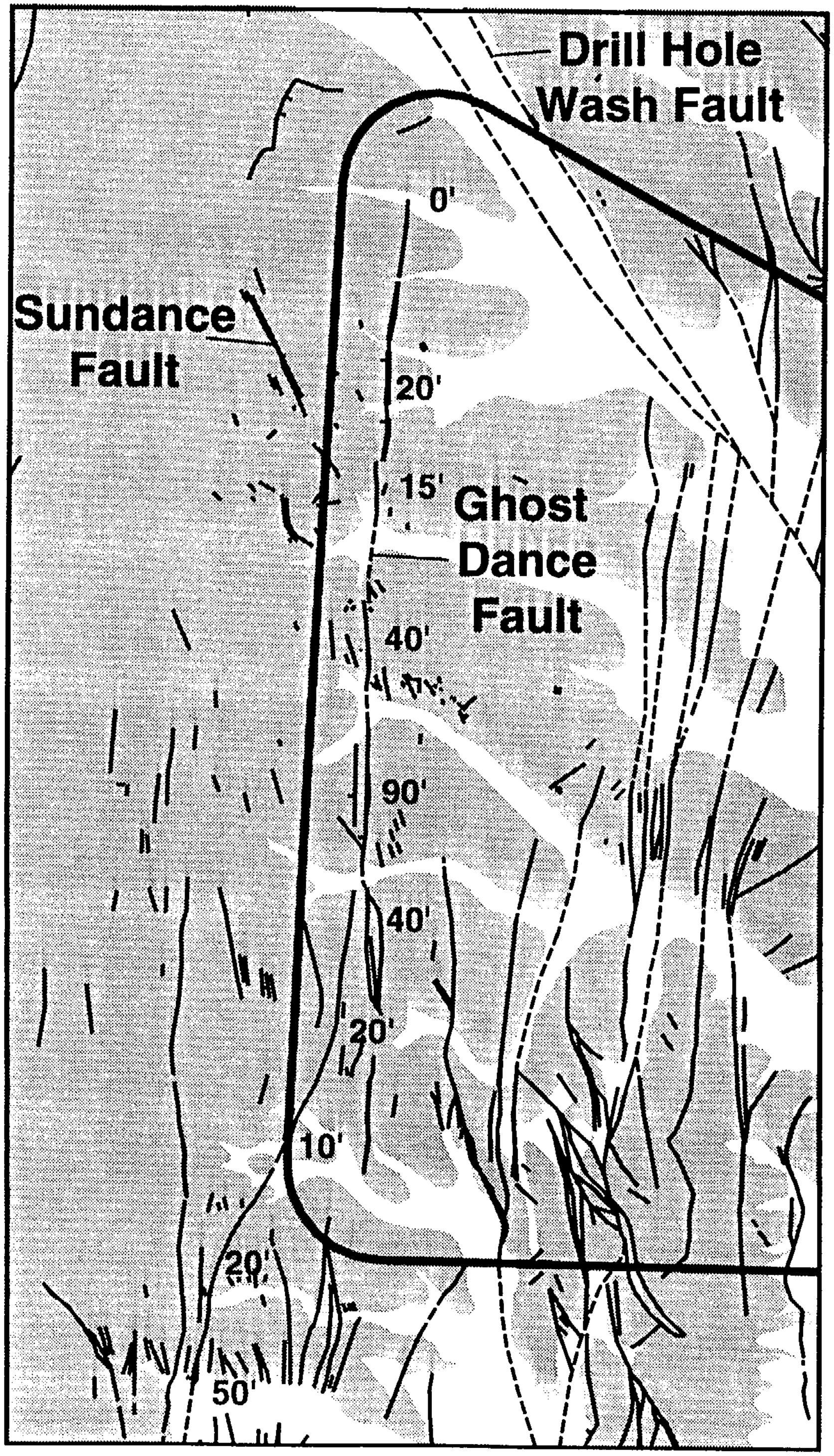

Faults in the Central Block Area

Miocene Volcanic Rocks

Faults - known and inferred (Day and others)

Exploratory Studies Facility

20' Displacement (Feet)

0 2,500 Feet

Preliminary Data for Information Only
USGS
July, 1996

Dra. #8A

Characteristics of Northwest-Striking Faults

Intrablock Faults (Drill Hole, Paganay Wash, Sever Wash)

- No evidence for Yucca Wash Fault (Units project continuously, geophysics inconclusive)
- Drill Hole, Paganay Wash, Sever Wash dip steeply to southwest
  - *Several different modes of origin possible*
- Slickensides and Reidel Shears indicate dextral offset
- "Scissoring" along Paganay Wash Fault
- Coeval with north-striking intrablock and block-bounding faults

Characteristics of Northwest-Striking Faults (continued)

Northwest-Striking Bridging Faults

- Formed as accommodation zones faults that transferred offset (bleed strain) between block-bounding faults
- Examples: faults that bridge the Solitario Canyon and Iron Ridge faults, Northern Windy Wash and Fatigue Wash, and Fatigue Wash and Solitario Canyon fault
- Incipient bridging faults developed in southern part of Central Block Area
  - Between Bow Ridge and Dune Wash faults form "canoe-shaped" en echelon grabens
  - These en echelon grabens will be penetrated by the ESF
- Capture of the Bow Ridge Fault south of Central Block Area

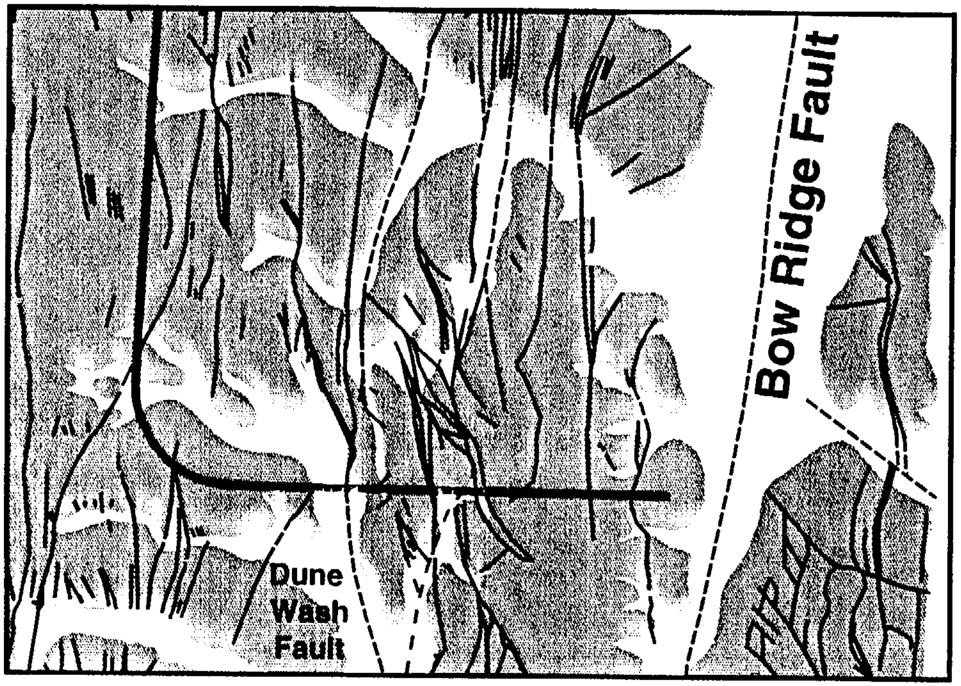

Faults in the Central Block Area

Miocene Volcanic Rocks

Faults - known and inferred (Day and others)

Exploratory Studies Facility

0 2,500 Feet

CROSS SECTION FROM 3-D GEOLOGIC MODEL

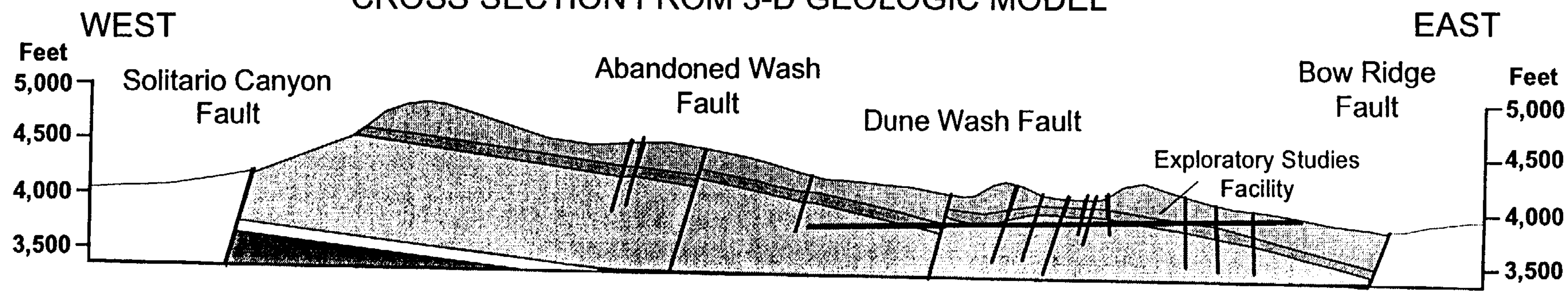

CROSS SECTION FROM NEW BEDROCK GEOLOGIC MAP

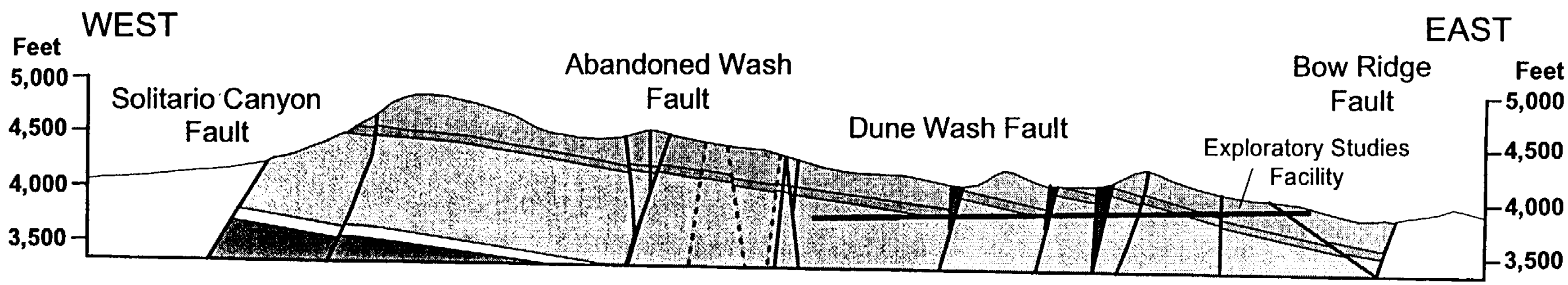

Explanation

- Breccia Zone
- Tiva Canyon Tuff
- PTn
- Topopah Spring Tuff
- Calico Hills
- Prow Pass

PRELIMINARY DATA
USGS (JULY, 1996)

Day 9

Conclusion
FY97 Activities—*Where We Are Going*

- Initiate publication cycle for Central Block Geologic Map
- Prepare integrated geologic and geophysical report for the PISA report
- Prepare Expanded Site Area Geologic Map
  - (1:24,000-scale)
- Help the Project Develop the 3-d Geologic Framework Model
- Update the Fracture Synthesis Report to incorporate new research on fracture networks associated with the ^{36}CL studies
- Input Structural Framework into the 3-d Unsaturated Zone Hydrologic Models
- Work with the Design Team for Construction and Expansion Area issues

Valid Type of Fault Classification Scheme for the Yucca Mountain Area

Offset (m)	Class	Length (km)	Type
0-3	I	<0.5	A
3-10	II	0.5-1	B
10-30	III	1-3	C
30-100	IV	3-10	D
100-300	V	>10	E
>300	VI		

For Example: A fault classified as a IIIE fault would be a fault (or segment) that has between 10-30 m of offset over a length of >10 km.

Problem: Faults with <1 m offset very difficult to confidently identify and follow over any distance in the field

U.S. Department of Energy
OFFICE OF CIVILIAN RADIOACTIVE WASTE MANAGEMENT

YUCCA MOUNTAIN SEISMIC SOURCE CHARACTERIZATION WORKSHOP #2 HAZARD METHODOLOGIES

SUBJECT: FRACTURES AND FAULTS MAPPED IN THE ESF

PRESENTER: ROBERT C. LUNG, GEOLOGIST,
U.S. BUREAU OF RECLAMATION

SALT LAKE CITY, UTAH
OCTOBER 16-18, 1996

LAYOUT OF THE EXPLORATORY STUDIES FACILITY

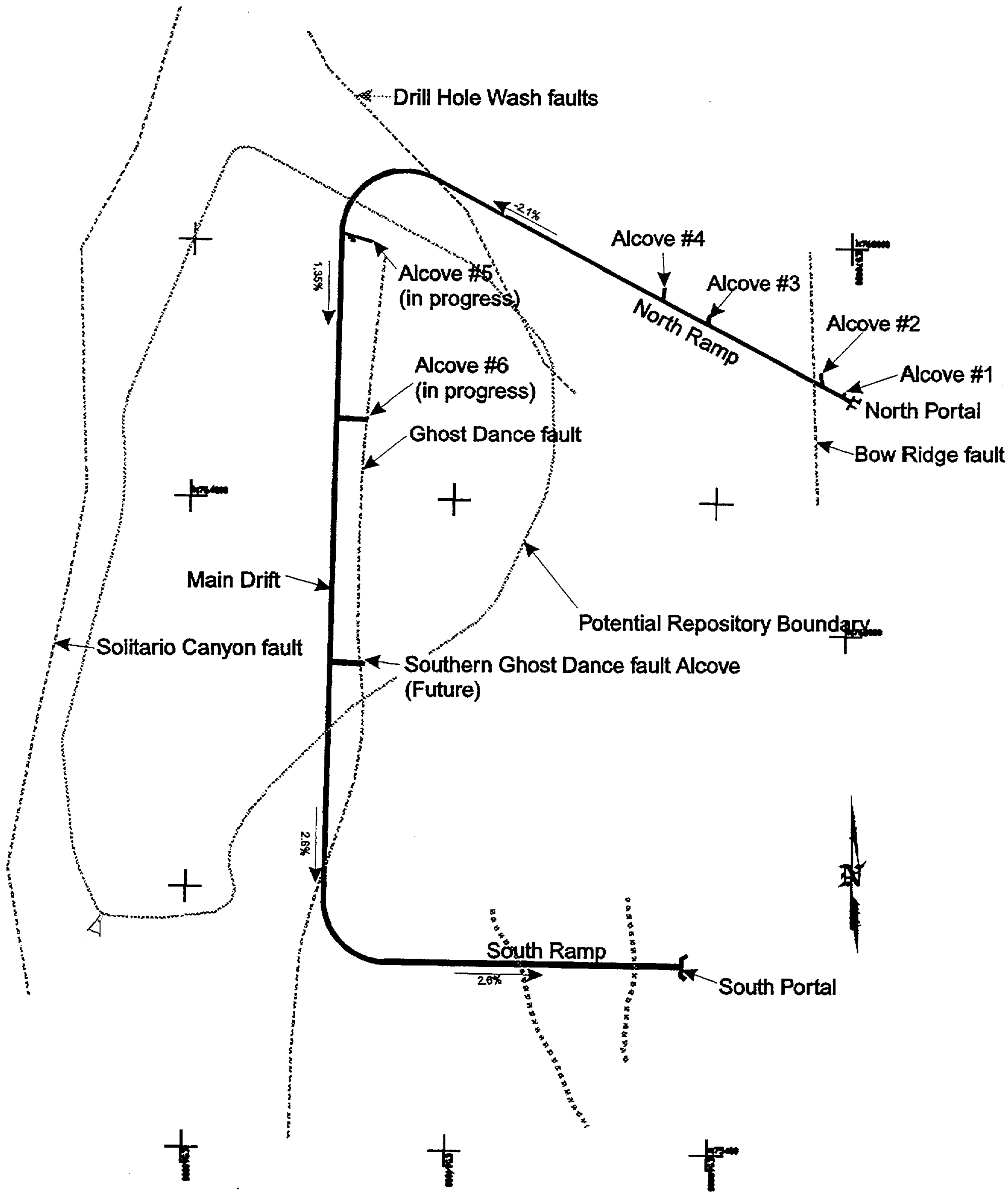

FULL PERIPHERY GEOLOGIC MAPS

- Maps are compiled into 100 meter sections
- Discontinuities greater than or equal to 1 meter in length are mapped
- Noteworthy geologic features are mapped and described, i.e. fracture zones, fault zones, shear zones, and breccia zones.
- Sample and geotechnical instrumentation locations are included
- "Q" ground support is mapped
- A generalized geologic cross-section is included
- Excavation rates and rock mass classification data are displayed at the top of the map

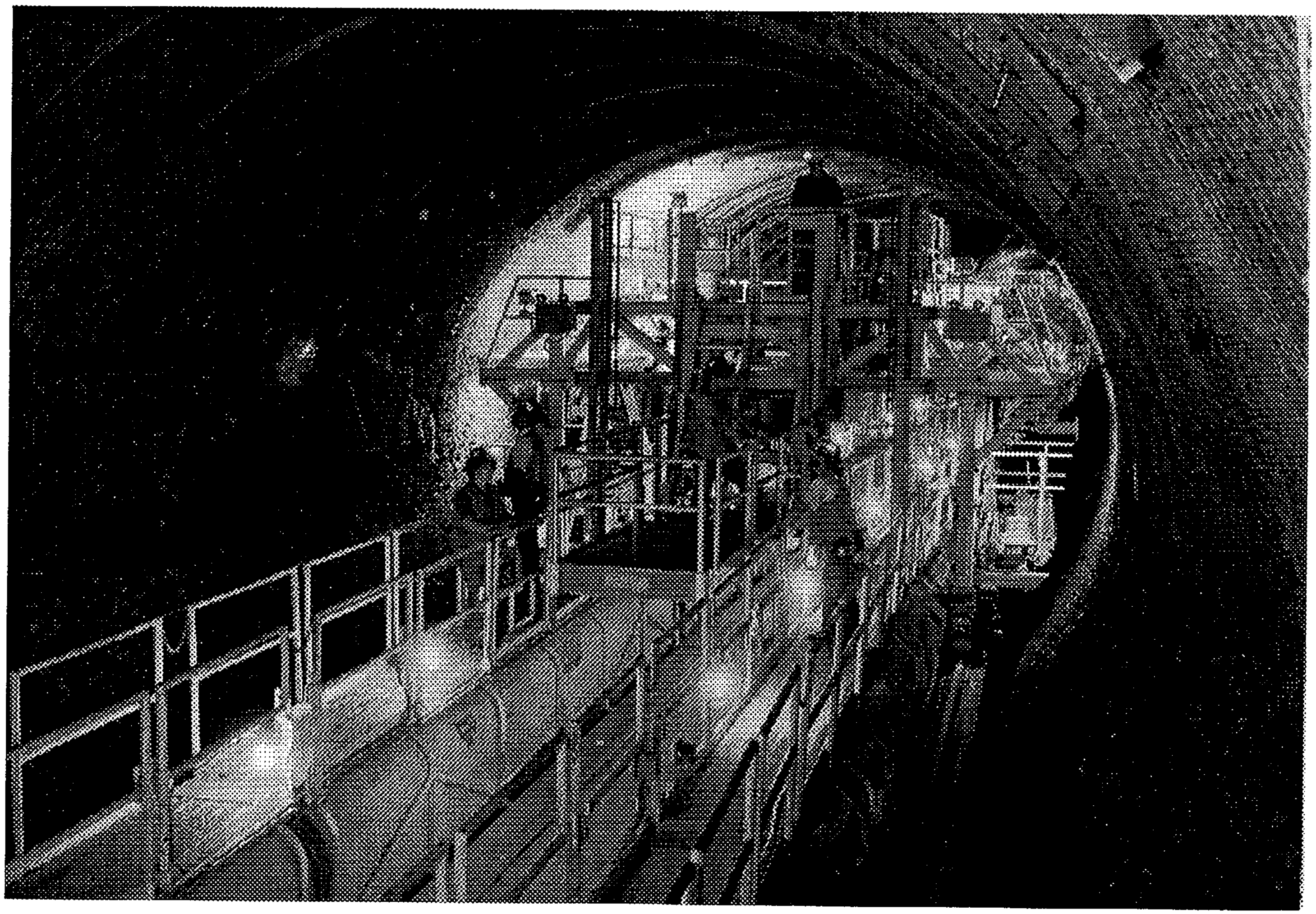

Photo
YM11095.

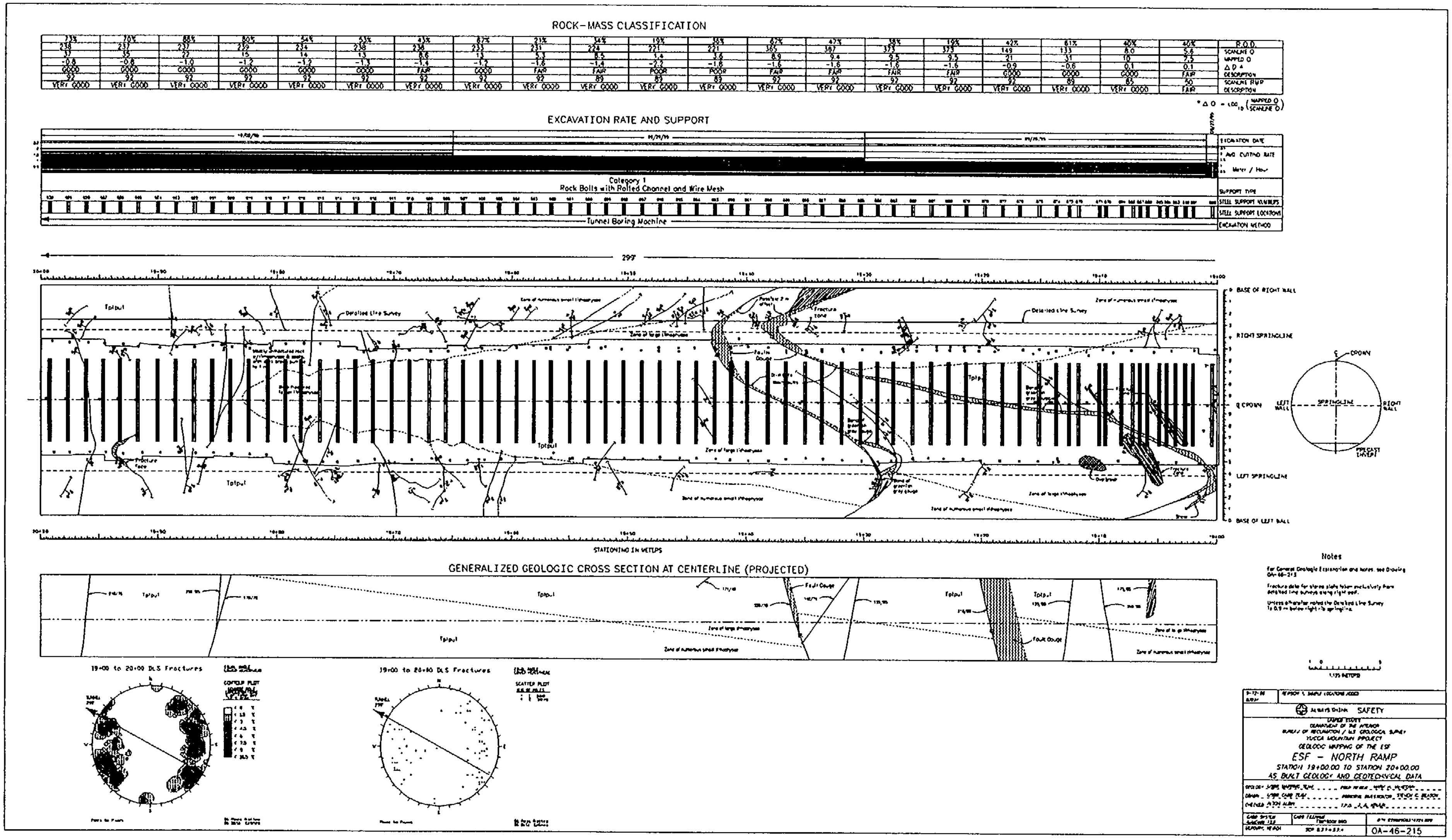

FULL PERIPHERY GEOLOGIC MAP

with Excavation Rates, Ground Support, and Rock Mass Classification

DETAILED LINE SURVEY

- Tapeline on right wall approximately 1 meter below springline
- All discontinuities greater than or equal to 1 meter in length are documented
- 19 Attributes are described for each feature:

1) STATION
2) TYPE
3) AZIMUTH
4) DIP
5) TRACE LENGTH ABOVE TAPE
6) TRACE LENGTH BELOW TAPE
7) HEIGHT
8) WIDTH
9) ENDS
10) UPPER TERMINATION
11) LOWER TERMINATION
12) PLANARITY
13) JOINT ALTERATION NUMBER
14) APERTURE MINIMUM
15) APERTURE MAXIMUM
16) OFFSET
17) INFILLING TYPE
18) INFILLING THICKNESS
19) COMMENTS

- So far, 16,000 plus fractures have been recorded

Fracture Density in the ESF
Station 0+60 to 62+70

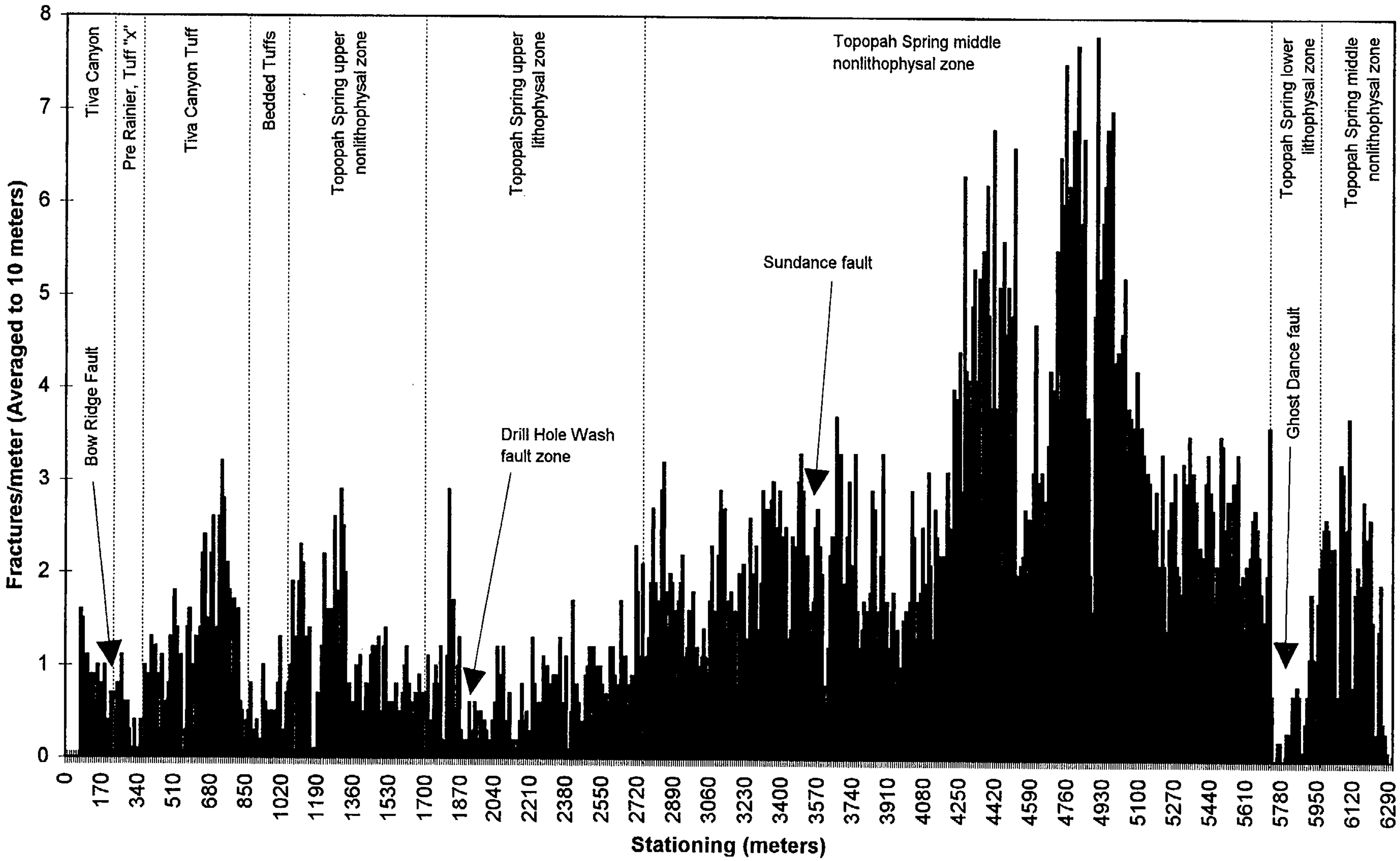

FAULTS AND SHEARS

- Structures with undeterminable or less than 0.1m of offset are termed shears

- Structures with greater than 0.1m of offset are termed faults

- Several criteria can be used to determine offset:
  a) Displacement of lithologies
  b) Displacement of discontinuties (fractures, joints, vapor phase partings)
  c) Pumice and lithic clasts

- Strike slip is the most difficult displacement to discern due to the lack of lateral markers. Slickensides show direction but not amount of movement

- Ground support can make the determination of offset difficult (Steel bar reinforcement) for safety

- So far, 220 faults and 655 shears have been recorded

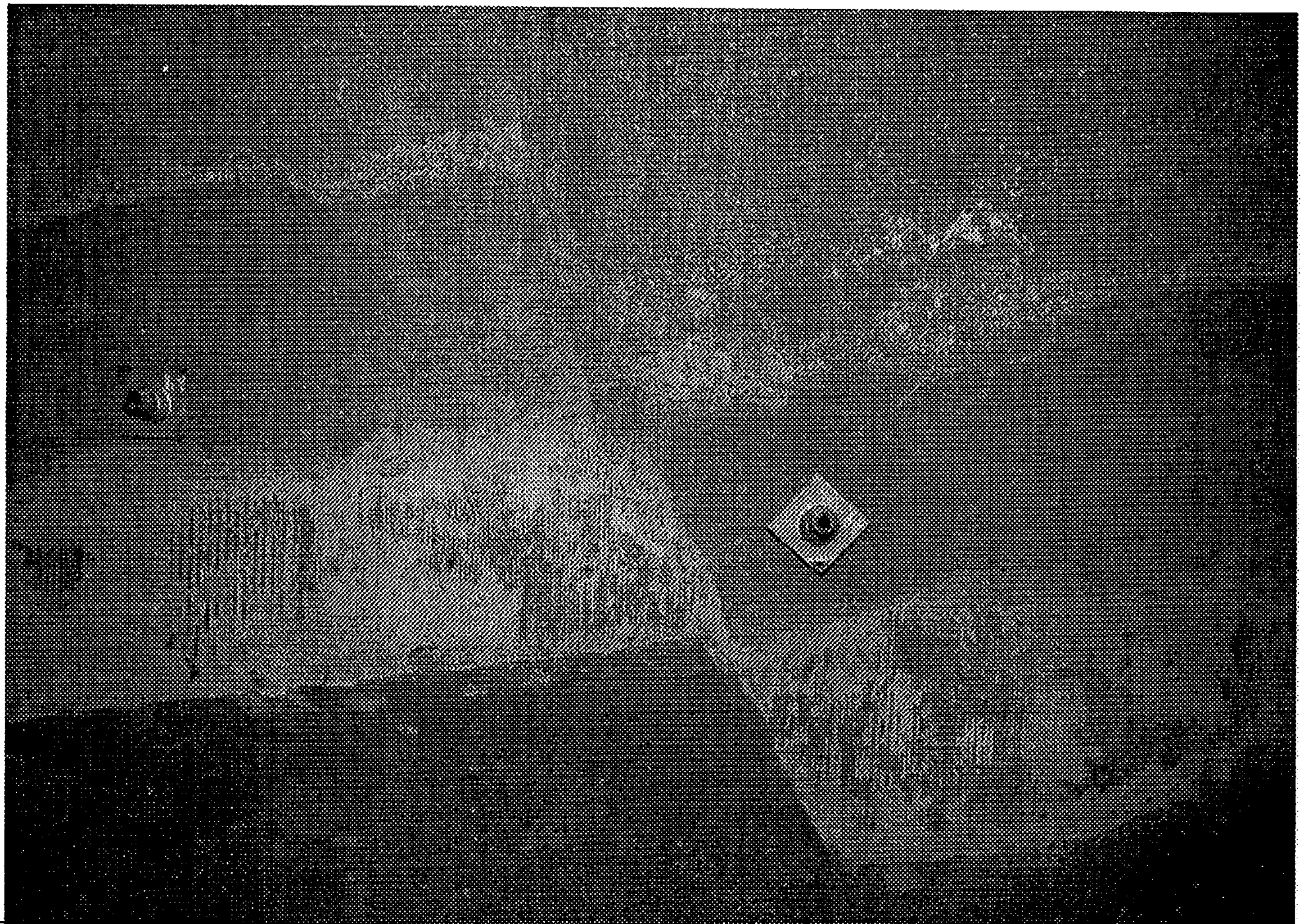

Photo
YM10227

Fault and Shear density in the ESF
Station 0+60 to 62+70

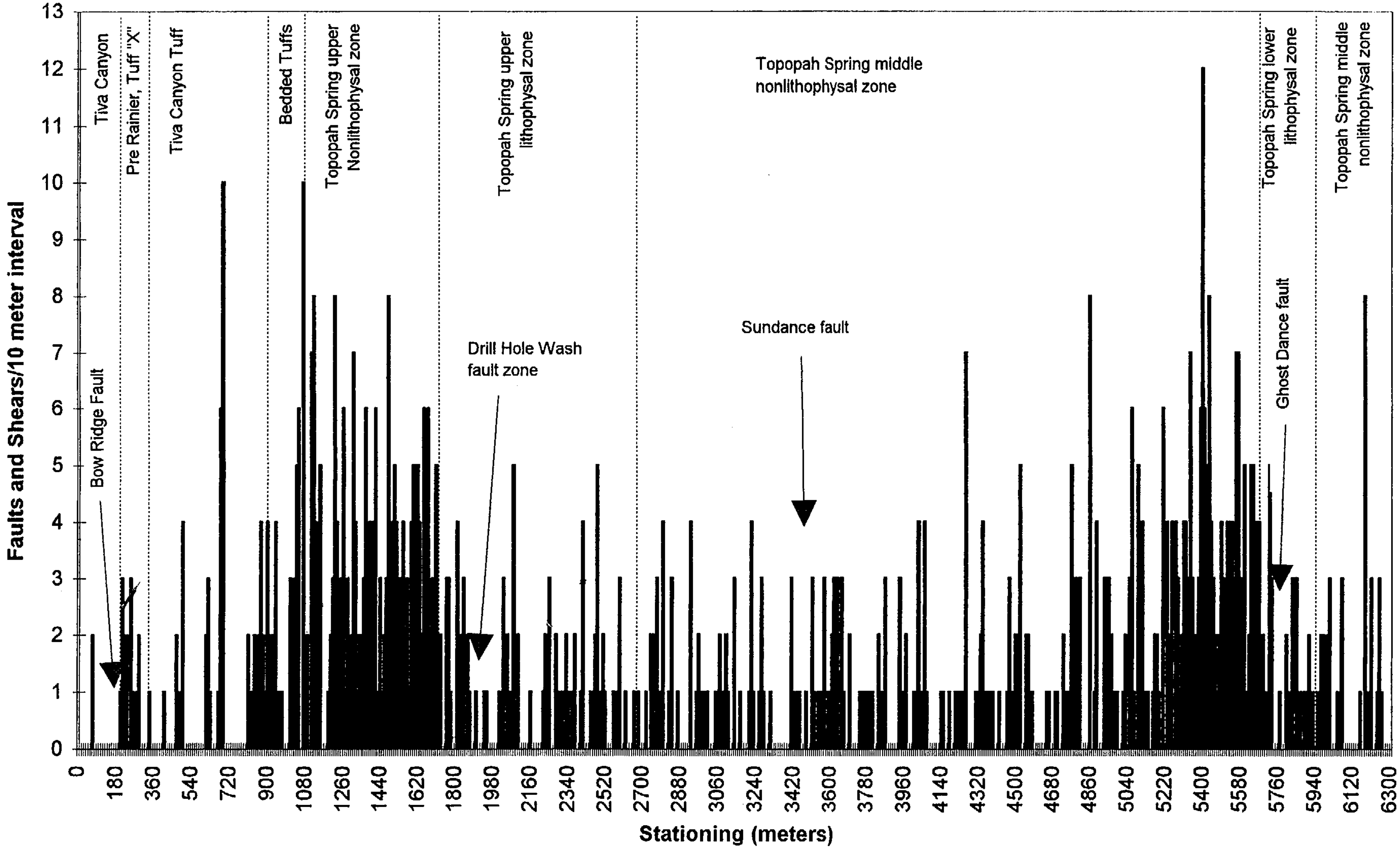

ESF NOTABLE STRUCTURAL FEATURES

Name	Station	Thickness	Offset	Characteristics
Bow Ridge fault	2+00	2 m	100 m	Uncemented breccia - Wall rock relatively unfractured, no distinct calcite veins visible associated with the zone
"Imbricate" fault zone	4+30-11+70	Multiple zones up to 5 m thick	Multiple offsets up to 18 m	Numerous individual faults, many with offsets >5 m offset, typically uncemented fault rubble with little or no cemented breccia
Drill Hole Wash fault zone	19+00	0.5 m	6 m	Composed of 2 separate faults, horizontal slickensides, no mineralization along fault trace
Sundance fault	35+94	0.5m	<1 m	Composed of a series of discontinuous shears and small fault planes, no mineralization along fault trace
Ghost Dance fault	57+30	0.5m	1.2 m	Distinct plane (205°/90°) with in a small zone. Less offset the anticipated

Geological Structure at Yucca Mountain

Correlation between Surface and ESF mapping

- Imbricate fault zone

  Surface mapping helped define faults obscured by support in the ESF at station 5+50

  Underground mapping showed several faults not easily visible at the surface

- Drill Hole Wash faults

  Surface and underground mapping agreed on location of the main faults

  Underground mapping defined the limited size of the faults

- Northern extent of the Ghost Dance Fault

  Both surface and underground mapping confirm that the fault does not extend as far north as the ESF

Geological Structure at Yucca Mountain

Correlation between Surface and ESF mapping
(Continued)

- Sundance Fault

  Surface and underground mapping confirmed the minor and discontinuous nature of the fault zone

  The difference in fault location between the surface and underground suggests a vertically discontinuous nature for the fault

- Intensely Fractured Zone

  Surface Mapping confirms that the zone is apparently stratabound (not visible at surface)

- South Ramp Surface Mapping

  Detailed mapping and cross-section provide the basis for design

  Help underground team correctly identify fault zones with know surface features

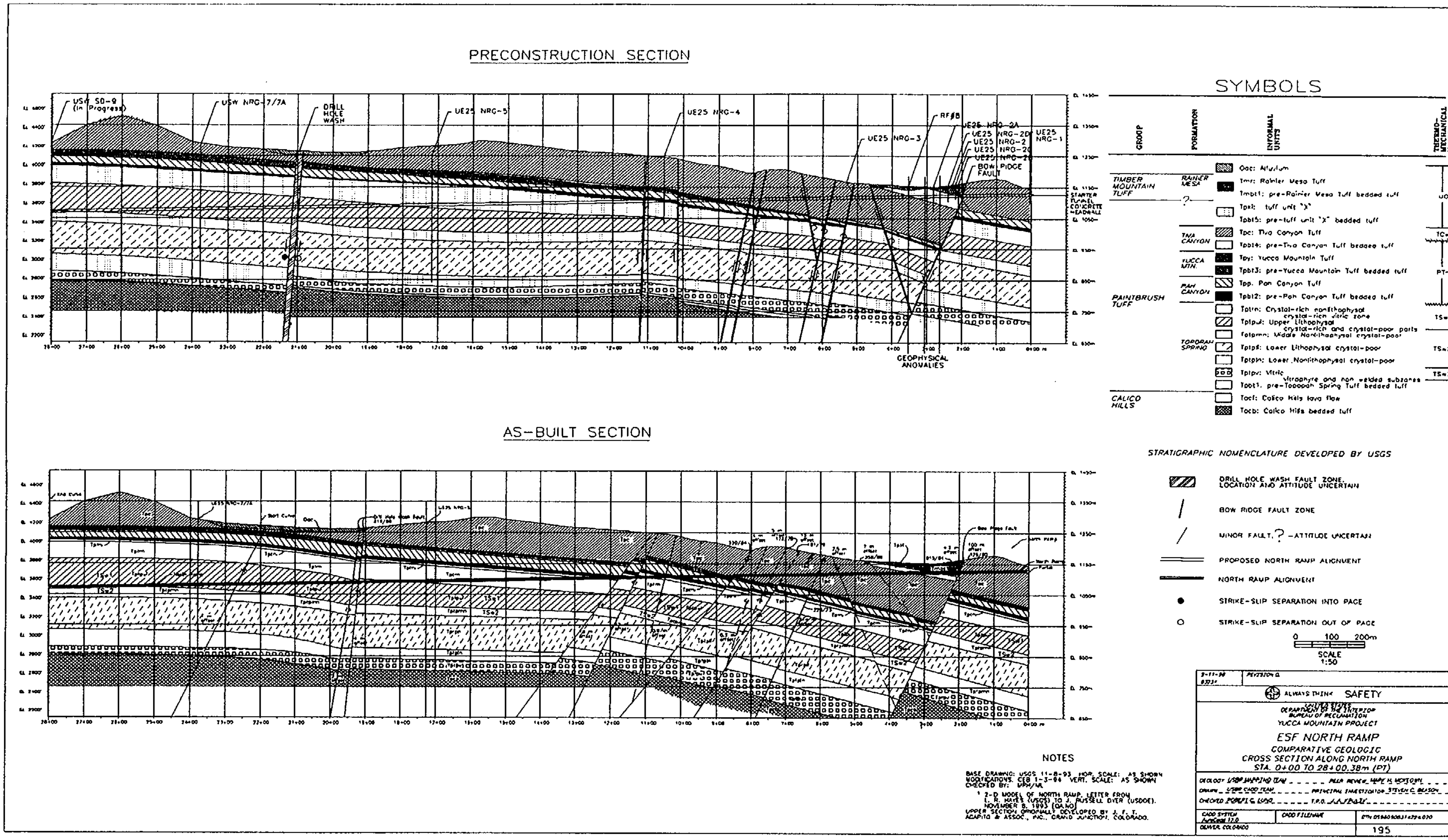

NORTH RAMP STATION 0+00 TO 28+00
PRECONSTRUCTION & AS-BUILT CROSS-SECTION COMPARISON

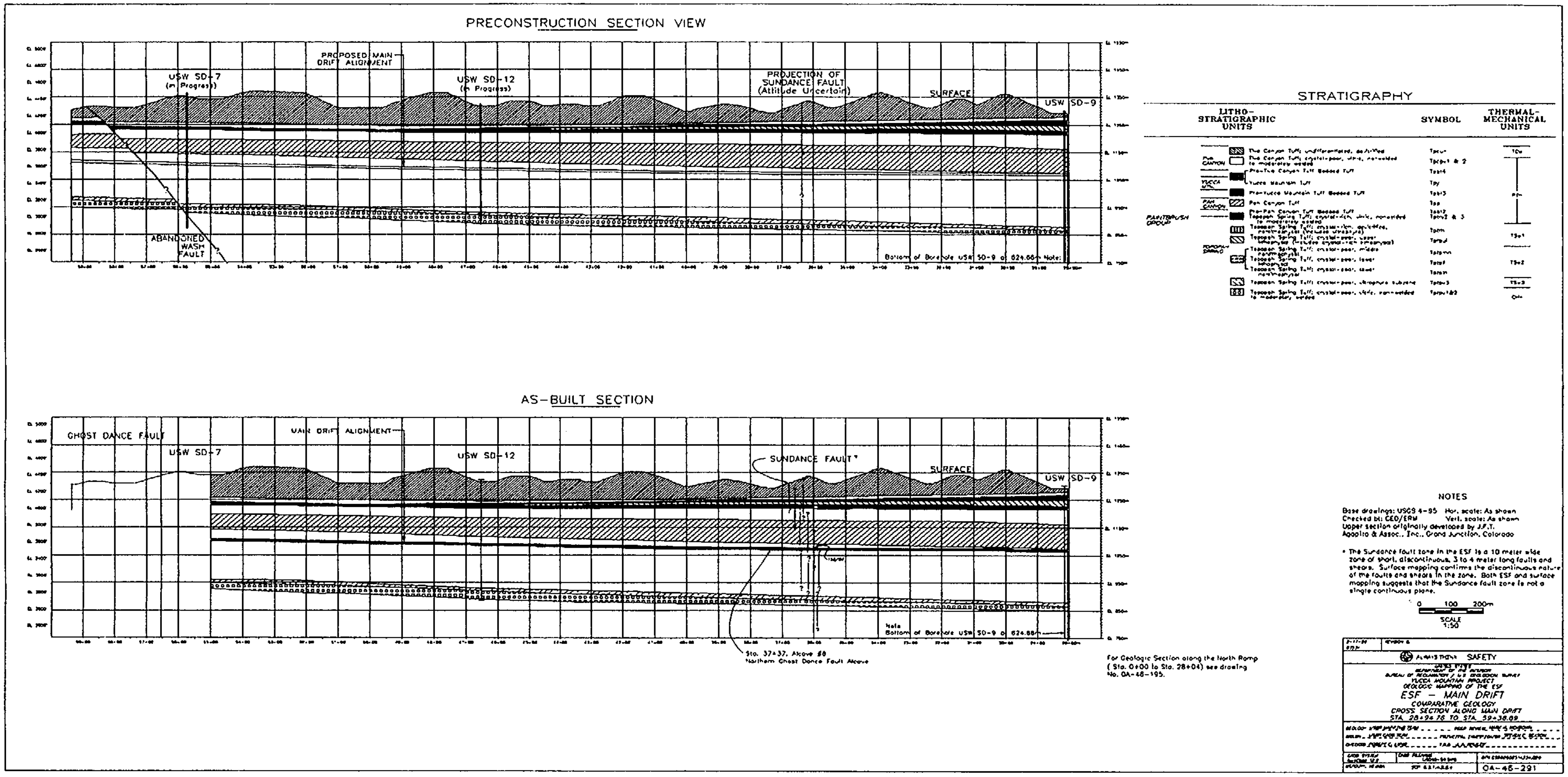

MAIN DRIFT STATION 28+00 TO 55+00
PRECONSTRUCTION & AS-BUILT CROSS-SECTION COMPARISON

Yucca Mountain Geophysical Data

presented by:
Mark A. Feighner
Lawrence Berkeley National Laboratory

[Principal Investigator - Ernest L. Majer, with: L. Johnson, T. Daley, E. Karageorgi, K. H. Lee, K. Williams, and T. McEvilly]

Presented at the:
Yucca Mountain Seismic Source Characterization
Workshop #2 - Hazard Methodologies
October 18, 1996

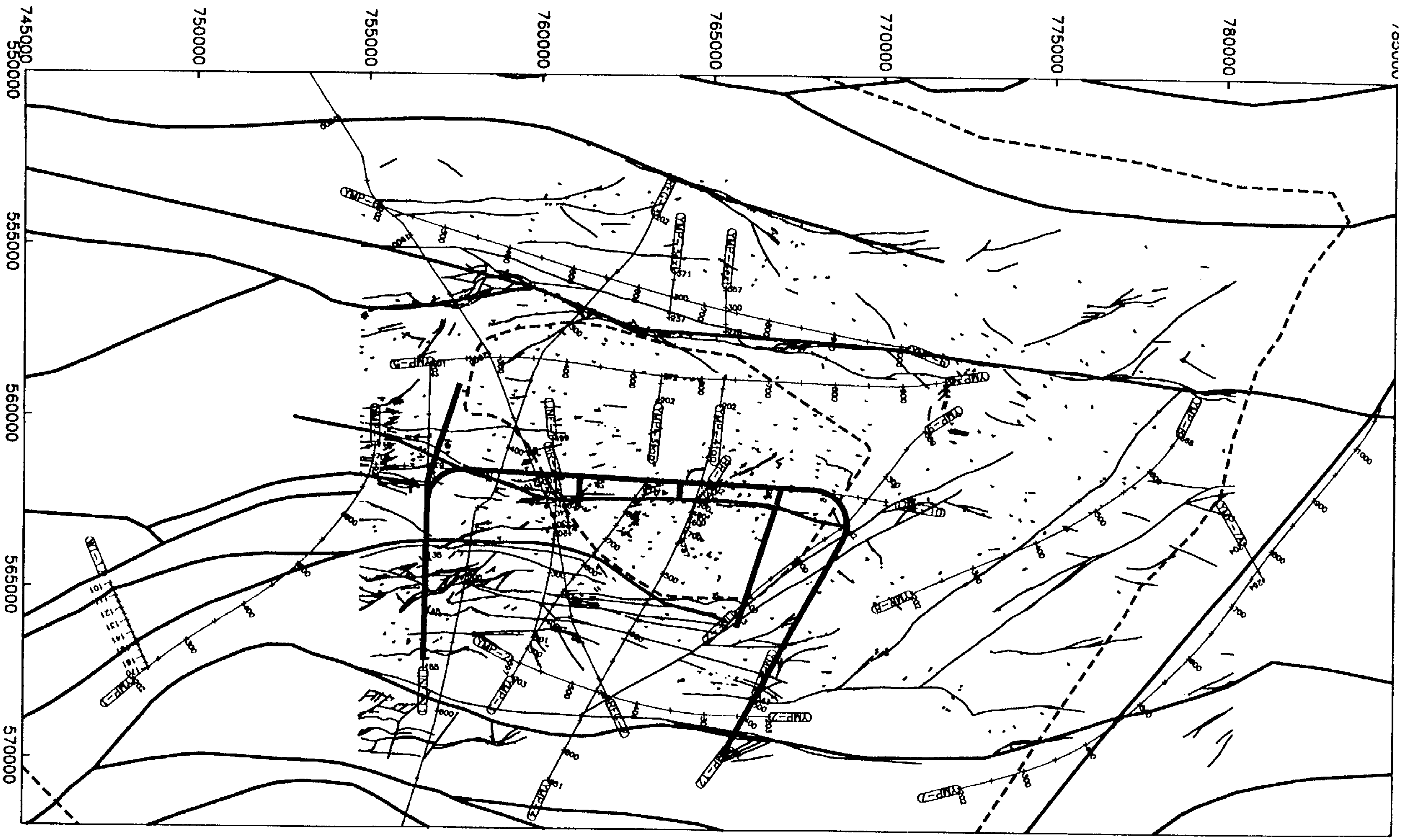

BLUE Lines - Geophysical Data; RED Lines - Faults from geologic model [Zelinski & Clayton, 1996];
BLACK Lines - Faults from Day et al. (1996); and GREEN Lines are ESF and repository boundaries.

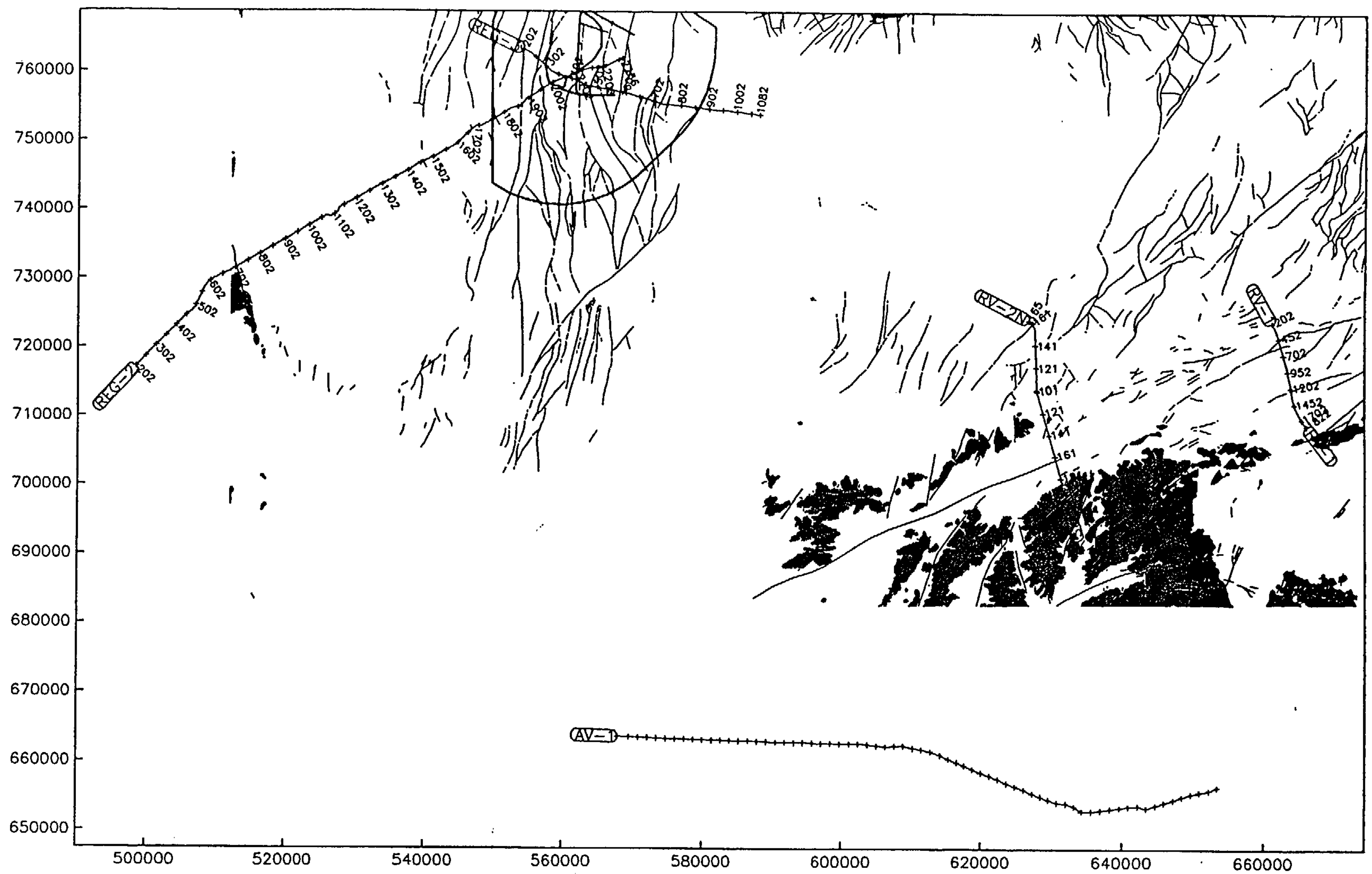

Figure 2. Common Depth Point (CDP) locations of the regional lines REG-2, REG-3, and RV-1. The location of seismic line AV-1 is also shown. The station locations for the gravity only line RV-2 (South and North) are shown. Gray areas are Paleozoic outcrops and faults are thin black lines (Data from Sawyer et al., 1995).

TABLE 1. GEOPHYSICAL DATA COLLECTED

Line	Seismic	Gravity	Magnetics	Vertical Seismic Profile (VSP) Well	Magneto-tellurics (MT)
YMP-1	X	X	X		
YMP-2	X	X	X	RF-4, RF-7a	
YMP-3	X	X	X	SD-12, UZ-16	X
YMP-3ext	X	X			
YMP-3top	X				
YMP-4	X	X	X		
YMP-4ext	X	X			
YMP-4top	X				
YMP-5	X	X	X		
YMP-6	X	X	X		
YMP-7	X		X		
YMP-7a	X	X	X		
YMP-8	X	X	X	G-2	
YMP-9	X	X	X		
LINE-10		X	X		
LINE-11		X			
YMP-12	X	X	X		
YMP-13a YMP-13b	X X				
YMP-14a YMP-14b	X X				
HR-1	X				
HR-2	X				
LINE-1	X			WT-2	
LINE-2	X			G-4, NRG-6	
WT-17		X			
RV-1	X	X			
RV-2		X			
REG-2 (Regional)	X	X	X		
REG-3 (Regional)	X	X	X		

Figure 101. Plan view of basement structure derived from gravity data. Elevation is given in feet. Dark areas are paleozoic outcrops, the black lines are faults (geologic data are from Sawyer et al. 1995). The black dots in the Rock Valley area are epicenter locations of aftershocks from the Little Skull Mountain earthquake sequence.

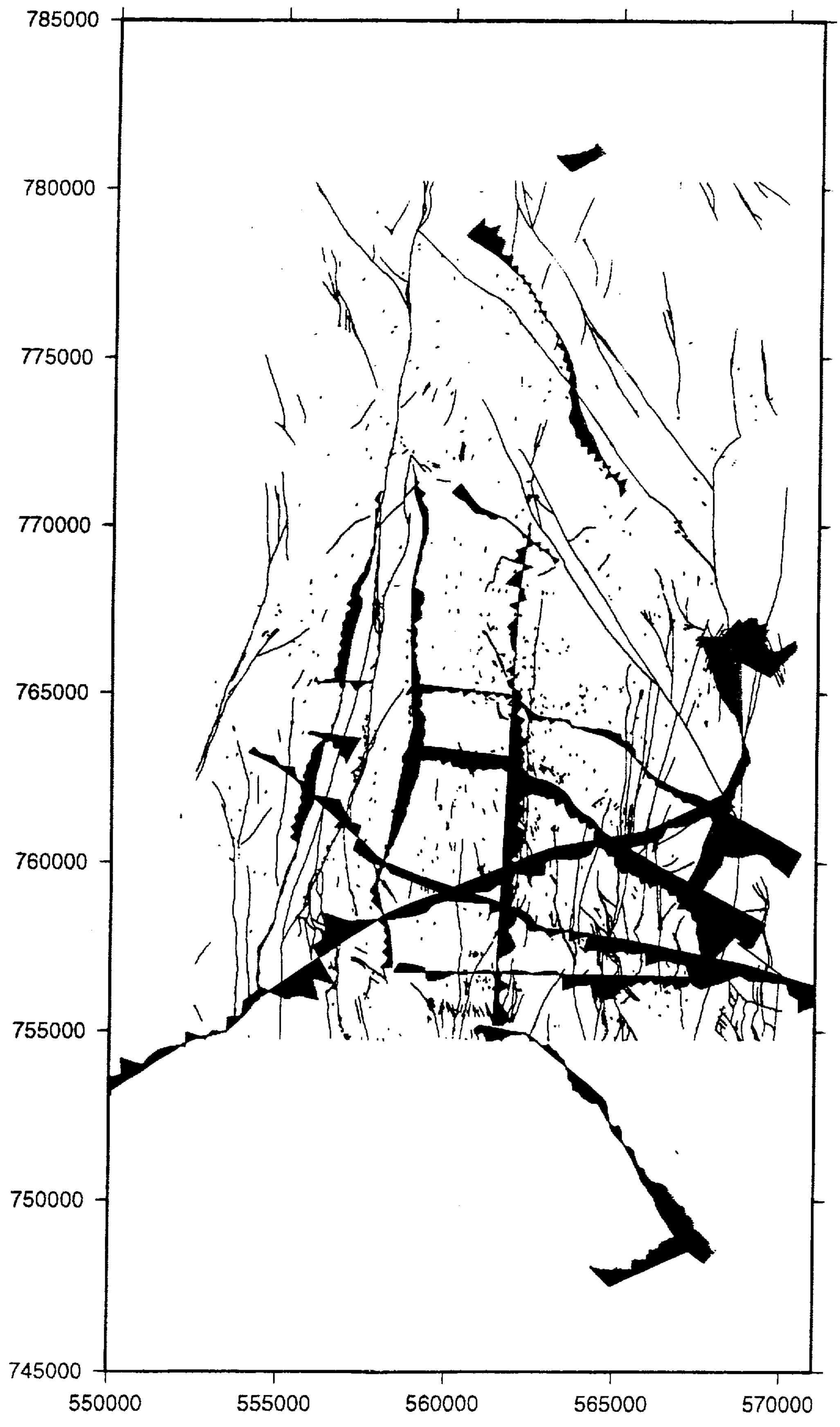

Figure 100. Repository residual gravity lines shown as wiggle lines along track where one inch equals 5 mGals. The red areas are negative values and the blue areas are positive values. Faults from Day et al. (1996).

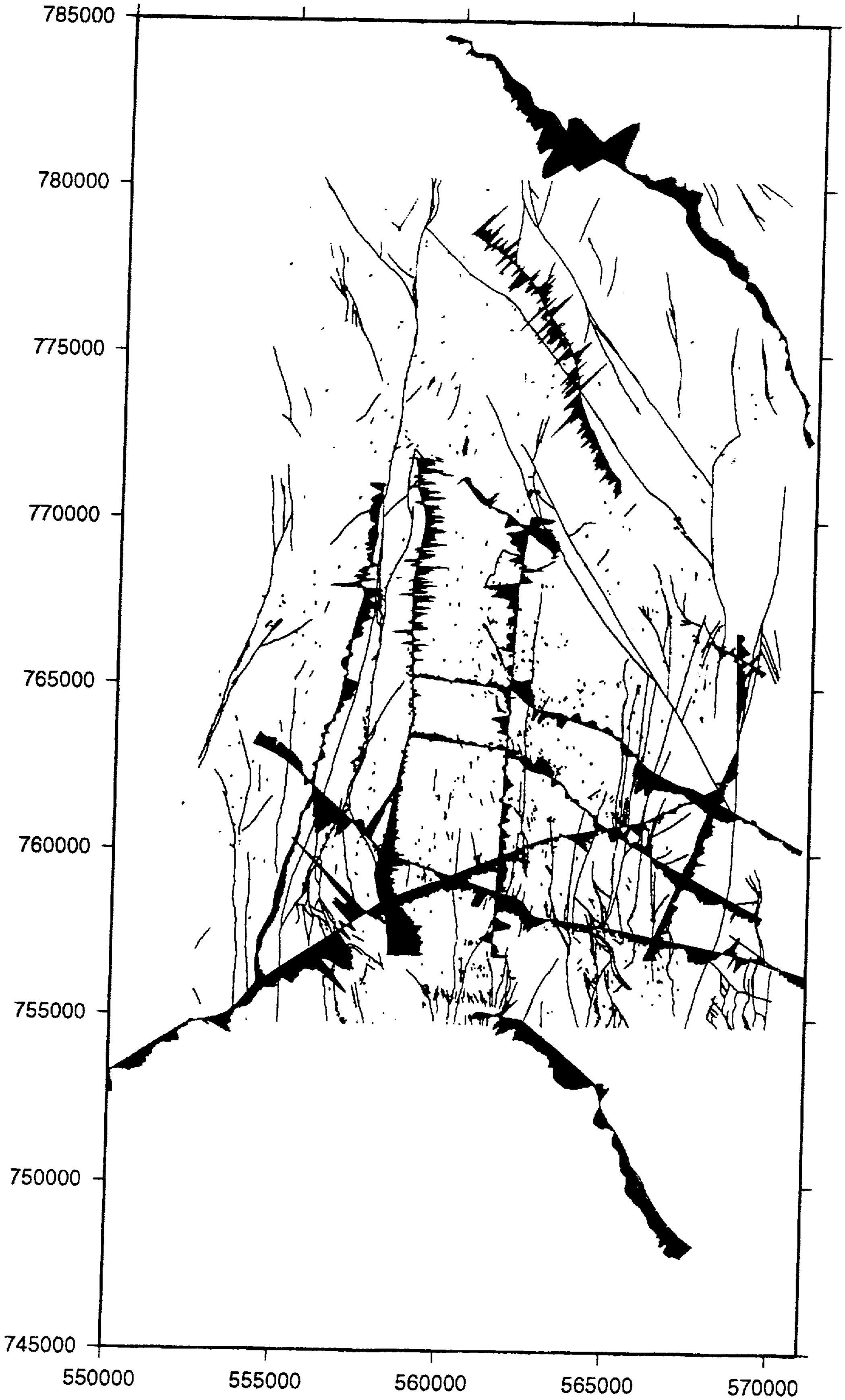

Figure 63. Repository ground magnetic lines shown as wiggle lines along track where one inch equals 2000 nT. The red areas are values less than 50900 nT and the blue areas are values greater than this value. Faults from Day et al. (1996).

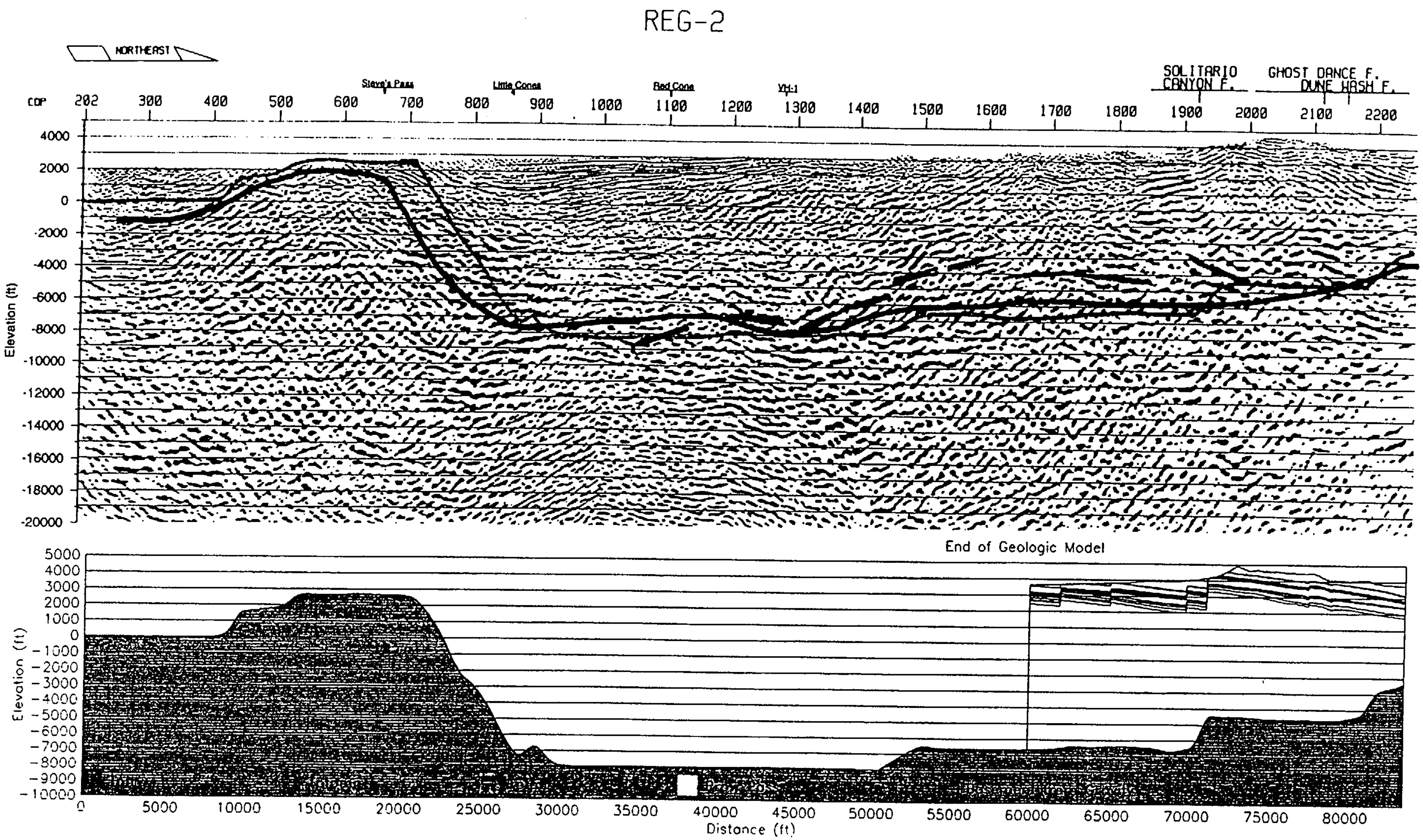

Figure 47a. Seismic line REG-2 with Paleozoic basement as derived from gravity, and geologic cross section (where available). Red line on section is basement from gravity, green is from Brocher et al., 1996b, blue is our interpretation. Note that Brocher et al., 1996b, did not interpret basement east of CDP 1900 on this line.

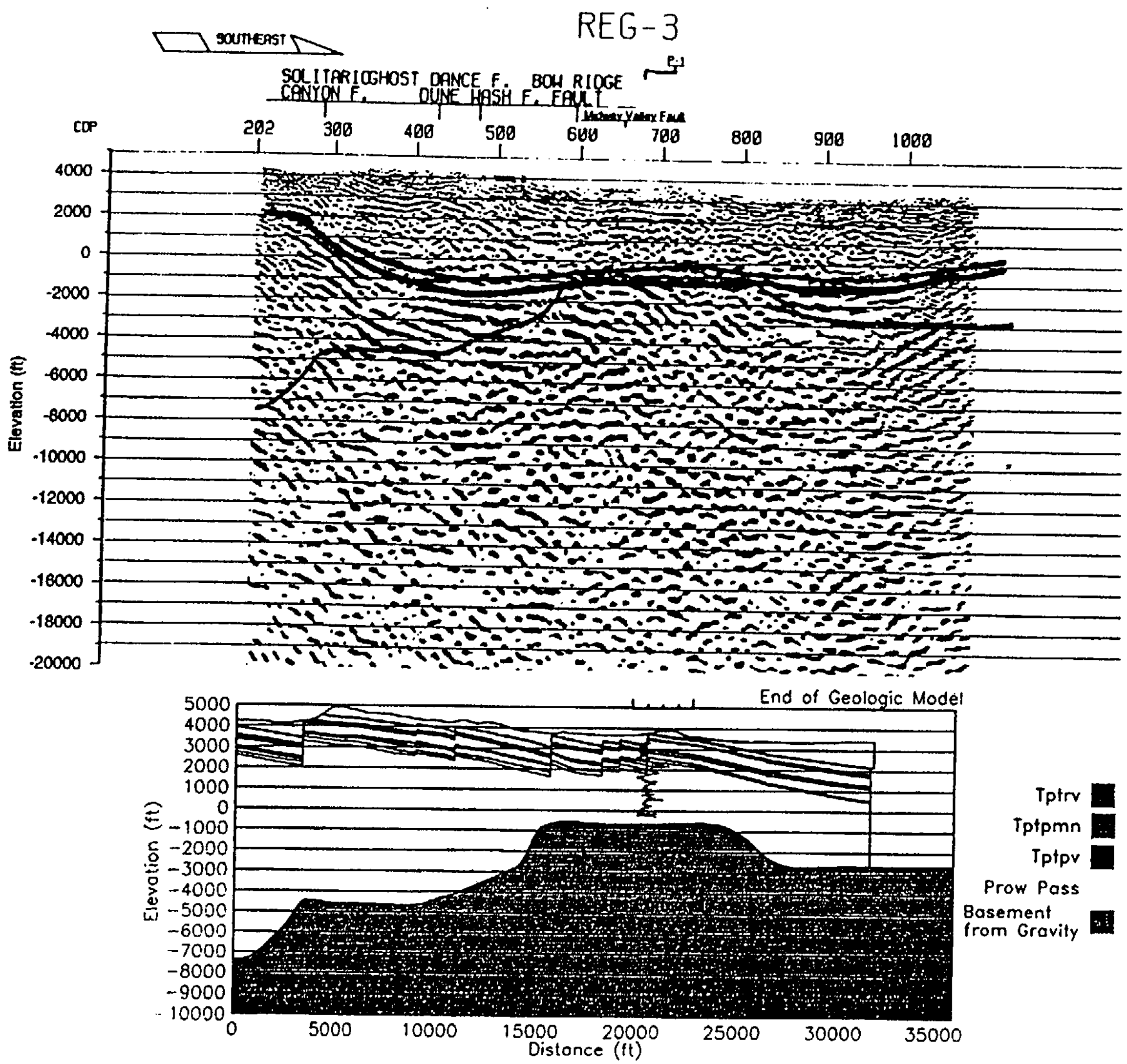

Figure 48. Seismic line REG-3 with paleozoic basement as derived from gravity; also shown is the geologic cross section where available. The red line is the basement from the gravity, green is from Brocher et al., 1996b, and the blue is our seismic pick, if one assumes that the top of the low frequency high amplitude data is the top of the basement.

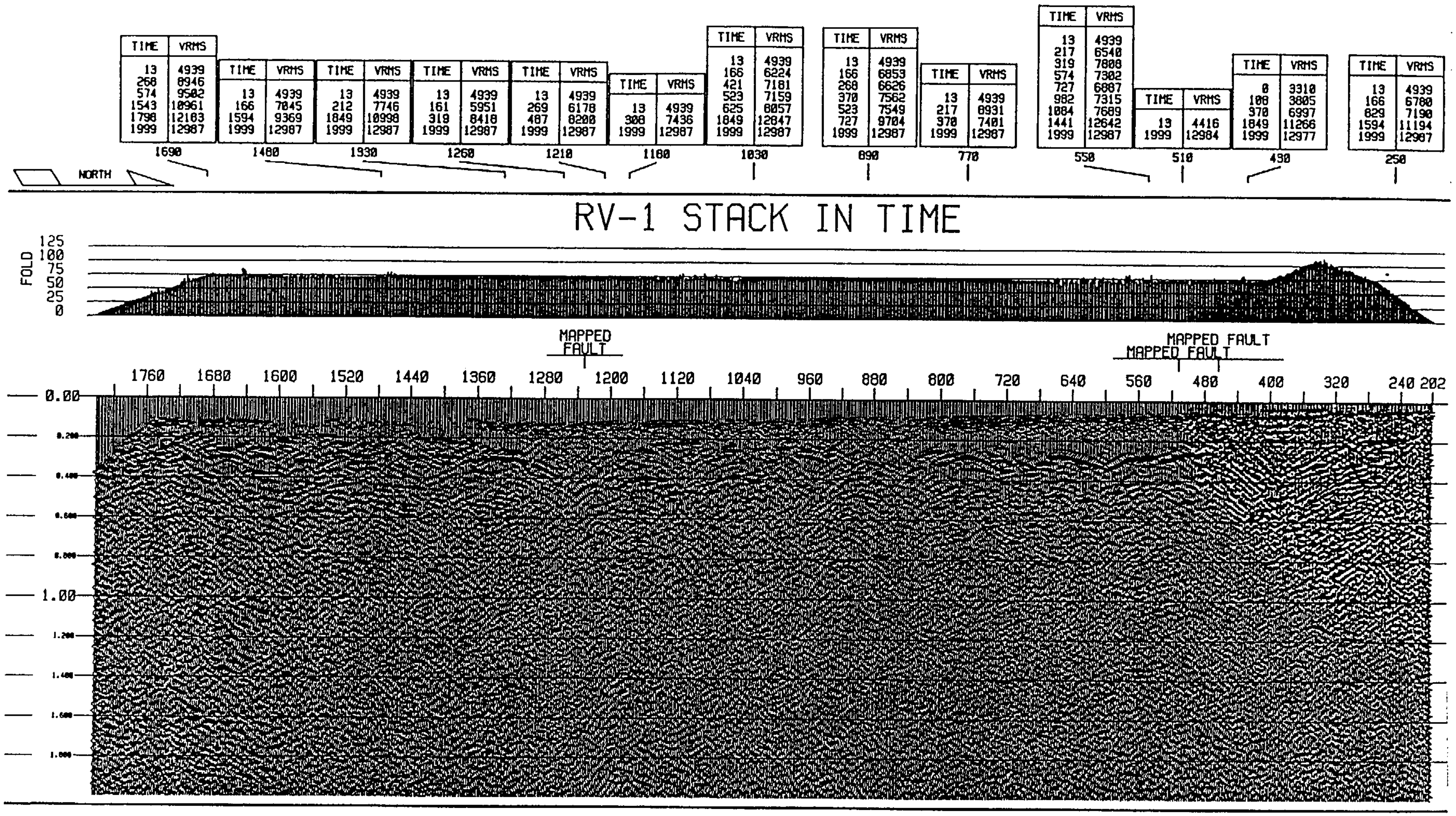

Figure 33a. RV-1 stack in time with stacking velocities shown at top.

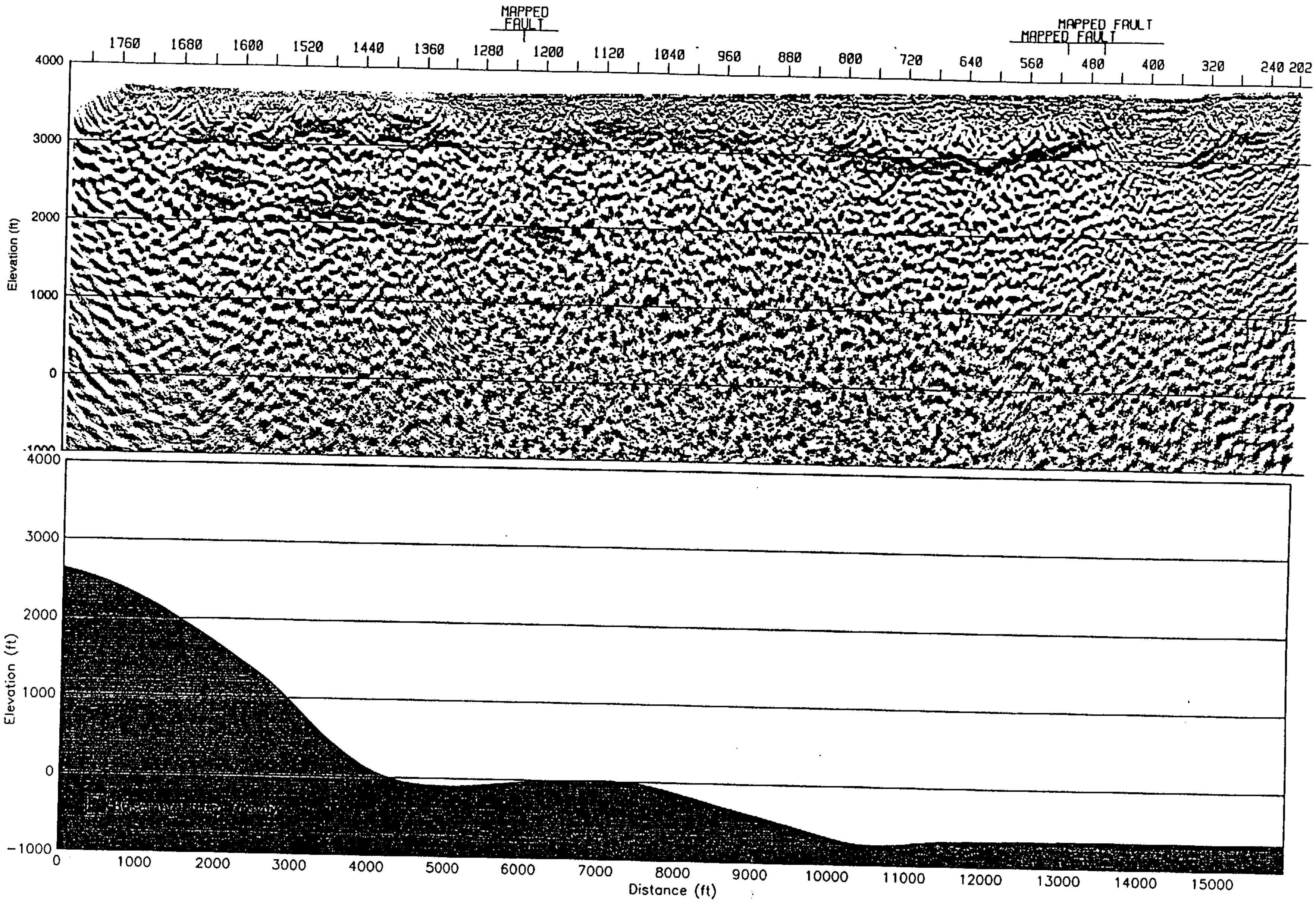

Figure 46. Seismic line RV-1 with Paleozoic basement derived from gravity. Two prominent seismic reflectors are colored green and red.

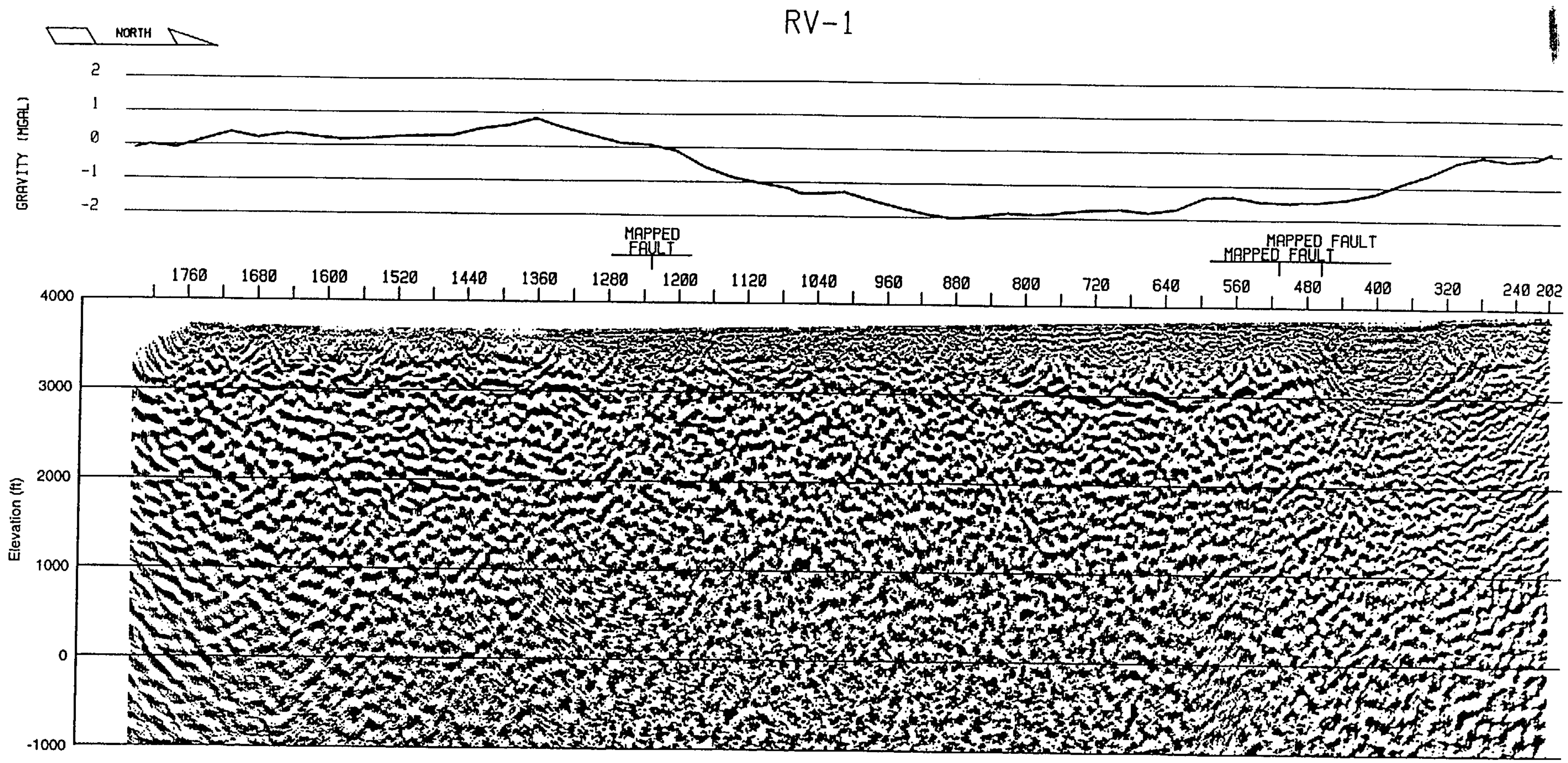

RV-1
NORTH
GRAVITY (MGAL)
2
1
0
-1
-2
MAPPED FAULT
MAPPED FAULT
MAPPED FAULT
1760 1680 1600 1520 1440 1360 1280 1200 1120 1040 960 880 800 720 640 560 480 400 320 240 202
Elevation (ft)
4000
3000
2000
1000
0
-1000

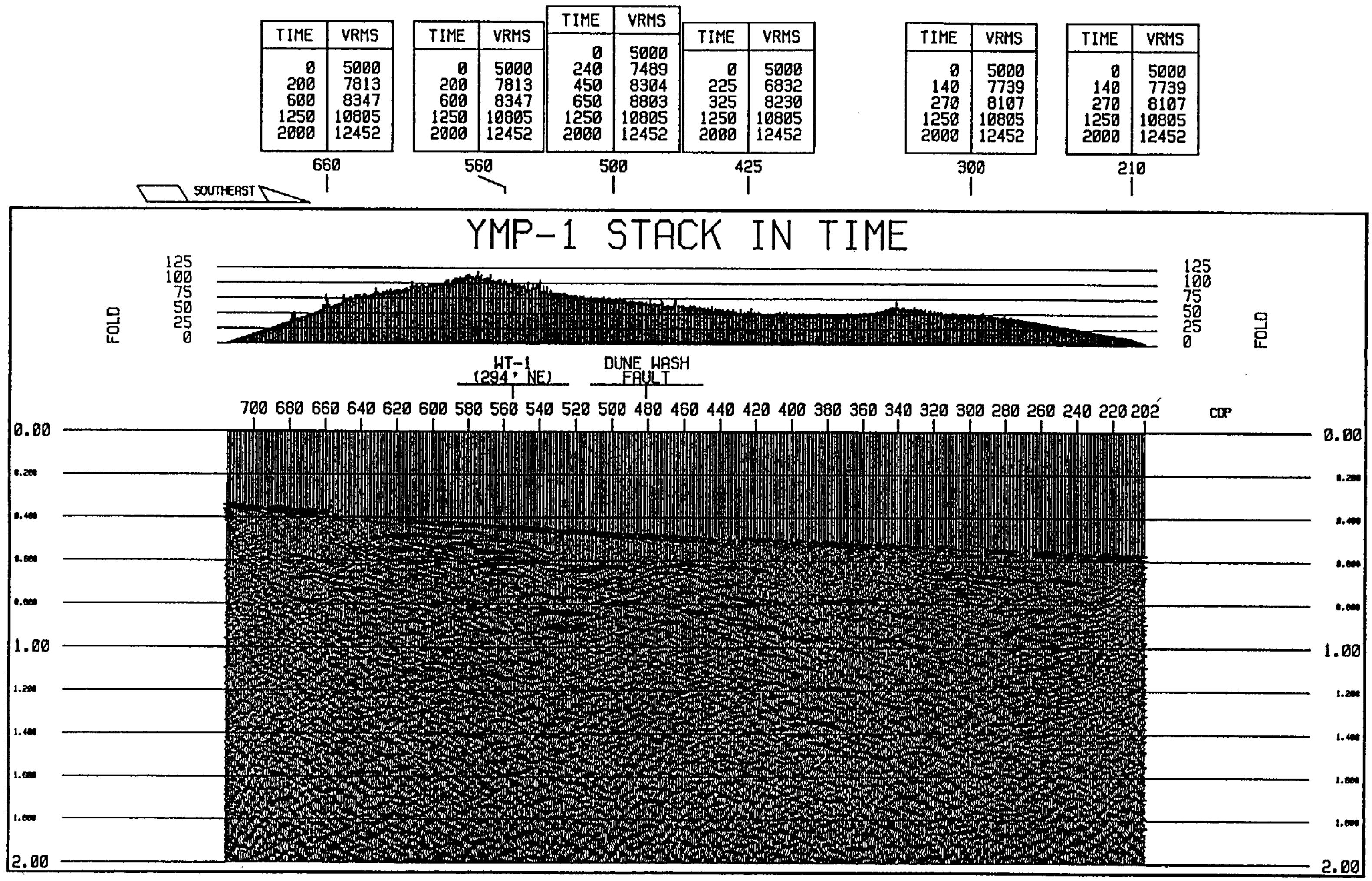

Figure13a. YMP-1 stack in time with stacking velocities shown at top.

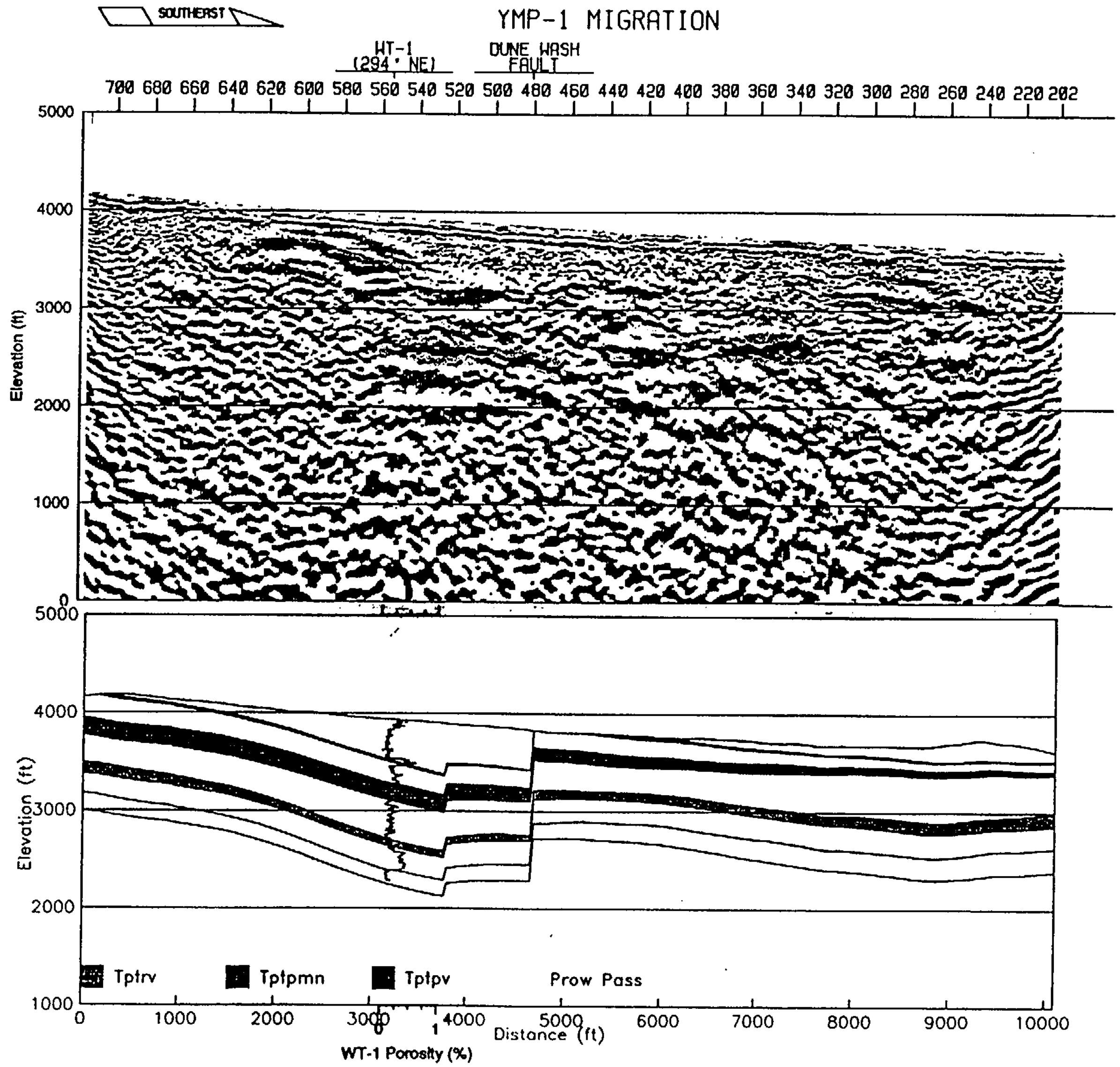

Figure 35. Seismic line YMP-1 with interpreted marker horizons and current geologic cross section. The seismic section is a migrated depth section at 1:1 scale, 1 inch = 1200 ft. Computed porosity log (if available) for all wells within 1000 ft. of seismic line is plotted on the geologic cross section.

YMP-1

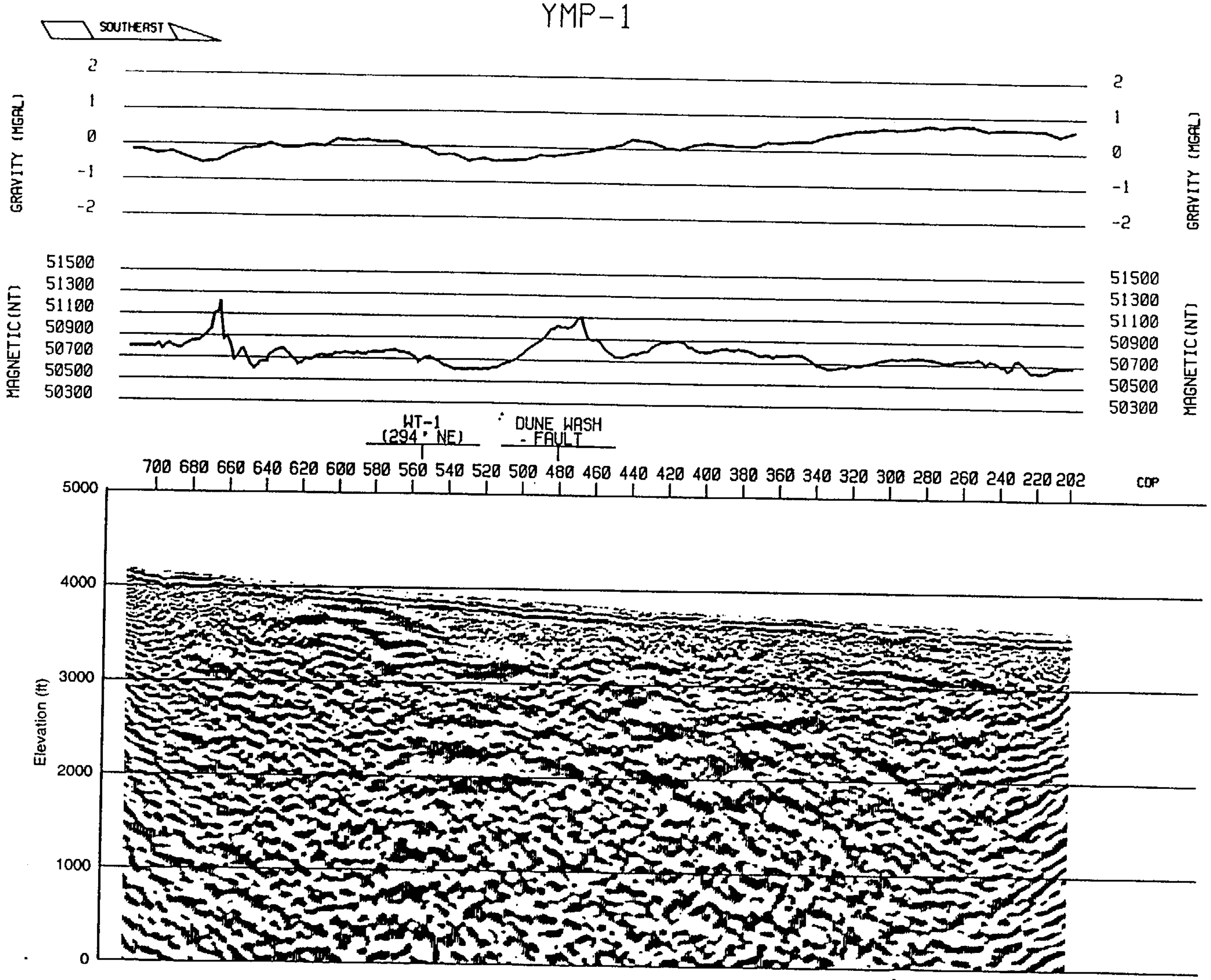

SOUTHEAST
GRAVITY (MGAL)
2
1
0
-1
-2
MAGNETIC (NT)
51500
51300
51100
50900
50700
50500
50300
WT-1
(294 ° NE)
DUNE WASH
- FAULT
700 680 660 640 620 600 580 560 540 520 500 480 460 440 420 400 380 360 340 320 300 280 260 240 220 202
CDP
Elevation (ft)
5000
4000
3000
2000
1000
0

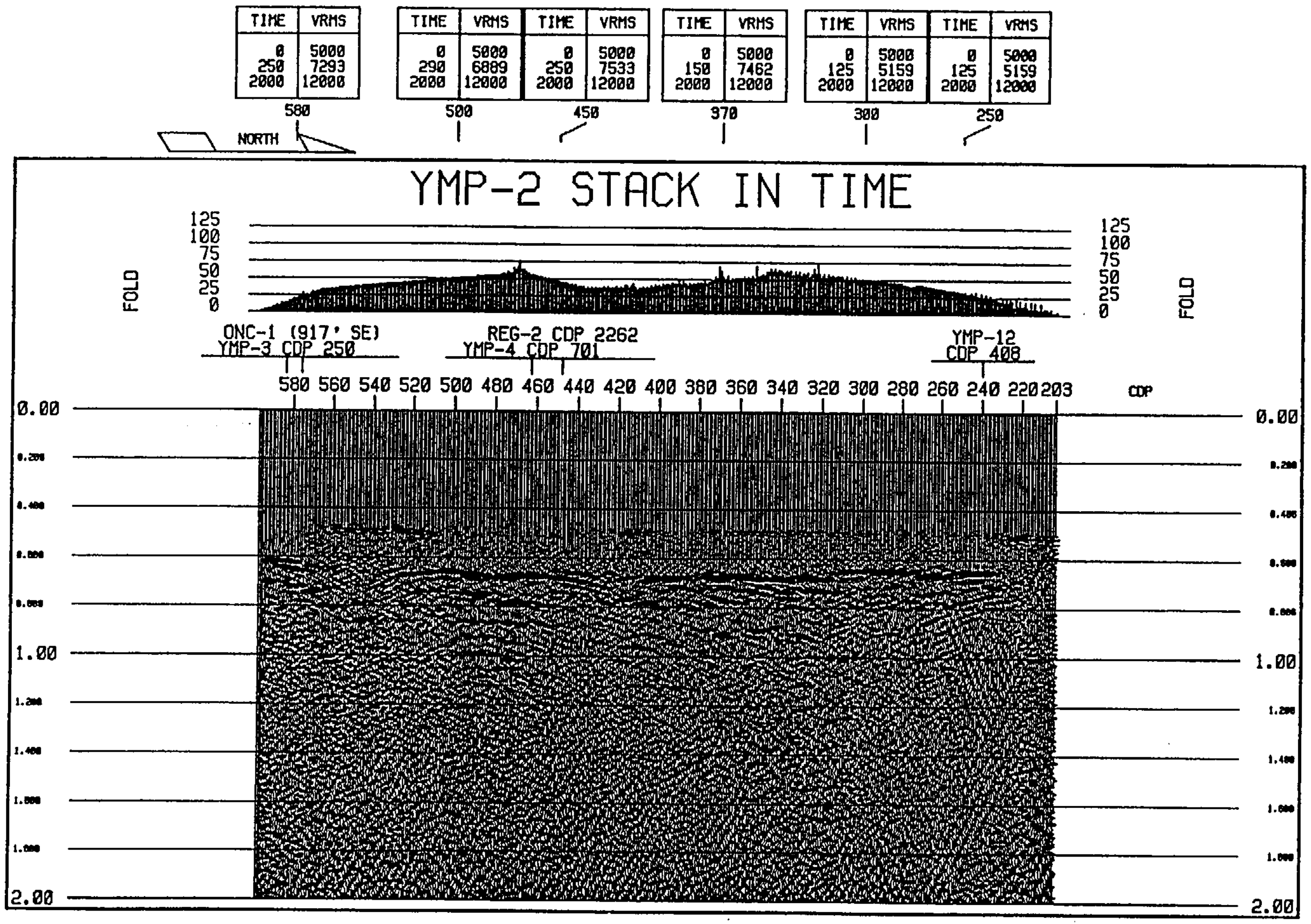

Figure 14a. YMP-2 stack in time with stacking velocities shown at top.

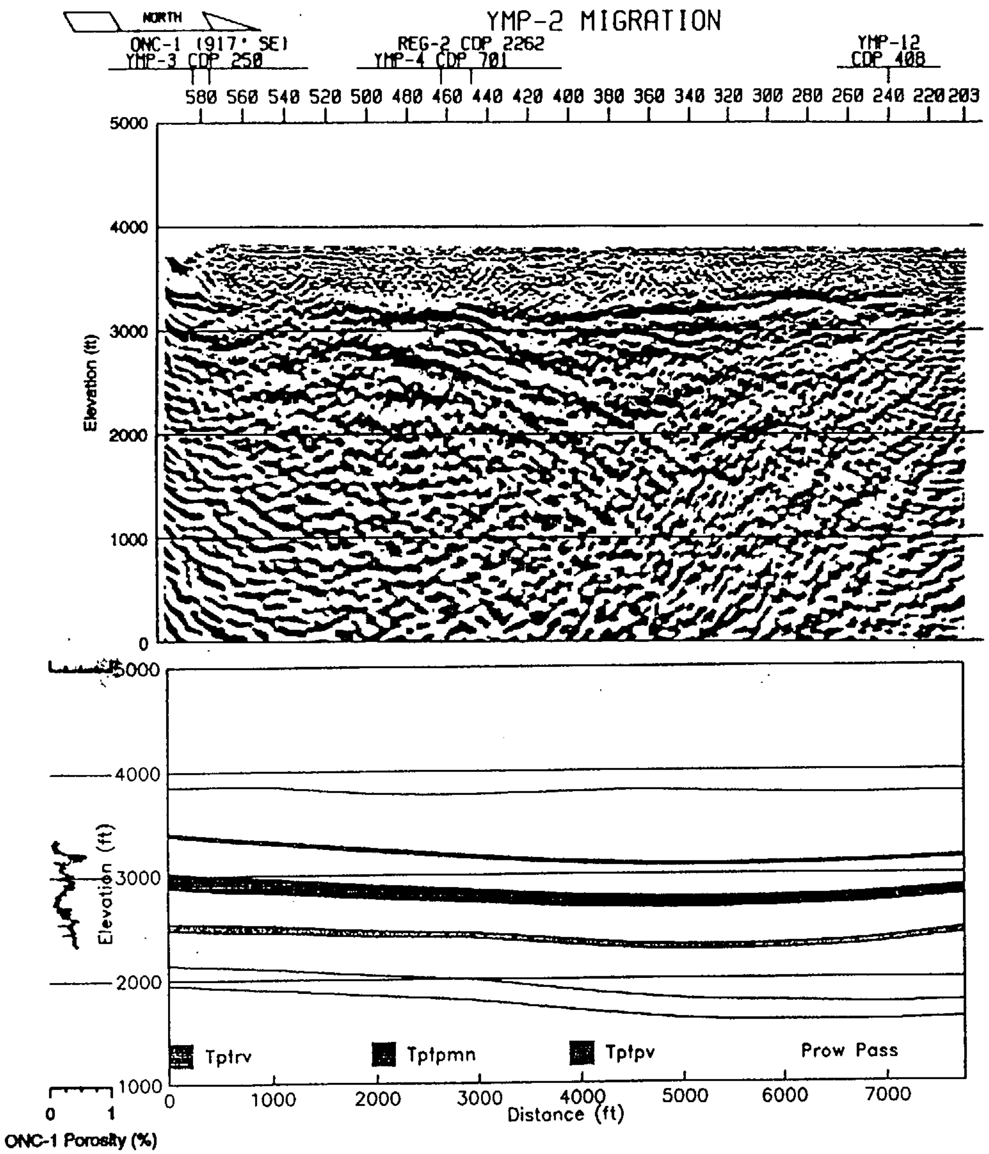

NORTH
YMP-2 MIGRATION
ONC-1 (917' SE)
YMP-3 CDP 250
REG-2 CDP 2262
YMP-4 CDP 701
YMP-12
CDP 408
580 560 540 520 500 480 460 440 420 400 380 360 340 320 300 280 260 240 220 203
Elevation (ft)
5000
4000
3000
2000
1000
0
Tptrv
Tptpmn
Tptpv
Prow Pass
0 1000 2000 3000 4000 5000 6000 7000
Distance (ft)
0 1
ONC-1 Porosity (%)

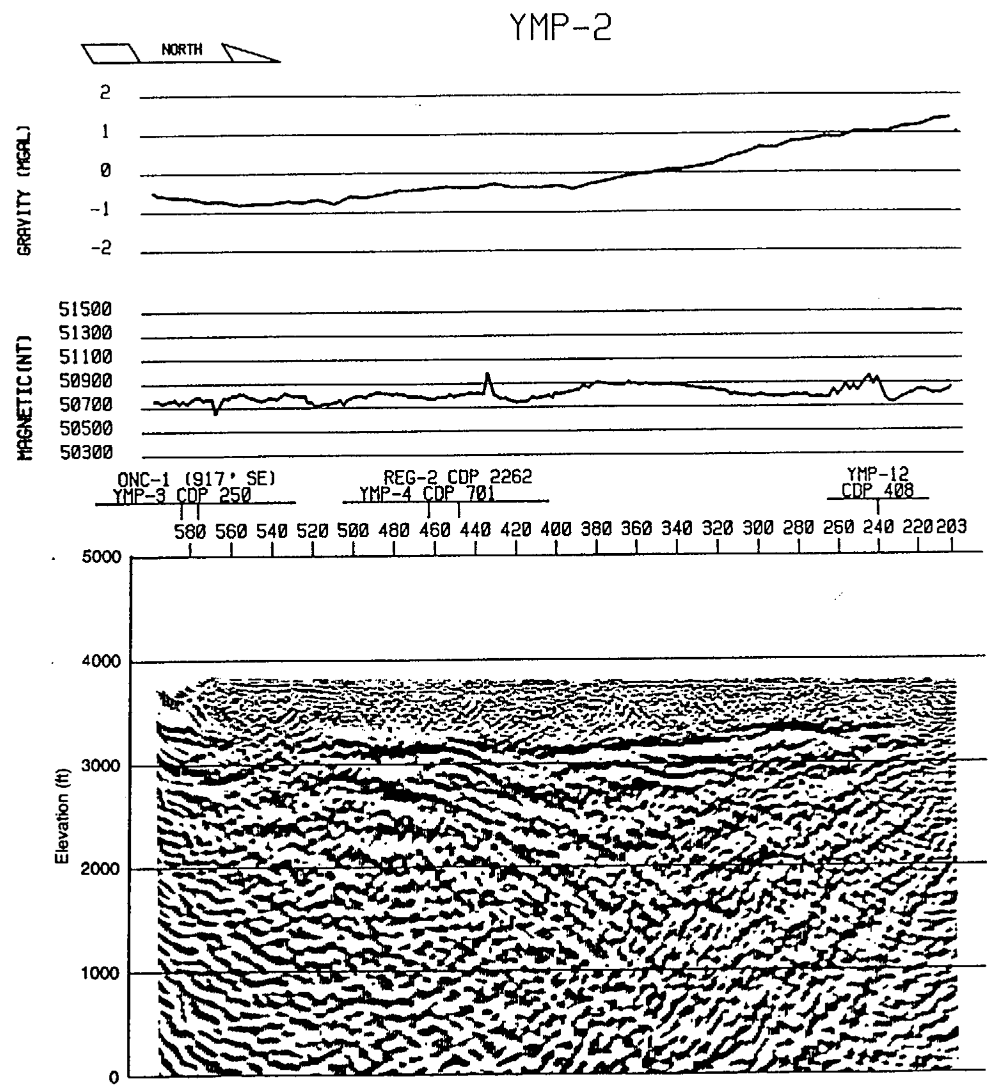

YMP-2
NORTH
GRAVITY (MGAL)
2
1
0
-1
-2
MAGNETIC(NT)
51500
51300
51100
50900
50700
50500
50300
ONC-1 (917' SE)
YMP-3 CDP 250
REG-2 CDP 2262
YMP-4 CDP 701
YMP-12
CDP 408
580 560 540 520 500 480 460 440 420 400 380 360 340 320 300 280 260 240 220 203
Elevation (ft)
5000
4000
3000
2000
1000
0

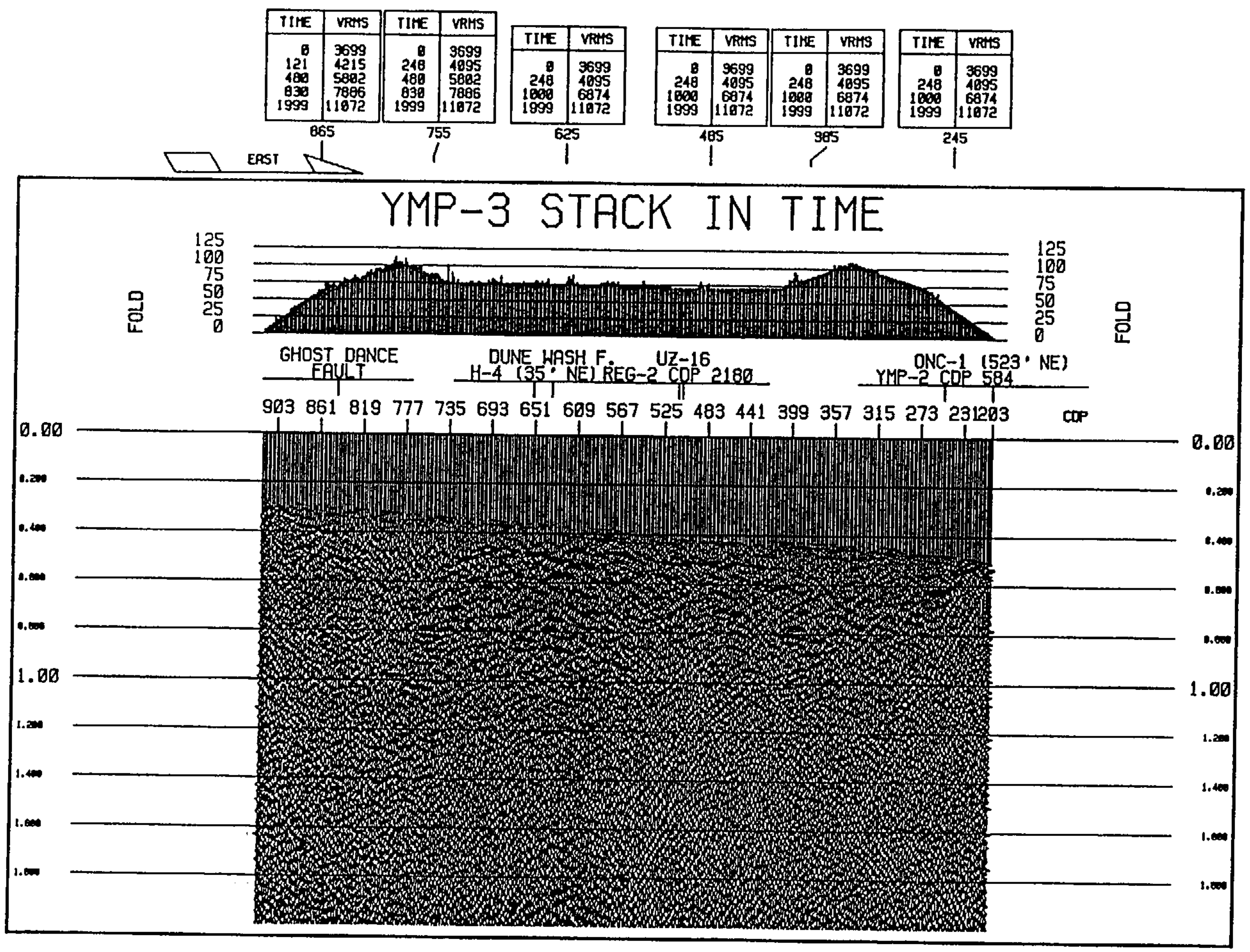

Figure 15a. YMP-3 stack in time with stacking velocities shown at top.

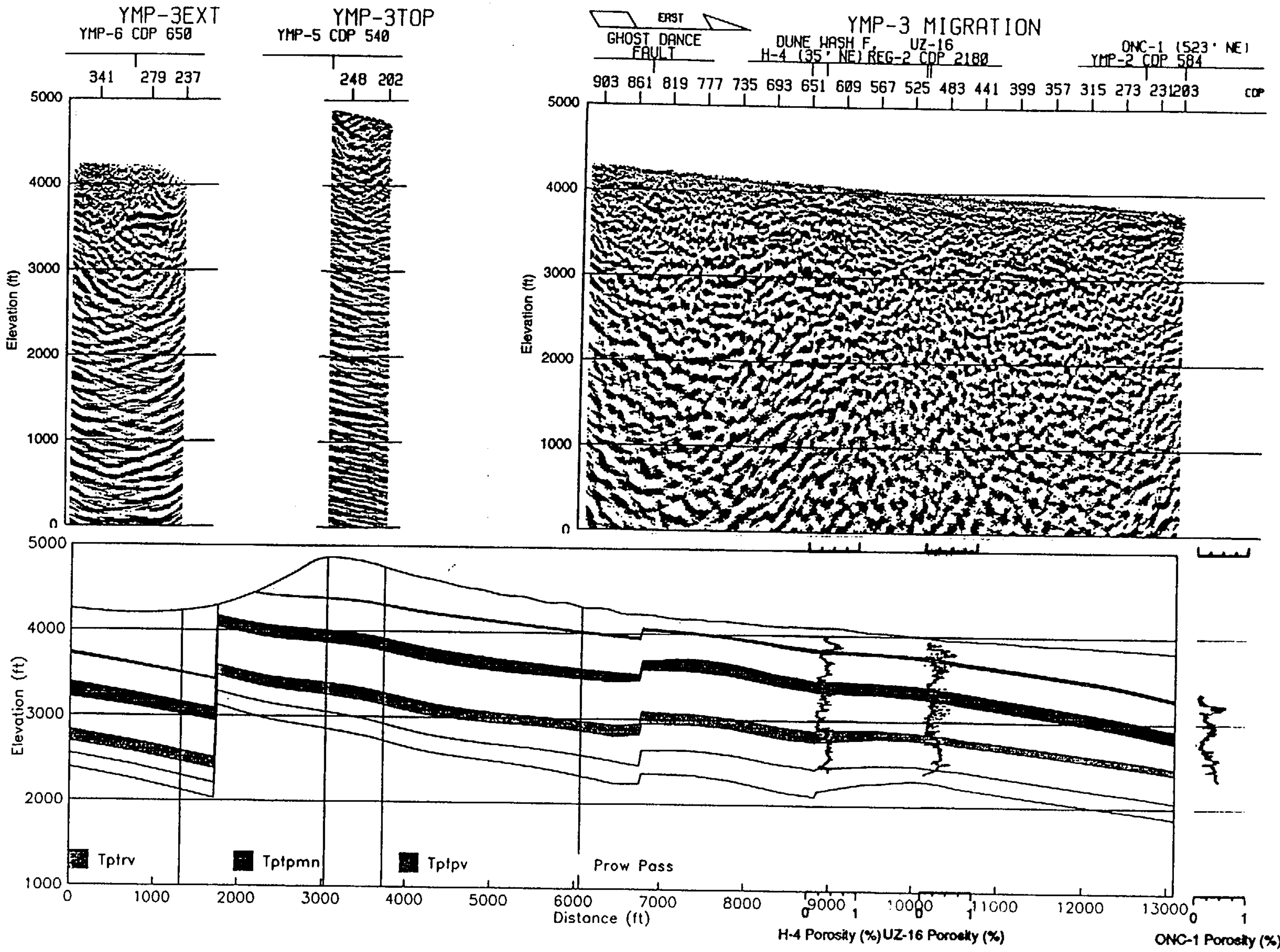

Figure 37. Seismic lines YMP3-ext, YMP3top, and YMP-3 with interpreted marker horizons and current geologic cross section. The seismic section is a migrated depth section at 1:1 scale, 1 inch = 1200 ft. Computed porosity log (if available) for all wells within 1000 ft. of seismic line is plotted on the geologic cross section.

YMP-3

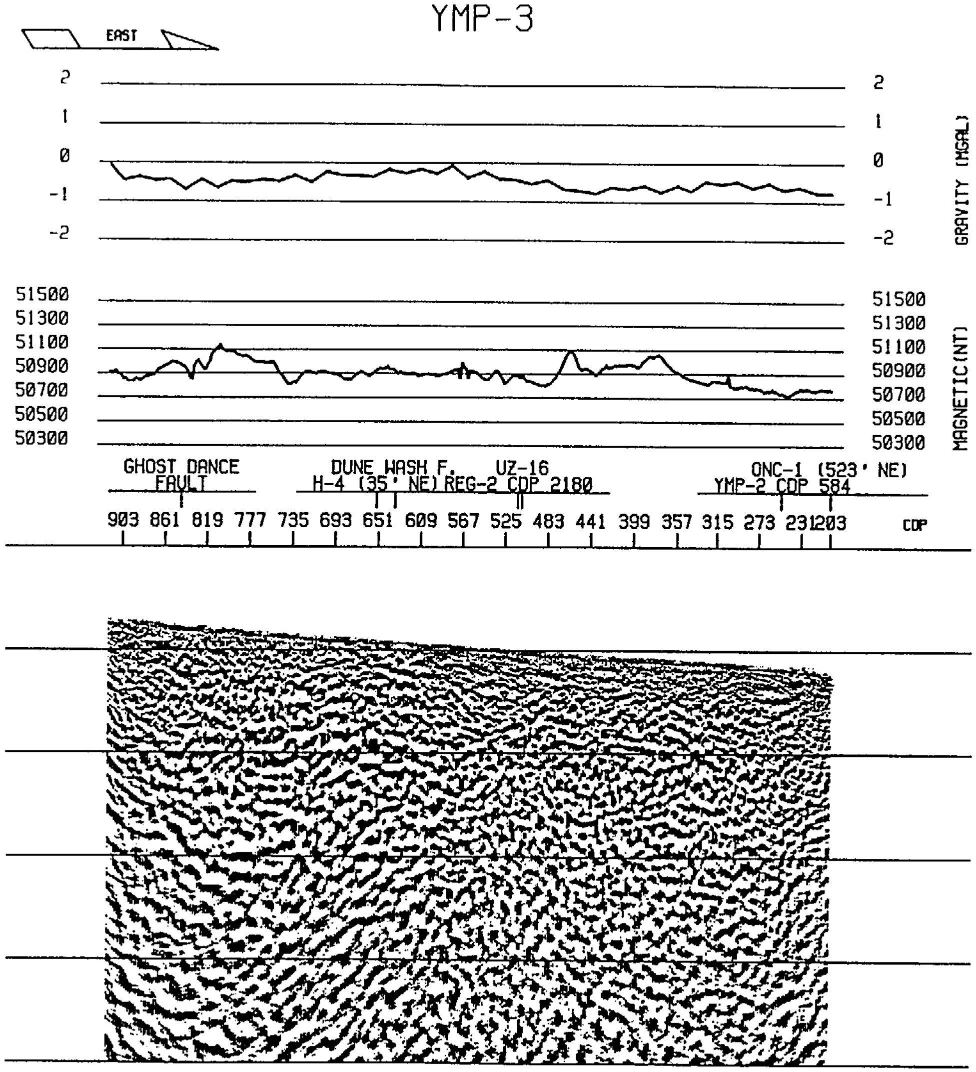
EAST
GRAVITY (MGAL)
2
1
0
-1
-2
MAGNETIC(NT)
51500
51300
51100
50900
50700
50500
50300
GHOST DANCE FAULT
DUNE WASH F.
H-4 (35' NE)
UZ-16
REG-2 CDP 2180
ONC-1 (523' NE)
YMP-2 CDP 584
903 861 819 777 735 693 651 609 567 525 483 441 399 357 315 273 231203
CDP

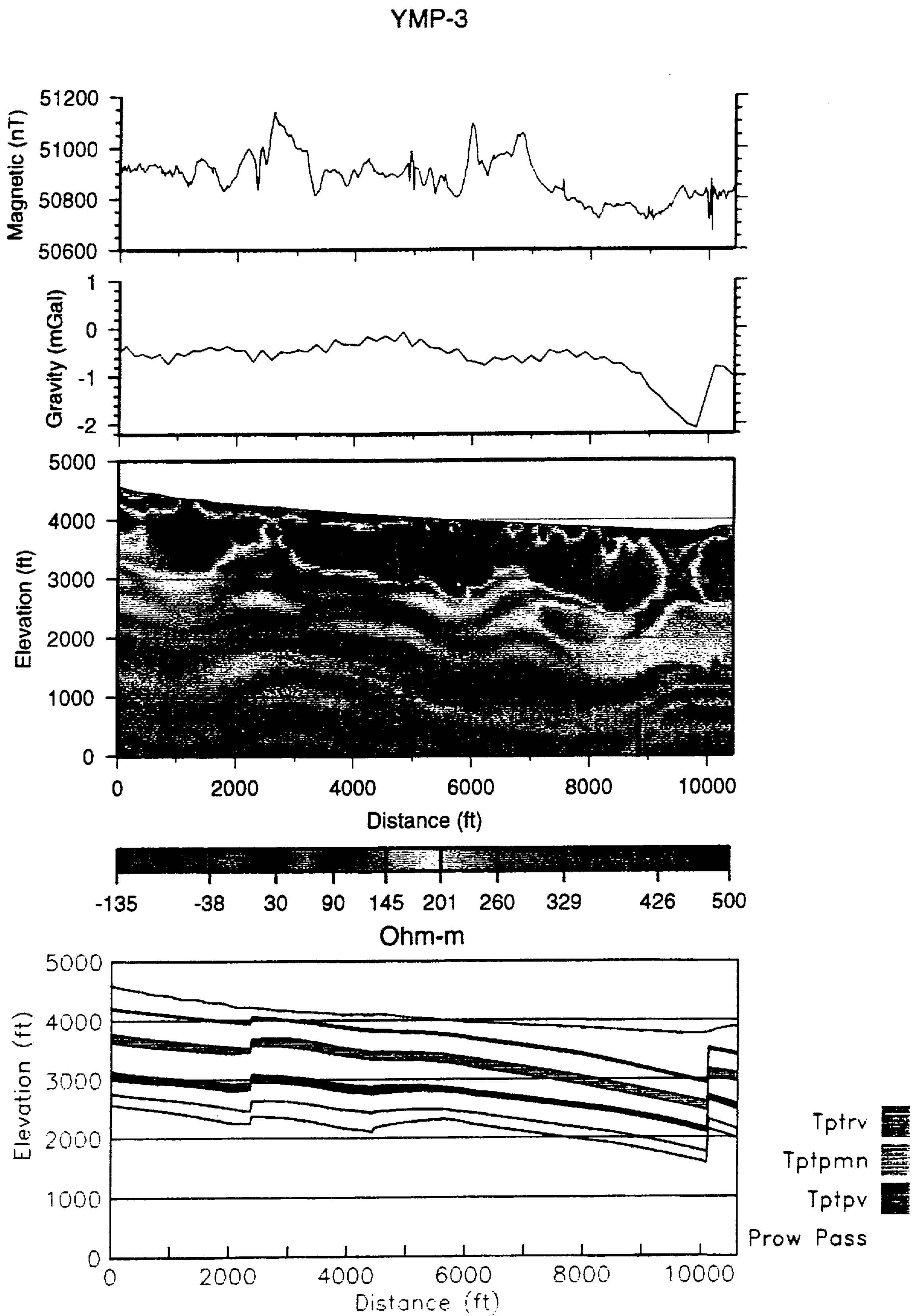

Figure 93D. Geophysical data for Line YMP-3. Magnetic (top), gravity (second from top), magnetotellurics (third from top) and geologic cross section (bottom). All data sets are on the same distance scale.

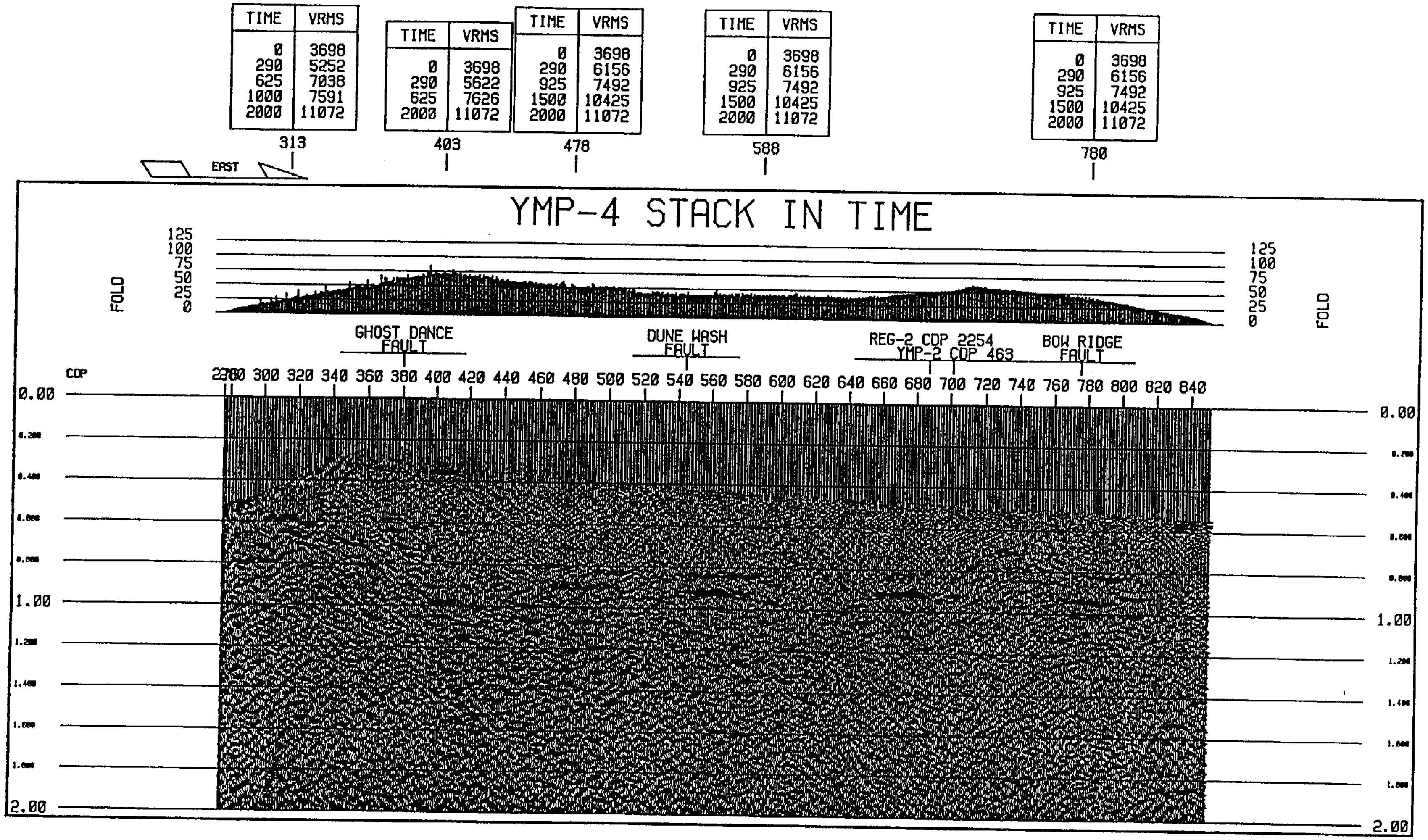

Figure 18a. YMP-4 stack in time with stacking velocities shown at top.

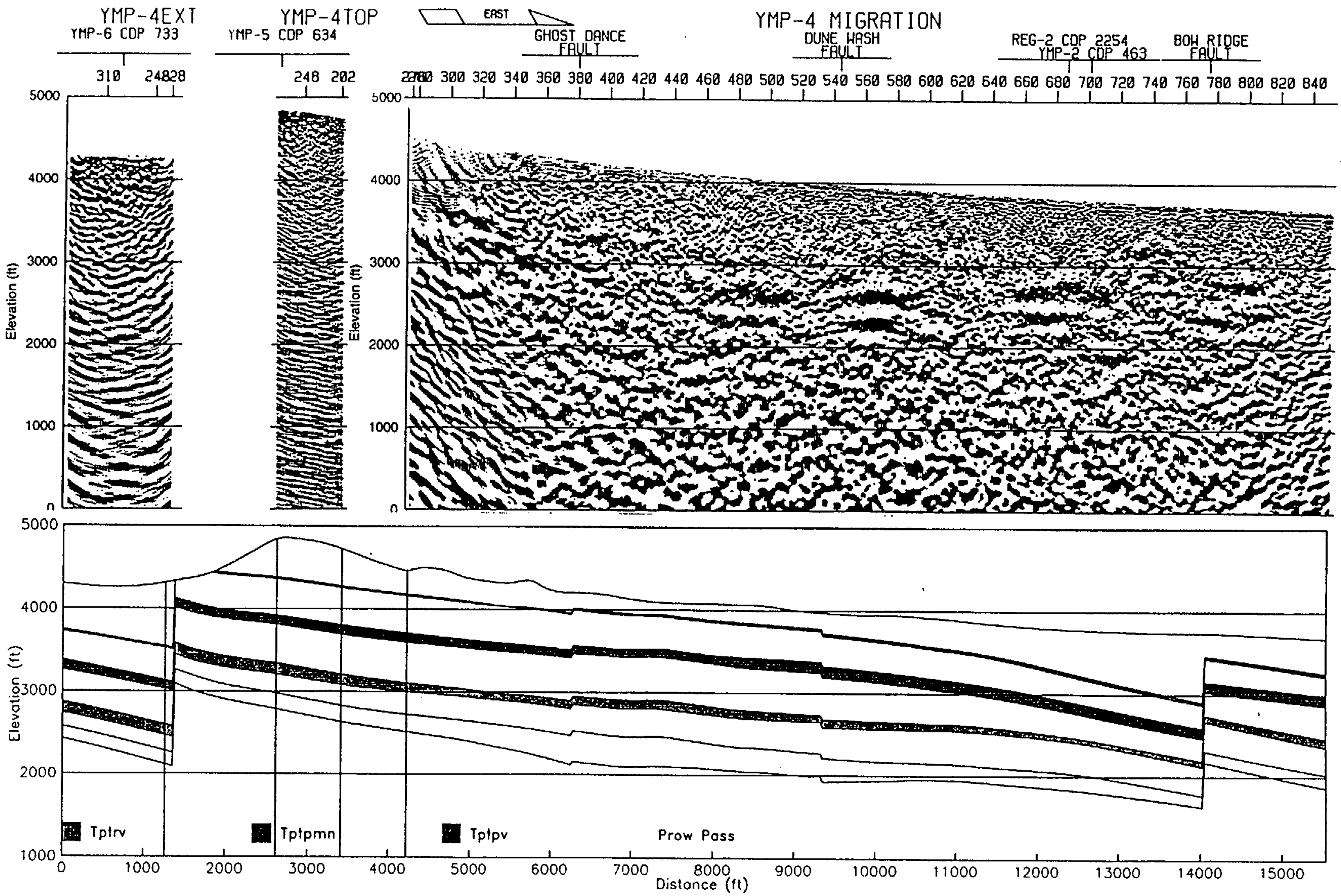

Figure 38. Seismic lines YMP-4ext, YMP-4top, and YMP-4 with interpreted marker horizons and current geologic cross section. The seismic section is a migrated depth section at 1:1 scale, 1 inch = 1200 ft. Computed porosity log (if available) for all wells within 1000 ft. of seismic line is plotted on the geologic cross section.

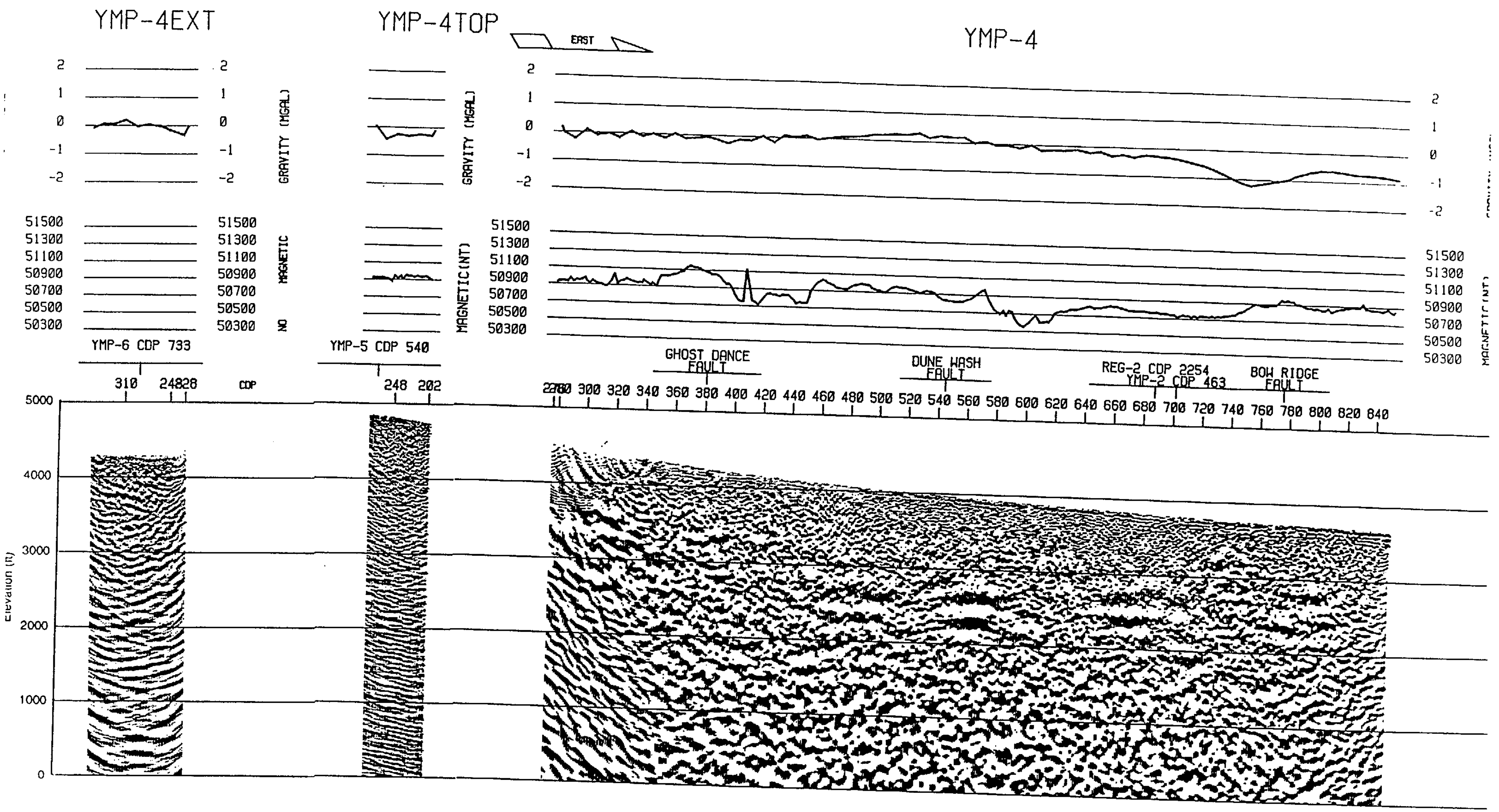

YMP-4EXT
YMP-4TOP
EAST
YMP-4
GRAVITY (MGAL)
MAGNETIC (NT)
YMP-6 CDP 733
YMP-5 CDP 540
GHOST DANCE FAULT
DUNE WASH FAULT
REG-2 CDP 2254
YMP-2 CDP 463
BOW RIDGE FAULT
CDP
Elevation (ft)

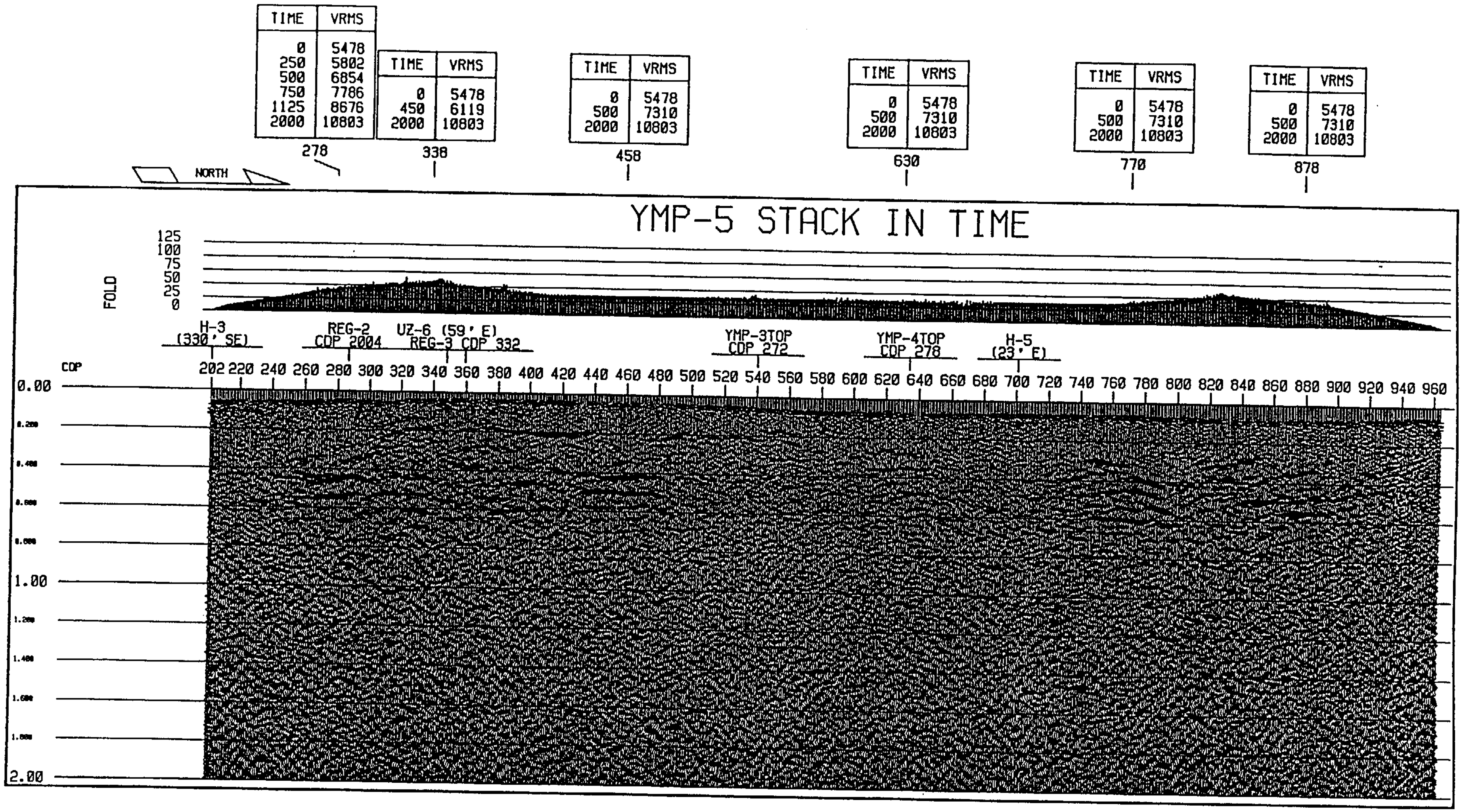

Figure 21a. YMP-5 stack in time with stacking velocities shown at top.

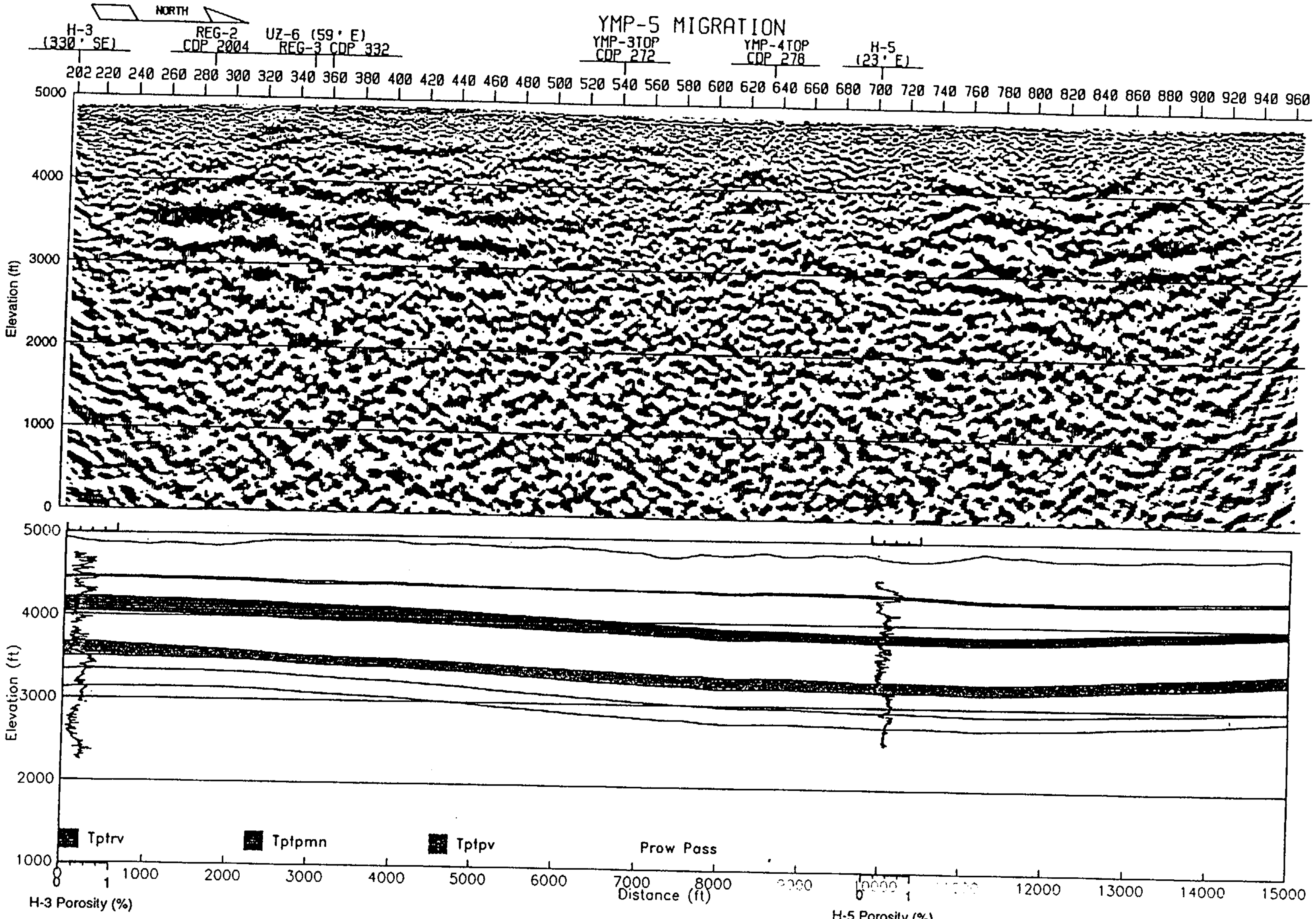

Figure 39. Seismic line YMP-5 with interpreted marker horizons and current geologic cross section. The seismic section is a migrated depth section at 1:1 scale, 1 inch = 1200 ft. Computed porosity log (if available) for all wells within 1000 ft. of seismic line is plotted on the geologic cross section.

YMP-5

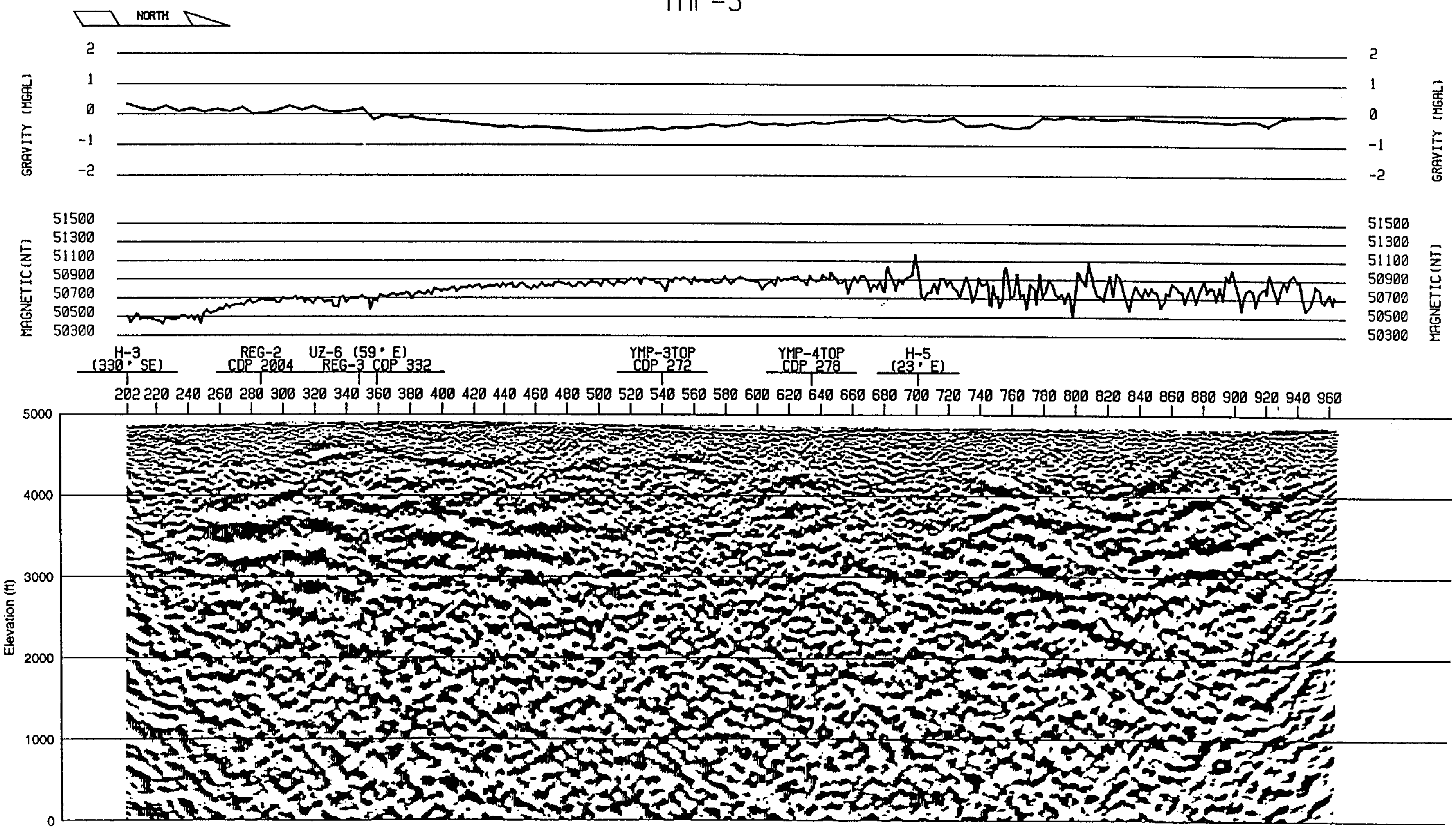

NORTH
GRAVITY (MGAL)
2
1
0
-1
-2
MAGNETIC(NT)
51500
51300
51100
50900
50700
50500
50300
H-3 (330' SE)
REG-2 CDP 2004
UZ-6 (59' E) REG-3 CDP 332
YMP-3TOP CDP 272
YMP-4TOP CDP 278
H-5 (23' E)
202 220 240 260 280 300 320 340 360 380 400 420 440 460 480 500 520 540 560 580 600 620 640 660 680 700 720 740 760 780 800 820 840 860 880 900 920 940 960
Elevation (ft)
5000
4000
3000
2000
1000
0

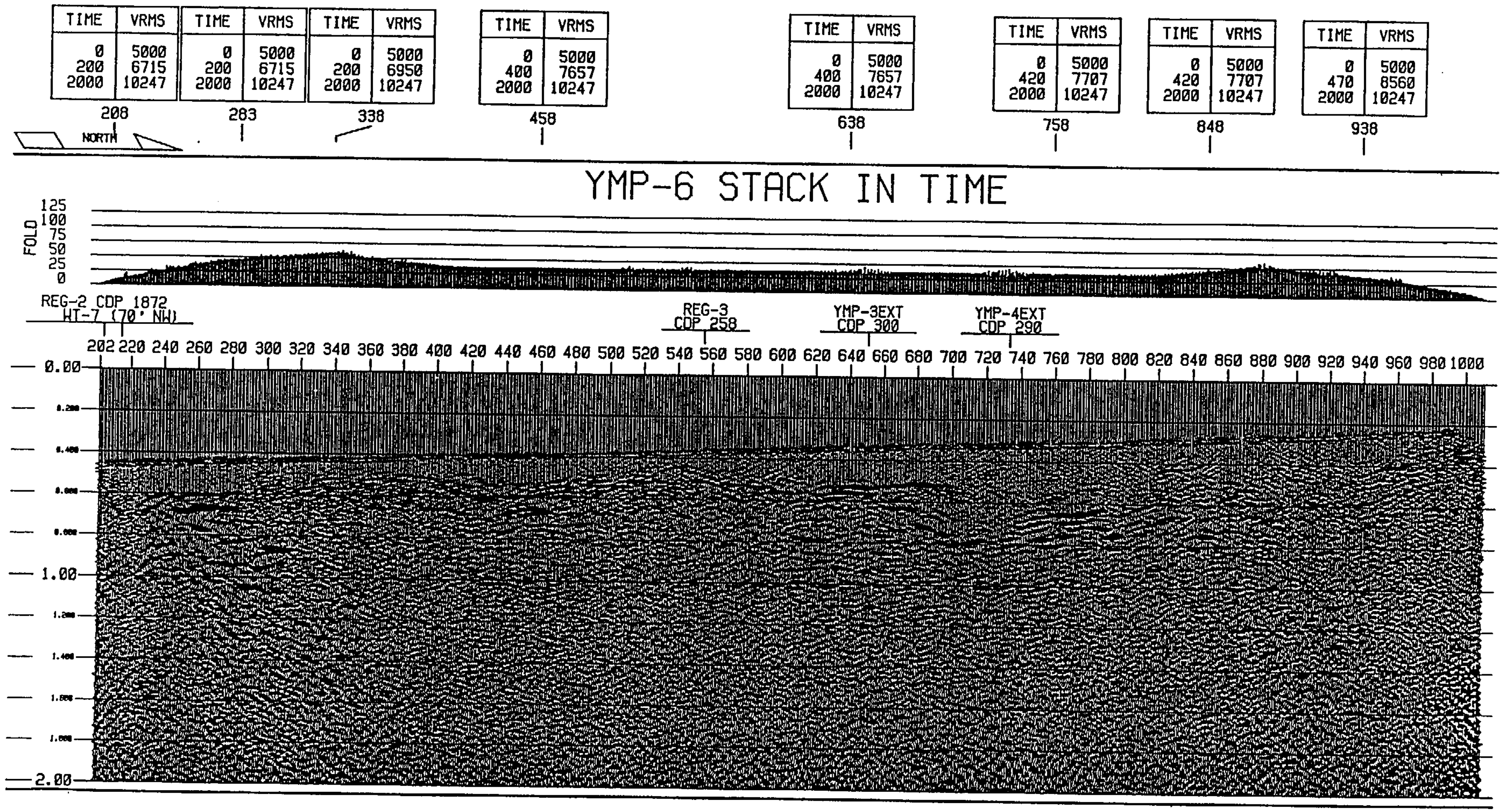

Figure 22a. YMP-6 stack in time with stacking velocities shown at top.

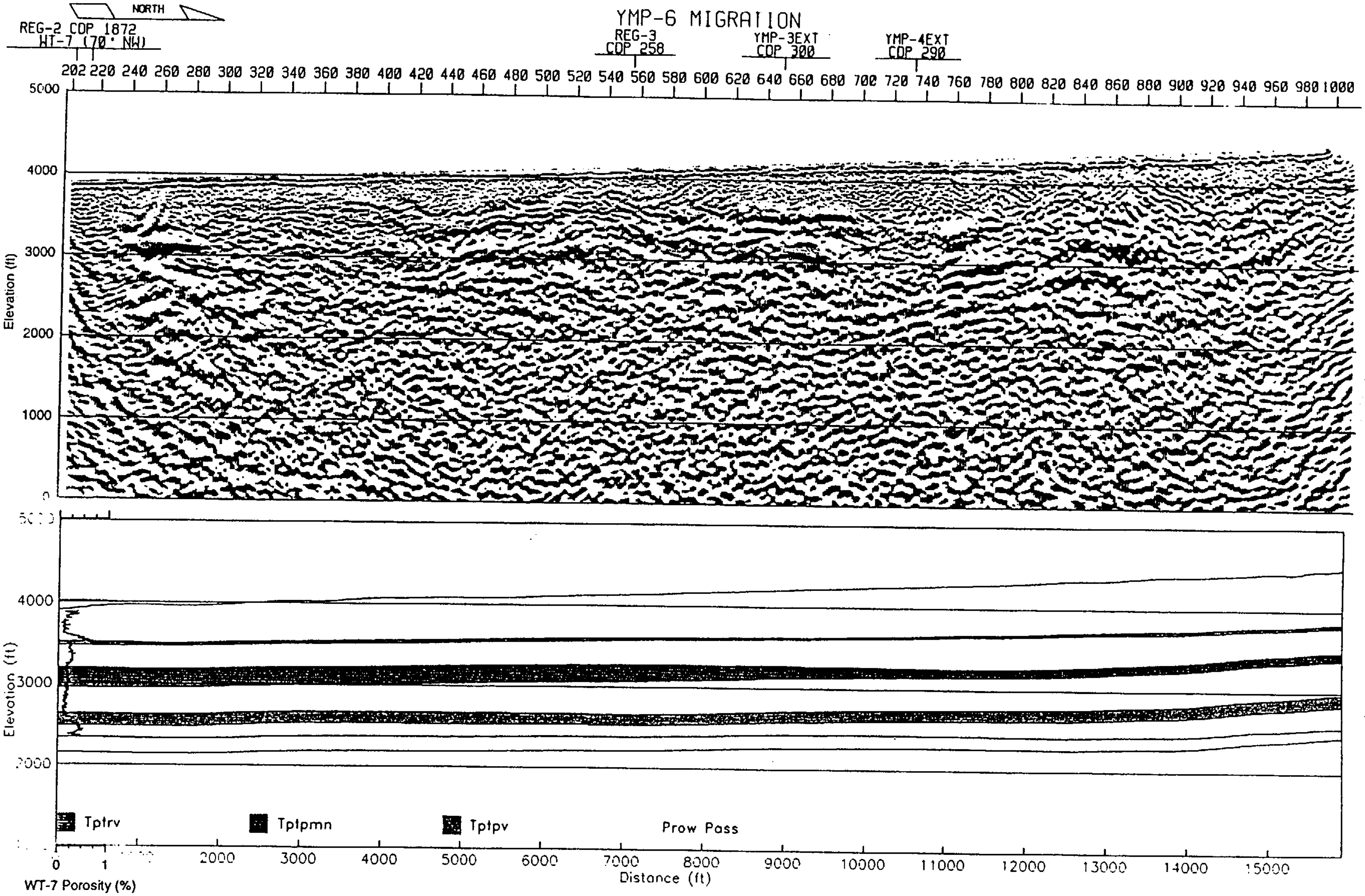

Figure 40. Seismic line YMP-6 with interpreted marker horizons and current geologic cross section. The seismic section is a migrated depth section at 1:1 scale, 1 inch = 1200 ft. Computed porosity log (if available) for all wells within 1000 ft. of seismic line is plotted on the geologic cross section.

YMP-6

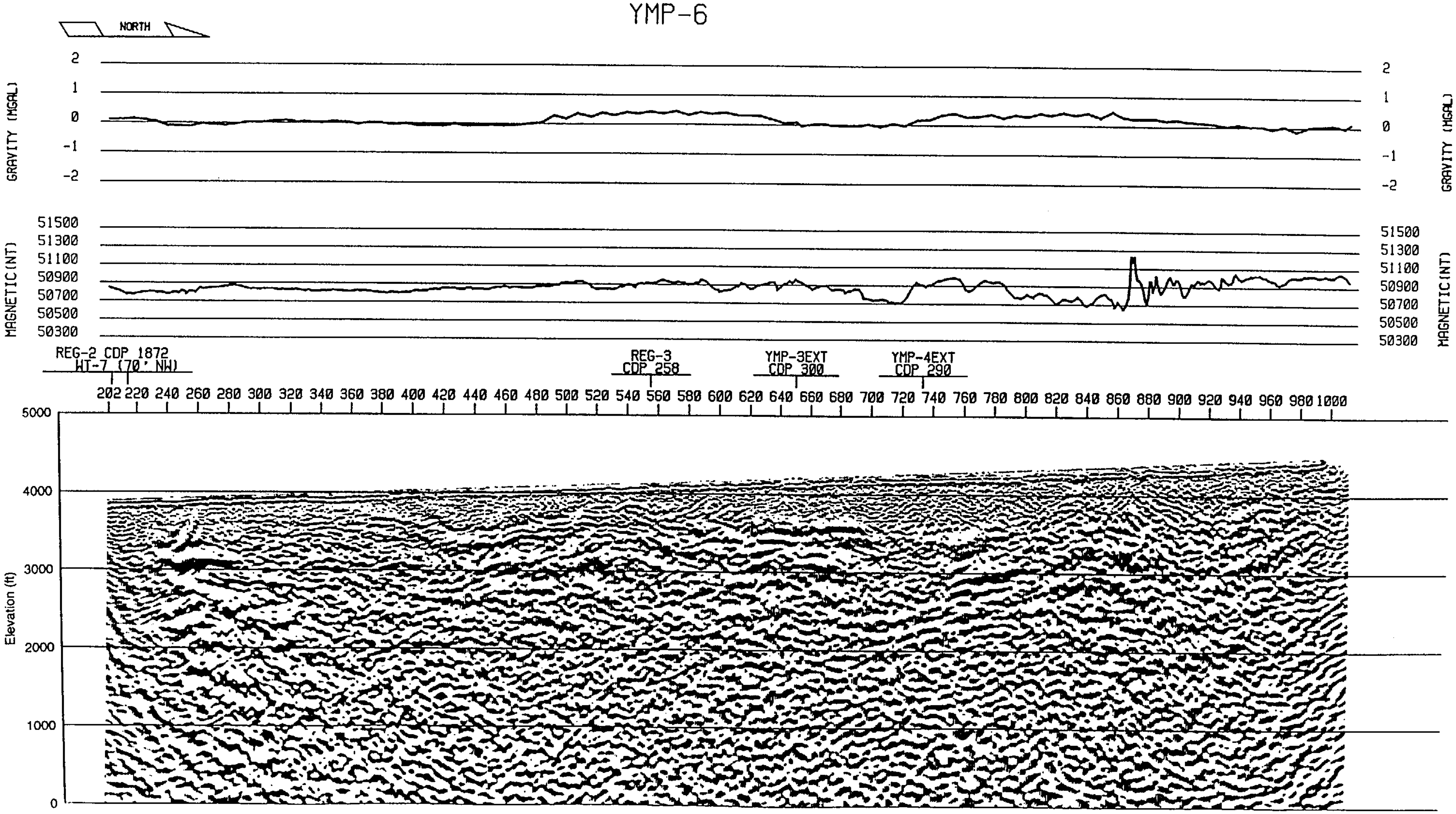
NORTH
GRAVITY (MGAL)
2
1
0
-1
-2
MAGNETIC(NT)
51500
51300
51100
50900
50700
50500
50300
REG-2 CDP 1872
WT-7 (70' NW)
REG-3
CDP 258
YMP-3EXT
CDP 300
YMP-4EXT
CDP 290
202 220 240 260 280 300 320 340 360 380 400 420 440 460 480 500 520 540 560 580 600 620 640 660 680 700 720 740 760 780 800 820 840 860 880 900 920 940 960 980 1000
Elevation (ft)
5000
4000
3000
2000
1000
0

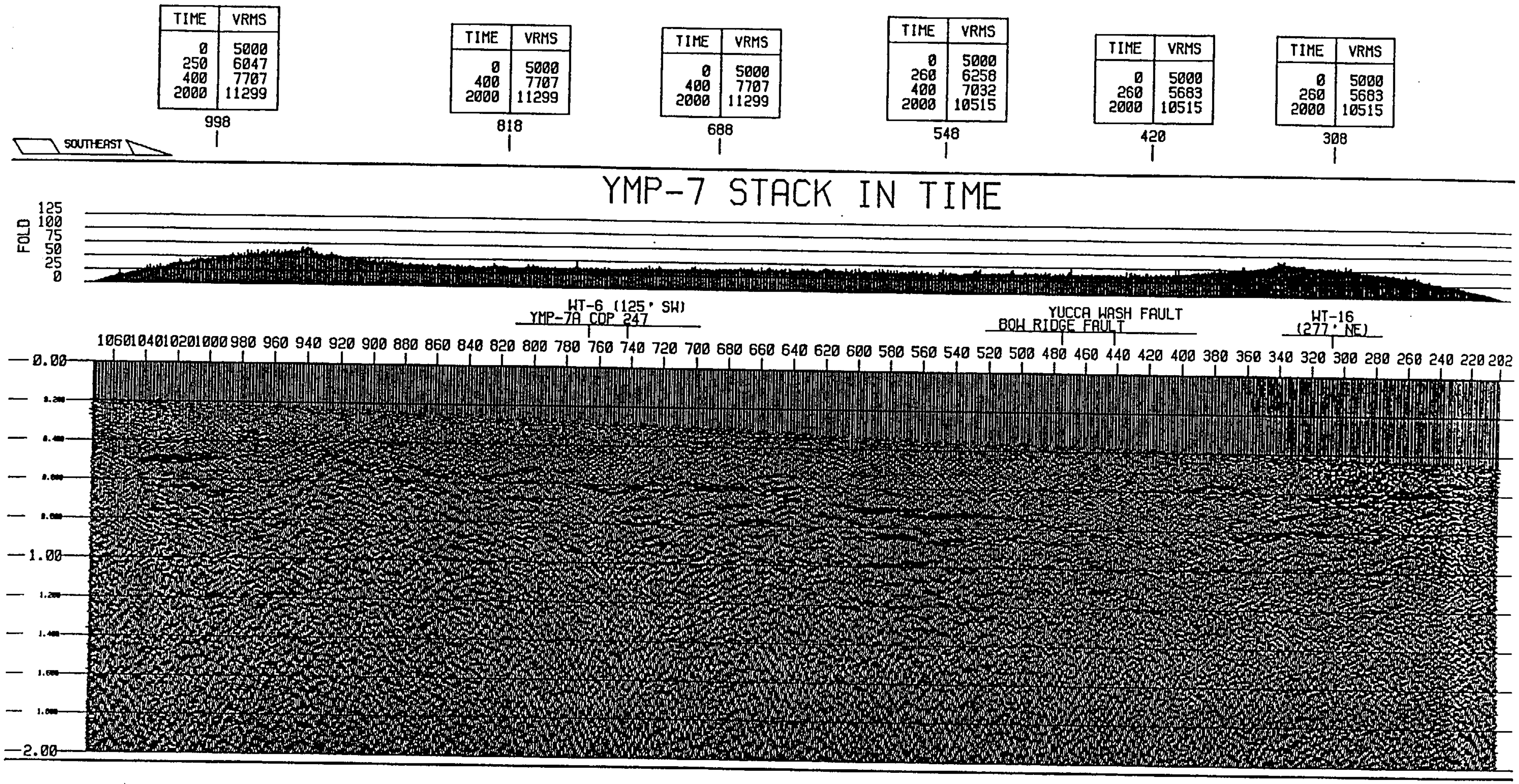

Figure 23a. YMP-7 stack in time with stacking velocities shown at top.

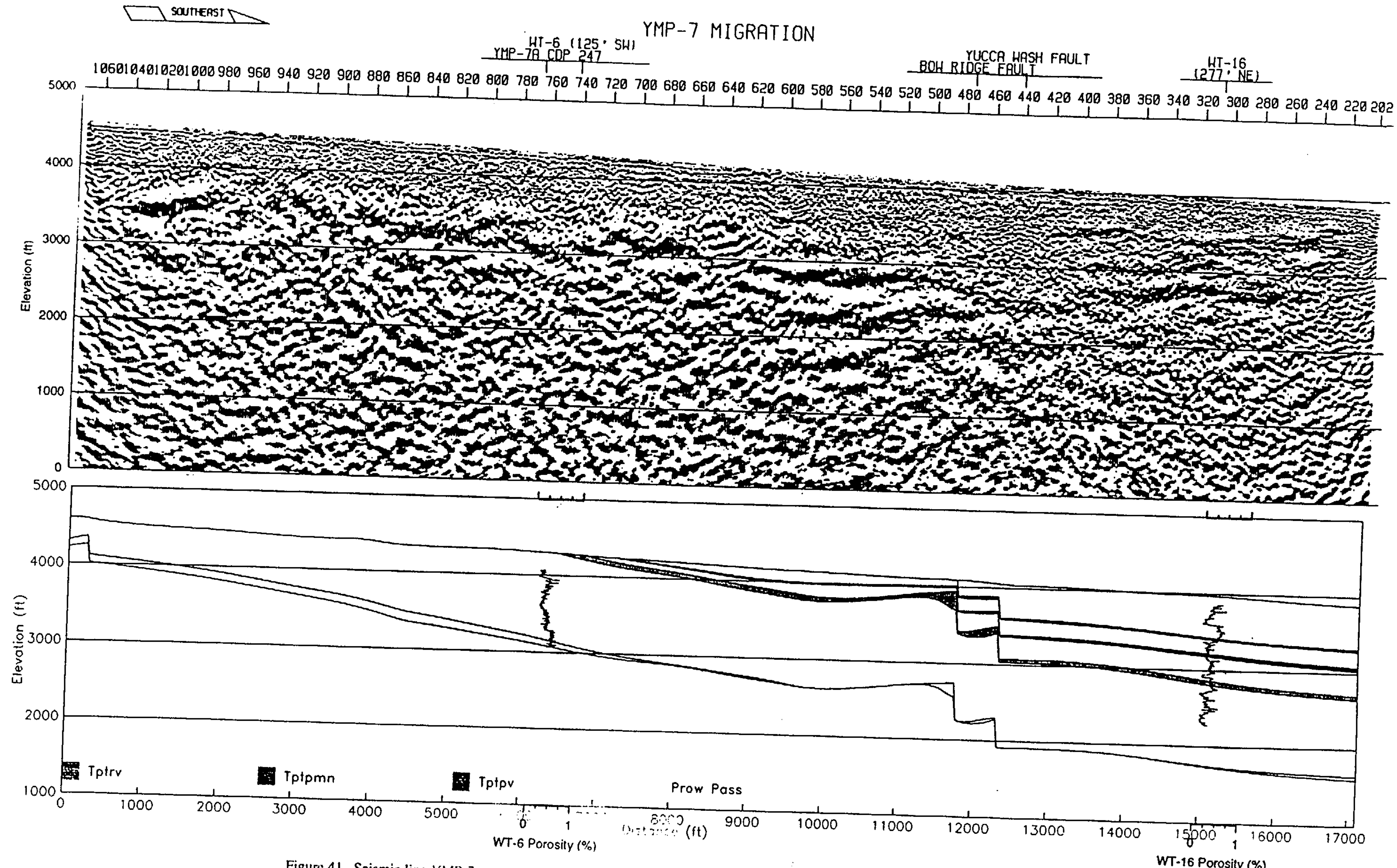

Figure 41. Seismic line YMP-7 with interpreted marker horizons and current geologic cross section. The seismic section is a migrated depth section at 1:1 scale, 1 inch = 1200 ft. Computed porosity log (if available) for all wells within 1000 ft. of seismic line is plotted on the geologic cross section.

YMP-7

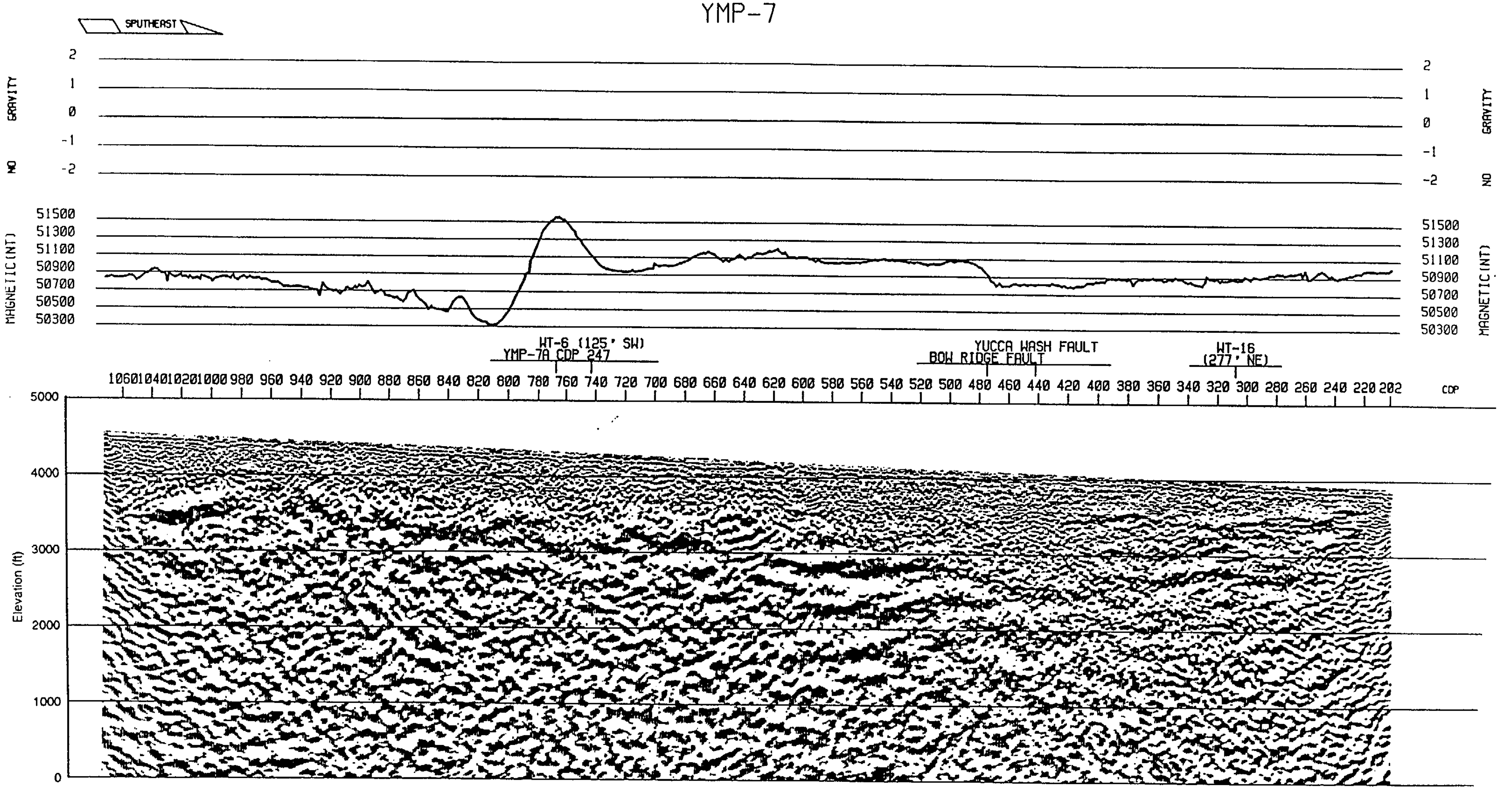

SOUTHEAST
GRAVITY
NO
2
1
0
-1
-2
MAGNETIC(NT)
51500
51300
51100
50900
50700
50500
50300
WT-6 (125' SW)
YMP-7A CDP 247
YUCCA WASH FAULT
BOW RIDGE FAULT
WT-16
(277' NE)
1060 1040 1020 1000 980 960 940 920 900 880 860 840 820 800 780 760 740 720 700 680 660 640 620 600 580 560 540 520 500 480 460 440 420 400 380 360 340 320 300 280 260 240 220 202
CDP
Elevation (ft)
5000
4000
3000
2000
1000
0

TIME	VRMS	TIME	VRMS	TIME	VRMS	TIME	VRMS	TIME	VRMS	TIME	VRMS
0	4000	0	4000	0	4000	0	4000	0	4000	0	4000
250	4591	250	4591	250	5130	250	4856	250	4658	250	4658
600	4878	700	5368	650	5885	650	5885	400	5066	400	5066
2000	8063	2000	8063	2000	8063	2000	8063	2000	8063	2000	8063
536		485		415		330		270		234	

TIME	VRMS	TIME	VRMS	TIME	VRMS
0	5000	0	5000	0	5000
400	6482	400	6482	400	6482
1000	8228	1000	8228	1000	8228
1200	8717	1200	8717	1200	8717
2000	10929	2000	10929	2000	10929
370		305		230	

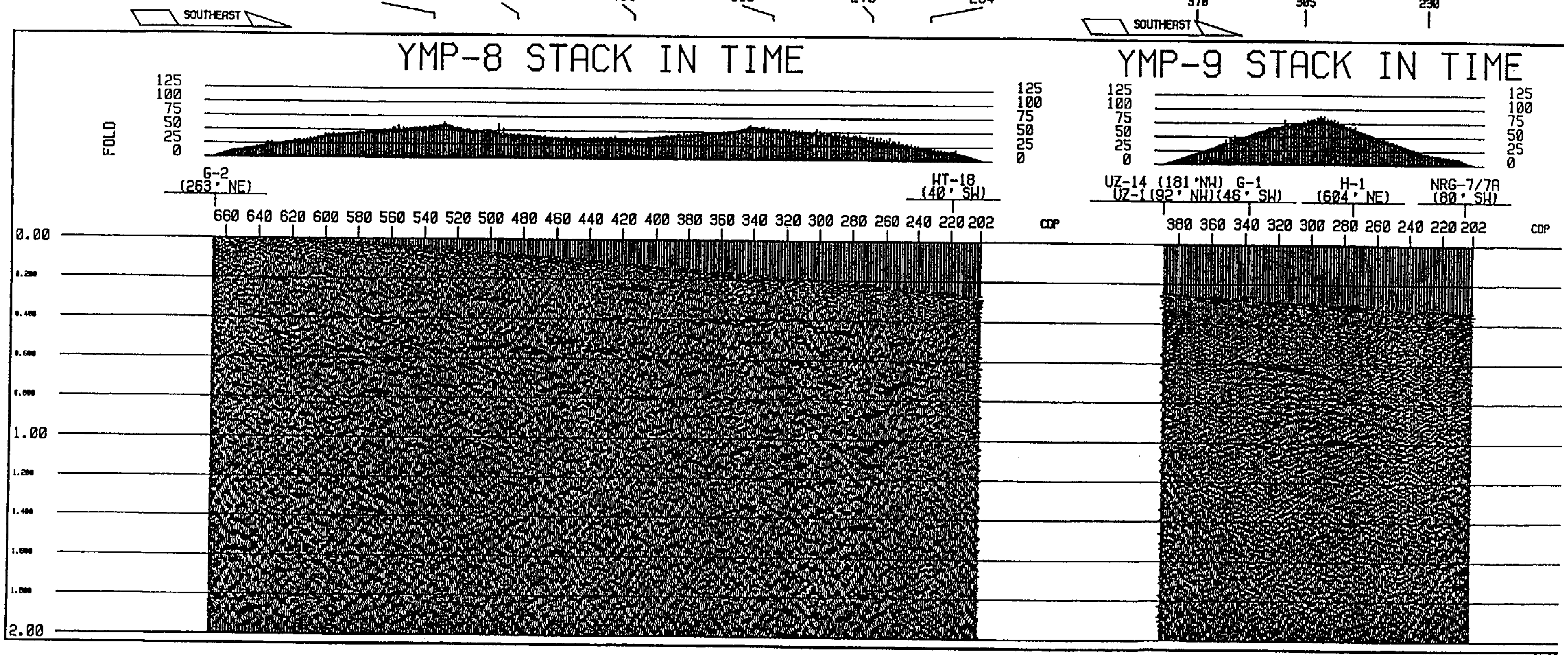

YMP-8

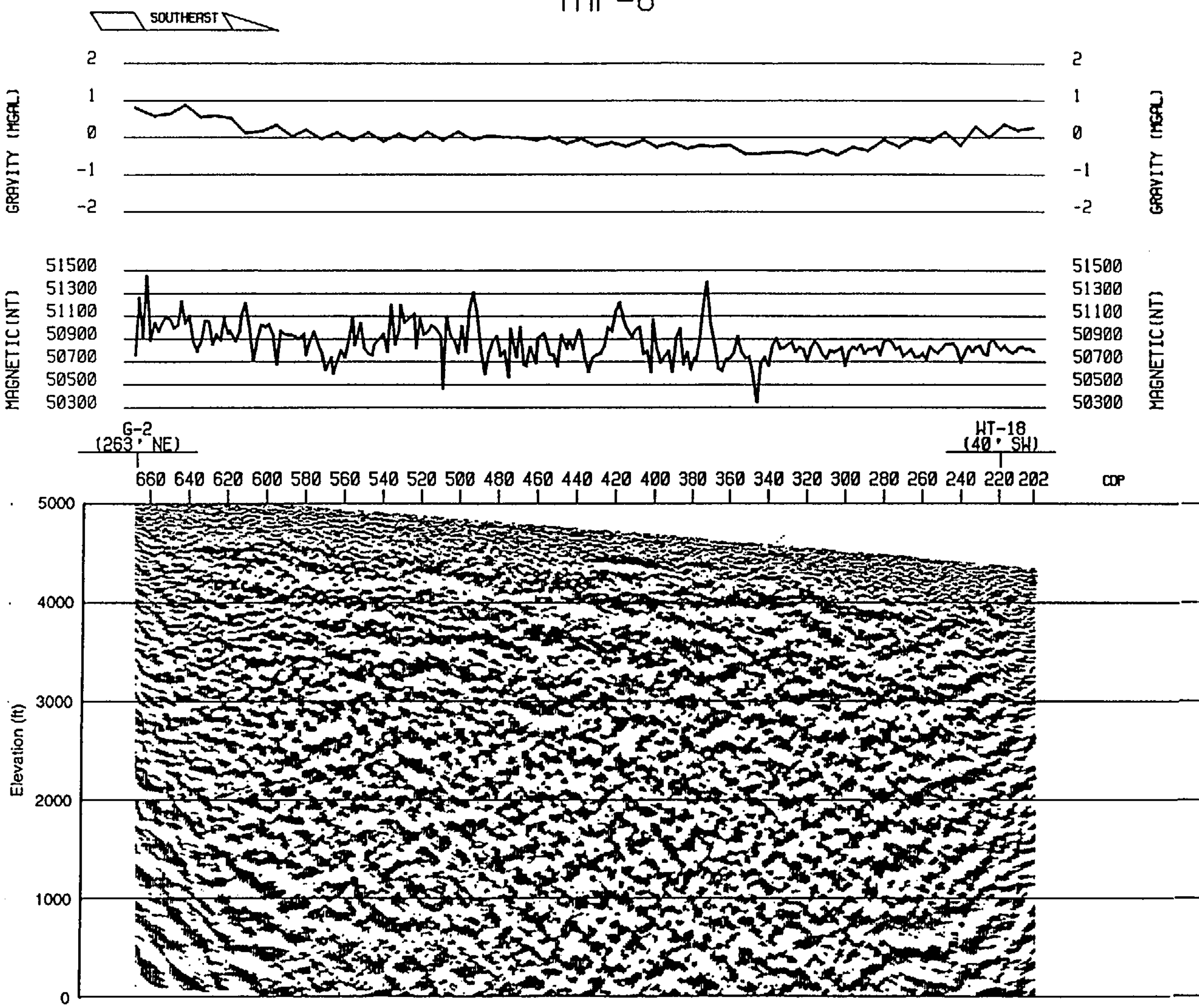
SOUTHEAST
GRAVITY (MGAL)
2
1
0
-1
-2
MAGNETIC (NT)
51500
51300
51100
50900
50700
50500
50300
G-2
(263' NE)
WT-18
(40' SW)
660 640 620 600 580 560 540 520 500 480 460 440 420 400 380 360 340 320 300 280 260 240 220 202
CDP
Elevation (ft)
5000
4000
3000
2000
1000
0

YMP-9

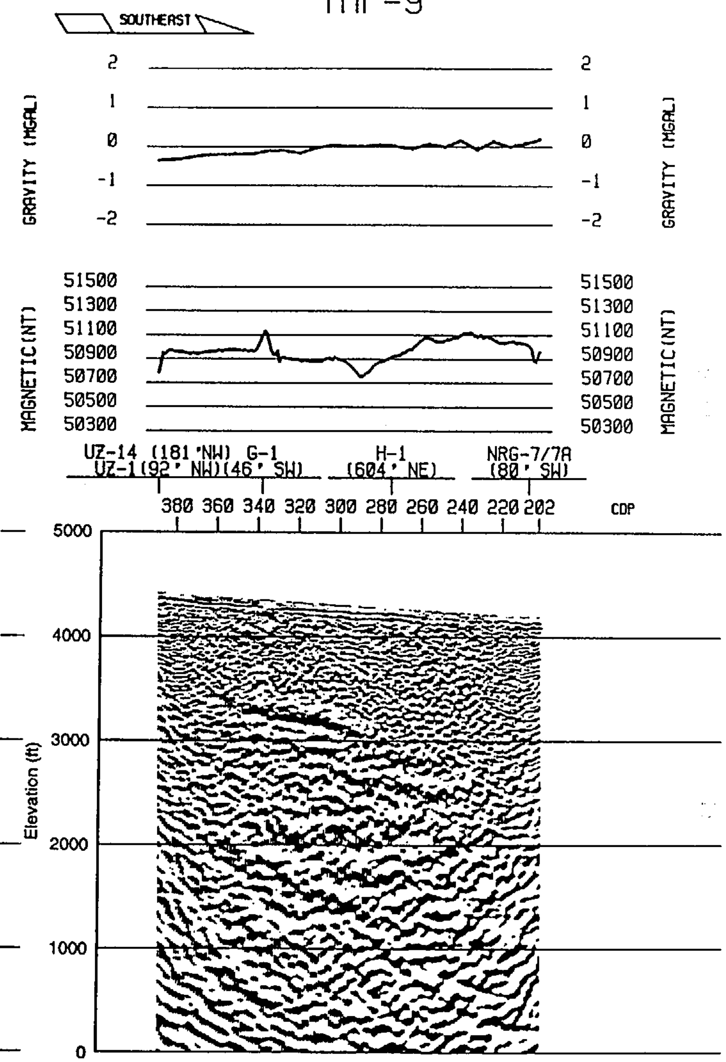
SOUTHEAST
GRAVITY (MGAL)
2
1
0
-1
-2
MAGNETIC (NT)
51500
51300
51100
50900
50700
50500
50300
UZ-14 (181' NW) G-1
UZ-1 (92' NW)(46' SW)
H-1
(604' NE)
NRG-7/7A
(80' SW)
380 360 340 320 300 280 260 240 220 202
CDP
Elevation (ft)
5000
4000
3000
2000
1000
0

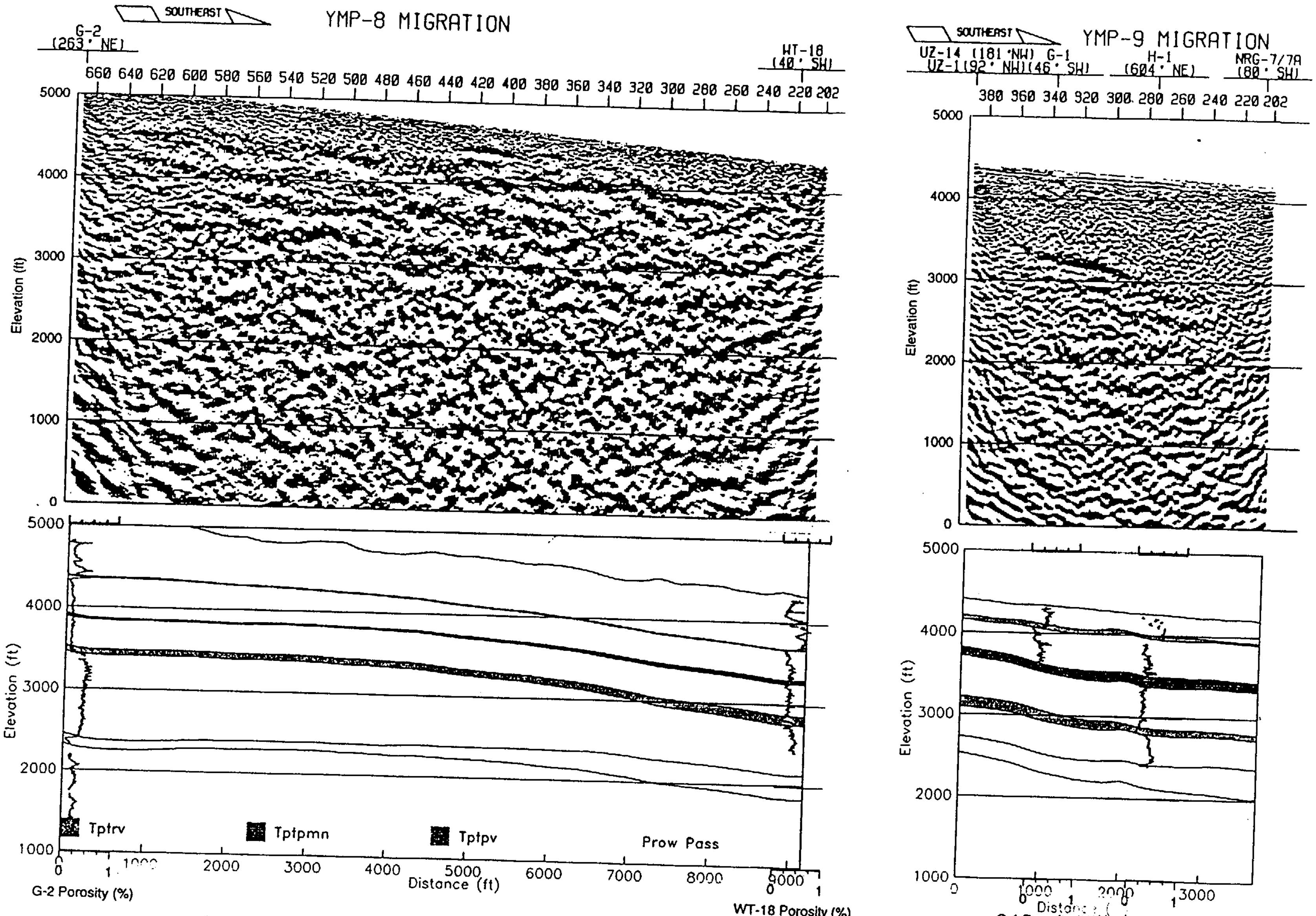

Figure 42. Seismic lines YMP-8 and YMP-9 with interpreted marker horizons and current geologic cross section. The seismic section is a migrated depth section at 1:1 scale, 1 inch = 1200 ft. Computed porosity log (if available) for all wells within 1000 ft. of seismic line is plotted on the geologic cross section.

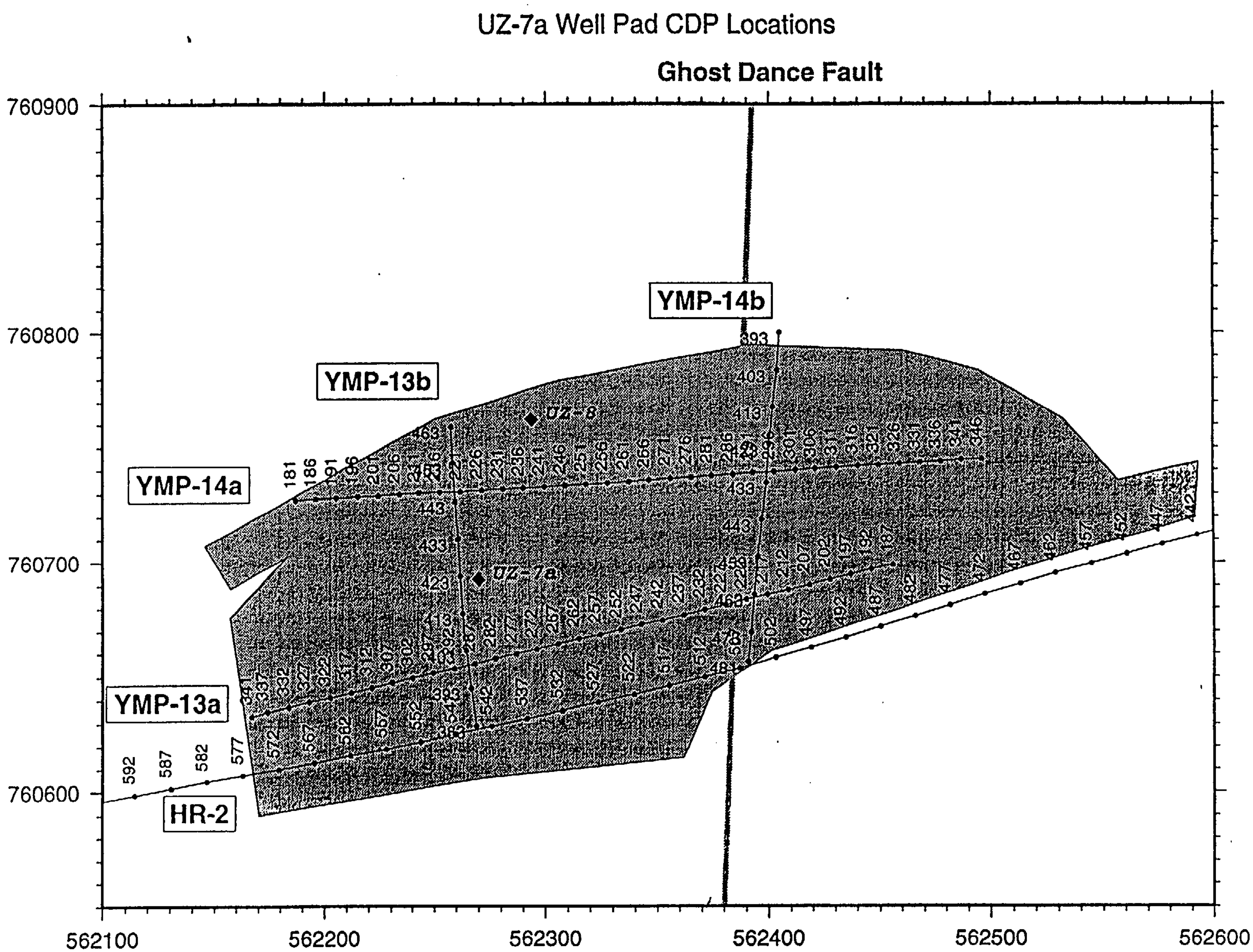

Figure 1b. Detailed map of the UZ-7a well pad for seismic lines YMP-13a, 13b, 14a, 14b, and HR-2. The thick gray line is the Ghost Dance Fault from the geologic model of Zelinski and Clayton (1996).

YMP 13a

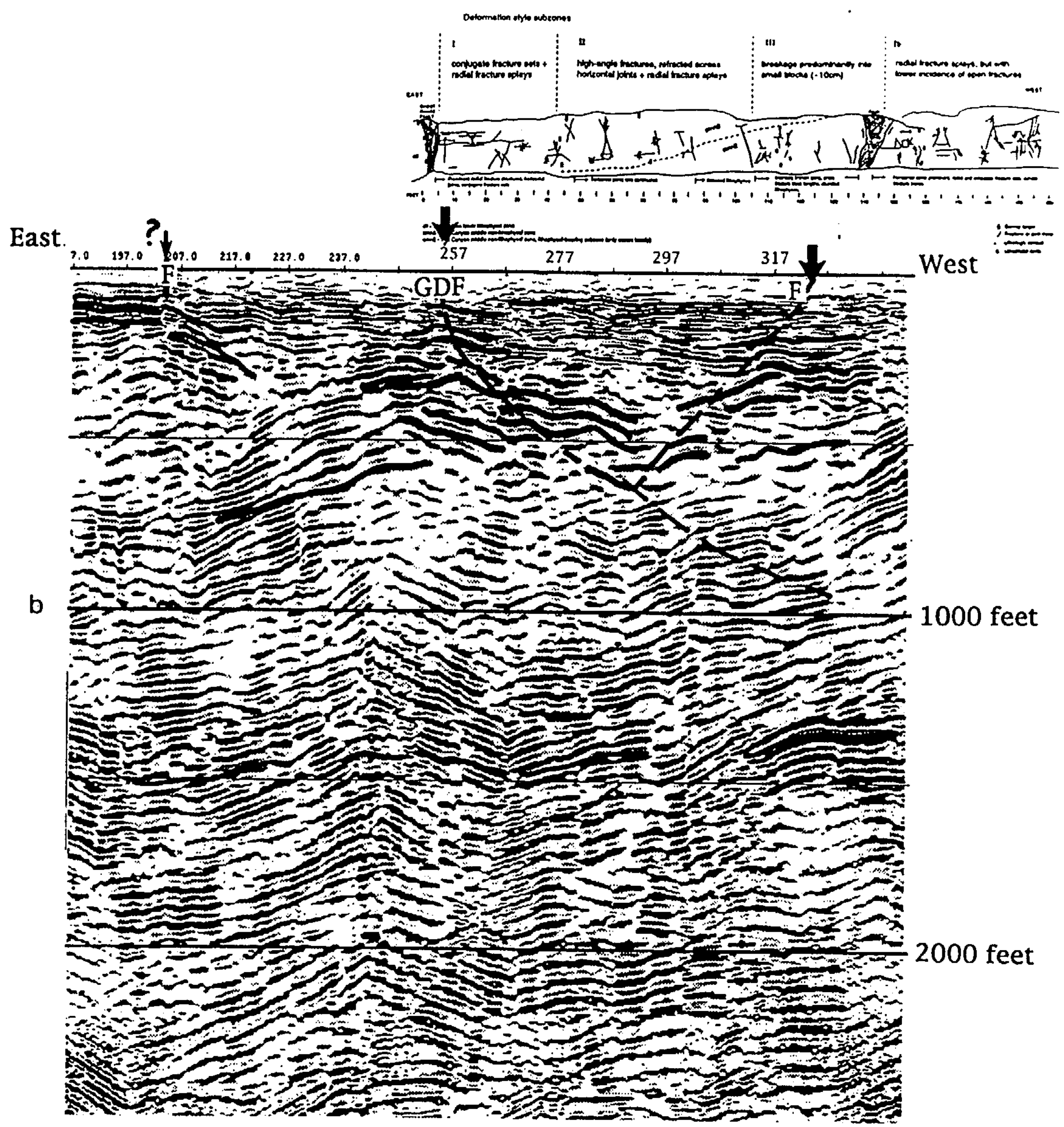

Deformation style subzones
I
conjugate fracture sets + radial fracture splays
II
high-angle fractures, refracted across horizontal joints + radial fracture splays
III
breakage predominantly into small blocks (~10cm)
IV
radial fracture splays, but with lower incidence of open fractures
East
West
?
F
GDF
F
7.0
197.0
207.0
217.0
227.0
237.0
257
277
297
317
b
1000 feet
2000 feet

YMP 14a

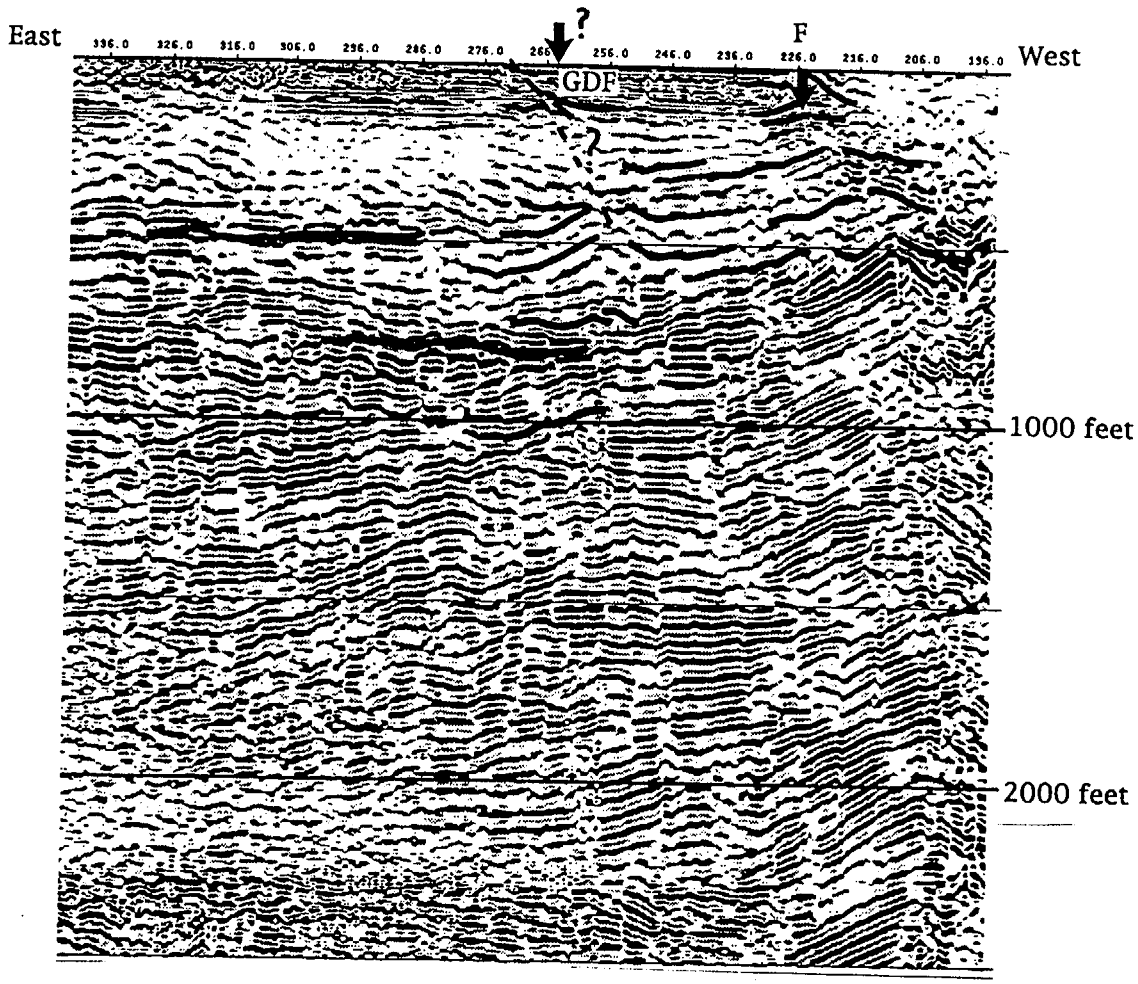

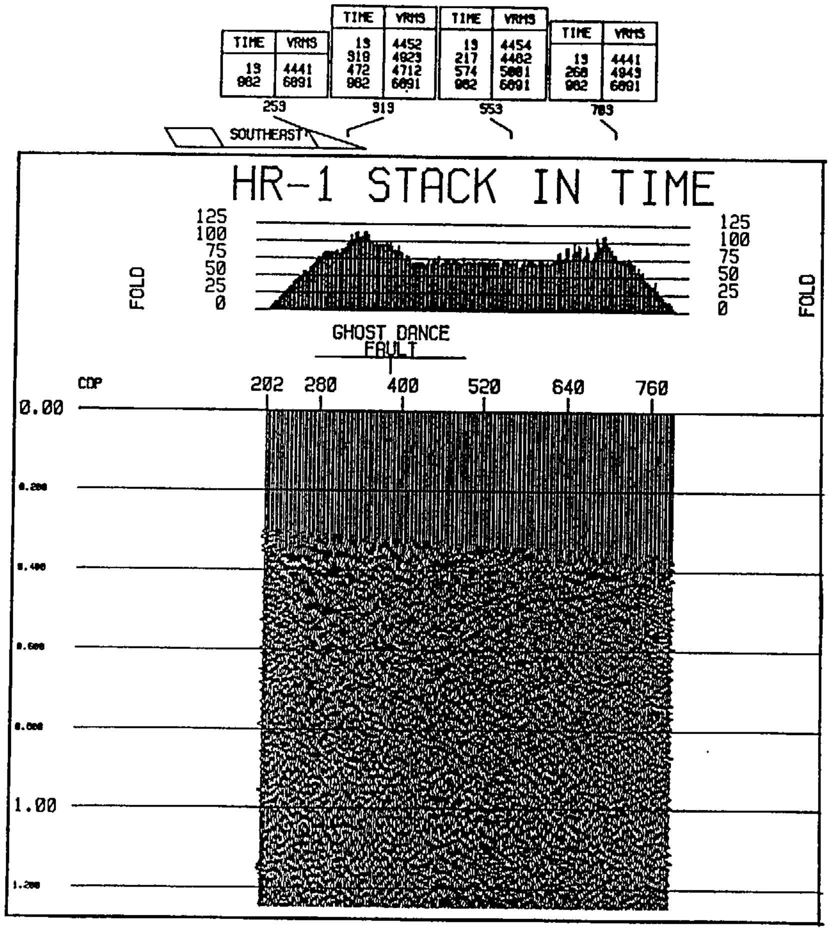
TIME VRMS
19 4441
982 6891
259
TIME VRMS
19 4452
318 4923
472 4712
982 6891
919
TIME VRMS
19 4454
217 4482
574 5001
982 6891
553
TIME VRMS
19 4441
260 4943
982 6891
703
SOUTHEAST
HR-1 STACK IN TIME
FOLD
125 100 75 50 25 0
GHOST DANCE FAULT
CDP
202 280 400 520 640 760
0.00
1.00

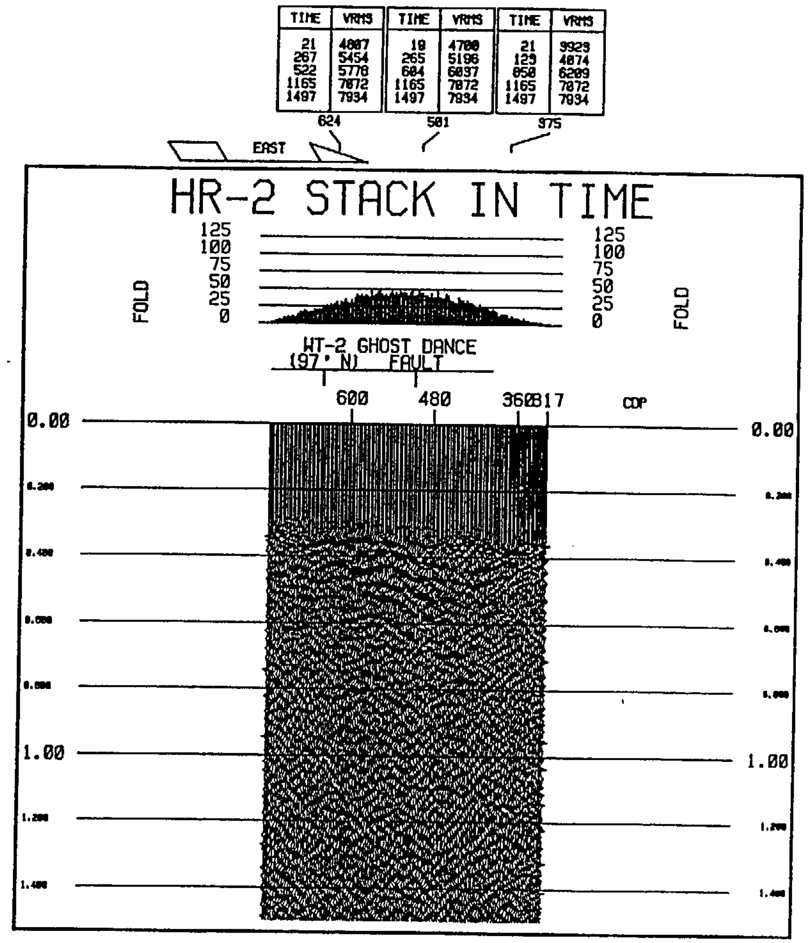
TIME VRMS
21 4007
267 5454
522 5770
1165 7072
1497 7034
624
TIME VRMS
18 4700
265 5196
604 6037
1165 7072
1497 7034
501
TIME VRMS
21 3929
129 4074
850 6209
1165 7072
1497 7034
375
EAST
HR-2 STACK IN TIME
FOLD
125 100 75 50 25 0
WT-2 (97' N)
GHOST DANCE FAULT
600 480 360 317
CDP
0.00
1.00

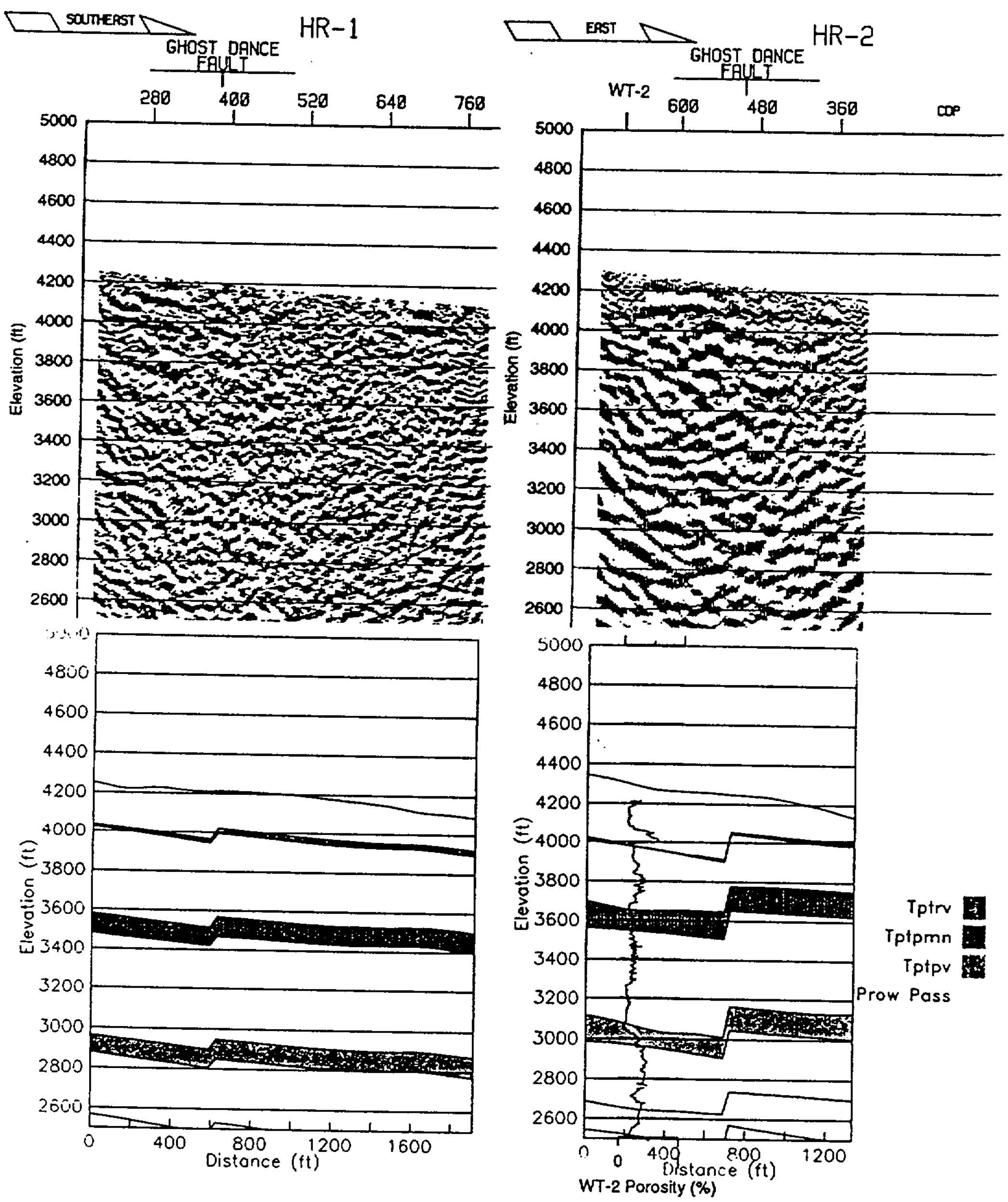

Figure 43. Seismic lines HR-1 and HR-2 with interpreted marker horizons and current geologic cross section. The seismic section is a migrated depth section at 1:1 scale, 1 inch = 1200 ft. Computed porosity log (if available) for all wells within 1000 ft. of seismic line is plotted on the geologic cross section.

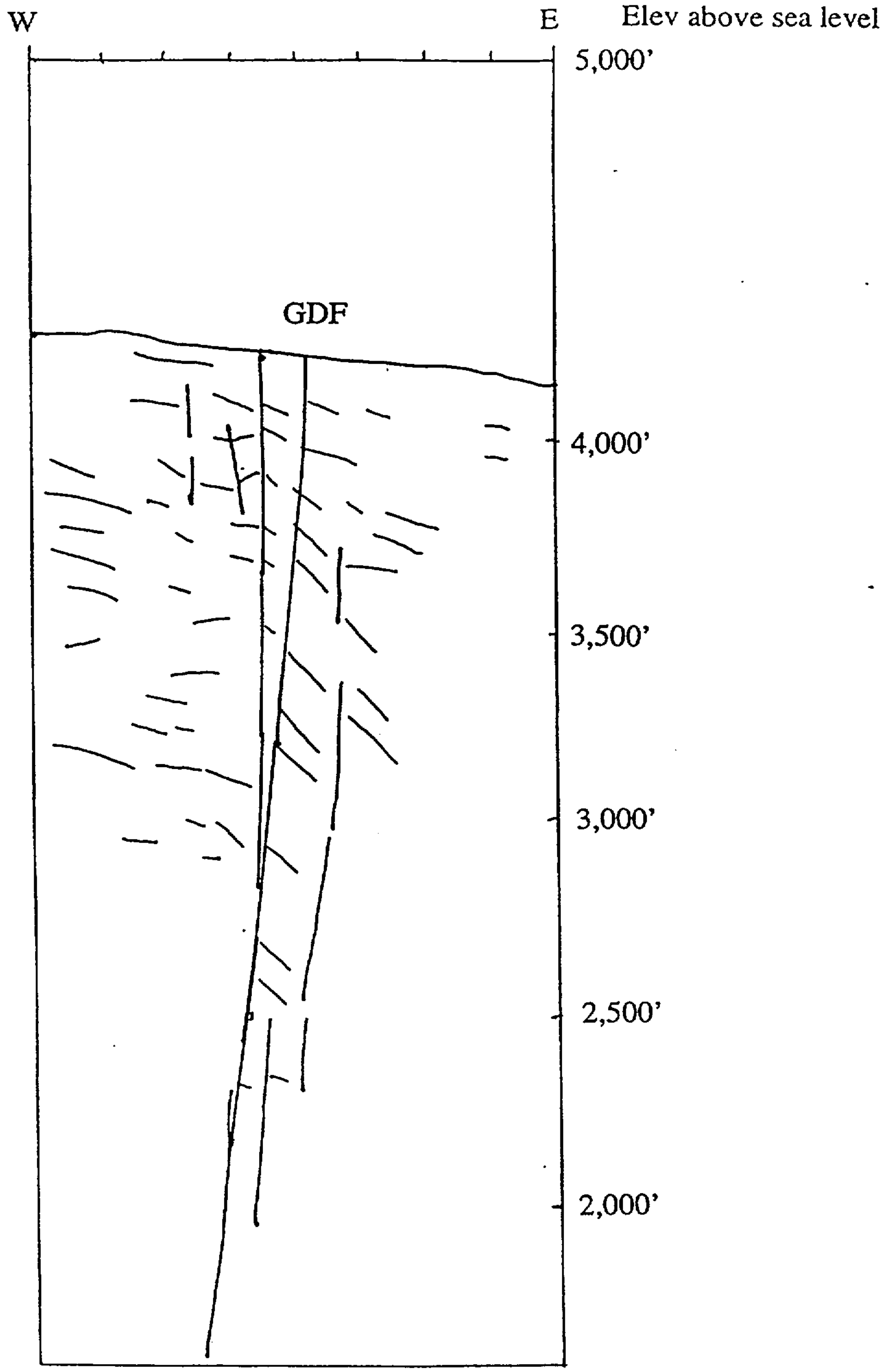

Figure 99B. Interpretation of Faulting on seismic line HR-2 based on unmigrated section. Scale is 1 inch equals 475 feet. V.E. = 1.1. From Day (1996, personal communication).

CONCLUSIONS

- At the present time we cannot discriminate between variation in porosity caused by fracturing or large scale changes in matrix properties. However, in cases where there is good surface evidence for faulting, it appears that the faulting and fracturing is the main cause for the variability in the geophysical data.

- There is abundant evidence of multiple sub-parallel fracture zones or faults associated with major mapped faults, most definitively for the Ghost Dance fault. It was difficult, however, to trace the faulting from one geophysical line to another, also an indication of the complexity of this area.

- In the repository region no seismic reflections were identified as a Paleozoic interface. This is attributed to the combination of the small amount of energy penetrating to depth (high attenuation of the tuffs), and a smaller than expected contrast in the acoustic impedances between the Paleozoic rocks and the overlying tuffs.

- Surface and borehole velocity studies across Yucca Mt. indicated that in addition to local heterogeneity, there is a general trend from north to south of increasing seismic velocity, implying increasing porosity to the north.

- East-west seismic lines show fewer reflections than north-south lines, probably due to the abundance of north-south faults. The high degree of faulting and "broken up" nature of the repository volume would make it difficult to store enough energy to produce a damaging event located in the tuffs.

  i.e. large EQ

Ghost Dance Fault Paleoseismic Data

Quaternary Description of an Interblock Fault

presented by

John Whitney
US Geological Survey

Data from Chapter 4.5 and recently logged trench GDF - 5

LOCATION MAP OF MAJOR FAULTS AND TRENCHES AT YUCCA MOUNTAIN

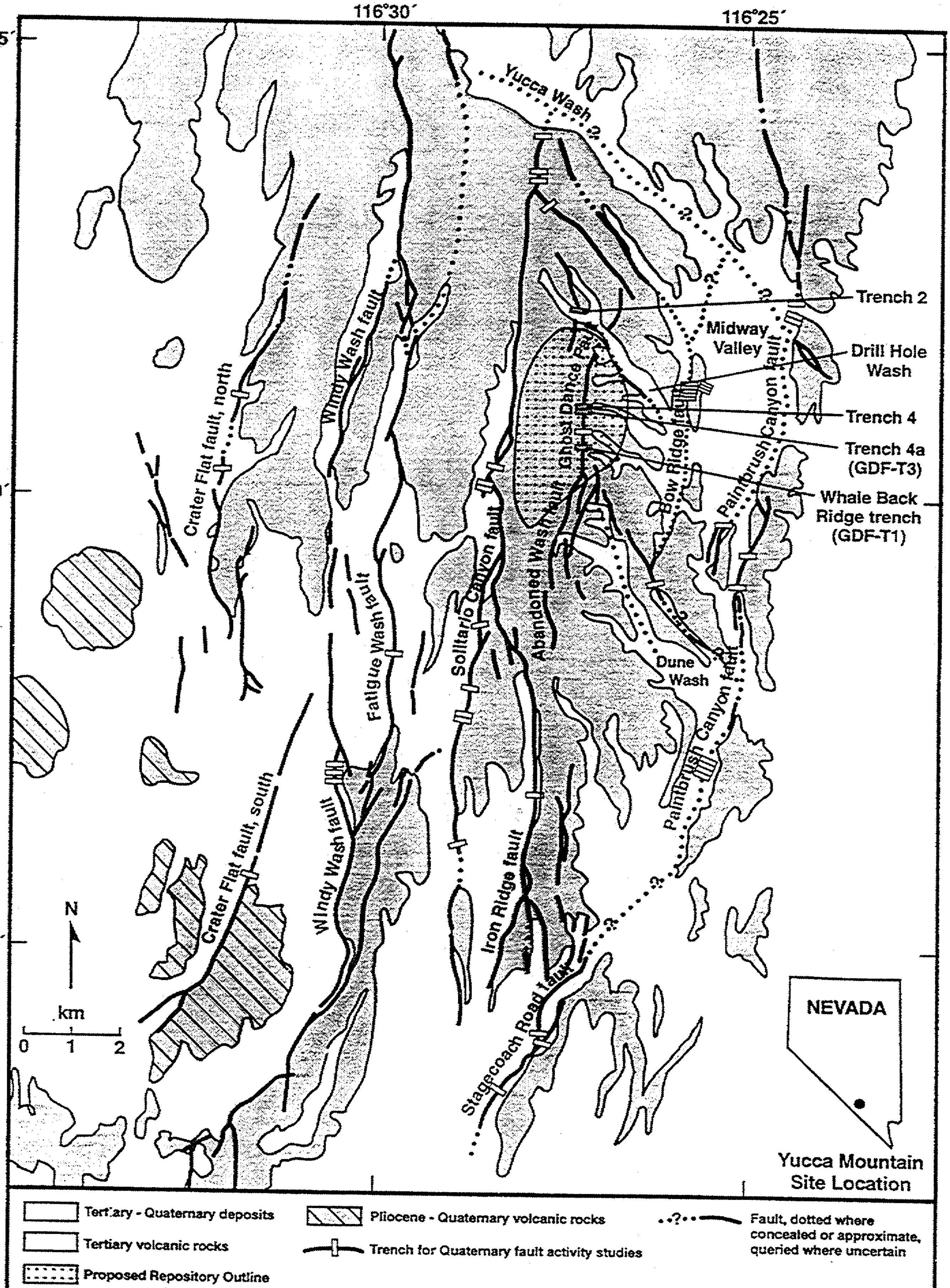

GEOXSECT.CDR.123/5-22-95

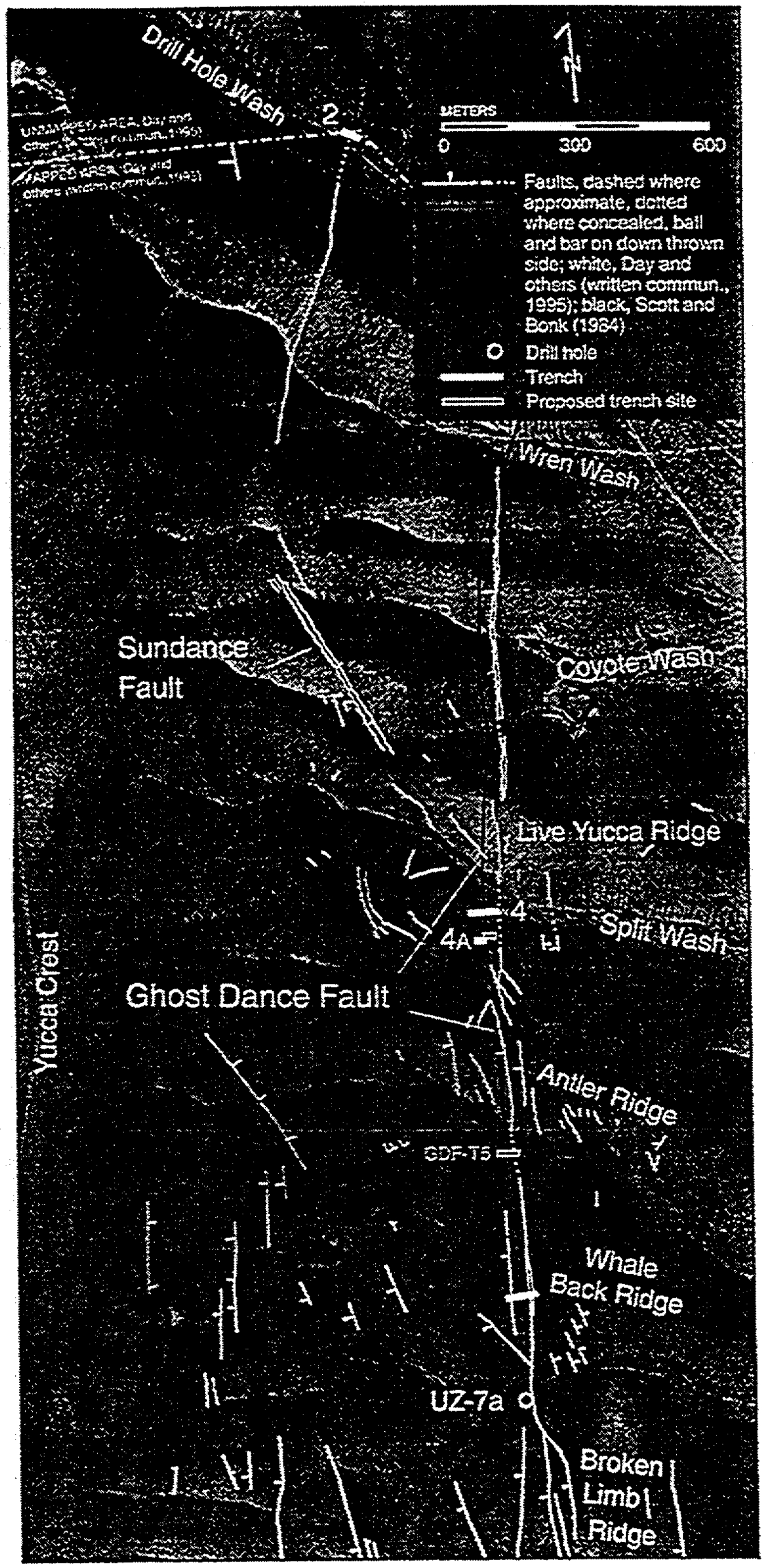

Figure 4.5.2. Location of the Ghost Dance and Sundance faults, and trenches in Quaternary deposits that intersect the bedrock fault projections. Fault traces are modified from Day and others (written commun., 1995) and Scott and Bonk (1984).

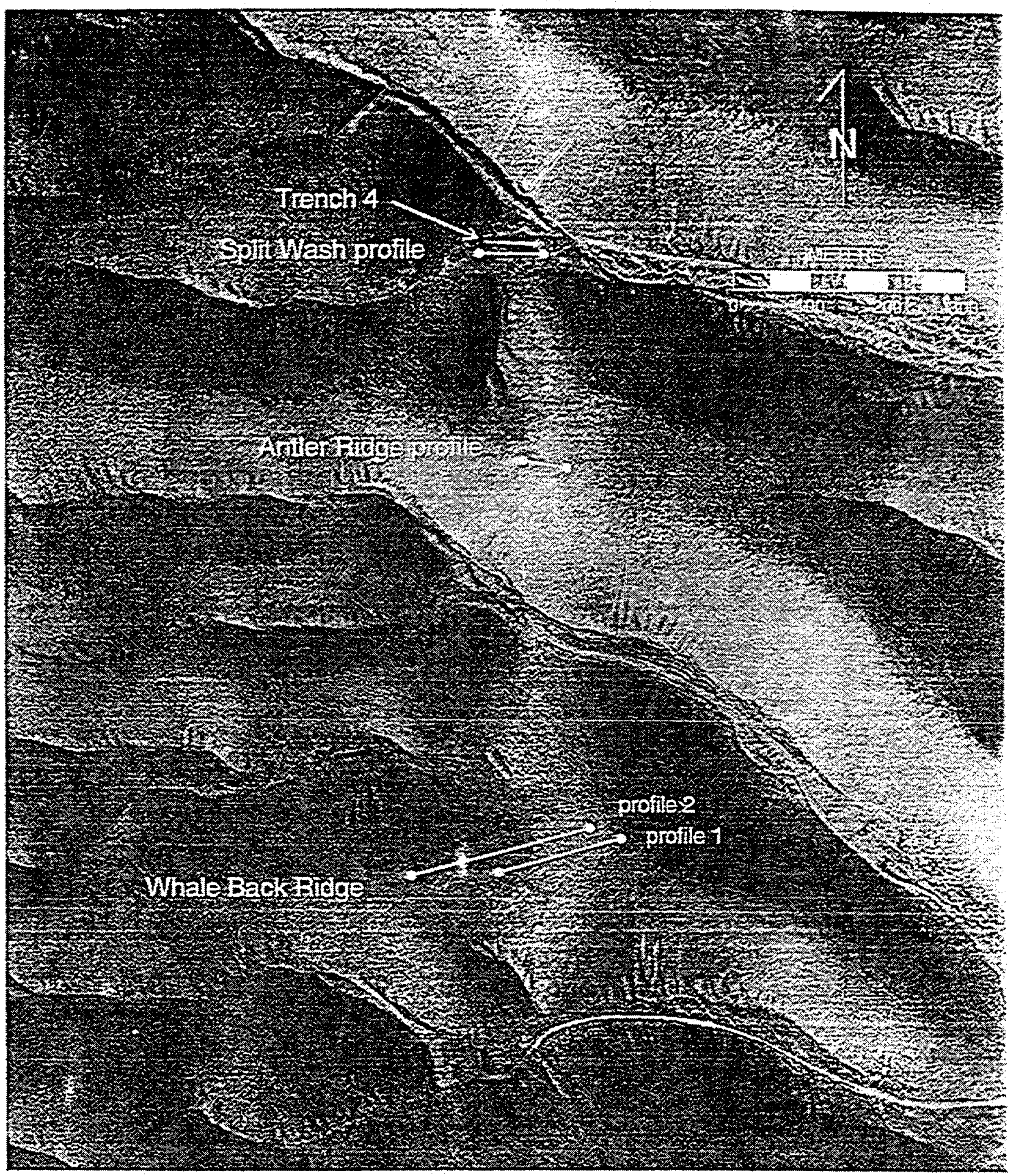

Figure 4.5.4. Location of profile transects measured across the Ghost Dance fault on Whale Back Ridge, Antler Ridge, and in Split Wash.

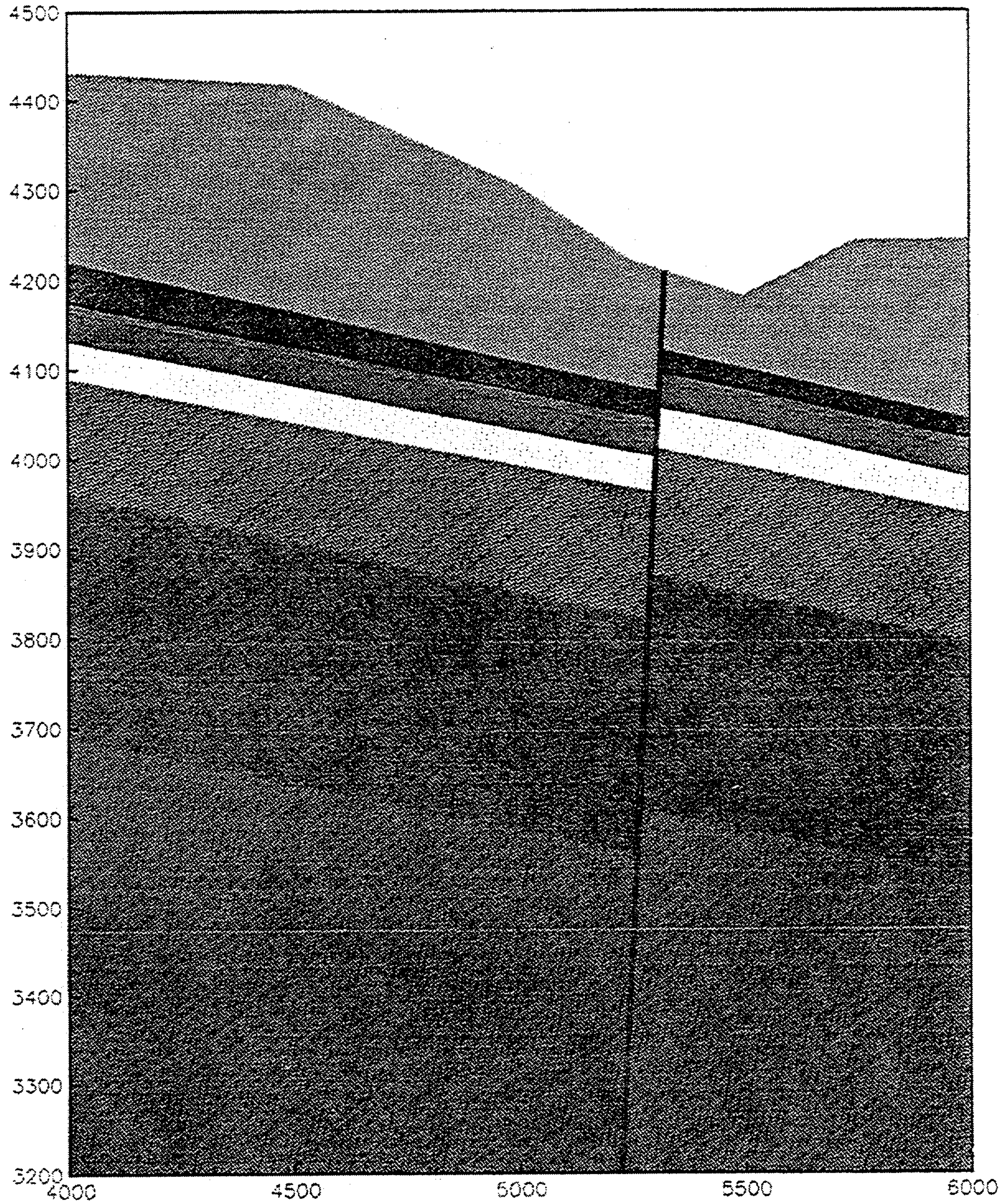

Ghost Dance Fault

YMP-95-285.0

ANTLER Ridge, Ghost Dance Fault, Trench GDF-5

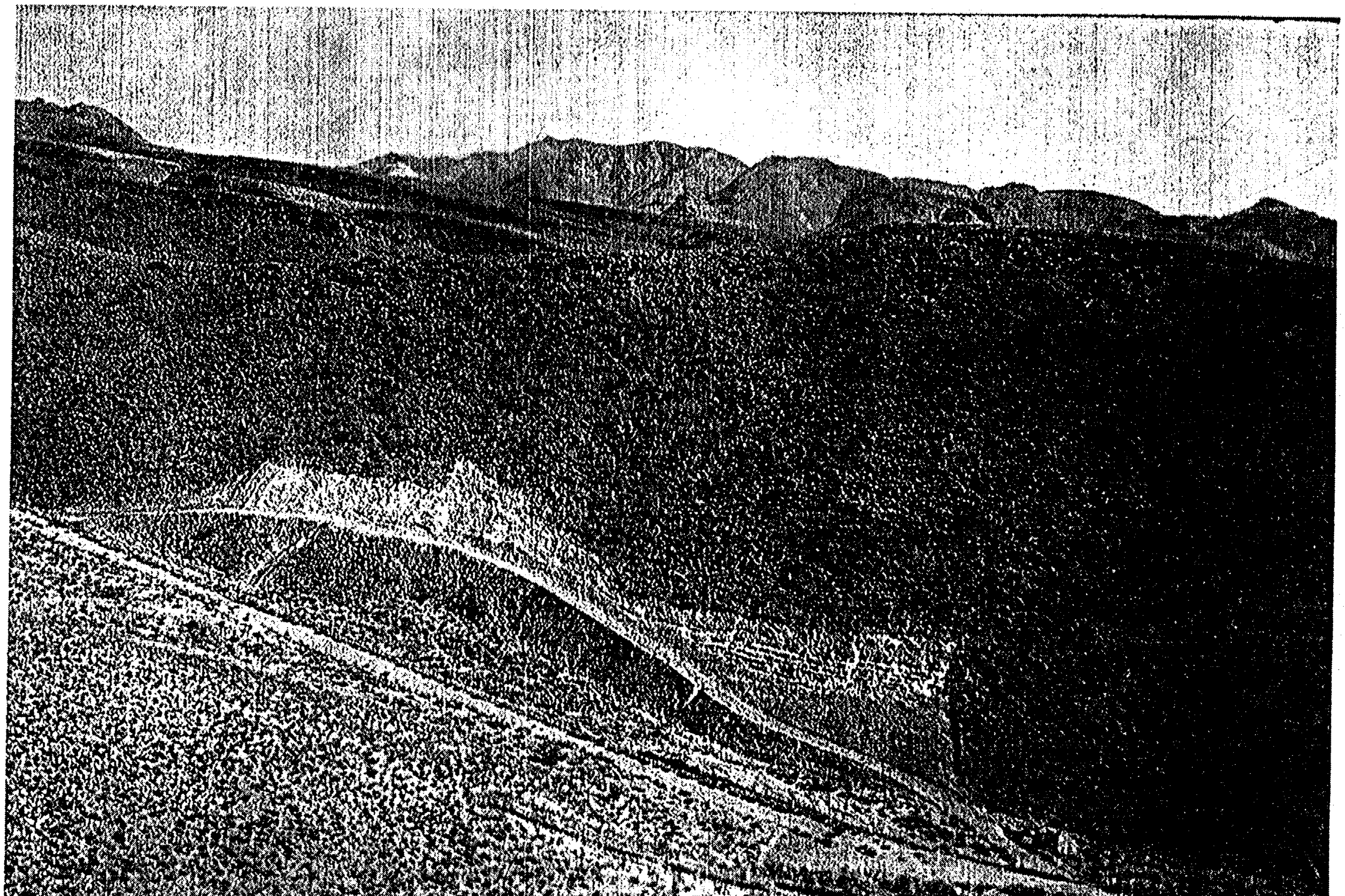

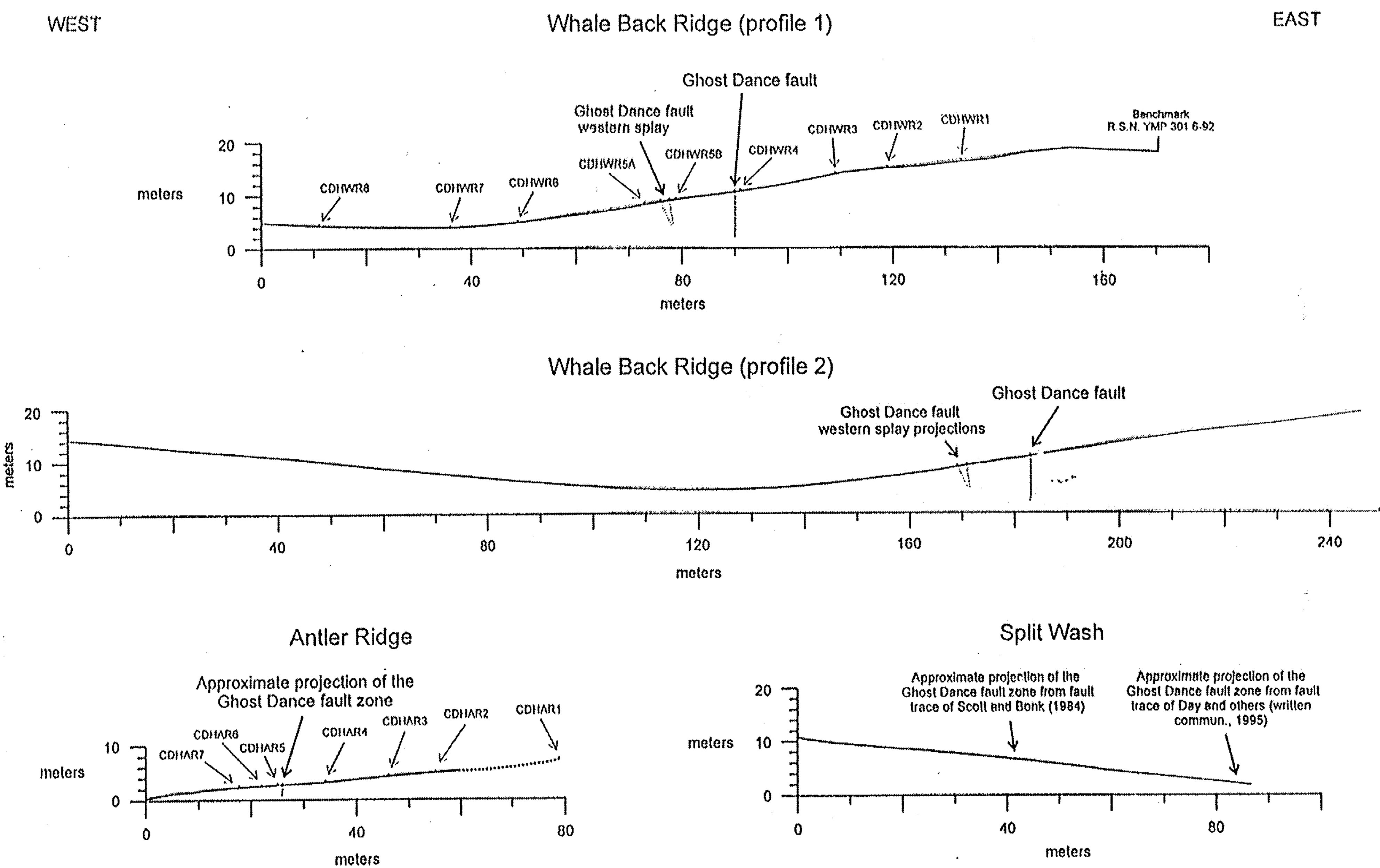

Figure 4.5.5. Profile transects and related cosmogenic radionuclide sample localities. See figure 4 for profile locations. Fault trace projections of Day and others (written commun., 1995) and Scott and Bonk (1984) were used for Split Wash, see figure 2. All profiles are shown without vertical exaggeration.

^{10}Be exposure ages (ka)
along the crest of Antler Ridge

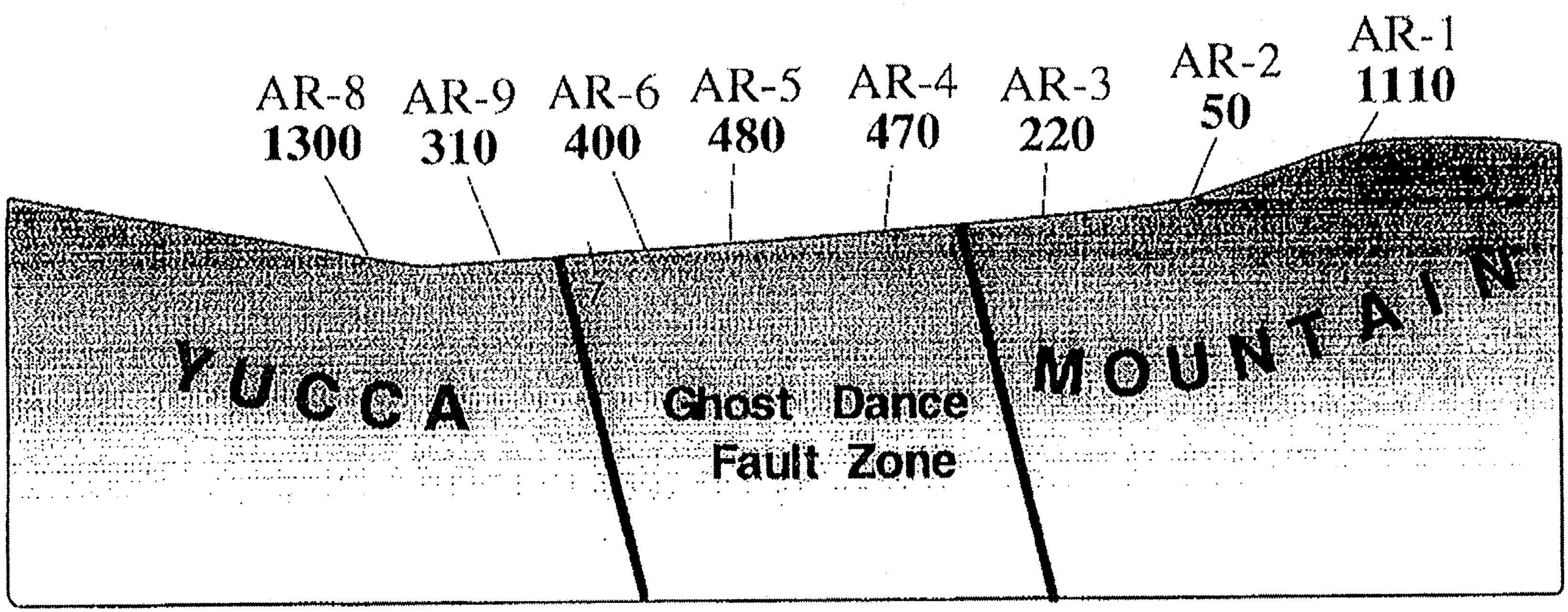

single nuclide ages, no adjustment for erosion rate (minimum ages)

unpublished data from Gosse, Harrington, & Whitney

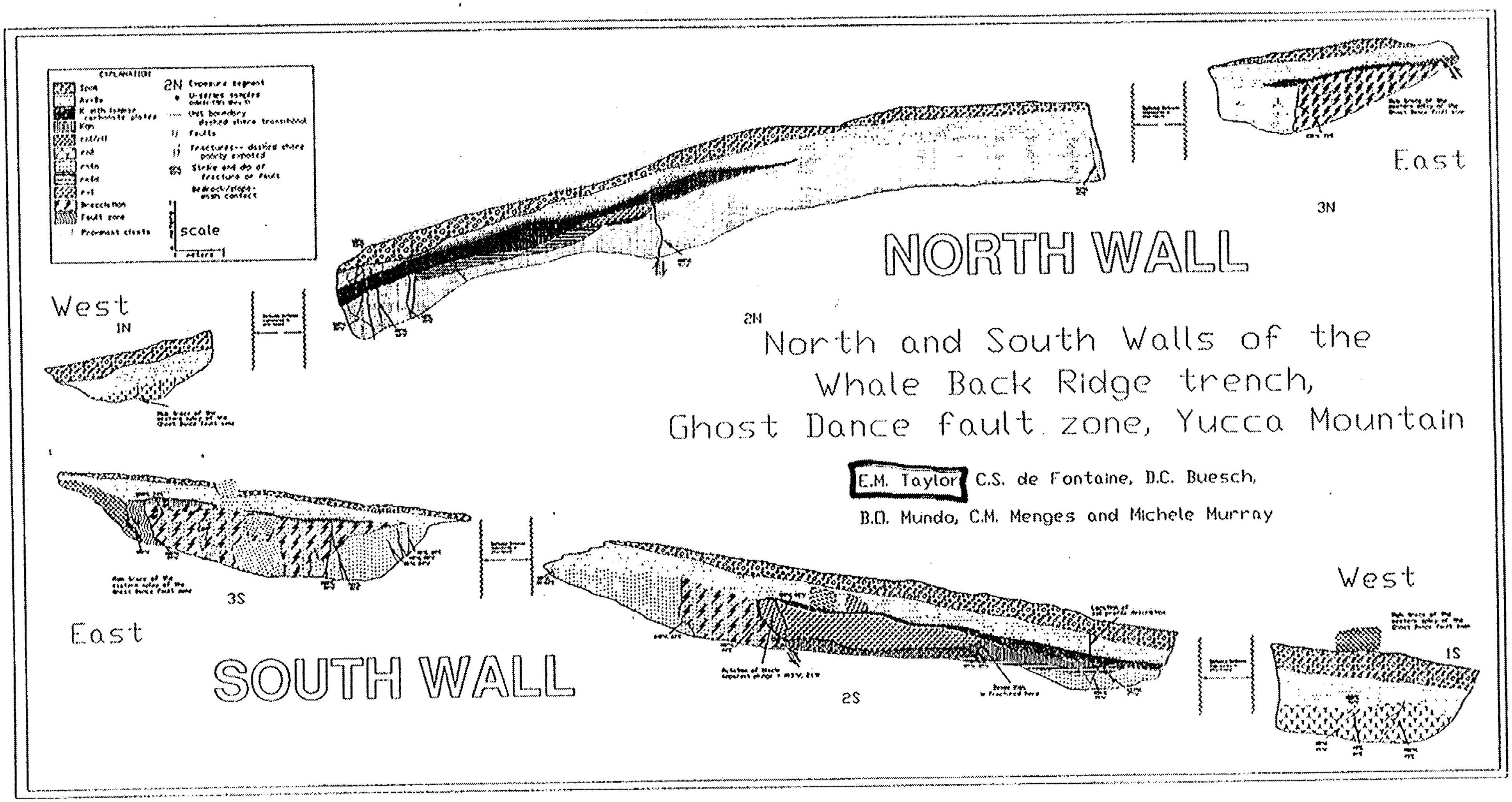

4.5.7. North and South walls of the Whale Back Ridge trench, Ghost Dance fault zone, Yucca Mountain

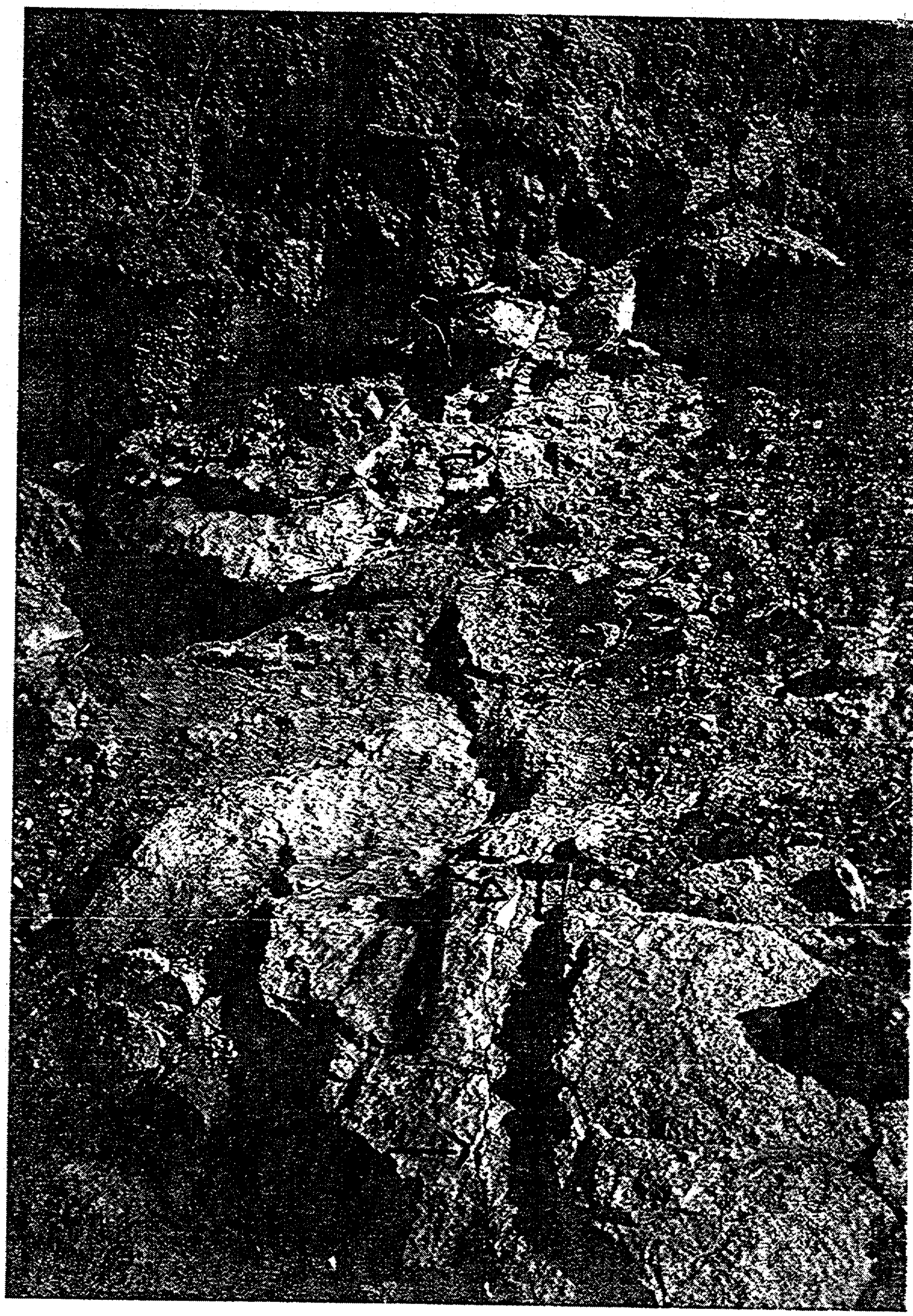

FRACTURED STAGE IV K horizon
in Whaleback Trench on the
Ghost Dance Fault

SiO-cemented breccia in Ghost Dance fault — Antler Ridge Pavement

Note Discontinuous younger crack

Close up photograph of discontinuous $CaCO_3$-filled crack at Antler Ridge Pavemen

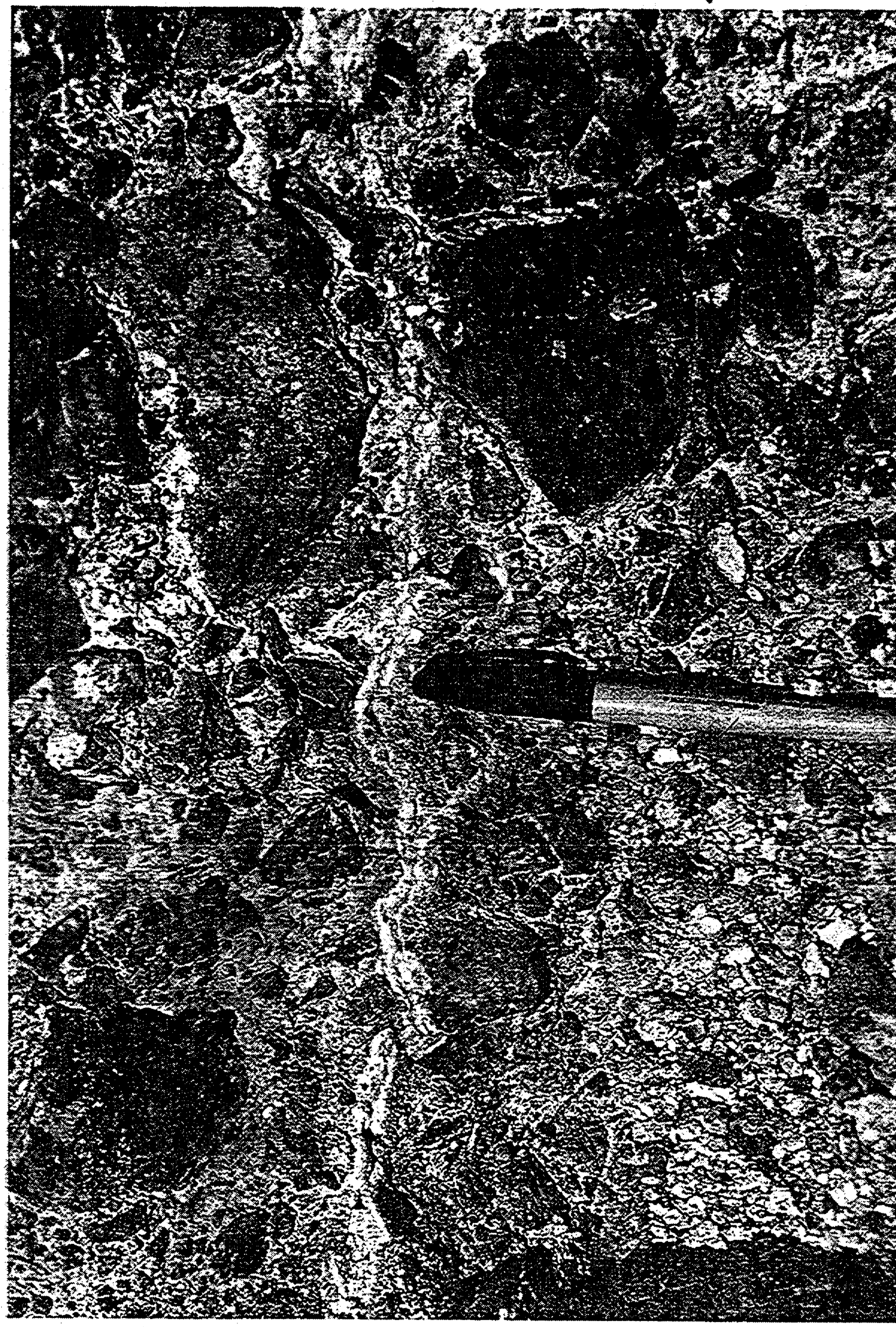

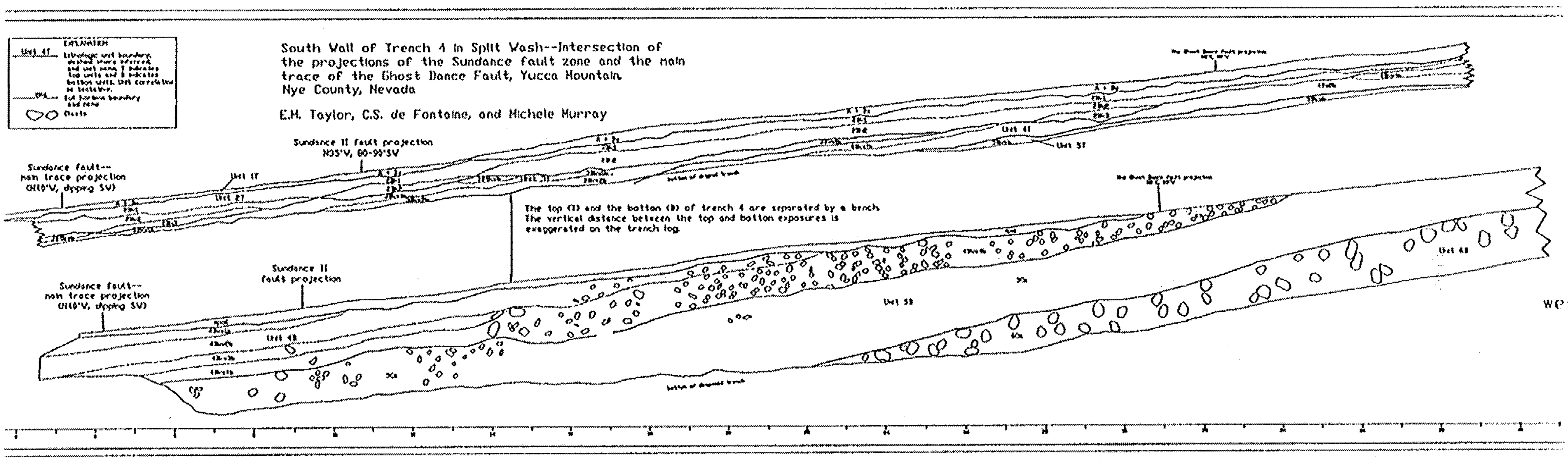
EXPLANATION
Clasts
South Wall of Trench 4 in Split Wash--Intersection of the projections of the Sundance fault zone and the main trace of the Ghost Dance Fault, Yucca Mountain, Nye County, Nevada
E.H. Taylor, C.S. de Fontaine, and Michele Murray
Sundance II fault projection
N35°W, 80-90°SW
Sundance fault--
main trace projection
(N10°W, dipping SW)
Sundance II
fault projection
Unit 41
Unit 57
Unit 58
Unit 68
The top (T) and the bottom (B) of trench 4 are separated by a bench. The vertical distance between the top and bottom exposures is exaggerated on the trench log.

Figure 4.5.12

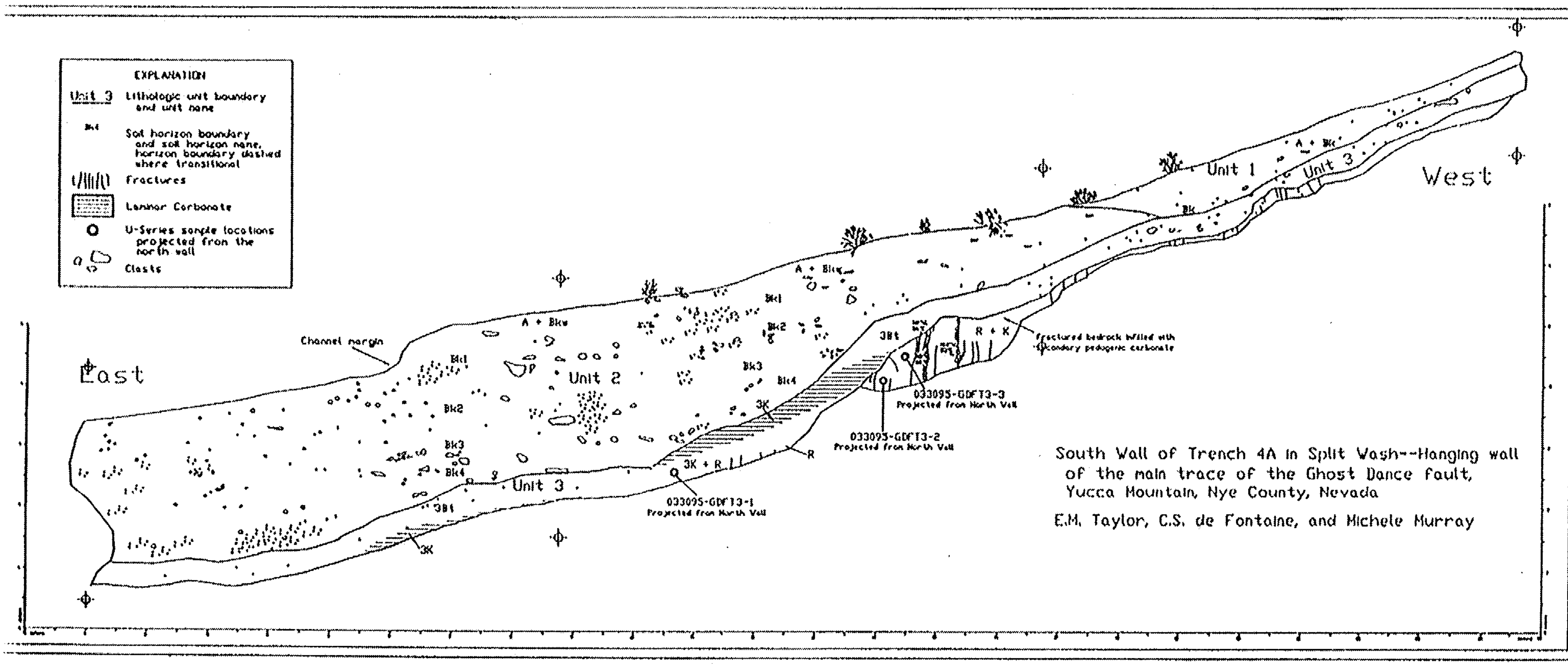

EXPLANATION
Unit 3 Lithologic unit boundary and unit name
Soil horizon boundary and soil horizon name, horizon boundary dashed where transitional
Fractures
Laminar Carbonate
U-Series sample locations projected from the north wall
Clasts
East
West
Channel margin
Unit 1
Unit 2
Unit 3
A + Bkv
Bk1
Bk2
Bk3
Bk4
3Bt
3K
3K + R
R
R + K
Fractured bedrock infilled with secondary pedogenic carbonate
033095-GDFT3-1
Projected from North Wall
033095-GDFT3-2
Projected from North Wall
033095-GDFT3-3
Projected from North Wall
South Wall of Trench 4A in Split Wash--Hanging wall of the main trace of the Ghost Dance fault, Yucca Mountain, Nye County, Nevada
E.M. Taylor, C.S. de Fontaine, and Michele Murray

Figure 4.5.13

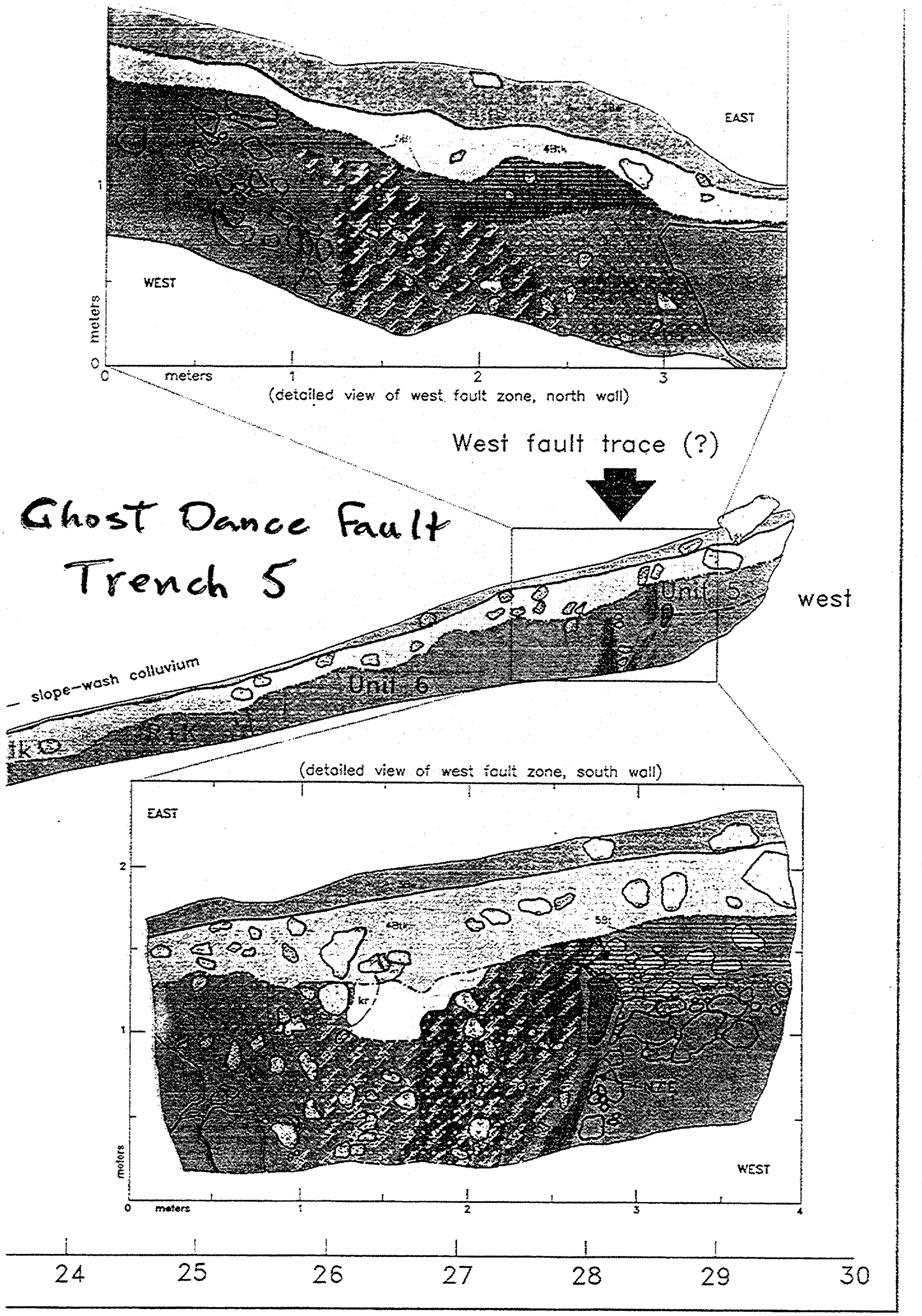
Ghost Dance Fault
Trench 5
EAST
WEST
meters
0
1
2
3
(detailed view of west fault zone, north wall)
West fault trace (?)
west
Unit 5
Unit 6
slope-wash colluvium
(detailed view of west fault zone, south wall)
EAST
WEST
kr
4
24
25
26
27
28
29
30

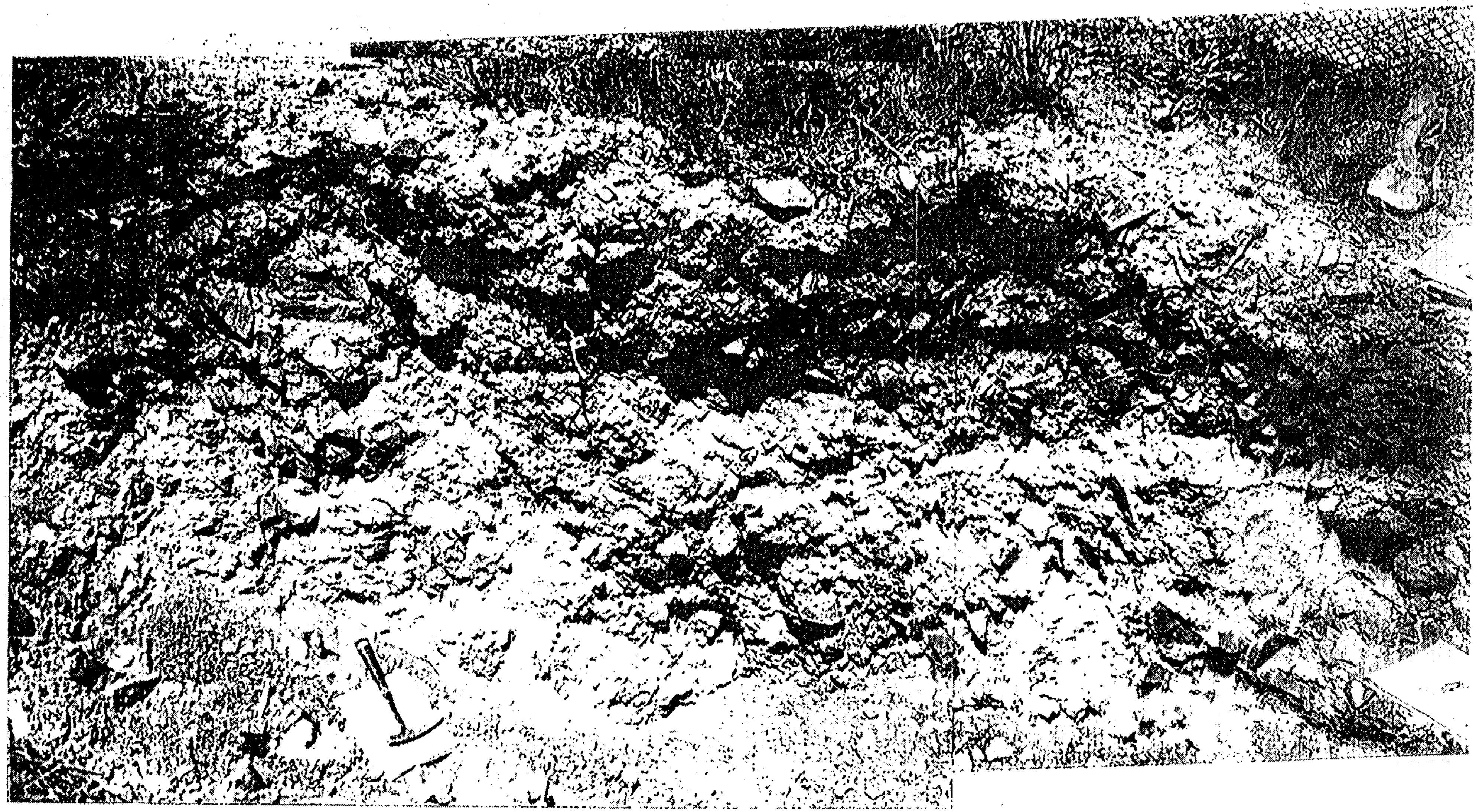

West end of north wall –
Trench GDF-5 : possible
Quaternary Paleoevent

MAGNITUDE AND SURFACE RUPTURE LENGTH, AVERAGE, AND MAXIMUM FAULT DISPLACEMENTS

B. SLEMMONS
YUCCA MOUNTAIN SSC#2 WORKSHOP
OCTOBER 18, 1996

Table 1 Linear regressions of magnitude, M, and surface rupture length for all fault types. M - A + B log L for rupture lengths in km, except * for length in m.

NO.	REFERENCE	REGION	EVENTS	A	B	M FOR 20 KM	M FOR 30 KM	STD. DEV
1	Tocher, (1958)	W. U.S.	10	5.65	0.98	6.93	7.10	0.7
2	Iida (1959)	Worldwide	34	6.27	0.63	7.09	7.20	—
3	Iida (1965)	Worldwide	54	6.02	0.76	7.01	7.34	—
4	Bonilla and Buchanan (1970)	Worldwide	53	3.76*	0.76*	7.02	7.11	0.78
5	Slemmons (1977)	Worldwide	75	1.61*	1.18*	6.69	6.90	0.60
6	Slemmons (1982)	Worldwide	56	2.06*	1.07*	6.66	6.84	0.30
7	Bonilla and others (1984)	Worldwide	45	6.04	0.71	6.96	7.09	0.31
8	Slemmons and others (1989)	Worldwide	48	5.39	1.03	6.73	6.91	0,30
9	Coppersmith (1991)	Worldwide	60	5.00	1.20	6.56	6.77	0.30
10	Wells and Coppersmith (1994)	Worldwide	68	5.03	1.19	6.57	6.78	0.28

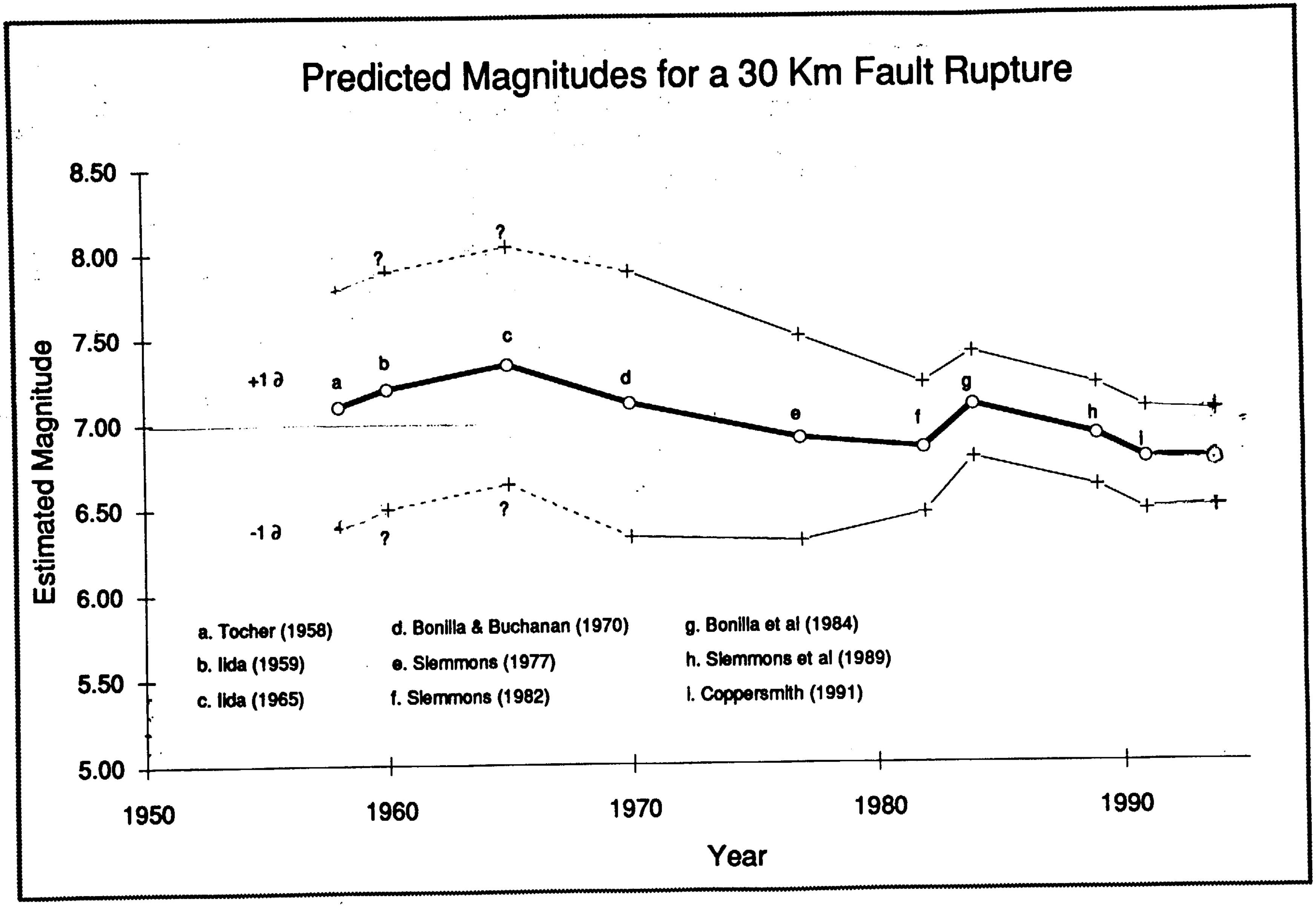

McCleary & Slemmons (199?)

Tocher (1958) made the first regresion analyses of M vs. SRL, and M vs. SRL x Dmax, based on 10 events in western United States:

1906 San Francisco
1915 Pleasant Valley
1932 Cedar Mountain
1934 Excelsior Mountain
1947 Manix
1952 Kern County
1954 Rainbow Mountain
1954 Stillwater
1954 Fairview Peak
1954 Dixie Valley

Wells & Coppersmith, ...

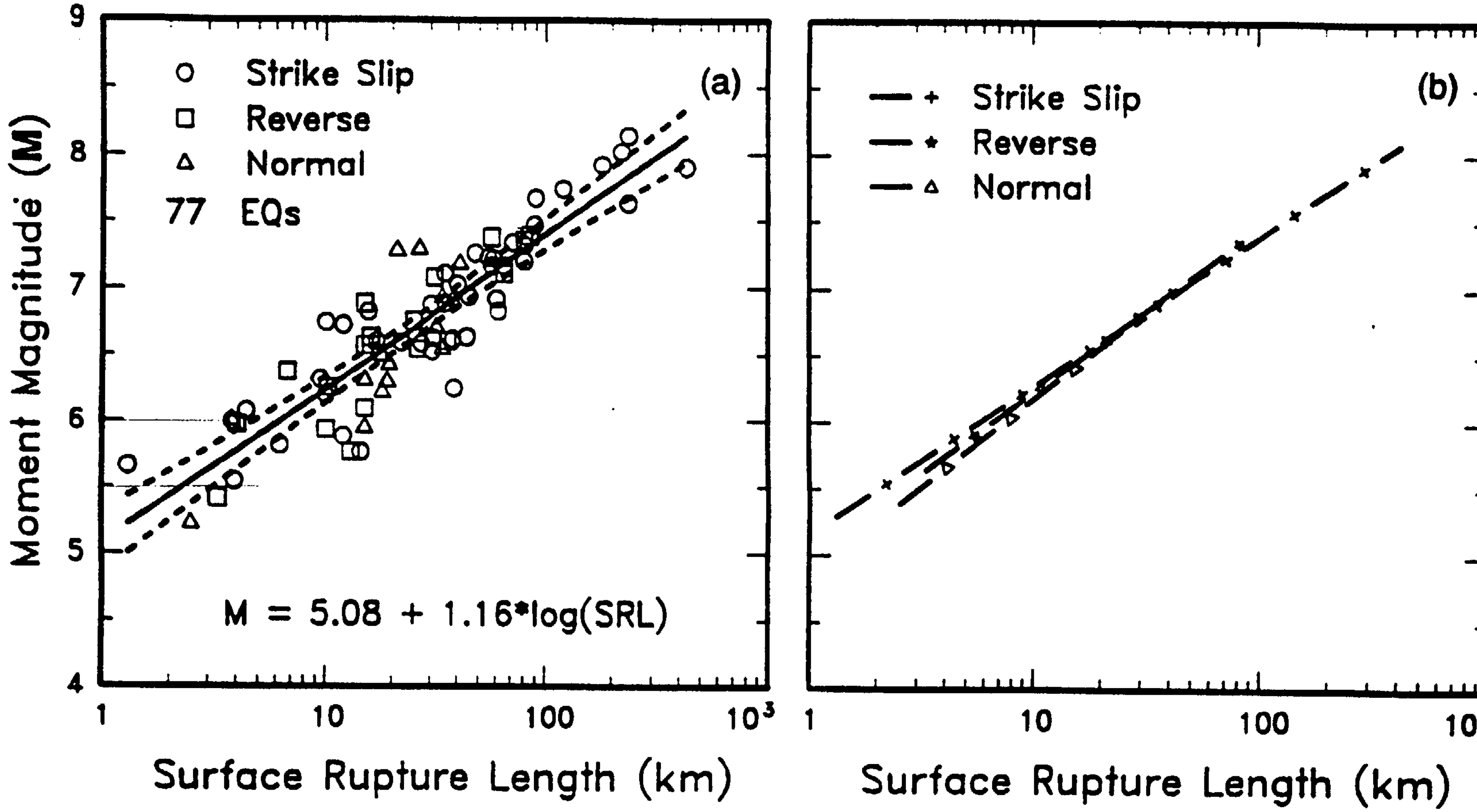

Figure 9

REGRESSIONS FOR SURFACE RUPTURE LENGTH, MAXIMUM DISPLACEMENT, AND MOMENT MAGNITUDE FOR ALL FAULT TYPES (WELLS AND COPPERSMITH, 1994)

EQUATION	TYPE	EVENTS	10 KM SRL	20 KM SRL	30 KM SRL
M=5.08+1.16 LOG (SRL)	ALL	77	6.24	6.59	6.81
M=5.16+1.12 LOG (SRL)	SS	43	6.28	6.62	6.81
M=5.00+1.22 LOG (SRL)	R	19	6.22	6.59	6.80
M=4.86+1.32 LOG (SRL)	N	15	6.18	6.58	6.81
			MD=0.5	MD=1.0	MD=1.5
M=6.69+0.74 LOG (MD)	ALL	80	6.47	6.69	6.82
M=6.81+0.78 LOG (MD)	SS	43	6.58	6.81	6.95
{M=6.52+0.44 LOG(MD)	*R*	*21*	*6.39*	*6.52*	*6.99}*
M=6.61+0.71 LOG(MD)	N	16	6.40	6.61	6.74
			AD=0.25	AD=0.50	AD=0.75
M=6.93+0.82 LOG(AD)	ALL	56	6.44	6.68	6.83
M=7.04+0.89 LOG (AD)	SS	43	6.50	6.77	6.93
{M=6.64+0.13 LOG (AD)	*R*	*15*	*6.56*	*6.60*	*6.62*
N=6.78+0.65 LOG (AD)	N	12	6.39	6.58	6.70O

Wells & Coppersmith

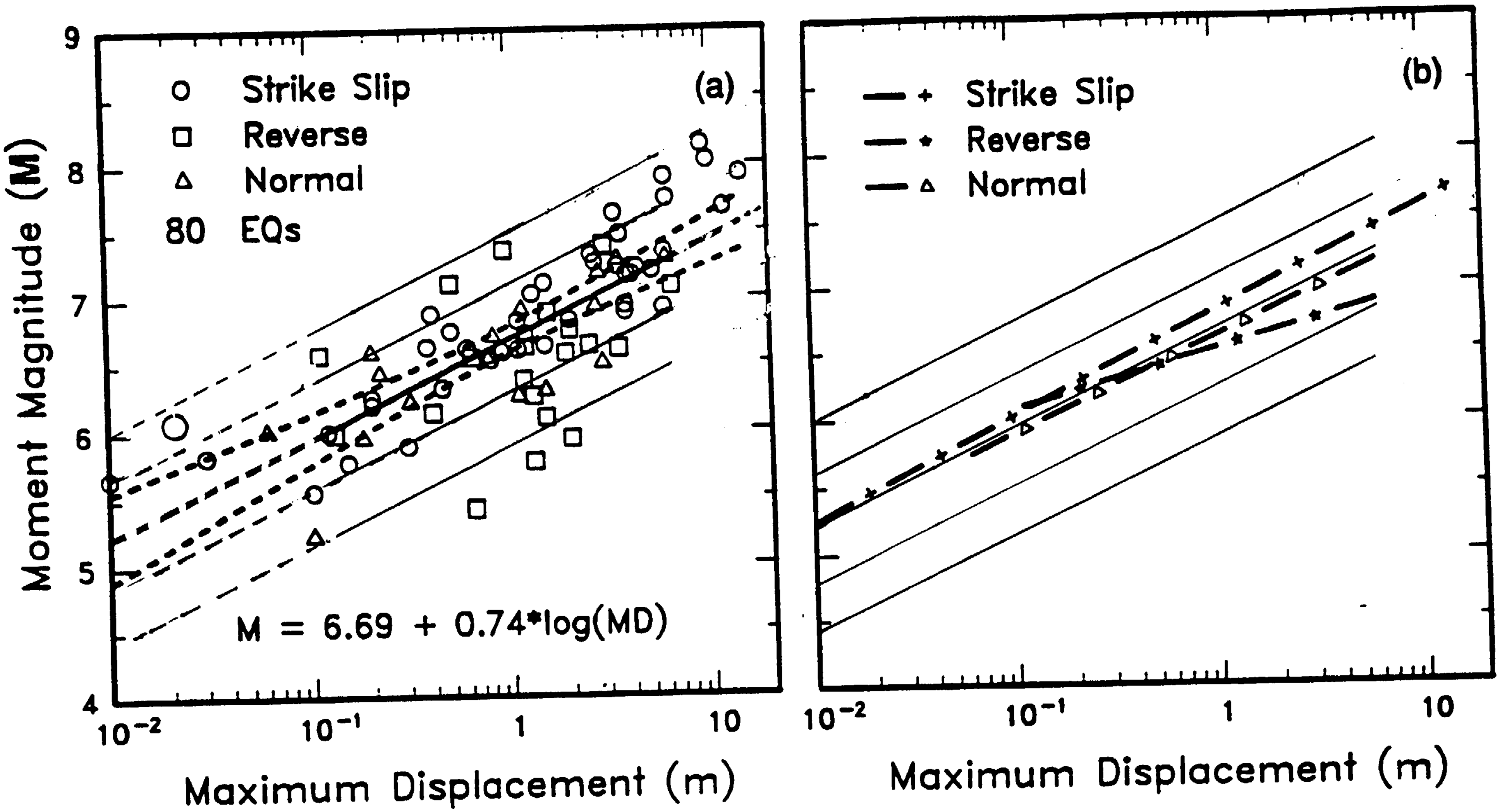

Figure 10

NUMBER	EQN	DATE	LENGTH (KM)	MCALC, SD RATIO	Mw
1	7	1906	432	-1.57	7.8
2	10	1920	220	-1.47	8.02
3	17	1931	180	-0.92	7.92
4	52	1957	236	-1.82	8.14
5	112	1976	235	-1.82	7.63
6	233	1990	120	-1.10	7.72
7	1	1957	297?, or 360?	-1.10	(7.85)
8	3	1972	108	-0.37	(7.61)
9	20	1932	148	-1.40	(7.60)
10	25	1939	360	-1.20	(7.81)
11	29	1943	280	-1.70	(7.58)
12	30	1944	180	-1.22	(7.59)

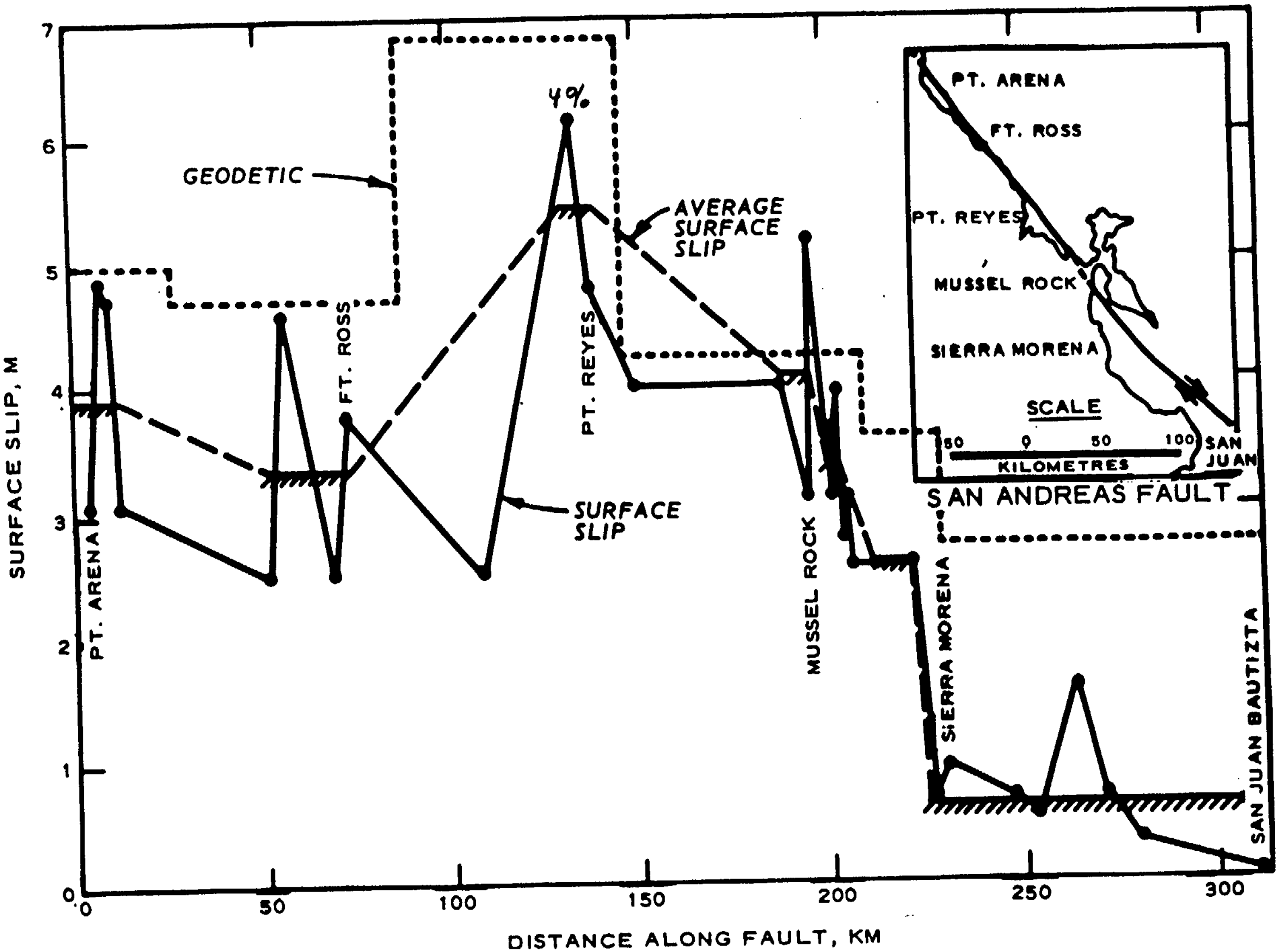

Figure 11. Observed fault displacements on the San Andreas fault from the 1906 earthquake. Dots are actual observations; hatched line connected by dashes shows a rough average of these data. Bar graph is based on 6 geodetic profiles across the fault zone and the faulting model based on slip on segments of a 10-km-deep fault (Thatcher[37,40]). Many of the measured field observations appear to be smaller than the geodetic values as the result of local drag or distortion

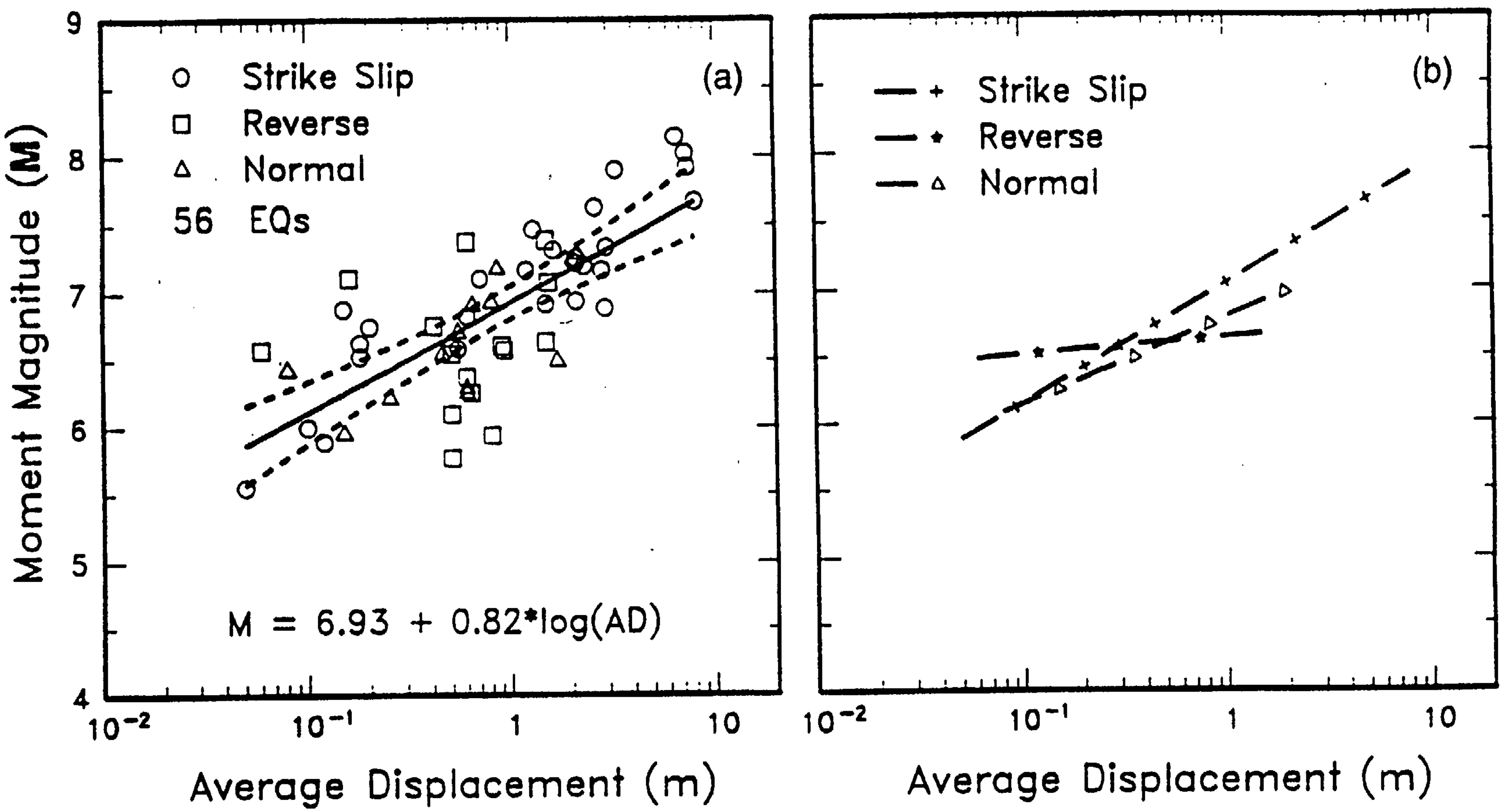

Strike Slip
Reverse
Normal
56 EQs
(a)
M = 6.93 + 0.82*log(AD)
Moment Magnitude (M)
Average Displacement (m)
(b)
Strike Slip
Reverse
Normal
Average Displacement (m)

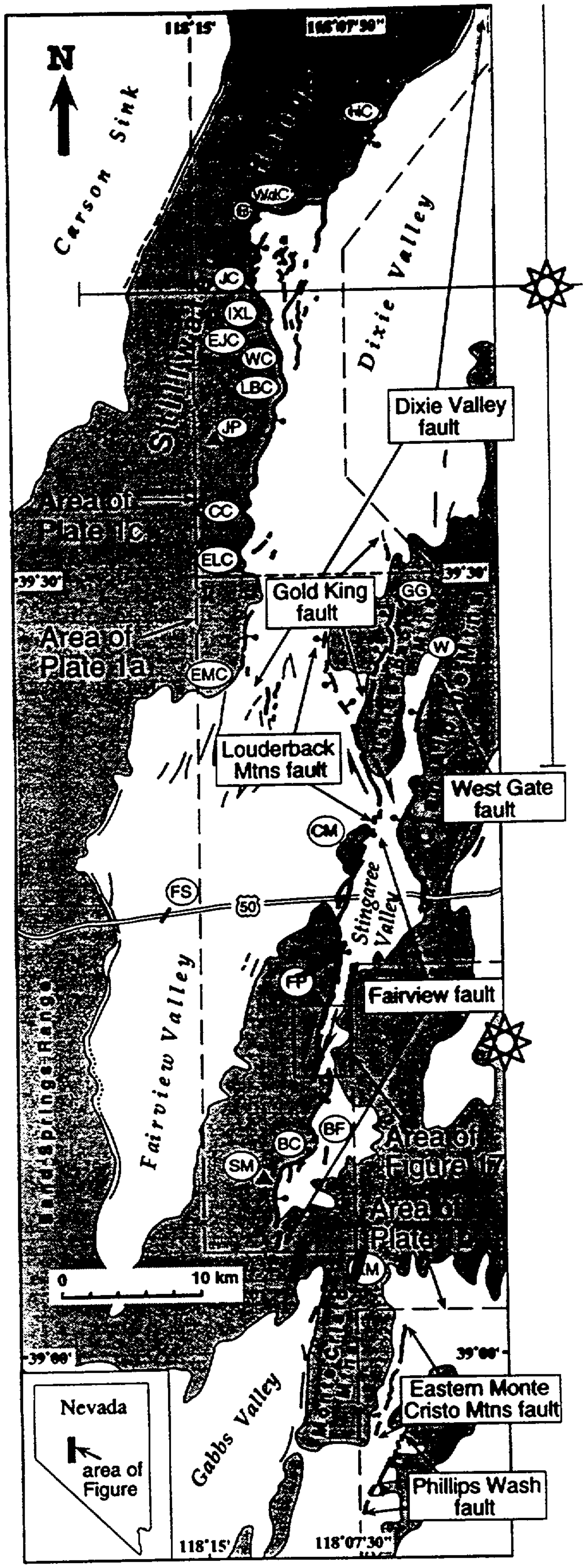
N
Carson Sink
Dixie Valley
Dixie Valley fault
Area of Plate 1c
Area of Plate 1a
Gold King fault
Louderback Mtns fault
West Gate fault
Stingaree Valley
Fairview Valley
Fairview fault
Area of Figure 17
Area of Plate 1b
Eastern Monte Cristo Mtns fault
Phillips Wash fault
Gabbs Valley
0 10 km
Nevada
area of Figure
39°30'
39°00'
118°15'
118°07'30"
HC
WdC
JC
IXL
EJC
WC
LBC
JP
CC
ELC
EMC
GG
W
CM
FS
50
FP
BF
BC
SM
KM

Figure 1

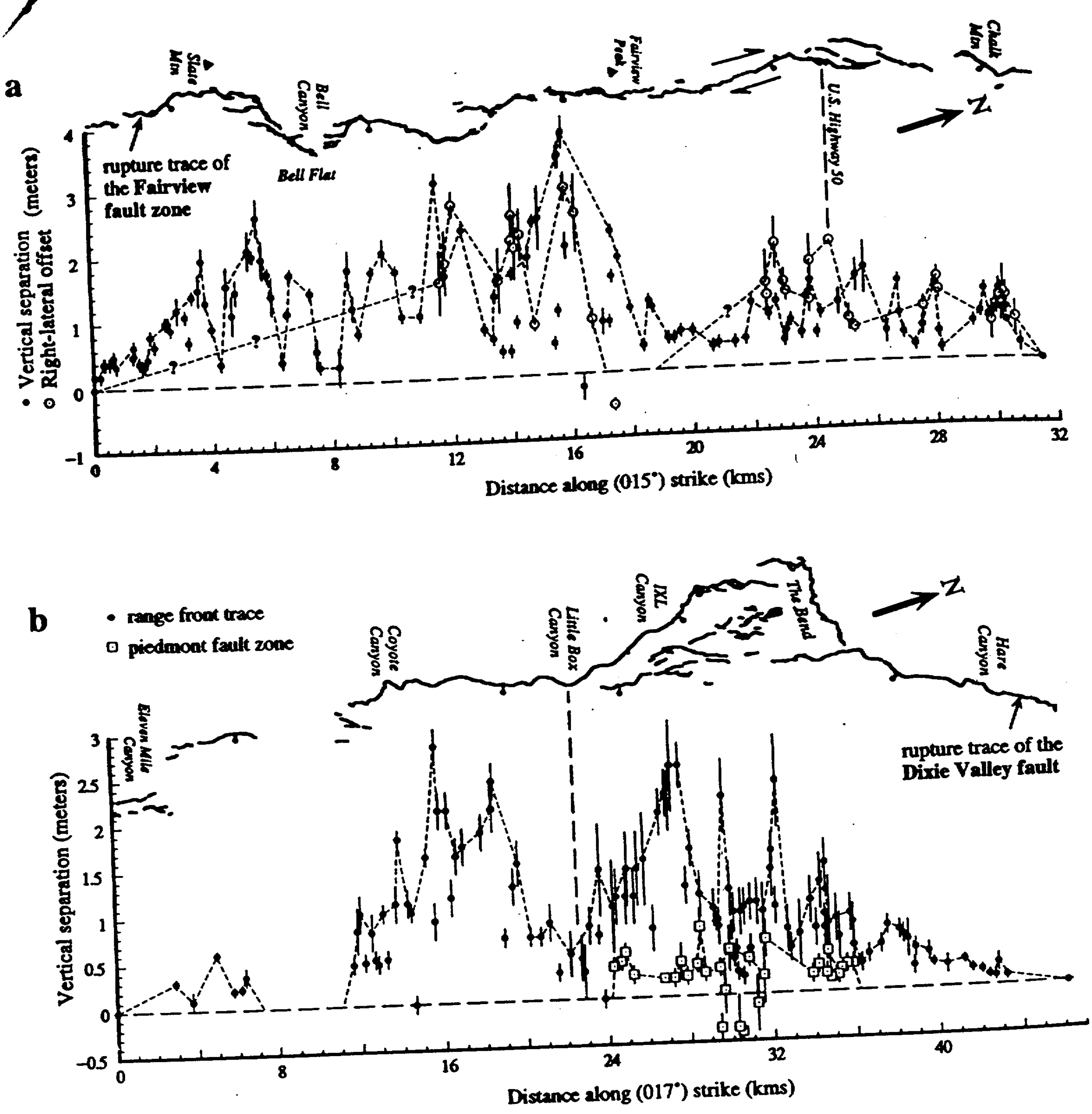

Figure 5. Measurements of vertical separation (solid dots and open squares) and lateral offset (open circles) versus distance along a line of average strike for (a) the Fairview fault, (b) the Dixie Valley fault (c) West Gate fault, (d) the Louderback Mountains fault, (e) the Gold King fault, (f) and the Phillips Wash fault surface ruptures. The mapped rupture traces are registered with the horizontal axis for each plot; ball and stick shown on down-thrown side of the faults; paired arrows indicate direction of lateral motion. Negative vertical separation values in (a) and (b) represent net down-to-the-west separations; those in (d) represent net down-to-the-east separations. The negative right lateral value in (a) represents a measurement of net left-lateral offset (see text, Plate 1a). In (a), strike-slip offset is projected to zero at the south end of Fairview fault trace to reflect previous observations of right slip outboard of the range-front fault in Bell Flat (Slemmons, 1957). Measurement error bars are shown as thin vertical lines through data points. Where rupture strands overlap at map scale, measurements that fall on (or very close to) a given line perpendicular to the average strike line of the fault are combined for net lateral offsets and net vertical separations. Measurements of lateral offset in areas of multiple fault strands are generally considered minimum net values because lateral displacement is seldom well expressed or preserved on all overlapping ruptures. Where rupture strands overlap, error estimates on all strands are assumed to be additive and are therefore generally greater than error estimates where only a single fault

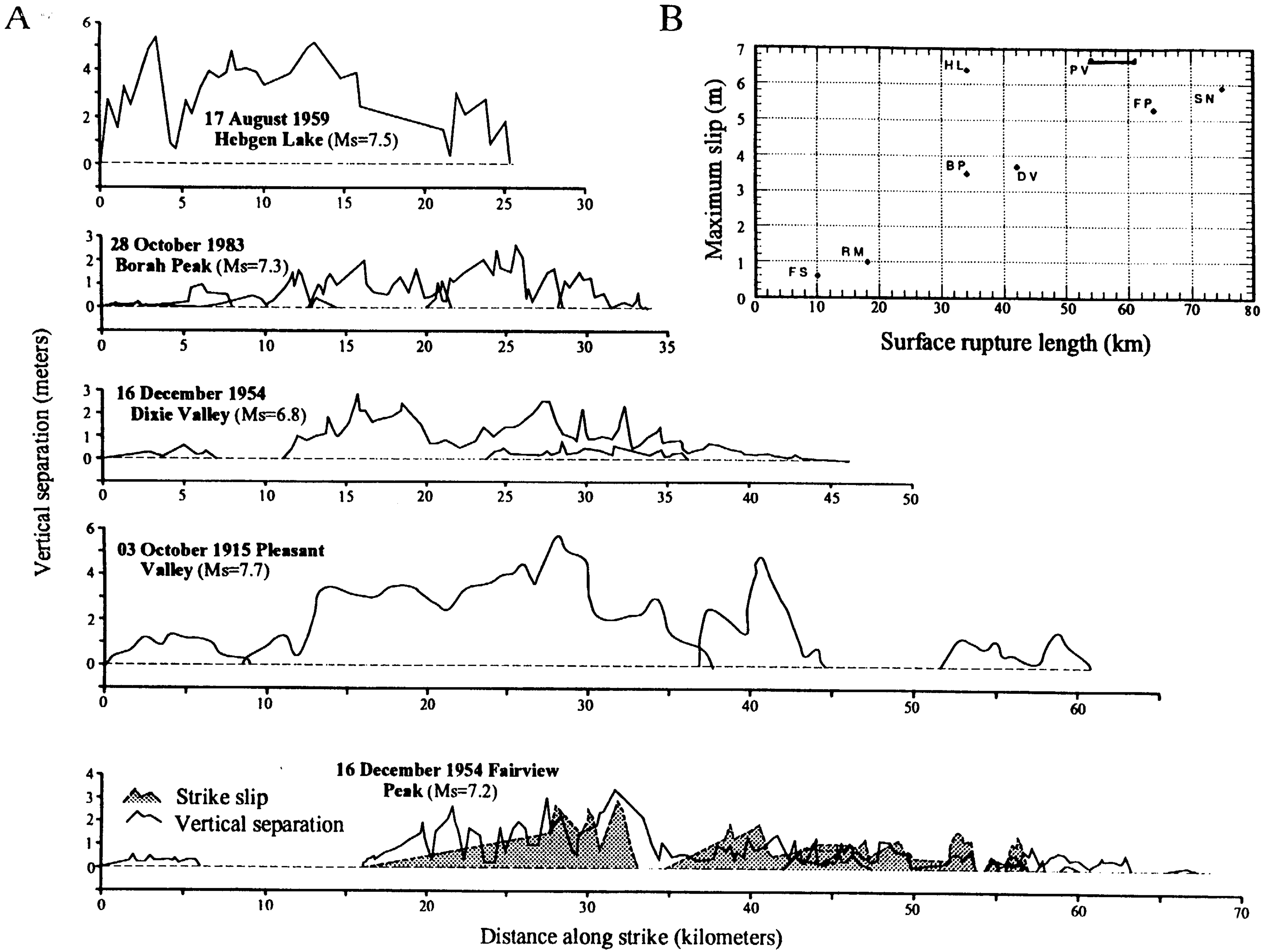

Figure 20. (a) Slip distributions for historical normal and normal-oblique surface

Table 1

Summary of surface rupture characteristics for faults activated during the 1954 Fairview Peak and Dixie Valley earthquakes

Fault	Rupture length (kms)	Average strike	Dip	VS_{max} (m)	VS_{avg} (m)	SS_{max} (m)	SS_{avg} (m)	u_{max} (m)	u_{avg} (m)	M_0^g(max) ($x10^{26}$ dyne cm)	M_0^g(avg) ($x10^{26}$ dyne cm)	M_w(max)	M_w(avg)
Dixie Valley fault	42.0	017°	30-50°E	2.80	0.90	—	—	3.66	1.17	9.04	2.89	7.27	6.94
Fairview fault zone	31.6	015°	50-70°E	3.80 (3.80)	1.20	2.90	1.00	5.26	1.71	8.63	2.80	—	—
Gold King fault	8.5	005°	50-70°W	1.00	0.45	—	—	1.15	0.52	0.51	0.23	—	—
Louderback Mtns fault	14.0	345°	60-80°W	0.80 (0.70)	0.20	1.70	0.50	1.86	0.54	1.25	0.36	—	—
Phillips Wash fault	6.2	027°	50-70°E	0.48 (0.30)	0.25	0.80	0.60	0.87	0.67	0.28	0.22	—	—
West Gate fault	10.0	003°	50-70°W	1.15 (0.65)	0.40	1.20	0.60	1.41	0.76	0.73	0.39	—	—
Fairview Peak event totals										11.40	4.00	7.34	7.03

Abbreviations: VS_{max} (maximum vertical separation of the ground surface) is taken to approximate maximum vertical displacement (throw) (numbers in parentheses represent vertical separation measured at location of maximum strike slip offset and these values are used to determine dip slip component for u_{max} calculations); SS_{max} (maximum lateral offset); VS_{avg} (average vertical separation (approximates average throw)) and SS_{avg} (average lateral offset) calculated using generalized linear point-to-point functions that define slip distribution curves (Figure 5). Areas beneath the slip distribution curves (Figure 5) were determined and these areas were then divided by rupture length to determine average values. SS_{avg} for Phillips Wash fault was determined by assuming a constant proportion of strike slip to dip slip along the entire rupture length as at the location of the single strike slip measurement (Figure 5f). u_{max} (maximum surface displacement) is determined at a single location along the fault (e.g.(Wells and Coppersmith, 1994)) and is equal to the vector sum of the dip slip and strike slip components. Along the Fairview fault, VS_{max} and SS_{max} were measured within 100 m of each other, so in this case, these measurements are used to calculate u_{max}. Dip slip (DS) is determined from the relation $DS=VS/\sin\theta$, where θ is the fault dip angle. The average fault dip from the range of dip values shown in Table were used to calculate dip slip except for the Dixie Valley fault where a 50° fault dip was used because this dip angle is well constrained for the fault in areas north of The Bend (Okaya and Thompson, 1985). As well, it is not known if the low angle of dip at the surface along parts of the fault south of The Bend (discussed in text) projects down to seismogenic depths. Ranges for dip values shown in the Table are based generally on field observations (Plates 1a-c) where available. Otherwise, ranges for dip values are assumed. u_{avg} (average slip resolved) is calculated from the vector sum of DS_{avg} ($=VS_{avg}/\sin\theta$) and SS_{avg}; M_0^g(max) and M_0^g(avg) (maximum and average geologic moments) for each fault ruptured were calculated from the relationship $M_0^g=\mu wLu$ (Aki and Richards, 1980) where μ is the shear modulus ($3x10^{11}$ dyne/cm^2), w is fault width (assuming the same fault dips used for dip slip calculations and a fault depth of 15 km which is consistent with microearthquake studies in the Fairview Peak area (Ryall and Malone, 1971; Stauder and Ryall, 1967), L is fault surface rupture length, and u is net displacement. Maximum and average geologic moments were calculated using u_{max} and u_{avg}, respectively; M_w(max) and M_w(avg) (maximum and average moment magnitudes) were calculated from the relation $M_w=2/3\mathrm{Log}M_0^g-10.7$ (Hanks and Kanamori, 1979) for maximum and average geologic moments. Moments and moment magnitudes for the Fairview Peak event totals assume that the Fairview, Gold King, Louderback Mountains, Phillips Wash, and West Gate fault all ruptured during this earthquake. Because the west-dipping Gold King, Louderback Mountains, and West Gate faults may not extend down to 15 km depth (i.e. they may be antithetic to and therefore terminate at the Fairview and Dixie Valley faults at a shallower depth) both M_0^g(max) and M_0^g(avg) and corresponding moment magnitudes are considered maximum values for these estimates.

EQN	DATE	M_w	RUPTURE LENGTH (KM)	D_{MEDIAN}	D_{AVG}	D_{MAX}	FAULT % WITH D NEAREST 0	FAULT % WITH D NEAREST D_{AVG}	FAULT % WITH D NEAREST D_{MAX}	RATIO
1	1857	(7.85)	RL, FT. TEJON, CA 1 L= 315 KM MODEL L= 360 KM MODEL* L= 400+ KM SIEH MODEL		5.33 5.04 4.34	9.4 9.4 9.4	6 11* 12	79 75* 76	15 14* 12	0.58 0.54* 0.46
2	1872	(7.61)	RL, OWENS VALLEY, CA 2 MODEL 1; L=CA.100 KM MODEL 2: L=108+ KM MODEL 1: L=108 KM		4.37 4.57 3.87	11.0 11 11	20 11* 18	52 >55* 74	28- <34* 8	0.40 0.39* 0.35
4	1887	(7.31)	N, PITAYCACHI, MEX 18	?	1.9(2.2)	5.1(5.9)				0.37
7	1906	7.9	RL, SAN FRANCISCO, CA 3 (DATA FOR 60% OF L=432 RUPTURE LENGTH)	-2.7	2.5	6.1	(23)	(69)	(8)	0.41
9	1915	7.18	NS, PLEASANT VALLEY, NV4 CASKEY MODEL		1.9(2.2)	5.8(6.7)	41	49	10	0.33
10	1920	8.02	LL, HAIYUAN, CHINA 5 L=225 KM (Modified from Weflin et al)	3.0	4.4	11.6	29	57	14	0.38
15	1930	6.89	LL-R, NORTH IZU, JAPAN 6 L=35	0.6	1.35	3.8	49	29	22	0.36

FLTMEAS.96C-October 13, 1996

SUMMARY OF PRELIMINARY RESULTS FOR 17 EVENTS

	Percentage
Displacements nearest maximum displacement	16 ± 12
Displacements nearest average displacement	61 ± 13
Displacements nearest zero	23 ± 7
	100

The median displacement value is subequal to the average displacement for events with numerous and accurate field measurements.

The average displacement is about 37 % of the maximum displacement value (not 50 %).

Surface Ruptures of Historic Earthquakes in the Basin and Range

Data Related to the Along-Strike and Across-Strike Distribution of Fault Displacement

presented by

Silvio Pezzopane

U.S. Geological Survey

Yucca Mountain Project

The Data and Approach

- 24 Surface-Faulting Earthquakes in the Extensional Cordillera of the Western US
- 20 Surface Rupture Maps
  - » ~12 High Quality (Distributed SR — since 1950's)
- 9 Along-Strike Slip Distributions
  - » 6 High Quality
- Data Quality Varies w/ Time and Magnitude

- Characterization Parameters
  - » Magnitude
  - » Focal Depth
  - » Slip Vector
  - » Primary Surface Rupture Length
  - » Displacement Max. and Ave.
  - » Along-Strike Slip Distribution
  - » Geometric Segmentation
  - » Max. Width of Surf.Rupt. Zone
  - » Max. Secondary Rupture Length & Displacement

in USGS Seismotectonic Report—Chapter 9

24 Transtensional Surface-Rupturing B&R Earthquakes

YEAR	LOCATION, NAME (ABBREV)	MAGNITUDE
1869	Nevada, Olinghouse (OL)	6.5
1872	California, Owens Valley (OV)	7.6
1887	Mexico, Sonora (SN)	7.4
1903	Nevada, Wonder (WO)	6.0
1915	Nevada, Pleasant Valley (PV)	7.3
1932	Nevada, Cedar Mtn. (CM)	7.2
1934	Nevada, Excelsior Mtn. (EM)	6.3
1934	Utah, Hansel Valley (HV)	6.6
1947	California, Manix (MX)	6.4
1950	California, Fort Sage (FS)	5.6
1954	Nevada, Rainbow Mtn. (RM)	6.6
1954	Nevada, Stillwater (ST)	6.8
1954	Nevada, Fairview Peak (FP)	7.1
1954	Nevada, Dixie Valley (DV)	6.8
1959	Montana, Hebgen Lake (HL)	7.4
1975	California, Galway Lake (GL)	5.2
1979	California, Homestead Valley (HM)	5.5
1980	California, Mammoth Lakes (ML)	6.1
1981	California, Mammoth Lakes (MM)	5.8
1983	Idaho, Borah Peak (BP)	6.8
1986	California, Chalfant Valley (CV)	6.2
1992	California, Landers (LD)	7.4
1993	California, Eureka Valley (EV)	6.1
1995	California, Ridgecrest (RC)	5.8

Data Sources

- Earthquake Source Parameters
  - » D. Doser (Doser and Smith, 1989)
  - » Stover and Coffman, 1993 (USGS)
  - » a few from published literature
- Rupture Maps
  - » many many many different rupture mappers
  - » V.P. Gianella
    - – Verdi, Fort Sage, Sonora, Cedar Mtn
  - » D.B. Slemmons
    - – Dixie-Fairview, Olinghouse, Wonder
  - » M.M. Clark
    - – Owens, Mammoth, Chalfant, Mono
  - » many recent re-investigations

in USGS Seismotectonic Report—Chapter 9

Location, Date, and Magnitude of Surface-Rupturing Earthquakes in the Basin and Range

- 20 of 24 Events in the Western Great Basin
  - » YM is Yucca Mtn
- 5 of 24 Events in or near Mojave Desert
- 10 of 24 Events are Pre-1950's
  - » Poor—Moderate Data Quality
- Minimum Faulting Earthquakes (< M 6.0) are Post-1950's
  - » Post-1978

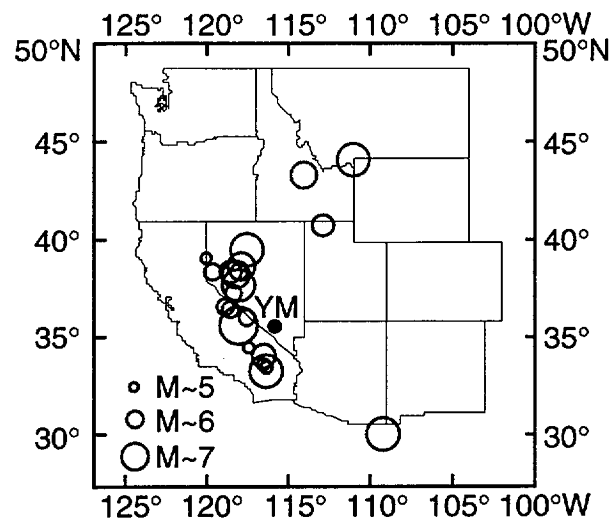

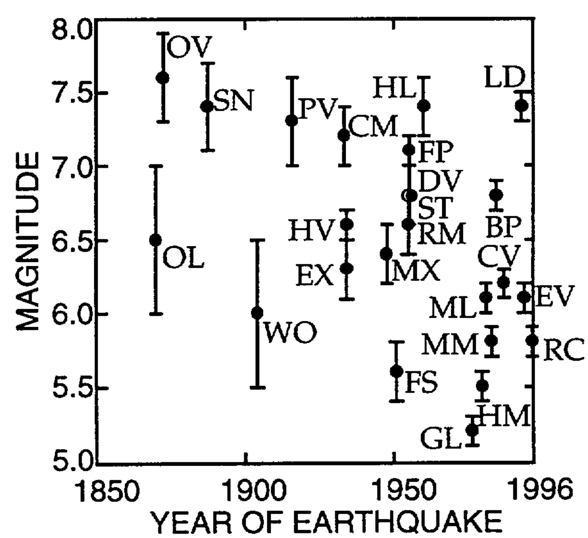

in USGS Seismotectonic Report—Chapter 9

Focal Depth and Faulting Style of Surface-Rupturing Earthquakes in the Basin and Range

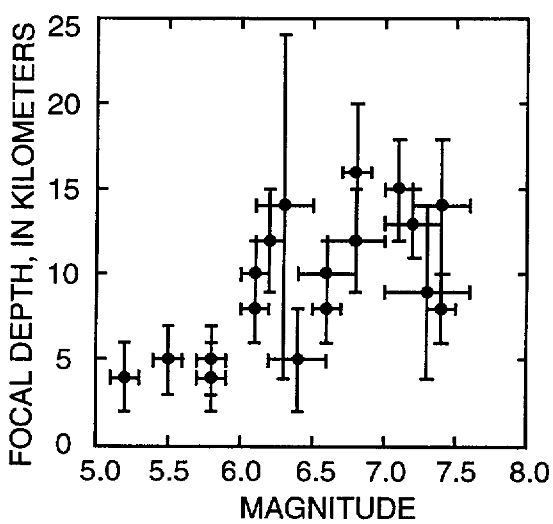

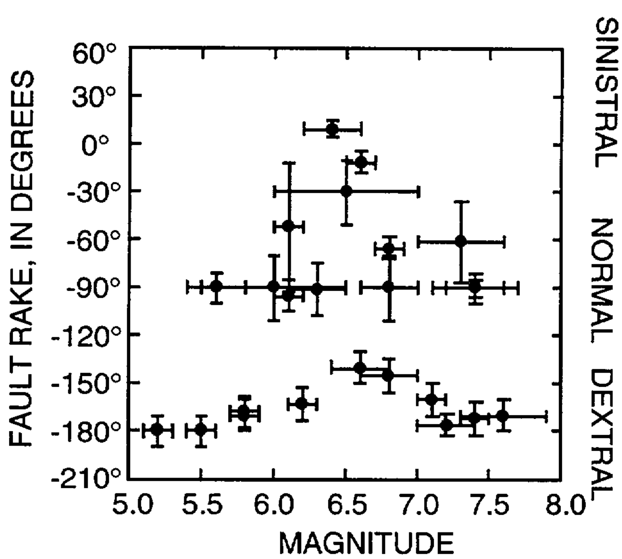

in USGS Seismotectonic Report—Chapter 9

- 19 of 24 Events have Determined Depths
  - » waveform modeling
- 5 Events (M < 6.5) have Depths < 7 km
- 9 Events (M > 6.5) have Depths > 7 km
- 10 of 24 Events are Dominantly Normal Faulting
- 11 of 24 Events are Dominantly Right-Lateral Faulting
- 3 of 24 Events are Dominantly Left-Lateral Faulting

Rupture Length & Segmentation of Surface-Rupturing Earthquakes in the Basin and Range

- Surface Rupture Length and Moment Magnitude Scale w/ (WC) Wells and Coppersmith, 1994
  - » some exceptions
  - » (BML) Bonilla and others, 1984

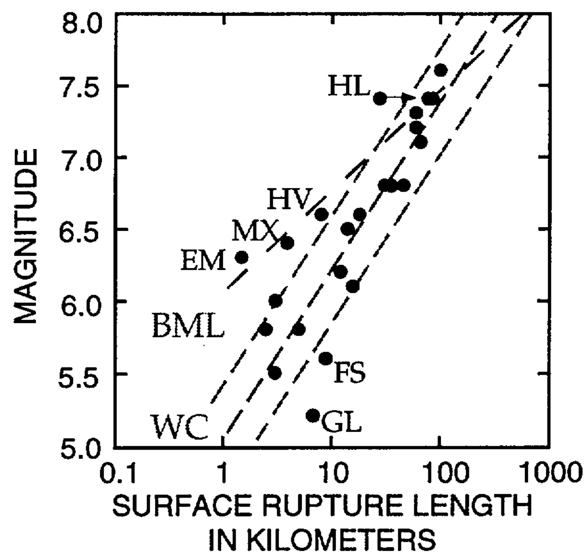

- Number of Geometric Fault Segments Scale w/ Surface Rupture Length and Moment Magnitude
  - » Length/Segment = 15 to 20 km
  - » Seismogenic Crustal Thickness??

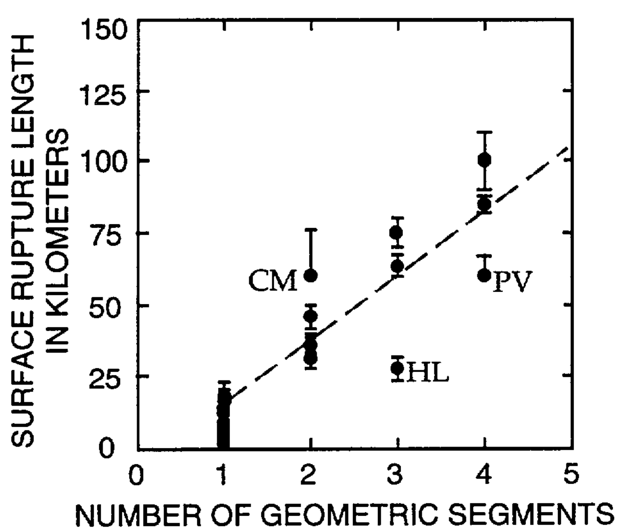

in USGS Seismotectonic Report—Chapter 9

Along-Strike Fault Slip Distributions of Surface-Rupturing Earthquakes in the Basin and Range

in USGS Seismotectonic Report—Chapter 9

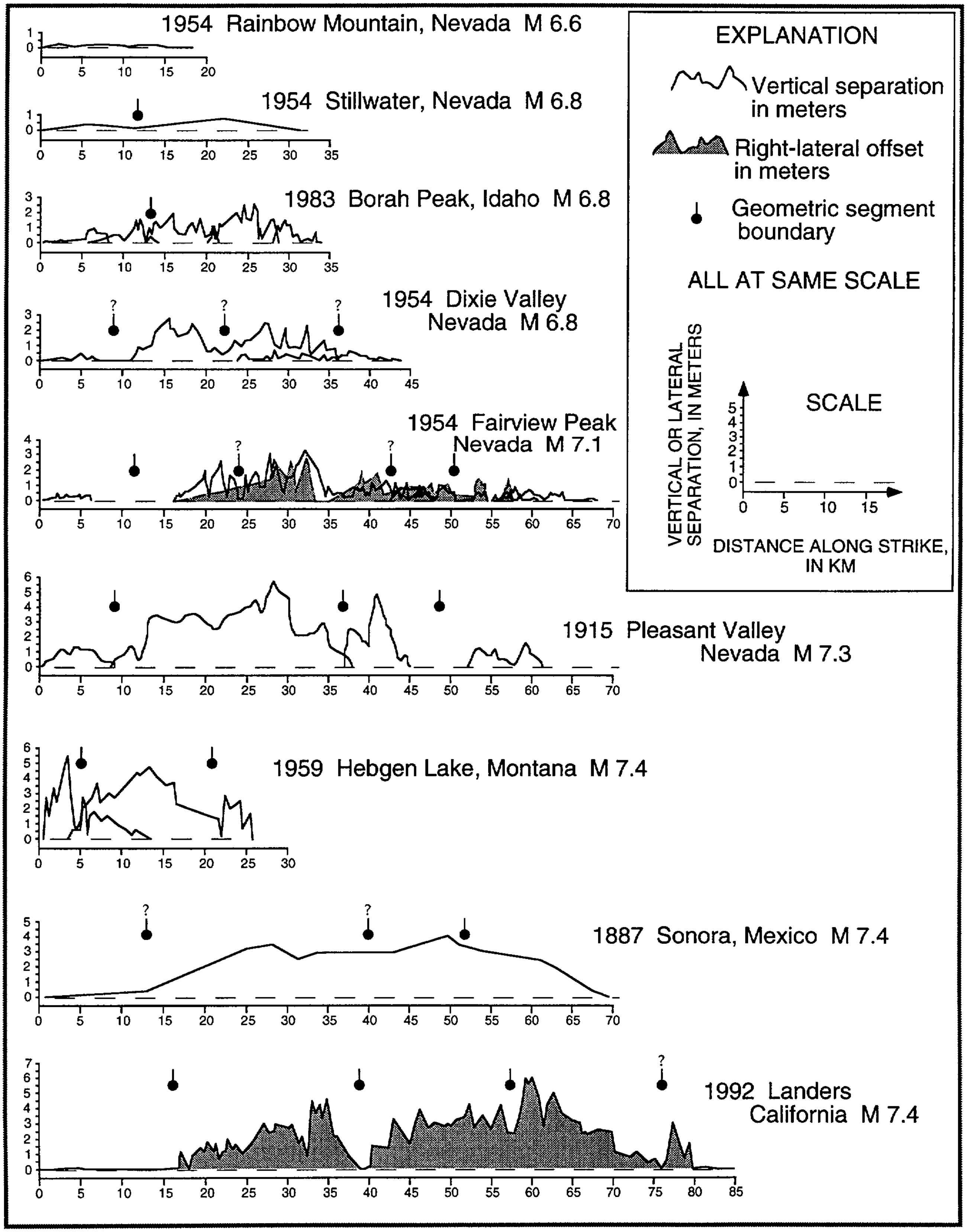

USGS-YMP Pezzopane Oct 96

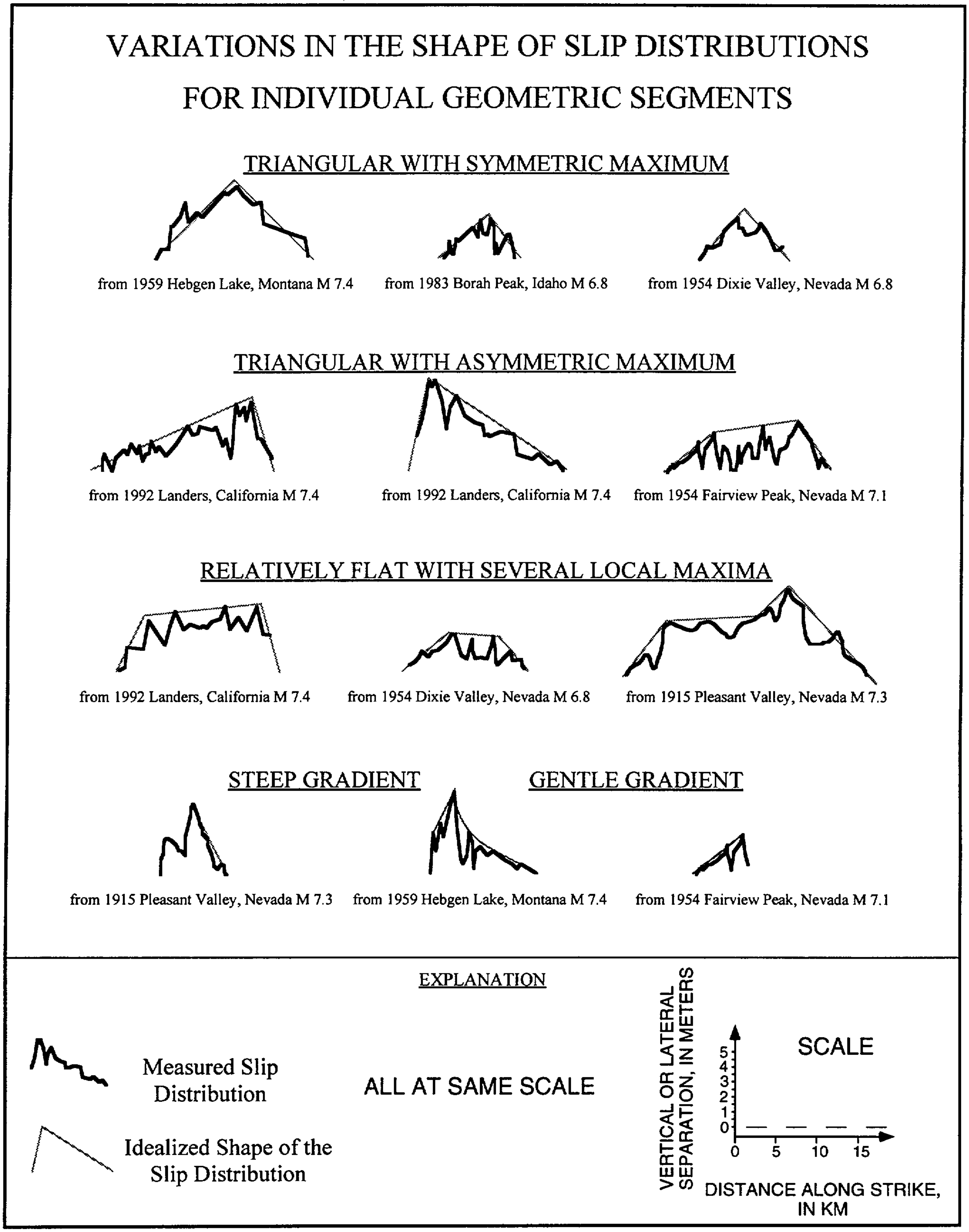

in USGS Seismotectonic Report—Chapter 9

Example Surface Rupture Characterization
1959 Hebgen Lake, Montana M 7.4

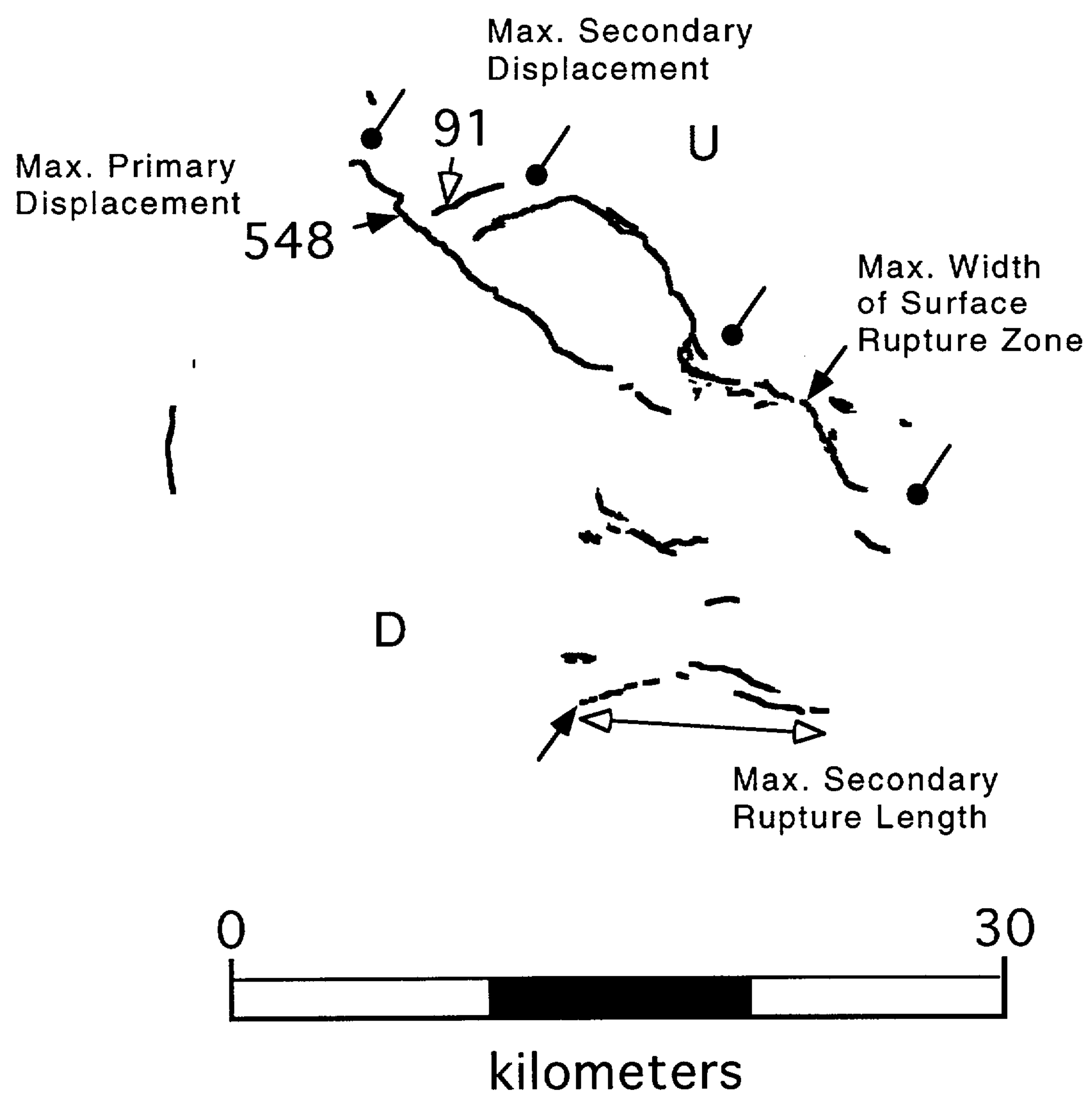

in USGS Seismotectonic Report—Chapter 9

Maximum Width of Surface Rupture Zone of Surface-Rupturing Earthquakes in the Basin and Range

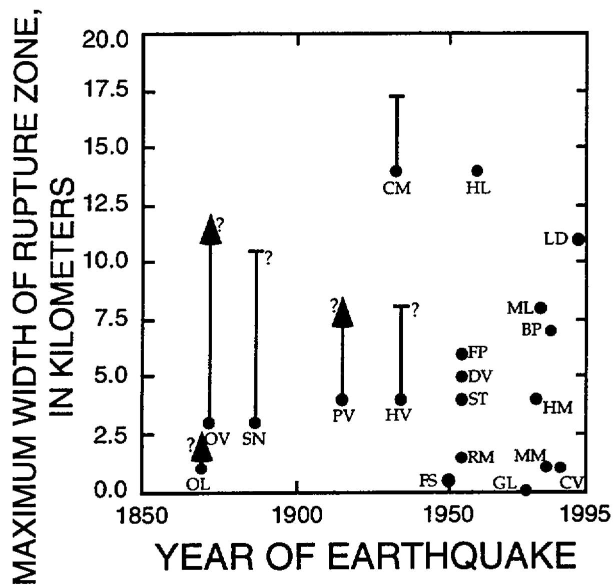

- Max. Width of Surface Rupture Zone may be <u>Minimum</u> Width for Older (pre-1950) Events
  - » error bars based on modern events of similar Mw

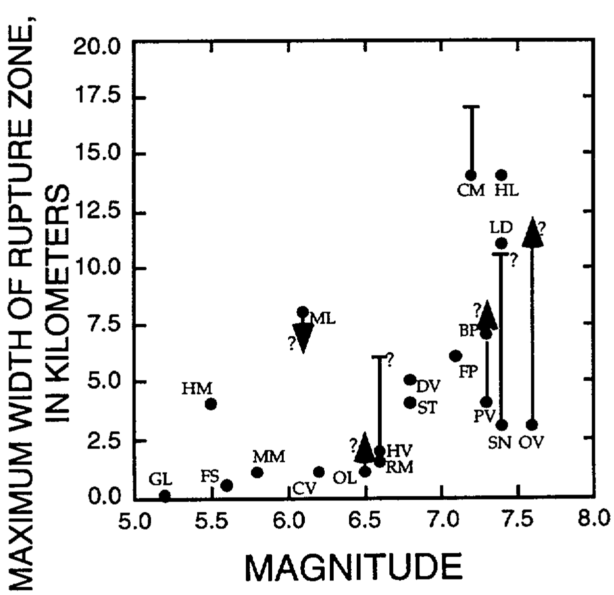

- Max. Width of Surface Rupture Zone Increases for Increasing Mw
  - » Max. Width 0-5 km for Mw < 6.5 (± 0.3)
  - » Max. Width 5-15 km for Mw > 6.5 (± 0.3)

in USGS Seismotectonic Report—Chapter 9

USGS-YMP Pezzopane Oct 96

Maximum Width of Surface Rupture Zone of Surface-Rupturing Earthquakes in the Basin and Range

- Max. Width of Surface Rupture Zone may Increase with Shallower Fault Dips
  - » data are poorly constrained

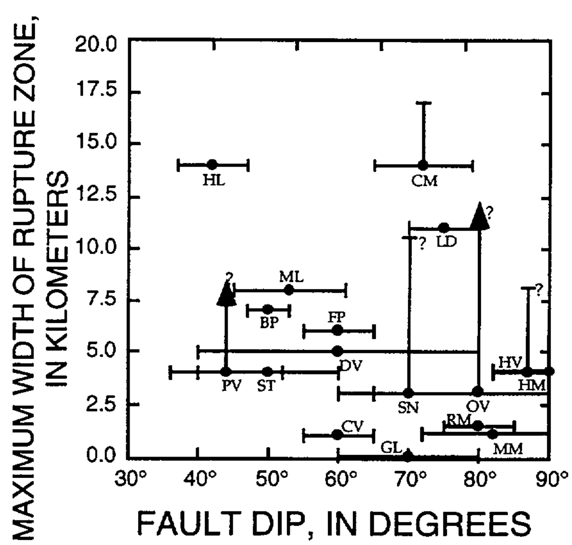

- Max. Width of Surface Rupture Zone may Increase with Deeper Focal Depths
  - » data are poorly constrained

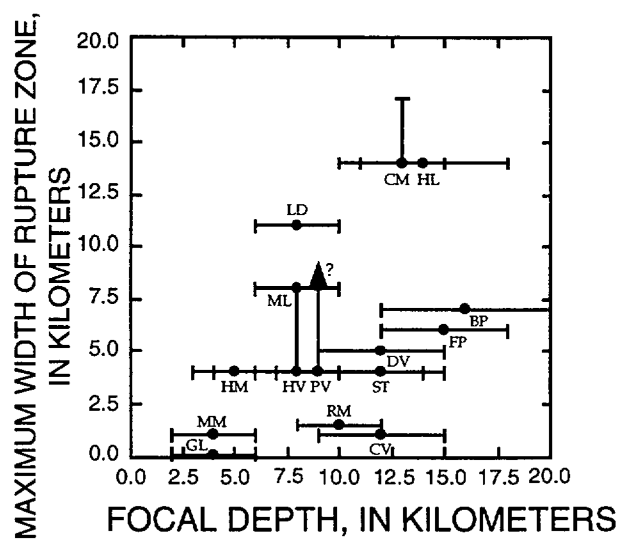

in USGS Seismotectonic Report—Chapter 9

Secondary Rupture Lengths of Surface-Rupturing Earthquakes in the Basin and Range

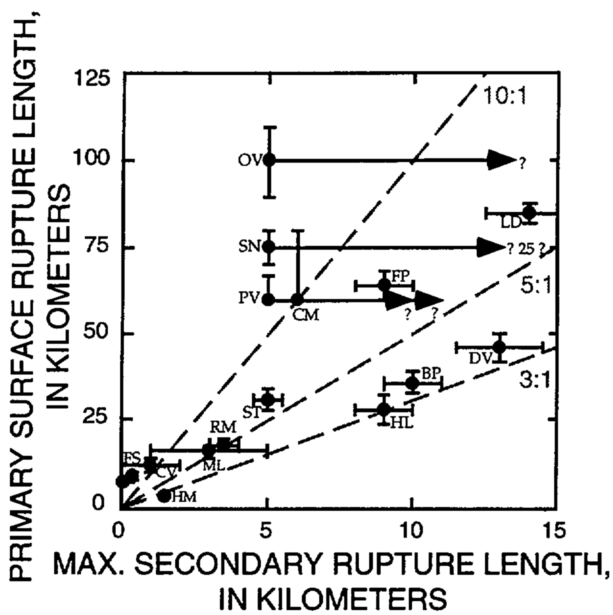

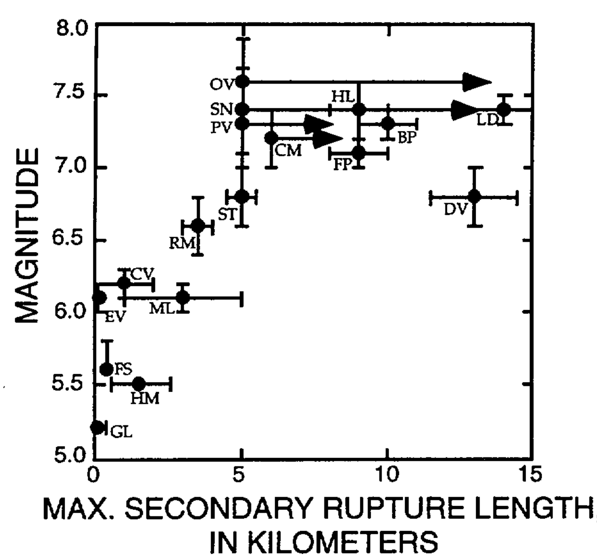

- Max. Secondary Surface Rupture Length Scales with Primary Surface Rupture Length
  - » ratio of P/S is about 5:1
- Max. Secondary Surface Rupture Length Scales with Magnitude
  - » exponential
  - » plot as straight line in log-linear coordinates

in USGS Seismotectonic Report—Chapter 9

Secondary Displacement of Surface-Rupturing Earthquakes in the Basin and Range

- Ratio of Max. Primary to Max. Secondary Displacement Scales with Mw
  - » ratio of P/S is commonly 1:1 to 3:1
  - » all < 6:1

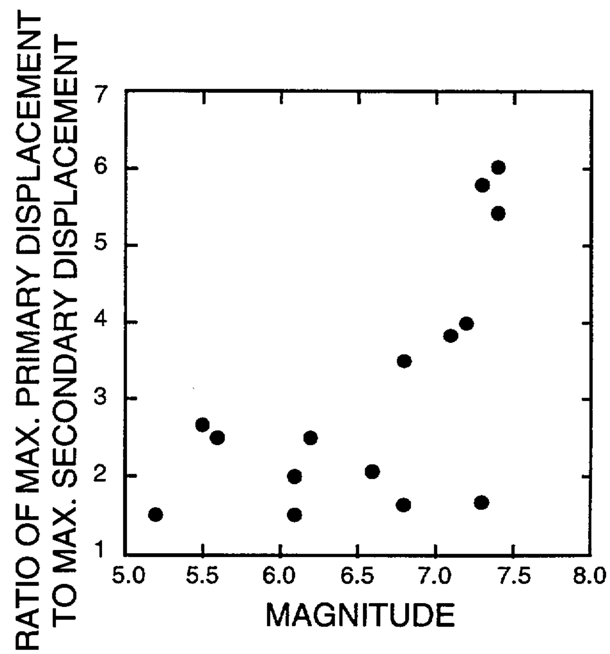

- Ratio of Ave. Primary to Max. Secondary Displacement Scales with Mw
  - » ratio of P/S is commonly ~ 1:1
  - » all < 3:1

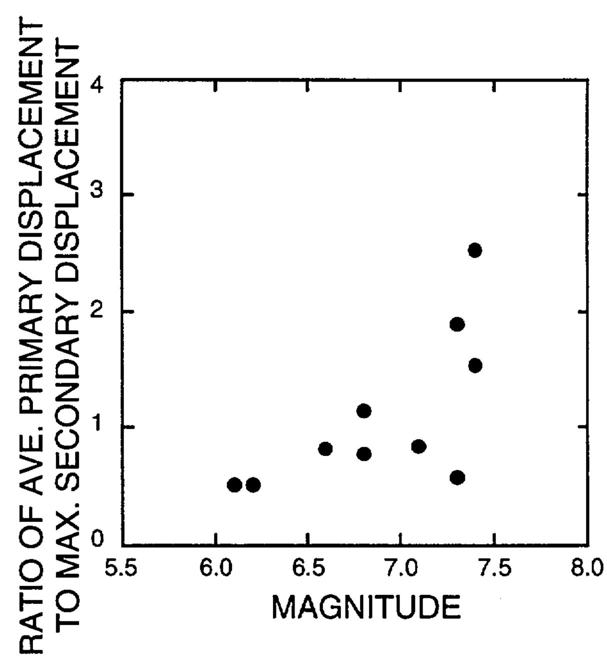

Relations Among Secondary Rupture Length & Displacement of Surface-Rupturing Earthquakes in the Basin and Range

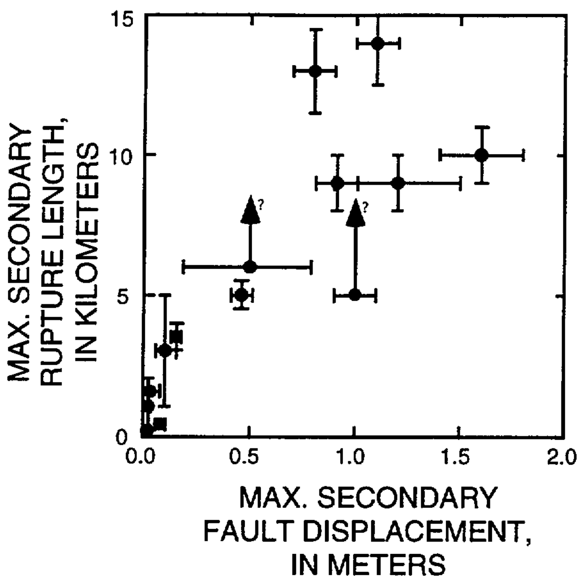

- Max. Secondary Displacement Scales with Max. Secondary Rupture Length
  - » exponential ??

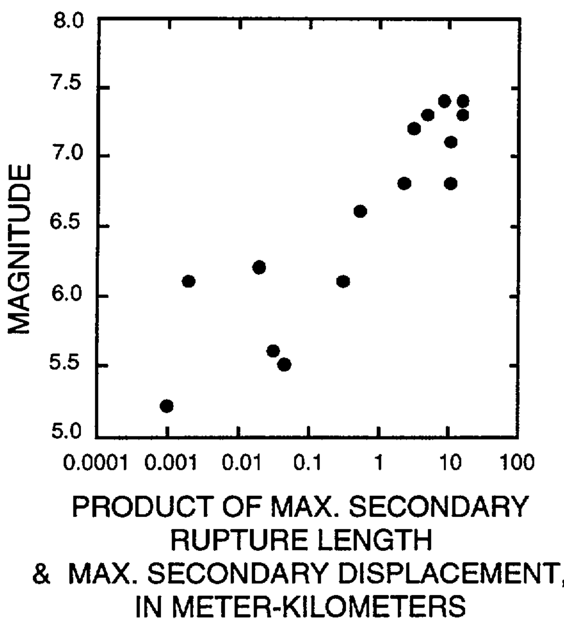

- Product of Max. Secondary Rupture Length & Max. Secondary Displacement Scales with Mw
  - » distributed faulting shows scaling relations

in USGS Seismotectonic Report—Chapter 9

Same-Scale Comparisons of Selected Surface Ruptures and Yucca Mountain Faults

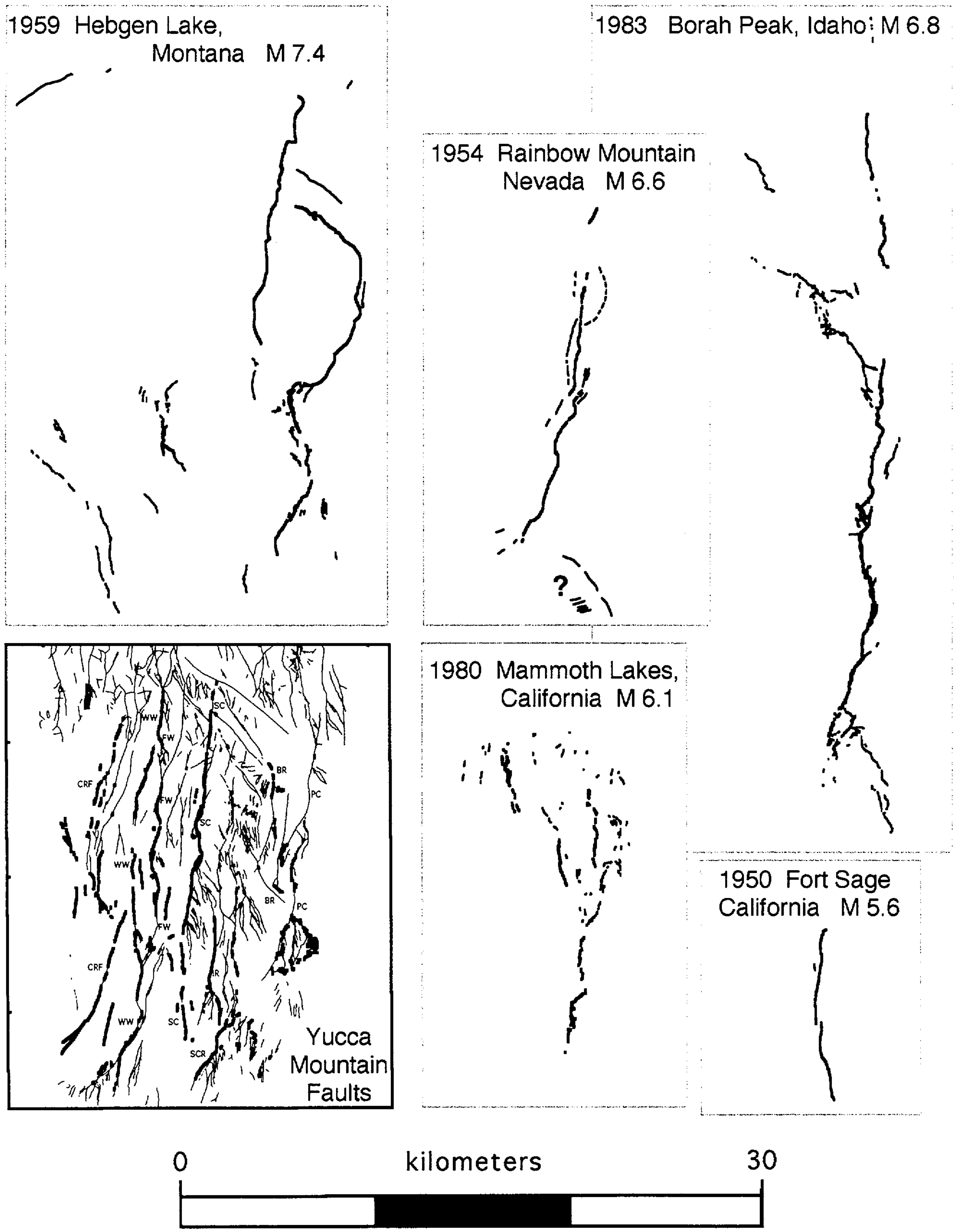

USGS-YMP Pezzopane Oct 96

Global Empirical Data for Normal and Oblique-Normal Earthquakes

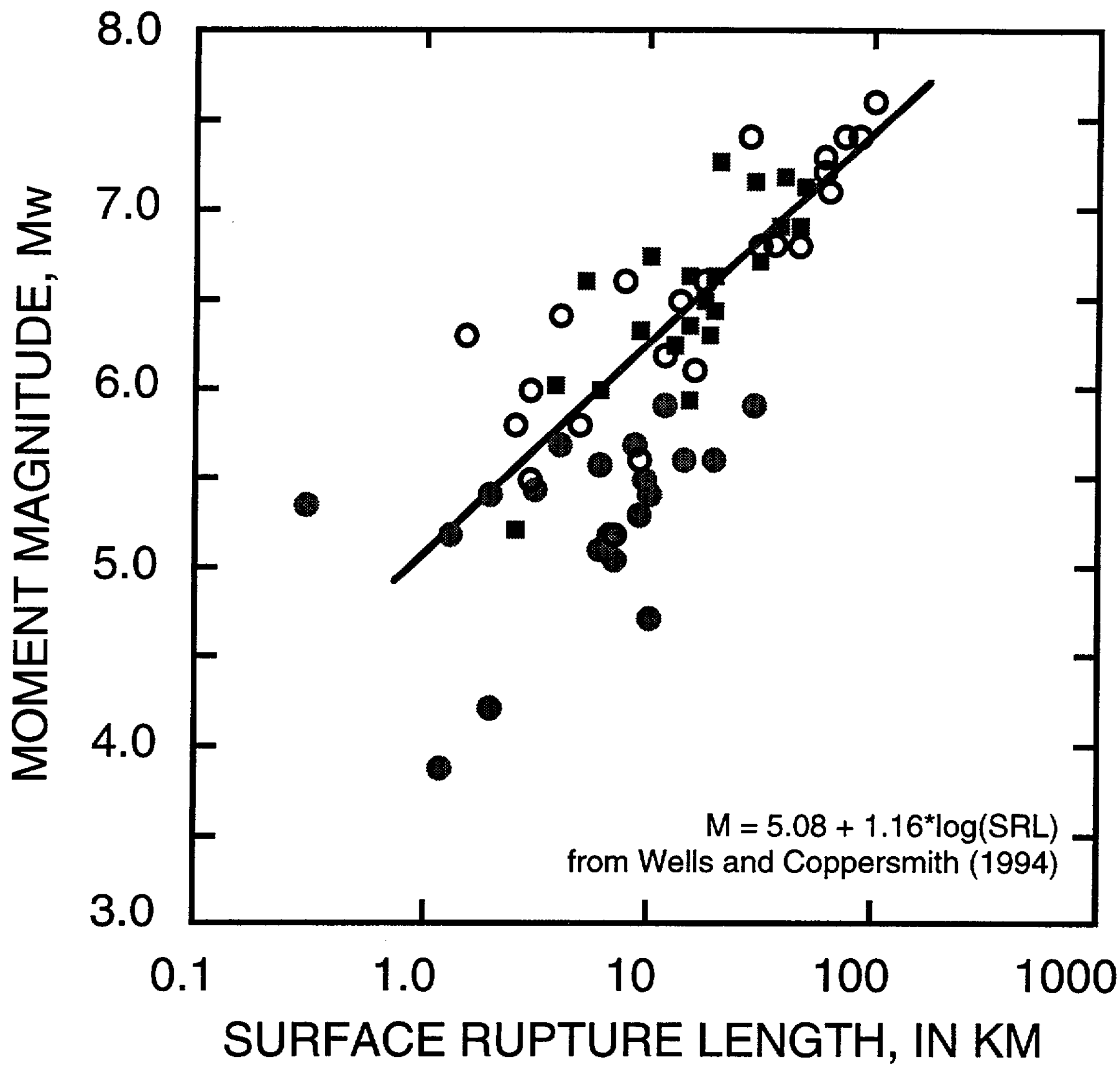

- ● from Bonilla (1988)
- ■ from Wells and Coppersmith (1994)
- o from Basin and Range Data Set
  USGS Seismotectonic Report—Chapter 9

Global Empirical Data for Normal and Oblique-Normal Earthquakes

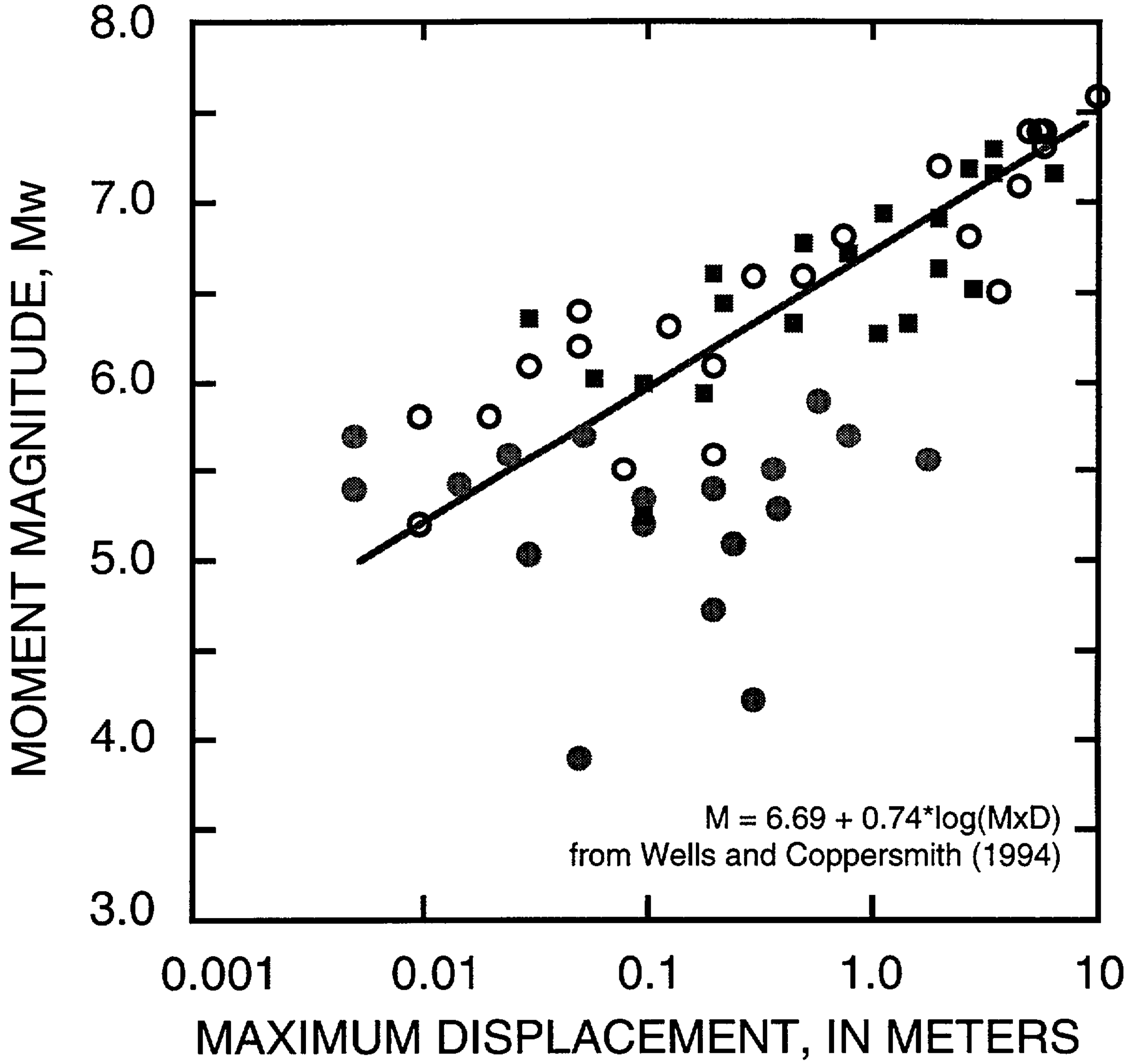

- ● from Bonilla (1988)
- ■ from Wells and Coppersmith (1994)
- ○ from Basin and Range Data Set
  USGS Seismotectonic Report—Chapter 9

USGS-YMP Pezzopane Oct 96

—Summary—
Distributed Surface Faulting Basin and Range Earthquakes

- 24 Surface Rupturing Events—Normal and Strike-Slip Faulting Mechanisms
- Primary Surface Rupture Length, Displacement, & Geometric Segmentation Scale with Magnitude
- Along-Strike Slip Distributions show Considerable Variation
- Across-Strike Width of Surface Rupture Zone Increases with Increasing Magnitude
- Secondary Rupture Length and Displacement (Distributed Ruptures) Scale Exponentially with Magnitude
- Historical Surface Ruptures are Analogs for Yucca Mtn. Distributed Faulting and Rupture Scenarios

Dynamic Wave Effects on Particle Motions in Thrust, Normal and Strike Slip Faulting

James N Brune (Seismological Laboratory, University of Nevada, Reno, NV 89554; 702-784-4974; email: brune@seismo.unr.edu)

Dynamic wave effects generated by the faulting process can destroy the plane symmetry often assumed in models of faulting. In the idealized symmetric models there are no fault-normal stresses propagated ahead of the rupture front. However, on actual faults a number of effects can destroy this symmetry and cause fault-normal stresses ahead of the rupture front, with consequent fault rupture and particle motions deviating significantly from the idealized models.

In strike-slip ruptures, fault-normal stresses ahead of the rupture front can be caused by differences in material properties on the two sides of the fault (Weertman waves), asperity impact during fault slip, or Riedel shears in the zone of fault gouge. The tensile stresses propagated ahead of the rupture front by Riedel shears are approximated by the formula: $\sigma_t = 0.1\ (r^2/R^2)\ \sigma$, where σ_t is the tensile stress, R is the distance along the fault ahead of the Riedel shear, and r and σ the radius and stress-drop of the Riedel shear. Depending on the fault failure conditions, fault-normal stresses can radically alter the rupture propagation and particle motions.

In shallow angle thrust faulting, a dislocation starting at the heel of the hanging-wall wedge sends a compressional wave upward and forward in the hanging-wall plate, which changes polarity upon reflection at the free surface, and then impinges on the fault plane as a tensile wave, reducing the normal stress and destabilizing the fault, thus altering the dynamics and particle motions. In a foam rubber model of shallow angle (25deg.) thrust faulting, interface waves associated with fault opening are reinforced by the reflected wave, decoupling the overlying hanging-wall plate from the foot-wall plate, thus trapping energy in the hanging-wall wedge and resulting in a spectacular increase in particle motions at the fault tip (Brune, SRL, V 67, No. 2, 1996; Proc. Indian Acad. Sci. (Earth Planet. Sci.), V. 105, No. 2, June 1996, pp. L197-L206).

In shallow angle normal faulting, a dislocation at the heel of the hanging-wall wedge sends a dilatational wave upward and forward in the hanging-wall wedge, which changes polarity upon reflection at the free surface, and then impinges on the fault as a compressional wave, which stabilizes the fault. A foam rubber model of a shallow angle (25 deg.) normal fault dramatically illustrates the differences between normal faulting and thrust faulting. The shallow angle normal faulting is accomplished by numerous small dislocations which have very weak ground motion at the hanging-wall fault tip.

Although the strong motion data set for ground motions near the outcrop of large normal and thrust earthquakes is very limited, it appears to be consistent with these dynamic effects being operative in some large earthquakes. If so, they may have drastic effects on the resulting near-source ground motions and on estimates of seismic hazard, with surface intersecting thrust faults being more dangerous, and surface intersecting normal faults less dangerous.

Teleseismic Tomographic Imaging of the Yucca Mountain Region

Glenn P. Biasi

University of Nevada-Reno
Seismological Laboratory
Reno, NV, 89557

YMP Activity Number: 8.3.1.1.7.4.1.2
YMP WBS Number: 1.2.3.2.8.4.1
Draft — October 15, 1996

Summary

Relative teleseismic delays to permanent and portable southern Great Basin (SGB) stations from 117 events were inverted to image crustal and upper mantle velocity structure under and around Yucca Mountain. Important structures of the regional models include the 2-3% high velocity Timber Mountain/Silent Canyon structure, which extends to a depth of 200 km or more, 1-3% low velocities to ~150 km depth south, east, and northeast of Timber Mountain, and 1-2% high velocities under the Panamint Range southwest of NTS. Detailed modeling of Crater Flat and Yucca Mountain indicates that the majority of teleseismic delays here can be explained by structures shallower than 3 to 4 km seen in earlier refraction studies. Residual mid-crustal structure is inferred to derive from deeper offsets on the Bare Mountain Fault than were resolved by refraction. There is no large low-velocity zone under Crater Flat or Yucca Mountain that would suggest a major volcanic hazard. Partial melt in small fractions cannot be ruled out, particularly deeper than 45 km beneath southern NTS and Crater Flat and the adjacent portions of Amargosa Valley. Refraction corrections account for virtually all of the inferred eastern structural boundary of Crater Flat without major deeper structures. Moderate low velocities in the crust and upper mantle are imaged in a wide band beneath southern Jackass Flats, Skull Mountain and Rock Valley. The depth of wide features is difficult to resolve using tomographic methods. The relative range of velocities imaged within the lower crust is about 0.4 km/sec, A very large increase in mid- and lower-crustal temperature could account for the velocity anomaly, but not for the the lack of a heat flow anomaly or for the significant crustal density decrease to the northwest. A more consistent interpretation of this lower velocity region is as a lithological contrast where dense but relatively silicic mid- and lower-crustal rocks predominate below and south of Little Skull and Skull Mountains. Structural effects may contribute to the apparently lower velocities; basement rocks are a kilometer or more deeper northwest across Rock Valley. A thickening of the crust by ~2 km under Skull Mountain and Rock Valley would reduce apparent seismic velocity and regional gravity by about the degree observed. A crustal explanation is also preferred because the anomaly is strongly attenuated below the first upper mantle layer. Other possible explanations of upper mantle low velocities include a small partial melt fraction or perhaps a petrologic contrast. The Calico Hills area is imaged as 1-3% higher than the model average and connected to high velocities of Timber Mountain to the north. High velocities rooted in Timber Mountain occur beneath Yucca Mountain north of Yucca Wash and unrooted, <2% high velocities occur south of the ESF beneath a local gravity high. This structure may derive from a local basement high or perhaps from a local inclusion of a high-velocity block within the basement rocks. Overall, results at crustal depths can be explained by shallow velocity contrasts and reasonable deeper petrologic and structural variations. Below 45 km partial melt could be present south of the project area, although the anomaly here could be explained by sub-solidus mechanisms as well. Low velocities beneath Rock Valley, Skull Mountain, and to the east follow a long-standing

lithospheric weakness. Considering the long-term amagmatic history of this region, it seems that the region of low mantle velocities southeast of Jackass Flats is stable and perhaps crustal in origin.

Introduction

Teleseismic tomography is a recognized method of evaluating the seismic velocity structure and by inference the physical state of the deep crust and upper mantle. Teleseismic P-waves are the higest frequency body waves that are routinely available to study these depths. An important aspect of site characterization in the vicinity of Yucca Mountain is the credibility of a volcanic hazard to a proposed high-level nuclear waste repository. Several Quaternary volcanic centers occur near Yucca Mountain, the youngest of which erupted small volumes of pyroclastic and flow basalt approximately 100,000 years ago. The clear long-term regional trend of volcanism since the mid-Miocene has been toward smaller volumes and more basic volcanism, but the timing between eruptions has been irregular and the regional trend does not speak directly to the hazard at Yucca Mountain. This study uses compressional waves from teleseisms to infer the physical state of the lower crust and upper mantle beneath Yucca Mountain and Crater Flat.

Teleseismic tomography has been used in several places to probe crustal and upper mantle physical properties. Humphreys and Dueker (1994a, b) review regional-scale tomographic results in the Western U.S. and inferences that can be drawn about the state of the upper mantle. Compared to global averages, teleseismic arrivals to most western US stations are approximately 2 seconds late. Considering the high regional heat flow, widespread Cenozoic volcanism, evident extensional tectonism, and attenuation of teleseismic shear waves, the upper mantle is probably near its solidus, and most of the velocity variations imaged by tomography reflect perturbations around this hot and perhaps slightly molten state. Supersolidus mantle conditions are clear in places like Yellowstone, and likely at mantle depths beneath the Snake River Plains and the Long Valley Caldera. Some partial melt in the present-day upper mantle seems necessary to explain distributed latest Tertiary and Quaternary volcanism in the Basin and Range from the eastern Sierra Nevada to western Utah. Set in this regional view several local studies have sought to use teleseismic phases to delineate crustal structures associated with magmatism (See Iyer and Dawson, 1993 for a review and further references).

Data and Data Reduction

The methods of data development and reduction used here generally follow recognized practice for teleseismic tomographic studies. Readers most interested in the final results may wish to skip this portion of the report, and return to it later to see how data handling might have affected the conclusions.

Event List

Events from July 1995 through July 1996 were used in this inversion (Figure 1, Table 1). Events were selected to maximize ray parameter and azimuth coverage. Core phases (PKiKP, PKP) were included to improve ray coverage near the edges of the array. Of the 117 events used, 101 of them were recorded by both the SGBSN and SGBDSN, and 16 of them were recorded by the SGBDSN alone. No events were included if only portable station picks were available.

Event and Station Locations

Station locations for this study are shown in Figure 2. Teleseismic delays depend on the event-to-station great circle distance. Both event and station location accuracy contribute to the absolute travel time, but relative delays only strongly depend on station locations. The amount of the relative delay variation due to station mislocation can be estimated as $\delta t = \delta distance / phase\ velocity$, where $\delta distance$ is the component of station mislocation in km in the direction of the event, and the phase velocity is in km/sec. For nearest teleseisms δt can range up to ~.075 seconds per km mislocation along the back-azimuth. This error will not be removed in a station correction term since station mislocation increases delays from one back-azimuth and decreases by an equal amount delays from the opposite direction, with no net affect on the average station delay.

Locations for the SGBSN and five SGBDSN stations (SYM, SCF, NCF, CAF, and LSC) were determined by the USGS. Later SGBDSN stations were located by UNRSL personnel using topographic maps and single fix GPS values. Differential-mode GPS surveying, however, of selected SGBSN and SGBDSN stations revealed 12 stations that were mislocated by over 100 meters and 5 that were mislocated by over 400 meters. The improvement in delay time data quality is illustrated in Figure 3. In practice moderate station mislocations probably get mapped into data misfit and relatively little into the velocity structure. Differential mode GPS locations were used where they were available (all southern SGBDSN stations and 7 SGBSN stations near Little Skull Mountain, Table 2). Portable stations were located with multiple GPS fixes and checked on 7½ minute USGS topological sheets. Unfortunately not all stations have been resurveyed, so station mislocations away from Crater Flat and Yucca Mountain may contribute somewhat to both data misfit and model structure.

Array timing

Appreciable effort was required to correct all teleseismic picks to a common time base. Both the digital upgrade and analog systems required some time adjustments.

Digital Upgrade: Timing for the digital upgrade array is provided by a GPS system at the UNRSL. The GPS unit receives a digital time code from GPS satellites. Time is transmitted via modem through the Nevada State microwave system, the radio command transmitter, and the Digital Acquisition System (DAS) internal modem to the DAS signal processing system. The DAS time-stamps all data it records using this time, filling in from an internal clock when GPS time is unavailable. This multi-element system involves several delays totaling several tens of milliseconds, mostly in the transmit and receive modems. The delay would cause a simultaneous signal recorded at the UNRSL and the SGBDSN to appear early in the SGBDSN records.

This delay is compensated by a factor called the RF delay. The RF delay is programmed into the field recorders as a recording parameter. Based on manufacturer's data the array was operated until 1995:275 with a delay of 0.024 seconds. Around 1995:275 it was noticed that local earthquakes recorded at analog station WCT and digital station WLD did not yield simultaneous arrivals, despite these stations being co-located (< 6 meters apart). An RF delay of 0.090 seconds reconciled the difference, and was adopted for the whole array for the period from 1995:276 through 1995:305. Around 1995:304 a calibrated GPS clock was taken to the WLD/WCT site for the purpose of checking the RF delay directly. The results showed that a delay of 0.044 was correct. This result was confirmed in July 1996 with another GPS clock. Thus the WCT station is ~0.046 ahead of SGBDSN station WLD. The teleseismic data reflect this difference (Figure 4); WCT picks are on average 0.05 seconds ahead of WLD picks for the same event. Unfortunately the 0.05 second estimate appears to be site-dependent. Portable station CFY2 was collocated with analog station YM2 and timed by GPS receiver. Thirty eight events recorded by both recorders were picked. A histogram of differences between CFY2 and YM2 picks (Figure 4) indicates no systematic timing differences within the precision of the data. Figure 3 shows that after the RF-delay adjustment, neighboring stations LSC and LTS also share the same time base. It is not known at present whether the WCT-WLD difference is unique to the site or common to all sites with similar hardware configurations. It is also not known whether the RF delay at WLD is common to all SGBDSN recorders or whether it is unique to the recorder at that site. Unfortunately this means that some timing uncertainty exists in the picks and therefore in the relative delays used in the inversion. The potential for timing uncertainty exists in the SGBSN data used by Evans and Smith (1992, 1995) as well.

For this report the SGBDSN array timing with an RF delay of .044 seconds was regarded as the datum. Picks for periods with an RF delay of .024 seconds were delayed by 0.020; picks for periods with an RF delay of 0.090 were made earlier by 0.046 seconds.

During some intervals SGBDSN data also required another correction, amounting to an advance of 1.000 seconds. A communications logic problem caused the GPS time received by field units to "skip" a 1-second pulse, causing units to label all subsequent data 1 second behind the true time. The exact conditions under which the "skip" occurred were unclear, but they appeared to be correlated with periods when the quality of two-way communications were degraded. Once the "skip" occurred, further skips forward or back did not occur, and true time was restored whenever the array was reinitialized. Unit 1-second skips in the data are conspicuous in relative teleseismic delay data by the size and pattern delays that result, and by the large differences seen between ordinarily similar stations (e.g., WCT-WLD, LTS-LSC). Table 3 shows periods during which the 1-second skip in known to have been on or off. Firmware upgrades in March 1996 resolved the 1-second problem, and it has not been seen since that time. One second was added to pick times of affected stations before relative delays were calculated.

Analog Array: Analog data for events until April 1996 were taken from continuous backup tapes. Until 1995:274 an error in the automatic time decoding software caused the system to record signals precisely 0.10 seconds late. This delay was recognized and fixed so that it does not affect data after that date. The exact time of the fix was apparently not recorded, but the time-code is recorded with the data, and was picked with all SGBSN data to ensure both the time of the fix and that no other problems were present. Times for picks before 1995:274 were advanced by 0.100 seconds before relative delays were calculated.

Sensor Response Correction

Some stations (TAR, RPY, TIM, SPC, CFLC, and CFQN) used Guralp broadband sensors with nominally flat instrument responses from periods of .02 to 30 seconds. The balance of SGBDSN and SGBSN stations use mechanical sensors with a 1 Hz free period and slight under-damping. The relative sensor responses are such that the short-period sensors are nominally 90 degrees out of phase with the broadband sensors, or for 1 Hz signals, about 0.25

seconds. To standardize responses to a common sensor we convolved the nominal short-period sensor response with the broadband signals so all picks were made on similar instruments. Signals were subsequently filtered to pass from 0.5 to 1.5 Hz with a 2-pass 2-pole Butterworth filter before picking.

Computing Relative Delays

Raw teleseismic residuals are calculated by adding the event-to-station predicted travel-time of a spherical-earth model $\Delta t(x_0,y_0,z_0)_{ij\ pred}$ to the event origin time $t_{j\ origin}$, then subtracting the picked phase arrival time t_{ij}. Teleseismic phases are usually emergent so we picked a first peak or trough. As long as the early part of the waveform does not change shape much across the array, this procedure simply adds a constant to all of the raw residuals. The raw travel-time delay is

$$\Delta t_{ij\ raw} = t_{j\ origin} + \Delta t(x_0,y_0,z_0)_{i\ pred} - t_{ij} \qquad i=1,2,\ldots,n_j \ \ stations \tag{1}$$

Teleseismic delays used for inversion are ordinarily found by demeaning the raw residuals. This approach removes the arithmetic average travel-time delay associated with the event origin time and location errors, and the travel-time model. As long as the station coverage is spread uniformly over the area of interest, this approach also removes the average delay beneath the array. The demeaned delay is

$$\Delta t_{ij} = \Delta t_{ij\ raw} - \sum_{i=1}^{n_j} \left(\frac{\Delta t_{ij\ raw}}{n_j} \right) \tag{2}$$

When station coverage has a significant fraction of its total number concentrated in a small area, then the "average delay beneath the array" can become strongly weighted to the average beneath that subset. In the SGB stations are concentrated around Yucca Mountain and Crater Flat. The concentration does distort array averages, forcing outlying station delays earlier for most back-azimuths, and much later for NE back-azimuth events coming through the Timber Mountain upper mantle anomaly. Figure 5 shows the effect of the Crater Flat/Yucca Mountain concentration on relative delays.

The demeaning bias caused by station coverage heterogeneity was approximately removed by selecting a subset of more uniformly distributed stations and using them to establish a level for demeaning all stations (Figure 6). Most stations away from Yucca Mountain were included in the uniform subset, but only 4 were retained near Yucca Mountain. The impact of the demeaning method on delay maps is seen in Figure 7. For this event the difference is 0.20 seconds, and can be a bit larger. The effect of demeaning on the delay-azimuth plots of example stations near Yucca Mountain and away from it is illustrated in Figure 8. For station WLD using the homogeneous station mean increases the peak-to-peak amplitude of delays on the line N20E/S20W by 0.4 seconds, or nearly double the range compared to the raw demeaning method. On NW/SE azimuths, the range is increased by only 0.1 seconds. The inverse effect occurs for stations away from the Yucca Mountain station concentration.

Crustal Delays

Shallow crustal velocity heterogeneities around the Yucca Mountain area can delay teleseismic arrivals by 0.25 seconds or more. Since the amplitude of upper-mantle-derived teleseismic delays is 0.5 to 1.5 seconds peak to trough, crustal delays do not usually obscure the major features of the velocity structure. However, for detailed studies and shallow depths, crustal delays must be considered. Geologic features that can cause crustal delays include alluvial cover, block changes in petrology, buried topography, and pervasive alteration or fracturing. Crustal corrections can be worthwhile even for stations sited on rock. For example, the Tertiary volcanic rocks that comprise Yucca Mountain have seismic velocities substantially lower than those in nearby Paleozoic ranges, and are mostly 2 km or more thick. Teleseismic rays do not cross in the upper crust for typical station spacings of ≥5 km, so these delays cannot be directly resolved by inversion.

There are three basic strategies to correct for shallow crustal variation. The first is to include a layer of model parameters shallow enough that teleseismic rays do not cross in it. The model parameters can take the form of a crustal layer of blocks and treated like other model blocks, or can be model parameters dedicated to each station as station statics. The model block method differs from the station static in that a shallow block can have two or more stations on it, in which case the block is assigned the average crustal velocity, and unaccounted delays, if there are any, are distributed elsewhere in the model. Also, (potentially hidden) a priori limits on model amplitude can keep the shallowest block from attaining the 10-30% equivalent velocity variation needed to account for shallow structure. A station static parameter need not have this limitation. Unfortunately station statics tend to absorb the average delay for the site, including delays originating in the upper mantle, so they tend to decrease model amplitude as a result. The station static will be similar in sign to the average delay at the station but generally smaller in magnitude. Average delays for stations around Yucca Mountain are plotted in Figure 9.

Shallow crustal delays can also be estimated from local active-source refraction lines. The two refraction lines of greatest use in the Yucca Mountain area were described by Mooney and Schapper (1995, p. 103, 107). Stations WCT and WLD were used as a datum, since they are located on Paleozoic limestones of Bare Mountain. Thicknesses and velocities from those lines, extrapolated along strike where necessary, yield the delays listed in Table 4 and plotted in Figure 10. Refraction delays compare reasonably with those calculated by Snyder and Carr (1984, their Figure 5). The thicknesses and velocities, and the code used to estimate delays are in Appendix 1. Crustal delays were estimated only to stations from Bare Mountain to the northern Specter Range. Both refraction corrections and station statics can be used in the same inversion. In this applications the station statics absorb the major crustal effects at outlying stations, and to compensate for velocity variations deeper than the refraction-based correction. Examples of inversions with and without crustal correction are given in a later section.

Inversion Methods

Relative delays may be qualitatively inverted for structure by comparing delay maps for events from different back-azimuths (Figure 11). Velocity anomalies near the surface will project to the same stations from all back-azimuths, whereas delay patterns from deep structure "move" with event back-azimuth. Deep structure clearly accounts for the shifts observed from NNE versus SSW (Figure 7a and 11a, resp.). A deep Timber Mountain anomaly causes the delay pattern in southwest NTS and Crater Flat to change sign, shifting from ~0.5 seconds early for NNE events to ~0.25 seconds late from SSW. A similarly deep source is required to explain the 0.4 to 0.6 second shift NE of NTS. This pattern indicates that the lowest velocity mantle is NNE of these stations. To stations NW of NTS no major shifts are present, suggesting that slightly higher velocity crust and/or upper mantle prevail there. Figure 11b shows similar slightly early arrivals NW of NTS for easterly events, but not from the west. Together this pattern suggests shallow high velocities with deeper low velocities outside the array to the west (Figure 11c). The very late arrivals to stations NE of NTS from the NNE do not appear for events from the east or west, indicating either a deep source outside the array to the NE, or a narrow NE-trending structure near the edge of the array. The latter case will be confirmed by inversion. Figure 11b and 11c show that delays to southern Yucca Mountain and Crater Flat stations are 0.1 to 0.25 seconds late, suggesting that most of the delay observed here is relatively shallow, and that the early arrivals from NE through Timber Mountain overwhelm this shallow delaying effect. It also shows that using the mean station delay as the crustal correction could lead to serious mis-estimation. Thus a qualitative examination of delay patterns provides a good idea of what structures to expect from formal inversion. Station delay patterns (Figure 8) provide a related perspective that is more localized but more complete in ray parameter and back-azimuth coverage.

A linearized block model for velocity structures is applied here. The raw travel-time delay d of a given teleseismic ray is the integral of the slowness perturbation over the path S_i of the ray from the source to the receiver:

$$d = \int_{S_i} \Delta S(x,y,z)\,ds \qquad (3)$$

For slowness perturbations of a few percent or less rays, path S_i can be traced through the unperturbed velocity model with minimal effect on resolution.

When relative delays are inverted, structure along S_i outside the model is assumed to have been removed with the demeaning. Thus one must assume that the scale of velocity variations outside the model space is large compared to the model itself. Structure deriving from outside the model will be forced into the model, usually with some penalty of data misfit. Assuming that a sensible model can be proposed, the event-to-station path integral can be replaced by the sum of the slowness perturbations through blocks in the model domain:

$$\Delta t_i = \sum_{j=1}^{J} \Delta s_j \Delta l_{ij} \tag{4}$$

where Δs_j is the slowness perturbation of the j^{th} block and Δl_{ij} is the length of the i^{th} ray in the j^{th} block. If matrix **G** is comprised of lengths l_{ij}, **d** is the vector of relative delays, and **m** is the vector of model slownesses, Equation 4 becomes:

$$\mathbf{d} = \mathbf{Gm} \tag{5}$$

We invert relative delays for velocity structure using a modified SIRT (Simultaneous Iterative Reconstruction Technique) algorithm (Humphreys and Clayton, 1988; Dueker et al., 1993). The SIRT algorithm converges to a least-squares estimate $\hat{\mathbf{m}}$ of **m** (Ivansson, 1983; Vander Sluis and Van der Vorst, 1987; Trampert and Leveque, 1990) by iteratively constructing an inverse to G. Iterative techniques are required for large models and datasets because of the dimensions of G (number of blocks by the number of delays, or about 9900 by 7000). The salient points of the SIRT algorithm are reviewed below.

The data consist of $i = 1,...,I$ rays, the model domain is discretized into $j = 1,...,J$ blocks, and G_{ij} is the length of the i^{th} ray of the j^{th} event. Each block is further divided into bins by ray parameter and back-azimuth. Five bins are used: four for ray parameters greater than 4.4 seconds/degree (0-90°, 90-180°, 180-270°, and 270-360° back-azimuths), and one for PKiKP and PKP core phases. γ_{jb} is the ray length in the b^{th} bin of the j^{th} block:

$$\gamma_{jb} = \sum_{i=1}^{N} G_{ij} \delta_{ib} \tag{6}$$

$\delta_{ib} = 1$ if the i^{th} ray in the b^{th} bin, and 0 otherwise. Model block slownesses are initialized to zero: $m_j^0 = 0$. The residual delay not explained by the the q^{th} iteration ($q = 1,2,...$) is the observed delay minus sum of the ray's length in the j^{th} block times its slowness perturbation:

$$r_i^q = d_i - \sum_{j=1}^{J} G_{ij} m_j^q, \tag{7}$$

Each bin contributes Δm_{jb}^q to the block model update:

$$\Delta m_{jb}^q = \sum_{i=1}^{I} \frac{r_i^q G_{ij} \delta_{ib}}{\rho_i}, \tag{8}$$

where ρ_i is the length of the i^{th} ray. Bin contributions are weighted by their hit quality W_{jb} The j^{th} block slowness update is the sum of its bin contributions, Δm_{jb}^q:

$$\Delta m_j^q = \frac{1}{H_j} \sum_{b=1}^{n_b} \frac{W_{jb}}{\gamma_{jb} + \mu} \Delta m_{jb}^q \tag{9}$$

where

$$W_{jb} = \frac{1}{n_b} \left\{ \begin{array}{ll} 1 & \gamma_{jb} \geq \alpha th(z) \\ \frac{\gamma_{jb}}{\alpha} & \gamma_{jb} \geq \alpha th(z) \end{array} \right\}. \quad (10)$$

W_{jb} is the weight given to the b^{th} bin update, and is limits the maximum weight of a bin contribution. α is called the bincut, and is set to 5 in the inversions shown here.

$$H_j = \sum W_{jb} \quad (11)$$

is the hit quality, a qualitative measure of resolution. Blocks with 25 rays in 1 bin receive a hit quality of 0.20 whereas $H_j = 1.0$ for 25 rays distributed 5 each in 5 bins. In the first case the 25 rays are largely redundant, whereas in the second case rays cross at high angles, a geometry ideal to resolve block slowness. Binning prevents a cluster of events from a single back-azimuth from dominating the solution by limiting the cluster's weight to a single bin contribution.

The SIRT algorithm has certain advantages and also some drawbacks. In many iterative methods the solution is weighted to minimize structure in poorly sampled regions of the model domain. This precludes pure artifacts in regions where no rays pass, but it also tends to force delays of the rays that pass through the poorly sampled regions into velocity structure elsewhere in the model. The SIRT algorithm, by contrast, initially projects delays proportional to the ray length in the blocks the ray passed through, and only revises that projection when information exists (i.e. residuals with ray length in that block) to change it. Thus the forward projection of delays and residuals amounts to a minimum information, or equivalently, a maximum entropy starting point for modeling. This could be considered a liability if an *a priori* model was available. SIRT has another potential drawback in that it updates block slowness estimates in inverse proportion to the ray length in a block (Equation 9). The algorithm here avoids this problem by limiting the model update in two respects. First, it divides the model update into bin estimates, so blocks with a low hit quality converge more slowly. Second, the parameter μ' sets a floor value to the denominator $(\gamma_{jb} + \mu')$ in Eqn 9. Thus a single, very short ray length in a block cannot dominate Δm_j^q. We set μ' to approximately the average ray length in a bin as a compromise between convergence rate and model amplitude. See Dueker et al. (1993) and Trampert and Leveque (1990) for details.

When a block model is applied to irregularly spaced station or data coverage, the resulting model depends to some extent on exactly where block boundaries fall relative to the stations. In detail both model amplitude and apparent resolution can change if the applied grid is moved by even a couple of kilometers. This effect cannot be removed by spatial smoothing of a single model since no "information" exists in a single model about what would be imaged in a different grid. The modelization problem can be addressed (Evans and Achauer, 1993) by producing several models with a slightly shifted grid while keeping the same data and station coverage. Models are then stacked on the central model grid. For the images interpreted in this report, we shifted the grid by approximately 1/3 of a block width north, northwest, west, southwest, south, southeast, east, and northeast. Shifted models were weighted by .09 each, and the central model received .28 weighting. The stacked models are more coherent, especially in regions of marginal ray coverage, but all are similar in their major features.

Resolution

Resolution when using iterative inversion methods can be evaluated by using the data to reconstruct known structures. Single block anomalies reconstruct as a "point spread function" (Humphreys and Clayton, 1988), typically spreading along ray paths with the same sign, and with smaller, opposite sign in adjoining blocks. An example reconstruction of a single block structure in SW NTS is shown in Figure 12. For all inversion methods resolution depends on ray coverage, and thus varies significantly throughout the model.

Resolution in the detailed models is illustrated in Figure 13. The input anomaly consists of posts on 3×3 block centers 1% faster than background, extending from 12 to 60 km in depth. In map view ray coverage is good in the mid-crust beneath Crater Flat, Yucca Mountain, Jackass Flats west of Little Skull Mountain, and in most of Rock Valley. Within this area 50 to 80% of the structure is restored to the blocks it derives from. Negative lobes are a quarter to more typically a tenth of the synthetic input. Outside the region of good ray coverage, restored energy is typically 30 to 50%, and the side-lobes are a larger fraction of the input. Resolution improves in both area and quality with depth. The property of improving resolution with depth is illustrated in Figure 14, which shows north-south cross-sections spaced 4½ km apart along the axes of Yucca Mountain and stepping east to Little Skull Mountain. Spreading of post structures in depth is seen to be relatively small.

Plate-like synthetic structures are more difficult to reconstruct if they are large enough that all rays in a region go through them. In Figure 15 an irregular plate shown by open squares is 1% fast in a 30×30×6, 60 km deep block model. Only blocks with 4 or more rays in them are plotted. Figure 15b-e are north-south profiles through Little Skull Mountain where the input structure is moved successively deeper in the model. When the input is shallow (12-20 km), the reconstruction is poor, and the structure is mapped at comparable amplitudes well into the upper mantle. This is an example of the cone of resolution discussed by Evans and Archauer (1993). Deeper structures are successively better resolved. Structure in the bottom layer has less tendency to smear upward because more stations are contributing to resolution. These synthetics show that a structure in the crust or uppermost mantle would be difficult to restore to its proper depth if it is areally extensive.

Velocity Scaling

Bulk seismic velocity variations can be caused by variations in temperature, composition, and partial melt content.

Temperature: Christiansen and Wepfer (1989) summarize temperature derivatives for various crustal rock types. They fall in a range of 0.45 to 0.55 m/s/°K (~130°C/%ΔV_p) for silicic to mafic lithologies, respectively. Under upper mantle conditions, Anderson and Bass (1984) estimated a sub-solidus temperature derivative as $\partial V / \partial T$ = -0.5 m/s/°K, or about 160°C/%ΔV. Near the peridotite solidus Sato et al. (1989) proposed a temperature derivative of 50°C/%ΔV by extrapolating ultrasonic measurements to seismic frequencies. Karato and Spetzler (1990) show that this extrapolation is probably inappropriate as it implies unreasonably high activation energies for crystalographic relaxation mechanisms. Temperature-dependent anelastic mechanisms near the solidus, however, could cause delays of up to 1% per 50°C variation (Karato, 1993).

Composition: Jordan (1979) studied the velocity effects of peridotite depletion with basalt extraction. Iron preferentially fractionates into the melt, so the residual olivine becomes increasingly magnesium rich, and both the melt and the residuum become less dense. He estimates that a 10% basalt depletion would result in a 1% increase in mantle V_p. In the crust composition can account for the first-order variations in P-wave velocity. Fountain and Christiansen (1989, their Table 8) summarize this data for a variety of petrologies. The central range they give for likely lower crustal velocities (6.3 to 7.1 km/sec) could be present in the project area if the lower crustal composition varied from quartzofeldspathic gneiss to gabbro (e.g., from lower plate lithologies in the Bullfrog Hills (Maldonado, 1990) to intrusive equivalents of widespread basalts).

Partial Melt. The effect of partial melt on teleseismic P-waves depends on melt geometry. For small fractions, ΔV_p (%) $\approx A \phi$ (Mavko, 1980; Schmeling, 1985), where A is in the range of 1 to 3 for expected likely pore aspect ratios.

Apparent bulk velocity variations can be caused by two other mechanisms. Anisotropy, especially in upper mantle peridotite, can be quite large. Olivine crystals exhibit over 20% V_p velocity variation, among its crystalographic axes. Tectonic influences can preferentially align the olivine in peridotite (Ribe, 1989), and the statistical alignment causes the velocity anisotropy. Limited shear-wave splitting measurements to SGBDSN stations indicates the presence of anisotropy in the SGB upper mantle, but from the magnitude of the measurements, the dominant velocity anisotropy is probably horizontal. P-waves cross this fabric at high angles and so should not be strongly affected. Any residual effect is averaged in a block-wise isotropic inversion, with some penalty to the data misfit. Still, some influence of anisotropy on velocity images of the outer areas of the array cannot be excluded.

The second mechanism that can cause apparent bulk velocity variations is topography on internal surfaces separating large velocity contrasts. Layer thicknesses themselves do not matter much since any error applies to all stations equally. This type of error is removed by demeaning. Local variations in thickness, however, are not removed. The amount of time for a vertical ray is estimated as $(1/V_1 - 1/V_2)$ in seconds per km of topography. For layers with small velocity contrasts (e.g. 5-30 km and 30-300 km) thickness variations cause only small relative delays. However, at 5 and 30 km in the detailed models, velocity variations (4.43 to 6.01 km/s, and 6.42 to 7.90 km/s) yield 0.059 and 0.029 seconds of apparent delay, respectively, per kilometer. This apparent delay is distributed into adjacent layers as a fractional bulk velocity variation. Since the data consist of only relative delays, the contributions of thickness and velocity variations cannot be separated. Velocity variations in Crater Flat and Rock Valley may reflect this phenomenon. A detailed velocity model using crustal phases could help independently constrain variations imaged by tomography.

Results

Regional Model

To get a "big-picture" view of the context of the Yucca Mountain region a 450×450×300 km (EW×NS×depth) region centered on Yucca Mountain are discussed in this section (Figure 16). Data was reduced using the homogeneous station coverage datum (Figure 6). Crustal corrections around Yucca Mountain and Crater Flat were removed from delays before inversion, and elevation differences were corrected to the average elevation of all stations (1390 m) with a velocity of 5500 m/sec. Station static corrections were not used because they reduce the true amplitude of large-scale upper mantle features and because crustal effects generally affect only the shallowest upper mantle layers. Station spacing away from Yucca Mountain is not adequate to resolve crustal velocity, so it is not discussed for the regional model.

Model amplitudes are important to any interpretation. The model rms amplitude (Figure 16) is 1.073 percent and the data rms is 0.233 seconds. The model explains 69% of the data rms. Model fit would improve to 78% by including station static corrections. Some under-reconstruction of model amplitude seems likely. Qualitatively the model rms amplitude is consistent with the data rms — 1.073% anomaly over 185 km yields approximately the .233 seconds. However, checking the amplitude of the major anomalies this way indicates that, for example, Timber Mountain is under-reconstructed by ~1/3. Absolute velocity information is lost when relative delays are used, so there is some unavoidable uncertainty in the interpretation of any particular region as slower or faster. The relative differences however, are more reliable, and any reinterpretation of the zero anomaly level must be handled consistently across the model.

Principle Deep Features

Below ~150 km high velocities associated with Timber Mountain upper mantle anomaly are the only prominent structure. The base of this structure is ~200 km or perhaps a bit more. The center of the anomaly at depth is 15-30 km NE of its shallower expression. The spatial association of the upper mantle anomaly with the Timber Mountain-Silent Canyon Caldera Complex strongly suggests a genetic relationship (as others have noted: Spence, 1974; Monfort and Evans, 1982; Biasi and Humphreys, 1992). This spatial association and the prominent gravity decrease to the north imply that the upper mantle anomaly represents the results of chemical depletion and in virtue of its high velocity eventual melt depletion. A gravity contrast of opposite sign would result if the anomaly were comprised of thermal lithosphere that sank into its present position. The depth of the anomaly is significant because it means that melt evolved from the SWNVF from an unusually great depth, and that the source or trigger for melting must have been significantly deeper. Its depth is also significant in that it shows that at least since ~15 Ma the crust and upper mantle of this part of southern Nevada have been in contact with one another. The Timber Mountain region has apparently not participated in any regional detachment at least since the onset of major volcanism ~15 My ago. It also implies that this portion of the Basin and Range upper mantle has been exempt from large-scale convective overturning and significant channel flow at asthenospheric depths.

Low velocities (1 to 3%) southeast and east of Timber Mountain are imaged to a depth of 120 to 150 km. The depth of this structure leads to 0.6 to 0.8 second delays to stations above it.

Principle Shallow Features

The deeper pattern of high velocities beneath the SWNVF and low velocities south, east and northeast of NTS extends up to Moho depth. In addition, above 70 km 1-2% higher velocities are imaged west NW of Timber Mountain. The 30-40 km western extension of the Timber Mountain anomaly generally follows the caldera boundary, but includes some of eastern Sarcobatus Flat. This region is something of an enigma, since the basalts of Sleeping Butte occur 15 km west of the NTS boundary, and Quaternary basalts in small quantities occur in Sarcobatus Flat 25 km farther west. If there is more partial melt in the upper mantle in the high velocity portions of Timber Mountain, then it must be in relatively small volumes or melt fractions. Alternatively, it may be present in areas not well-sampled by teleseismic rays. Station density in these areas does not permit a definitive answer in this. Petrologic studies of post-Miocene basalt compositions are consistent with a trend toward smaller melt fractions and deeper sources (Vaniman et al., 1982). High velocities beneath the southern Silver Peak Range may be associated with a high velocity lower crust or depleted mantle lithosphere attached to the Precambrian through Mesozoic basement rocks exposed there. Station density there is not sufficient to separate crustal and shallow upper mantle velocities.

West and southwest of southern NTS is 1-2% below the regional velocity average. A weak low-velocity region appears south of NTS beneath the Amargosa Valley. This could be the continuation of the larger NE-trending low-velocity region, or be due to more local causes. This structure has been interpreted (Humphreys and Dueker, 1994a) as the SW continuation of the St George Volcanic Trend (Smith and Luedke, 1984). Low velocities might be due to higher temperatures and could include a small fraction of partial melt based on accepted velocity scaling. The region above it and for ~ 100 km SE has been amagmatic, however, throughout the Cenozoic (Smith and Luedke, 1984), and except near the St George Volcanics, heat flow is a normal or low for the Basin and Range (Sass et al., 1995; Sass et al., 1994). The lowest velocities do not underly late Tertiary volcanic centers in southern Nevada.

No structure is suggested beneath the Funeral Mountains, despite the exposure in outcrop there of rocks from a lower crustal pressure regime. High velocities (1-2%) are present 30 km west beneath the northern Panamint Range, but cannot be detailed with the present station coverage. This anomaly was imaged in the same place by Evans and Smith (1995, their Figure 7a).

They described it as beneath the Funeral Mountains, but this appears to have been a geographic misstatement. The approximately arch-shaped line (dashed line, Figure 14, 30-50 km layer) separating higher velocities beneath the Panamints north to Timber Mountain closely follows the -140 mgal gravity contour of Eaton et al. (1978), indicating a thinner or denser crust or higher upper mantle densities inside the arch.

Detailed Inversions

Around Yucca Mountain and Crater Flat the station density is adequate to do a more detailed inversion (Figure 17). A 90×90 km area centered on Yucca Mountain was considered. Stations in the smaller model area from the homogeneous coverage (Figure 6) were used to set the mean level for relative delay calculation. This model covers the area of the Evans and Smith (1992, 1995) in a similar block size. Only refraction crustal corrections were applied. Evans and Smith used station corrections, so a direct comparison with their results will be deferred to a later section.

Detailed inversions involve the same technical assumptions as for larger models. Most importantly, the spatial wavelength of upper mantle structure on raypaths outside the model space is assumed to be large compared to the model itself. Inversions assume that the model space accounts for all of the observed delay data. The larger scale inversions show that the high velocity Timber Mountain structure and northeast trending low-velocity structure are relatively sharp and quite deep, so delays they cause will be mapped into smaller models. The best way to conduct detailed modeling would be to inset a region of small model blocks into the larger regional model, but software to do this was not yet available. Unfortunately this leads to some ambiguity in the true amplitudes of detailed anomalies.

The dependence of model amplitude on the total depth of the model is illustrated in Figure 18. The relatively linear relationship between model amplitude and depth illustrates the point that relative delays tightly constrain only the product of model slowness and ray length, and not slowness directly. Thus a model twice as deep requires half the slowness perturbation to account for the same delay. Fit quality, however, improves with model depth. When the model depth was increased without increasing the number of degrees of freedom (i.e., without increasing the number of fitting parameters), an improvement in fit means that the deeper model better reflects the true depth of the slowness structure. When an additional layer was added (plus sign, Figure 18), the fit and model rms did not materially improve over the 6 layer model of the same depth, confirming that the fit here depends on model depth and not on the number of degrees of freedom available with which to fit the data. Based on this evaluation, an 80 km depth model was used in the detailed model discussion.

Detailed Inversion: Crust

In the mid- and lower crust (Figure 17), the region beneath and east of Little Skull and Skull Mountains exhibits 1-3% lower velocities than the model average. This low-velocity region is a detailed view of a portion of the larger structure noted in the regional image. Crustal velocity reductions of 1-3% can be due to petrologic variations within the crust (e.g., a reduction of 6.3 to 6.11 km/sec is -3%). Rock Valley is the boundary of 1 km or more of vertical structural relief, with the northwest side down. In addition, the largest clearly active fault in the project area trends NE above the low-velocity region of the crust and upper mantle. Thus this lower velocity crust corresponds with a structurally controlled contrast in lithospheric strength. The observed velocity reduction could be due to heating and thermal weakening of the lithosphere, but the fault trend is a relatively long-standing feature and heat flow in this area is only about average for the Basin and Range (Sass et al., 1995), so this seems unlikely. One might also expect volcanism along the Rock Valley-Mine Mountain trend if it was a zone of pervasive heating. A relatively sharp gradient in Bouguer gravity in this region implies that there is a significant reduction in crustal bulk density on the NW side of the Rock Valley-Skull Mountain region (Saltus and Thompson, 1995) Considered together, the simplest explanation is that low velocities primarily mark a crustal petrologic boundary, with a lower velocity, less dense, and perhaps more silicic phase on the down-dropped northwest. Granitic intrusive equivalents of the rhyolitic and dacitic Wahmonie Formation with these qualities outcrop 8 km north of Skull Mountain (WAH, Figure 17), consistent with this hypothesis.

The Crater Flat midcrust is generally 1½% or less below model average. Lower velocities follow the Bare Mountain Fault. This probably means that the refraction corrections taken from the upper 3 to 4 km underestimate the true upper crustal contribution. This would be expected if the Bare Mountain Fault juxtaposes rocks of different velocities to its full depth. Ferrill et al. (1996) interpret geomorphic evidence along the Bare Mountain Fault to indicate greater offsets and a higher rate of offset on the south end of the Bare Mountain Fault, compared to the north end where refraction data are available. Undercorrection to station CFSO and perhaps SCF (Figure 10), perhaps explained by that differential offset, is probably responsible for the 2-3½% slowness blocks in the 5-12 km layer of southeast Crater Flat. The Lathrop Cone is not associated with low velocities or perceptibly larger delays to southerly stations SYM, CFQN or CFSO, all of which interrogate its likely source in the deep crust or upper mantle. Its source area may be very small, significantly deeper (>45 km), or extinct. No prominent structural boundary is imaged between Crater Flat and Yucca Mountain beyond what is removed by the refraction correction. Crustal corrections here, however, are substantial (Figure 10). The southern edge of high velocities associated with Timber Mountain is clear in the 20-30 km layer and extends southward beneath the Calico Hills as it shallows. The origin of the 1½% faster blocks near the ESF is unclear. Arrivals from westerly back-azimuths are systematically early to stations FRG and YM2/CFY2 (Figure 2), and average delays (Figure 9) are somewhat smaller here, so it is unlikely to be an artifact of the station corrections. Brune et al. (unpublished UNR manuscript) observed small amplitude, anomalously early P-wave phases that require an isolated high velocity structure between the Little Skull Mountain earthquake source area and northern Crater Flat and Bare Mountain stations. Ponce and Oliver (1995, their Figure 2.3) and Snyder and Carr (1984) show a local gravity high in this region as well. Snyder and Carr interpret this feature as a basement ridge or high, but a high-density, high-velocity inlier in the basement should also be considered. Basement topography is probably responsible for the abrupt 0.1 second increase in average delays (Figure 9) from station CFWW near Windy Wash and CFSW and STO in Solitario Canyon (Figure 9). A deeper origin for this difference is unlikely because of the relatively long wavelength of teleseismic P-waves. The anomaly does not continue along the strike of Solitario Canyon; delays at stations CFY2 and YM2 are similar to that at CFWW. Snyder and Carr (1984) note a closed 4-8 mgal Bouguer anomaly centered on north Solitario Canyon that would include the stations with larger average delays. A kilometer of Tertiary volcanic fill in a closed depression here could account for both the gravity and teleseismic observations. The lack of significant structural offsets in the Yucca Mountain tuffs above this region implies that any deeper structure has been inactive since ~11-13 Ma. To the northeast the south and east sides of the Timber Mountain Caldera are imaged a few kilometers toward the center of the caldera from its mapped boundary, indicating that the structural effects of volcanism extend out farther than do its effects on crustal velocity.

Detailed Inversion: Mantle

In the upper mantle (Figure 17, 30-80 km layers) the general pattern of low velocities under Rock Valley and high velocities beneath Timber Mountain is still present. The Timber Mountain structure is somewhat more sharply defined using the smaller model blocks. Lowest Moho depth velocities are imaged 5 km or so south of Little Skull Mountain beneath the SW terminus of Rock Valley. Low velocities are prominent here ohly in the 30-45 km layer, which generally favors a crustal origin, for example, by a local thickening of the crust. The uppermost mantle beneath southern Yucca Mountain and Crater Flat is almost exactly at the regional average, and no anomalous structure is even suggested. Some of the 2-3% low-velocity structure south of the SW NTS corner in the 60-80 km depth slice actually belongs beneath and west of the state line at greater depth and lower amplitude, as can be seen from regional inversions. Here and beneath Timber Mountain two characteristics of "out-of-box" structure are illustrated: the bottom is not imaged, and amplitudes are large or extreme relative to the model as a whole. Elevated temperatures and perhaps some partial melt are possible here, especially considering the history of extension in and west of Amargosa Valley.

Comparisons Without Crustal Correction

To test the importance of crustal correction to the results, we compare the preferred model of

Figure 17 to identical inversions that use no crustal corrections at all, that use both refraction and station static corrections, and that use only station static corrections (Figure 19). The last of these is most directly analogous to the crustal correction approach of Evans and Smith (1992, 1995). Only representative profiles are shown in the interests of space.

In the north-south profiles along the axis of Yucca Mountain (Figure 19a), principle features include high velocity structure from deeper Timber Mountain, and low velocity structure to the south, partly from outside the model space. With no crustal corrections (Figure 19b) 1-2% low velocity structure is introduced in southern Yucca Mountain and generally slower velocities prevail everywhere south of the ESF. Comparing Figures 19a to 19b, it is clear that delays originating in the upper 3-4 km are streaking downward throughout the crust and into the uppermost mantle. Amplitudes of the main structures would be approximately doubled if the model was truncated at a depth of 41 km (Evans and Smith, 1992, 1995), essentially by forcing structure up vertically. Station static corrections alone (Figure 19c) remove virtually all structure beneath the ESF, confirming that whatever caused high velocities there is crustal in origin. Figure 19d shows that virtually all crustal structure on this profile can be explained by a combination of station statics and crustal correction. The model using both refraction and station corrections shows essentially no structure in the crust except near Timber Mountain, but recovers the main upper mantle structures.

In east-west profiles through central Crater Flat and Skull Mountain, the refraction crustal correction accounts for most of the Crater Flat velocity structure above ~45 (Figure 19e vs. Figure 19f). The contrast between Bare Mountain and Crater Flat emerges as a 5-7% contrast when refraction corrections are not applied. The importance of shallow corrections can be estimated from the top two layers of Fig 19f. Compared to Bare Mountain, Crater Flat is imaged as 5 and 7% slower in the 0-5 and 5-12 km layers, respectively. These anomalies account for a total delay of ~0.135 seconds. The balance of the known crustal delays (.05 to about .12 seconds in Crater Flat) is mapped deeper into the model with some penalty to the fit. To some extents this reflects a weakness of iterative inversions methods. The first projection of delays into the model assumes each block on the raypath is as likely as the next to have caused the observed delay, and the delay is prorated along the raypath accordingly. In theory, by iterating one eventually restores delays to their true source. In practice the crustal delays can be much bigger than others in the model, and the restorative "force" is weak when the structure is a few blocks or more wide. The damped least-squared algorithm (Aki and Richards, 1980; Evans and Smith, 1992, 1995) suffers from the same problem if a constant is used in place of the explicit model covariance matrix. An inversion method designed to recover large variations in block slowness would be required to pursue this. Station statics (Figure 19g) incompletely account for crustal structure, but in combination with the refraction corrections, account for all of the Yucca Mountain area crustal structure. Additional east-west cross-sections are shown in Appendix 2.

Overall, the refraction-derived corrections are of greatest importance, but one would draw similar inferences from a model corrected by station statics alone. Some form of crustal correction is required to prevent very shallow structure from mapping deeper in the model than it belongs. Modest low velocities in the crust beneath Crater Flat and southern Yucca Mountain probably derive from undercorrection of crustal structure. At least along the western side of the Crater Flat, structural offset on the Bare Mountain Fault is surely deeper than the 3-4 km depth included in refraction correction. The strong velocity contrasts between Crater Flat and southern Yucca Mountain in the upper crust are largely recovered by the refraction survey. A weak boundary may be present within and bounding the west side of southern Yucca Mountain, but it is not in evidence north of the profile in Figure 19a (See Figure 17 and Appendix 2). The strong contrast interpreted by Evans and Smith (1995) as a possible caldera or faulting boundary is an image of and perhaps an undercorrection for crustal structure revealed by refraction.

The prominent low velocity region along the Rock Valley trend does not vary as much with the crustal correction strategy. Some velocity variation may derive from undercorrection of local structures, since the refraction lines ran several km from the key stations on Little Skull Mountain. Lower relative velocities there may derive from a local thickening of the crust by perhaps 2 km. A 1 km downward deflection of the Moho is equivalent in delay time to a -2% velocity contrast over the 10 km from 20-30 km or 1.5% over 30 to 45 km depth. If the imaged lower velocities are due to crustal velocity variation, they could be explained by realistic variations in silica content of the lower crustal rocks.

Comparison With the Results of Evans and Smith

Evans and Smith (1992, 1995) inverted similar data from the project area. They reported suggestive low velocities beneath Crater Flat and southern Yucca Mountain, and registered concern for a volcanic hazard to a potential repository. The models shown here substantially repeat their experiment, but with a widened area of good resolution due to improved analog station coverage around Rock Valley, 22 new SGBDSN stations, and a number of portable instruments.

The regional model of Evans and Smith and the one presented here are similar in imaged patterns and amplitudes. Any comparison of models is necessarily approximate, since one can only estimate which portions of their models are well resolved.

Minor differences are expected between models because of differences in data reduction and inversion. Evans and Smith did not mention any attempt to remove the potential problem of high station density around Crater Flat and Yucca Mountain (Figure 5). As shown above, a locally high density of stations tends to reduce model amplitude in the central region around Crater Flat and Yucca Mountain, increase model amplitude in outlying areas, and increase data misfit. Test inversions suggest that this effect is not crucial, but may be why their model amplitudes are 1/2 to 1% larger in the Panamint Mountains and Bullfrog Hills. In a related way, using events recorded only by a small aperture array causes similar problems. To illustrate by way of an extreme, an array with multiple stations and zero aperture would see no relative delay from any back-azimuth. Evans and Smith did not say how many of their events were recorded by only their portable array. Combining data from small and large arrays tends to increase the apparent noise in the data, since one might see a small delay from a given source location with a small array, and a larger delay when the full SGBSN array is used. In a SIRT inversion this effect can be approximately removed with an event static calculation, although it was not needed for this study.

A difference in developing crustal corrections may account for the crustal difference between the detailed models of Evans and Smith and those in Figure 17. Evans and Smith compensated for shallow crustal structure by an iterative solution. The approach (Evans and Achauer, 1993) involves making a form of one-layer model (one block per station, actually), inverting the data, and using the resulting model as the starting model for successive inversion, until the results converge. The average-delay crustal correction strategy was discussed with Figure 9. The magnitude of their station corrections were not listed in the Evans and Smith papers. A typical large value can be estimated from their detailed model (1995, their Figure 7a) to be -12% relative to the earliest station on Bare Mountain. An 12% anomaly in a 5 km of 4.43 km/sec layer corrects for about .15 seconds. This compares to a typical value based on refraction of .23 for Crater Flat stations. Thus .08 seconds on average would be unaccounted in the crustal correction, and mapped systematically into about 1.5% of crustal slowness structure. This apparently contributed to the crustal differences between the "stripped" models of Evans and Smith, and those in Figure 17. The general correspondence of their "unstripped" model and the average delays of Figure 9 indicate that the two studies "see" similar features, including the depression beneath Solitario Canyon.

The upper mantle differences in southern Crater Flat and southern Yucca Mountain between Evans and Smith and Figure 15 derive from the difference in the depth of the model used. Model amplitude is approximately controlled by the product of the model depth and the slowness perturbation ($\delta t = l\,\delta s$). Model evaluation was discussed above, where it was shown that deeper models can fit the data better without increasing the number of degrees of freedom. For shallow models southern Crater Flat delays come from deeper structure near the state line, and are mapped at higher amplitude by both inversion methods into the deepest layer of the model.

A similar situation should obtain for the Timber Mountain structure in Evans and Smith (1995, figure 7c) but they did not use stations north of the middle of the Timber Mountain Caldera in their detailed inversion.

Discussion and Conclusions

Results presented here suggest that the Bare Mountain Fault is a high-angle master fault with somewhat greater offset to the south. No similarly profound eastern boundary of Crater Flat is apparent either in the inversion or in the raw data. The modest internal structure in the tomographic images of crustal Crater Flat are most consistent with an origin in basement structure. A basement topographic low is required to explain the difference in average arrivals between Windy Wash and Solitario Canyon, and this low seems to extend eastward somewhat beneath northern Yucca Mountain. Some high-velocity basement structure is also inferred beneath and west of Fran Ridge, under Yucca Mountain, and eastern Crater Flat. Neither of these structures seems to correlate with the tectonic development Yucca Mountain. Northern Crater Flat internal structure is reasonably accounted for by refraction studies there. To the south there are indications of somewhat greater offsets on the west side Crater Flat, consistent with reflection and geologic evidence. The Lathrop Cone is not associated with low velocities or perceptibly larger delays to southerly stations. Its source area may be in the deep crust but too small to detect, or may be significantly deeper. Seismicity within Crater Flat is consistent with the tectonic picture of slow basin response to opening on the Bare Mountain Fault; only a few small earthquakes have been recorded within Crater Flat in the first 20 months of SGBDSN operation.

Low velocities beneath southern Jackass Flats, Little Skull and Skull Mountains, and Rock Valley in the crust and upper mantle are coherent and relatively pronounced. The depth of the anomalous region cannot be strongly constrained. Petrologic variations and some uncorrected basement and Moho topography seem likely causes. Station LSC on Little Skull Mountain has the largest average station delay of any SGB station (Figure 9). Locally high temperatures (+200-400°C) could lead to the observed low velocities, but would not explain the lack of a heat flow anomaly or the crustal density gradient above and NE of the low velocities. Active Little Skull Mountain/Rock Valley faulting above the low velocity region implies that the low velocities mark a zone of through-going weakness. Partial melt cannot be excluded as a cause especially for upper mantle low velocities, but neither is it required. A detailed crustal velocity and Pn-time-term model would reduce the interpretational ambiguity.

The mantle structure beneath Timber Mountain is too deep and too localized to be explained without a deep point source of heat or volatiles. A general association of volcanism as far south as the SWNVF with the Yellowstone hotspot has been proposed (Saltus and Thompson, 1995). A hot-spot origin for the Timber Mountain upper mantle anomaly is unlikely, however, on two grounds. First, the effects of the passage of the Yellowstone hotspot are well-imaged beneath the Snake River Plain as leaving low and not high velocity upper mantle beneath associated volcanism. Second, it is hard to see how a thermal pulse at great depth could deliver enough heat rapidly to the relatively small area imaged in Figure 16. Also, if the source was longer-lived and associated with the hot-spot, it should migrate with Yellowstone in the hot-spot reference frame (25 km/My NE), which this anomaly apparently does not.

The more likely alternative is that the Timber Mountain upper mantle anomaly is due to a temporal flux of fluids, probably of water. Water strongly lowers the melting point of upper mantle assemblages so that little or no influx of heat is required to precipitate a significant fraction of buoyant melt. The ultimate source of such water would be subduction off the west coast of North America. Several hundred kilometers of oceanic crust apparently subducted at this latitude beneath western North America after the end of the Laramide orogeny and before the margin of western North America transitioned to strike-slip tectonics (Atwater, 1970; Severinghaus and Atwater, 1990). This subduction resulted in relatively little volcanic expression (Moore and Dodge, 1980; Loomis and Burbank, 1988) but is known to have taken significant volumes of water into the upper mantle, based on evidence as nearby as Long Valley (Ormerod et al., 1988). The rapid onset, large volumes, and rapid shutdown of explosive volcanism of the SWNVF are consistent with the introduction of volatiles. Later basaltic phases including those in Crater Flat exhibit anomalous geochemistries consistent with an unusual source (Vaniman et al, 1982) including some water. Water is unusual in late-Tertiary basaltic volcanism elsewhere in the southern Basin and Range.

The hypothesis above about the deep origin and structure of the Timber Mountain anomaly is relevant to the Yucca Mountain project in that the origins of the anomaly are explained by processes that are unlikely to be operating today. Water is no longer being fluxed by subduction into the deep upper mantle beneath southern Nevada. Water has such a reducing effect on the melting point of upper mantle assemblages that if it were there in significant volumes with Basin and Range geotherms, it would result in volcanism. Instead, volcanism in the region is waning in volume and violence, and transitioning to milder basaltic forms. In addition late Cenozoic volcanism has been associated with significant cooling of the crust near volcanic centers (Perry et al., 1993), so the overall likelihood of volcanism is probably declining as well.

Table Captions

Table 1. Event list.

Table 2. Station locations checked by differential GPS.

Table 3. Periods of the 1-second jumps are only accurate enough to resolve the timing issue for the events used in this study. RF delay changes are noted in Scientific Notebook for data acquisition and in the data log files.

Table 4. Crustal corrections. Crustal velocities and thicknesses used to arrive at these values are in Appendix 1.

Figure Captions

Figure 1. Events used in this study. Small circles are 30, 65, and 100 degrees from Yucca Mountain.

Figure 2. Station locations. (a) Regional coverage. (b) Near Yucca Mountain. Stations used include analog SGBSN, digital SGBDSN, and digital portable recorders.

Figure 3. The effect of station relocation on teleseismic delays. About 100 events were picked at both LSC and LTS, which are neighboring stations on Little Skull Mountain. The dashed line is a histogram of differences in hundredths of seconds between relative delays to LSC and LTS using the original station locations. Differences after correction (solid line) to the station locations improve data precision from ±35 to ±20 milliseconds.

Figure 4. Timing differences between delays at WCT/WLD and YM2/CFY2. Differences in hundredths of seconds between relative delays at co-located stations WCT and WLD (dashed) reveal a systematic difference of about 50 milliseconds with WCT delays advanced relative to WLD. The origin of the mode at -15 msec is unknown. Analog station YM2 and portable station CFY2 were collocated, and do not reflect a significant timing difference between them.

Figure 5. Effect of a dense cluster of stations in an otherwise distributed array. (a) Circles show relative delays calculated using an arithmetic mean of all absolute delays, plotted versus their great-circle distance from an event in the north Atlantic. Dashed line shows the mean level using more uniform station coverage (Figure 6). The difference in mean levels in this case makes all delays later by 0.11 seconds. (b) The difference between arithmetic and uniform station means as a function of event back-azimuth. The zero-shift amount is added as a relative advance to all arithmetically demeaned delays. The event above (back-azimuth = 44 degrees) falls among several with comparable means, reflecting the stability of the estimate for similar back-azimuths, distances, and station coverages. The vertical scatter elsewhere is largely due to variations in event ray-parameter (~distance). The two points with negative shifts near 50° back-azimuth were picked for the upgrade stations only. Despite its over 50 km aperture, the SGBDSN array mean is far from the regional mean for this back-azimuth.

Figure 6. Station coverage used to demean data in this study. Stations away from Yucca Mountain are relatively uniformly spaced and almost all were included. The stations near Yucca Mountain were selected qualitatively to maintain uniformity. Delays to this station set provide a regional average as representative as can be practically achieved.

Figure 7. Delay maps computed with (a) the Figure 6 station coverage; and (b) a raw average delay. The back-azimuth for this event is 19 degrees. Squares and positive relative delays indicate late arrivals, triangles are relatively early. For this event deep Timber Mountain structure appears as early arrivals to Yucca Mountain and Crater Flat stations. Using the correct mean level causes 0.19 seconds more delay to be explained by structure around Yucca Mountain.

Figure 8. Ray parameter versus back-azimuth delay plots for station WLD in Crater Flat using (a) raw demeaning; and (b) Figure 6 station demeaning. Squares are relatively late: triangles are relatively early. Inner and outer circles are 4.5 and 9 sec/degree ray parameters, respectively. Peak-to-peak delays are greater than arithmetic demeaning by over 0.4 seconds on the NNW/SSE line, and 0.1 second greater along the NW/SE line. Arithmetic demeaning would cause 0.4 seconds of apparent anisotropy across the SGB array. (c) and (d) present arithmetic and Figure 6 demeaning to station PAN in the Panamint Range.

Figure 9. Plot of average relative delays for Yucca Mountain stations. Average delays should not be interpreted as purely crustal in origin; long-wavelength upper mantle structure can and locally does control averages. Large differences between neighboring stations, on the other hand, must be relatively shallow in origin. The increase from stations CFWW and CFY2 to CFSW and STO originate in the shallow crust. The likely cause is a structural depression in the Paleozoic or Proterozoic basement now filled by Tertiary volcanics.

Figure 10. Refraction-derived crustal corrections. Corrections have been extrapolated along strike where necessary from the nearest lines of Mooney and Schapper (1995). Corrections are in seconds and adjusted to an average teleseismic ray parameter.

Figure 11. Delay maps from various back-azimuths. (a) 203°. The opposing back-azimuth is shown in Figure 7a. (b) 91°. (c) 284°. The size of the spatial shift of a delay patterns increases with the depth to structure responsible for the delay. Low velocities NE of NTS and the Timber Mountain structure are clearly in the upper mantle; early arrivals NW of NTS are relatively shallow.

Figure 12. Single block anomaly at 30-45 km in SW NTS. The open square indicates the amplitude of the input structure. Station coverage in this area (Figure 2) is not exceptional. Little of the structure leaked into adjacent blocks, and 67% is restored to the source block. The hit quality for this block is 0.53.

Figure 13. Synthetic post structure for the detailed model. Blocksize is 4½x4½ km. Post structures are 1% fast and extend from layer 3 through layer 6 (12 to 60 km). Model total depth is 80 km. Post input magnitude is shown by the open squares. Solid lines

enclose a hit quality of 0.40 (Eqn. 11), requiring 10 or more rays split among 2 or more bins. Dashed lines include a hit quality of ≥0.28, requiring 7 rays split among 2 or more bins. Blocks with fewer than 4 rays are not plotted. The best-resolved area centers on Yucca Mountain and Crater Flat. Hit quality contours are a function of the ray coverage, and thus are the same for all detailed models.

Figure 14. North-south profiles through the structure of Figure 13. Plotting conventions are as for Figure 13. The improvement in resolution with depth is evident. Profile NS-7 runs up the western NTS boundary. Successive profiles step east one block at a time, so the fourth (Profile NS-10) shows resolution beneath Little Skull Mountain. Side-lobe energy in resolved regions of Profiles NS-8 and NS-9 is clearly very much smaller than the input. In the well-hit region, isolated block anomalies will be well located in space and somewhat under-reconstructed in amplitude.

Figure 15. Synthetic plate structure illustrating depth resolution of areally extensive anomalies. Blocks with 4 or more rays in them are shown. (a) Amplitude reconstruction is poor for the plate at 12-20 km. In cross-sections (b-e) this plate is moved successively deeper. (b) North-south cross-section through the Little Skull Mountain (LSM) area, showing that the plate is virtually unresolved. (c) Plate input at 20-30 km. (d) Plate at 30-45 km. Downward blurring remains, but upward blurring is attenuated. (e) Plate at 45-60 km. 60-75% of input amplitudes is recovered because the anomaly cannot blur downward. Shallow structure can be introduced along poorly hit ray-paths.

Figure 16. Regional model of the southern Great Basin area. 30×30×11 blocks cover 450×450×300 km, so blocks are 15 km on a side. Full block amplitude is 3%. Blocks with hit qualities lower than 0.28 are not plotted. Black is relatively fast; gray is slow. Only refraction-based crustal corrections were applied and station delays are not removed by station statics. As a result the crustal layers appear somewhat noisy. SPR: Silver Peak Range; SF: Sarcobatus Flat; FM: Funeral Mountains; PAN: Panamint Range. The dashed line is discussed in the text.

Figure 17. Detailed inversion. Blocks are 4.5×4.5 km. Blocks with hit quality < 0.28 (~7 rays with crossing ray constraint) are not plotted. ESF: Exploratory Surface Facility; LSM: Little Skull Mountain; SkM: Skull Mountain; BMF: Bare Mountain Fault; CH: Calico Hills; WAH: Wahmonie. Crustal corrections are described in the text.

Figure 18. Model size versus Data Misfit. Teleseismic delays directly constrain the product of model amplitude (size) times model thickness (upper line). The improvement in data fit with model total depth and no increase in degrees of freedom means the true structure is better explained by deeper models. The 41 km model depth was used by Evans and Smith (1992, 1995). The *plus* sign is the model size with another model layer added.

Based on this figure detailed models used a total depth of 80 km.

Figure 19. Profiles illustrating Crater Flat and SW NTS structure for various crustal correction strategies. (a-d) North-south profiles along the axis of Yucca Mountain. (a) Refraction corrections only, (Figure 17). A modest high velocity structure extends up and southward from the Timber Mountain structure. Synthetic testing of the block south of the ESF at 5-12 km restored 40% of the block structure with modest blurring to the blocks above and below it. (b) No crustal correction at all. Strong crustal effects map downward in the southern Yucca Mountain area. The small high velocity south of the ESF appears here without any crustal correction at all. (c) Station static corrections alone. (d) Station static and refraction corrections together. (e-h) East-west profiles with crustal corrections as (a-d) respectively. See the text for a discussion.

References

Aki, K. and Richards, P.G., 1980, *Quantitative Seismology*, W.H. Freeman and Co., New York, 932 p.

Atwater, T., 1970, Implications of plate tectonics for the Cenozoic tectonic evolution of western North America, *Geol. Soc. Amer. Bull., 81*, 3513-3536.

Biasi, G.P. and Humphreys, E.H., 1992, P-wave image of the upper mantle structure of central California and southern Nevada, *Geophys. Res. Lett., 19*, 1161-1164.

Christiansen, N.I. and Wepfer, W.W., 1989, Laboratory techniques for determining seismic velocities and attenuations, with applications to the continental lithosphere, *in*, Pakiser, L.C., and Mooney, W.D., eds., *Geophysical Framework of the Continental United States*, Boulder, Colorado, *Geol. Soc. Am. Memoir 172*, 91-102.

Dueker, K., E. Humphreys and G. Biasi, 1993, Teleseismic imaging of the western United States upper mantle structure using the simultaneous iterative reconstruction technique, *Seismic Tomography: Theory and practice*, H.M. Iyer and K. Hirahara, eds., Chapman and Hall, London.

Eaton, G.P., Wahl, R.R., Prostka, H.J., Mabey, D.R., and Kleinkopf, M.D., 1978, Regional gravity and tectonic patterns: Their relation to late Cenozoic epiorogeny and lateral spreading in the western Cordillera, *Geol. Soc. Am. Mem., 152*, 51-91.

Evans, J.R. and Achauer, U., 1993, Teleseismic velocity tomography using the ACH method: theory and application to continental-scale studies, *Chapter 13* in *Seismic Tomography: Theory and practice*, H.M. Iyer and K. Hirahara, eds., Chapman and Hall, London

Evans, J.R., and Smith, M. III, 1992, Teleseismic tomography of the Yucca Mountain Region: volcanism and tectonism, *American Nuclear Society, Proceedings of the Third International Conference on High-Level Radioactive Waste Management, 2*, 2372-2380.

Evans, J.R. and Smith, M. III, 1995, Teleseismic investigations, Chapter 7 *in*, Major Results of Geophysical Investigations at Yucca Mountain and Vicinity, Southern Nevada, H.W. Oliver, D.A. Ponce, and W.C. Hunter, Eds., *USGS Open File Report 95-74*, 190 p.

Farmer, G.L., Perry, F.V., Semken, S., Crowe, B., Curtis, D., and DePaolo, D.J., 1989, Isotopic evidence on the structure and origin of subcontinental lithospheric mantle in southern Nevada, *J. Geophys. Res., 94*, 7885-7898.

Ferrill, D.A., Stamatakos, J.A., Jones, S.M., Rahe, B, McKague, H.L., Martin, R.H., and Morris, A.P., 1996, Quaternary slip history of the Bare Mountain fault (Nevada) from the morphology and distribution of alluvial fan deposits, *Geology, 24*, 559-562.

Fountain, D.M. and Christiansen, N.I., 1989, Composition of the continental crust and upper mantle; A review, *in*, Pakiser, L.C., and Mooney, W.D., eds., *Geophysical Framework of the Continental United States*, Boulder, Colorado, *Geol. Soc. Am. Memoir 172*, 711-742.

Hudson, M.R., Sawyer, D.A., and Warren, R.G., 1994, Paleomagnetism and rotation constraints for the middle Miocene southwestern Nevada volcanic field, *Tectonics, 13*, 258-277.

Humphreys, E. and Clayton, R. W., 1988, Adaptation of back projection tomography to seismic travel time problems, *J. Geophys. Res. 93*, 1073-1085.

Humphreys, E.D., and Dueker, K.D., 1994a, Western U.S. upper mantle structure, *J. Geophys. Res., 99*, 9615-9634.

Humphreys, E.D., and Dueker, K.D., 1994b, Physical state of the western U.S. upper mantle, *J. Geophys. Res., 99*, 9635-9650.

Ivansson, S., 1983, Remark on an earlier proposed iterative tomographic algorithm, *Geophys. J.R. astr. Soc., 75*, 855-860.

Iyer, H.M, and Dawson, P.B., 1993, Imaging volcanos using teleseismic tomography, *Chapter 17* in *Seismic Tomography: Theory and practice*, H.M. Iyer and K. Hirahara, eds., Chapman and Hall, London.

Jordan, T.H., 1979, Mineralogies, densities and seismic velocities of garnet lherzolites and their geophysical implications, *in* The Mantle Sample: Inclusions in kimberlites and other volcanics, Boyd, F.R. and Meyer, H.O.A., eds., Proceedings of the Second International Kimberlite Conference, Vol 2, American Geophysical Union, Washington, D.C.

Loomis, D.P., and Burbank, D.W., 1988, The stratigraphic evolution of the El Paso basin, southern California: Implications for the Miocene development of the Garlock fault and uplift of the Sierra Nevada, *Geol. Soc. Am. Bull., 100*, 12-28.

Maldonado, F., 1990, Structural geology of the upper plate of the Bullfrog Hills detachment fault system, southern Nevada, *Geol. Soc. Am. Bull., 102*, 992-1006.

Monfort, Mary E. and Evans, John R., 1982, Three-dimensional modeling of the Nevada Test Site and vicinity from teleseismic P-wave residuals, *USGS Open File Report 82-409*, 66 p.

Mooney, W.D. and Schapper, S., 1995, Seismic Refraction investigations, Chapter 5 *in*, Major Results of Geophysical Investigations at Yucca Mountain and Vicinity, Southern Nevada, H.W. Oliver, D.A. Ponce, and W.C. Hunter, Eds., *USGS Open File Report 95-74*, 190 p.

Moore, J.G. and Dodge, F.C.W., 1980, Late Cenozoic volcanic rocks of the southern Sierra Nevada, California: I. Geology and petrology: Summary, *Geol. Soc. Amer. Bull., 91*, 515-518.

Ormerod, D.S., Hawksworth, C.J., Rogers, N.W., Leeman, W.P., and Menzies, M.A., 1988, Tectonic and magmatic transitions in the western Great Basin, USA, *Nature, 333*, 349-353.

Perry, F.V., DePaolo, D.J., and Baldridge, W.S., 1993, Neodymium isotopic evidence for decreasing crustal contributions to Cenozoic ignimbrites of the western United States: Implications for the thermal evolution of the thermal evolution of the Cordilleran crust, *Geol. Soc. Am. Bull., 105*, 872-882.

Ponce, D.A. and Oliver, H.W., 1995, Gravity Investigations, Chapter 2 *in*, Major Results of Geophysical Investigations at Yucca Mountain and Vicinity, Southern Nevada, H.W. Oliver, D.A. Ponce, and W.C. Hunter, Eds., *USGS Open File Report 95-74*, 190 p.

Saltus, R.W. and Thompson, G.A., 1995, Why is it downhill from Tonopah to Las Vegas?: A case for mantle plume support of the high northern Basin and Range, *Tectonics, 14*, 1235-1244.

Sass, J.H., Lachenbruch, A.H., Galanis, S.P. Jr., Morgan, P., Priest, S.S., Moses, T.H. Jr., and Munrow, R.J., 1994, Thermal regime of the southern Basin and Range province: 1. Heat flow data from Arizona and the Mojave Desert of California and Nevada, *J. Geophys. Res., 99*, 22093-22119.

Sass, J.H., Dudley, W.W. Jr., and Lachenbruch, A.H., 1995, Regional Thermal Setting, Chapter 8 *in*, Major Results of Geophysical Investigations at Yucca Mountain and Vicinity, Southern Nevada, H.W. Oliver, D.A. Ponce, and W.C. Hunter, Eds., *USGS Open File Report 95-74*, 190 p.

Severinghaus, J. and Atwater, T., 1990, Cenozoic geometry and thermal state of the subducting slabs beneath western North America, *in* Wernicke, B.P., ed., Basin and Range extensional tectonics near the latitude of Las Vegas, Nevada, *Geol. Soc. Amer. Memoir 176*, 1-22.

Smith, R.L., and Luedke, R.G., 1984, Potentially active volcanic lineaments and loci in western conterminous United States, in *Explosive Volcanism: Inception, Evolution, and Hazards*, 47-66, National Academy Press, Washington, D. C.

Snyder, D.B. and Carr, W.J., 1984, Interpretation of gravity data in a complex volcano-tectonic setting, southwestern Nevada, *J. Geophys. Res.*, *89* 10193-10206.

Spence, William, 1974, P-wave residual differences and inferences on an upper mantle source for the Silent Canyon Volcanic Centre, southern Great Basin, Nevada, *Geophys. J. R. astr. Soc.*, *38*, 505-523.

Trampert, J., and Leveque, J.-J., 1990, Simultaneous iterative reconstruction technique: Physical interpretation based on the generalized least squares solution, *J. Geophys. Res.*, *95*, 12553-12559.

Van Der Sluis, A., and van der Vorst, H.A., 1987, Numerical solution of large, sparse linear algebraic systems arising from tomographic problems, *in* Nolet, G. *ed.*, Seismic Tomography, D. Reidel Publ. Co., p. 49-83.

Vaniman, D.T., Crowe, B.M., and Gladney, E.S., 1982, Petrology and geochemistry of hawaiite lavas from Crater Flat, Nevada, *Contrib. Mineral Petrol.*, *80*, 341-357.

Appendix A: Crustal correction input data and delay computation.

Appendix B: East-west profiles through north Jackass Flats and southern Timber Mountain. E-W 10 passes just south of the ESF, E-W 11 just north, and E-W 12 4.5 km north of the ESF. In each, (a) uses only refraction; (b) uses no crustal corrections; (c) uses only station static corrections; (d) uses refraction and station static corrections.

SGB Event Distribution

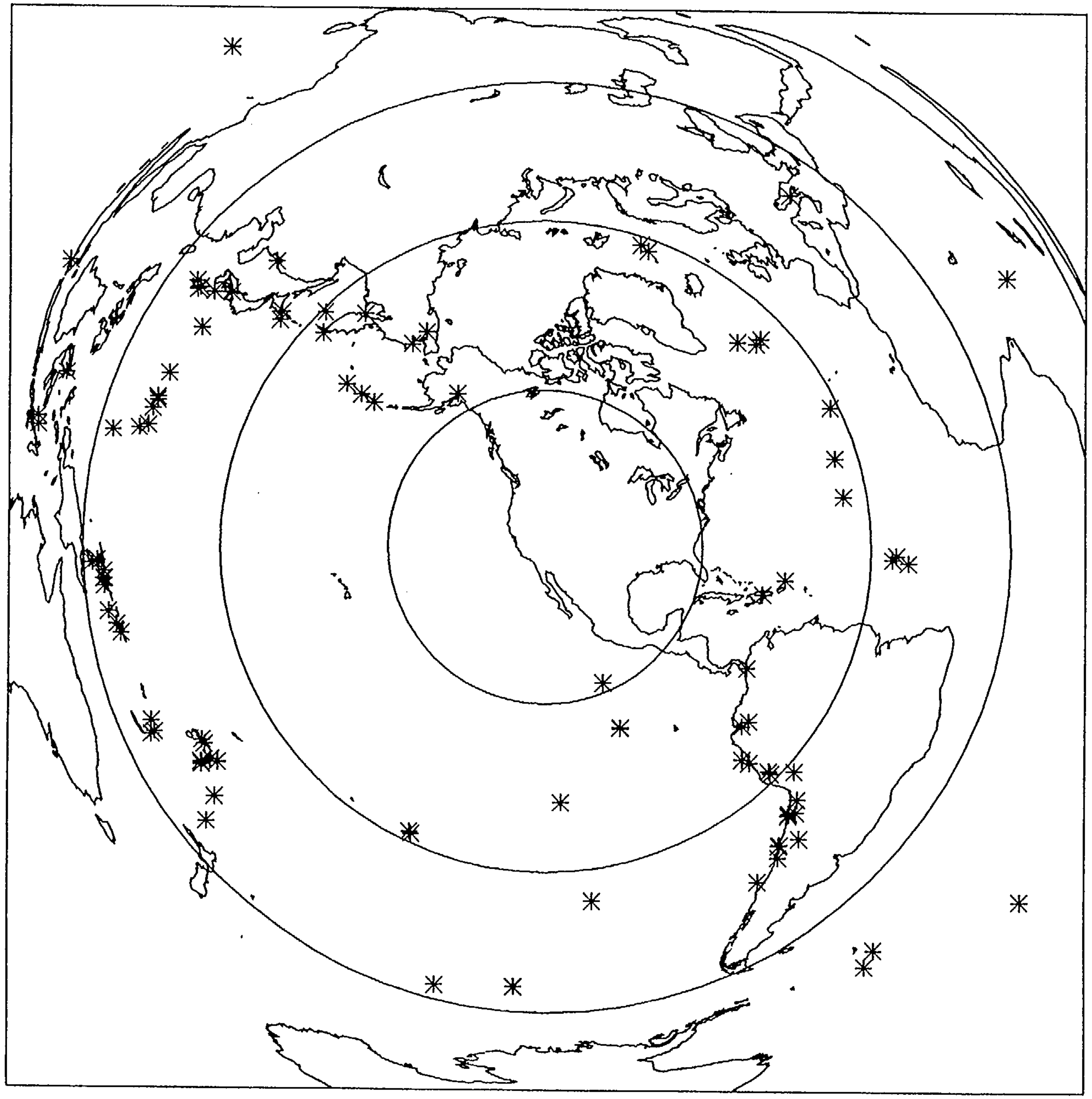

Figure 1

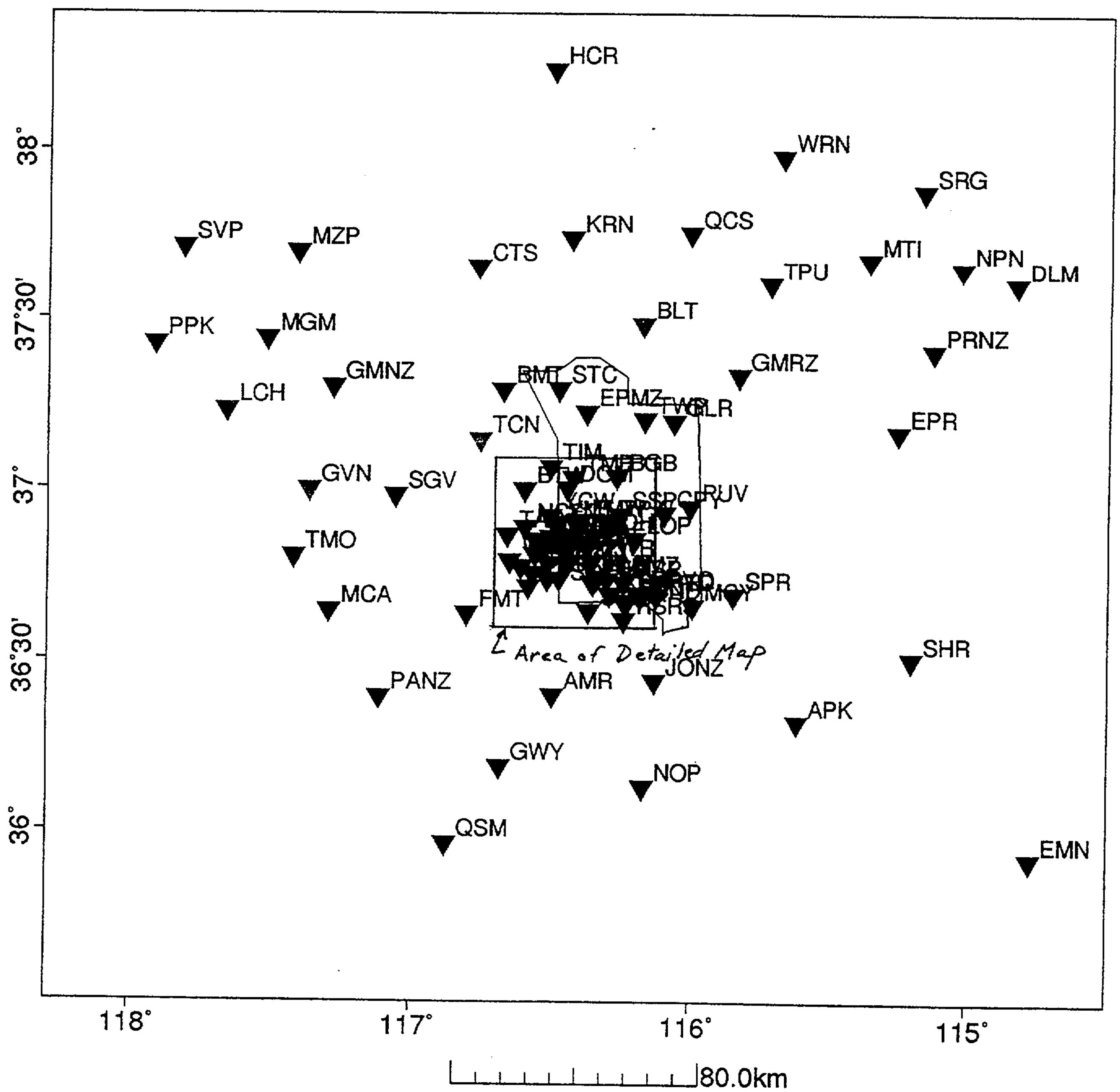

HCR
WRN
SRG
SVP
MZP
CTS
KRN
QCS
MTI
NPN
DLM
TPU
PPK
MGM
BLT
PRNZ
GMNZ
LCH
STC
GMRZ
EPR
TCN
TIM
GVN
SGV
RUV
TMO
MCA
FMT
SPR
SHR
Area of Detailed Map
JONZ
PANZ
AMR
APK
GWY
NOP
QSM
EMN
38°
37°30'
37°
36°30'
36°
118°
117°
116°
115°
80.0km

Figure 2a

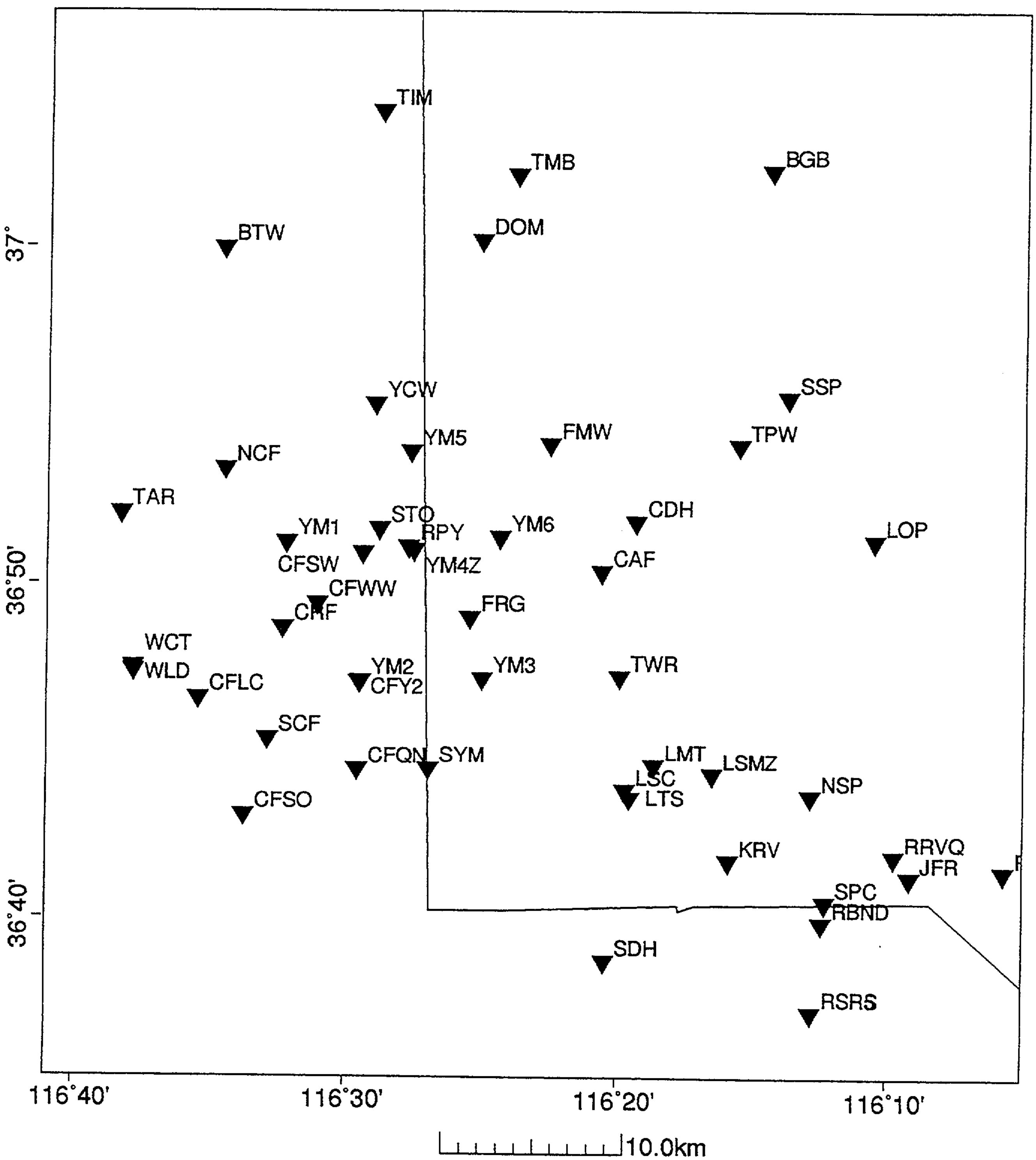
TIM
TMB
BGB
BTW
DOM
37°
YCW
SSP
YM5
FMW
TPW
NCF
TAR
STO
CDH
YM1
RPY
YM6
LOP
CFSW
YM4Z
CAF
36°50'
CFWW
CRF
FRG
WCT
WLD
CFLC
YM2
CFY2
YM3
TWR
SCF
CFQN
SYM
LMT
LSMZ
LSC
LTS
NSP
CFSO
KRV
RRVQ
JFR
SPC
RBND
36°40'
SDH
RSRS
116°40'
116°30'
116°20'
116°10'
10.0km

Figure 2b

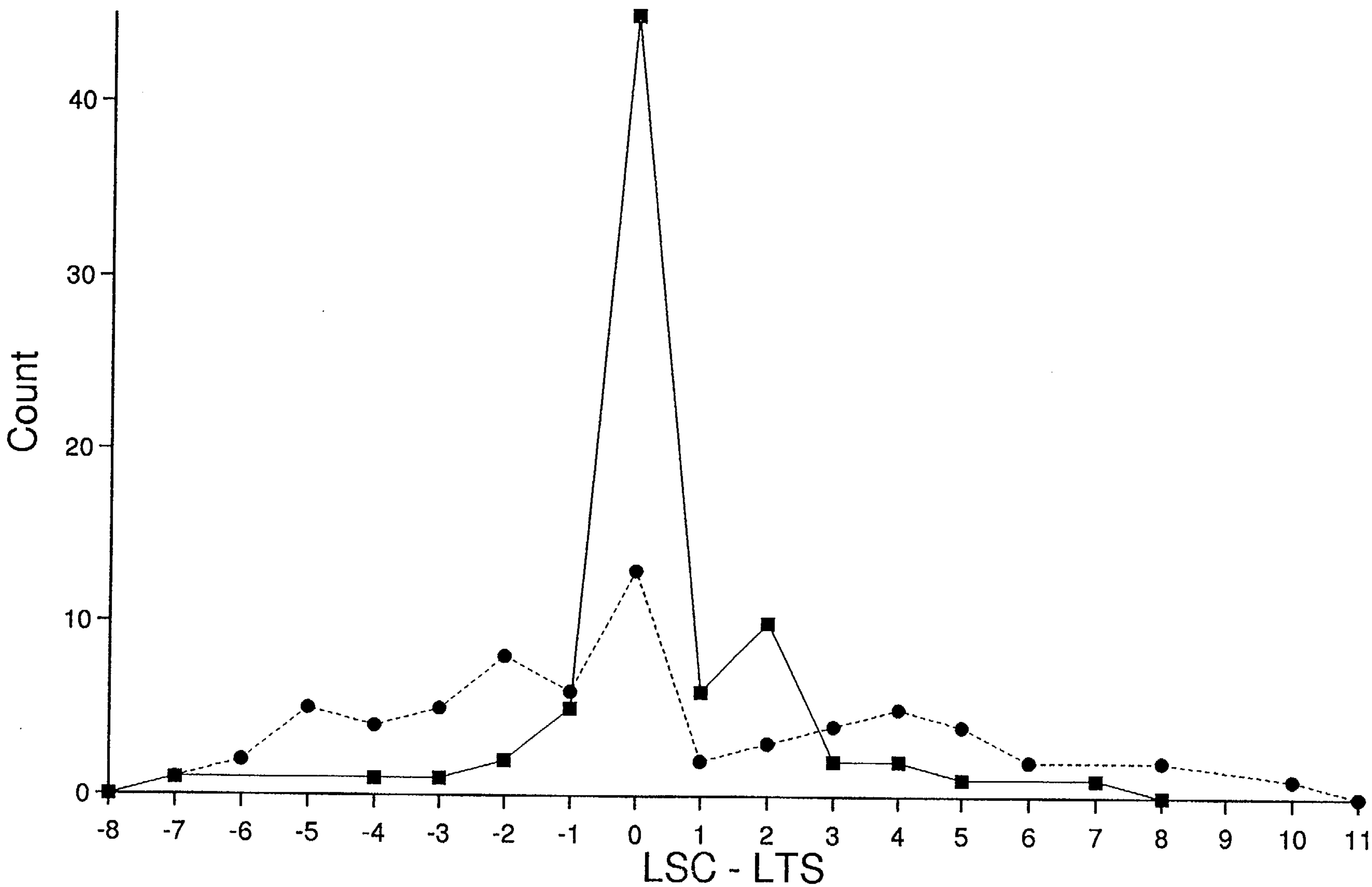

Before location correction.
After location correction.

Figure 3

YM2 & WLD Differences

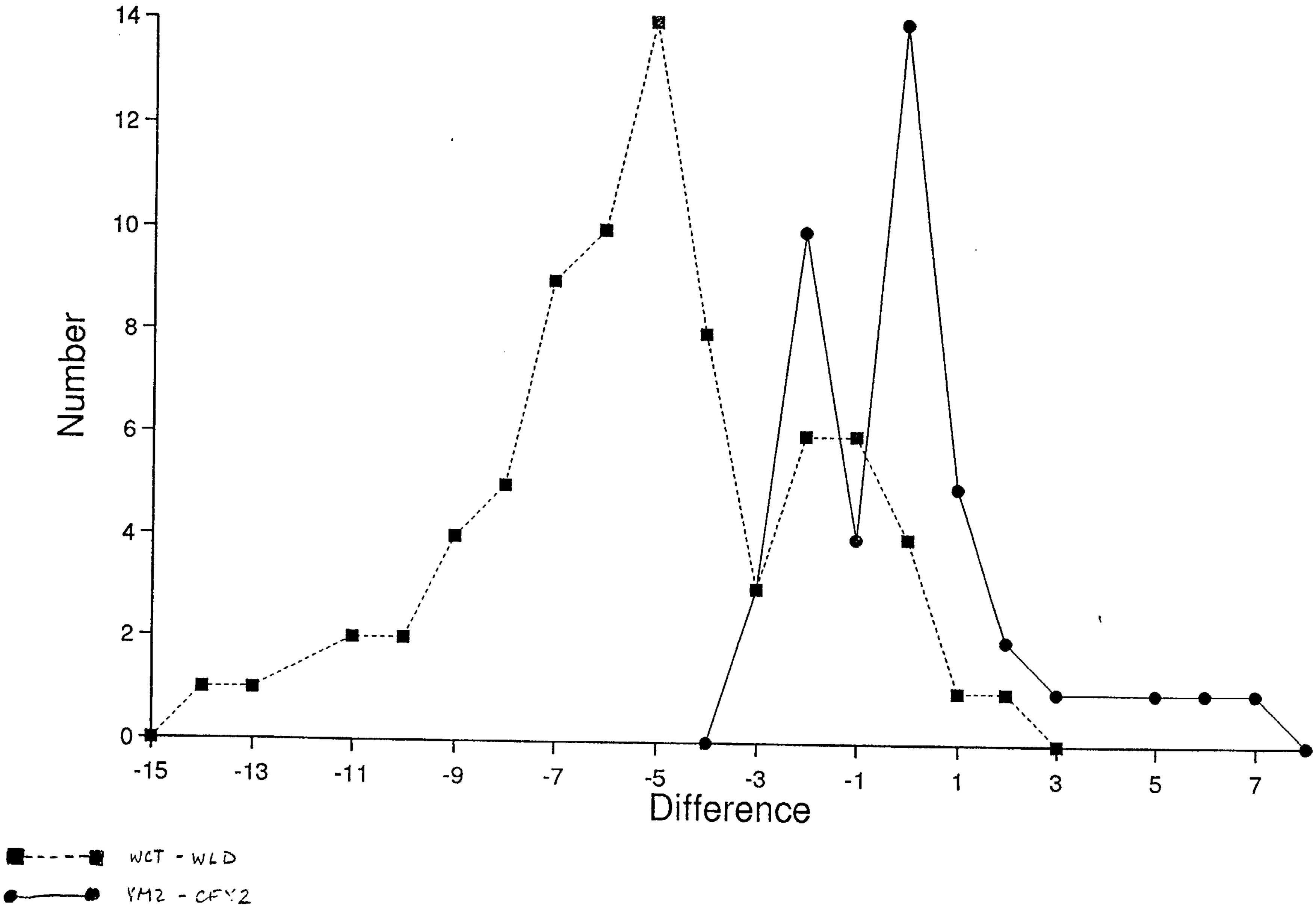

FIGURE 4

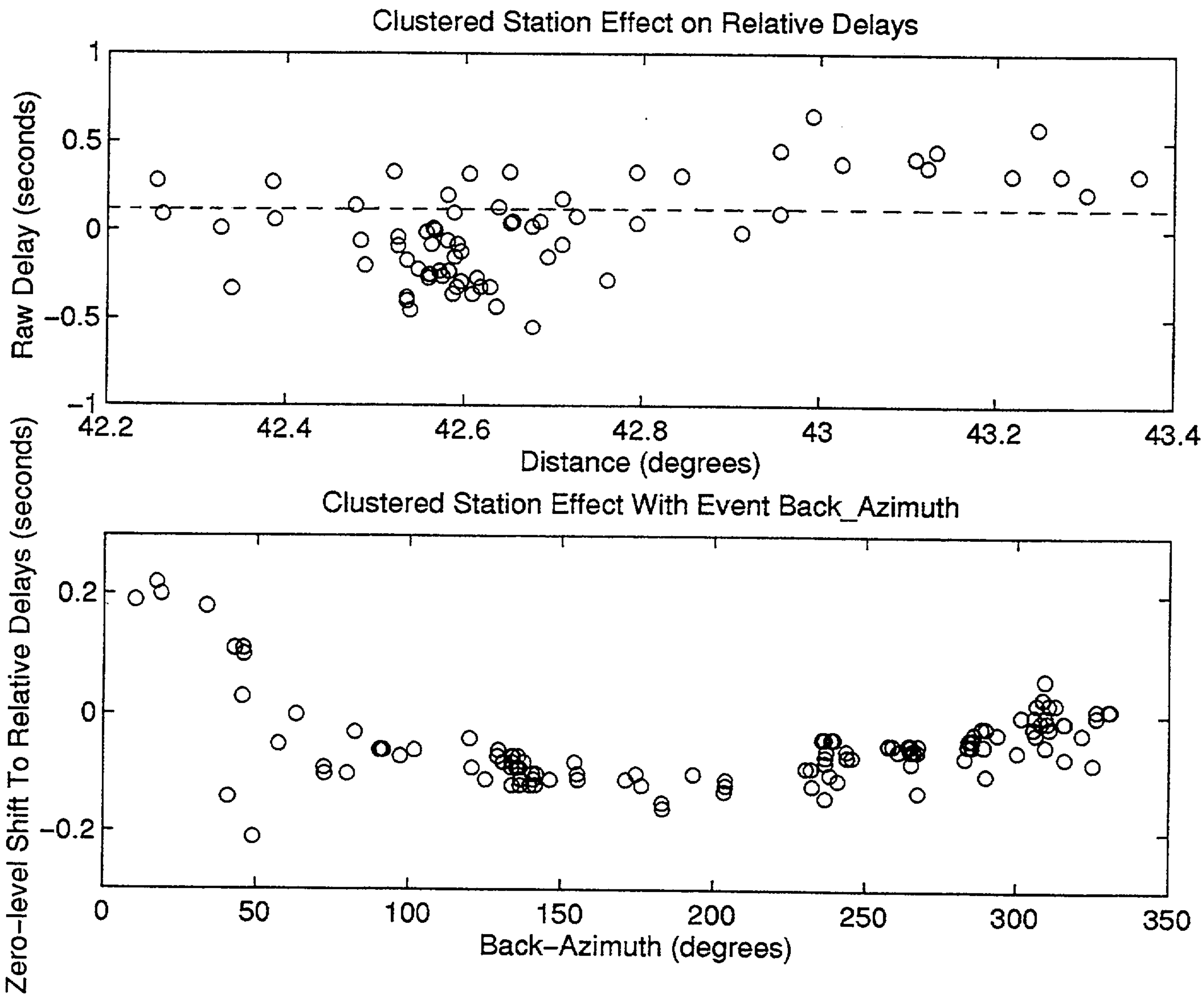
Clustered Station Effect on Relative Delays
Raw Delay (seconds)
1
0.5
0
−0.5
−1
42.2
42.4
42.6
42.8
43
43.2
43.4
Distance (degrees)
Clustered Station Effect With Event Back_Azimuth
Zero−level Shift To Relative Delays (seconds)
0.2
0
−0.2
0
50
100
150
200
250
300
350
Back−Azimuth (degrees)

FIGURE 5

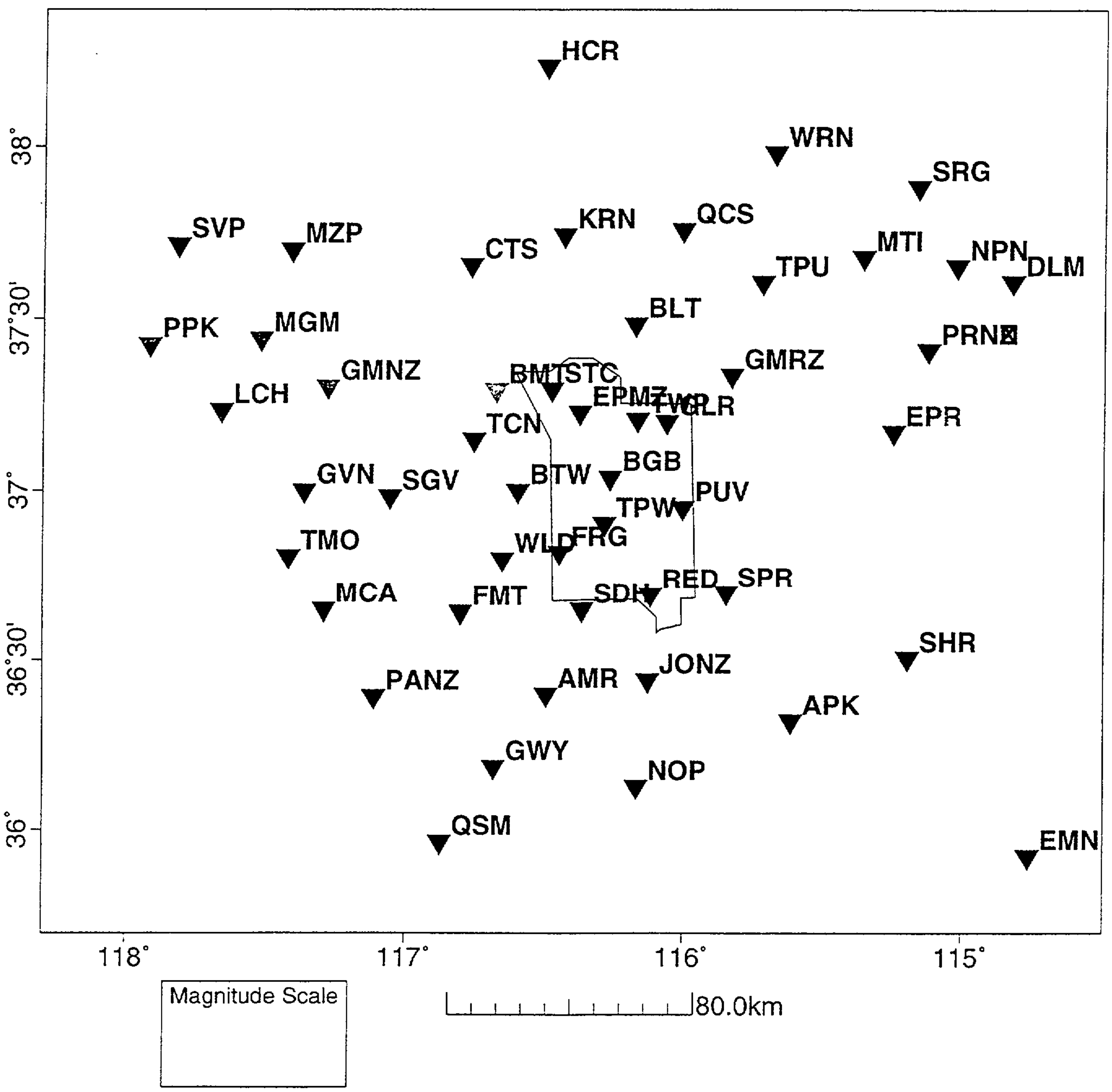
HCR
WRN
SRG
SVP
MZP
KRN
QCS
CTS
MTI
NPN
DLM
TPU
BLT
PPK
MGM
PRN
GMRZ
GMNZ
BMT
STC
LCH
EPR
TCN
BGB
GVN
SGV
BTW
PUV
TPW
TMO
WLD
FRG
RED
SPR
MCA
FMT
SDH
SHR
PANZ
AMR
JONZ
APK
GWY
NOP
QSM
EMN
38°
37°30'
37°
36°30'
36°
118°
117°
116°
115°
Magnitude Scale
80.0km

Figure 6

95:196:11:03:31 p: 6.71 baz: 18.76 sp2

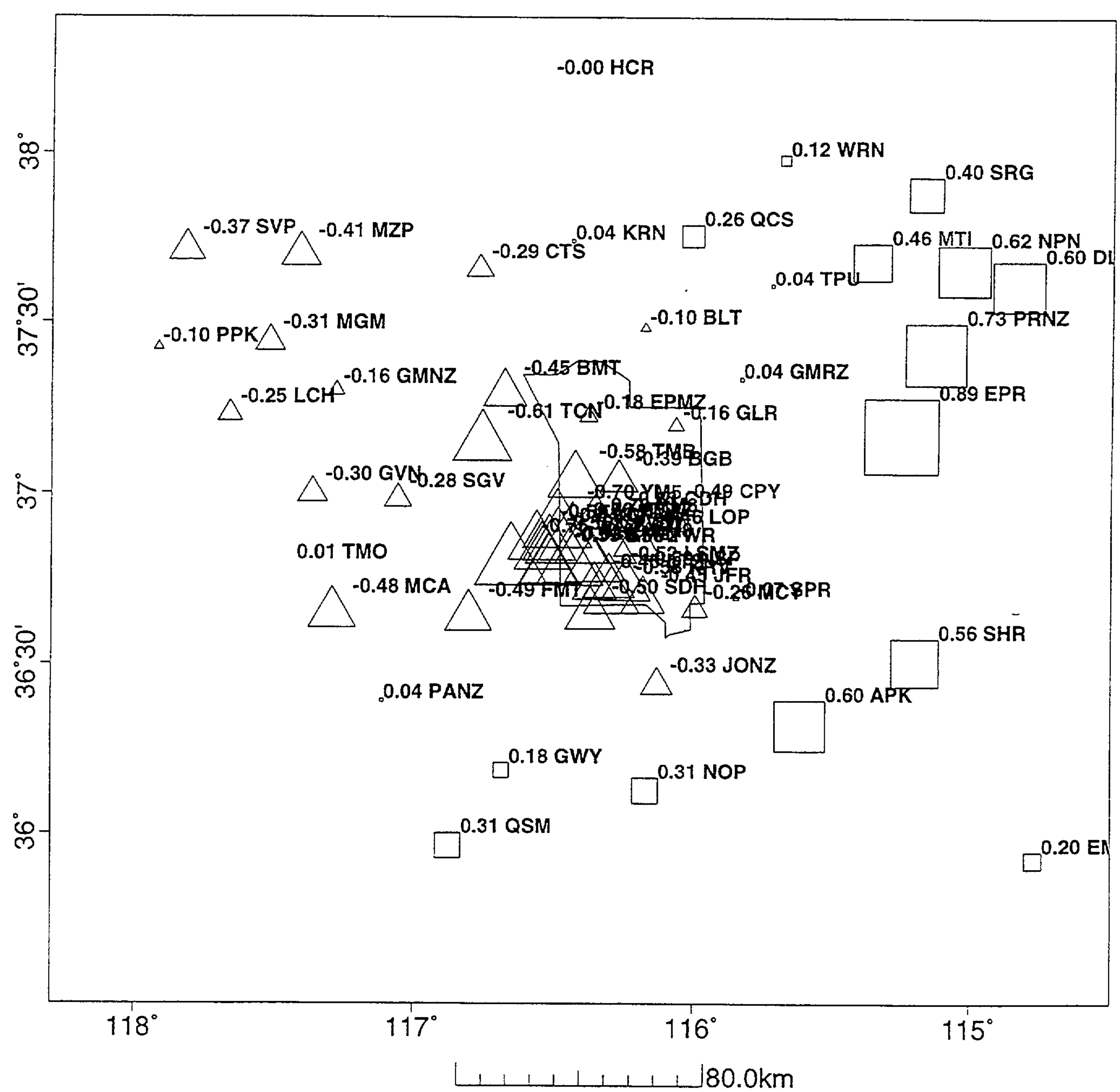

95:196:11:03:31 p: 6.70 baz: 18.74

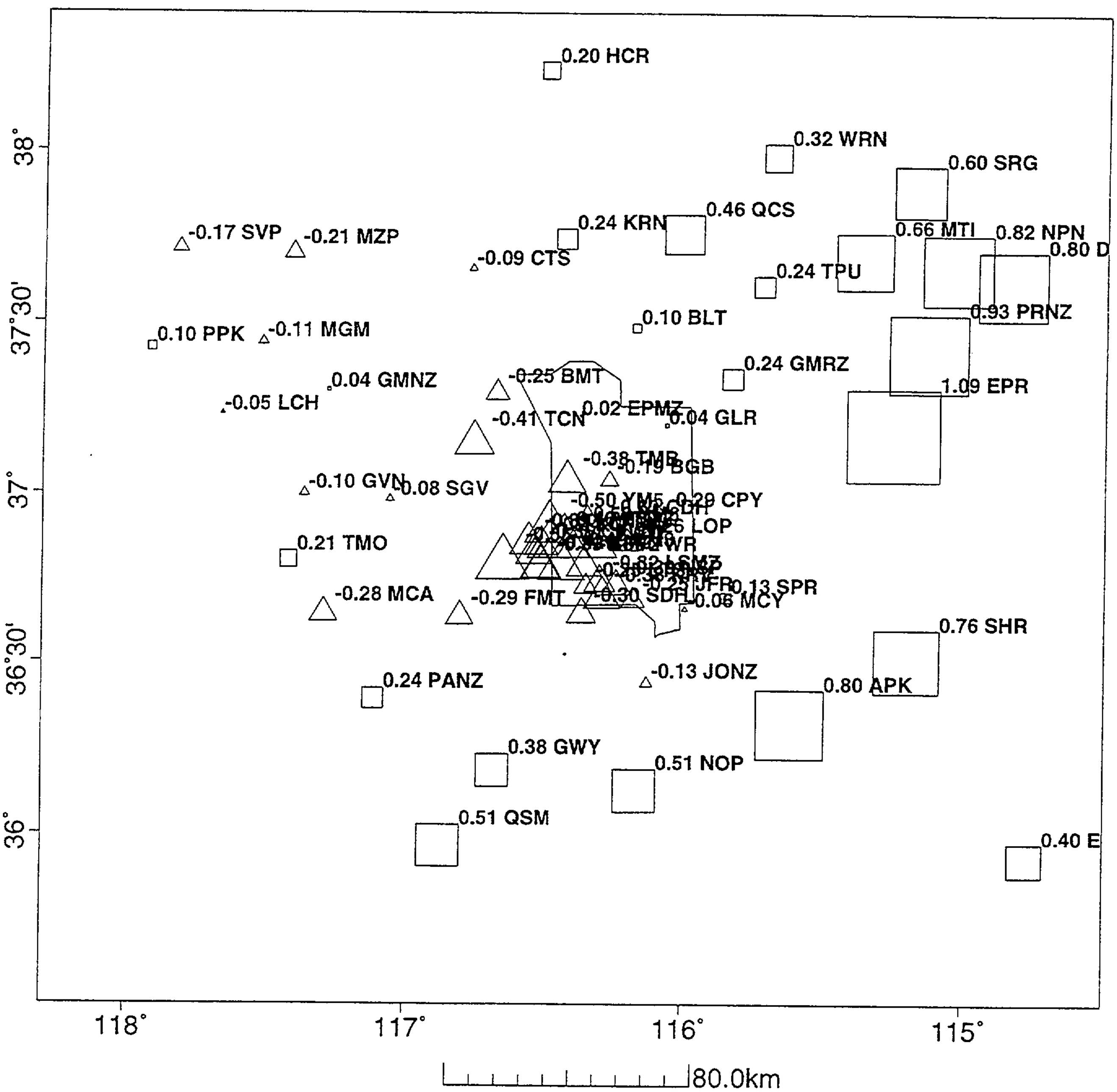

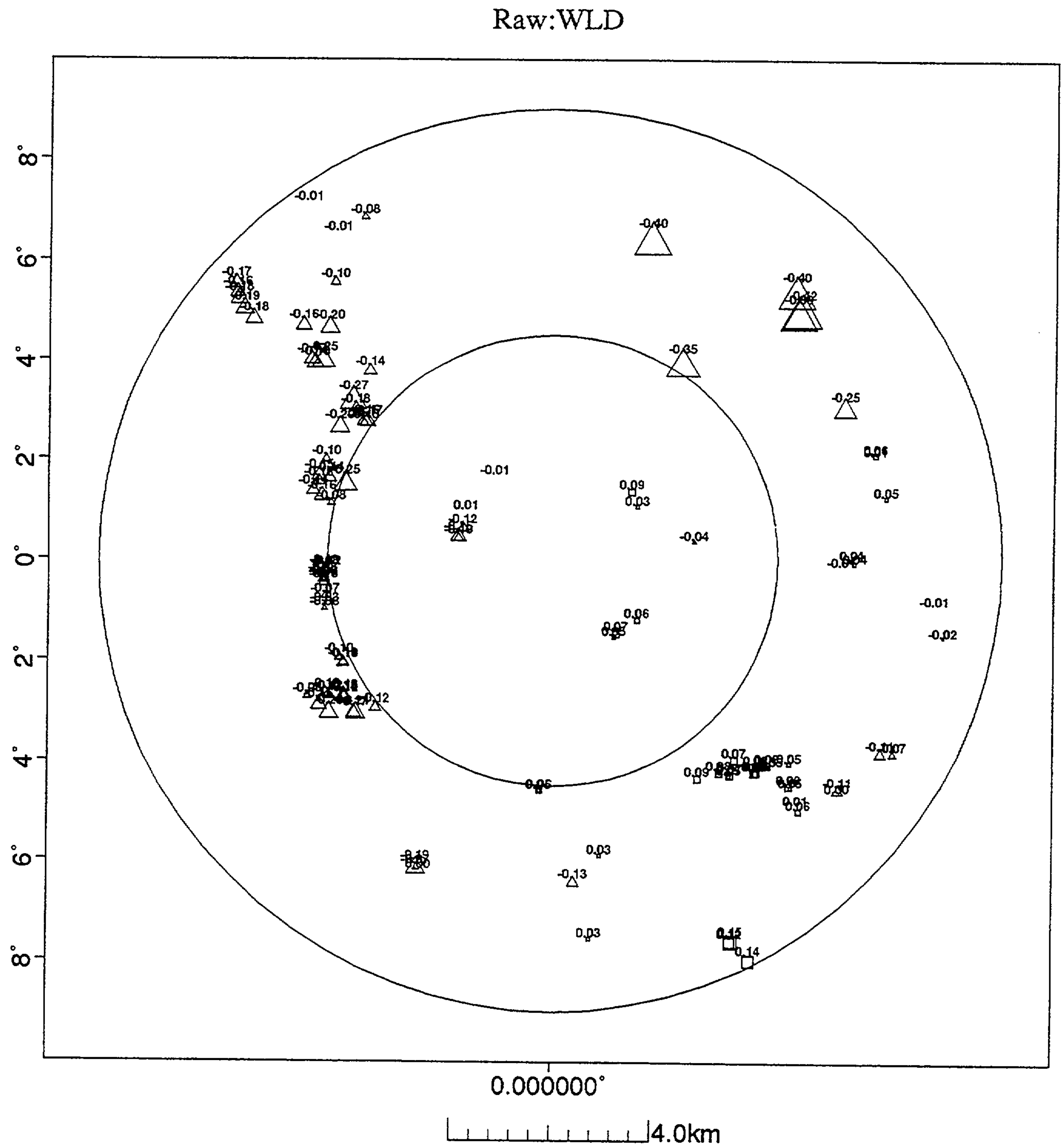

FIGURE 8a

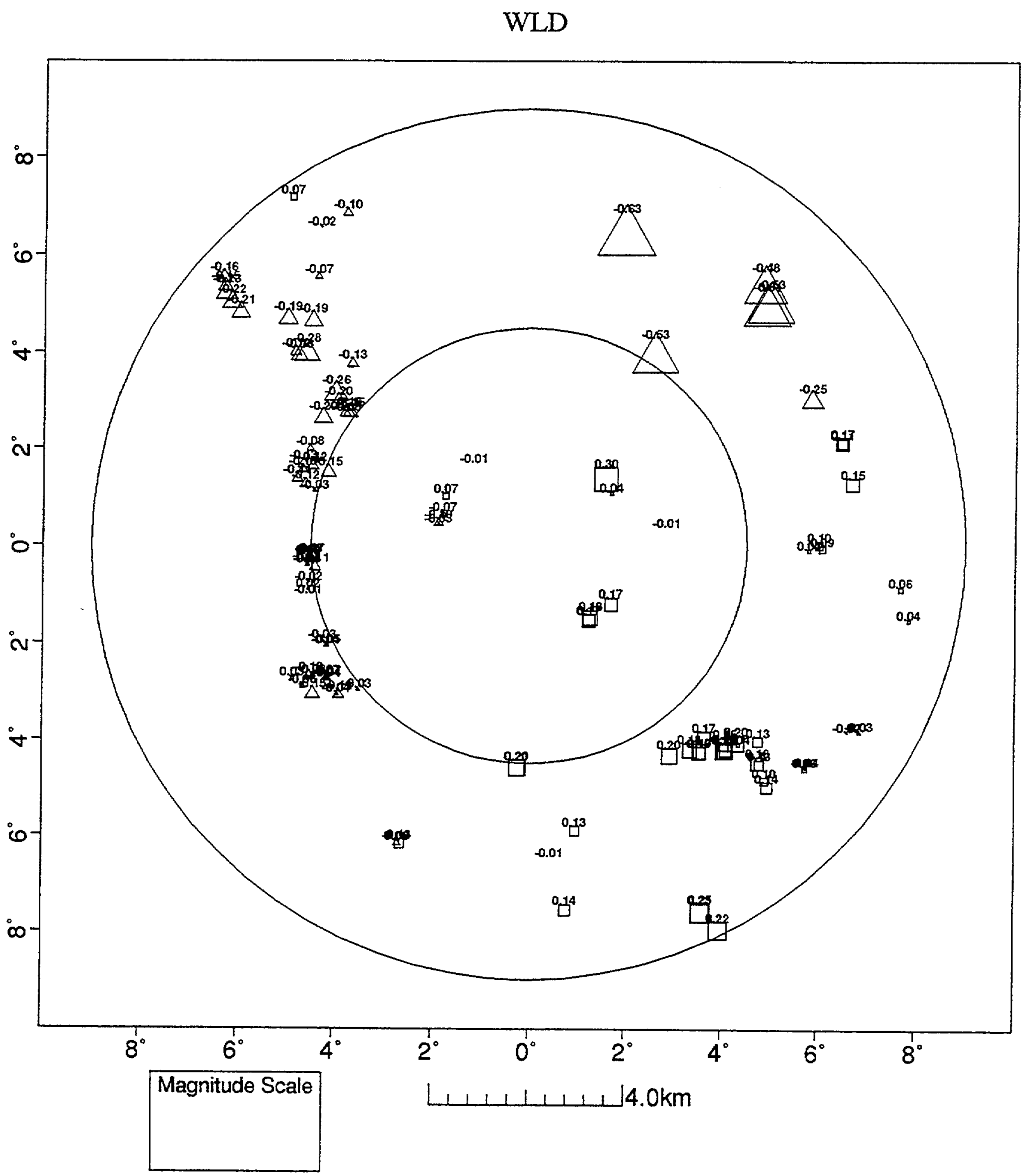

FIGURE 8b.

Raw:PANZ

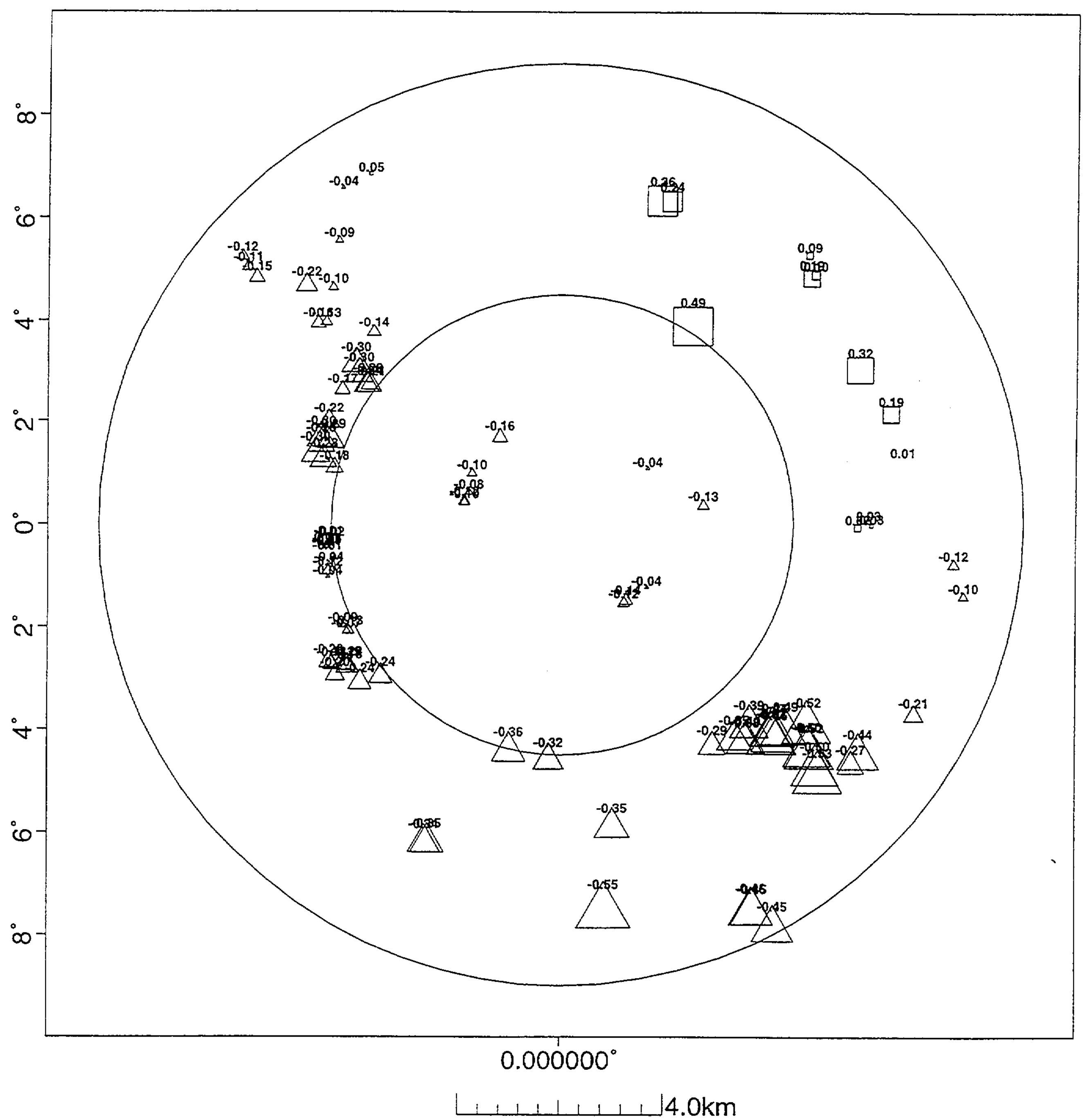

PANZ

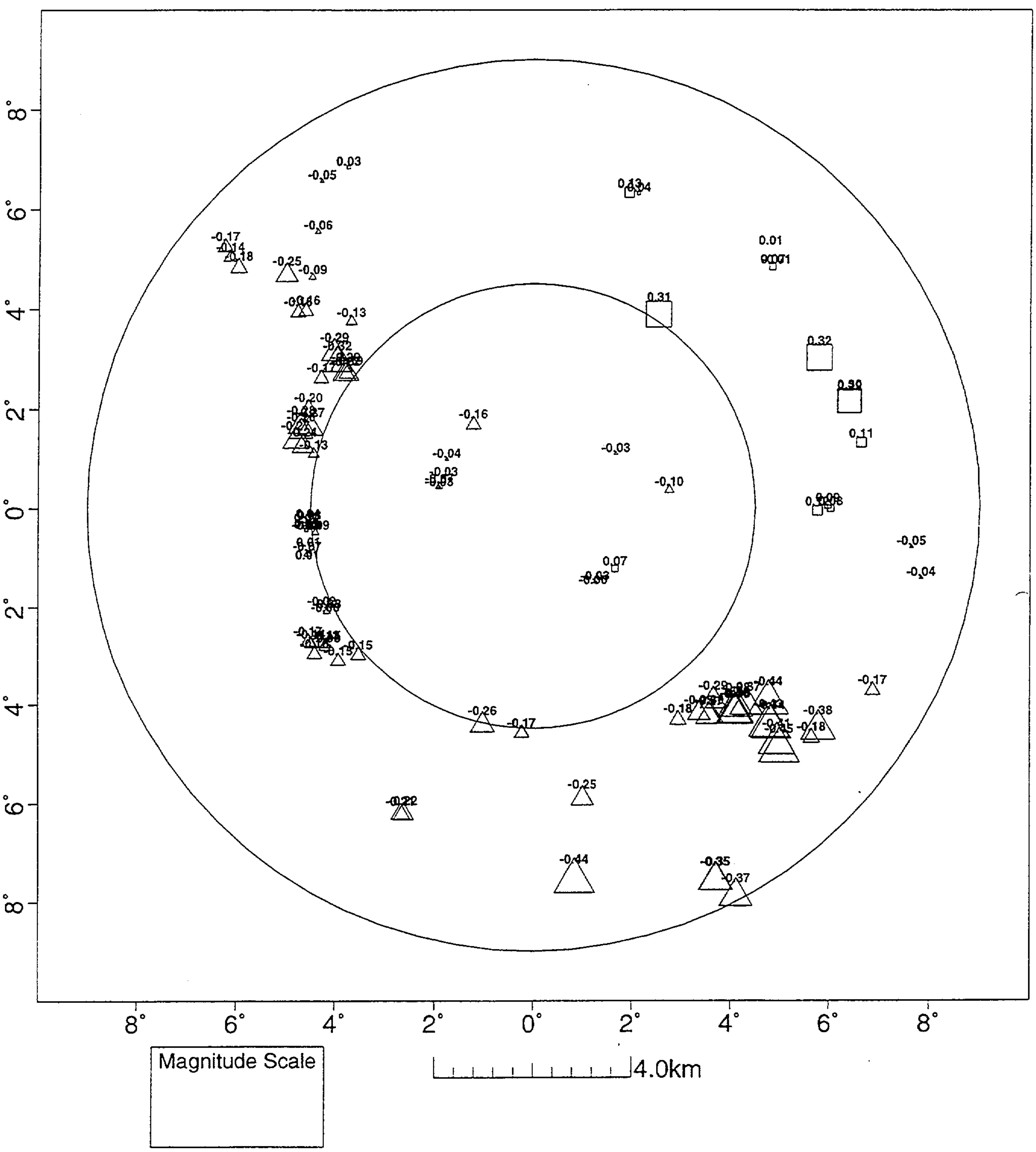

Average Station Delays

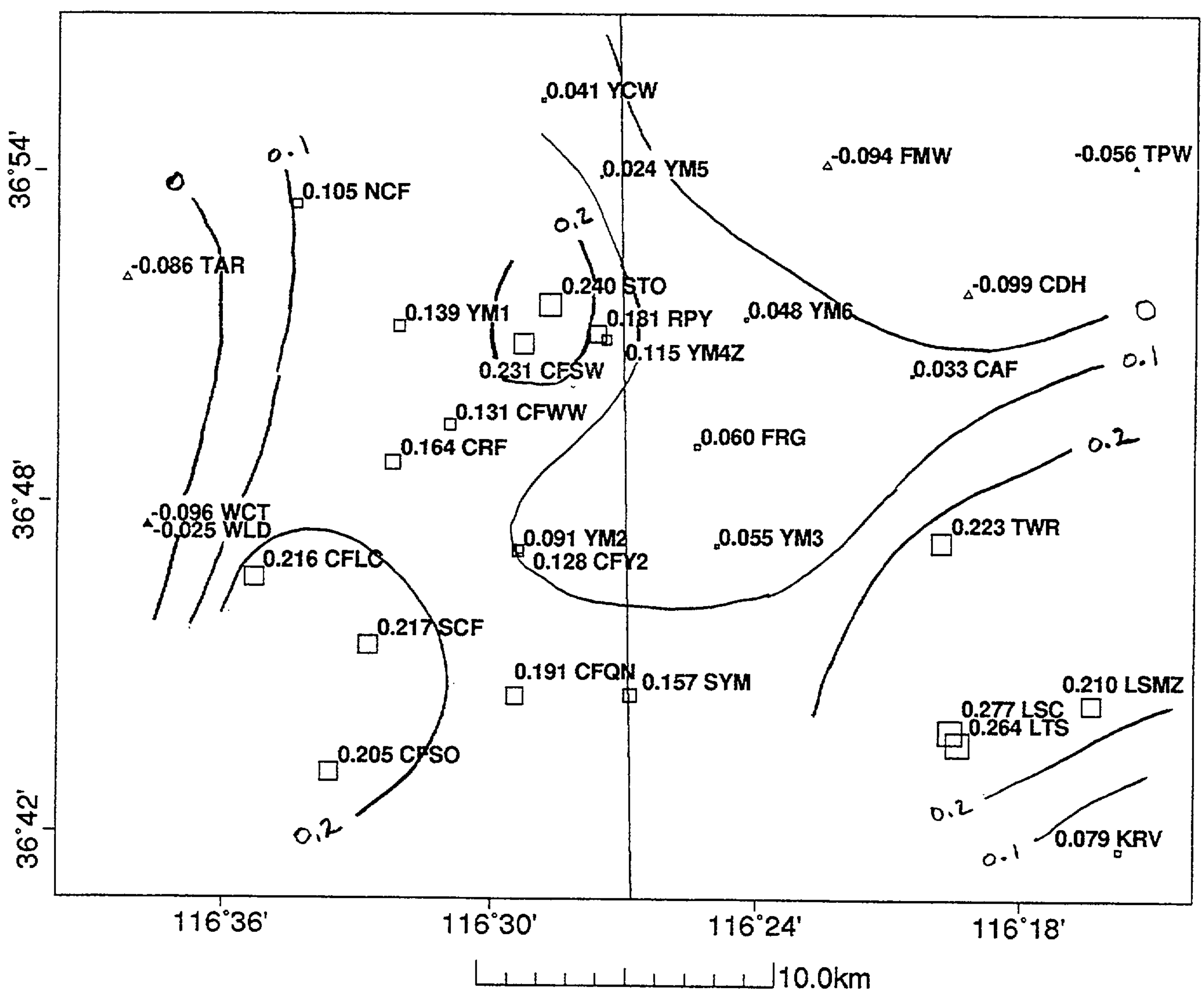

FIGURE 9

Refraction Crustal Corrections

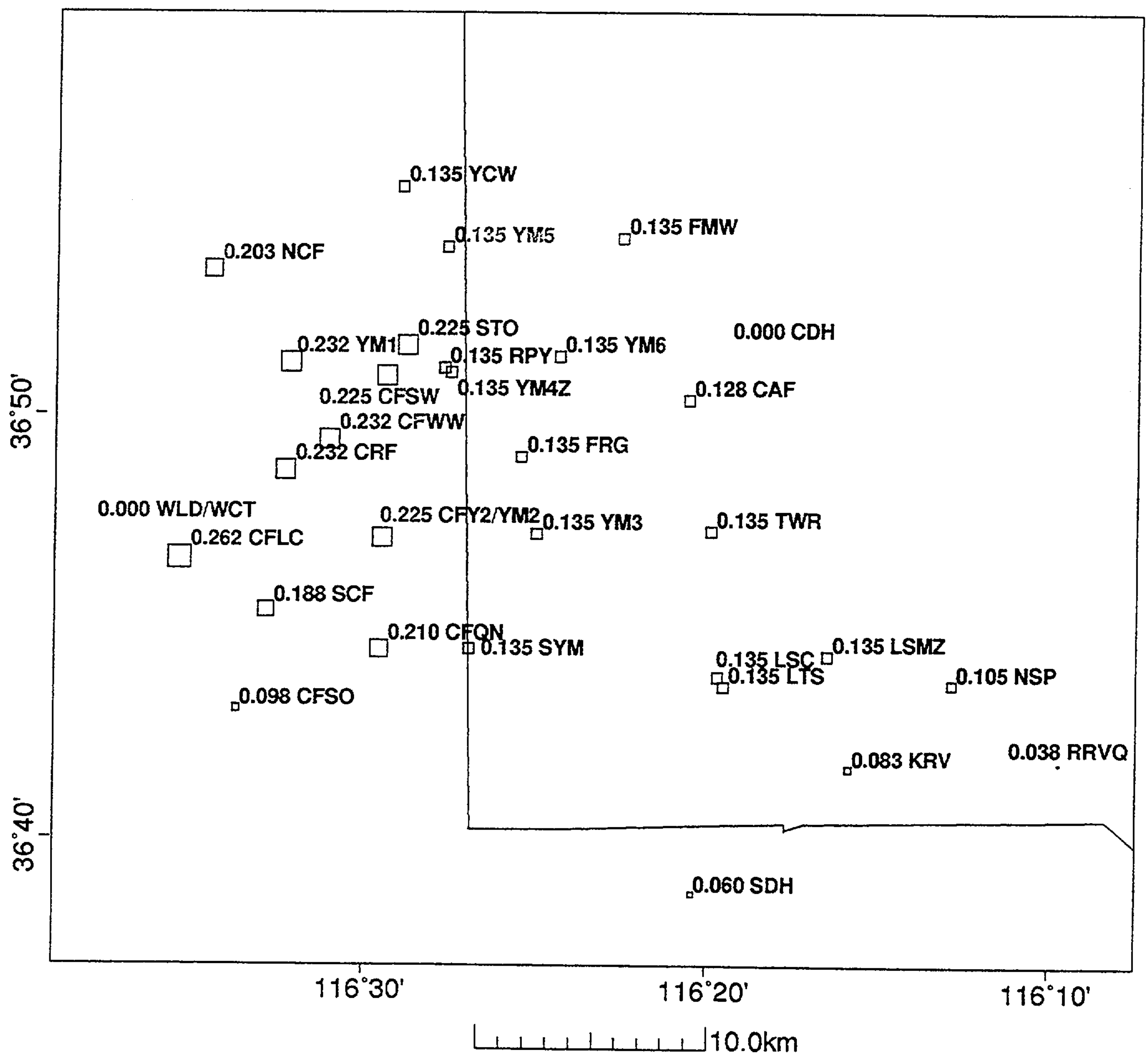

FIGURE 10

95:274:23:39:15 p: 6.70 baz: 203.46 sp

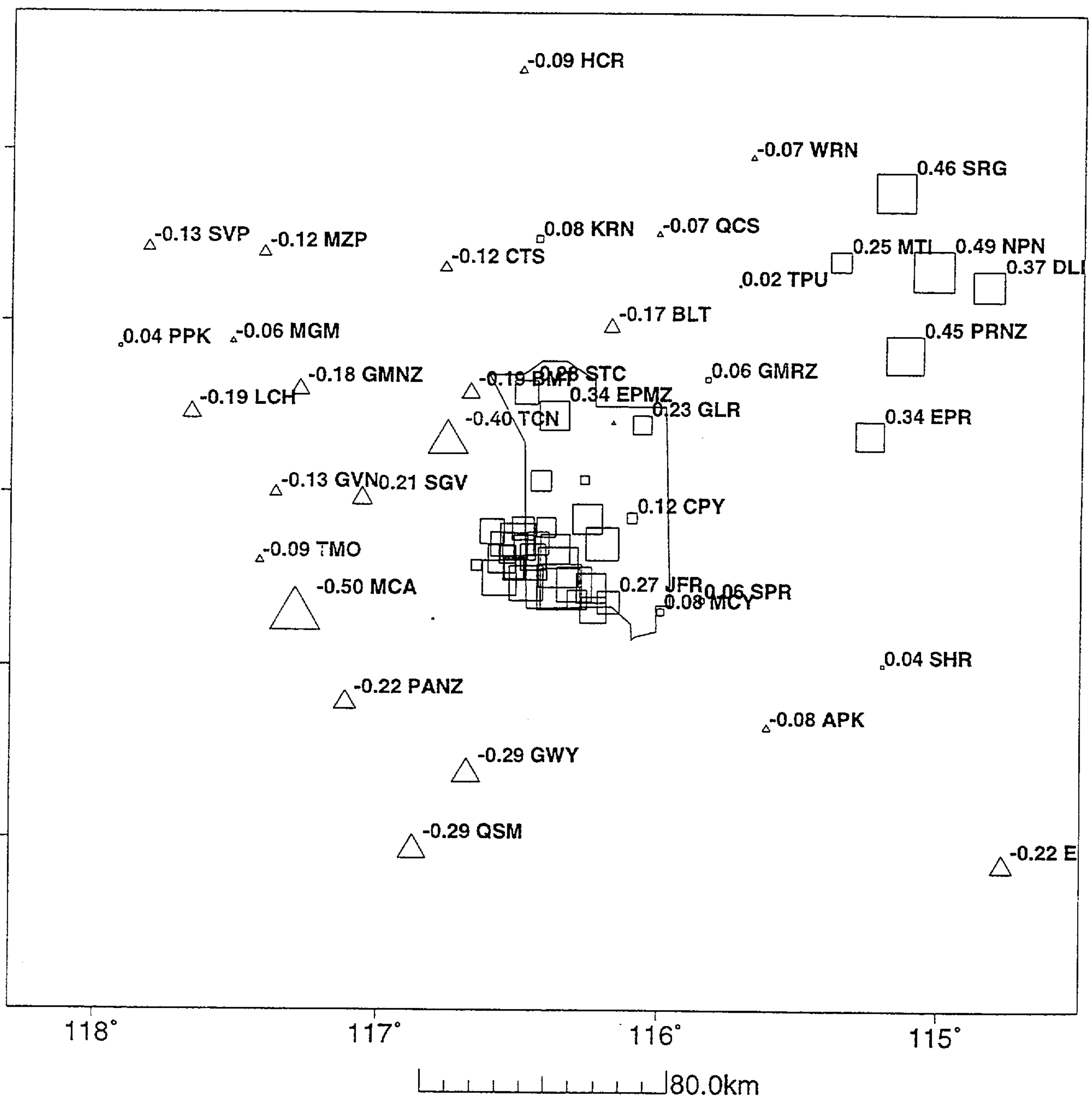

Figure 11a

96:154:03:01:17 p: 6.08 baz: 90.97 sp

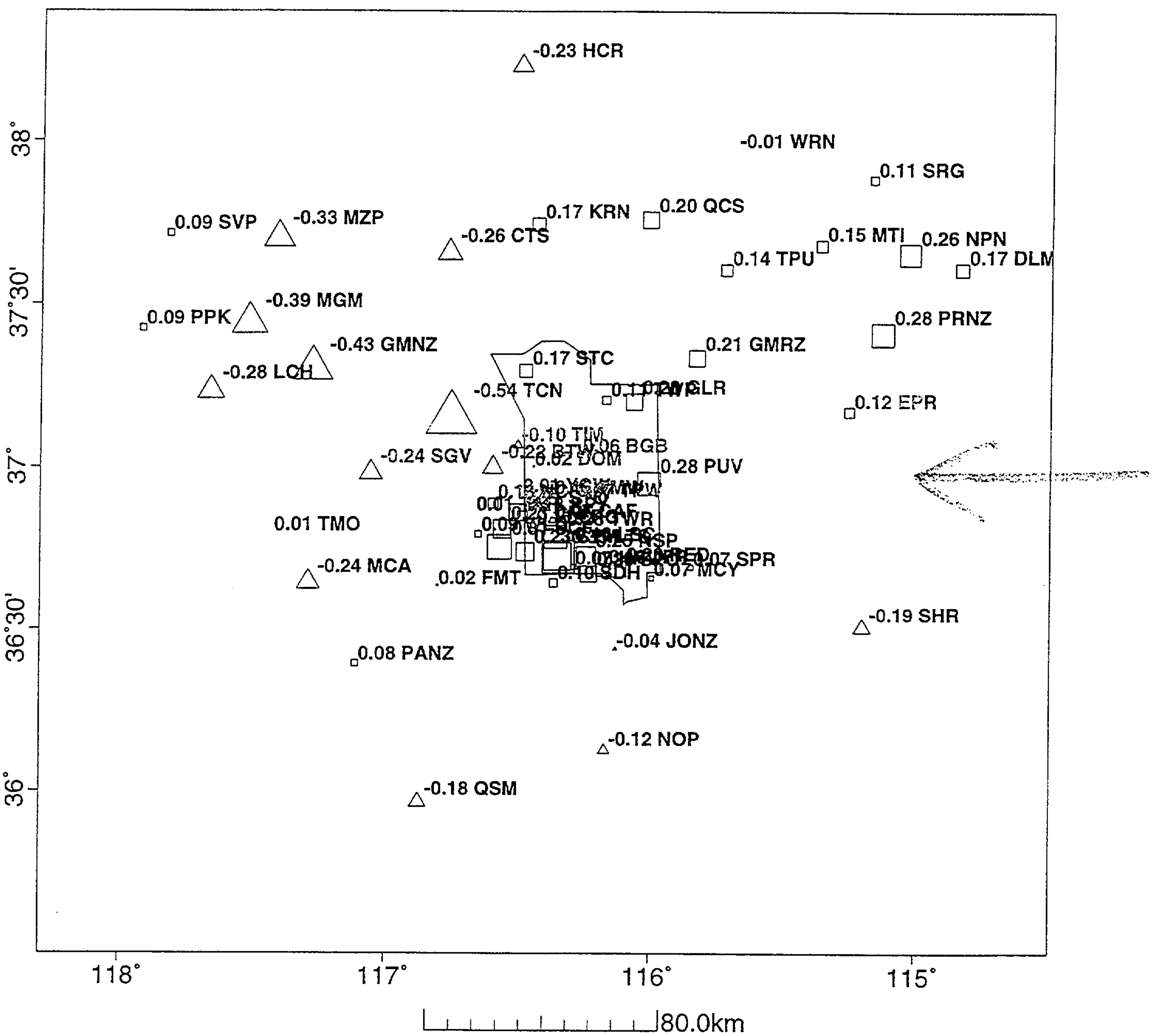

FIGURE 11b

96:186:16:02:45 p: 4.56 baz: 284.37 sp

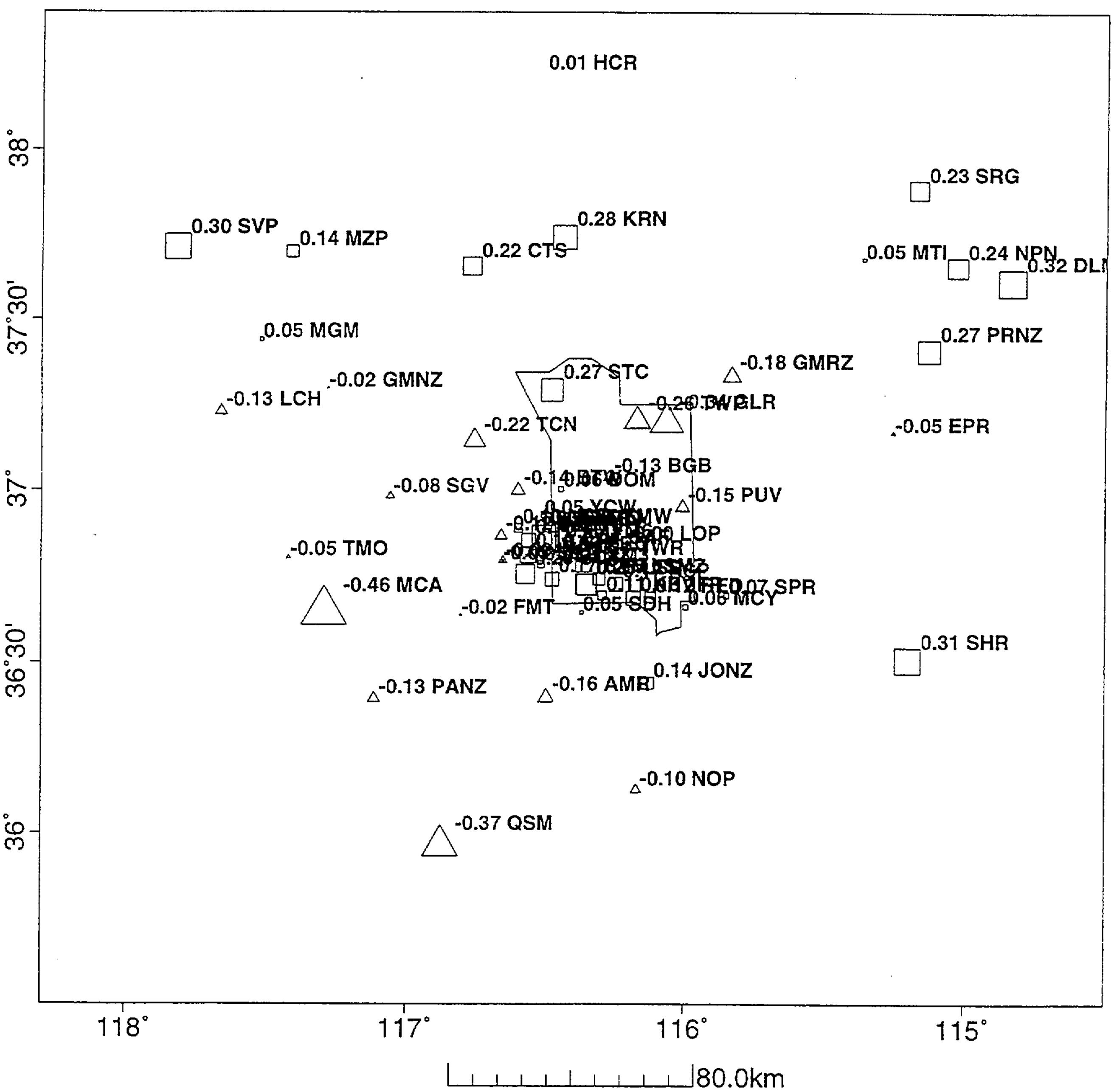

FIGURE 11C

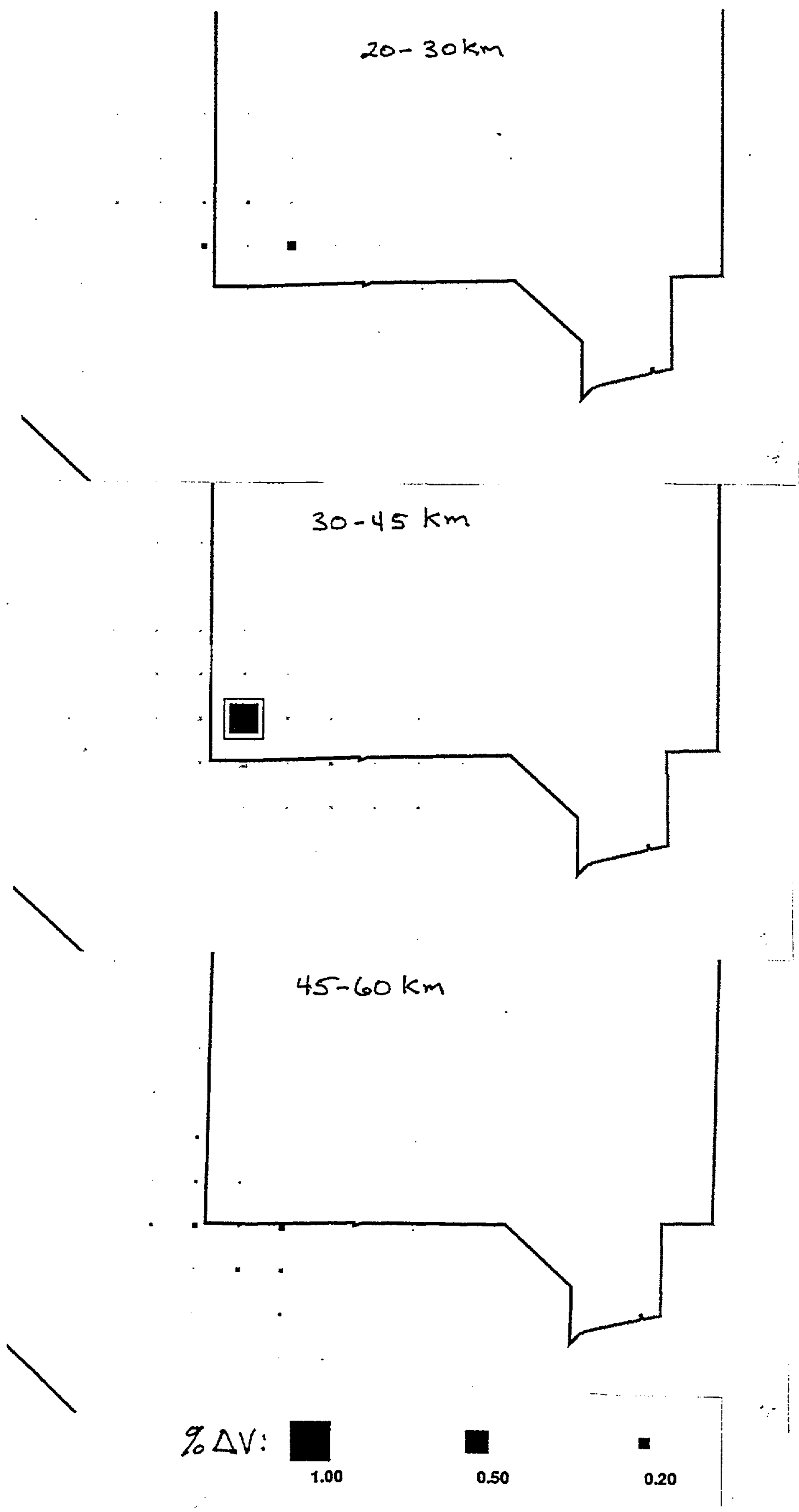

FIGURE 12

ymp_t3.3.11

Layer 2
Slow clip 1.0
Hit clip 0.15
Depth 5.0 - 12.0

20x20 x7 Posts
Basis for Fig Synth_1

numit 12
bincut & thksum 5. - 80.0
synthethic noise levels
Resid: 0.001 Stn: 0.000 Evt: 0.001

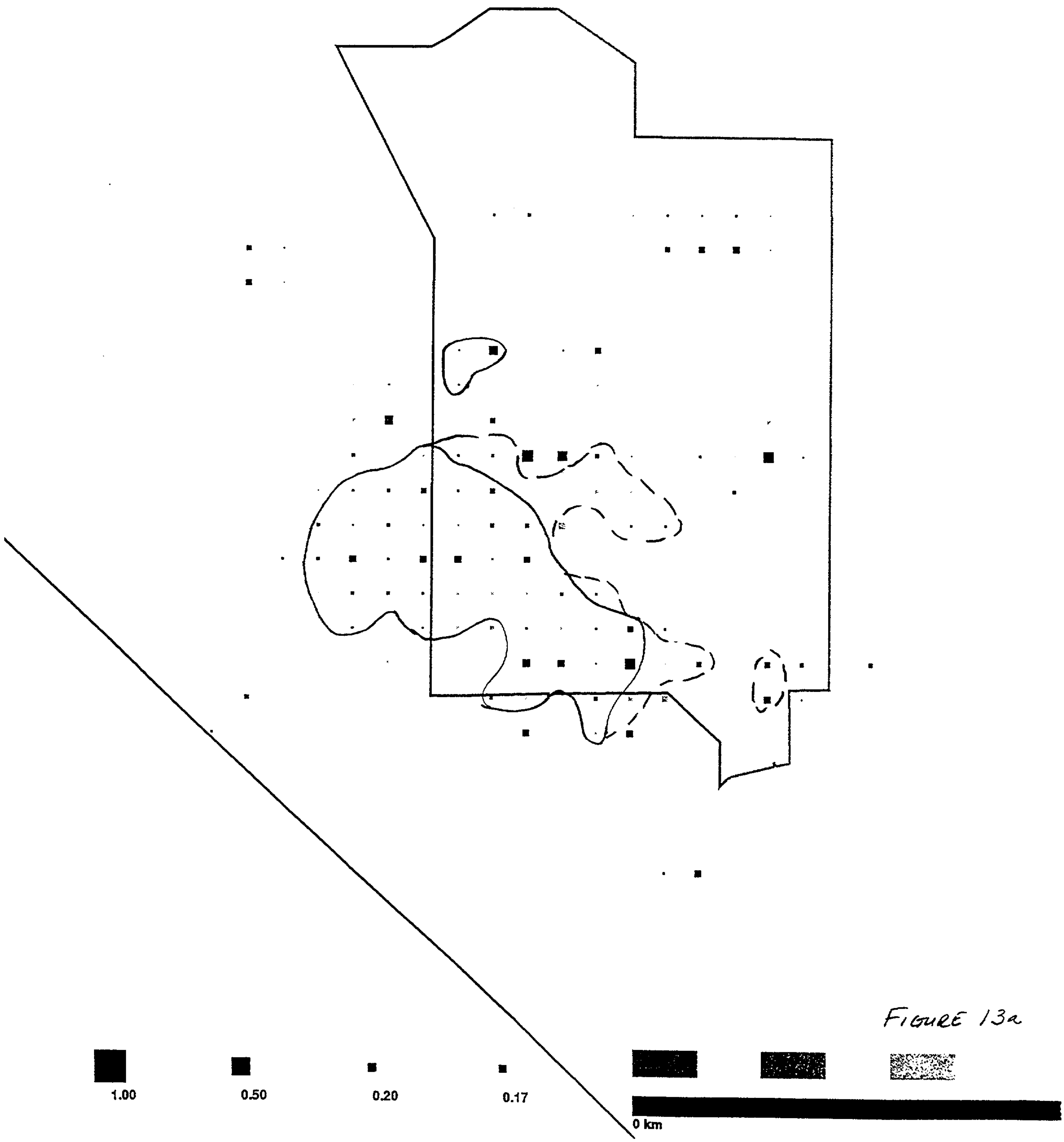

FIGURE 13a

ymp_t3.3.11

Layer 3
Slow clip 1.0
Hit clip 0.15
Depth 12.0 - 20.0

numit 12
bincut & thksum 5. - 80.0
synthethic noise levels
Resid: 0.001 Stn: 0.000 Evt: 0.001

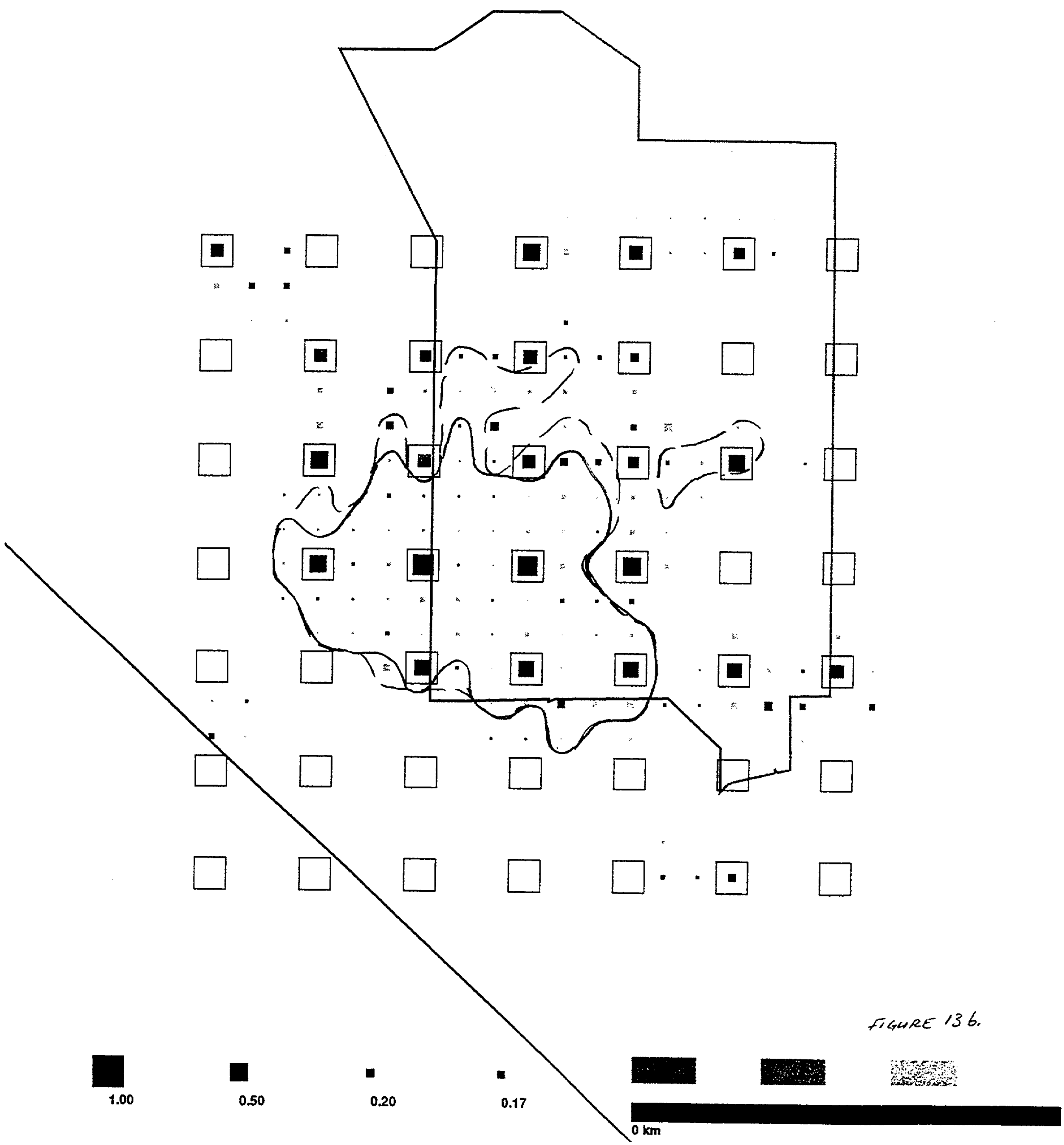

FIGURE 13b.

ymp_t3.3.11

Layer 4
Slow clip 1.0
Hit clip 0.15
Depth 20.0 - 30.0

numit 12
bincut & thksum 5. - 80.0
synthethic noise levels
Resid: 0.001 Stn: 0.000 Evt: 0.001

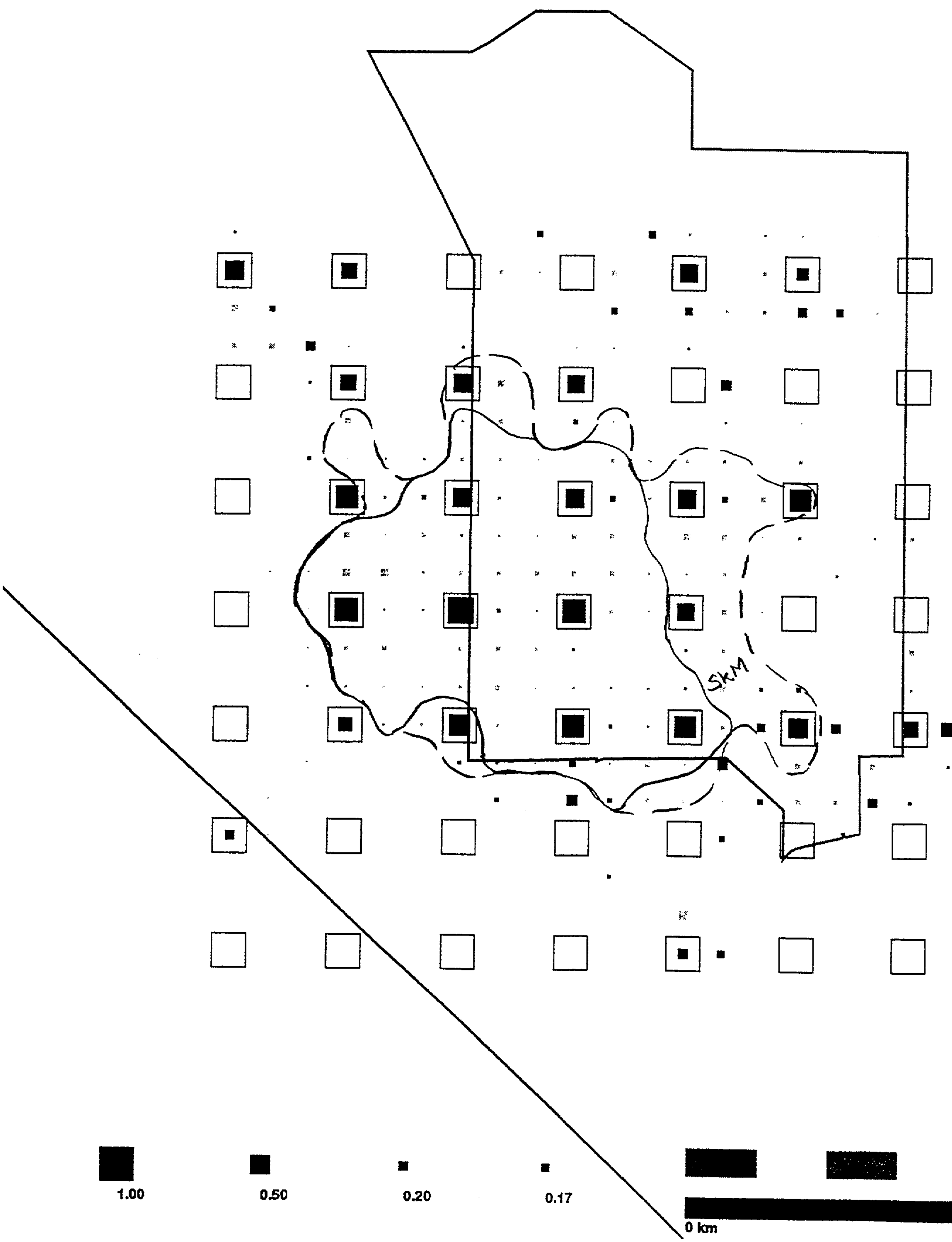

FIGURE 13 C

1.00 0.50 0.20 0.17

0 km

ymp_t3.3.11

Layer 5
Slow clip 1.0
Hit clip 0.15
Depth 30.0 - 45.0

numit 12
bincut & thksum 5. - 80.0
synthethic noise levels
Resid: 0.001   Stn: 0.000   Evt: 0.001

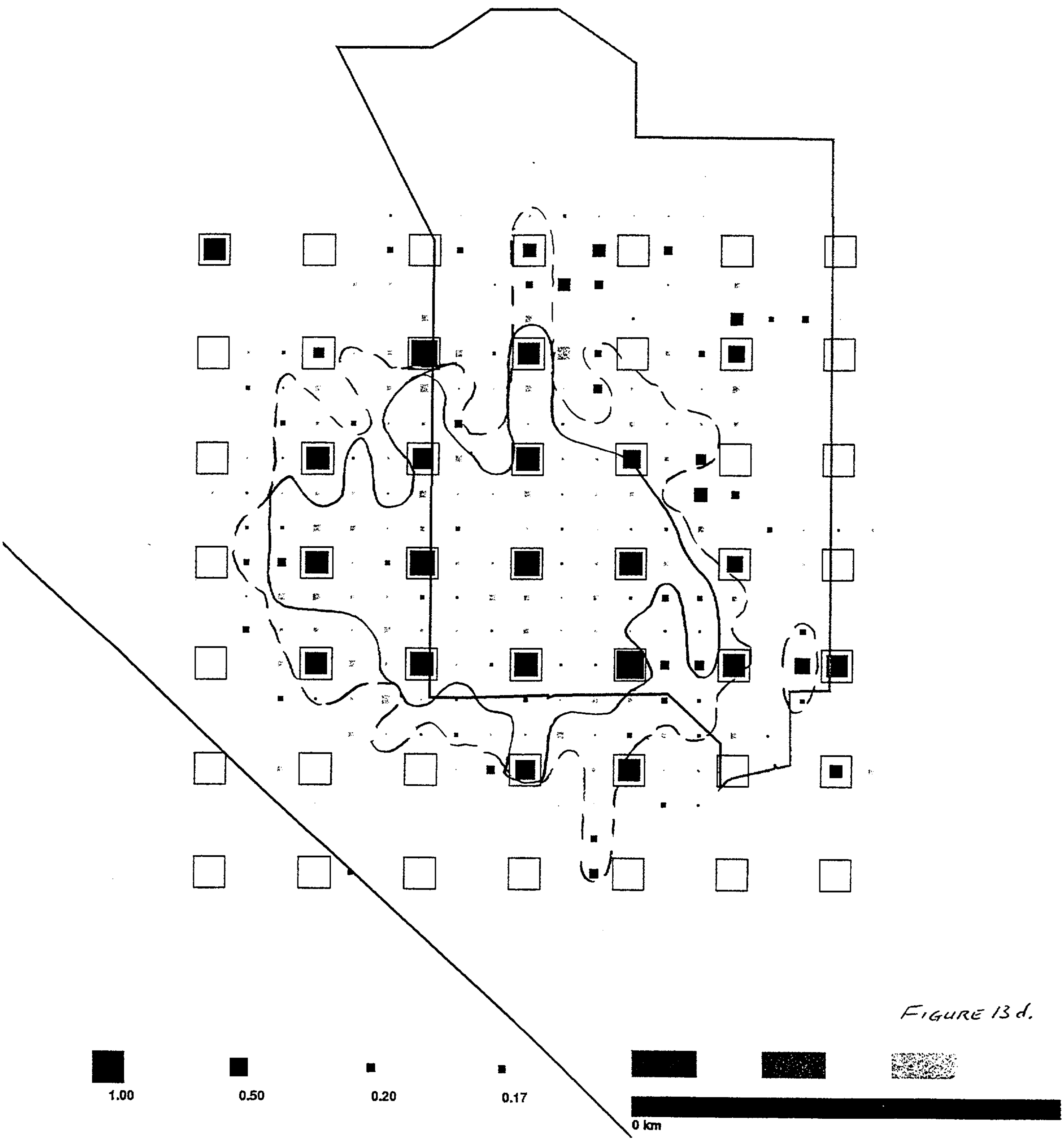

FIGURE 13 d.

ymp_t3.3.11

Layer 6
Slow clip 1.0
Hit clip 0.15
Depth 45.0 - 60.0

numit 12
bincut & thksum 5. - 80.0
synthethic noise levels
Resid: 0.001 Stn: 0.000 Evt: 0.001

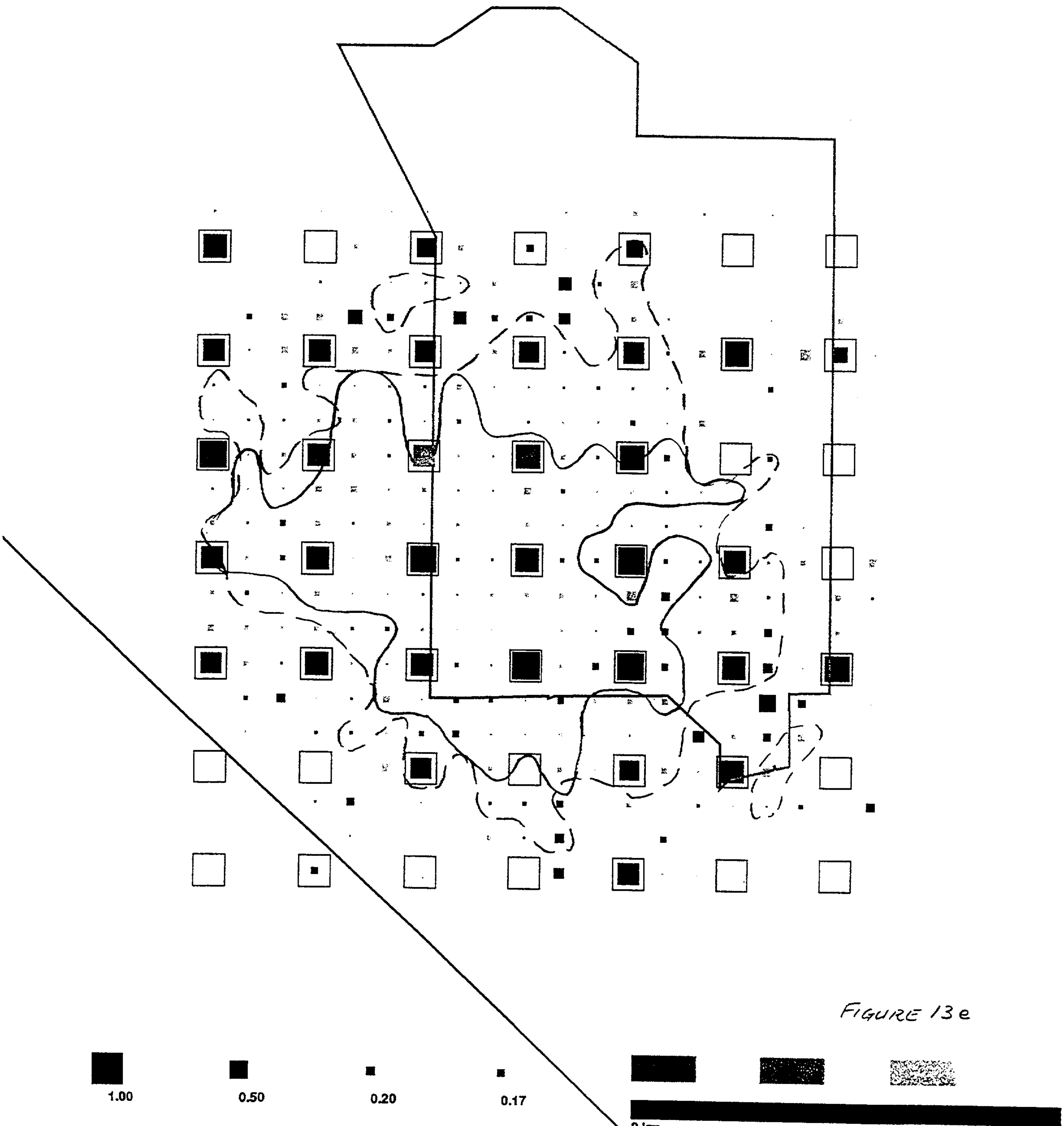

FIGURE 13e

ymp_t3.3.11

Layer 7
Slow clip 1.0
Hit clip 0.15
Depth 60.0 - 80.0

numit 12
bincut & thksum 5. - 80.0
synthethic noise levels
Resid: 0.001 Stn: 0.000 Evt: 0.001

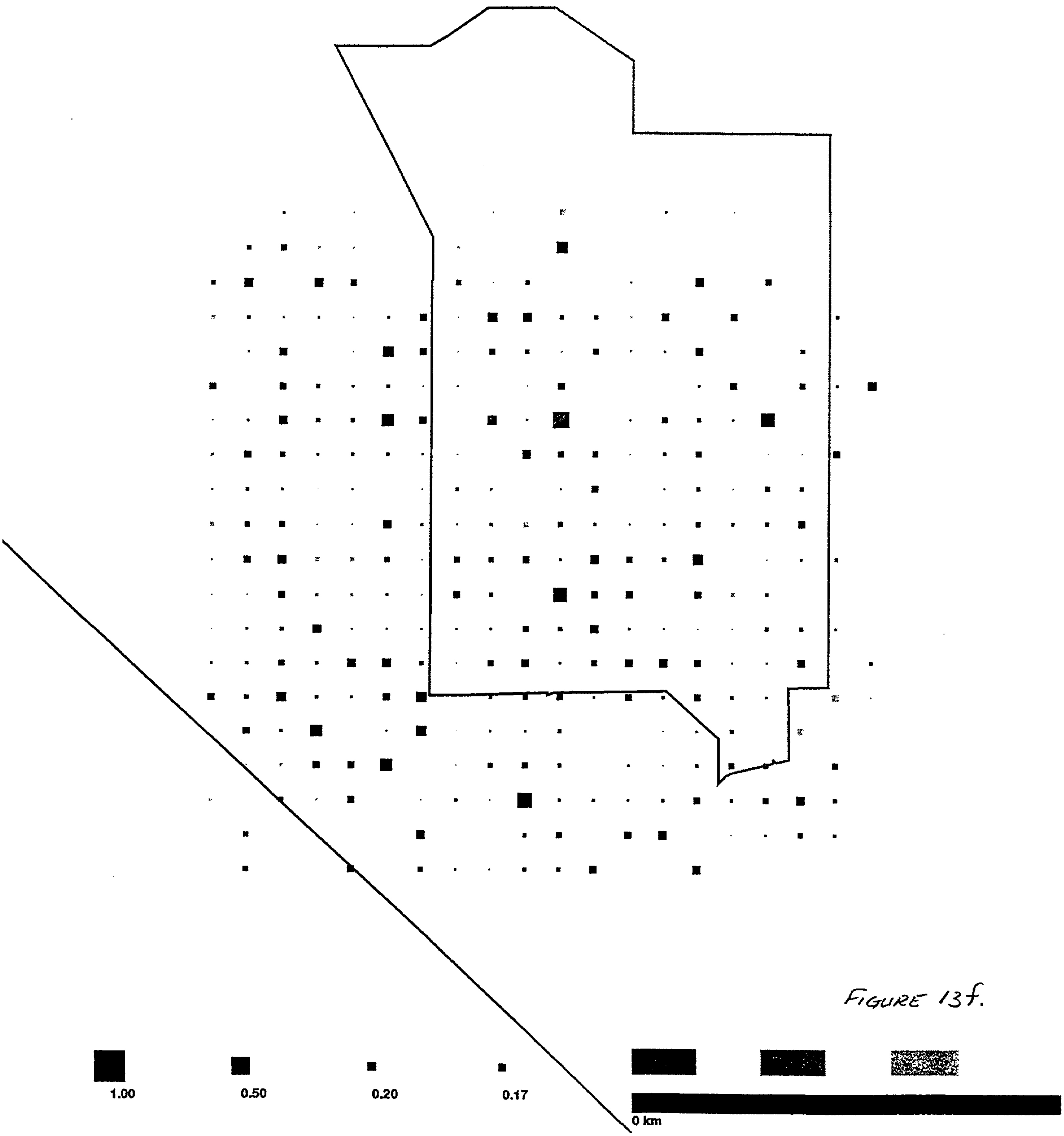

FIGURE 13f.

ymp_t3.3.11

N-S 7
Slow clip 1.0
Hit clip 0.15
Depth 0.0 - 80.0

Basis for Fig Synth_2

numit 12
bincut & thksum 5. - 80.0
synthethic noise levels
Resid: 0.001   Stn: 0.000   Evt: 0.001

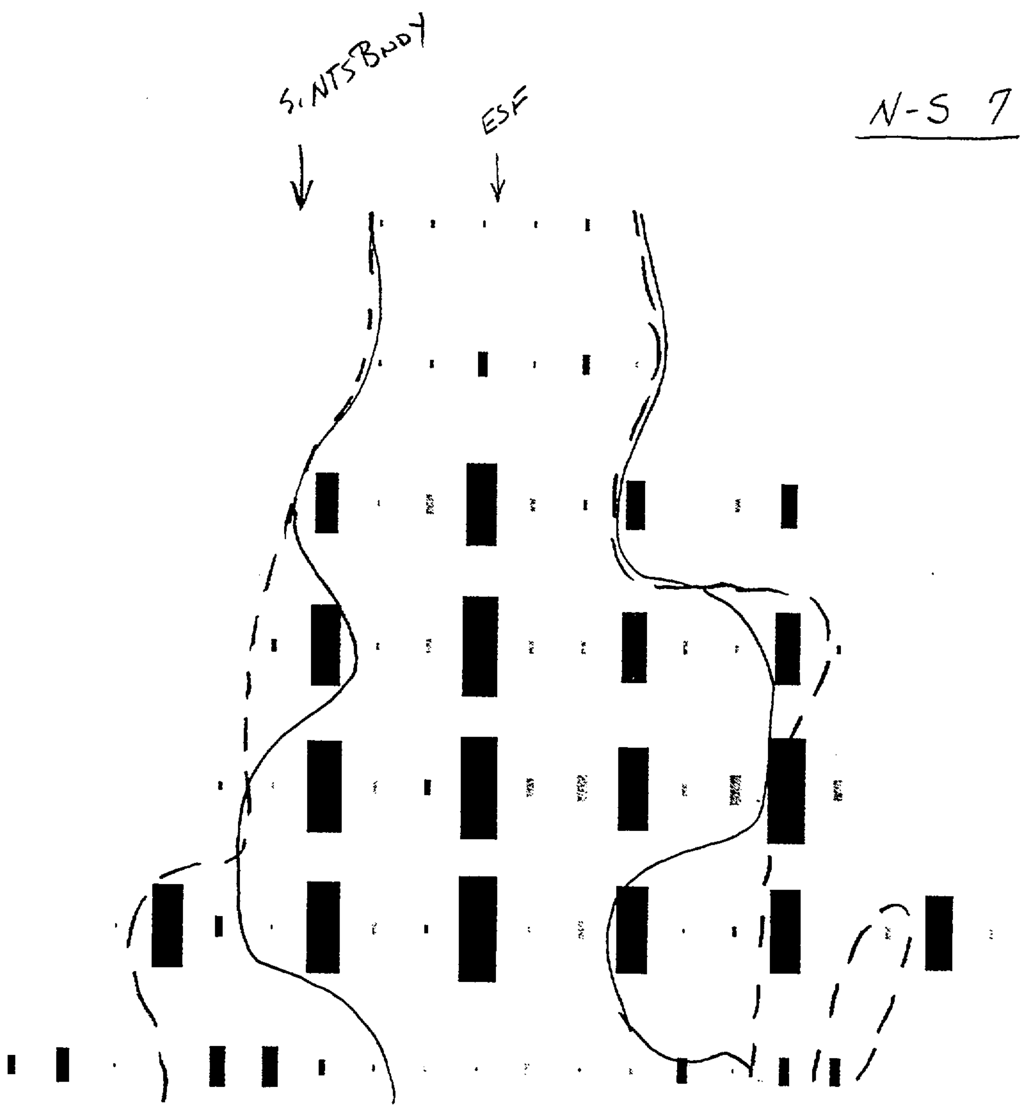

FIGURE 14a

ymp_t3.3.11

N-S 8
Slow clip 1.0
Hit clip 0.15
Depth 0.0 - 80.0

numit 12
bincut & thksum 5. - 80.0
synthethic noise levels
Resid: 0.001   Stn: 0.000   Evt: 0.001

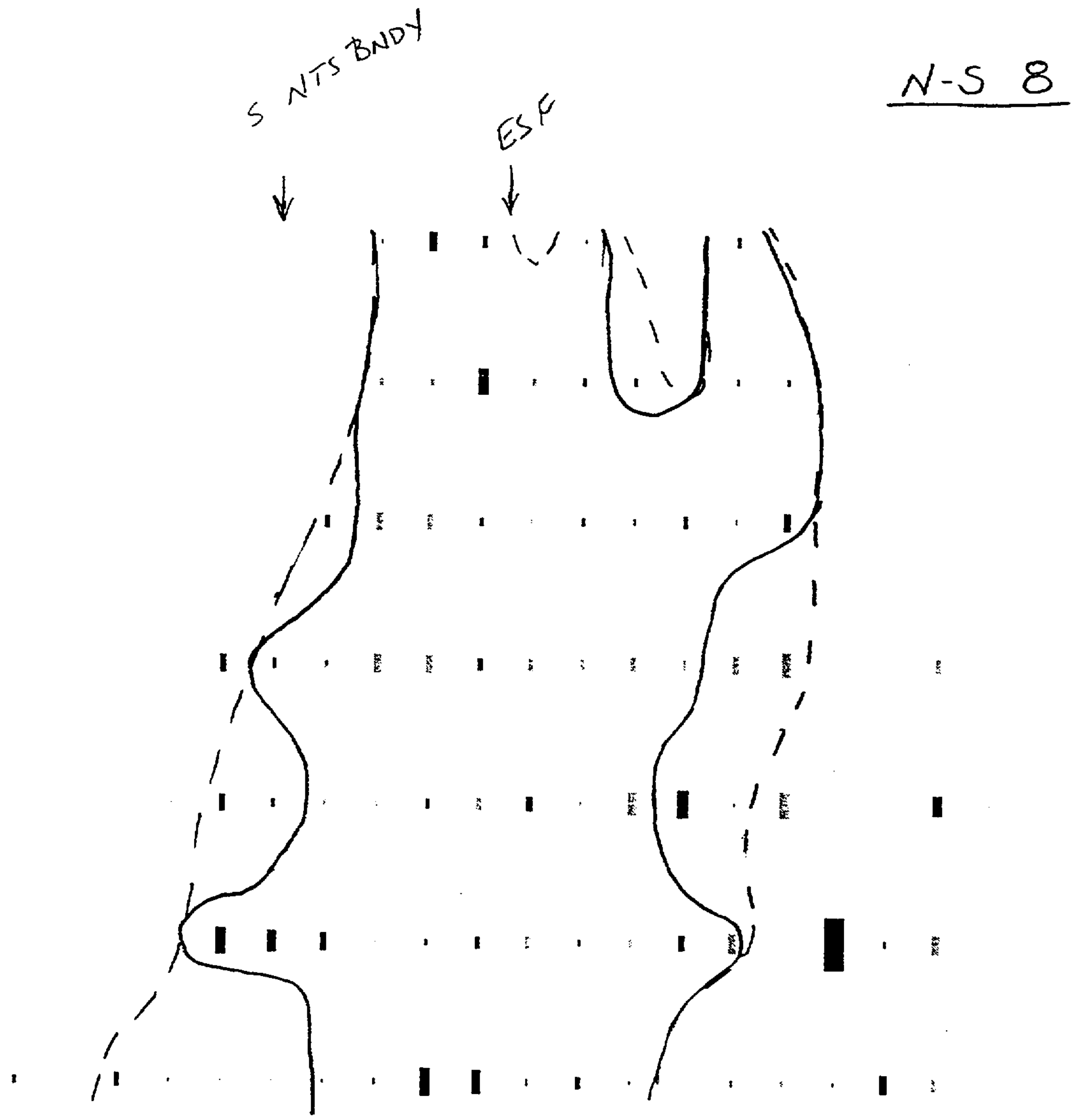

FIGURE 14b

ymp_t3.3.11

N-S 9
Slow clip 1.0
Hit clip 0.15
Depth 0.0 - 80.0

numit 12
bincut & thksum 5. - 80.0
synthethic noise levels
Resid: 0.001 Stn: 0.000 Evt: 0.001

N-S 9

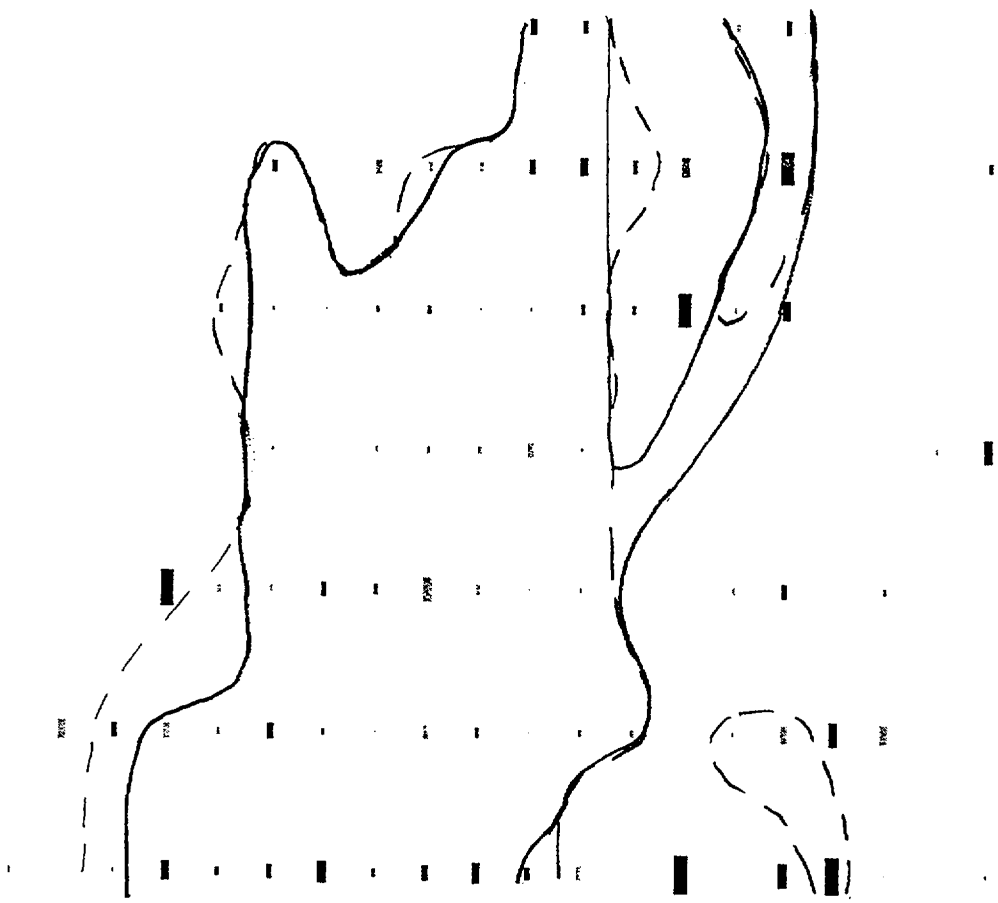

FIGURE 14C

ymp_t3.3.11

N-S 10
Slow clip 1.0
Hit clip 0.15
Depth 0.0 - 80.0

numit 12
bincut & thksum 5. - 80.0
synthethic noise levels
Resid: 0.001   Stn: 0.000   Evt: 0.001

N-S 10

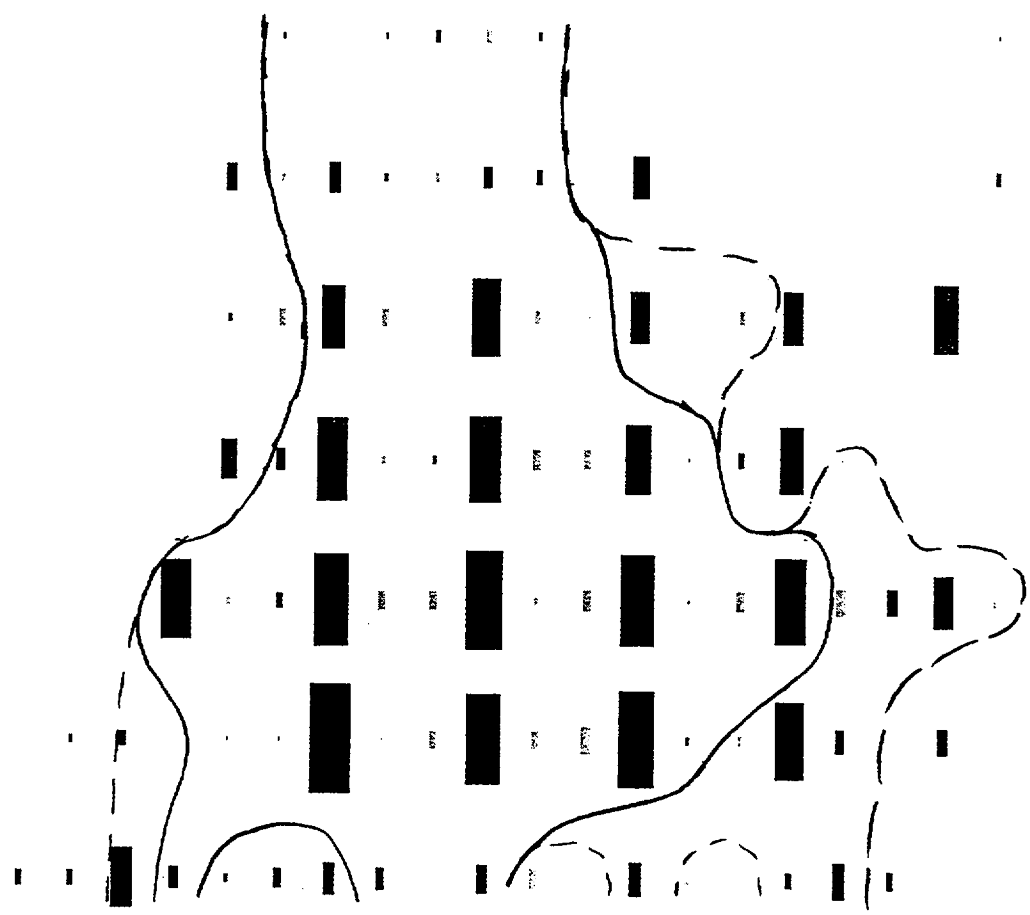

FIGURE 14d

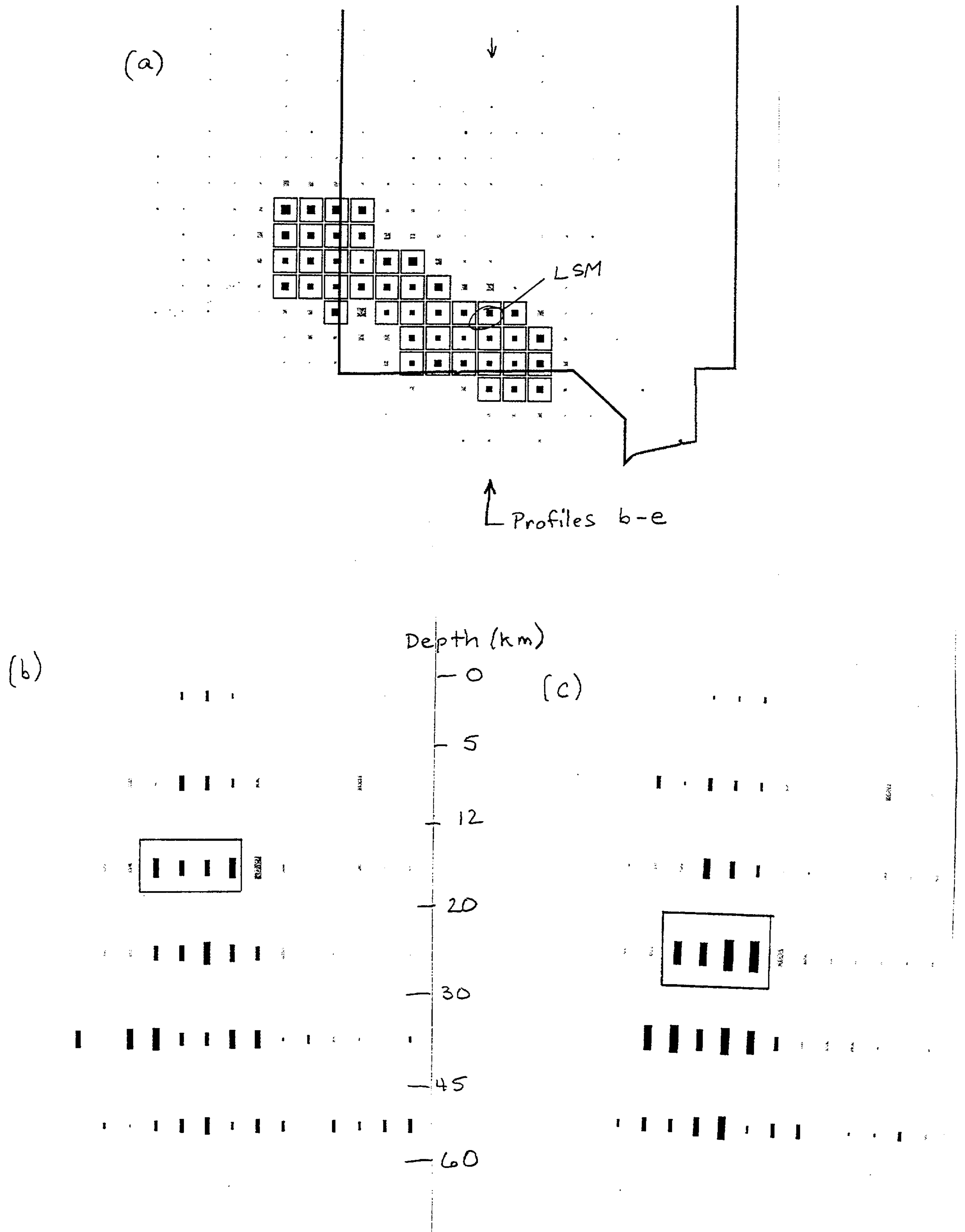

FIGURE 15

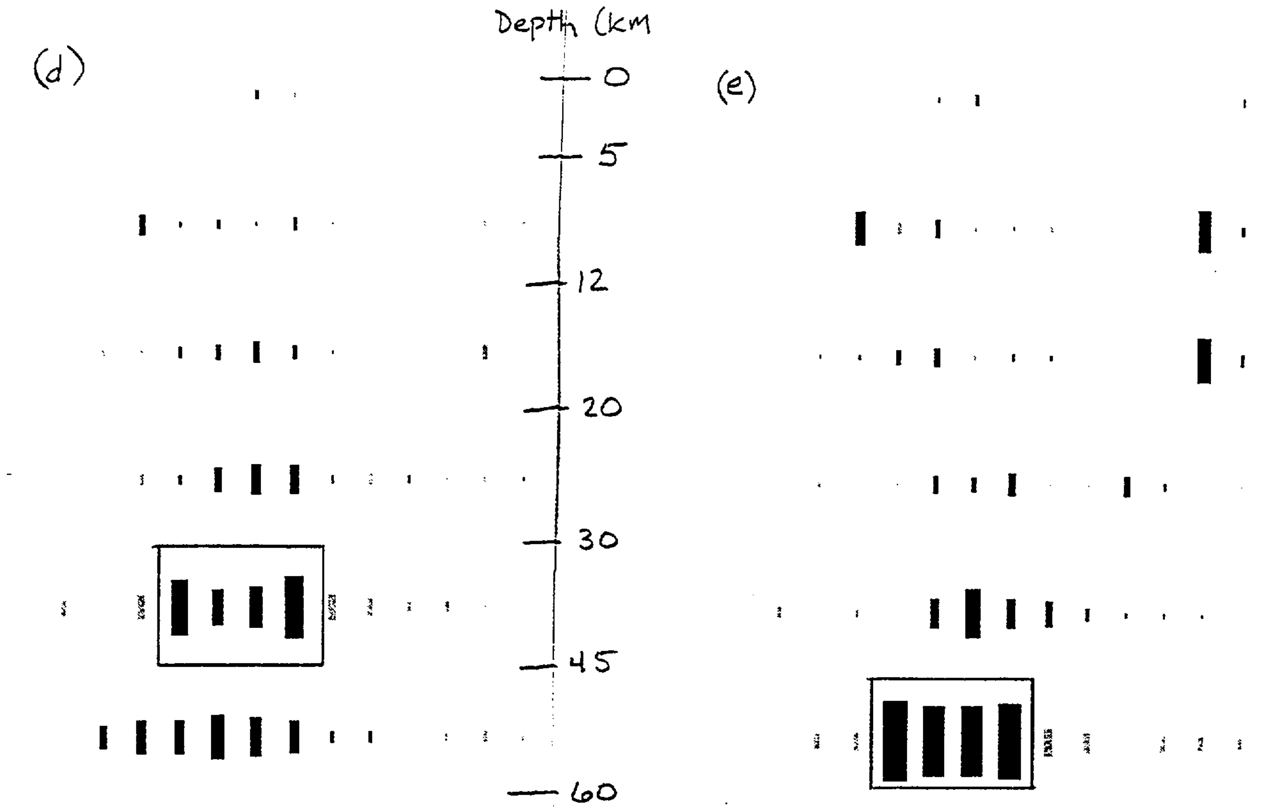

FIGURE 15 (cont)

FIGURE 16

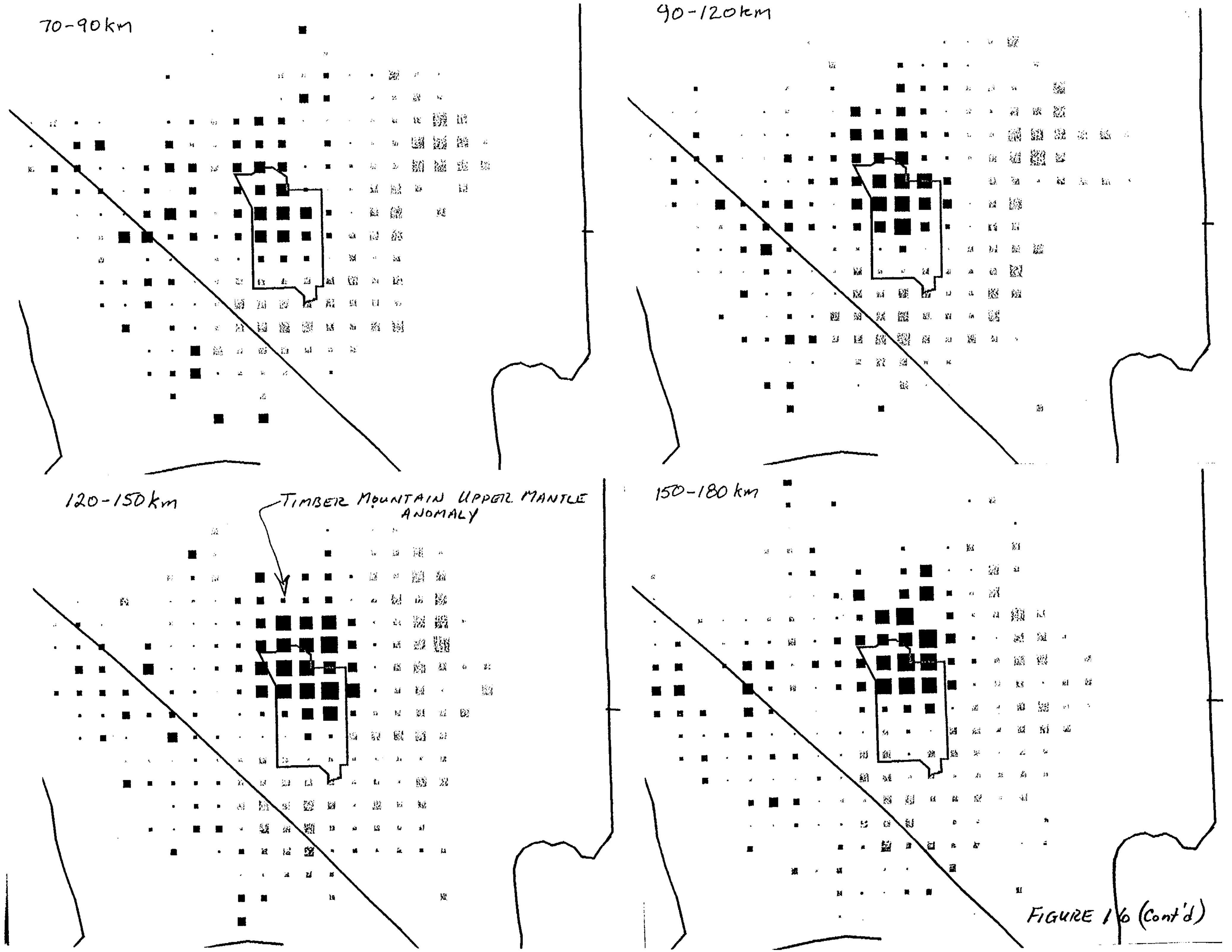

FIGURE 16 (Cont'd)

FIGURE 16 (cont)

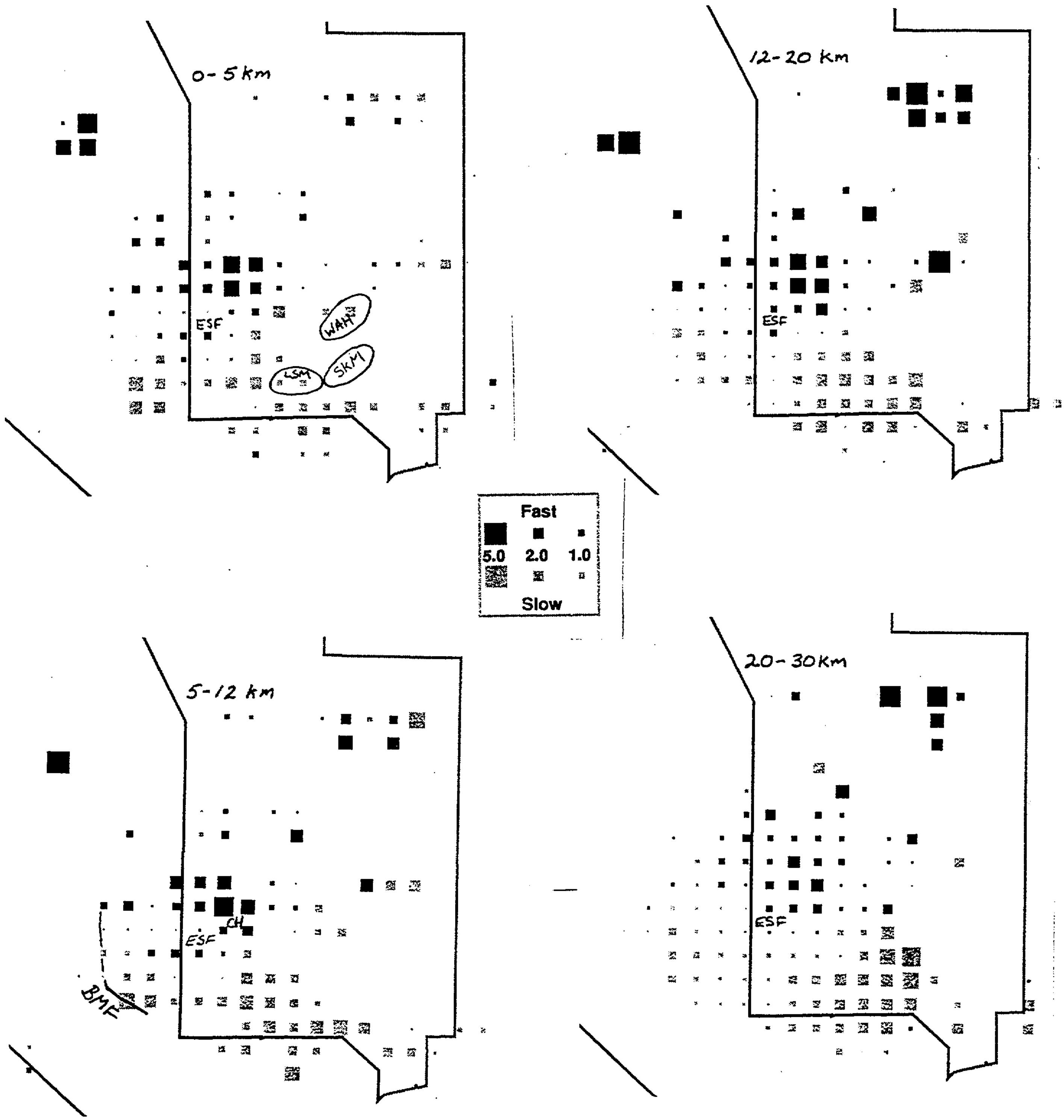
0-5 km
ESF
WAH
SKM
LSM
12-20 Km
ESF
Fast
5.0
2.0
1.0
Slow
5-12 km
ESF
CH
BMF
20-30Km
ESF

FIGURE 17

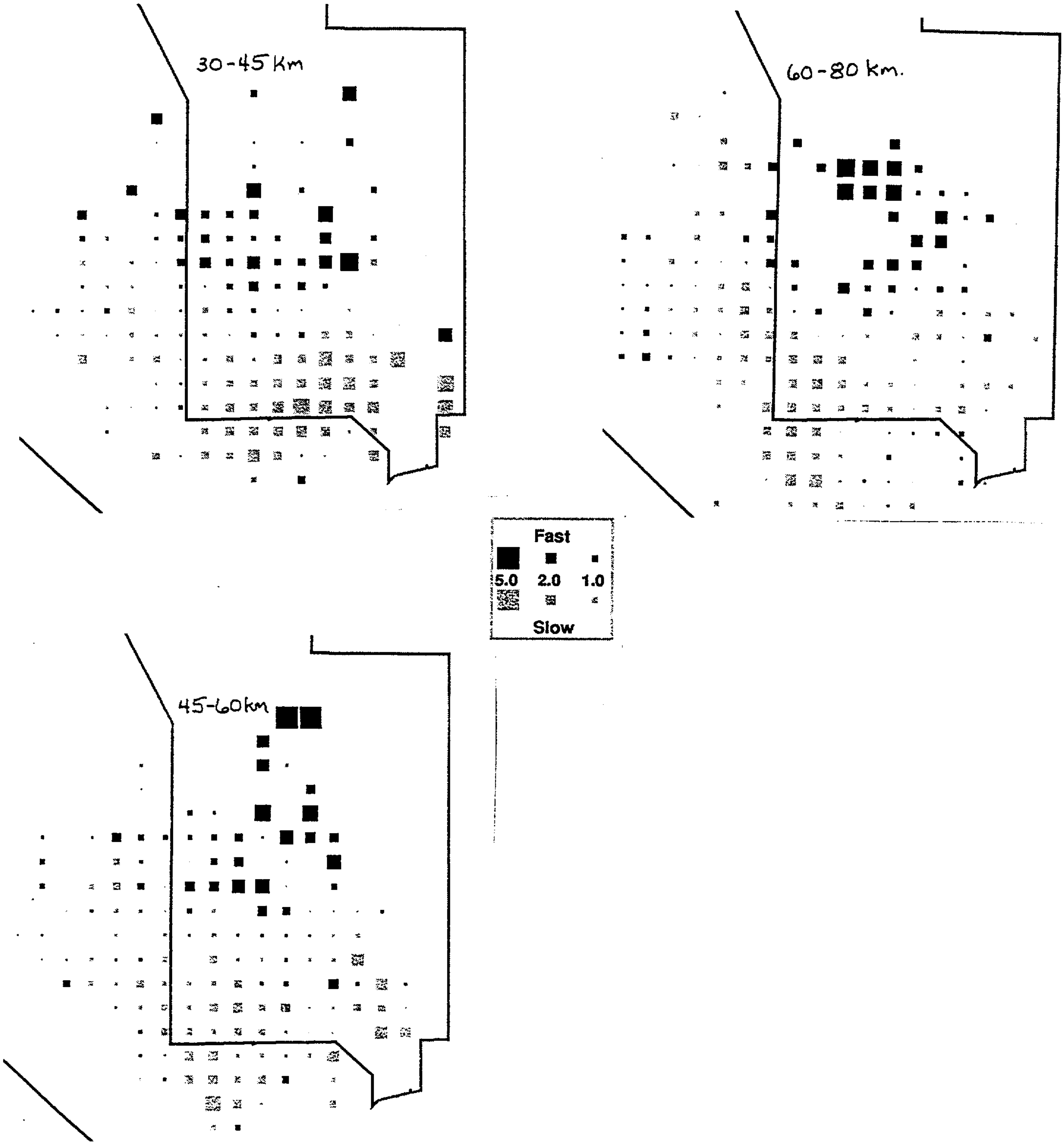

FIGURE 17 (Cont'd)

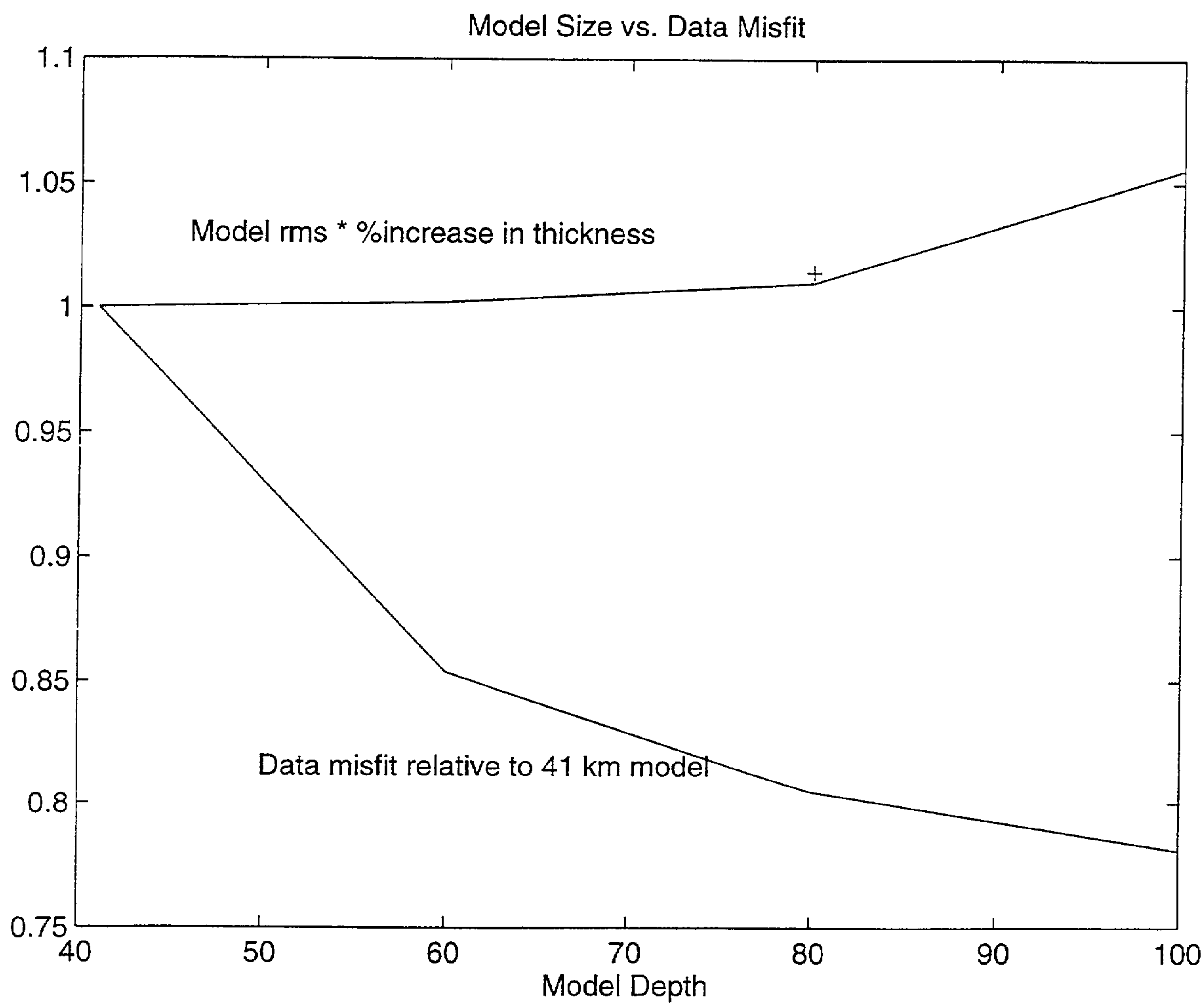
Model Size vs. Data Misfit
1.1
1.05
1
0.95
0.9
0.85
0.8
0.75
Model rms * %increase in thickness
Data misfit relative to 41 km model
40
50
60
70
80
90
100
Model Depth

FIGURE 18

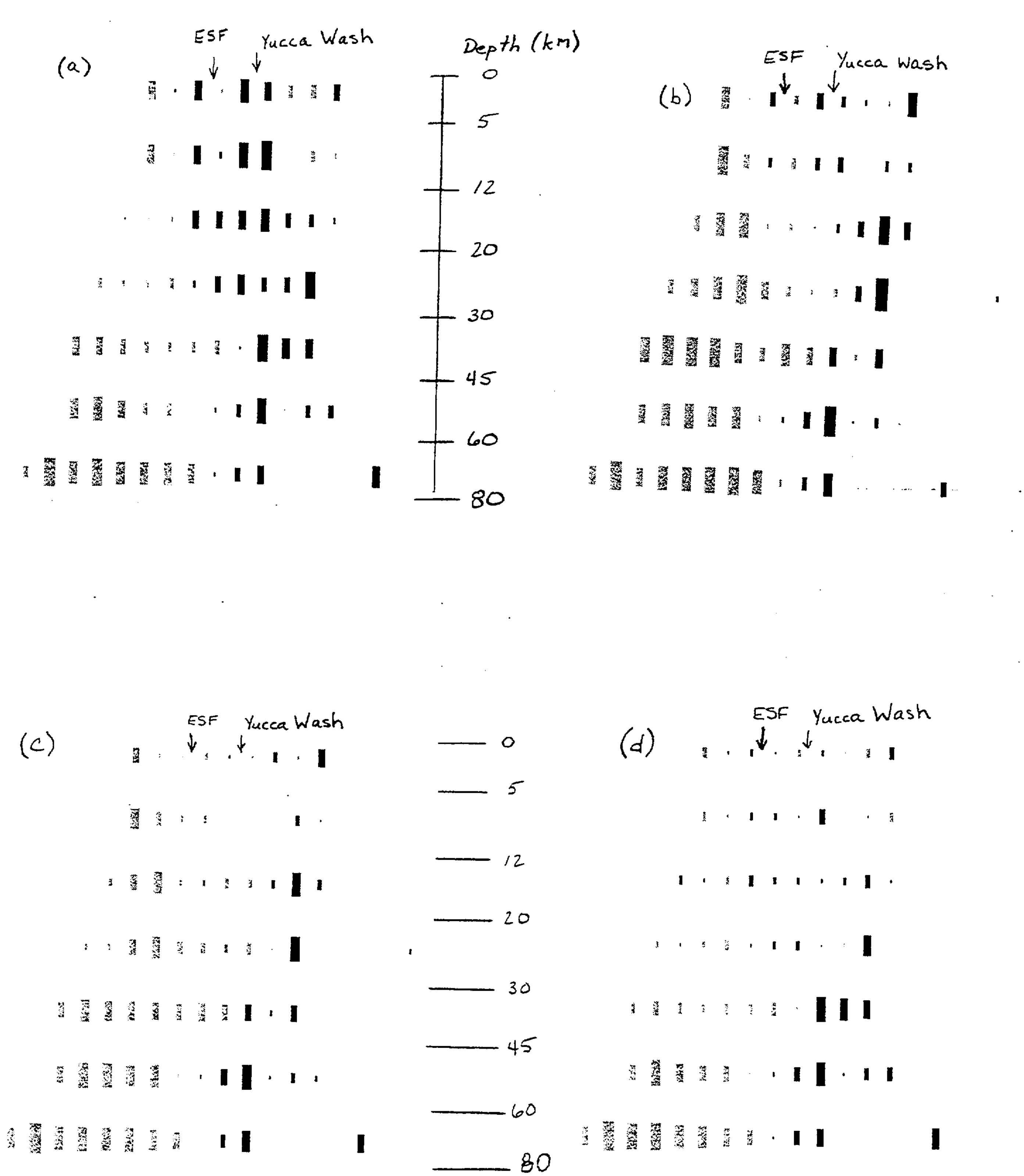

FIGURE 19
N.S-8

1 Picked with analog and digital arrays together

2	95	196:01:45:37	900	80.5	236.6	013514.6	19.900S	177.547W	358y	5.5	0.0	0.0	999	
3	95	196:11:03:31	900	62.8	18.6	105417.7	71.837N	1.494W	10y	5.4	4.9	0.0	999	
4	95	205:19:21:51	1800	56.0	0.0	191321.5	55.626N	35.059W	10G	5.4	5.2	0.9	198	NORTH ATLANTIC OCEAN
5	95	206:15:22:19	2400	71.9	0.0	151326.5	10.669N	41.196W	10G	5.5	5.5	0.9	159	NORTHERN MID-ATLANTIC RIDGE. Mw
6	95	208:06:08:36	2400	152.2	0.0	055118.2	12.608S	79.233E	10G	6.2	6.0	0.6	88	S INDIAN OCEAN.
7	95	226:03:39:04	1800	120.8	141.8	082144.0	57.896S	25.584W	33N	5.3	4.7	0.8	64	SOUTH SANDWICH ISLANDS REGION
8	95	228:10:38:07	7200	92.9	264.9	102729.0	5.320S	154.194E	33N	6.5	7.8	1.2	221	SOLOMON ISLANDS.
9	95	228:15:13:46	1800	91.0	230.1	150401.5*	31.707S	179.098E	462y	5.8	5.8	0.7	71	KERMADEC ISLANDS REGION
10	95	228:23:21:02	7200	92.9	0.0	231028.0	5.719S	154.128E	71D	6.4	7.2	0.8	85	SOLOMON ISLANDS.
11	95	228:23:56:49	900	48.9	0.0	235037.2	50.632N	176.125E	33y	5.3	5.3	0.8	64	RAT ISLANDS, ALEUTIAN ISLANDS
12	95	229:00:26:33	3600	93.1	0.0	001553.0*	5.852S	153.961E	33N	6.1	6.6	1.0	54	NEW IRELAND REGION
13	95	229:18:20:39	900	93.1	0.0	180959.2*	5.874S	154.035E	33N	5.4	5.6	0.8	36	SOLOMON ISLANDS
14	95	231:21:40:20	900	92.8	0.0	212821.3*	4.952S	153.650E	86y	5.3	5.3	0.8	39	NEW IRELAND REGION
15	95	233:07:53:47	900	60.9	0.0	074604.5*	24.884N	45.388W	10G	4.8	4.6	0.8	35	N. MID-ATLANTIC RIDGE
16	95	235:13:25:38	3600	95.6	0.0	131443.1*	56.738S	141.085W	10G	5.8	5.5	1.0	25	PACIFIC-ANTARCTIC RIDGE.
17	95	236:02:04:40	1800	85.4	0.0	015534.5	18.970N	144.914E	588y	5.7	5.7	0.7	86	MARIANA ISLANDS.
18	95	239:18:09:40	1200	154.3	126.0	175059.6*	47.909S	31.952E	10G	5.3	4.7	0.7	11	SOUTH OF AFRICA
19	95	244:05:27:13	900	63.6	133.5	051804.5*	13.323S	74.613W	109y	5.1	5.1	0.8	56	CENTRAL PERU
20	95	244:06:47:45	1800	113.8	289.1	063040.8	0.028S	123.285E	191y	5.2	5.2	1.0	69	MINAHASSA PENINSULA, SULAWESI
21	95	246:01:23:56	300	82.5	308.2	011325.1?	34.730N	134.990E	374y	4.4	4.4	0.8	28	NEAR S. COAST OF WESTERN HONSHU
22	95	246:16:11:35	1200	38.2	154.9	160526.4*	1.055N	101.278W	10y	5.1	5.1	0.9	49	E. PACIFIC OCEAN
23	95	251:00:39:52	3600	92.9	183.1	002749.2*	56.215S	122.029W	10G	5.0	5.7	1.0	18	S. EAST PACIFIC RISE.
24	95	251:01:27:31	3600	92.9	183.2	011528.7*	56.188S	122.252W	10G	5.4	6.3	1.0	28	S. EAST PACIFIC RISE.
25	95	254:04:29:02	1800	38.3	155.0	042252.6	0.989N	101.339W	10G	5.2	4.7	0.8	74	E. PACIFIC OCEAN
26	95	255:12:54:54	300	83.2	236.6	124440.9	21.602S	179.574W	601y	4.6	4.6	0.6	30	FIJI ISLANDS REGION
27	95	257:12:34:37	900	80.0	239.6	122434.6	17.289S	179.275W	533y	5.2	5.2	0.5	80	FIJI ISLANDS REGION
28	95	260:07:36:38	3600	82.2	146.3	072530.7	35.540S	74.038W	33N	5.8	4.8	0.8	110	COAST CENTRAL CHILE
29	95	260:19:35:11	1800	90.0	243.8	192322.0?	20.77 S	169.85 E	33N	5.0	4.6	1.2	12	VANUATU ISLANDS
30	95	262:03:42:03	1800	72.7	133.6	033157.1?	20.560S	68.880W	108y	5.9	5.9	0.7	90	CHILE-BOLIVIA BORDER REGION.
31	95	264:20:40:13	900	46.4	326.8	203257.3*	63.826N	179.366E	10y	4.9	4.9	0.8	50	EASTERN SIBERIA
32	95	265:09:09:38	1800	124.5	57.5	085149.5*	1.035N	19.475E	10G	5.2	5.0	1.2	12	ZAIRE
33	95	266:16:23:46	6000	131.8	299.9	160547.1*	5.651S	103.985E	33N	5.7	5.7	1.2	12	S. SUMATERA, INDONESIA
34	95	266:22:40:40	3600	59.4	135.0	223156.0	10.639S	78.242W	70y	6.3	6.3	0.8	99	COAST OF PERU
35	95	269:22:43:47	900	85.2	232.0	223238.5*	26.329S	177.620W	165y	5.0	5.0	0.8	44	S. FIJI ISLANDS
36	95	273:10:26:21	900	90.4	33.4	101434.2	41.777N	15.901E	33N	5.3	5.2	0.8	102	S. ITALY.
37	95	273:10:56:51	3600	60.3	313.3	104756.3	50.703N	157.406E	33N	5.8	5.5	0.8	156	KURIL ISLANDS
38	95	274:13:01:10	900	80.2	141.8	125015.4	31.356S	71.023W	65y	5.4	5.4	0.9	65	COAST CENTRAL CHILE.
39	95	274:17:16:33	1800	83.3	301.8	170602.8	29.287N	139.020E	425y	5.5	5.5	0.9	185	S. OF HONSHU, JAPAN.
40	95	274:23:39:15	900	62.5	203.3	232957.8	22.287S	138.788W	0y	5.5	5.5	0.6	82	TUAMOTU ARCHIPELAGO
41	95	275:01:43:07	900	47.0	331.1	013546.5	67.058N	178.614E	10G	5.3	4.8	0.7	76	E. SIBERIA
42	95	276:01:59:30	7200	53.3	128.9	015125.1	2.705S	77.862W	33N	6.4	6.9	0.8	136	PERU-ECUADOR BORDER
43	95	279:11:50:09	1800	79.6	235.6	113936.4	19.786S	176.071W	209y	5.5	5.5	0.6	85	FIJI ISLANDS REGION.
44	95	284:00:44:00	900	64.1	62.8	003436.9	36.211N	33.974W	10y	5.0	5.0	0.8	31	AZORES ISLANDS REGION
45	95	285:23:07:31	900	73.9	136.2	225710.1*	23.042S	70.278W	33N	5.3	4.9	1.2	52	N. CHILE
46	95	285:23:52:02	900	72.5	170.9	234146	35.180S	105.870W	10Q	5.6	5.6	0.0	000	E. PACIFIC RISE
47	95	291:10:49:12	7200	90.0	305.7	103726.3	27.934N	130.350E	27G	6.5	6.9	1.2	297	RYUKYU ISLANDS.
48	95	292:00:43:51	3600	89.7	306.1	003203.8	28.396N	130.268E	10G	5.9	6.4	0.9	89	RYUKYU ISLANDS.
49	95	293:08:00:44	900	79.6	315.8	074931.3	42.366N	131.612E	514y	4.8	4.8	0.7	63	E. RUSSIA-N.E. CHINA BORDER
50	95	298:14:03:38	1800	118.1	282.7	134713.8*	7.151S	123.642E	656y	5.3	5.3	1.3	18	BANDA SEA
51	95	300:22:09:10	3600	62.3	203.8	215957.8	21.916S	139.145W	0y	5.5	5.5	0.6	69	TUAMOTU ARCHIPELAGO
52	95	302:19:51:10	3600	83.2	236.7	194056.4	21.567S	179.672W	600y	5.5	5.5	0.7	90	FIJI ISLANDS REGION
53	95	303:20:32:09	3600	42.3	310.0	202529.4	52.029N	173.373W	33N	5.6	5.3	1.0	97	ANDREANOF ISLANDS
54	95	305:00:46:18	3600	78.0	140.7	003532.4	28.943S	71.390W	20G	6.3	6.4	1.1	181	CENTRAL CHILE.
55	95	305:01:22:55	900	78.0	140.4	011210.5	28.768S	71.184W	33y	5.3	5.3	0.8	49	CENTRAL CHILE
56	95	306:16:20:34	3600	91.0	258.9	160844.3*	9.529S	159.395E	33N	5.5	5.6	0.7	51	SOLOMON ISLANDS
57	95	309:09:32:23	900	52.9	130.6	092428.3	3.235S	79.171W	91y	5.1	5.1	1.2	79	COAST ECUADOR
58	95	310:04:49:16	900	118.1	139.8	043143.5*	55.267S	28.930W	33N	5.4	5.2	1.1	18	S SANDWICH ISL.
59	95	318:04:13:58	3600	96.0	267.1	040146.2	5.853S	150.422E	33N	5.6	5.3	0.6	49	NEW BRITAIN REGION
60	95	318:16:27:36	900	58.5	45.2	161852	52.540N	32.250W	23Q	4.9	4.9	0.0	000	N. ATLANTIC OCEAN
61	95	318:17:20:14	900	86.1	306.8	170805.0?	31.340N	132.850E	33y	5.2	5.2	0.8	45	SE OF SHIKOKU, JAPAN
62	95	329:04:23:33	1800	147.6	82.9	040501	26.760S	26.920E	5Q	5.1	5.1	0.0	000	SOUTH AFRICA
63	95	330:14:05:11	900	79.9	137.7	135426.5	28.653S	67.412W	127y	5.0	5.0	0.9	37	LA RIOJA PROVINCE, ARGENTINA
64	95	331:05:34:47	900	73.8	136.1	052427.0	22.869S	70.215W	35*	5.3	4.6	1.1	61	NORTHERN CHILE.
65	95	334:15:19:10	3600	70.3	311.0	150922.8	44.142N	145.673E	145y	6.0	6.0	0.8	184	HOKKAIDO, JAPAN
66	95	335:05:25:15	3600	28.8	153.8	052028.5	10.139N	104.048W	10G	5.6	6.2	1.0	111	MEXICO.
67	95	336:19:33:00	120	74.8	91.1	192140.2*	8.137N	39.460W	10y	5.2	5.2	1.2	26	CENTRAL MID-ATLANTIC
68	95	342:07:50:31	900	63.2	17.0	074113.5	72.581N	2.993E	10G	5.2	5.2	1.1	67	NORWEGIAN SEA
69	96	115:19:03:11	900	44.0	101.0	185622	18.81 N	70.39 W	79Q	5.2	5.2	0.0	000	DOMINICAN REPUBLIC REGION
70	96	122:09:33:23	2800	93.0	264.0	092123	6.59 S	154.64 E	33Q	6.0	6.0	0.0	000	SOLOMON ISLANDS
71	96	125:17:00:58	1200	87.5	285.5	164924	13.90 N	146.22 E	33Q	5.7	5.7	0.0	000	S. OF MARIANA ISLANDS
72	96	128:21:53:02	900	67.8	130.5	214340	14.93 S	69.69 W	242Q	5.1	5.1	0.0	000	PERU-BOLIVIA BORDER REGION
73	96	128:23:29:51	2800	69.4	309.8	231959	43.67 N	147.58 E	50Q	6.2	6.2	0.0	000	KURIL ISLANDS
74	96	131:10:28:52	900	64.3	133.6	101938	13.88 S	74.25 W	101Q	5.3	5.3	0.0	000	CENTRAL PERU
75	96	132:02:26:10	1800	48.1	96.6	021845	19.28 N	64.95 W	37Q	5.4	5.4	0.0	000	VIRGIN ISLANDS

TABLE 1

76	96	132:16:51:20	120	59.9	45.1	164144								
77	96	134:05:01:01	900	46.5	119.3	045347	52.11 N	30.02 W	10Q	4.8	4.8	0.0	000	N MID-ATLANTIC RIDGE
78	96	135:12:46:56	1200	80.0	238.8	123659	7.19 N	76.88 W	27Q	5.1	5.1	0.0	000	N COLOMBIA
79	96	139:07:52:44	900	74.7	135.2	074225	17.80 S	178.74 W	606Q	5.5	5.5	0.0	000	FIJI ISLANDS REGION
80	96	153:00:35:15	900	50.2	174.4	002730	23.11 S	68.91 W	96Q	5.3	5.3	0.0	000	N CHILE
81	96	154:00:59:15	900	57.8	135.5	005037	13.38 S	112.07 W	10Q	5.2	5.2	0.0	000	CE PACIFIC RISE
82	96	154:02:28:31	900	61.0	71.9	021932	9.62 S	79.52 W	33Q	5.4	5.4	0.0	000	N PERU
83	96	154:02:57:49	330	61.0	71.8	024846	30.51 N	41.33 W	33Q	5.1	5.1	0.0	000	N MID-ATLANTIC RIDGE
84	96	154:03:01:17	3600	71.0	90.7	025209	30.53 N	41.73 W	10Q	5.2	5.2	0.0	000	N MID-ATLANTIC RIDGE
85	96	154:09:49:38	3600	91.4	306.5	093747	10.64 N	42.29 W	10Q	6.8	6.8	0.0	000	N MID-ATLANTIC RIDGE
86	96	155:08:27:36	3600	92.7	260.7	081538	27.51 N	128.53 E	44Q	5.9	5.9	0.0	000	RYUKYU ISLANDS
87	96	156:03:36:12	900	94.6	267.4	032419	9.10 S	156.88 E	33Q	6.1	6.1	0.0	000	SOLOMON ISLANDS
88	96	158:06:38:42	3600	91.1	243.7	062651	4.77 S	151.34 E	150Q	5.0	5.0	0.0	000	NEW BRITAIN REGION
89	96	158:15:00:56	900	89.5	245.3	144913	21.53 S	169.03 E	33Q	5.5	5.5	0.0	000	LOYALTY ISL REGION
90	96	160:23:26:18	3600	45.3	309.4	231914	19.24 S	169.24 E	33Q	5.2	5.2	0.0	000	VANUATU ISLANDS
91	96	161:01:23:29	3600	85.6	288.6	011217	51.42 N	178.13 W	33Q	6.3	6.3	0.0	000	ANDREANOF ISL
92	96	185:16:58:49	1200	74.0	136.5	164827	17.50 N	145.74 E	146Q	6.0	6.0	0.0	000	MARIANA ISL
93	96	186:11:44:56	1800	33.1	330.9	113936	23.28 S	70.38 W	33Q	5.6	5.6	0.0	000	COAST N CHILE
94	96	186:15:54:22	600	119.1	283.7	153751	61.96 N	150.95 W	60Q	5.5	5.5	0.0	000	S ALASKA
95	96	186:16:02:45	1800	94.4	284.3	155039	7.11 S	122.37 E	600Q	5.2	5.2	0.0	000	FLORES SEA
96	96	187:18:46:22	1200	90.3	257.6	183435	8.77 N	141.36 E	33Q	5.5	5.5	0.0	000	W CAROLINE ISLANDS
97	96	188:12:08:07	1200	85.4	286.2	115644	10.13 S	160.75 E	33Q	5.8	5.8	0.0	000	SOLOMON ISL
98	96	188:21:47:26	1800	85.1	293.9	213628	15.72 N	147.52 E	33Q	5.7	5.7	0.0	000	MARIANA ISL
99	96	189:10:58:37	1200	57.2	321.9	105003	22.06 N	142.80 E	240Q	5.7	5.7	0.0	000	VOLCANO ISLANDS
100	96	191:12:11:15	900	63.1	316.3	120247	58.67 N	157.86 E	33Q	5.6	5.6	0.0	000	KAMCHATKA
101	96	196:19:31:40	900	83.1	237.0	192128	51.90 N	151.55 E	500Q	5.1	5.1	0.0	000	SEA OF OKHOTSK
102	96	197:17:02:27	1200	85.1	289.9	165121	21.23 S	179.75 W	616Q	5.0	5.0	0.0	000	FIJI ISLANDS REGION
103							18.82 N	145.40 E	176Q	5.7	5.7	0.0	000	MARIANA ISLANDS
104	Picked with only digital array data.													
105	95	222:00:58:21	1800	151.1	0.0	004105.1*	15.557S	41.217E	10G	5.3	5.2	1.0	10	MOZAMBIQUE CHANNEL
106	95	226:04:47:53	3600	94.5	267.4	043717.2	4.800S	151.421E	127y	6.3	6.3	0.9	128	NEW BRITAIN REGION
107	95	228:08:25:27	900	66.0	0.0	081711.9	29.277S	112.613W	10G	5.3	5.3	0.6	56	EASTER ISLAND REGION
108	95	231:21:49:34	3600	48.9	0.0	214332.0	4.992N	75.673W	126D	6.2	5.9	0.8	155	COLOMBIA
109	95	235:07:15:06	7200	85.2	0.0	070602.5	18.885N	145.167E	597y	6.1	6.1	0.9	116	MARIANA ISLANDS
110	95	252:21:08:46	3600	72.2	133.5	205840.6	20.128S	69.170W	79y	5.6	5.6	0.7	103	NORTHERN CHILE
111	95	255:14:33:46	900	83.0	236.7	142333.2	21.444S	179.516W	599y	5.1	5.1	0.6	67	FIJI ISLANDS
112	95	260:03:46:57	900	40.6	310.6	034029.0*	52.450N	170.673W	33y	4.7	4.7	1.1	29	FOX ISLANDS
113	95	280:21:36:11	2400	53.4	128.7	212805.6*	2.737S	77.685W	33N	5.5	5.2	0.7	77	PERU-ECUADOR BORDER
114	95	287:08:11:57	1800	84.8	232.4	080051.3	25.751S	177.612W	161y	5.7	5.7	0.9	195	SOUTH FIJI ISLANDS
115	95	298:10:25:59	120	38.4	311.4	101952.5	52.831N	167.036W	33y	4.8	4.8	1.1	50	FOX ISLANDS
116	95	317:02:23:24	3600	77.8	240.8	021241.4*	14.841S	178.479W	33N	4.8	6.4	0.7	16	FIJI ISLANDS
117	95	325:21:40:14	60	62.2	203.8	212958.6*	21.798S	139.116W	0y	5.0	5.0	0.8	27	TUAMOTU ARCHIPELAGO REGION
118	95	328:17:33:58	3600	68.1	309.8	172412.0	44.385N	149.132E	33N	6.1	6.4	0.8	235	KURIL ISLANDS.
119	95	333:14:45:10	120	32.8	325.7	143916.2	59.391N	153.386W	121y	4.1	4.1	0.9	56	SOUTHERN ALASKA
120	95	333:18:50:43	900	77.7	238.2	184037.0	16.689S	176.560W	372y	5.1	5.1	0.5	62	FIJI ISLANDS

TABLE 1 (CONT)

Site locations checked with differential GPS.

Dx ~~meters~~ km E/W. > 0 means new is east of the old one
Dy ~~meters~~ km N/S. > 0 means new is north of the old one
Dist in ~~meters~~ km.
Az is heading in degrees from old to new location.

Site	Dist	Az	Dx	Dy
SYM	0.081	262.1	-0.080	-0.011
SCF	0.089	277.2	-0.089	0.011
NCF	0.037	252.7	-0.036	-0.011
CAF	0.115	292.7	-0.107	0.044
LSC	0.791	48.7	0.595	0.522
FRG	0.076	125.5	0.062	-0.044
CRF	0.049	226.9	-0.036	-0.033
STO	0.223	198.7	-0.071	-0.211
FMW	0.977	299.3	-0.852	0.477
WLD	0.437	195.4	-0.115	-0.422
TWP	0.054	281.8	-0.053	0.011
STC	0.083	254.5	-0.080	-0.022
PUV	0.161	277.9	-0.160	0.022
TPW	0.087	247.4	-0.080	-0.033
TAR	0.014	38.6	0.009	0.011
YCW	0.239	222.0	-0.160	-0.178
RED	0.361	79.3	0.355	0.067
RPY	0.018	90.0	0.018	0.000
SPC	0.127	29.2	0.062	0.111

Analog array

LSMZ	0.403	187.7	-0.053	-0.400
KRV	0.044	270.0	-0.044	0.000
NSP	0.126	315.0	-0.089	0.089
LMT	0.612	146.5	0.337	-0.511
LTS	0.021	122.0	0.018	-0.011
TWR	0.057	321.4	-0.036	0.044
JFR	0.024	158.1	0.009	-0.022
WCT	0.437	195.4	-0.115	-0.422

Table 2

Periods of 1-second differences between SGBDSN and analog arrays:

1/08/1996	0:00:00.000	to	1/13/1996	0:00:00.000
11/30/1995	0:00:00.000	to	12/09/1995	0:00:00.000
9/21/1995	0:00:00.000	to	9/30/1995	0:00:00.000
8/31/1995	0:00:00.000	to	9/17/1995	0:00:00.000
7/15/1995		to	8/02/1995	0:00:00.000

Events falling in these time windows were corrected for the 1-second difference. The precision of window ends is only accurate enough to decide the timing state of events used here.

Table 3

Stations examined for refraction crustal correction. Refraction lines are from Mooney and Schapper (1995). Delays here correct for Pn raypaths. Teleseismic delays are 0.75 of the value shown.

Stn	Lat	Lon	Elev	Refraction Corr.	
WCT	36.7927	-116.6257	930	0.00	Datum
WLD	36.7927	-116.6257	930	0.00	Datum
CDH	36.8637	-116.3162	1353	0.00	= 0.
RRVQ	36.6971	-116.1597	1070	0.05	
SDH	36.6453	-116.3397	1050	0.08	
KRV	36.6950	-116.2623	1077	0.11	= between NSP and SDH
CFSO	36.7181	-116.5592	855	0.13	
NSP	36.7280	-116.2108	1239	0.14	
CAF	36.8391	-116.3377	1110	0.17	
FMW	36.9021	-116.3688	1146	0.18	
FRG	36.8169	-116.4195	1155	0.18	
LSC	36.7307	-116.3255	1238	0.18	
LTS	36.7269	-116.3227	1242	0.18	
RPY	36.8515	-116.4563	1301	0.18	
SYM	36.7416	-116.4460	995	0.18	
YM5	36.8985	-116.4542	1355	0.18	
YM6	36.8560	-116.4003	1090	0.18	= FMW
LMT	36.7434	-116.3075	1092	0.18	= LSC
LSMZ	36.7389	-116.2716	1113	0.18	= LSC
YCW	36.9223	-116.4756	1498	0.18	= RPY
YM4Z	36.8498	-116.4530	1248	0.18	= RPY
YM3	36.7868	-116.4125	1060	0.18	= FRG
TWR	36.7879	-116.3276	1099	0.18	split LSC-CAF
SCF	36.7568	-116.5440	909	0.25	
NCF	36.8899	-116.5682	1151	0.27	
CFQN	36.7414	-116.4896	963	0.28	
CFSW	36.8485	-116.4844	1310	0.30	
CFY2	36.7853	-116.4875	1065	0.30	
STO	36.8603	-116.4742	1359	0.30	
YM2	36.7857	-116.4870	1006	0.30	
CFWW	36.8236	-116.5126	1140	0.31	
CRF	36.8118	-116.5340	1032	0.31	
YM1	36.8537	-116.5310	1006	0.31	= CFWW
CFLC	36.7772	-116.5861	923	0.35	

TABLE 4

Appendix A: Crustal correction input data and delay computation.

```
      program crust
c
c     calculates crustal delays.
      parameter(MAX = 10, MAXSTA = 10000)
      real p, vh, v(MAX), th(MAX), theta(MAX)
      character stname*6

      open(1, file = 'crust.in', status = 'old')

      read(1,*) vh
      read(1,*) raypar
c                 input in sec/degree
      p = raypar / 111.17
c                 convert to sec/km
      vb = 1 / p

      thetah = asin(p * vh)
      write(6,'(3(a, f6.3, 2x))') "Vh: ", vh, "Ray param: ", raypar,
     &        "Refractor vel: ", vb

      do 100, j = 1, MAXSTA
         read(1, '(a)') stname
         if (stname .ne. 'LAST') then
            dt = 0.
            totthk = 0.
            ttanth = 0.
            do 10, i = 1, MAX
               read(1, *, err = 11) th(i), v(i)
               theta(i) = asin(p * v(i))
               totthk = totthk + th(i)
               ttanth = ttanth + th(i) * tan(theta(i))
               dt = dt + th(i)/(v(i) * cos(theta(i)) ) -
     &                          th(i)/(vh * cos(thetah))
10          continue
11          backspace(1)

               dt = dt + (totthk * tan(thetah) - ttanth) / vb
               write(6,'(a6, f5.2)') stname, dt
         else
            goto 999
         endif
100   continue
      close(1)
999   end


c # Purpose:  To compute Pn delays due to crustal structure from
c # shallow refraction lines.  Pn is used since it is a fairly standard
c # velocity, and "flat earth" geometry applies.  code doesn't rely on flat
c # earth, however.

c #
c # Algorithm:  From geometric considerations the relative delay in
c # terms of thicknesses T(i) (km), velocities V(i) (km/sec), Vh = slowest
c # 1-D velocity, and ray parameter p (sec/deg):

c #
c # p = 1/Vr  where Vr is the refraction velocity.  For teleseisms
c #    Vr >> Vp at that depth because of the curvature of the earth.
c #
```

```
c # p = sin(th(i))/V(i)  gives the angle th(i) of ray passage from
c #   vertical in the ith layer.  th(n+1) is the angle through Vh.
c #   The n layers have velocities < Vh.
c #
c # Single layer delay:
c #     dt = T(1)/[V(1)*cos(th(1))] - T(1)/[Vh*cos(th(2))] -
c #                          [T(1)*tan(th(1))] / Vr
c #
c #
c # For multiple layers:
c #     dt = sum { T(i)/[V(i)*cos(th(i)))] - T(i)/[Vh*cos(th(n+1))]} +
c #               {sum(T(i)) tan (th(n+1) - sum T(i) tan (th(i))} / Vr

c # where th(n+1) = sin-1(Vh)/p, and indices 1 = 1, ..., n layers.
c #
c # Reference:  Dix, C.H., Seismic Prospecting for Oil, 1981, p. 104.
c #
c # Input:
c # Line 1:  Vh, velocity of the layer at which velocity
c #    variations are 0.  Any label to the right of Vh is ignored.
c #    All velocities above must be strictly less than Vh.
c # Line 2:  raypar, the ray parameter.
c #    Any label tothe right of raypar is ignored. The ray parameter for
c #    Pn is 111.17/V(Pn), or around 14.07 sec/degree for the SGB.
c # STN(1)
c # T(1) vel(1)    whitespace or comma delimited
c # T(2) vel(2)
c # ...            up to MAX = 10 layers.
c # STN(2)
c # T(1) vel(1)
c # T(2) vel(2)
c # ...
c #
c # Out:
c #
c # for i = 1, n:
c # STN(i) Pn_delay(i)
c #
c # Notes:  trigonometric functions work in radians.
```

Vh: 5.500 Ray param: 14.000 Refractor vel: 7.941

SYM	0.18
SCF	0.25
NCF	0.27
CAF	0.17
LSC	0.18
FRG	0.18
CRF	0.31
STO	0.30
FMW	0.18
RPY	0.18
CFWW	0.31
CFSW	0.30
CFY2	0.30
CFSO	0.13
CFQN	0.28
CFLC	0.35
RRVQ	0.05
SDH	0.08
NSP	0.14
YM5	0.18

```
5.5     1-D velocity at and below this
14.00   ray parameter in seconds/degree AAA 1. 2.5
SYM
0.25  2.3
0.25 3.0
0.55 3.5
SCF
0.05 3.5
0.30 2.5
0.5 3.5
0.5 3.8
1.5 4.8
NCF
0.05 1.5
0.25 2.5
0.8 3.9
0.8 4.1
1.1 4.7
CAF
.15 1.5
.15 2.2
.20 2.7
LSC
0.25  2.3
0.25 3.0
0.55 3.5
FRG
0.25  2.3
0.25 3.0
0.55 3.5
CRF
0.5 2.4
0.5 3.5
0.7 3.9
1.4 4.8
STO
0.5 2.4
0.4 3.5
0.5 3.6
1.6 4.8
FMW
0.25  2.3
0.25 3.0
0.55 3.5
RPY
0.25  2.3
0.25 3.0
0.55 3.5
CFWW
0.5 2.4
0.5 3.5
0.7 3.9
1.4 4.8
CFSW
0.5 2.4
0.4 3.5
0.5 3.6
1.6 4.8
CFY2
0.5 2.4
0.4 3.5
0.5 3.6
1.6 4.8
CFSO
0.5 3.5
0.4 4.1
```

1.2 4.9
CFQN
0.15 1.5
0.1 2.5
0.65 3.6
1.0 4.1
0.6 4.8
CFLC
0.2 1.5
0.3 2.4
0.5 3.5
0.5 3.9
1.5 4.8
RRVQ
0.1 1.5
SDH
0.6 3.7
0.8 5.1
NSP
0.25 2.3
0.55 3.5
YM5
0.25 2.3
0.25 3.0
0.55 3.5
LAST

Appendix B: East-west profiles through north Jackass Flats and southern Timber Mountain. E-W 10 passes just south of the ESF, E-W 11 just north, and E-W 12 4.5 km north of the ESF. In each, (a) uses only refraction; (b) uses no crustal corrections; (c) uses only station static corrections; (d) uses refraction and station static corrections.

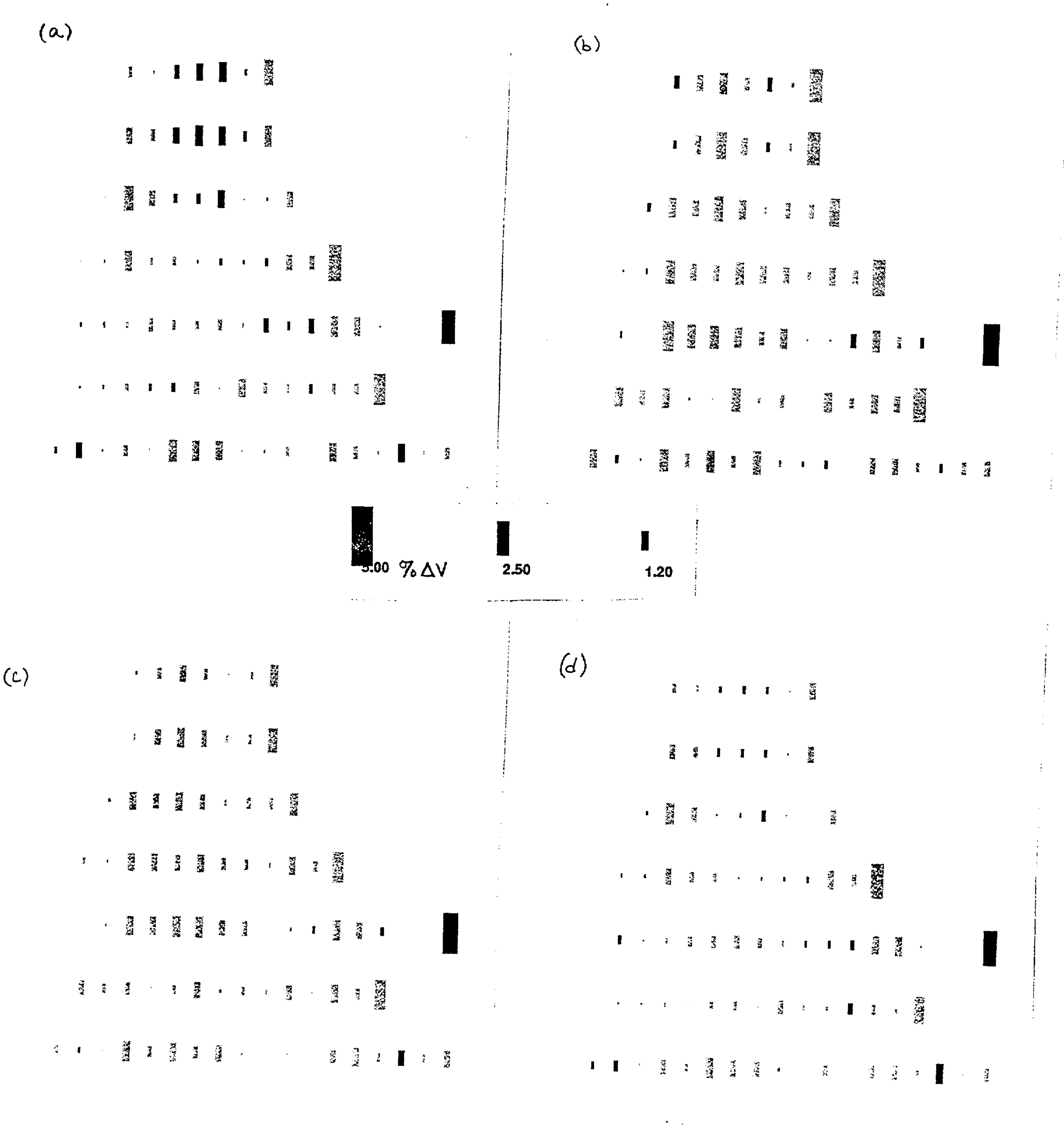

Appendix B East-West 10

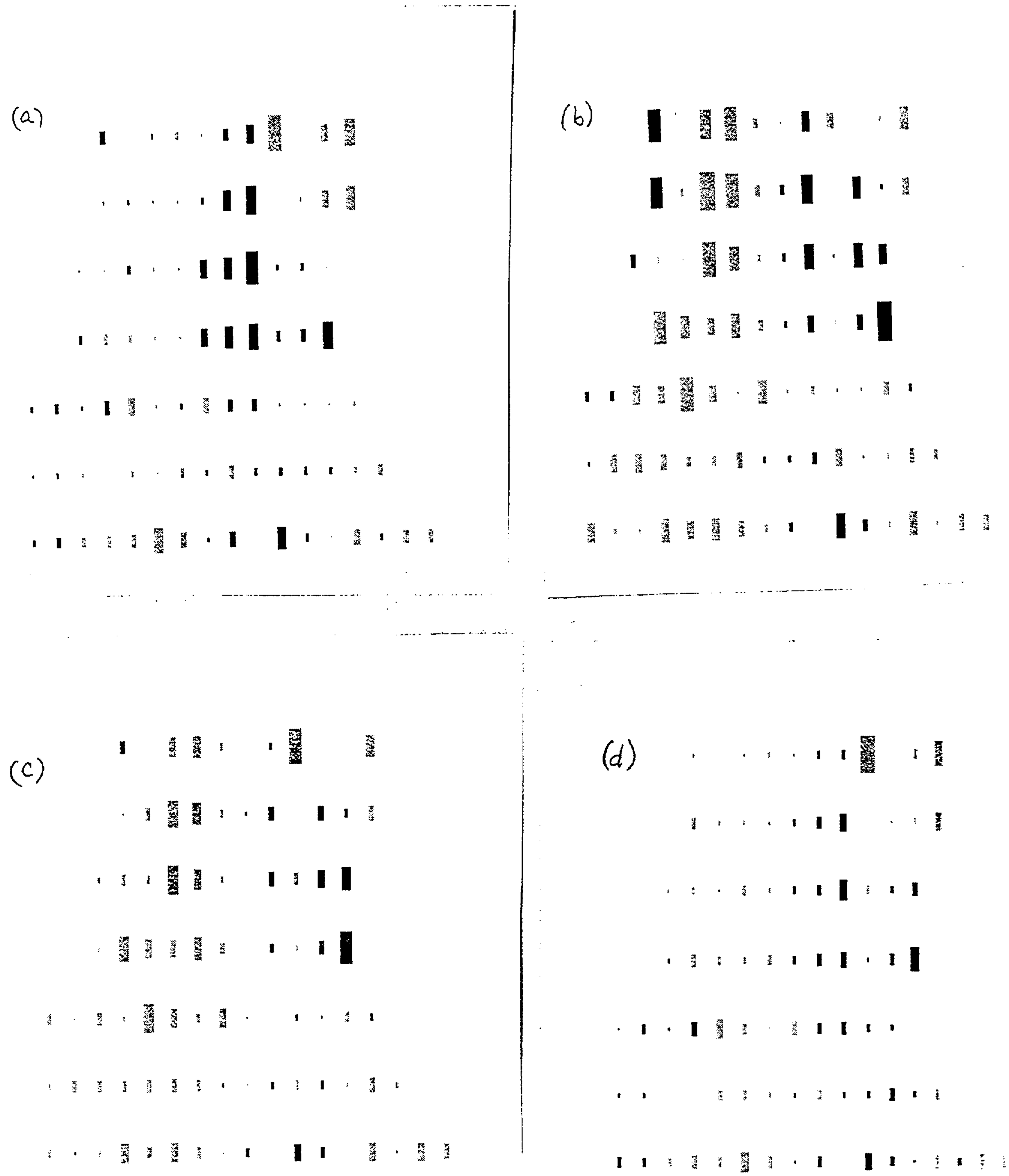

Appendix B East-West 11

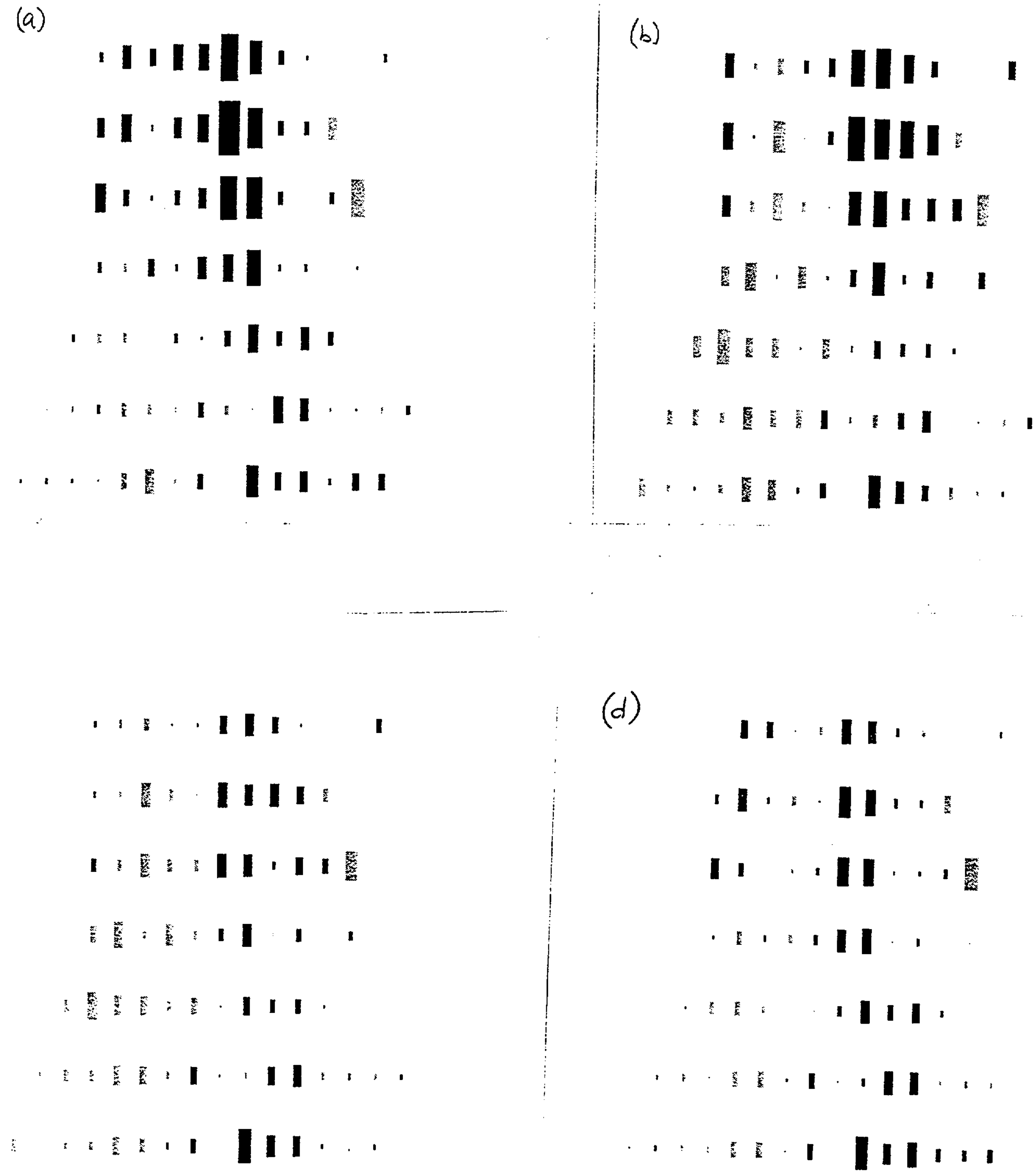

Appendix B. East-West 12

On the Scaling of Slip with Rupture Length for Shallow Strike-Slip Earthquakes: Quasi-static Models and Dynamic Rupture Propagation

Paul Bodin
Center for Earthquake Research and Information
The University of Memphis,
Memphis, TN 38152

James N. Brune
Seismological Laboratory
Mackay School of Mines
University of Nevada
Reno, NV 89557

In Press, BSSA Oct. '96

Abstract

We explore whether observations of average surface rupture properties among strike-slip earthquakes reflect the underlying mechanics. We compare the observed relationship between average slip and rupture length for 27 surface-ruptures (18 plate boundary earthquakes and 9 away from transform plate boundaries) with predictions from two families of uniform-stress-drop models. Purely elastic models with a rupture-limiting locking depth predict a non-linear relationship while a quasi-dynamic model with no locking depth predicts a linear relationship. We explore whether observations of fault slip at the Earth's surface distinguish which, if either, of these two families of models may be favored. We find that the data provide insufficient constraints to rule out either a linear or a non-linear relationship. This might arise from uncertainties in the observations, or from reasonable (but unrecoverable) variations in locking depths and uniform stress drops among earthquakes. We advance an alternative interpretation, that the complexity amongst the observations is consistent with dynamic rupture models featuring spatially-varying stress drops.

Uniform Stress Drop

Scaling relations between measurable quantities associated with a physical process may reveal underlying, yet hidden, mechanics. In this paper we consider the scaling relationship between rupture length, **L**, and average displacement, **d**, for strike-slip earthquake ruptures. Our ultimate goal is to interpret the scaling relationship between **L** and **d** in terms of processes that take place during rupture. At the heart of this matter lies the question of whether **d** is observed to be directly proportional to **L** or whether a "knee" may be observed in the relationship, with slip being independent of rupture length for long ruptures. Several studies have arrived at differing conclusions on this issue from different data sets and analyses. We will argue that neither model provides a convincing fit to updated observations, and suggest reasons why this may be the case. We will proceed to interpret the observations in a new way, which provides some insight into rupture processes.

A non-linear relationship between **L** and **d** is expected for a uniform stress drop rupture in an elastic Earth where earthquake slip is confined to a shallow layer (the seismogenic zone). The depth extent of the seismogenic zone is often assumed to coincide with the depth of microearthquakes--about 10-20 km. Theoretically, for uniform stress-drop shear cracks driven by a uniform background stress field (Kanamori and Anderson, 1975):

$$\mathbf{d} = \frac{C\Delta\sigma X}{\mu} \, , \tag{1}$$

where $\Delta\sigma$ is the static stress drop (for a total stress drop earthquake, *i.e.* when the frictional stress is zero, this is equal to the component of shear stress in the surrounding crustal rocks resolved on the rupture plane), μ is the rigidity of the crustal rocks, X is the smallest dimension of the rupture within the fault plane (either length, **L**, or the down-dip rupture width, **W**, depending on the rupture geometry, (Eshelby, 1957)) and C is a variable whose value depends on the shape and aspect ratio of the rupture, and on the sense of slip (dip slip or strike-slip). For ruptures confined to a shallow seismogenic zone, X may be replaced with **L** only if the fault is equidimensional or deeper than it is long. Otherwise, X signifies **W**. Analytical expressions for C have been obtained only for certain rupture geometries: circular ruptures (Keilis-Borok, 1959), elliptical ruptures (Eshelby, 1957), infinitely long strike-slip ruptures (Knopoff, 1958), and infinitely long dip-slip faults (Starr, 1928). Numerical solutions for C have also been computed for rectangular ruptures (*e.g.* Bodin and Bilham, 1994).

We adopt the common definition of small strike-slip ruptures as those that do not completely rupture the width of the seismogenic zone and may be nearly equidimensional (**L**~**W**). Amongst large ruptures **W** is essentially constant, and **L** exceeds **W**. From equation (1), given a constant stress drop, **d** should rise with increasing **L** asymptotically toward a constant value related to **W** (so-called **W**-models).

Scholz (1982) suggested that despite this expectation the relationship between **L** and **d** is linear over a wide range of **L** (so-called **L**-models), based on data for 14 plate boundary earthquakes compiled by Sykes and Quittmeyer (1981). Scholz (1982) pointed out that in L-models co-seismic slip at the base of the seismogenic zone must be unconstrained, so that **W** never limits the final average slip. He suggested a "quasi-dynamic" model in which shallow co-seismic slip represented a rapid extension to the surface of deep slip that had already taken place. Such a model would suggest very long rise times at any point on large ruptures. In order for a point on a fault to "know" when to stop slipping, it must get information back from the "end" of the fault as to when to stop. If information is transmitted with the speed of seismic waves, this could take a long time, implying very long rise times. For example, the duration of slip (the rise time) at the center of a 200 km long rupture would exceed 40 seconds, the two-way travel time between rupture initiation at the center of the rupture area and the farthest edge of the rupture assuming a rupture propagation velocity less than 5 km/sec. Such long durations have not been observed. In fact, Heaton (1990) suggests that rise times are on the order of a fraction of a second to several seconds.

Romanowicz (1992) found evidence for **W**-scaling in the relationships between fault length and scalar seismic moment, M_O. If **d** is constant for long earthquakes then M_O should scale with $\mathbf{L}^3$ for small earthquakes and **L** for large earthquakes. Pacheco et al. (1992) argued that a change in scaling of **d** with **L** would lead to a "kink" in the b-values for transform seismicity at magnitudes for ruptures with **L** ~ **W**, M~5.8. Romanowicz and Rundle (1993) argued that the magnitude-occurrence statistics expected from ruptures of different sizes that completely cover a given fault surface suggest that the kink reported by Pacheco et al. (1992) was consistent with **W**-models rather than **L**-models.

We claim that updated versions of the observations used by Scholz (1982) do not sufficiently permit the distinction between **L**- and **W**- models, in which the fault offset is determined by the average stress drop and the boundary conditions at the edge of the rupture. The results may be consistent with dynamic slip models, in which local stresses and conditions on the fault during the rupture process control the slip distribution. To test this, we compute the expected scaling relationships for shallow rectangular complete stress-drop earthquakes from a numerical model. We compare our expected relationships with the most recent data compilation available (Wells and Coppersmith, 1994). We find that the data are explained equally well by **W**-models, **L**-models, or dynamic models given the assumptions of each of the models. This finding permits us to re-interpret the evidence in terms of mechanics governing earthquake rupture consistent with equation 1 and with fewer contradictions with the observations.

Partial Stress Drop

In contrast to the above discussion, it is also possible that the slip at each point would be controlled by the dynamics of rupture, not by the final dimension (either **L** or **W**). The above scaling considerations all start from an analogy with models that have a uniform constant stress drop over the whole fault surface. It is difficult to imagine how this would occur in nature unless the final stress along the fault were zero. Otherwise, the slip along the fault would be controlled by the stress and friction history at each point (up to the point in time at which the fault is locked at a stress greater than zero by the non-zero coefficient of friction). In a given complex dynamic rupture process, the final locked stress at each point would be expected to be a complicated result of the dynamics, and not constant.

Brune (1970) suggested that in reality it was unlikely that a fault could slip to 100% of the dynamic stress drop over the complete fault plane, and that the consequent "partial stress drop" model would produce an intermediate spectral slope of approximately ω^{-1} (ω is the angular frequency). He suggested that this could be caused by a complex, multiple event stress drop, or a type of slip drop out of and into a "potential well" as would be appropriate for a crystal dislocation where a molecule on one side of the dislocation slips over another on the other side, and might be appropriate for interlocking asperities on a fault. Brune (1976) called this the "abrupt locking" model.

The partial stress drop, abrupt locking ω^{-1}, model has a second corner frequency, related to the size of the roughness, barriers, asperities or sub-events, beyond which the fall-off is ω^{-2}. Several recent studies have suggested that many earthquakes have an ω^{-1} spectral shape near the corner frequency, lending support to the partial stress drop model (Anderson et al. 1986, Smith et al. 1991, Mayeda and Walter 1995).

In the time domain, the partial stress drop model has the stress drop and slip velocities temporarily and/or locally higher than would be the case if the final static stress drop had been applied permanently (Brune et al., 1986). Thus, the stress must drop and then increase, but not back to the original stress level, leaving a permanent stress drop smaller than the transient stress drop. This model for earthquake stress change was originally suggested by Housner (1955) and is obviously appropriate for a crystal dislocation or interlocking strong bumps or asperities. Heaton (1990) calls this model the self-healing model (the fault heals and leaves a final stress level higher than the sliding frictional stress--Haskell, 1994), Quin (1990) refers to it as a "moving window of radiation."

For dynamic dislocation models there is no reason to expect a simple **L** or **W** scaling, since the slip at any point is controlled by the dynamic properties of fault slip in addition to effects from fault boundaries. Heaton (1990) has documented that all of the recent earthquakes with detailed determination of dislocation time histories by inversion techniques have shown local rise times much shorter than would be the case for the uniform stress drop model (where slip near the center of the fault continues until a "healing" signal arrives from the edges, giving a relatively long rise time). The data he presents illustrate that a complex multiple event or multiple asperity stress drop model is appropriate for nearly all of the events considered. Anderson et al. (1986) found that the shape of the integrated time function for the 1985 Michoacan earthquake was consistent with a dynamic slip model since the duration of slip at a particular point on the fault was short compared to the overall rupture time. The dynamic model of the 1979 Imperial Valley earthquake developed by Quin (1990) clearly shows the abrupt-locking, self-healing character of the rupture ("moving window of radiation"). Beroza (1991) also found short rise times for the 1989 Loma Prieta earthquake. In order to investigate the dynamic properties of fault slip, a large-scale foam rubber model of dynamic interface slip in a shear field has been developed (Brune et al. 1990, Brune et al. 1993, Anooshehpoor and Brune 1994). In this model the length of the dislocation pulse is approximately 10 cm, whereas the dimension of the final slip surface (unconstrained edge) is on the order of 1.5 meters. Therefore, the dynamic dislocation in this model corresponds to the partial stress drop/abrupt locking/self-healing model, and the fault slip is controlled by the dynamics of rupture, not simply by the final fault dimensions. In the foam rubber model, the normal stress is decreased to zero during the dislocation slip and the two sides of the fault temporarily separate, then close together, abruptly locking the fault. Brune et al. (1993) suggested that this mechanism could explain the long-standing paradox of lack of frictional heat generation along the San Andreas fault, and Anooshehpoor and Brune (1994) documented that the mechanism leads to significantly reduced frictional heat generation at high normal stresses.

Models

In order to facilitate the comparison of the observations to uniform total stress drop models, we compute the theoretical relationship between **d** and **L** for a range of stress-drops and locking-depths using a 3D boundary-element method (Figure 1)(Gomberg and Ellis, 1994; Bodin and Bilham, 1994). The rectangular ruptures completely relieve the stress on a vertical strike-slip fault. The stress field is a fault-parallel simple shear stress imposed on the entire half-space. To compute the mean slip we break the fault into 121 equal sub-faults, and average the slip on all segments.

The modeled displacement rises quickly with rupture length for short ruptures, and then reaches a "knee" with strongest curvature at **L**~2**W**, thereafter rising asymptotically toward a constant value that depends on **W** and $\Delta\sigma$ (Figure 2). Our model assumes that a rectangular rupture breaks the surface first when **L** = **W**, thus we do not predict surface slip for ruptures with **L** < **W**. The genesis of the shape of the curves is discussed by Bodin and Bilham (1994). Figure 2a clarifies the point that for a given stress drop, an **L**-model is the bound of **W**- models with increasing **W**. The "knee" in the relation between **d** and **L** is not strongly affected by the detailed shape of the rupture. Elliptical ruptures have the same general features (*e.g.* Eshelby, 1957, Bodin et al., 1987).

Figure 2b illustrates the wide range of both **W**- and **L**-models, given various plausible stress drops. The physical significance of the term "stress drop" differs between **L**- and **W**-models, however. Bodin and Bilham (1994) demonstrate that for **W**-models, stress available to drive the rupture may derive from a region extending one locking depth (**W**) or so from the rupture (they call this an ε-model). In **L**-models the stress driving the rupture is drawn from a region extending approximately one rupture length into the surrounding crust.

It is clear from Figure 2 that **d** and **L** for any given earthquake does not identify any given **L**-model, nor any given **W**-model, uniquely. A reasonable range of stress drops and material properties leads to a wide range of possible displacements for any given rupture length. Moreover, uncertainties in parameter estimates from real earthquake ruptures will exacerbate difficulties in resolving the scaling relations. Although for any given earthquake both **d** and **W** are uncertain, **d** may be the more poorly constrained observable. **W** may be estimated by the depth of the brittle-plastic transition, which is often associated with the depth cutoff of micro earthquakes. Geodetic observations for many recent transform earthquakes are consistent with W coinciding with the depth of the brittle-plastic transition, given uniform slip on a rupture. If one allows slip in geodetic models to die off with depth, however, it is difficult to set an absolute bound on W. The correlation of geodetic and seismological slip estimates suggests that deep slip, if it occurs, is not an important contributor to the overall seismic moment. Stress-drops may provide the greater source of variability amongst a collection of earthquakes. Stress drops may be difficult to determine, and may depend on the model used to calculate them (Bodin et al., 1987). Additionally, variations and uncertainty in the assumed material properties may contribute to the range of applicable models.

Comparison of Models with Data

Direct observations to constrain rupture scaling relations are not ideal. **W** is never observed directly and must be inferred, usually from seismic data or, in the best of cases, from geodetic observations. **L** may be inferred from aftershock zones, or estimated from a zone of surface faulting. **d** may be inferred from seismic or geodetic data, or estimated from surface faulting. These observations have been collected most carefully for seismic hazards studies (*e.g.* Bonilla, 1984; Slemmons, 1982; Wells and Coppersmith, 1994). These studies have tended not to include physically-motivated models in their analyses, but rather to fit mathematically simple functions to the data.

We use estimates of source parameters of 18 strike-slip earthquakes from the compilation by Wells and Coppersmith (1994). For reasons discussed below, it is difficult to assess the uncertainties of these estimates. For consistency, we use the observations of surface rupture length. The mean displacement values may derive from several sources, but are chiefly based on surface observations of slip. Such observations tend to provide minimum estimates of the true mean displacement over the entire rupture plane although for long earthquakes, elastic models suggest that they may be quite close to the overall value (Bodin and Bilham, 1994).

Figure 3 shows **L**- and **W**-models together with observations of **d**(**L**) for strike-slip earthquakes. The data have been separated into inter- and intra-plate earthquakes, and are further shaded as to geographical region of origin. We have found it a challenge to defend any single scheme to use existing observations to constrain the relation of **d**(**L**) for strike-slip ruptures in general. Difficulties arises from:

i) variations in how the parameters have been estimated for different ruptures,

ii) variations in the assignment of uncertainties among the estimates, and

iii) the possibility that systematic variations may exist between ruptures from different tectonic environments. In the following paragraphs we discuss briefly each of these in turn.

Estimates of slip and rupture length from observations of the surface rupture have the benefit of being direct, but the drawback of being incomplete. Their relationship to the slip at depth is not clear. Surface slip distribution during the 1992 Landers earthquake, for example, does not match the distribution of slip at depth modeled from geodetic and seismic data (Wald and Heaton, 1994). Interestingly, however, although the distributions differ for this event the average slip at depth was very similar to the average slip at the surface. Geodetic observations help constrain slip at depth, but lose resolution with depth of slip, and suffer from non-unique interpretations as to causative fault slip (*e.g.* Savage, 1990). Seismically-determined slip functions also constrain slip at depth, but are available for few earthquakes and may be controversial, even for well-instrumented earthquakes like the 1989 Loma Prieta earthquake (*e.g.* Beroza, 1991, Steidl et al., 1991; Wallace et al., 1991; Wald et al., 1991).

To maximize the number of earthquakes to compare models and data, it is necessary to use older and more remote earthquakes, for which source parameters may be relatively poorly known. A well known example is the length of the 1906 San Francisco earthquake, for which length estimates vary between 350 and 450 km, depending on one's interpretations of ground breakage observed at one site, Shelter Cove (*e.g.* Brown, 1994;

McLaughlin et al., 1979). The depth of ruptures is frequently estimated from the depth of regional microearthquakes. The relationship between this estimate and the mechanics that control a large earthquake is still controversial.

Systematic variations between different tectonic environments may result in scatter if observations from different environments are combined. All such distinctions are made moot, however, since systematic variations in rupture scaling must be inferred from the same noisy data. In the matter we are studying it is most frequently suggested that the difference between inter- and intra-plate earthquakes may be a first order effect (*e.g.* Kanamori and Allen, 1986; Scholz, 1982; Hanks and Johnston, 1992). For this reason we attempt to distinguish between these two tectonic settings amongst the observations. We find such distinctions challenging and debatable. In this paper we include as plate-boundary earthquakes those which occur on transform fault zones that root into a system of faults that, taken together, comprise a transform plate boundary. Thus, the 1956 rupture on the San Miguel fault in Baja California, and the 1992 Landers rupture are regarded as plate boundary earthquakes. Also earthquakes associated with the Anatolian fault in Turkey are regarded as plate boundary earthquakes, despite continuing debate about whether the fault system represents a true plate boundary. However, the 1890 Nobi earthquake in Japan is regarded as an intraplate earthquake. We recognize that all such distinctions are subject to interpretation, but we assert that our principal conclusions are not substantially affected by such differences in interpretation.

Our principal conclusion from Figure 3 is that the field observations of **d** and **L** are not well fit by a single **L**- or **W**-model. Rather, a range of **W**, μ and $\Delta\sigma$ for **W**-models, and of μ and $\Delta\sigma$ for **L**-models must be invoked to explain the scatter if we insist on quasi-static dislocation models. The data could be consistent with dynamic models since in these models the final slip need not be simply related to the final fault dimensions. However, given likely uncertainties in the data, it is likely to be fruitless to examine each data point much further. Nevertheless, we suggest that existing data, while they do not rule out either

L- or **W**-models, may reflect underlying **W**-scaling mechanics (*i.e.*, the existence of a locking depth), with additional features resulting from dynamic rupture propagation. Figure 4 illustrates this point. On the figure, the observations used by Scholz (1982) to argue for **L**-scaling have been added to data previously discussed. Figure 4 also contains the **L**-model Scholz (1982) fit to the observations, and a specific **W**-model we calculate (**W** = 15 km, $\Delta\sigma$ = **3 Mpa**). We note that with the exception of the 1857 Fort Tejon earthquake, the data for the larger earthquakes are not consistent with a L-model of a single stress-drop but could be bounded by a W- model with $\Delta\sigma$ somewhat larger than 4 Mpa. Because the 1857 earthquake was not subject to immediate and direct observations, we regard the estimate of average slip for this earthquake with additional skepticism.

Non-Uniform Stress-Drop

Can we interpret these somewhat messy scaling relations in terms of general features of earthquake source mechanics? The observations do not demand either an **L**-model or a **W**-model. Although (with the exception of the 1857 rupture) they seem to be bounded by **W**-mechanics for transform plate boundaries, they do not rule out a tendency for slip to increase with rupture length in excess of that predicted by any given **W**-models. They are consistent with the expected complexity and variability for dynamic rupture models.

Perhaps the simplest approach to explain the results is to modify the **W**-model assumption of uniform stress drop along the rupture plane as would be appropriate for dynamic models. We propose three possible modifications:

i) A rupture that starts out with an unusually large stress drop will tend to propagate farther than a rupture that starts with a low stress drop. This is because the increased energy density in the crack tip will increase the probability that the ruptures will pass through asperities and barriers. Ellsworth and Beroza (1995) present observations about the scaling of the earliest portion of seismograms from earthquakes of differing sizes that may be consistent with this suggestion.

ii) If the preexisting stress on a fault, or the strength of the fault, varies along strike, then a long rupture may be more likely than a short rupture to encounter conditions promoting large slip. Failure of a high stress drop area may send additional pulses of displacement both directions along a fault.

iii) Longer ruptures may more efficiently rupture the surface layers than do shorter ruptures. It is plausible that a longer duration of shaking will increase the probability that deep slip will propagate to the surface, or that sections of the fault that do not slip during the first passage of the rupture will do so subsequently as part of a complex multiple-event rupture process. Because stress will concentrate on near the margins of sections of the fault that do not slip during the first passage of the rupture, slip of the unruptured sections may be triggered by continued shaking from slip on more distant parts of the fault. This may result in "overstress" sub-events, as suggested by Brune et al. (1986). Alternatively, longer shaking might help to overcome frictional resistance to the rupture that might be expected in a velocity-strengthening regime in shallow sediments (e.g., Marone and Scholz, 1988)

All of the above processes might be expected once we give up trying to explain the data by purely quasi-static constant stress drop models, and anticipate the complexities that are expected to occur during real dynamic rupture propagation.

Acknowledgements

CERI contribution # 293. Numerous readers and critics helped to shape the arguments we present. We thank Scott Davis for useful comments, and Arch Johnston for enlightening discussions about intraplate earthquakes. Max Wyss read and contributed to an early version of the paper. We also gratefully acknowledge the influence and assistance of Burt Slemmons in helping to understand the significance of surface measurements of offset.

References

Anderson, J., P. Bodin, J. Brune, J. Prince, S. Singh, R. Quaas, and M. Oñate, (1986). Strong ground motion from the Michoacán, Mexico Earthquake. *Science*, **233**: p. 1043-1049.

Anooshehpoor, A. and J.N. Brune (1994). Frictional heat generation and seismic radiation in a foam rubber model of earthquakes. *Pure and Applied Geophysics, .* **142**, 735 - 747.

Beroza, G.C. (1991). Near-source modeling of the Loma Prieta Earthquake: evidence for heterogeneous slip and implications for earthquake hazard. *Bull. Seism. Soc. Am.*, **81**, 1603-1621.

Bodin, P., and R. Bilham (1994). 3-D Geometry of velocity fields at transform plate boundaries: implications for seismic rupture. *Geophys. Res. Lett.*, **21**, 2523-2526.

Bodin, P., J.N. Brune, D.B. Slemmons, and X. Zhang (1987). "Scaling relations among the source parameters of shallow earthquakes" *EOS, Trans. Am. Geophys Un.*, **68**, 1243.

Bonilla, M.G., R.K. Mark, and J.J. Lienkamper, (1984). Statistical relations among earthquake magnitude, surface rupture length, and surface fault displacement. *Bull. Seism. Soc. Am.*, **74**, 2379-2411.

Brown, R.D. (1995). 1906 Surface faulting on the San Andreas fault near Point Delgada, California, *Bull. Seism. Soc. Am.*, **85**, 100.

Brune, J.N., (1970). Tectonic stress and the spectra of seismic shear waves from earthquakes. *J. Geophys. Res.*, **75**, 4997 - 5009.

Brune, J.N. (1976). *The physics of earthquake strong motion.* In: C. Lomnitz and E. Rosenblueth (Eds.), Seismic Risk and Engineering Decisions, Elsevier, New York, pp. 140-177.

Brune, J.N., J. Fletcher, F. Vernon, L. Haar, T. Hanks, and J. Berger, (1986). Low stress-drop earthquakes in the light of new data from the Anza, California, telemetered digital array. In: S. Das, J. Boatwright and C.H. Scholz (Eds), *Earthquake Source Mechanics. Geophys. Monogr. Am. Geophys. Union*, **37**, 237-245.

Brune, J.N., P.A. Johnson, and C. Slater, (1990). Nucleation, predictability, and rupture mechanism in foam rubber models of earthquakes. *J. Himalayan Geol.*, **1(2)**, 155-166.

Brune J.N., S. Brown, and P.A. Johnson, (1993). Rupture mechanism and interface separation in foam rubber models of earthquakes: a possible solution to the heat flow paradox and the paradox of large overthrusts. *Tectonophysics*, **218**, 59 - 67.

Ellsworth, W.L. and G.C. Beroza (1995). Seismic evidence for an earthquake nucleation phase. *Science*, **268**, 851-.

Eshelby, (1957). The determination of the elastic field of an ellipsoidal inclusion, and related problems. *Proc. Roy. Soc. London, Series A*, **241**, 376-396.

Gomberg, J. and M. Ellis (1994). Topography and tectonics of the central New Madrid seismic zone: Results of numerical experiments using a three-dimensional boundary element program, *J. Geophys. Res.*, **99**, 20,299 - 20310.

Hanks, T.C., and A.C. Johnston (1992). Common features of the excitation and propagation of strong ground motion for North American earthquakes. *Bull. Seism. Soc. Am.*, **82**, 1-23.

Haskell, N.A. (1964). Total energy and energy spectral density of elastic wave radiation from propagating faults, *Bull. Seism. Soc. Am.*, **54**, 1811-1841.

Heaton, T.H. (1990). Evidence for and implications of self-healing pulses of slip in earthquake rupture. *Phys. Earth Planet. Int.*, **64**, 1-20.

Housner, G.W., (1955). Properties of strong-motion earthquakes. *Bull. Seism. Soc. Am.*, **45**, 197 - 218.

Kanamori, H. and D.L. Anderson (1975). Theoretical basis of some empirical relations in seismology. *Bull. Seism. Soc. Am.*, **65**, 1073-1095.

Kanamori, H. and C.R. Allen (1986). Earthquake repeat time and average stress drop. *Earthquake Source Mechanics. Maurice Ewing Volume 6.* Edited by Das, S., J. Boatwright, and C.H. Scholz, AGU, Washington. D.C.

Keilis-Borok, V. (1959). On estimation of the displacement in an earthquake source and of source dimensions, *Ann. Geofis (Rome)*, **12**, 205-214.

Knopoff, L. (1958). Energy release in earthquakes, *Geophys. J.*, **2**, 44-52.

Marone, C.J., and C.H. Scholz (1988). The depth of seismic faulting and the upper transition from stable to unstable slip regimes, *Geophys. Res. Lett.* **15**, 621-624.

Mayeda, K., and W.R. Walter (1995). Source parameters of western U.S. earthquakes: moment, energy, stress drop and source spectra from regional coda envelopes. submitted to *J. Geophys. Res.*

McLaughlin, R.J., D.H. Sorg, J.L. Morton, J.N. Batchelder, R.A. LeVeque, C. Heropoulos, H.N. Ohlin, and M.B. Norman II (1979). Timing of sulfide mineralization and elimination of the San Andreas Fault at Point Delgada, California. *EOS Trans. Am. Geophys. Un.*, **60**, 883.

Pacheco, J., C.H. Scholz, and L. Sykes(1992). Changes in frequency-size relationship from small to large earthquakes. *Nature*, **355**, 61-73

Quin, H. (1990). Dynamic stress drop and rupture dynamics of the Oct. 15, 1979 Imperial Valley, CA earthquake. *Tectonophysics*, **175**, 93-117.

Romanowicz, B. (1992). Strike-slip earthquakes on quasi-vertical transcurrent faults: inferences for general scaling relations, *Geophys. Res. Lett.*, **19**, 481-484.

Romanowicz, B. and J.G. Rundle (1993). On scaling relations for large earthquakes, *Bull. Seism. Soc. Am.*, **83**, 1294-1297.

Savage, J.C. (1990). Equivalent strike-slip earthquake cycles in half-space and lithosphere-asthenosphere Earth models, *J. Geophys. Res.*, **95**, 4873-4879.

Scholz, C.H. (1982). Scaling laws for large earthquakes: consequences for physical models, *Bull. Seism. Soc. Am.*, **72**, 1-14.

Scholz, C.H. (1992). A reappraisal of large earthquake scaling. *Bull. Seism. Soc. Am.*, **82**, 215-218.

Slemmons, D.B. (1982). Faults and earthquake magnitudes: U.S. Army Engineer Waterways Experiment Station, Vicksburg, MS, *State of the Art of Assessing Earthquake hazards in the United States Series, Rept. 6., Misc. Paper 5-73-1*, 166 p.

Smith, K.D., J.N. Brune, and K.F. Priestley (1991). The seismic spectrum, radiated energy, and the Savage and Wood inequality for complex earthquakes. Tectonophysics, **188**, 303 - .

Steidl, J.H., R.J. Archuleta, and S.H. Hartzell. (1991). Rupture history of the 1989 Loma Prieta, California, Earthquake. *Bull. Seism. Soc. Am.*, **81**, 1573-1602.

Starr, A.T. (1928). Slip in a crystal and rupture in a solid due to shear, *Proc. Cambridge Phil. Soc.,* **24**, 489-500.

Sykes, L.R., and R.C. Quittmeyer (1981) Repeat times of great earthquakes along simple plate boundaries, in: *Third Maurice Ewing Symposium on Earthquake Predictions*, **4**, edited by D.W. Simpson and P.G. Richards, AGU, Washington, D.C.

Wallace, T.C., A. Velasco, J. Zhang, and T. Lay (1991). A broadband seismological investigation of the 1989 Loma Prieta, California, earthquake: evidence for deep slow slip? *Bull. Seism. Soc. Am.*, **81**, 1622-1646.

Wald, D.H., and T.H. Heaton (1994) Spatial and temporal distribution of slip for the 1992 Landers, California, earthquake. *Bull. Seism. Soc. Am.*, 84, 668-691.

Wald, D.J., D.V. Helmberger, and T.H. Heaton (199**21**). Rupture model of the 1989 Loma Prieta earthquake from the inversion of strong-motion and broadband teleseismic Data. *Bull. Seism. Soc. Am.*, **81**, 1540-1572.

Wells D.L., and K.J. Coppersmith (1994). New empirical relationships among magnitude, rupture length, rupture width, rupture area, and surface displacement. *Bull. Seism. Soc. Am.*, **84**, 974-1002.

Table 1. Earthquake Ruptures On or Near Transform Plate Boundaries. Source: Wells and Coppersmith (1994). Earthquakes in italic font were earthquakes for which average slip was not considered sufficiently reliable for regressions by Wells and Coppersmith. They are included in the table for completeness, but are not shown on Figures 3 and 4.

Country*, Yr	Date	Place or Fault	Length (km)	Avg. Slip (cm)
US 1857	09 Jan	Fort Tejon	297	640
US 1906	13 Mar	San Francisco	432	330
US 1940	19 Apr	Imperial Valley	60	150
TK 1944	01 Feb	Bolu	180	180
TK 1953	18 Mar	Canakkale	58	210
MX 1956	09 Feb	San Miguel	22	50
TK 1957	26 May	Abant	40	55
TK 1966	19 Aug	Vaarto	30	15
TK 1967	22 July	Mudurnu	80	163
US 1968	09 Apr	Borrego Mtn.	31	18
IR 1968	31 Aug	Dasht-e-Bayaz	80	23
GU 1976	04 Feb	Motagua	235	260
TK 1976	24 Nov	Caldiran	55	205
IR 1977	19 Dec	Bob-Tangol	12	12
US 1979	15 Mar	Homestead Valley	3.9	5
US 1979	15 Oct	Imperial Valley	30.5	18
US 1987	24 Nov	Superstition Hills	27	54
US 1992	28 Jun	Landers	71	295
TK 1939	*26 Dec*	*Erzincan*	*360*	*185*
TK 1943	*26 Nov*	*Kastamonu*	*280*	*57*
TK 1971	*22 May*	*Bingol*	*38*	*25*
US 1987	*24 Nov*	*Elmore Ranch*	*10*	*23*

*GU=Guatemala, IR=Iran, MX=Mexico,TK=Turkey, US=United States

---

Table 2. Earthquake Ruptures Not Clearly Associated with Transform Plate Boundaries. Same format as Table 1.

Country*, Yr	Date	Location or Fault	Length (km)	Avg. Slip (cm)
JP 1891	27 Oct	Nobi	80	504
CH 1920	16 Dec	Kansu	220	725
CH 1951	18 Nov	Damxung	90	800
MO 1957	04 Dec	Gobi-Altai	236	654
CH 1970	04 Jan	Tonghai	48	210
CH 1973	06 Feb	Luhuo	89	130
AL 1985	27 Oct	Constantine	3.8	10
CH 1988	06 Nov	Lancang-Gengma	35	70
CH 1988	06 Nov	Gengma, Yunnan	15.6	60
JP 1943	*10 Sep*	*Sikano*	*33*	*50*

*AL=Algeria, CH=China, JP=Japan, MO=Mongolia

Figure Captions

Figure 1. We model the slip that results on a frictionless vertical rectangular rupture with one edge at the surface of a uniform half space with rigidity, μ (assumed to be $3X10^{10}$ Mpa); the rupture is **L** km long by **W** km deep, and is driven by a regional stress field, σ. The rupture is divided into 11 segments in the strike and dip directions, and the slip on each sub-element is determined by the boundary-element method. This process models a uniform stress-drop of $\Delta\sigma$ across the fault plane, with a variable slip-function that decays to 0 at the buried rupture edges. The average slip, **d**, is computed by numerically averaging all 121 sub-elements.

Figure 2. The effect of variations in locking depth and stress-drops on theoretical scaling relationships. **W**- models are computed as described in the text and Fig. 1, **L**- models are from Scholz (1982). A) Theoretical scaling for ruptures with uniform constant stress drop of 3 Mpa. Increasing **W** straightens the knee and shifts it to larger values of rupture length. As **W** increases, the **W**- models asymptotically approach the **L**- model with the same stress drop. B) Theoretical scaling for ruptures with a uniform locking depth of 10 km. Increasing the stress drop multiplies each **W**- model and the slope of each **L**- model by a constant.

Figure 3. Observations, from Wells and Coppersmith (1994), and theoretical scaling relations. A) Ruptures on or near transform plate boundaries, as described in text. Symbols correspond to ruptures in Times-Roman font in Table 1 coded as follows: circles = California / Baja California, stars = Turkey, triangles = Iran, square = Central America. Models are: dashed line = **L**- model from Scholz (1982); higher **W**- model = $\Delta\sigma$ 3 Mpa, **W** = 15 km; lower **W**- model = $\Delta\sigma$ 1 Mpa, **W** = 15 km. B) Ruptures not near known transform plate boundaries. Symbols correspond to earthquakes listed in Times-Roman font in Table 2. coded as follows: stars = China, triangle = Algeria, circle = Mongolia, square = Japan. Models are: dashed line = **L**- model $\Delta\sigma$ 5 Mpa; solid line = **W**- model $\Delta\sigma$ 2.8 Mpa, **W** = 25 km

Figure 4. Slip vs. rupture length for transform plate-boundary ruptures from Wells and Coppersmith (1994) [symbols as in Figure 3A], with additional values from Scholz (1982) [indicated by **x**]. Where the same rupture was used in both studies, an arrow connects the two values. This demonstrates the level of uncertainty associated with many of the observations.

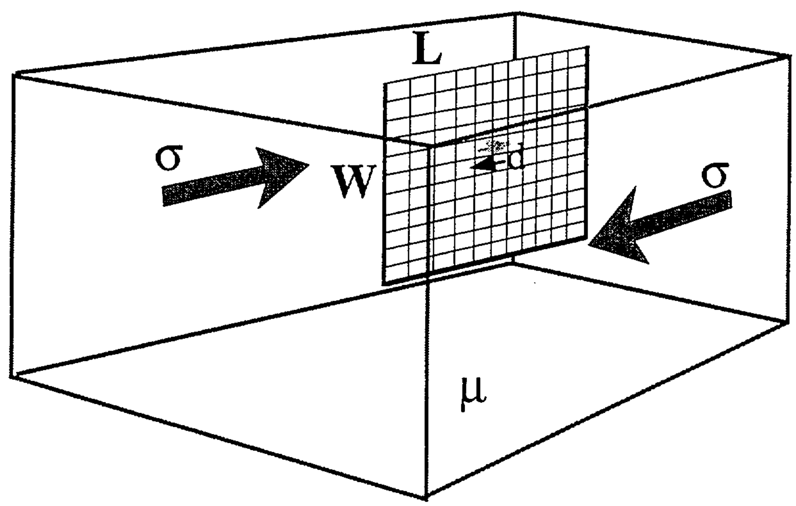
L
σ
W
d
σ
μ

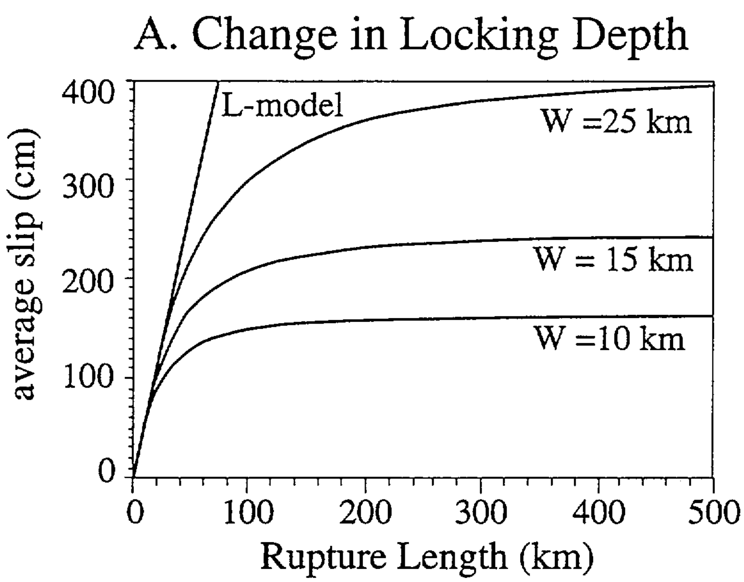
A. Change in Locking Depth
L-model
W =25 km
W = 15 km
W =10 km
average slip (cm)
Rupture Length (km)
0
100
200
300
400
500

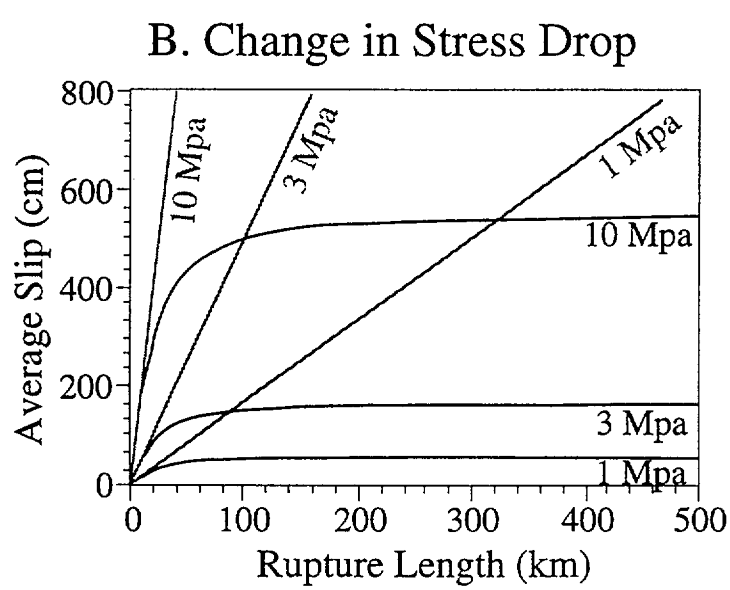
B. Change in Stress Drop
10 Mpa
3 Mpa
1 Mpa
10 Mpa
3 Mpa
1 Mpa
Average Slip (cm)
Rupture Length (km)
0
200
400
600
800
100
300
500

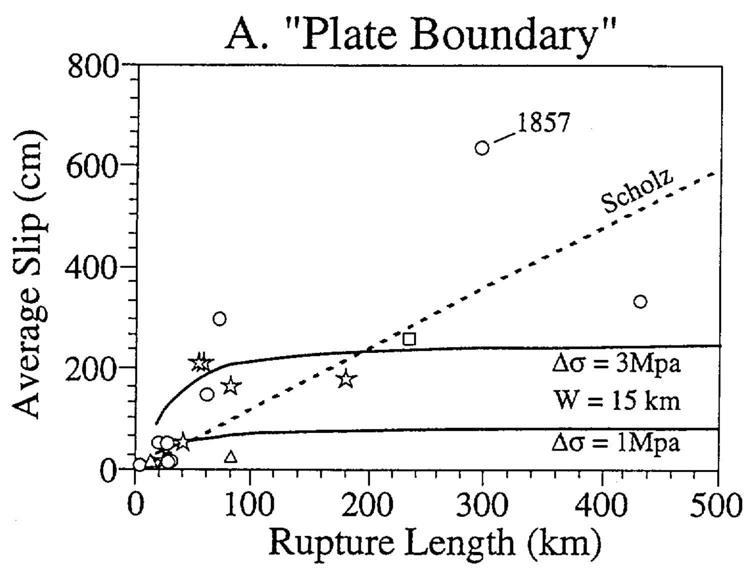

A. "Plate Boundary"
Average Slip (cm)
800
600
400
200
0
1857
Scholz
Δσ = 3Mpa
W = 15 km
Δσ = 1Mpa
0
100
200
300
400
500
Rupture Length (km)

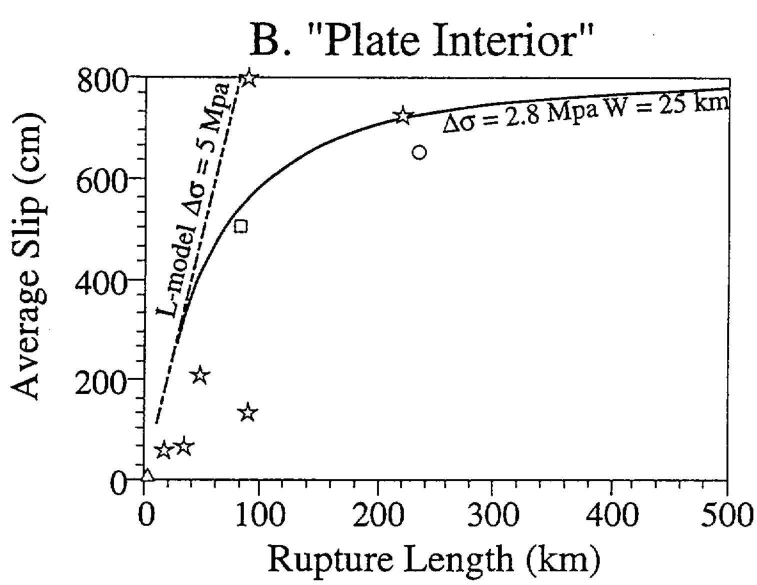

B. "Plate Interior"
Average Slip (cm)
800
600
400
200
0
L-model Δσ = 5 Mpa
Δσ = 2.8 Mpa W = 25 km
0
100
200
300
400
500
Rupture Length (km)

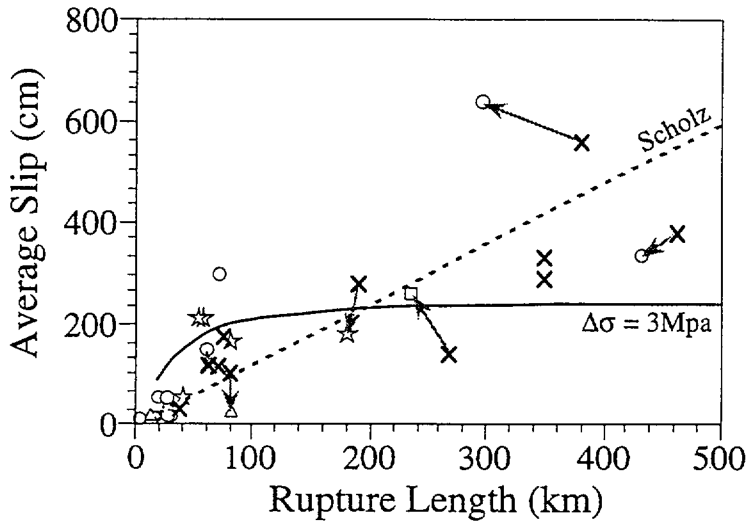

800
600
400
200
0
Average Slip (cm)
0
100
200
300
400
500
Rupture Length (km)
Scholz
Δσ = 3Mpa

Methodology for Using Precarious Rocks in Nevada to Test Seismic Hazard Models

John G. Anderson and James N. Brune

Seismological Laboratory and Department of Geological Sciences, Mackay School of Mines, University of Nevada, Reno, Nevada 89557

Abstract

Fields of precariously balanced rocks indicate that strong earthquake motions have not occurred at that site since the precarious rocks developed. These fields can be characterized with an estimate of the peak acceleration that would be sufficient to topple the rocks, and an estimate of how long the rocks have been precarious. This paper uses this information to test the input to probabilistic seismic hazard analysis. The fundamental assumption is that the probability of exceeding a ground motion capable of toppling a precarious rock during a time period equal to the age of the rock is equal to the confidence level at which the inputs to the probabilistic seismic hazard analysis can be rejected.

We performed a probabilistic seismic hazard analysis for 26 sites of observed precarious rocks in Nevada, using preliminary estimates of the toppling acceleration and the age of the features. Following standard practice, the first probabilistic seismic hazard analysis used both faults and diffuse area seismic sources. The area sources had a minimum magnitude of 5.0. The

Submitted to Bull. Seism. Soc. Am., July 1996

attenuation relationship allowed ground motions of up to + 3 sigma. Two models of this type are rejected with over 95% confidence by most of the precarious rock observations. Clearly, some aspect of analysis is wrong.

We considered possible explanations for the inconsistency of the precarious rock observations and the probabilistic seismic hazard analysis. As in southern California (Brune, 1996), a probabilistic seismic hazard analysis which eliminates the area sources and only includes faults is consistent with the precarious rock observations at essentially all of the sites. However, additional calculations indicate that it may not be necessary to totally reject the inclusion of diffuse zones from the probabilistic seismic hazard analysis. The physics of rock stability may allow increasing the minimum magnitude to 6.0 in the area sources, since the short duration of high frequency accelerations in smaller events may not topple all precarious rocks. Alternatively, because the precarious rocks are generally sited on relatively good quality rock outcrops, truncating the attenuation relationship to eliminate above-average accelerations may be appropriate. Individually, each of these effects allow more of the precarious rock sites to be consistent with the area source zones, and if both are effective only about 20% of the precarious rock sites are inconsistent with the probabilistic seismic hazard analysis input including diffuse zones. Changes in diffuse source zone geometries might further reduce the number of discrepancies. Thus, with the present uncertainties in interpretation of the precarious rocks, it is premature to reject the concept of area sources in general.

Introduction

Brune (1996) reported on the existence of precarious rocks in southern California, and proposed that their presence could place a constraint on probabilistic seismic hazard analysis. This study develops a more rigorous procedure to utilize that constraint. We also use this procedure to evaluate the input to some probabilistic seismic hazard analyses for Nevada.

A major question that has developed from the Brune (1996) study is whether area source zones are generally valid in probabilistic seismic hazard analysis. In southern California, analysis that includes the diffuse zones seems to give hazards that are much too high to be consistent with the observed precarious rocks but when faults only are used as input to the analysis there is no contradiction. The relevance of this result in another region, such as Nevada, needs to be carefully examined.

Precarious Rocks in Nevada

Figure 1 shows locations of precariously balanced rocks identified and documented by Jim Brune in field trips during 1994 and 1995. Each site is also listed in Table 1. Additional analysis and field study is needed to reduce the uncertainties on peak accelerations sufficient to topple the most precarious rocks in each formation. The accelerations listed in Table 1 are estimates based on field examinations of each field of rocks, combined with experience developed from laboratory experiments to topple scale models of precarious rocks and field experiments measuring the force to move some precarious rocks (Shi et al., 1996). Likewise, the age of the precarious rocks is based on visual inspections in the field of the geomorphic setting and, in some cases, the development of desert varnish on surfaces that, once exposed, assure that the rock is precariously balanced. The uncertainties in these ages can be reduced by radiocarbon dating of the desert varnish, analysis of the desert varnish layering, and determination of cosmogenic exposure times (Bell et al, 1996), but that has not been done yet in most cases reported in Table 1. Brune (in preparation) is preparing a more thorough documentation of these fields of precariously balanced rocks. We believe the preliminary estimates given in Table 1 are accurate enough to illustrate the proposed methodology and to draw preliminary conclusions.

Method

Precarious rocks with an age of T years demonstrate that shaking strong enough to knock down the rocks has not occurred within the past T years. For instance, if the input model for the probabilistic seismic hazard analysis implies that it is certain that ground motions capable of knocking down a precariously balanced rock would have occurred in the past T years, then it is necessary to reject that input model with certainty. The presence of the precarious rocks prove that the input is wrong.

This concept can be generalized. The initial output of a probabilistic seismic hazard analysis is a hazard curve, which gives the expected annual rate $(N(a))$ of ground motions with amplitude a or larger. Under the usual assumption that the earthquaks occur with a Poissonian distribution in time, then in the time interval T, the probability of a ground motion that equals or exceeds a is: $P(a)=1-exp(-N(a)T)$. If the presence of precariously balanced rocks at the site demonstrate that ground motion with amplitude a has not been exceeded in this time interval, then the confidence level in rejecting the seismicity model for that site is also *P(a)*.

An issue is whether we could reject any seismicity models altogether on the basis of this approach. In considering this question, it is important to bear in mind that the sites with precarious rocks are not chosen at random, and are not necessarily independent. For each site where precarious rocks have been discovered, there may be several where they are not present but could have been if an earthquake had not occurred recently. Thus, it is not valid to calculate the joint probability of all of these sites having precarious rocks. Thus, formally we can only use each site as an indication of whether the input to the probabilistic seismic hazard analysis is locally acceptable or not.

The parameters a and T are uncertain. This paper evaluates *P(a)* for a range of values for several sites of precariously balanced rocks in Nevada. Values in Table 1 are taken as best estimates of both. Sensitivity to these estimates is tested by considering values of a increased and decreased by 50%, and values of T increased and decreased by a factor of 2.

The probabilistic seismic hazard analysis is carried out with a revised version of program EQRISK (Anderson and Trifunac, 1978). The input includes faults (line sources) and diffuse seismicity zones (area sources). All earthquakes are given finite rupture lengths using a magnitude - rupture length relation given by Wells and Coppersmith (1994). The attenuation relation is the one given by Idriss (1991) for rock and stiff soil sites, truncated to disallow accelerations more than 3σ greater than the mean.

Seismicity models

This paper utilizes six different seismicity models to evaluate *P(a)*. They are summarized in Table 2. The first two models are in the category of standard inputs for probabilistic seismic hazard analysis. Model 1 is identical to the input used by Siddharthan et al. (1993), which includes both area sources and faults. The fault activity rates and seismicity in the diffuse zones in Model 1 are given by Siddharthan et al. (1993). Model 2 uses the same faults, but a different set of area sources. The diffuse zones in Model 2 are generally larger, and chosen with a somewhat different philosophy. The boundaries of both sets of source zones are shown in Figure 2. Table 3 lists activity rates for the source zones in Model 2, since they are not published elsewhere. Both of these models differ from the earlier model of Algermissen et al. (1982) by the inclusion of a comprehensive set of faults (Figure 3) in addition to area sources. Comparisons of the output of Siddharthan et al. (1993) and Algermissen et al (1982) did not reveal any major discrepancies. Because of the interest in the relative contributions of faults and area sources, Models 1 and 2 are more interesting for this study than the model by Algermissen et al. (1982). As will be seen, the results of the probabilistic seismic hazard analysis with models 1 and 2 are quite similar. Model 3 uses only the faults identified by Siddharthan et al. (1993), to test the effect of eliminating the area sources completely.

Brune (1996) points out that the precarious rocks are likely to be at sites with below average ground motions, and in addition that small earthquakes may not be able to topple precariously balanced rocks even when the acceleration peak is as high or higher than accelerations that can topple them in a large earthquake. Thus, Models 4 and 5 examine sensitivity to the minimum magnitude and attenuation relations, respectively, by introducing perturbations to Model 2.

Model 4 is equivalent of Model 2, except that it uses M_{min}=6.0 instead of 5.0. Thus in Model 4, earthquakes that cause only a brief pulse of high accelerations are removed. Model 5 is the equivalent of Model 2, except that the regression is truncated just above the mean prediction level, at $0.1*\sigma$. While precarious rocks are in locations of positive topography which could cause some amplification (e.g. Geli et al., 1988), this model assumes that the effect of having a more competent bedrock at the site, which tends to cause smaller amplitudes (e.g. Joyner et al., 1981; Day, 1996; Anderson et al., 1996), is more important and the net effect is below average ground motions. Lastly, Model 6 evaluates the joint effect of M_{min}=6 and a cutoff at $0.1*\sigma$, thus combining the effects of Models 4 and 5.

Figures 4 and 5 show hazard curves calculated using the six models as described above. At these two stations, as at most, there is little difference between the estimated hazard curves under Models 1 and 2, but both are much larger than the curves using faults only (Model 3). Thus, the background seismicity zones make the main contribution to the hazard curves at these stations. This is typical for sites in the Basin and Range province, because the recurrence times on faults are generally long. Compared to Model 2, Model 4 is mainly reduced at the lower amplitudes, due to the removal of the numerous magnitude 5 to 6 earthquakes from the seismicity model. Model 5 on the other hand shows a very sharply truncated hazard curve at larger amplitudes compared to Model 2, caused by elimination of the possibility that ground motions exceed the mean estimate at the regression at these sites. The difference between Model 5 and Model 2 shows that above-average motions have a very large influence on the hazard curve in the amplitude range of most interest. Finally, Model 6 is reduced at lower accelerations similar to Model 4, and is sharply truncated at larger amplitudes matching Model 5.

Evaluation

Figure 6 graphs the confidence levels with which various seismicity models could be rejected. Brune (1996) suggested that the presence of precarious rocks in locations away from faults in southern California, where the diffuse zones are driving up the hazard, is an indication that the diffuse zones are not universally valid. Indeed, based on the frequency with which they cause peak accelerations that would topple precariously balanced rocks, Models 1 and 2 are inconsistent with the observations at most of the sites in this study. The best estimates of age and peak acceleration to topple the rocks would lead to rejecting the model in the vicinity of 23 or 24 of the 26 sites in both Models 1 and 2. Within the assumed uncertainties in the age and peak acceleration, these models would still be rejected at 18 or 19 of the 26 sites. Considering the wide geographical distribution of the precarious rocks, there is no choice but to conclude that some part of the analysis based on Models 1 or 2 is wrong.

There are several assumptions in the analysis where we can look to remove the inconsistencies presented by Models 1 and 2. Some of these can be addressed by modifying the probabilistic seismic hazard analysis, and that is the purpose of Models 3, 4, 5, and 6. The analysis assumptions, and modifications where possible, are listed in Table 4. Since Models 1 and 2 give similar results, it is sufficient to modify only Model 2 in testing these ideas.

Model 3 is constructed in response to the possibility that the concept of diffuse zones is not valid. From Figure 6, it is evident that Model 3 causes the fewest contradictions. It is rejected only at site 21, when the uncertainty in age and toppling acceleration is considered. A simple interpretation is that moderate sized earthquakes are located in the vicinity of the major faults, rather than randomly located over much larger areas as is assumed by assigning them to diffuse zones in Models 1 and 2. If so, their large numbers would not over time cause toppling accelerations at the precarious rock sites. This interpretation is consistent with Brune (1996), who reported that in southern California the precarious rock locations correlate with minima in seismic hazard maps by Wesnousky (1986) that use only faults for input.

The models that retain the diffuse zones in some modified form are less successful. Using preferred values of toppling acceleration and age, Model 4 is rejected at 17 sites (65%), Model 5 is rejected at 14 sites (54%), and Model 6 is rejected at 13 sites (50%). As shown in Table 4, Models 4 and would be rejected at about half of the sites taking maximum advantage of uncertainties in toppling acceleration and age, and Model 5 would be rejected at about 25%. Model 6, which combines the modifications from Models 4 and 5, is of course a little better, being acceptable at about 80% of the sites. Since both the higher cutoff magnitude and the truncation of the attenuation relation are rather arbitrarily selected, it is clear that even more restrictive input could further enhance the extent to which individual models could be accepted. Other gains could be achieved by restricting the moderate sized earthquakes to occur near faults. A related factor, not investigated but potentially important, is the selection of the attenuation relationship. All of these modifications require more research to determine the extent to which they are justified. At the same time, the area sources in Models 1 and 2 should be reexamined as part of the effort to reconcile the probabilistic seismic hazard analysis with the precarious rock observations.

In summary, Model 3 (faults only) shows fewer inconsistencies with the precarious rocks than any other model. Models 1 and 2, which add diffuse zones as they are usually included in probabilistic seismic hazard analysis, are inconsistent with precarious rock observations.

However, Models 4, 5, and 6 indicate that the diffuse source zones might be reconciled with precarious rock observations if further research validates the assumptions that went into those models: earthquakes with magnitude under 6 have too short a duration to topple many of the rocks, and sites with precarious rocks generally have below-average levels of ground shaking. It is important to note that the ground motions that are considered by Models 1 and 2 but disallowed in Models 4-6 could be important for other types of structures or for locations with larger assumed site amplification. Thus it is premature to reject area sources as a general type of probabilistic seismic hazard analysis input, as in Models 1 or 2, on the basis of the precarious rock observations.

Discussion

Site effects at the precarious rock locations is a topic deserving further investigation. While we assumed that the attenuation relation was truncated essentially at the mean value, it may turn out that ground motions at precarious rock sites are generally even smaller. A preliminary analysis by Feng Su based on coda amplifications at sites near precarious rock locations in southern California suggests that ground motions at these sites could be 50% smaller than at average "rock" sites (i.e. type A sites). Measurements of ground motions are called for to resolve this issue.

The assumption that the probability of ground motion that equals or exceeds the peak ground motion a, $P(a)$, equals the confidence level in rejecting the seismicity model could also be debated. One might introduce an additional distribution giving the probability of toppling the rocks in a field of precarious boulders as a function of the amplitude of ground motion. The distribution would have two contributions: the range of toppling accelerations caused by the range of precarious rock geometries, and the chance that different time series with the same peak acceleration might not all allow a specific rock to remain in a precarious position. For the first contribution, the toppling acceleration of the remaining rocks would continue to provide a constraint on the ground motions that have affected the site. A distribution of effectiveness of different time series with the same peak acceleration might indicate that peak acceleration is an imperfect parameter to characterize whether precarious rocks will be toppled. If this distribution has a large standard deviation, the assumption that $P(a)$ gives the confidence level of rejecting the seismicity model should be modified appropriately, but we expect that the distribution is sufficiently narrow that the results will not be significantly affected.

Nonetheless, it has not yet been established that peak acceleration is the most appropriate ground motion parameter for the toppling of precarious rocks. It could, instead, be more correct to correlate with some other parameter such as a response spectral amplitude. If that is proven, it is of course straightforward to carry out the same type of analysis with that different parameter. Ultimately it might be best to use different parameters for different precarious rocks, depending on their geometry. More research is needed to establish this. Whatever the result, the methods presented in this paper introduce a quantitative method by which the presence of precarious rocks can be used as a constraint or a test on input to probabilistic seismic hazard analysis.

A factor not discussed here is the evolution of precarious rocks over time. In some situations, erosion can work to increase the precariousness of the rock over time. An example of this is some of the precarious rocks near Las Vegas, which are of the hoodoo type, where a hard protective boulder rests on top of a less resistant pillar (e.g. Brune and Anderson, 1996). Where this is the mechanism of formation, the fields of precarious rocks would have required greater accelerations to be toppled earlier in their development. To the extent that this factor is active, the probability of rejecting a seismicity model would tend to be overestimated. However, we believe that many of the fields of precarious rocks were actually developed by a different mechanism in which soft material that develops below the surface along joints is removed relatively quickly leaving piles with the resistant cores of rocks, with the ones on top precariously balanced. Rapid removal of the soft material might have occurred during the wetter climate late in the last glacial period that ended roughly 10000 years ago (Bell et al, 1996). With the combination of the dry climate that has persisted in Nevada since then, plus the decreased weathering rate of rocks when they are subareal, the erosional processes would be slow to nonexistent, as illustrated by the development of desert varnish, so a precarious formation could presist essentially unchanged for long time periods. However, this is a subject that deserves more detailed investigations.

None of the uncertainties discussed here present insurmountable obstacles. We are optimistic that precarious rock observations will be extremely useful for providing constraints to probabilistic seismic hazard analysis.

Acknowledgements

We appreciate helpful discussions with Tom Hanks, Mark Stirling, Steve Wesnousky, and Yuehua Zeng. Mark Stirling made several helpful suggestions for an earlier draft of the manuscript. John Anderson thanks the University of Nevada for granting a sabbatical leave, during which much of this research was completed. This project was supported by USGS

Contract ___,? and by DOE?.

References

Algermissen, S. T., D. M. Perkins, P. C. Thenhaus, S. L. Hanson and B. L. Bender (1982). Probabilistic estimates of maximum acceleration and velocity in rock in the contiguous United States, Open-File Report 82-1033, U. S. Geological Survey, Denver, Colorado, 99 pages.

Anderson (1978) eqrisk

Anderson, J. G., Y. Lee, Y. Zeng and S. Day (1996). Control of strong motion by the upper 30 meters, BSSA (in press)

Bell, J. W., J. N. Brune, T. Liu, M. Zreda and R. I. Dorn (1996). Surface-exposure dating of precariously balanced boulders: an application for seismic hazard studies in California and Nevada, Geological Society of America Abstracts with Program, v. 28, no. 5, p. 48.

Brune, J. N. (1996). Precariously balanced rocks and ground-motion maps for southern California, BSSA 86, 43-54.

Brune, J. N. and J. G. Anderson (1996). Precarious rocks and seismic risk in the Las Vegas region, (in preparation).

Day, S. M. (1996). RMS response of a one-dimensional half-space to SH, BSSA 86, 363-370.

Geli, L., P.-Y. Bard and J. Beatrice (1988). The effect of topography on earthquake ground motion; a review and new results, BSSA 78, 42-63.

Idriss, I. M. (1991). Selection of earthquake ground motions at rock sites, Report prepared for the Structures Division, Building and Fire Research Laboratory, National Institute of Standards and Technology, Department of Civil Engineering, University of California, Davis, September.

Joyner, W. B., R. E. Warrick, and T. E. Fumal (1981). The effect of Quaternary alluvium on strong ground motion in the Coyote Lake, California earthquake of 1979, BSSA 71, 1333-1349.

Shi, B., A. Anooshehpoor, Y. Zeng and J. N. Brune (1996). Rocking and overturning of precariously balanced rocks by earthquakes, BSSA (in press).

Siddharthan, R., J. W. Bell, J. G. Anderson and C. M. dePolo (1993). Peak bedrock acceleration for State of Nevada, Department of Civil Engineering, University of Nevada, Reno, 51 pages.

Wells, D. L. and K. J. Coppersmith (1994). New empirical relationships among magnitude, rupture length, rupture width, rupture area, and surface displacement, BSSA 84, 974-1002.

Wesnousky, S. G. (1986). Earthquakes, Quaternary faults, and seismic hazard in California, J. Geophys. Res. 91, 12587-12631.

Tables

Table 1.

Sites with precarious rocks in Nevada

This list gives locations of 26 sites in or immediately adjacent to Nevada where there are fields of precarious rocks. The peak accelerations sufficient to topple the rocks in each field (a_{max}) and the age of each field (Age) are preliminary estimates.

No.	Station Name	Longitude	Latitude	a_{max}	Age
21	Winnemucca Ranch	-119.75	39.95	0.15	10000.
22	Eureka E.	-115.92	39.41	0.30	10000.
23	West of Wabuska	-119.25	39.15	0.15	5000.
24	Wilson Canyon	-119.22	38.81	0.15	1000.
25	Palmetto Wash	-117.75	37.45	0.15	5000.
26	Belmont North	-116.83	38.60	0.15	10000.
27	Pink Butte	-116.95	38.25	0.15	2000.
28	Ash Springs	-115.15	37.55	0.15	10000.
29	Nelson Landing	-114.70	35.70	0.15	1000.
30	Yucca Mountain	-116.50	36.75	0.15	20000.
31	South Crater Flat	-116.52	36.77	0.30	2000.
32	Searchlight South	-114.80	35.20	0.20	5000.
33	Beatty	-116.76	36.91	0.20	5000.
34	40 Mile Wash	-116.38	36.82	0.20	10000.

35	North Crater Flat	-116.61	36.94	0.20	1000.
36	Tarantula Canyon	-116.63	36.87	0.30	5000.
37	Pahute Mesa	-116.20	37.10	0.20	2000.
38	Hancock Summit	-115.38	37.43	0.40	10000.
39	Red Rock Road	-119.92	39.81	0.30	10000.
40	Broken Hills West	-118.04	39.06	0.40	10000.
41	Owyhee South	-116.06	41.89	0.30	10000.
~~42~~	~~JARBIDGE~~	~~-115.43~~	~~42.00~~		
43	Contact	-114.75	41.77	0.40	10000.
44	South Lake Tahoe	-119.98	38.94	0.40	5000.
45	Sand Springs South	-118.35	39.20	0.40	10000.
46	New Pass Canyon	-117.53	39.58	0.40	5000.
47	Austin Summit	-117.03	39.48	0.40	10000.

Table 2

Seismicity Models

Model	Seismicity	Attenuation
1	Faults and area sources as given by Siddharthan et al. (1993). The faults are the only sources for events with magnitudes over 6.75, and the area sources are the only sources for earthquakes with magnitudes under 6.75.	Idriss (1991) model for peak ground acceleration on rock or firm soil. Regressions use a cutoff at +3 sigma.
2	Faults from Model 1. New area sources as given in Table 3. As in Model 1, the minimum magnitudes in area sources is 5.0.	Same as Model 1.
3	Only the faults from Model 1.	Same as Model 1.
4	Same as Model 2, except that the Minimum magnitudes in diffuse zones is 6.0.	Same as Model 1.

5	Same as Model 2.	Same regression as in Model 1, but with a cutoff at +0.1 σ.
6	Same as Model 4.	Same as Model 5.

Table 3

Diffuse Zones Used for Model 3

Zone	a*	b	Area (km2)	Coordinates of Corners (clockwise) longitude	latitude
1	3.88	0.80	37900	-121.83	41.20
				-119.51	39.47
				-119.51	38.87
				-118.07	37.77
				-119.27	37.77
				-120.26	38.45
				-120.26	38.94
				-122.58	40.76
2	3.53	0.81	163375	-121.83	41.20
				-121.83	42.48
				-112.58	42.48
				-113.18	42.02
				-112.73	41.42
				-115.21	40.30
				-120.62	40.30
3	3.88	0.81	53150	-120.62	40.30
				-117.28	40.30
				-117.28	37.50
				-118.07	37.50
				-118.07	37.77
				-119.51	38.87
				-119.51	39.47
4	3.24	0.82	13500	-117.28	40.30
				-115.21	40.30
				-112.73	41.42
				-112.27	40.81
				-112.47	38.80

				-113.43	38.04
				-114.73	37.50
				-117.28	37.50
5	4.52	0.83	7450	-119.27	37.77
				-118.07	37.77
				-118.07	37.12
				-119.27	37.12
6	3.91	0.81	109250	-118.07	37.50
				-114.73	37.50
				-113.43	38.04
				-112.47	38.80
				-112.27	40.81
				-113.18	42.02
				-111.45	43.20
				-110.42	43.20
				-111.03	41.84
				-111.30	38.47
				-112.38	37.55
				-114.31	36.85
				-117.84	36.85
				-118.07	37.12
7	3.35	0.83	160050	-117.84	36.85
				-114.31	36.85
				-112.38	37.55
				-111.27	37.00
				-111.27	34.00
				-115.40	34.00
				-116.56	35.70

* a is for an incremental relationship giving number of events in a magnitude range +- 0.25.

Note: All diffuse zones use Mmax=6.5.

Table 4

Possible explanations for failure of standard probabilistic seismic hazard analysis

	Assumption	Alternative	Modification to probabilistic seismic hazard analysis	Result (Using maximum range of uncertainties)
1.	The existence of area source zones in which moderate earthquakes are uniformly distributed. Brune (1996)	Only the large faults can cause significant motions.	Model 3, which eliminates all area sources.	Acceptable at 25/26 sites.
2.		The distribution of sources within the area zones is in reality very inhomogeneous.	Can only be tested with much longer records of seismicity and/or additional research. The small faults that cause the moderate will not generally be visible	Not tested.

			at the surface, so geological mapping is not helpful.	
3.	Peak acceleration is the appropriate parameter to study in the probabilistic seismic hazard analysis. Brune (1996)	Some other parameter such as a response spectral amplitude might be better to represent a threshhold for toppling the rocks.	Carry out probabilistic seismic hazard analysis with other parameters. Numerical and physical experiments on the physics of toppling precarious rocks.	Not tested.
4.	The assumption that a peak acceleration spike of short duration will cause the rocks to fall. Brune (1996)	An acceleration at the threshhold may require several cycles of motion.	Models 4 and 6, which eliminate small earthquakes (causing only short durations) from the seismicity model.	By itself, allowed at 13/26 sites.
5.	Site effects at sites of precarious rocks have the same distribution as where strong	The site amplifications could be systematically smaller.	Models 5 and 6, which eliminate ground motions greater than 0.1	By itself. allowed at 19/26 sites.

motion instruments have provided data for regression analysis. Brune (1996)	sigma above the average of the attenuation model.	Model 6 combined allowed at 21/26 sites.

Figures

Figure 1.

Map of Nevada showing locations of precariously balanced rocks used in this study. Site numbers are referenced to Table 1.

Figure 2.

Map of Nevada showing earthquakes and boundaries of diffuse seismicity zones used in this study. (A) Diffuse zones from Siddharthan et al. (1993) and Model 1. (B) Diffuse zones used in Model 2. Circles are at the sites of precariously balanced rocks as in Figure 1.

Figure 3.

Surface traces of faults as used by Siddharthan et al. (1993) and this study for input to probabilistic analysis. Assumed magnitudes of events and occurrence rates are given by Siddharthan et al. (1993). Most are based on a preliminary estimate of slip rate using geomorphic expression of the fault. Circles are at the sites of precariously balanced rocks as in Figure 1.

Figure 4.

Estimated hazard curves for the six probabilistic seismic hazard analysis models for Site 21, Winnemucca Ranch. Seismicity models are described in Table 2. The solid vertical line is drawn at the estimated peak acceleration sufficient to topple the most precarious rocks in the field. The solid horizontal line is drawn at an annual occurrence rate that corresponds to a Poisson probability of 95% that an event occurs in a time interval equal to the age of the precarious rocks, or 10000 years in this case (Table 1). An interpretation is that above this horizontal line at the threshhold for toppling the rocks (the vertical line), it is highly certain (>95%) that an earthquake would have caused the given acceleration. Thus if a seismicity model enters the upper right quadrant formed by these two criteria, we conclude that it contradicts the precarious rock observations, while if it enters the lower left quadrant there is no contradiction. For Site 21, all six of the hazard models considered in this paper are inconsistent with the precarious rock observations.

Figure 5.

Estimated hazard curves for the six probabilistic seismic hazard analysis models for Site 32, Searchlight South. See the legend for Figure 4 for an explanation of the figure. For this site, since Models 3, 4, 5, and 6 all enter the lower left quadrant formed by the age and peak acceleration, none of these models for the hazard at Site 32 can be rejected. Within the uncertainties in estimates of both acceleration and age criteria, Models 1 and 2 are also acceptable.

Figure 6.

Summary of rejection confidences for various seismicity models. Rejection confidence is the confidence with which the combination of seismicity model and attenuation model that are input for a probabilistic seismic hazard analysis can be rejected by the presence of precarious rocks. Models are described in Table 2. Frames are for the six different seismicity models. The central symbol at each site is probability of rejecting the seismicity model using the best estimate of the peak acceleration that will topple the rock and the best estimate of the age of the precarious rock. Other symbols are for 50% greater or smaller acceleration, and a doubling or halving of the age.

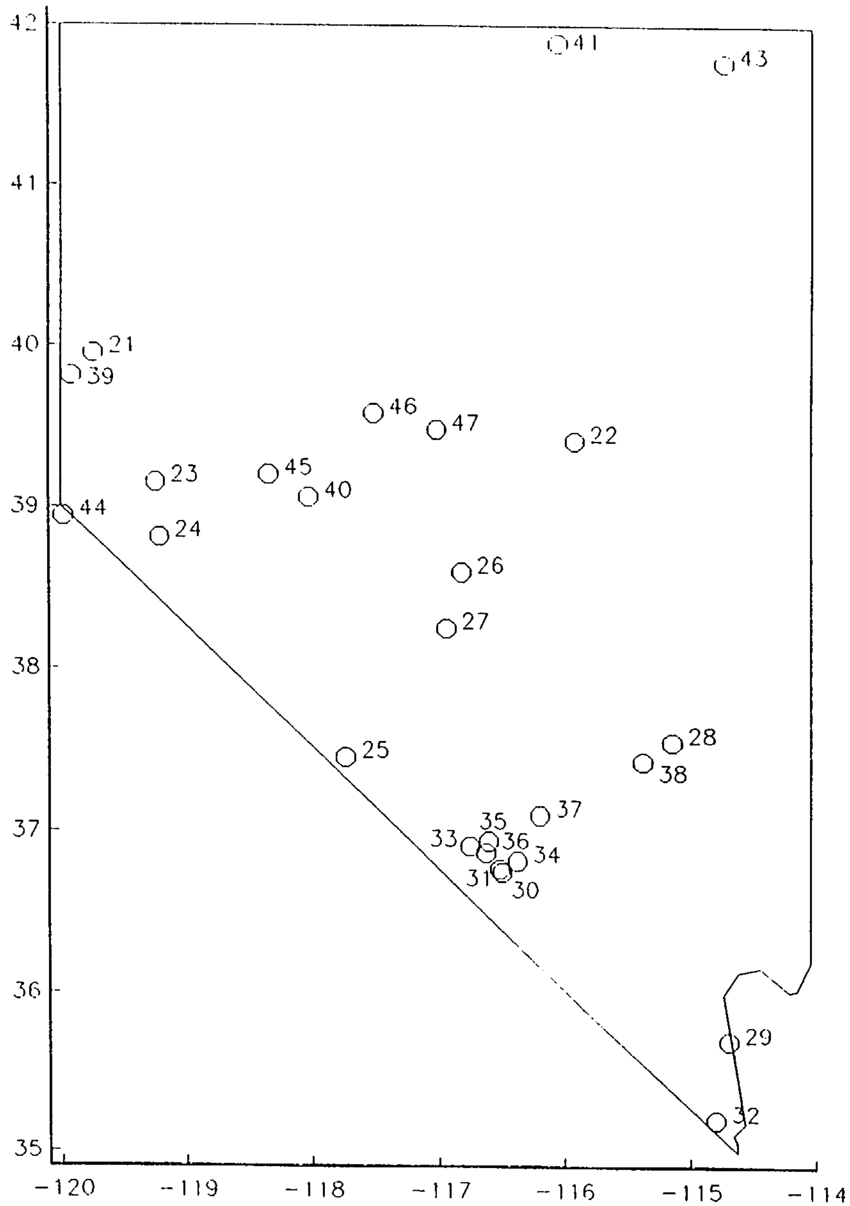
42
41
40
39
38
37
36
35
-120
-119
-118
-117
-116
-115
-114
41
43
21
39
46
47
22
23
45
40
44
24
26
27
25
28
38
37
35
33
36
34
31
30
29
32

Fig 1

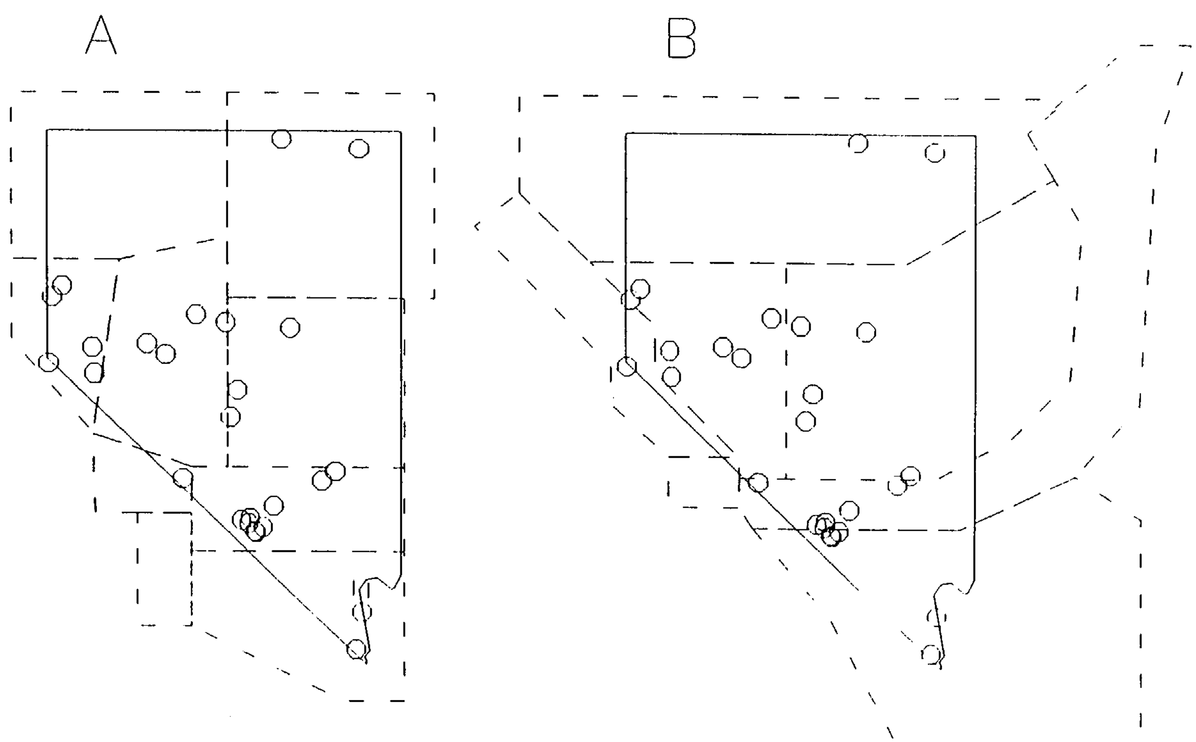

Fig 2.

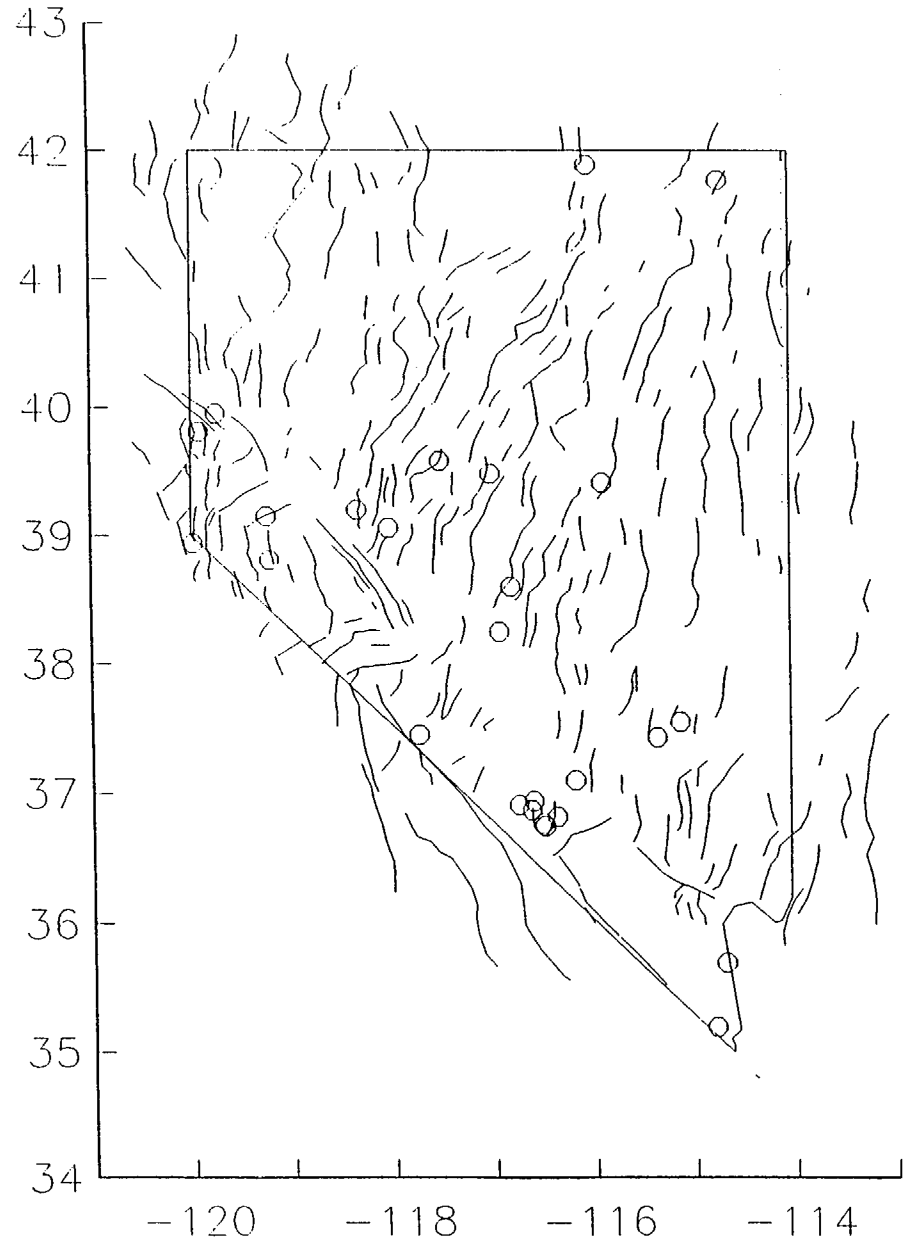

Fig 3

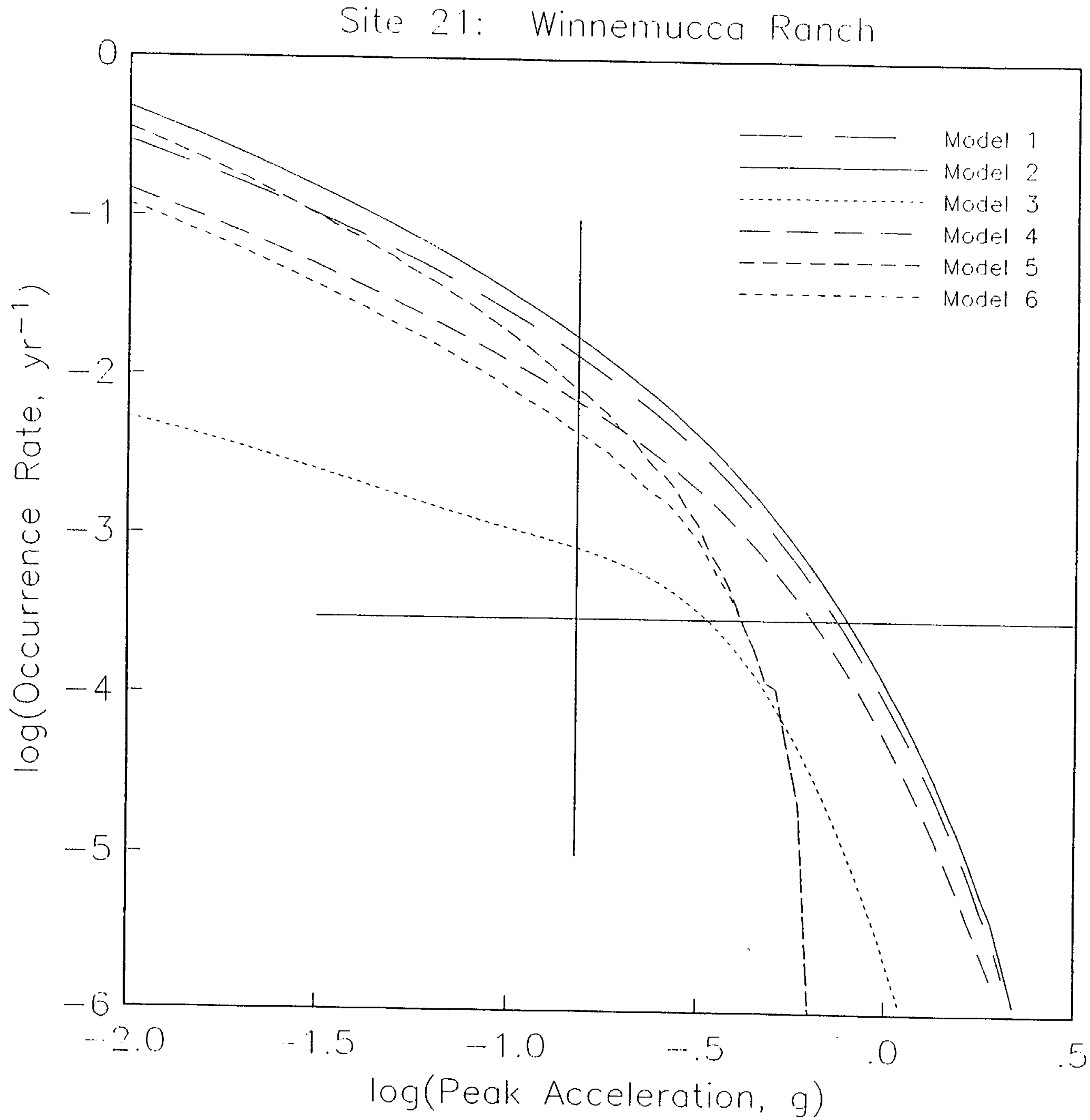
Site 21: Winnemucca Ranch
Model 1
Model 2
Model 3
Model 4
Model 5
Model 6
0
−1
−2
−3
−4
−5
−6
log(Occurrence Rate, yr^{-1})
−2.0
−1.5
−1.0
−.5
.0
.5
log(Peak Acceleration, g)

Fig 4

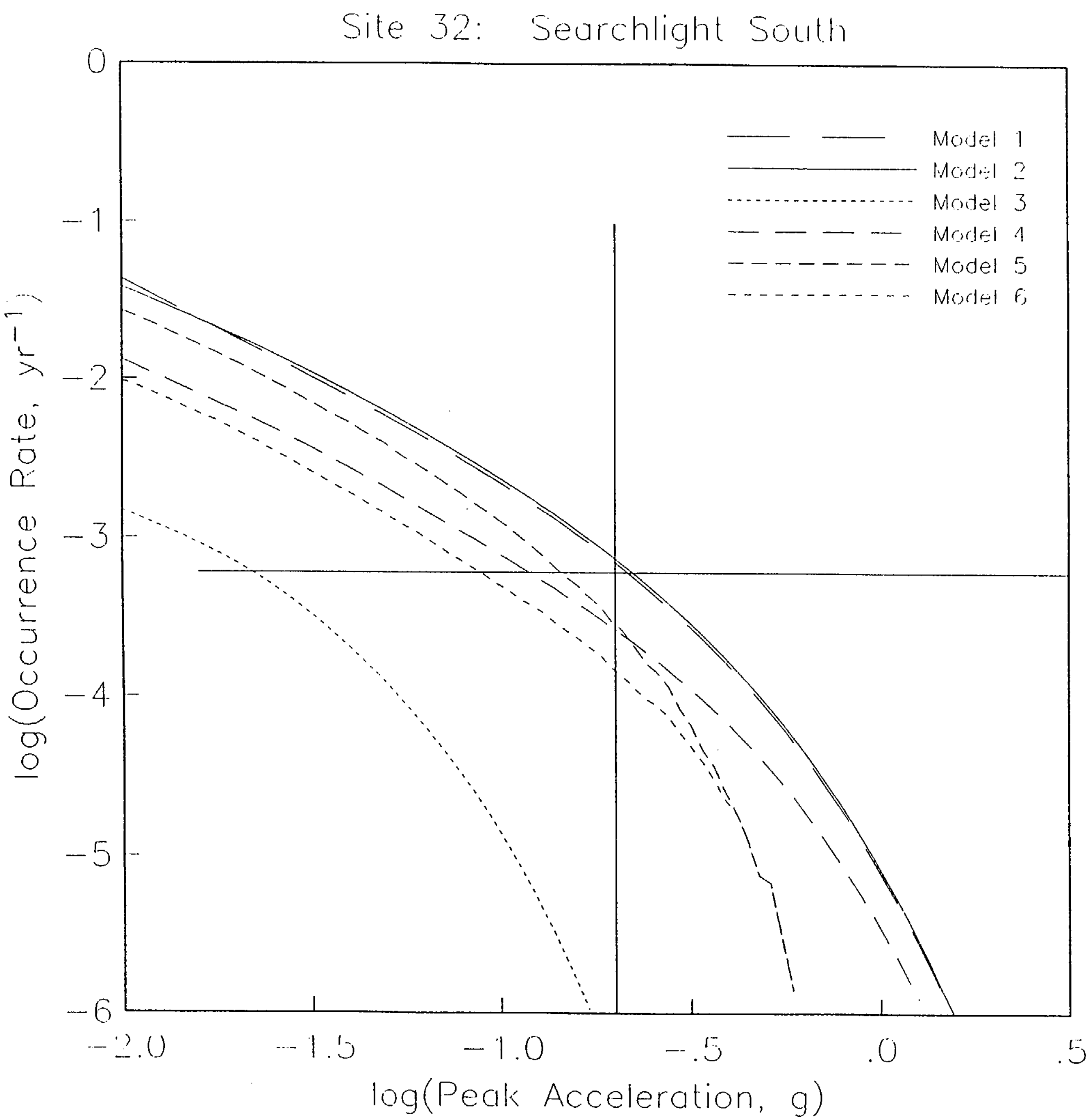

Site 32: Searchlight South
Model 1
Model 2
Model 3
Model 4
Model 5
Model 6
0
-1
-2
-3
-4
-5
-6
log(Occurrence Rate, yr^{-1})
-2.0
-1.5
-1.0
-.5
.0
.5
log(Peak Acceleration, g)

Fig. 5

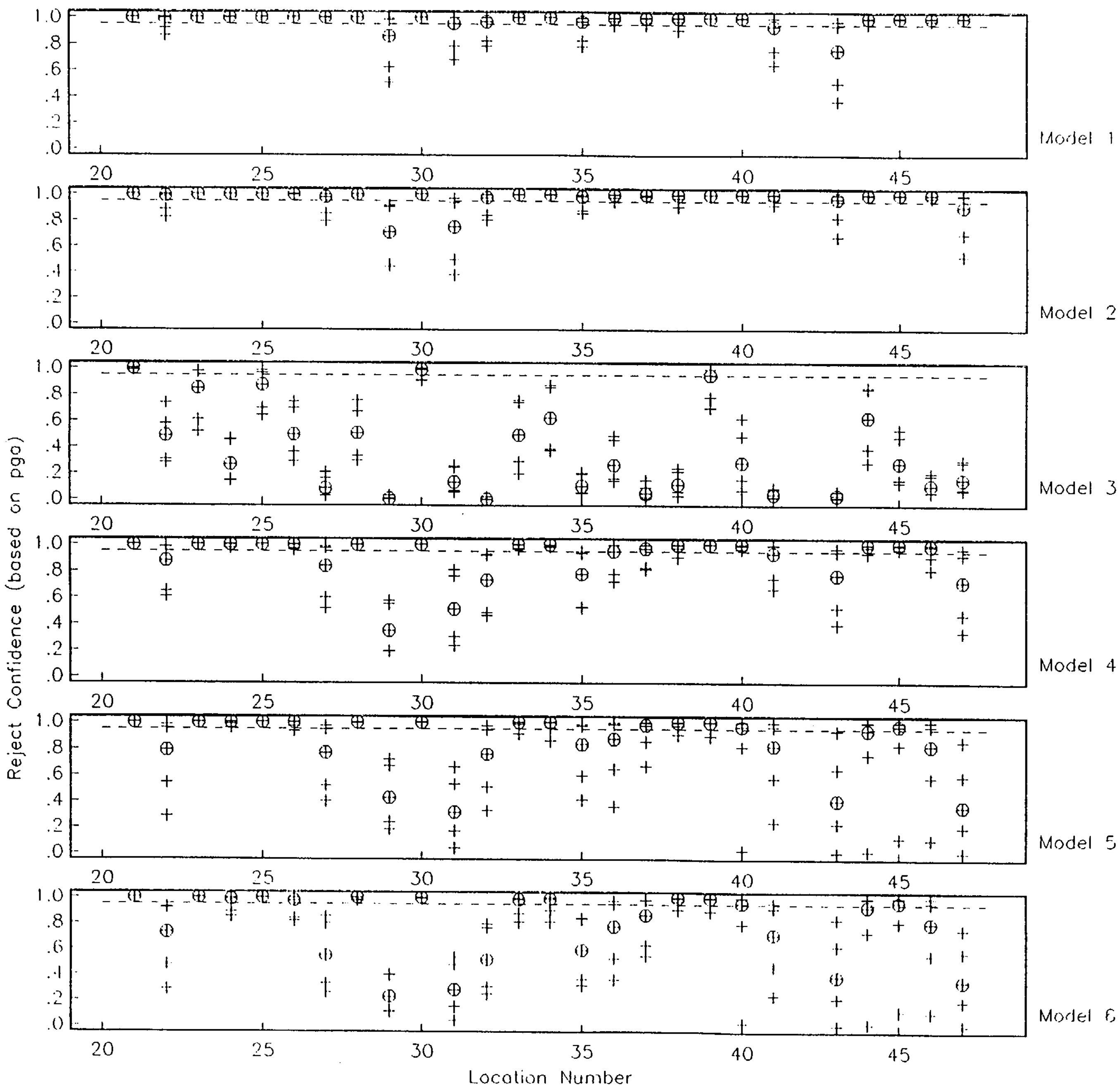
Reject Confidence (based on pgo)
Location Number
Model 1
Model 2
Model 3
Model 4
Model 5
Model 6

Fig 6.

Seismic Source

Experts

Dr. Jon P. Ake	U.S. Bureau of Reclamation
Mr. Larry W. Anderson	U.S. Bureau of Reclamation
Dr. R. Ernest Anderson	U.S. Geological Survey
Dr. Walter J. Arabasz	University of Utah
Dr. Ronald L. Bruhn	University of Utah
Mr. Craig M. dePolo	Nevada Bureau of Mines & Geology
Dr. Diane I. Doser	University of Texas at El Paso
Dr. Christopher J. Fridrich	U.S. Geological Survey
Dr. Peter L.K. Knuepfer	State University of New York at Binghamton
Dr. James P. McCalpin	GEO-HAZ Consulting
Dr. Christopher M. Menges	U.S. Geological Survey
Mr. Alan R. Ramelli	Nevada Bureau of Mines & Geology
Dr. Albert M. Rogers	U.S. Geological Survey
Dr. D. Burton Slemmons	Consultant
Dr. Kenneth D. Smith	University of Nevada at Reno
Dr. Robert B. Smith	University of Utah
Dr. Frank H. (Bert) Swan	Geomatrix Consultants
Mr. James C. Yount	U.S. Geological Survey

Attachment 7

Biosketch for Jon P. Ake

Jon P. Ake is a seismologist whose recent research interests have been focused primarily on seismic hazard analyses, engineering seismology and induced seismicity. He received his undergraduate degree in 1979 in geology and physics. He then worked at the New Mexico Engineering Research Institute where he conducted research dealing with strong ground motions generated by explosions, the dynamic response of earth media, and the applications of signal analysis techniques to ground shock problems. From 1983-1987 Mr.Ake attended graduate school at the New Mexico Institute of Mining and Technology where he received a Ph.D. in geophysics in 1987. His research dealt with the analysis of microearthquake data applied to studies of crustal structure, seismic sources and near-station effects. From 1987-1989 he had responsibility for operating a seismic network focused on assessing seismic hazard in the Colorado Front Range for Denver Water Department facilities. Research involved probabilistic seismic hazard analyses and application of inversion procedures. From 1989 to the present Mr. Ake has been employed by the U.S. Bureau of Reclamation as a senior seismologist in the Seismotectonic and Geophysics group. His duties include seismologic and tectonic fault assessments, estimation of strong ground motions by several techniques, and consultation on engineering geophysics. He has been responsible for review and coordination of seismic hazard and risk analyses and review of contract seismotectonic studies. Additional duties include operation, maintenance and data analysis from two seismic monitoring networks in western Colorado. Current research involves application of finite-source ground motion modelling to engineering analyses, risk-based seismic hazard assessment, and studies of induced seismicity.

Larry W. Anderson
Seismotectonics and Geophysics Group
U.S. Bureau of Reclamation
Box 25007, D-8330
Denver, Colorado 80225

BIOSKETCH FOR LARRY W. ANDERSON

Larry W. Anderson is a geologist with over 17 years experience in the identification, evaluation, and seismic hazard analysis of active and potentially active faults as applied to engineered facilities. Born in San Francisco, California, Larry attended Brigham Young University and the University of Colorado. He received a M.S. degree from the University of Colorado in 1976. From 1977 to 1980, Larry was employed by Fugro, Inc., where he worked on geotechnical investigations for major facilities including fault related studies for several existing or planned nuclear power plants in the western United States. While at Fugro, he compiled the first Quaternary fault map of the state of Utah. In 1981, Larry began work with the Seismotectonic Group of the Bureau of Reclamation. Since that date, Larry has personally conducted or been responsible for numerous seismic hazard studies for Reclamation dams and facilities in the western United States. Many of these studies included detailed fault evaluations such as those for the Ortigalita fault in California, the Pyramid Lake fault zone in Nevada, and the Horseshoe fault in Arizona. Results of these studies have been published in several publications. Since 1992, Larry has been the Principal Investigator on the study of "Quaternary Faulting within 100 km of Yucca Mountain, Including the Walker Lane" for the Yucca Mountain Project. The major emphasis for this study has been on evaluating the Quaternary paleoseismic history of the Death Valley-Furnace Creek fault zone and the Bare Mountain fault.

R. ERNEST ANDERSON

Ernie received his PhD from Washington University, St Louis in 1962 after which he spent 11 years working on AEC-sponsored geologic studies (mostly mapping at various scales) in and around NTS. This NTS background gives him a valuable perspective on a broad range of geologic problems in the YM area, but equally important, he has built on that background to become an expert on the structure and tectonics of the Basin and Range by his mapping and topical studies in more that 40 mountain ranges in the province. For the past 20 years, those studies have been dovetailed with a broad range of regional and site-specific investigations bearing on seismicity and paleoseismicity including: 1. mapping Quaternary fault scarps in western Utah and developing some of the first quantitative understanding of the time dependence of scarp degradation, 2. coordinating USGS paleoseismic studies of the Wasatch fault in Utah, 3. developing an understanding of integrated focal mechanism and fault-slip data in central Utah, 4. evaluating hazards aspects of basaltic volcanism in southern Utah and adjacent Arizona, and 5. advising other agencies such as the USBR and USSCS on seismic hazards aspects of dams in central and southwest Utah. Ernie has a strong interest in paleohydrology and has authored papers on paleohydrology of areas in Clark and Lincoln Counties, NV and a paper interpreting the impoundment-related seismicity at Lake Mead in terms of geographic contrasts in hydraulic continuity. His strongest current research interest is in improving understanding of the 3-D aspects of the deformation field in the Basin and Range and the role of plutonism in shaping that deformation field--two subjects of potentially great importance to understanding the tectonics of YM.

WALTER J. ARABASZ

Education: B.S., Geology, summa cum laude, Boston College, 1964; M.S., Geology, California Institute of Technology, 1966; Ph.D., Geology (minor in geophysics), California Inst. of Technology, 1971.

Professional Experience: Post-Doctoral Research Fellow, Department of Scientific and Industrial Research, Geophysics Division, Wellington, New Zealand, 1970-73; Research Scientist, Lamont-Doherty Geological Observatory, 1973-74; University of Utah (1974-present): Research Professor of Geology and Geophysics (since (1983); Director, University of Utah Seismograph Stations (since 1985).

Research Interests: Network seismology, earthquake-hazard analysis, tectonics and seismicity of the Intermountain area, statistical patterns of earthquake occurrence.

Current Professional Activities: Chair, Council of the National Seismic System; Member, Utah Seismic Safety Commission; Member, Board of Directors, Seismological Society of America, Member, National Research Council's Panel on Seismic Hazard Evaluation.

Relevant Experience: Member, Peer Review Group for *Early Site Suitability Evaluation of the Potential Repository Site at Yucca Mountain, Nevada* (1991); Member, Specialist Panel, *Earthquakes and Tectonics Expert Judgment Elicitation Project, Yucca Mountain High-Level Waste Repository* (1991-92); technical reviewer for reports on seismic hazard methodology for Yucca Mtn. and on seismic design inputs for the Exploratory Studies Facility (1993-94); Member, Seismic Hazard Methodology Team, EPRI Seismic Hazards Research Program (1984-87); varied consulting on earthquake hazard evaluation for engineering firms, the International Atomic Energy Agency, the Department of Energy, the Soil Conservation Service, Lawrence Livermore National Lab, U.S. Bureau of Reclamation.

Ronald L. Bruhn
Department of Geology and Geophysics
University of Utah
Salt Lake City, Utah 84112

Ronald Bruhn received his B.A. in Geology from Alaska Methodist University in 1971. He received his Ph.D. in Geology from Columbia University in 1976. He is a Professor of Geology in the Department of Geology and Geophysics at the University of Utah, where he has worked since 1976. He teaches courses in physical geology, structural geology, engineering geology and tectonics. Bruhn's expertise includes structural geology and tectonics, and the application of structural geology to problems in mining and petroleum geology, and seismic hazards. In earthquake hazards studies, he specializes in the applications of structural geology to infer rupture characteristics, including segmentation of fault zones, fluid flow in fault zones, and earthquake mechanics. He has conducted seismic hazards projects in strike-slip, normal and reverse faulting regimes in the western U.S., Alaska, Israel, South America, and South Korea. He has extensive experience with both regional and detailed studies of faulting in the Basin and Range Province, including the tectonic evolution of the Mesozoic and Cenozoic Cordillera. He has also completed studies on the seismogenic properties of faults in the Central Nevada Seismic Belt. Currently he is developing new methods to date paleo-earthquakes using cosmogenic isotopes. His research and consulting work is supported by the National Earthquake Hazards Reduction Program, the National Science Foundation, the Norwegian Petroleum Directorate, the Department of Energy, and private firms.

ANTHONY J. CRONE

Biographical Sketch

Anthony J. Crone is a geologist whose research interests focus on paleoseismology, earthquake geology, Quaternary tectonics, tectonic geomorphology, and subsurface geology. He has 17 years of national and international experience in paleoseismic investigations. His research focuses on the study problems related to the assessment of earthquake potential and seismic hazard with emphasis on the Mid-continent and Western United States. In his studies, he seeks to characterize the long-term prehistoric behavior of hazardous faults, which requires highly interdisciplinary skills in geomorphology, pedology, Quaternary geology, stratigraphy, subsurface and structural geology, reflection seismology, and neotectonics He has conducted and participated in paleoseismic and geophysical studies of hazardous faults in the New Madrid seismic zone of the Central Mississippi Valley and on Basin and Range normal faults throughout Utah, Idaho, Montana, and Nevada. He assumed lead responsibility for the team of USGS geologists who mapped the fault scarps that formed during the M_s 7.3 Borah Peak, Idaho earthquake in 1983, and conducted subsequent studies of the segmentation and long-term behavior of major range-front normal faults in the northern Basin and Range of Idaho and adjacent parts of Montana. He conducted the pioneering paleoseismic studies of the enigmatic Meers fault in southwestern Oklahoma and subsequently conducted studies of thrust faults in west-central China and central Australia. In recent years, he has continued studies in the central U.S and pursued his interest in examining the long-term behavior of active faults, particularly those in "stable" continental interior settings. He is currently involved in paleoseismic investigations of late Quaternary faulting in southeastern Colorado and central Nebraska, and field studies of Quaternary faults in the vicinity of Yucca Mountain, Nevada.

In addition to his broad and diverse reseach interests and skills, Dr. Crone functions as coordinator for the National/International component of the USGS's National Earthquake Hazard Reduction Program (NEHRP). He serves as a national and international consultant on paleoseismicity and neotectonics and conducts post-earthquake studies in the U.S. and abroad. He serves on expert scientific panels to evaluate neotectonic issues related to critical national facilities. His work has direct application to the characterization of urban earthquake hazards in various regions of the U.S. He also serves as an associate editor for major professional scientific journals.

CRAIG M. dePOLO

Craig DePolo is a Research Geologist for the Nevada Bureau of Mines and Geology. He has been involved with seismic hazard characterization and research for the last 18 years, 12 of which have been studying the Basin and Range province. He has been involved with the seismic hazard characterization of Yucca Mountain, Nevada for the last nine years. Craig has conducted aerial reconnaissance and photographic missions of active faults and historical earthquake ruptures, worked on logging and interpreting trenches, and has, to date, characterized the seismic hazard of several hundred faults. He has worked on fault segmentation theory using historical earthquakes as a data base and a fault slip rate theory using fault data from Nevada and California. Craig has mapped out the surface ruptures from the 1932 Cedar Mountain earthquake, and worked on trench studies along these breaks. Recent research has included an analysis of the maximum background earthquake for the Basin and Range province and studies of multiple segment and distributed surface ruptures. He is currently involved in devising and managing an earthquake scenario project in the Reno-Carson City urban corridor. Craig is an active participant in the Nevada Earthquake Safety Council, and is the past Chairman and currently serves on the Executive Committee of the Western States Seismic Policy Council.

Diane Irene Doser
Department of Geological Sciences, University of Texas at El Paso

Education:
B.S. Applied Geophysics, Michigan Technological University
M.S., Ph.D., Geophysics, University of Utah

Professional Experience:
Postdoctoral fellow, California Institute of Technology
Assistant (1986-1991), Associate (1991-present) Professor, Director, Kidd Memorial Seismic Observatory, University of Texas at El Paso

Experience Related to Seismic Sources: both M.S. and Ph.D. work related to earthquakes of the intermountain west, have published 16 papers related to source processes of U.S. intermountain earthquakes, including 4 papers on Nevada earthquakes, have published 5 papers related to source processes of earthquakes in other continental rifts (Baikal, east Africa), 6 papers on southern California-northern Baja California earthquakes, and 4 papers related to induced seismicity in west Texas oil fields

Experience Related to Siting of Nuclear Waste Facilities: co-PI on numerous grants (1987 to present) from Texas Low-Level Radioactive Waste Authority to assess seismic hazards associated with two proposed disposal sites in west Texas and to operate seismic monitoring networks in these regions

CHRIS FRIDRICH
Geologist/Hydrologist
U.S. Geological Survey

Chris Fridrich obtained both his doctorate and masters degrees in geology from Stanford University. He also has a bachelor's degree in geological engineering from Michigan Technical University. Dr. Fridrich has been working on the Yucca Mountain project since 1988, including both research and managerial duties. He is responsible for geologic mapping of the Crater Flat basin and structural analysis of the map data for the purpose of developing constraints on tectonic models to be used in seismic risk assessments of the Yucca Mountain site. He is also principal investigator for studies of tectonic effects on the hydrology of Yucca Mountain, which includes hydrogeologic studies, surface and subsurface mapping, and evaluation of several types of geological, geophysical and hydrologic data.

PETER L.K. KNUEPFER
UNIVERSITY OF NEW YORK AT BINGHAMTON

Dr. Peter L.K. Knuepfer has worked on paleoseismic studies in the Basin and Range of the western United States throughout his professional career. He wrote grant proposals and was a member of the Woodward-Clyde Consultants team that pioneered trenching of normal faults for paleoseismic analysis along the Wasatch fault in the late 1970s. As a graduate student at the University of Arizona in the early 1980s, he assisted in trenching studies of a low-slip-rate fault, the Santa Rita Piedmont fault, south of Tucson, Arizona, and he worked with Prof. William B. Bull and other students on studies of the 1887 surface rupture and previous breaks along the Pitaycachi fault in northern Sonora, Mexico. These two study areas bear particular resemblance to the Yucca Mountain area in that faults have long return times between surface ruptures, and faulting is closely related to volcanism. Since joining the faculty of Binghamton University in 1986, Dr. Knuepfer has studied the paleoseismicity of the Lemhi fault in Idaho with a group of students and (jointly with Woodward-Clyde Federal Services and personnel at the Idaho National Engineering Laboratory) more recently has been a team member and/or reviewer of trenching studies along the southern Lemhi and Lost River faults. This work led to Dr. Knuepfer's inclusion in an expert panel solicitation regarding earthquake hazards at the INEL, under the direction of Lawrence Livermore. Further work in Idaho, in early stages of research, focuses on the temporal relationship and possible strain partitioning between basaltic volcanic eruptions in the Eastern Snake River Plain and faulting on the Lemhi and Lost River faults. Other work on normal faulting has included unpublished studies of fault scarps in the Panamint Valley area of California, the Fairview Peak and Pleasant Valley areas of Nevada, and the Hebgen Lake area of Montana. Thus, although Dr. Knuepfer has not worked directly on paleoseismic studies in southern Nevada or near the Yucca Mountain area, he has extensive experience in paleoseismic and geomorphic analysis of active faults throughout the Basin and Range.

Dr. Knuepfer has other extensive experience in active tectonics and paleoseismic studies in California and overseas in Taiwan and New Zealand. Recent research in New Zealand has included studies of fault scarps formed during the youngest ruptures of the Alpine fault, as well as studies of terraces formed by river incision to deduce rates and styles of uplift in the Southern Alps. He and his students have been conducting similar studies in Taiwan, seeking to understand the response of rivers to rapidly uplifting mountains and how to use the river and terrace patterns to deduce uplift.

JAMES P. McCALPIN

Dr. McCalpin is President of GEO-HAZ Consulting, Inc., and is also Research Associate Professor of Geology at Utah State University and Special Graduate Faculty at the University of Colorado, Boulder. He has been performing neotectonic studies since 1976. Dr. McCalpin has developed an international reputation for trenching faults and using numerical dating techniques to reconstruct the magnitude and timing of paleoseismic events. He is currently editing the first reference book in paleoseismology ("Paleoseismology," Academic Press, 1995) along with 10 co-authors from government and academia. Between 1982 and 1992, Dr. McCalpin was the Principal Investigator on 10 research grants, funded by the U.S. Geological Survey and National Science Foundation, to decipher the Quaternary history of faulting on various large normal faults in the western U.S. During these studies, he developed (along with Dr. S.L. Forman) a technique for combined radiocarbon and thermoluminescence dating of fault-zone sediments that provides the best dating control yet achieved for many tectonic and climatic settings. His synthesis of the Holocene paleoearthquake history of the Wasatch fault zone, Utah, is the basis for the most up-to-date estimates of future earthquake probability (work with USGS collaborator S.P. Nishenko). More recently he has been an expert reviewer for seismic hazards assessments of two DOE facilities, the Rocky Flats Plant, Colorado, and Los Alamos National Laboratory, New Mexico. His current research involves statistical analysis of paleoseismic data for application to logic trees and probabilistic seismic hazard analyses, particularly with reference to normal faults and the western USA.

BIOSKETCH FOR CHRISTOPHER M. MENGES

Christopher M. Menges has worked on neotectonic problems in the Basin and Range Province of the southwestern United States for the past 20 years. Specifically, he received his undergraduate B.S. degree from the University of Washington in Seattle in 1973. He then worked from 1973 to 1974 with Woodward Clyde Associates in Satsop, Washington, on geologic investigations for a proposed nuclear power plant. Much of this work involved study of recency of faulting in the site area. From there, Menges attended the University of Arizona in a Masters program, receiving his M.S. in 1981. His thesis focused on the late Cenozoic evolution of a small Basin-Range basin in southeastern Arizona, including evidence for any Quaternary tectonic activity. While in attendance at UA, he also worked as a research assistant with Dr. W.B. Bull on the tectonic geomorphology of active faults and range fronts in southern California. Between 1980 and 1983, Menges conducted research with the Arizona Geological Survey as a Principal Investigator for a U.S. Geological Survey contract to investigate neotectonic activity in Arizona. This work involved statewide photointerpretive mapping, field investigations, and morphological analysis of Quaternary fault scarps. In 1983, Menges began a Ph.D. program at the University of New Mexico that was completed in 1988. His dissertation research centered on the tectonic geomorphology of a mountain front in the northern Rio Grande rift that included use of fault scarps to analyze the range-front fault as a seismic source. Between 1988 and 1992, he worked overseas with the U.S. Geological Survey on a groundwater resources evaluation for the United Arab Emirates. Part of this work involved neotectonic analysis of buried thrust faults. Since 1992 Menges has worked with the Yucca Mountain Project of the U.S. Geological Survey as the Principal Investigator for paleoseismic investigations of Quaternary faults in the Yucca Mountain site area in southwestern Nevada. Trenching studies are used to provide basic data for determination of paleoseismic parameters that will be applied to seismic source characterization for seismic hazard analyses. Preparation of reports summarizing these data and interpretations is currently underway.

ALAN R. RAMELLI
Research Geologist
Nevada Bureau of Mines and Geology
University of Nevada, MS 178
Reno, NV 89557-0088

Alan Ramelli has held a position as Research Geologist with the Nevada Bureau of Mines and Geology since 1986. He has been involved in research studies of active faulting and paleoseismology in the Basin and Range province and issues related to high-level nuclear waste storage since 1983. From 1983-1986, on a consulting basis, Alan conducted active-fault evaluations and reviews of environmental assessments and other documents for the Yucca Mountain, Deaf Smith, Hanford, and Davis Canyon proposed high-level nuclear waste storage sites. From 1986-1991, he conducted document reviews and original studies of the Yucca Mountain area, including planning of low-sun-angle aerial photography missions and mapping of faults and Quaternary geology, as part of studies conducted by the State of Nevada. From 1992-present, under contract to the U.S. Geological Survey, he has conducted paleoseismic studies, including exploratory trenching, of the Yucca Mountain area and has held primary responsibility for studies of the Solitario Canyon fault. Other recent projects include paleoseismic studies, including exploratory trenching, of the Carson Range fault system in western Nevada and studies of the 1994 Double Spring Flat earthquake.

Biography

Albert M. Rogers

A. M. Rogers is presently a research geophysicist with the U.S. Geological Survey in Golden, Colorado. He received a Ph. D. in Geophysics in 1970 and Bachelor of Science in 1965, both from Saint Louis University He has conducted research related to earthquake hazard assessment in Nevada, Utah, the west Texas-southern New Mexico region, and the Pacific Northwest. Dr. Rogers has conducted seismicity network studies to assess the seismic hazard to nuclear waste sites at the Waste Isolation Pilot Project in New Mexico, and at the proposed Yucca Mountain site in Nevada; he also led a study of induced seismicity at Lake Mead, Nevada. Dr. Rogers conducted a probabilistic seismic hazard assessment for DOE for the initial proposal for high-level nuclear-waste site at NTS, termed the Retrievable Surface Storage Facility. His principal research interest concerns earthquake strong-motion prediction, especially the effects of site geology on earthquake shaking levels. Dr. Rogers served as Branch Chief of the Branch of Geologic Risk Assessment from 1984 to 1988 and during that time also served as Coordinator of both the internal and external USGS Regional Earthquake Hazards Assessments Programs.

SPECIAL EXPERIENCE RELATED TO THE YUCCA MOUNTAIN AREA

Dr. D. Burton Slemmons has published numerous papers, abstracts, and edited volumes dealing with neotectonics, earthquake hazard evaluation, and paleoseismicity. While a professor at the University of Nevada-Reno, he supervised more than two dozen theses of graduate students including studies in the Yucca Mountain region, including Owens, Panamint, Saline, Death, Fish Lake, Amargosa, and Pahrump Valleys. He assisted the Lawrence Livermore National Laboratory as a consultant in making high-level nuclear waste assessments of the eleven sites considered by the U. S. Department of Energy. From 1985 to 1989, he directed the Yucca Mountain Project of the University of Nevada-Reno. He was one of the seven expert technical specialists selected by Geomatrix Consultants in the Electric Power Research Institute (EPRI) Earthquakes and Tectonics Expert Judgment Elicitation Project for the high-level waste repository at Yucca Mountain. He has consulted for Woodward-Clyde Federal Services in support of TRW from January 1992 to present on the Yucca Mountain Project, including activity as a member of the technical assessment team that prepared the report "Seismic Design Inputs for the Exploratory Studies Facility at Yucca Mountain" in 1994. During the past twenty-five years, he has also been an expert consultant for the U. S. Nuclear Regulatory Commission or industry at more than one dozen power plants in United States. Since 1984, he has been a technical expert for the International Atomic Energy Agency (IAEA) on missions to assess earthquake hazards at nuclear power plant sites in Armenia, Brazil, Croatia, and Indonesia.

KEN SMITH
Seismological Laboratory
University of Nevada, Reno

Ken Smith obtained his Ph.D. from the University of Nevada in 1991. He holds bachelors degrees in geophysics from Boise State University and in geology from Indiana University. Dr. Smith has been involved in studies of the seismotectonics of the western Basin and Range for over 10 years. During this time, he has had extensive experience in seismic network operations, portable seismic experiments, and seismic network data management for western Great Basin earthquake activity. Since 1992, these efforts have focused on evaluating the seismicity in and around the Yucca Mountain area. He was a primary author of a study of the source parameters and faulting behavior of 1992 Little Skull Mountain earthquake and of a study of recent earthquake activity in the Rock Valley fault zone. He participated in the data collection for the Little Skull Mountain earthquake, the 1993 Rock Valley earthquake sequence, and the 1993 NPE refraction experiment. Other research activities in the western Basin and Range have included determining the source parameters and complex faulting geometry of mainshock-aftershock sequences in the Mammoth Lakes, California area. Currently, he is involved in the operations and development of the digital upgrade for the southern Great Basin seismic network.

BioBib For
Robert B. Smith
Department of Geology and Geophysics
University of Utah
Salt Lake City, Utah 84112

Robert B. Smith received his B.S. and M.S. in Geology from Utah State University in 1960 and 1965 respectively. He received his Ph.D. in Geophysics from the University of Utah in 1967. He is a Professor of Geophysics in the Department of Geology and Geophysics where he has worked since 1967. He has also served as a Visiting Professor at the Swiss Federal Institute of Technology and the Cambridge University. Most recently he has taught courses in tectonophysics/elastic waves, earthquake seismology, theoretical seismology, and inverse theory. He has supervised 53 graduate students. Smith's expertise includes mechanics and processes of earthquakes, the relationship between seismicity and active tectonics, wave propagation, seismicity of the Intermountain Seismic Belt, GPS measurements of crustal deformation, numerical modeling of fault and volcano processes, and analyses of earthquake hazards. In earthquake risk , he has specifically worked on geometry and mechanics of normal faulting, scaling relations of surface fault parameters to magnitude, strong ground motion and attenuation of normal faulting earthquakes, and general seismotectonics. He has worked on seismic hazards projects in the Pacific northwest, the Basin and Range, and the Intermountain Seismic Belt. Smith has been Director and Associate Director of the University of Utah Seismograph Stations and he recently directed studies on the neotectonics of the Teton fault and paleoseismicty of the Intermountain Seismic Belt. His research and consulting work is supported by the National Science Foundation, the USGS National Earthquake Hazards Reduction and the Volcano Hazards programs, the National Park Service, as well as petroleum and mining companies. Smith has served as the President of the Seismology section of the American Geophysical Union, on the NSF Panel on Geophysics, the NSF Advisory Board in Earth Sciences, on the Advisory Committee of the Southern California Earthquake Center, on the NRC Committee on Seismology, on the Executive committee of the SSA, and was a founding member of IRIS.

Dr. Frank H. (Bert) Swan

Since 1973, Dr. Swan has participated in and directed projects for seismic hazard evaluations for critical facilities, including more than fifteen nuclear power plants, and other nuclear-related facilities. He has conducted fault studies in the eastern and western United States, Alaska, Central and South America, North Africa, the Middle East, Southeast Asia and Eastern Europe. From 1978 to 1985, Dr. Swan was the principal investigator for a series of research projects funded by the U.S. Geological Survey to investigate recurrence of moderate-to-large-magnitude earthquakes associated with past surface faulting along the Wasatch fault zone in Utah and to make a probabilistic assessment of the potential ground motion levels for selected urban areas along the Wasatch Front. From 1987 to 1993, Dr. Swan was Project Manager and principal investigator for a detailed paleoseismic investigation of the Meers fault, Oklahoma for the Research Division of the U.S. Nuclear Regulatory Commission. In 1992, he was a member of the International Atomic Energy Agency (IAEA) Geological and Seismic Hazards Safety Review Mission for the Crimea Nuclear Power Plant in the former Soviet Union. In 1993, Dr. Swan provided technical review of a probabilistic seismic hazard analysis of the Krško Nuclear Power Plant in the Republic of Slovenia. He is currently the principal investigator for studies being conducted at the Nuclear Test Site in Nevada to assess the potential for surface faulting at the proposed site for the waste-handling facilities where high level nuclear wastes will be received and packaged prior to their permanent burial in the proposed underground repository beneath Yucca Mountain.

From 1990 to 1993, Dr. Swan was a member of the Nuclear Management and Resources Council (NUMARC) Ad Hoc Advisory Committee to review and propose revisions to the U.S. Nuclear Regulatory guidelines for seismic and geological siting criteria for nuclear power plants. From 1990 to 1994, Dr. Swan was a member of the American Society of Civil Engineers (ASCE) Working Group on Dynamic Analysis and Design Considerations for High Level Nuclear Waste Repositories where he had the primary responsibility for preparing guidelines for investigations to assess the seismic potential of active faults and to assess the potential for fault rupture.

James C. Yount-Geologist, United States Geological Survey since 1975. B.S. University of Washington, 1968; M.S. University of Colorado, 1970.

Worked on delineation of seismotectonic framework of Puget Sound region, including research on liquefaction phenomena in Seattle area, and identification of youthful faults in offshore regions of Puget Sound, 1975-1983. Investigating active faulting in the Nevada Test Site area, 1983 to 1990 and 1994 to present. Studies include mapping and trench description of faulting features along the Rock Valley fault system and mapping of youthful faulting features along the Solitario Canyon fault system, the Wahmonie fault, the Mine Mountain fault, and the Cane Spring fault system. Past studies related to neotectonics include investigation of faulting along the Mohawk Valley fault system, northeast California, mapping of ground rupture following the 1979 Imperial Valley earthquake, and mapping of ground rupture following the 1980 Mammoth earthquake.

PSHA SSC Expert Teams

TEAM	EXPERT			AFFILIATION
SSC-1				
	Alan	R.	Ramelli	Nevada Bureau of Mines & Geology (U of NV-Reno)
	Walter	J.	Arabasz	University of Utah
	R.	Ernest	Anderson	U.S. Geological Survey
SSC-2				
	James	P.	McCalpin	GEO-HAZ Consulting, Inc.
	Jon	P.	Ake	U.S. Bureau of Reclamation
	David	Burton	Slemmons	Consultant (Woodward-Clyde Federal Services)
SSC-3				
	Larry	W.	Anderson	U.S. Bureau of Reclamation
	Albert	M.	Rogers	EQE International
	James	C.	Yount	U.S. Geological Survey
SSC-4				
	Peter	L. K.	Knuepfer	State University of New York at Binghamton
	Kenneth	D.	Smith	University of Nevada at Reno
	Ronald	L.	Bruhn	University of Utah
SSC-5				
	Christopher	M.	Menges	U.S. Geological Survey
	Robert	B.	Smith	University of Utah
	Craig	M.	dePolo	Nevada Bureau of Mines & Geology (U of NV-Reno)
SSC-6				
	Frank (Bert)	H.	Swan	Geomatrix Consultants
	Diane	I.	Doser	University of Texas at El Paso
	Christopher	J.	Fridrich	U.S. Geological Survey

CHAPTER 3 - SCIENTIFIC INVESTIGATION AND DESIGN CONTROL

SECTION 16 - SCIENTIFIC EXPERT ELICITATION

1. PURPOSE. This Quality Management Procedure (QMP) establishes the Yucca Mountain Project (YMP) - U.S. Geological Survey (USGS) process for elicitation of scientific expert interpretations to be used as inputs to design, site characterization, licensing, or performance assessment.

2. SCOPE OF COMPLIANCE. This procedure applies to the development of expert interpretations to be used as inputs to design, site characterization, licensing, or performance assessment. Elicitation of expert interpretations of scientific data may be used in situations wherein the available data would lend themselves to different interpretations and therefore, the combined interpretations of several experts, from somewhat different technical backgrounds, would provide a more comprehensive evaluation.

3. DEFINITIONS.

   3.1 Normative Expertise: Expertise in the statistical or mathematical principles of the response mode.

   3.2 Response Mode: The form used to ask the experts to give their interpretations. Some numeric response modes that are commonly used include probabilities, odds, intervals, ratings, logs, and pair wise comparisons. Qualitative response modes include verbal and written descriptions, classifications, categories, or preferences.

4. RESPONSIBILITIES.

   4.1 The Principal Investigator is responsible for identifying the need for using expert interpretation, for creating the project plan, and for overall management of the process.

   4.2 The Chief, Yucca Mountain Project Branch is responsible for approval of the project plan.

   4.3 The YMP-USGS Quality Assurance (QA) Manager is responsible for approval of the project plan and assignment of control numbers to expert elicitations.

   4.4 The Normative Expert is responsible for assuring that the expert elicitation is performed in a manner that does not introduce bias.

   4.5 The Methodology Team is responsible for:

   - assuring that the experts are provided equal access to available pertinent data and/or interpretations,

- organizing workshops,
- providing the scientific support needed by the experts,
- providing the facilitation and focusing the debates,
- presenting a clear definition to the expert(s) of the problem(s) to be addressed, and
- documenting the process of elicitation.

The Methodology Team Leader is also responsible for submittal of records to the Records Coordinator (see Para. 6.2).

5. PROCEDURE.

5.1 Project Plan: When the need for an expert elicitation is recognized, the Principal Investigator shall develop a project plan to address:

- project objective
- organization of the project and responsibilities of the participants,
- description of the problem to be solved (including a reference to the applicable Study Plan),
- the approach (see Para. 5.3),
- the parameters and uncertainty estimates needed from the experts,
- the selection of the team of experts (see Para. 5.2), and
- appropriate review and approval of the aggregated experts interpretations.

The project plan shall be submitted to the Chief, Yucca Mountain Project and to the YMP-USGS QA Manager for approval. Upon full approval, the QA Manager shall assign a control number for identification.

5.2 Selection of Experts: The project plan shall discuss the number of experts needed and whether they are expected to act as a team reaching consensus or whether they represent individual points of view necessary to define the range of expert interpretations. The plan shall describe the necessary education or experience required for the expert roles and how the experts will be chosen. The necessary and achievable level of independence of the experts shall be discussed. The balance between experts having site specific experience and generic experience shall be discussed. Documentation and verification of experts qualifications shall be in compliance with QMP-2.02 and QMP-2.08, and shall include a bibliography of relevant publications. Guidelines for selection of experts are:

- Individuals must have a professional reputation and recognized competence with tangible evidence provided by peer reviewed publications,
- Individuals must be willing to forsake a proponent role or a role as representative of a particular institution,
- Individuals must be open-minded,
- Individuals must be willing and able to spend the necessary time,
- The experts as a whole should represent the diversity of the scientific thought related to the issues being addressed.

5.2.1 If it becomes necessary to remove an expert after his selection and acceptance of the position, the reason for the dismissal or resignation shall be documented.

5.3 Approach:

5.3.1 A Data Needs Workshop will be conducted to explain the approach, to identify the issues, and to identify to the experts the available relevant data and data interpretations. The experts will be given the chance to request that other data be collected or finalized and made available when practical. Also, experts may contribute their own data sets, but must make them available to all other experts. All experts shall be provided equal access to the available data.

5.3.2 The experts are allowed sufficient time to develop their own initial interpretations of the data/interpretations provided. The experts may rely on software that has not been validated nor released in accordance with YMP-USGS software quality assurance (QA) requirements. Bibliographic references shall be provided for any key modelling software.

5.3.3 A preliminary input workshop shall be conducted as a forum for discussion of relevant issues and initial expert interpretations. This is an opportunity for the experts to critique each other's interpretations and readjust their own. It is a chance to challenge and evaluate each other's interpretations. At this time it is suggested that the normative expert provide each of the experts a detailed explanation of the elicitation process.

5.3.4 The preliminary expert interpretations(s) and a summary of relevant issues from the preliminary workshop shall be compiled and sent to all experts. Sufficient time shall be provided for review prior to the actual elicitation. Additional workshops will be held as required to investigate alternative interpretations.

5.3.5 The response mode used for the elicitation shall be documented with the role of the normative expert and the methodology team identified. A written record of the experts' interpretations shall be maintained. Application of the experts' interpretations (i.e., calculations made based on the interpretations) are provided immediately to him/her as feedback and a chance is given for the expert to alter his/her interpretations based on those calculations. Optionally, a feedback workshop is conducted to provide an immediate overall summary to the participants. Again, the experts may rely on software that has not been validated nor released in accordance with YMP-USGS software QA requirements. Individual or team experts' interpretations shall be authenticated by the participating experts and will be submitted to the records center as a records package which shall include a Technical Data Information Form (TDIF) (see YAP-SIII.3Q). The TDIF shall identify the source data used (by Data Tracking Number for YMP data and by references for other data) and shall include bibliographic references for key modelling software. The experts' interpretations shall be considered qualified. See QMP-3.04 for assignment of Data Tracking Numbers. The record package shall identify by YMP-USGS elicitation number that the interpretations of data were developed under this elicitation process which intrinsically provides technical review and feedback. Review and submittal under QMP-3.04 is not required. The experts' interpretations record packages shall contain sufficient detail to enable a colleague to follow the process used by the experts in reaching their interpretations. Each individual or team experts' interpretations shall contain a statement to the effect that this interpretation has not been reviewed for conformity with USGS standards. A colleague shall review the interpretation to determine if it contains sufficent detail to follow the process used in making the interpretation. The colleague shall not be one of the team of experts. The colleague shall document his/her determination. The experts' interpretations of data shall be submitted to the Geographic Nodal Information Study and Evaluation System, if appropriate (see YAP-SIII.3Q).

5.3.6 A discussion of the method used to aggregate the experts opinions and responsibility for this action shall be included in the project plan. The aggregated experts' interpretations will be submitted to the Local Records Center as a records package which shall include a Technical Data Information Form (see YAP-SIII.3Q) identifying the individual or team experts' interpretations as source data. An explanation of any changes from the methods described in the project plan will be included. The agregated experts' interpretations shall contain a statement to the effect that this interpretation has not been reviewed for conformity with USGS standards. The experts' aggregated interpretations of data shall be submitted to the Geographic Nodal Information Study and Evaluation System, if appropriate (see YAP-SIII.3Q).

5.3.7 Further use of the experts interpretations is governed by other pertinent procedures such as QMP-5.05, Scientific Notebook; and QMP-3.03, Software.

6. RECORDS MANAGEMENT.

6.1 Controlled Documents: None.

6.2 Records Center Documents: The following records shall be submitted to the Local Records Center as individual QA records by the Methodology Team Leader in accordance with QMP-17.01:

- Project plan
- Listing of available data provided to the experts
- Expert interpretations and summary of relevant issues discussed from each workshop
- Justification for dismissal or rejection of an expert after acceptance of the position

The following records shall be submitted as a QA records package to the Local Records Center by the Methodology Team Leader in accordance with QMP-17.01:

Individual or Team Expert Interpretations:

- Expert interpretations
- Technical Data Information Forms
- Statement by independent reviewer that the expert interpretations contain sufficent detail

Aggregated Expert Interpretations:

- Aggregated expert interpretations
- Discussion of method of aggregation

- Technical Data Information Form

NOTE: Personnel qualification records including bibliographic information is to be submitted as Privacy Act records under QMP-2.02 or QMP-2.08.

7. RELATED DOCUMENTS.

7.1 Superseded Documents: None.

7.2 References Cited:

- DOE/YMP YAP-SIII.2Q, Technical Information Flow to and From the Yucca Mountain Site Characterization Project Technical Data Base
- DOE/YMP YAP-SIII.3Q, Control and Transfer of Technical Data on the Yucca Mountain Site Characterization Project
- YMP-USGS-QMP-2.02, Federal Personnel Qualification
- YMP-USGS-QMP-2.08, Non-Federal Contractor Personnel Qualification
- YMP-USGS-QMP-3.03, Software
- YMP-USGS-QMP-3.04, Review and Approval of YMP-USGS Data, Interpretations of Data, and Manuscripts
- YMP-USGS-QMP-5.05, Scientific Notebooks
- YMP-USGS-QMP-17.01, YMP-USGS Records Management for Record Sources

8. ATTACHMENTS. None.

9. APPROVALS AND EFFECTIVE DATE.

EFFECTIVE DATE: 10/28/96

YMP-USGS Quality Assurance Manager	9/25/96 Date
Robert W. Craig Chief, Yucca Mountain Project Branch	9/26/96 Date
Assistant Chief Hydrologist for Technical Support	9/30/96 Date
Director, U.S. Geological Survey	10/2/96 Date

10. HISTORY OF CHANGES.

Revision/ Modification No.	Effective Date	Description of Changes
R0	10/28/96	Initial Issue.

9610250056-01

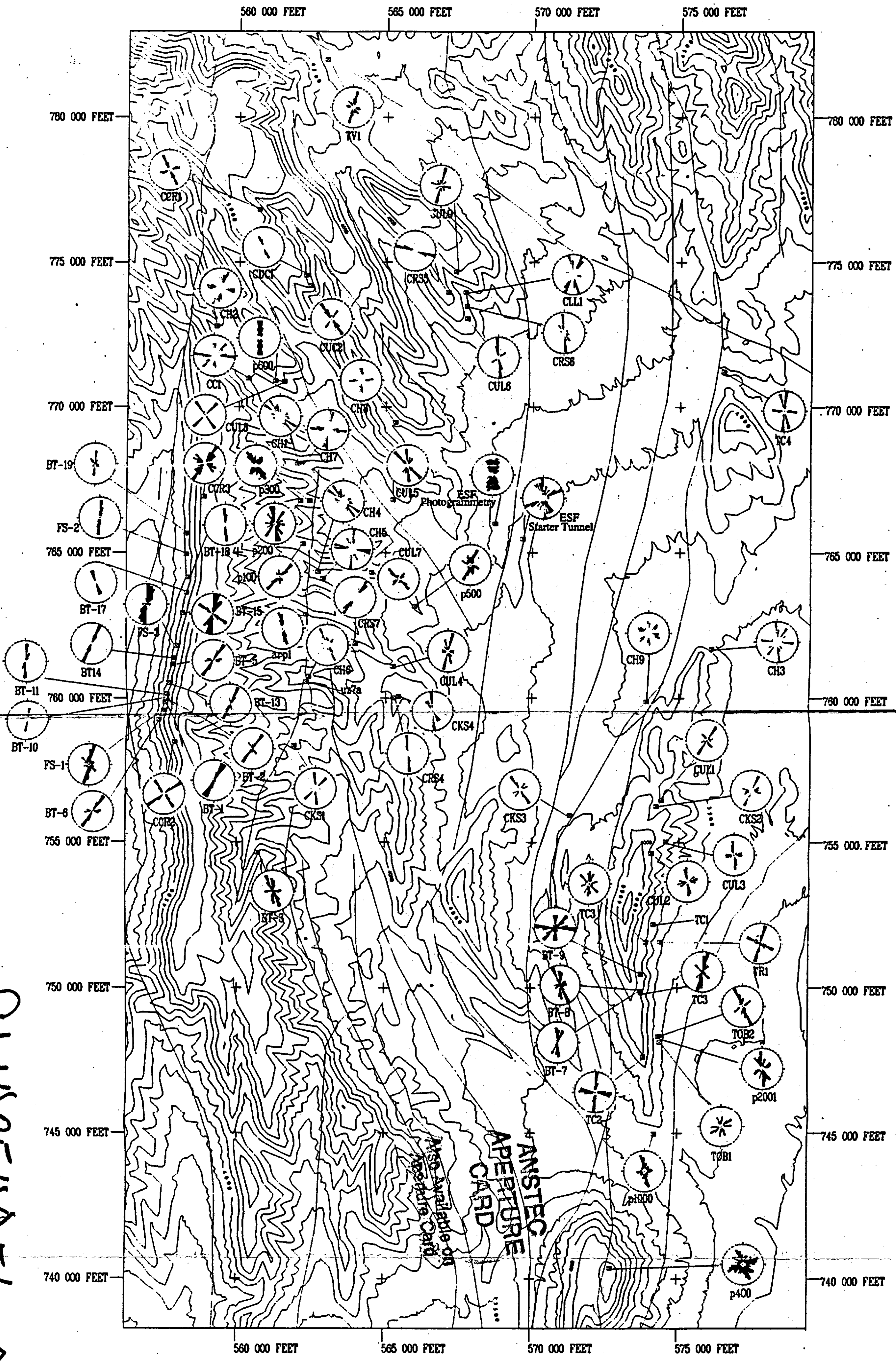

Figure 29.

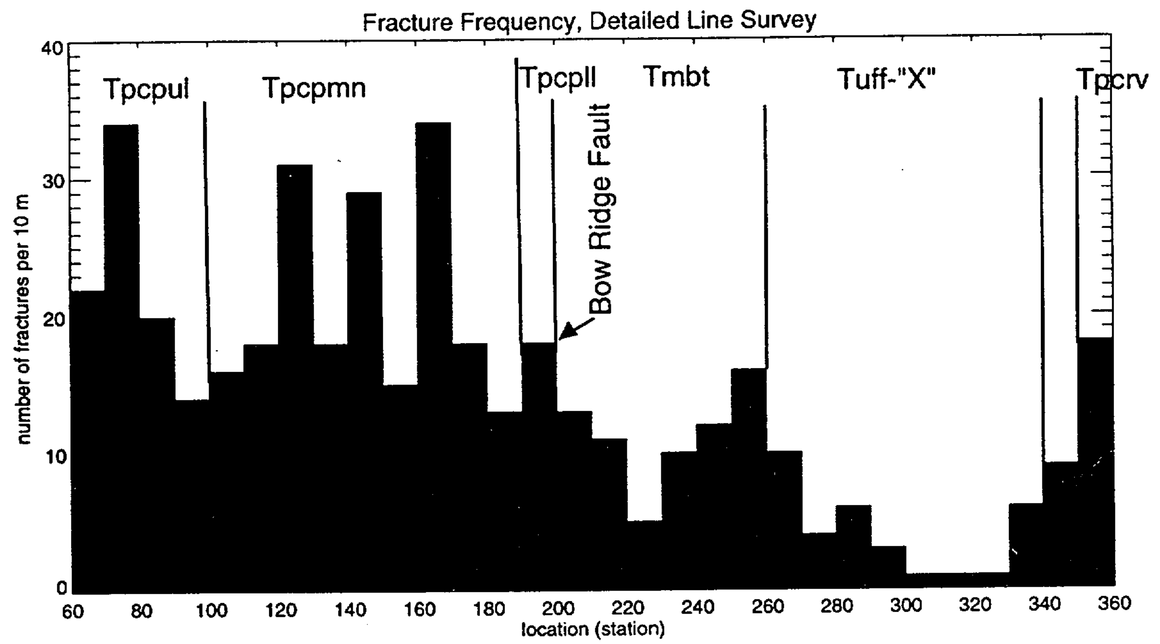
Fracture Frequency, Detailed Line Survey
number of fractures per 10 m
location (station)
Tpcpul
Tpcpmn
Tpcpll
Tmbt
Tuff-"X"
Tpcrv
Bow Ridge Fault
0
10
20
30
40
60
80
100
120
140
160
180
200
220
240
260
280
300
320
340
360

A

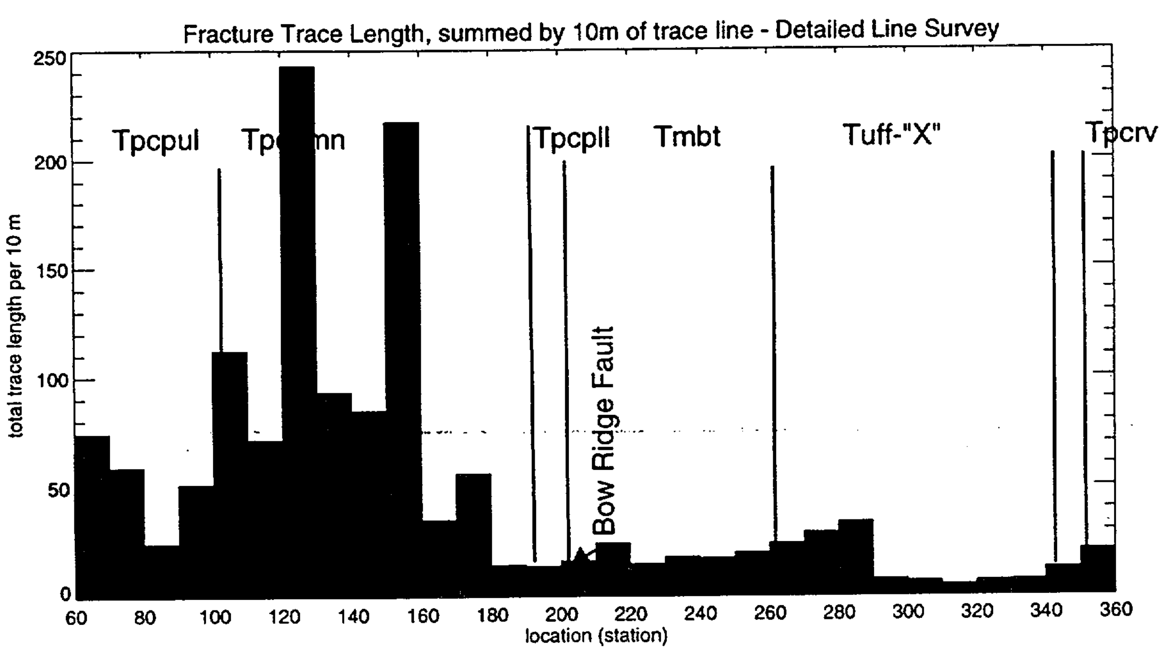
Fracture Trace Length, summed by 10m of trace line - Detailed Line Survey
total trace length per 10 m
location (station)
Tpcpul
Tpcpll
Tmbt
Tuff-"X"
Tpcrv
Bow Ridge Fault
0
50
100
150
200
250
60
80
100
120
140
160
180
200
220
240
260
280
300
320
340
360

B

Figure 30